NASA/CP—1999-208695

Ninth Thermal and Fluids Analysis Workshop Proceedings

November 1999

The NASA STI Program Office . . . in Profile

Since its founding, NASA has been dedicated to the advancement of aeronautics and space science. The NASA Scientific and Technical Information (STI) Program Office plays a key part in helping NASA maintain this important role.

The NASA STI Program Office is operated by Langley Research Center, the Lead Center for NASA's scientific and technical information. The NASA STI Program Office provides access to the NASA STI Database, the largest collection of aeronautical and space science STI in the world. The Program Office is also NASA's institutional mechanism for disseminating the results of its research and development activities. These results are published by NASA in the NASA STI Report Series, which includes the following report types:

- TECHNICAL PUBLICATION. Reports of completed research or a major significant phase of research that present the results of NASA programs and include extensive data or theoretical analysis. Includes compilations of significant scientific and technical data and information deemed to be of continuing reference value. NASA's counterpart of peer-reviewed formal professional papers but has less stringent limitations on manuscript length and extent of graphic presentations.

- TECHNICAL MEMORANDUM. Scientific and technical findings that are preliminary or of specialized interest, e.g., quick release reports, working papers, and bibliographies that contain minimal annotation. Does not contain extensive analysis.

- CONTRACTOR REPORT. Scientific and technical findings by NASA-sponsored contractors and grantees.

- CONFERENCE PUBLICATION. Collected papers from scientific and technical conferences, symposia, seminars, or other meetings sponsored or cosponsored by NASA.

- SPECIAL PUBLICATION. Scientific, technical, or historical information from NASA programs, projects, and missions, often concerned with subjects having substantial public interest.

- TECHNICAL TRANSLATION. English-language translations of foreign scientific and technical material pertinent to NASA's mission.

Specialized services that complement the STI Program Office's diverse offerings include creating custom thesauri, building customized data bases, organizing and publishing research results . . . even providing videos.

For more information about the NASA STI Program Office, see the following:

- Access the NASA STI Program Home Page at ***http://www.sti.nasa.gov***

- E-mail your question via the Internet to help@sti.nasa.gov

- Fax your question to the NASA Access Help Desk at (301) 621-0134

- Telephone the NASA Access Help Desk at (301) 621-0390

- Write to:
  NASA Access Help Desk
  NASA Center for AeroSpace Information
  7121 Standard Drive
  Hanover, MD 21076

NASA/CP—1999-208695

Ninth Thermal and Fluids Analysis Workshop Proceedings

Proceedings of a conference held at and sponsored by
NASA Glenn Research Center
Cleveland, Ohio
August 31—September 4, 1998

National Aeronautics and
Space Administration

Glenn Research Center

November 1999

Trade names or manufacturers' names are used in this report for identification only. This usage does not constitute an official endorsement, either expressed or implied, by the National Aeronautics and Space Administration.

This report is a preprint of a paper intended for presentation at a conference. Because of changes that may be made before formal publication, this preprint is made available with the understanding that it will not be cited or reproduced without the permission of the author.

Available from

NASA Center for Aerospace Information
7121 Standard Drive
Hanover, MD 21076
Price Code: A13

National Technical Information Service
5285 Port Royal Road
Springfield, VA 22100
Price Code: A13

TABLE OF CONTENTS

OVERVIEW
STEP—Progress, Status, & Impact
Eric Lebegue, Espri Concept, and Georg Siebes, Jet Propulsion Laboratory 1
STEP—TAS & STEP-NRF
Eric Lebegue, Espri Concept, and Georg Siebes, Jet Propulsion Laboratory 11
STEP—TAS Demonstrations
Eric Lebegue, Espri Concept, and Georg Siebes, Jet Propulsion Laboratory 23

EFFICIENT INTEGRATION OF CFD INTO PRODUCT DESIGN
Vedat Akdag, Al Magnuson, and Armin Wulf, ICEM CFD Engineering 27

COMPARISON OF INTEGRATED ANALYSIS METHODS FOR TWO MODEL SCENARIOS
Ruth M. Amundsen, NASA Langley 37

COMPARATIVE ANALYSIS BETWEEN NEVADA AND TSS USING A JET ENGINE EXHAUST NOZZLE TEST RIG
Joseph F. Baumeister and James R. Yuko, NASA Lewis 49

TWO-PHASE CENTRAL THERMAL CONTROL SYSTEM (TPS) OF INTERNATIONAL SPACE STATION «ALPHA» RUSSIAN SEGMENT
Y.I. Grigoriev, V.M. Cykhotsky, A.N. Sementsov, and Y.M. Prokhorov, Rocket-Space Corporation "ENERGIA," and G.A. Gorgenko and C.A. Malukhin, Center of Technical Physics of Kharkov Aviation Institute 69

THERMAL CONTROL OF A 195 KELVIN IR DETECTOR ON A SMALL LOW-EARTH ORBIT SATELLITE
H.Craig Heffner and George Firstbrook, Northrop Grumman Corporation 81

THERMAL ANALYSIS OF THE X-38 AFT FIN DURING RE-ENTRY
Andrew E. Hong, NASA Johnson 91

CONCEPT OF THE LOCAL THERMO-CHEMICAL SIMULATION FOR RE-ENTRY PROBLEM: VALIDATION & APPLICATIONS
Anatoliy F. Kolesnikov, The Institute for Problems in Mechanics in Russian Academy of Sciences 107

A STOCHASTIC APPROACH TO SPACECRAFTS THERMAL ANALYSIS
Felix Lamela Herrera, Construcciones Aeronauticas S.A., and Ana Laveron Simavilla, Instituto Universitario "Ignacio da Riva" 117

THERMAL MANAGEMENT OF AERO AND SPACE ELECTRONIC BOARDS
Greg Lazzaro, Dynamic Soft Analysis, Inc., and Tom Andrikowich, AlliedSignal Aerospace 131

MULTI-DISCIPLINARY ANALYSIS IN ENGINE DESIGN
Kamel G. Mahmoud and Andreas Ennemoser, AVL-LIST GmbH 139

THERMAL ANALYSIS AND DESIGN OF A PHASED ARRAY ANTENNA
James E. Marthinuss, Jr., Northrop Grumman Corporation 153

INTEGRATED MODELING TOOLS FOR THERMAL ANALYSIS AND APPLICATIONS
Mark H. Milman, Laura Needels, and Miltiadis Papalexandris, Jet Propulsion Laboratory 167

CATALYTIC EFFECTS OF HEAT SHIELD MATERIALS IN DISSOCIATED AIR
Masahito Mizuno and Yoshiki Morino, National Space Development Agency of Japan (NASDA), Yasuo Watanabe, National Aerospace Laboratory (NAL) 181

A CONCURRENT DESIGN ENVIRONMENT FOR DESIGNING SPACE INSTRUMENTS
Knut I. Oxnevad, Jet Propulsion Laboratory 205

TRUE CONCURRENT THERMAL ENGINEERING INTEGRATING CAD MODEL BUILDING WITH FINITE ELEMENT AND FINITE DIFFERENCE METHODS
Tim Panczak, Steve Ring, and Mark Welch, Cullimore and Ring Technologies 217

MODELING OF A DEPLOYABLE RADIATOR/LOOP HEAT PIPE SYSTEM
Michelle L. Parker and Bruce L. Drolen, Hughes Space and Communications, and P.S. Ayyaswamy, The University of Pennsylvania 233

INTEGRATING THERMAL TOOLS INTO THE MECHANICAL DESIGN PROCESS
Glenn T. Tsuyuki, Georg Siebes, Keith S. Novak, and Gary M. Kinsella, California Institute of Technology, Jet Propulsion Laboratory 239

NUMERICAL THERMAL MODEL OF A 30-CM NSTAR ION THRUSTER
Jon Van Noord and Alec Gallimore, University of Michigan, and Vincent K. Rawlin, NASA Lewis 251

A SHORT HISTORY AND A BRIGHT FUTURE FOR OPTO-MECHANICAL INTERFACE
Timothy D. Wise, Opto-Mech Interface Organization 263

Overview

STEP - Progress, Status, & Impact

Eric Lebegue
Espri Concept
Sophia-Entipolis, France

(Eric.Lebegue@esprico.fr)

Georg Siebes
Jet Propulsion Laboratory
Pasadena, California

Overview

This presentation has three parts

- About STEP
- STEP-TAS & STEP-NRF
- Demo

It is intended to be informal and we encourage questions

About STEP - Purpose and Name

- STEP purpose: To break down barriers to data exchange
- STEP name: ***STandard for the Exchange of Product model data***

About STEP - Objective

"STEP is an international standard, which provides an unambiguous, computer-interpretable definition of the physical and functional characteristics of a product throughout its life cycle."

Concept
Design
ISO 10303
Fabricate
Assemble
Test/Deliver
Support/Retire

About STEP - Business Environment

- Defense budgets continuing to decline
- Aerospace industry consolidating at all levels
- Auto industry under cost and time to market pressures
- Electronics industry becoming more competitive
- Supplier chain becoming a critical component of the business environment

About Step - Enabling

STEP enables:

- consistent and timely data sharing
- complete and accurate data exchange
- reuse of design, planning, and manufacturing data

About STEP - Roadmap

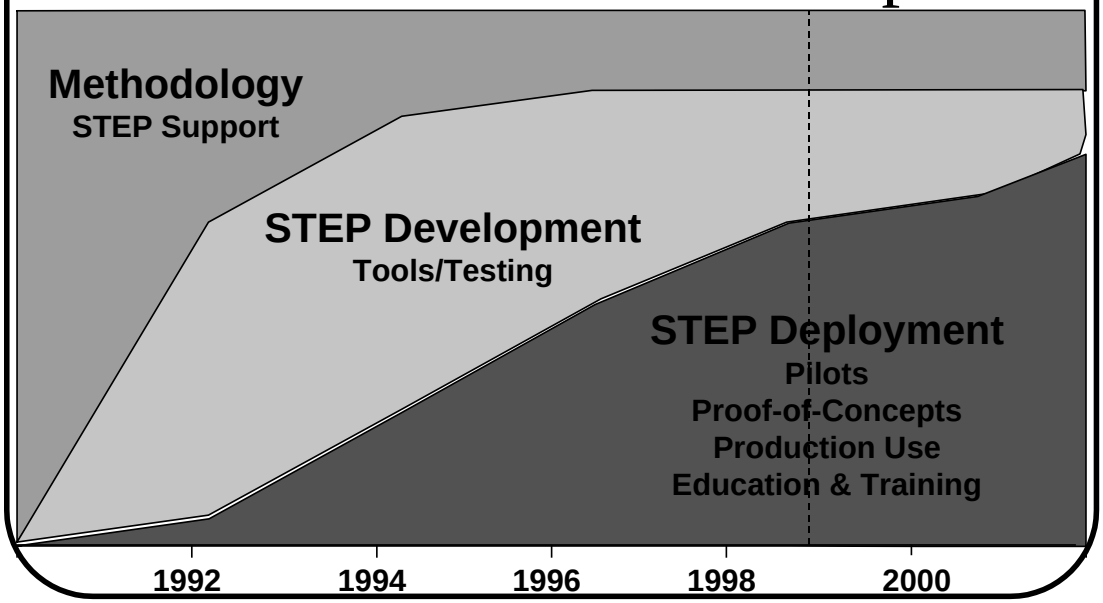

About Step - Characteristics

- STEP incorporates meaning of data into data structure
- STEP is shareable and extensible
- STEP provides a formal and computer sensible data modeling language
- STEP utilizes a development process that includes subject area experts

About STEP - Features

- **STEP is software-technology-independent**
  - **STEP representation of models is the "lingua-franca" for CAx tools**
  - **Use of STEP as standard data format allows CAx tool technology to evolve while retaining model information in a neutral data structure**
- **STEP is driven by CAx tool *users***
  - **Developed by major OEM's and NIST with help from tool vendors**
  - **Leading developers/users include major aerospace, automotive, shipbuilding, and manufacturing companies**
- **STEP spans CAx disciplines: MCAD, ECAD, CAE**
  - **STEP is the *only* standard that spans all engineering disciplines**
  - **Using its comprehensive models and mapping technology, STEP can be used to integrate heterogeneous data -- e.g.:**
    IGES, TCON/FEMAP, EDIF, IDF, VHDL, SPICE, IPC, Gerber, GENCAM, etc.

About STEP - original target

- Initially targeted at structural design and fabrication
  - Geometry, Tolerances, Features
  - Bill of materials: material, process specification, part identification, notes

About Step - Expansion

- Now expanding to: engineering analysis, electrical design, functionality …
- Multi-sector: aeronautics, aerospace, automotive, processing, shipbuilding, construction
- Organizations: PDES Inc (predominantly US), ProStep, GOSET, and Italian STEP center (Europe), JSTEP (Japan), also Australia, Canada, and China

About STEP - Architecture

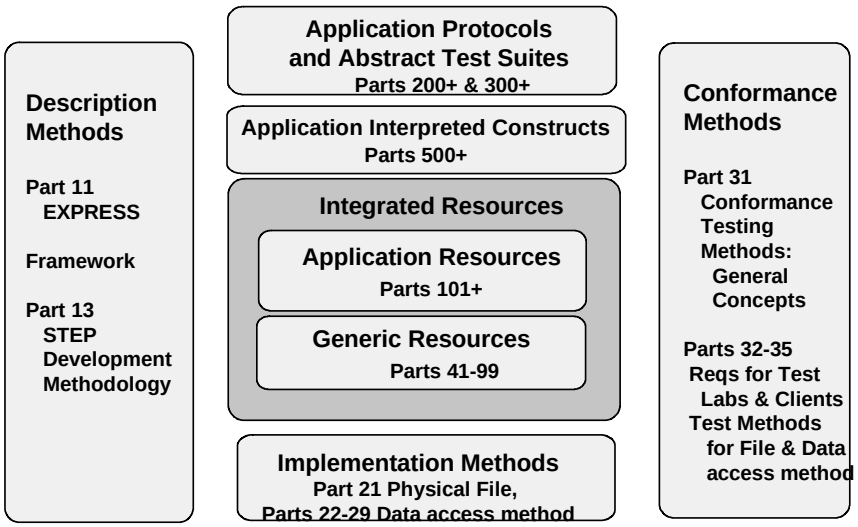

About STEP - EXPRESS

- Declarative object-like, Pascal-like, information modeling language
- Used to specify data semantics and structure for Data Architecture and other STEP specifications
- Entities, Types, Rules and Functions are basic constructs of EXPRESS
- Logical collections of data constructs are partitioned into Schemas
- Formal syntax permits automated processing of EXPRESS models

About STEP - Application Protocols

- AP201: Explicit Drafting
- AP 202: Associative Drafting
- AP 203: Configuration Controlled 3D Designs of Mechanical Parts and Assemblies
- AP204: Mechanical Design using boundary representation
- AP205: Mechanical Design using Surface Representation
- AP 207: Sheet Metal Die Planning and Design
- AP 208:Life Cycle Product Change Process
- AP209: Composite & Metallic Analysis & Related Design
- AP 210: Electronic Assembly, Interconnect and Packaging Design
- AP 212: Electromechanical Design and Installation
- AP 213: Numerical Control (NC) Process Plans for Machined Parts
- AP214: Core Data for Automotive Mechanical Design Processes

About STEP - Application Protocols

- AP 215-218: Ship Arrangement, Molded Forms, Piping, Structures
- AP 220 PCA Process Planning
- AP 221: Functional Data and their Schematic Representation for Process Plant
- AP222: Design to Manufacturing for Composite Structures
- AP 223: Exchange of Design and Manufacturing Product Information for Cast Parts
- AP224 Mechanical Product Definition for Process Planning Using Machining Features
- AP 225 : Building Elements Using Explicit Shape Representation
- AP 226: Ship Mechanical Systems
- AP 227: Plant Spatial Configuration
- AP 231: Process Design and Process Specifications of Major Equipment
- AP 232: Technical Data Packaging Core Information and Exchange
- AP 233: Systems Engineering

About Step - Maturity

Examples of production use:

- LMA Joint Strike Fighter, F-16, F-22
- Boeing C-17, 777, 767-400, cooperating with RR, Pratt & Whitney, and GE
- General Motors
- Ford
- Delco Electronics

Part 2

Now we look at “thermal” STEP:

– STEP-TAS

– STEP-NRF

Appendix - References

- Useful historical and business view at: ***http://www.ukcic.org/step/stpgolb1.htm***
- The one-page summary at: ***http://www.mel.nist.gov/sc5/soap/***
- US National Institute of Standards and Technology ***(NIST): http://www.nist.gov/sc4/***

Appendix - References

- PDESinc: International consortium promoting STEP: ***http://www.scra.org/pdesinc.html***
- ProSTEP: European focus for STEP in automotive industry: ***http://www.prostep.darmstadt.gmd.de/***
- The Product Data Technology Advisory Group: ESPRIT focus for STEP: ***http://www.cadlab.tu-berlin.de/~PDTAG/***

Appendix - References

- NASA STEP Central

  http://misspiggy.gsfc.nasa.gov/step
- ESPRI CONCEPT STEP-TAS

  http://cyclone.ceram.fr/step-tas/
- CAD translation service at:

  http://www.steptools.com/

Overview

STEP - TAS & STEP-NRF

Thermal Analysis Data Exchange In the European Space Industry

Eric Lebegue
Espri Concept
Sophia-Entipolis, France

(Eric.Lebegue@esprico.fr)

Georg Siebes
Jet Propulsion Laboratory
Pasadena, California

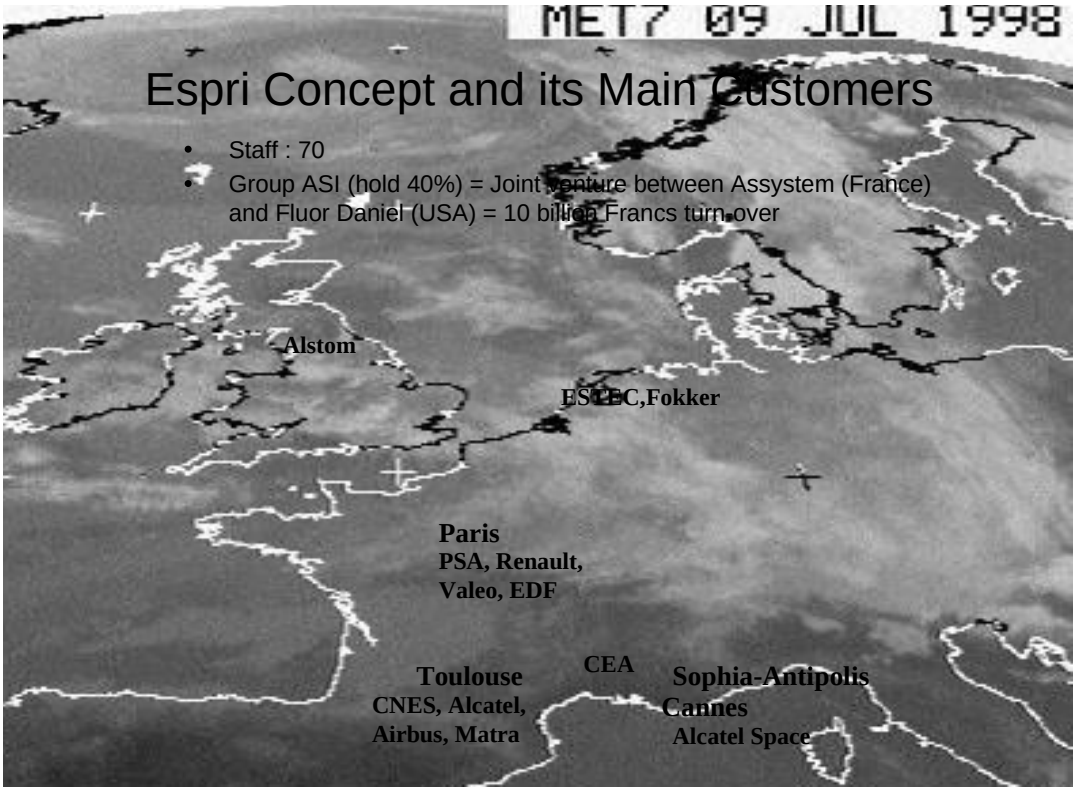

Espri Concept Share Holder

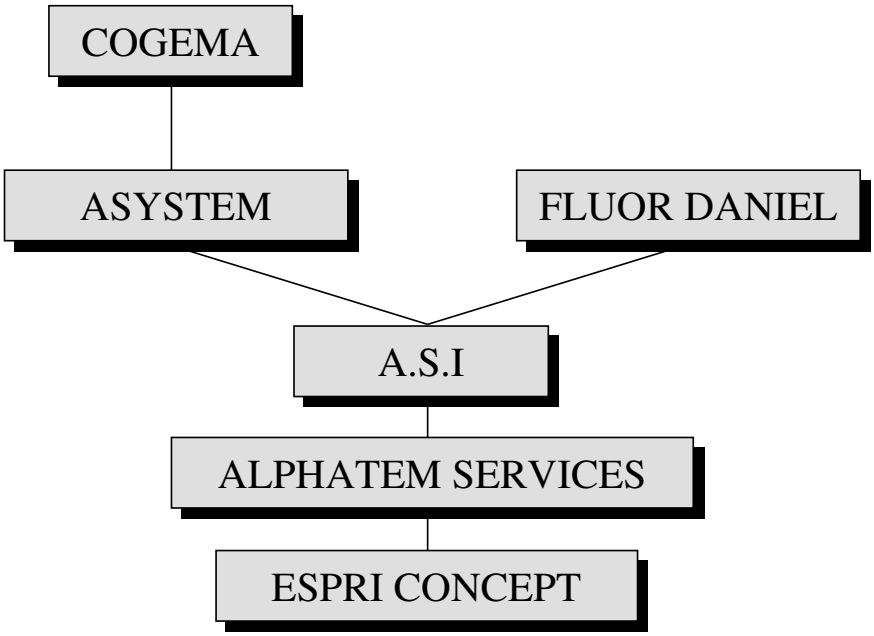

ASYSTEM SERVICES INTERNATIONAL

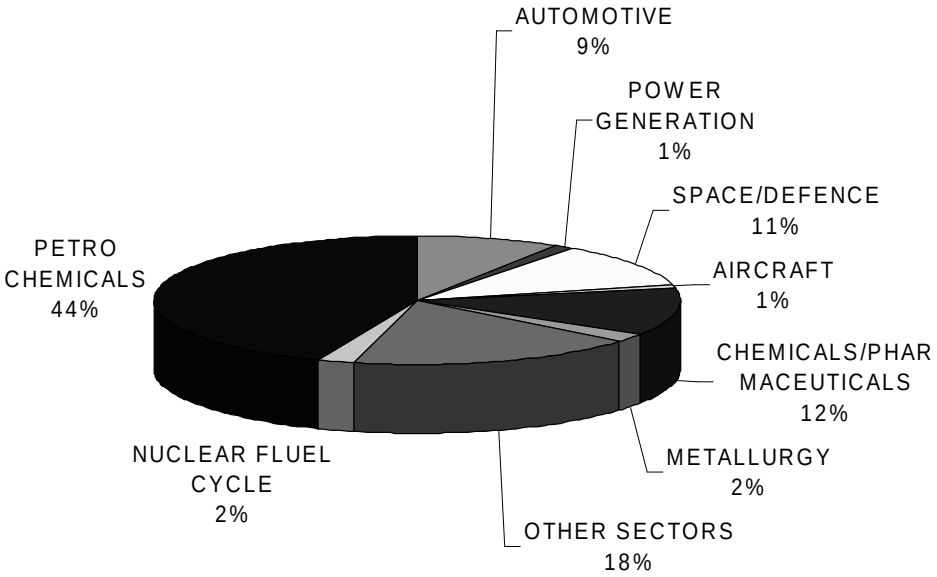

Yesterday situation in European space thermal analysis data exchange

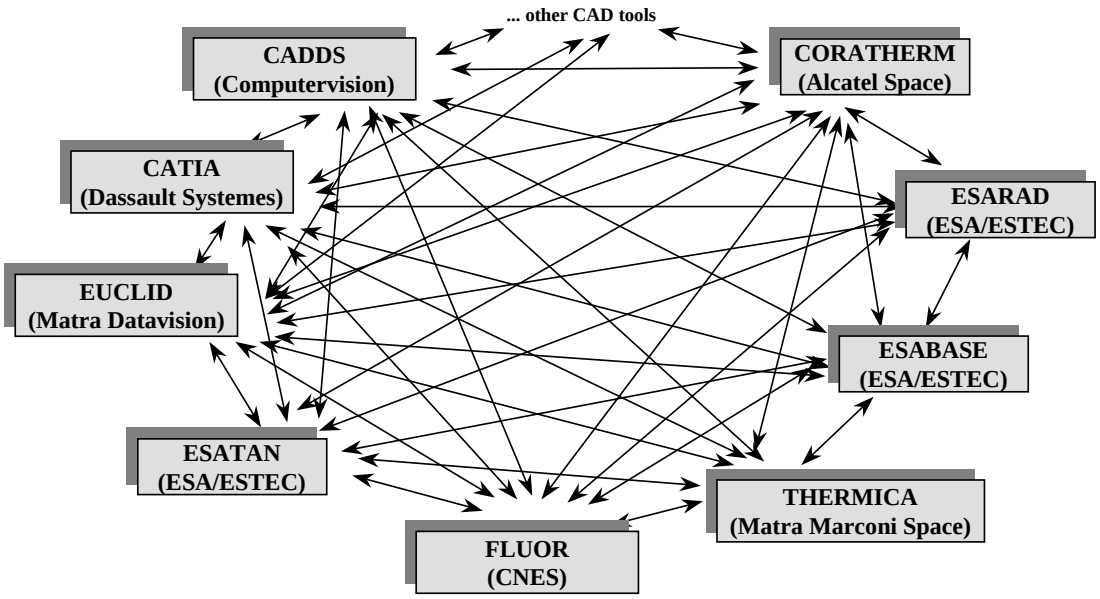

Today : a beginning of solution with SET (French Standard)

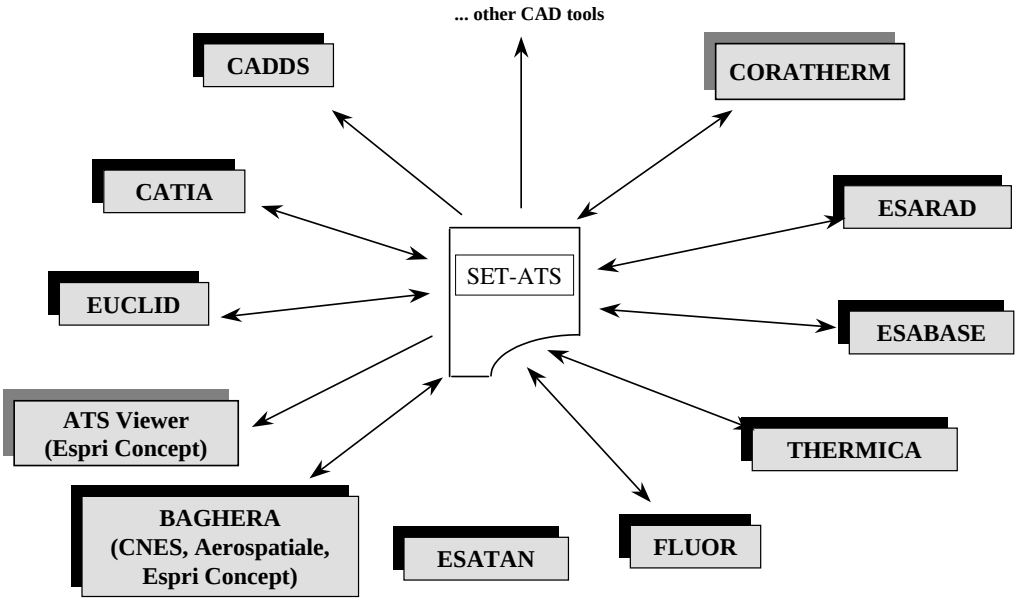

Tomorrow : more exchange with STEP (International Standard)

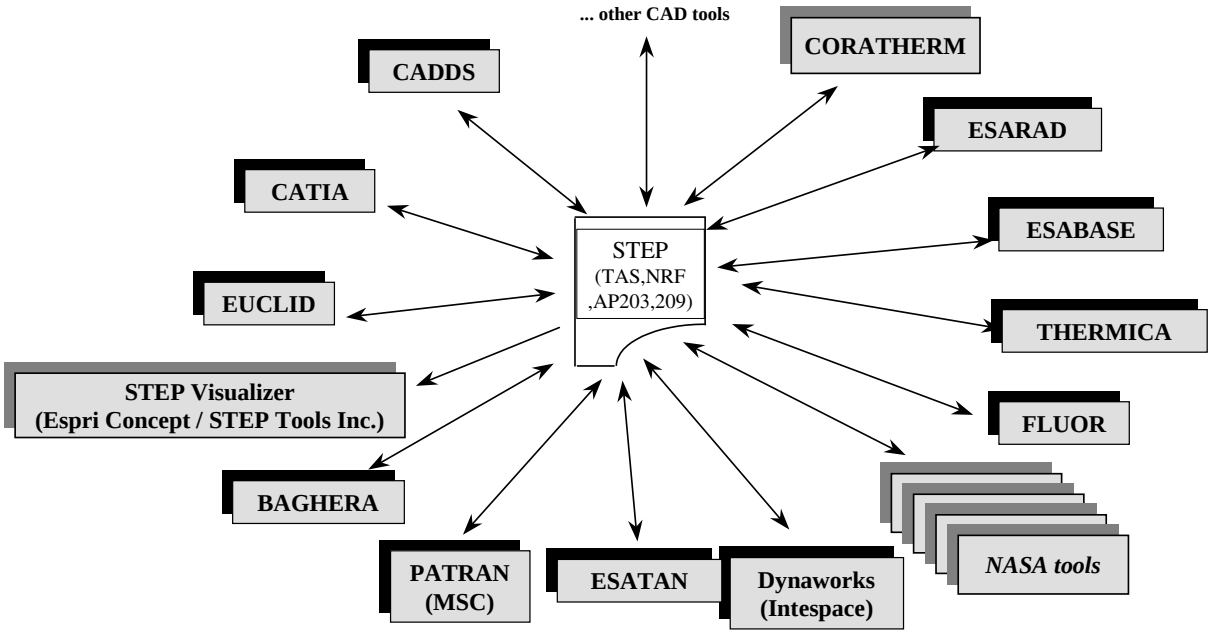

After tomorrow : data integration around database(s)

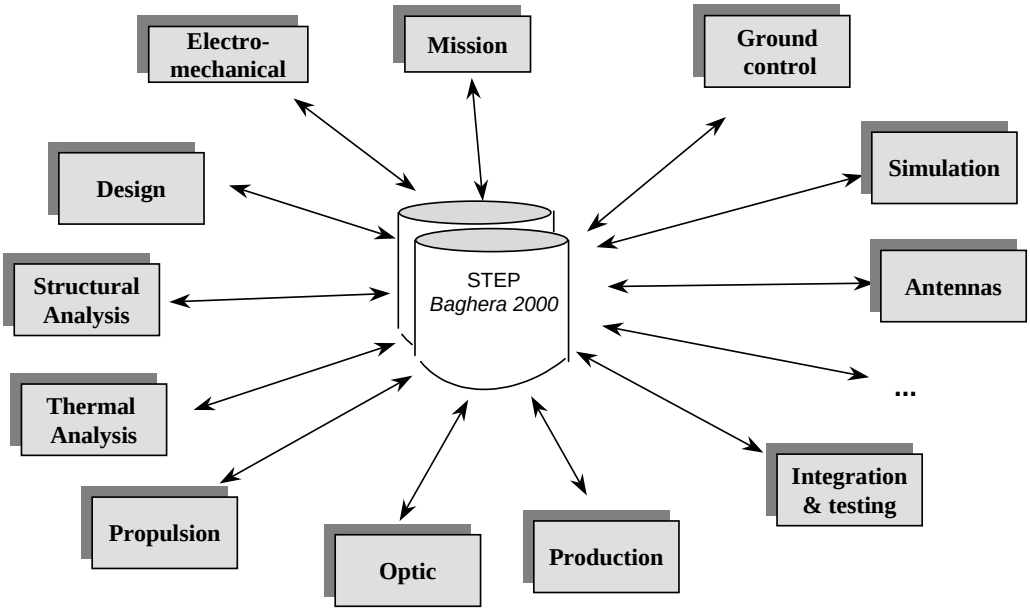

STEP : a complete technology

- **An ISO standard (10303) distributed in parts**

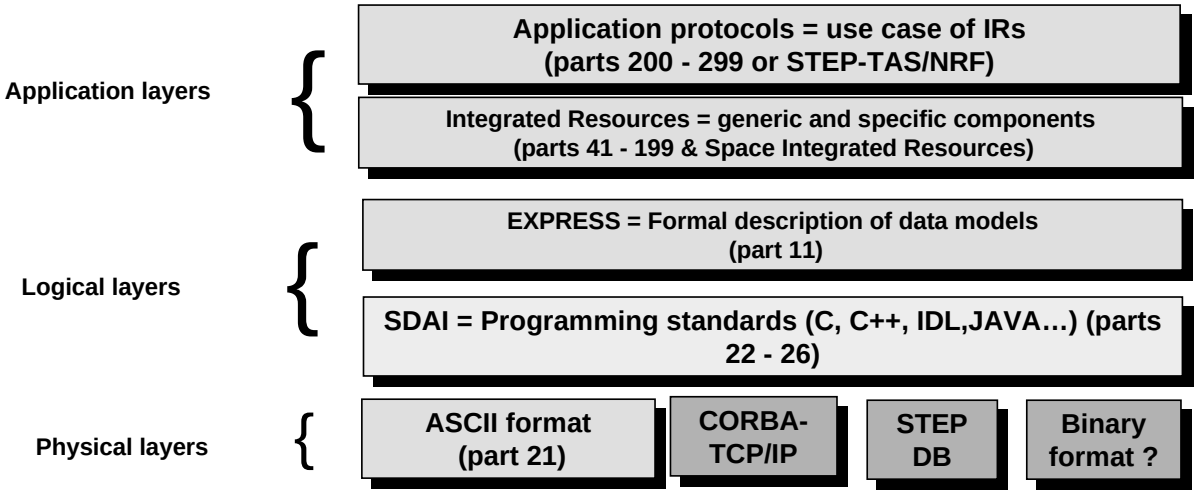

STEP is also a methodology...

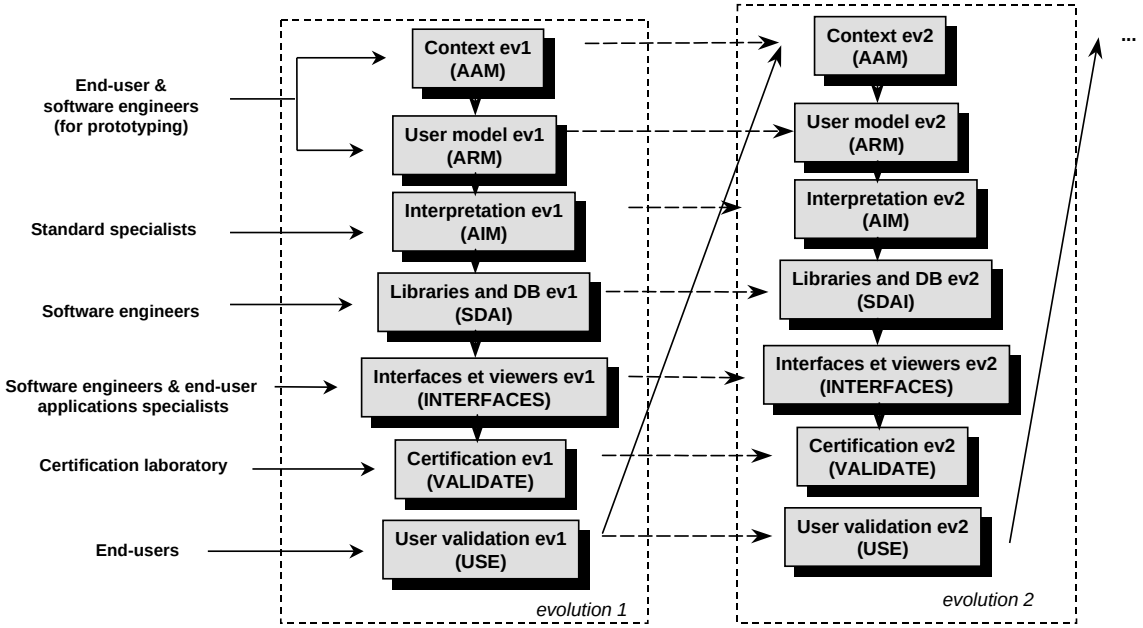

… and associated Tools

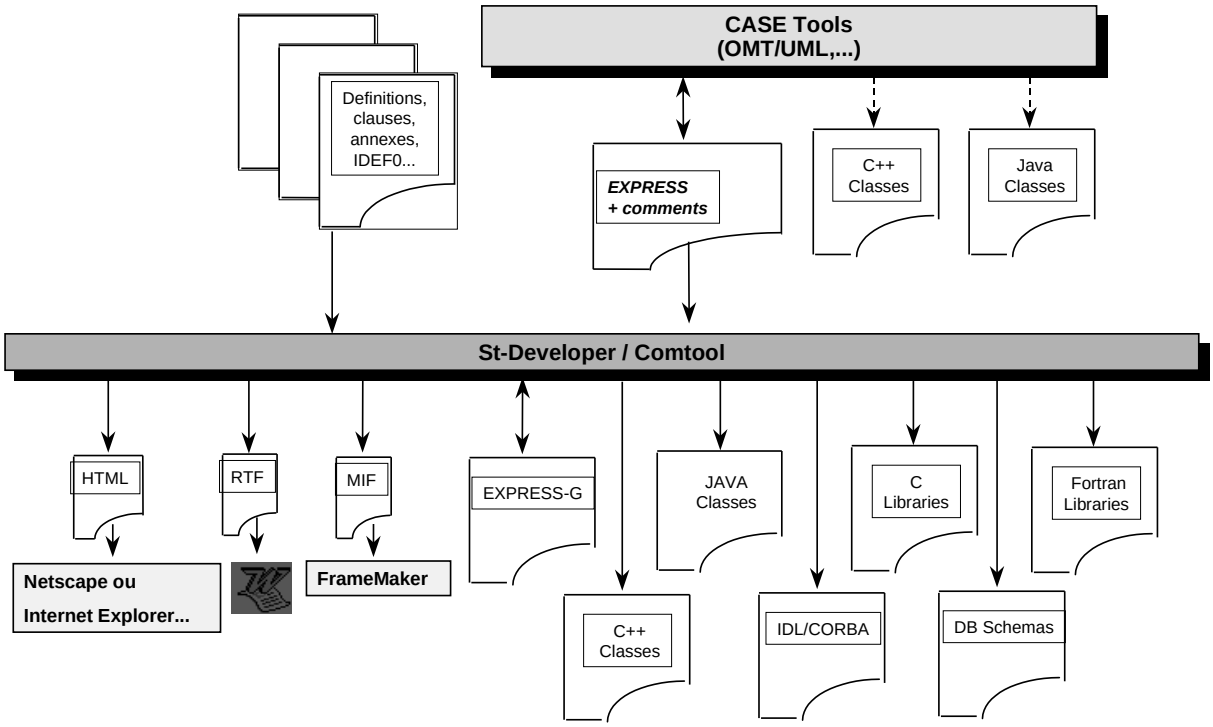

The choice of ESA and CNES

- Adoption of ISO STEP standards :
  - AP203 : CAD
  - AP209 : structural analysis
- Development of extensions for Spacecraft engineering
  - STEP-TAS : Thermal Analysis
  - STEP-NRF : Network based analysis model Results
  - Fluid network for Propulsion
  - Space configuration management
  - Mass & inertia budget

The Spacecraft STEP extensions development consortium

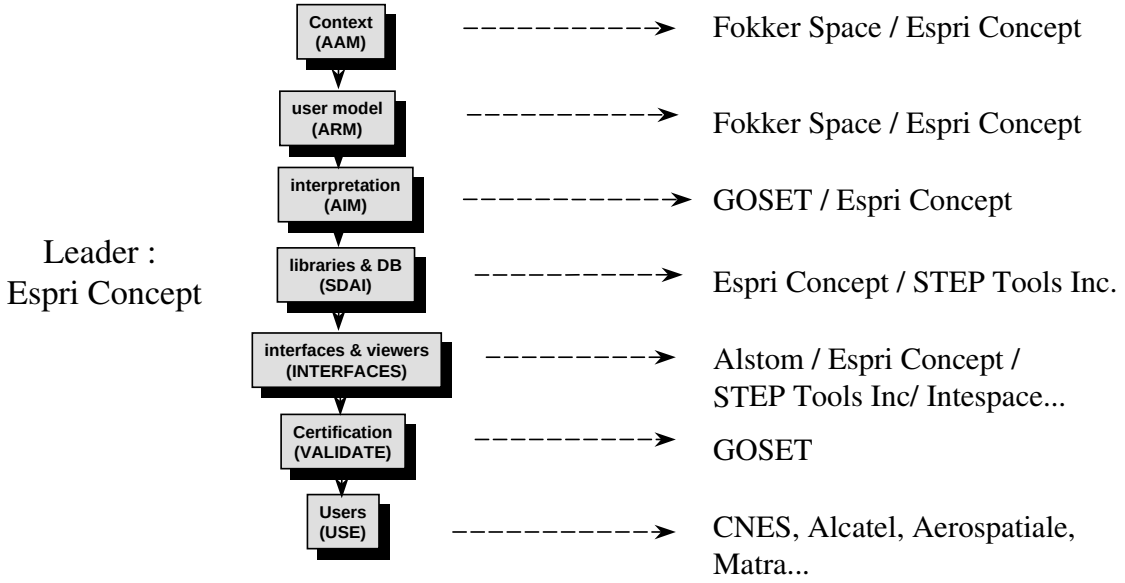

STEP-TAS : End-user geometry & orbits

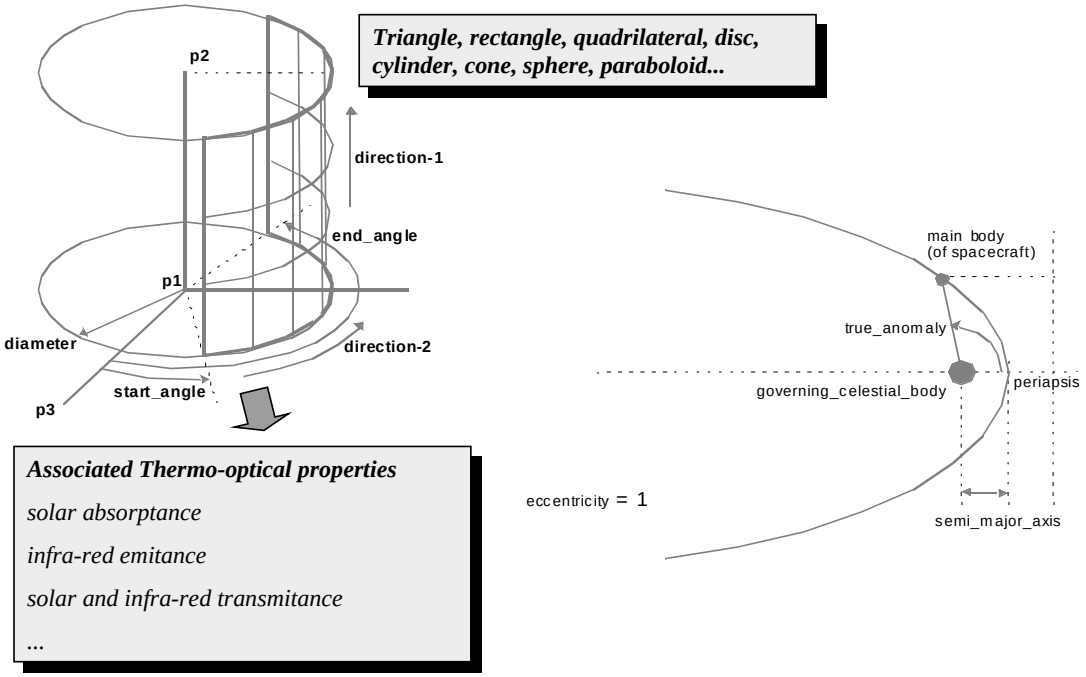

STEP-TAS : Product structure and kinematic

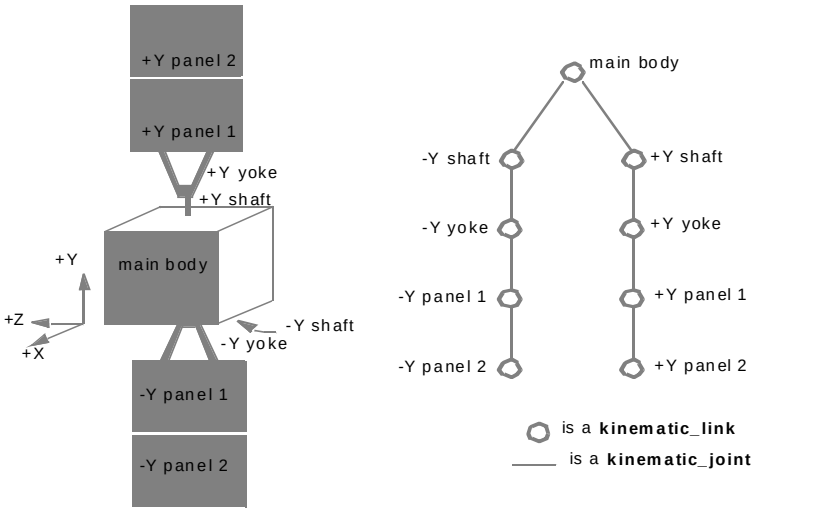

(a) Schematic shape model of a typical communications satellite with two fully deployed solar array wings

(b) The corresponding **kinematic_model** presented as a topological graph

STEP-NRF

Definition and results of Analysis, Test and Operation using Network Models

- ☛ Discipline generic
- Campaign
- Phases
- Cases
- Runs
- Nodes & nodes relationship
- Properties
- ☛ Future : HDF binary format

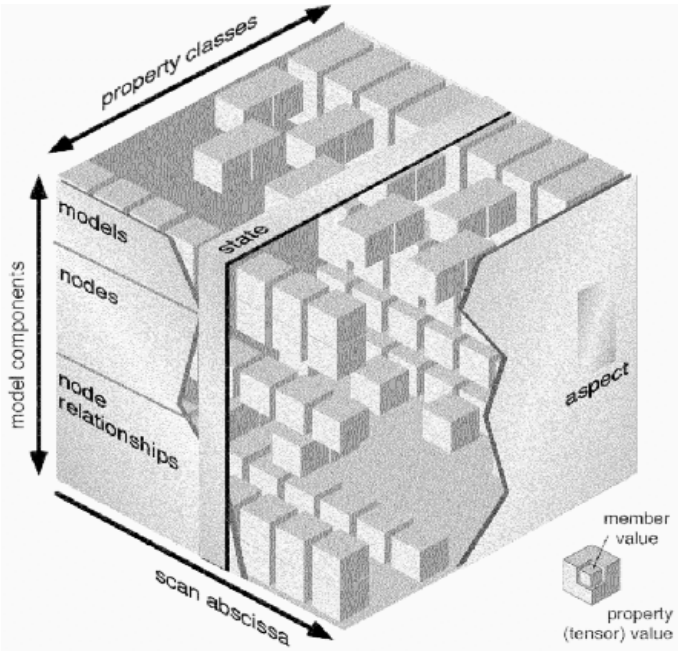

Editorial architecture

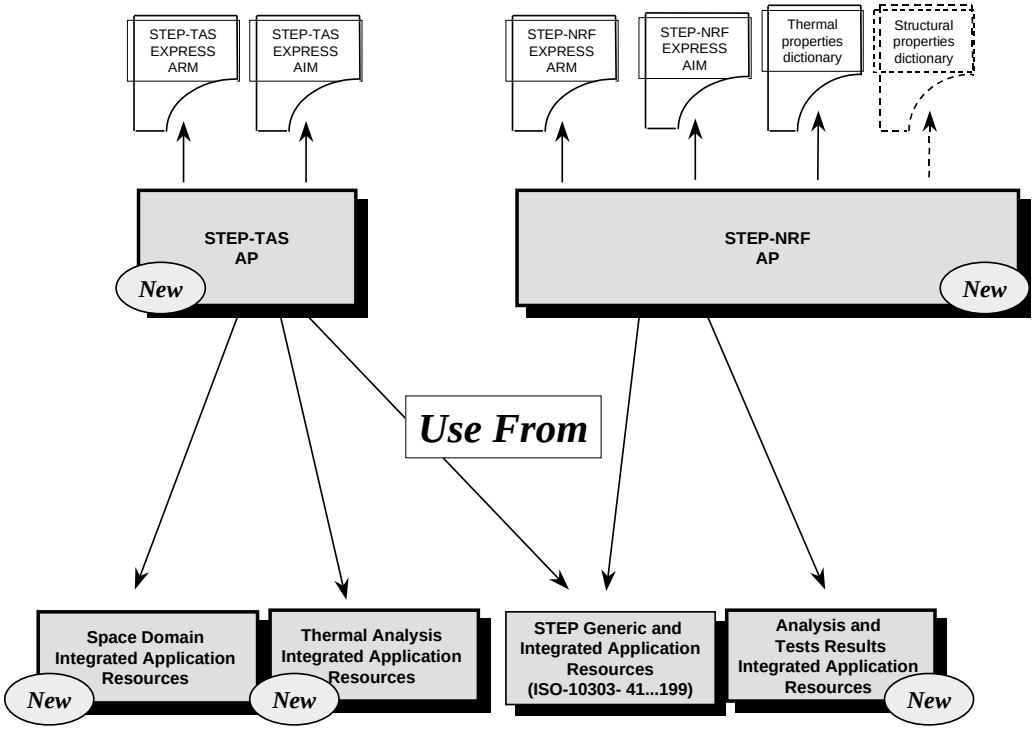

High Level Libraries

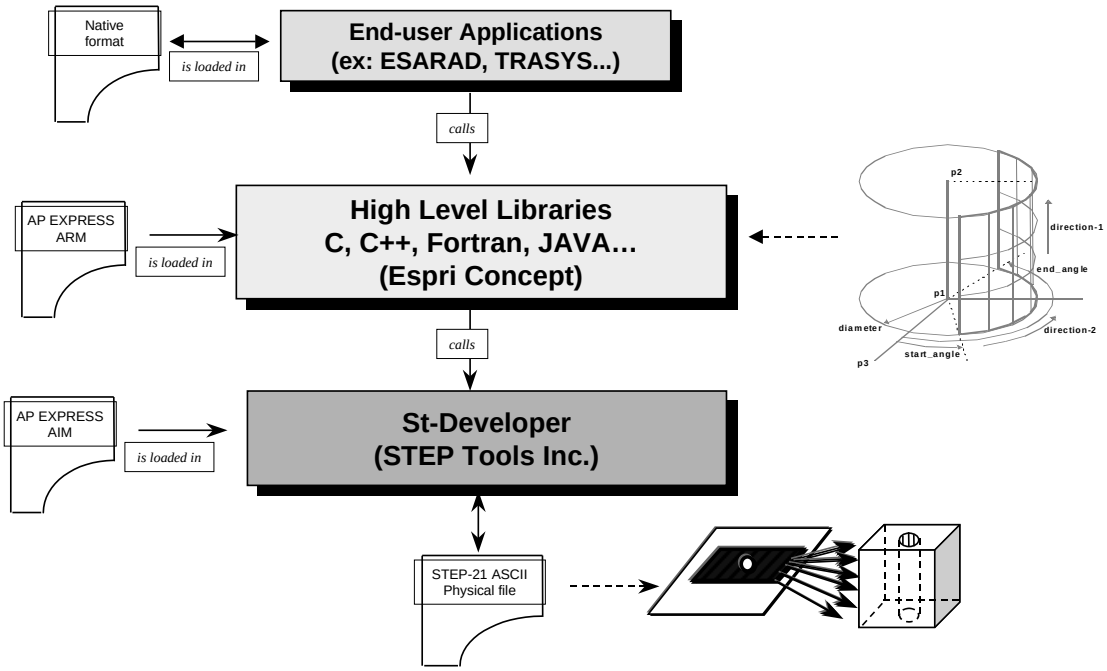

Libraries distribution

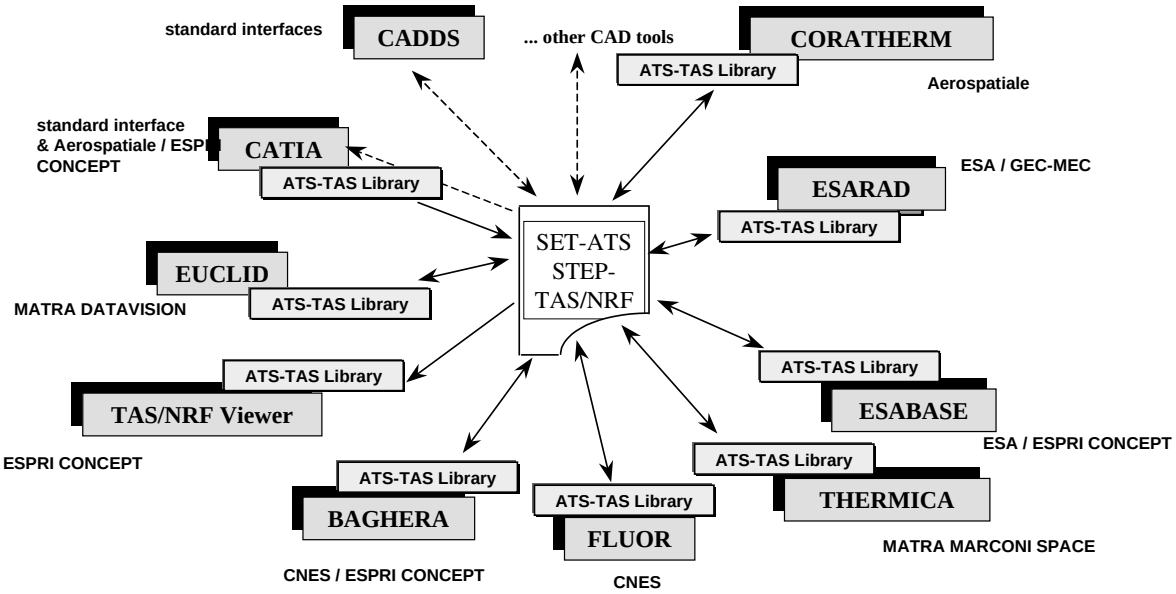

STEP Scientific Visualizer

☛ Checking and reporting

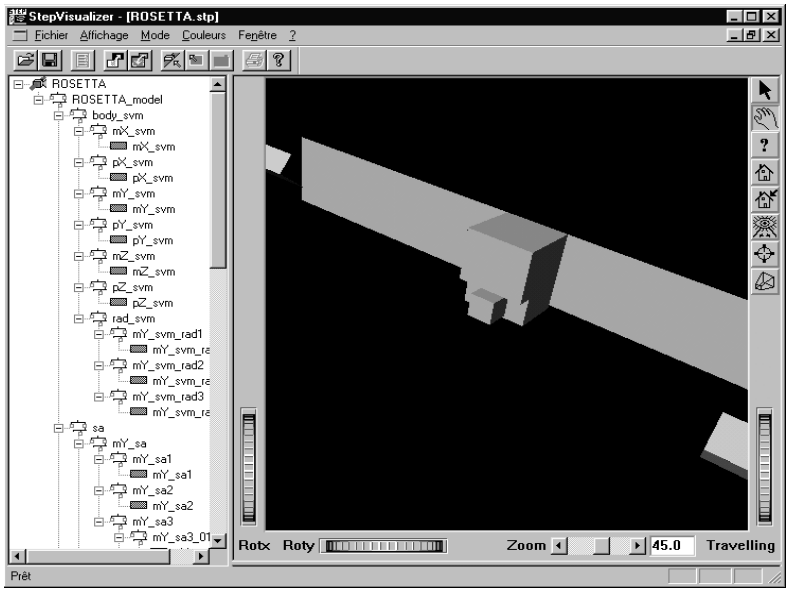

BAGHERA 2000

Engineering Design and Analysis Data Warehouse based on STEP

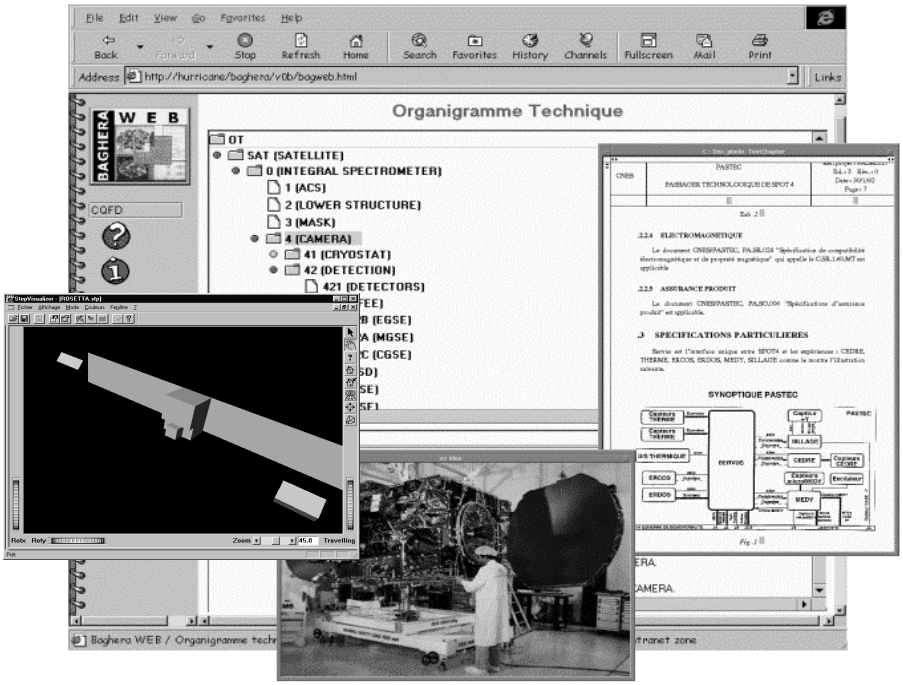

On-going activities

- STEP-TAS&NRF Editorial and associated software consolidation for ISO proposal
- STEP Visualizer : STEP-TAS&NRF.
  - Windows and Java platforms
- CAD / Analysis exchange consolidation
- STEP AP for Propulsion
- STEP AP for Spacecraft technical data and documentation configuration management
- Binary format for STEP with HDF (NCSA)
- STEP-NRF harmonisation with EDF and CEA
- STEP-NRF implementations (ESATAN,Dynaworks)

☛ Harmonisation with NASA ?

Overview

STEP - TAS Demonstrations

Eric Lebegue
Espri Concept
Sophia-Entipolis, France

(Eric.Lebegue@esprico.fr)

Georg Siebes
Jet Propulsion Laboratory
Pasadena, California

The demo map

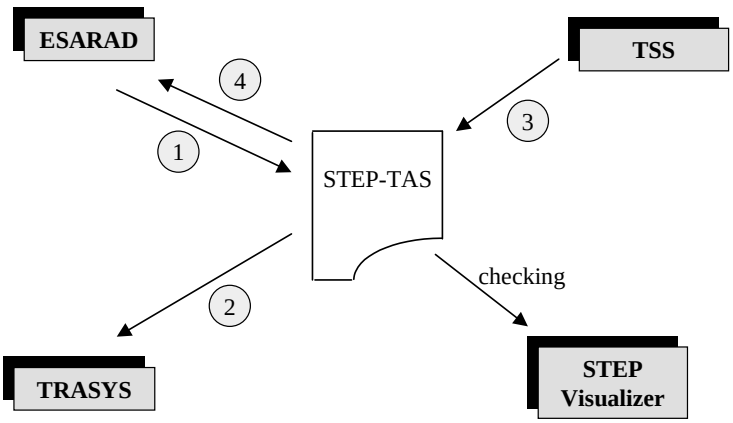

ESARAD to STEP-TAS

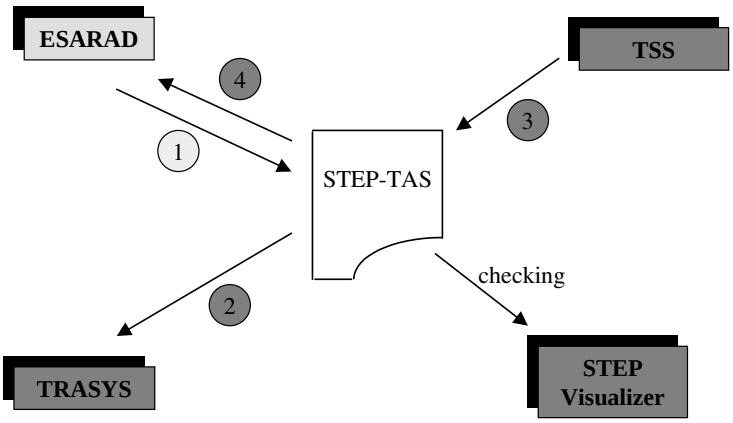

Checking ESARAD STEP-TAS file

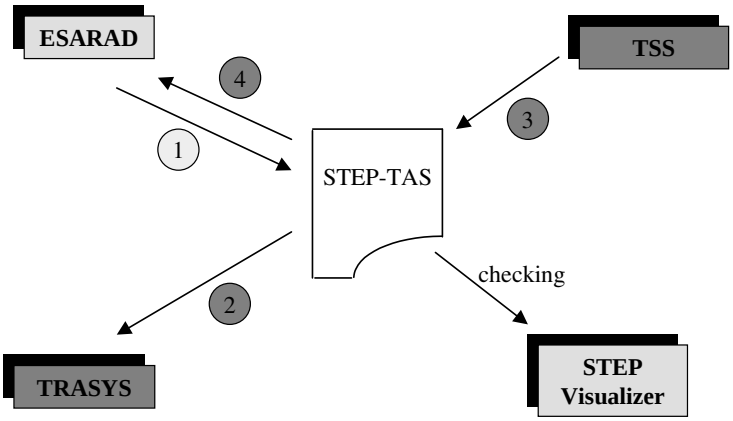

STEP-TAS to TRASYS

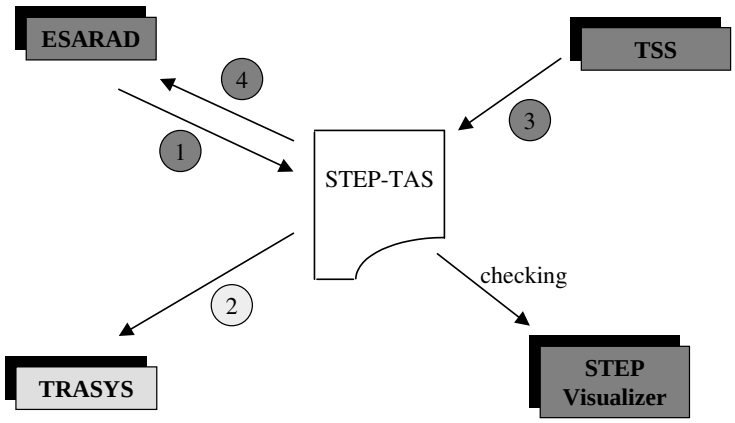

TSS to STEP-TAS

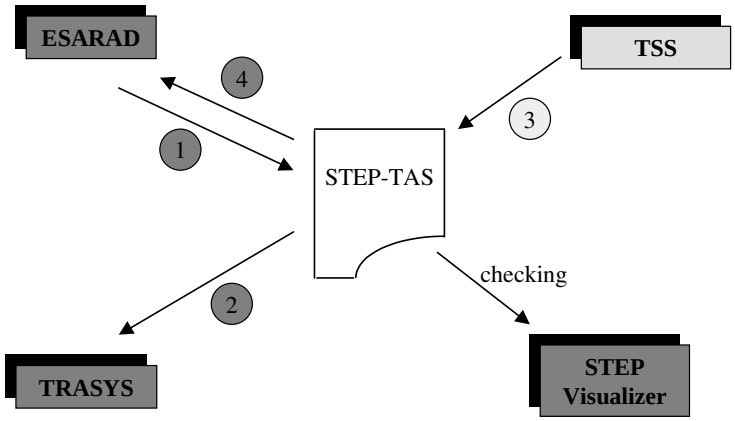

Checking TSS STEP-TAS file

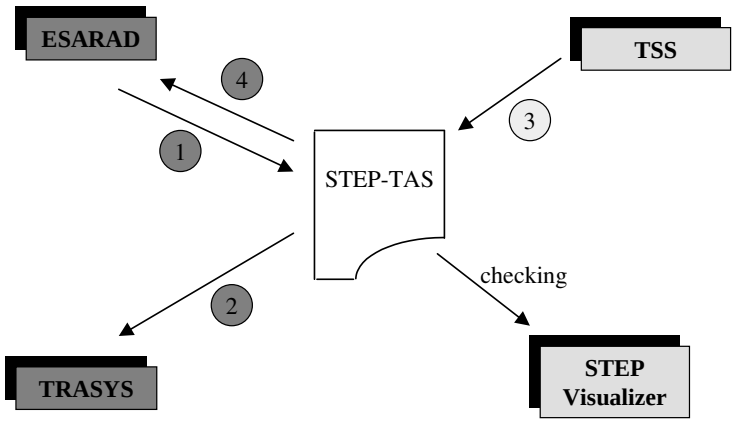

STEP-TAS to ESARAD

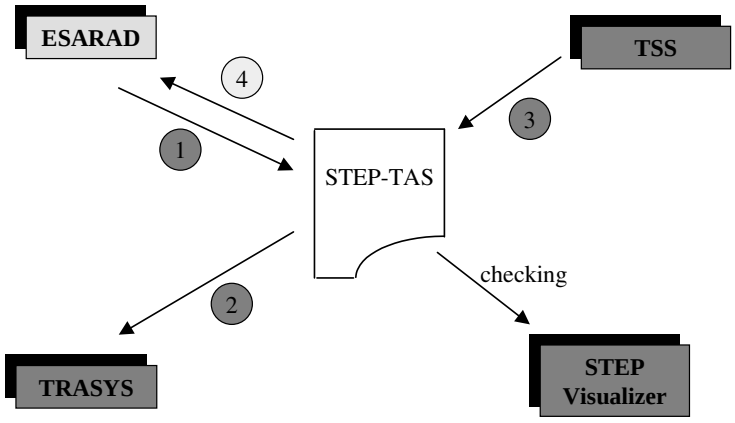

EFFICIENT INTEGRATION OF CFD INTO PRODUCT DESIGN

Vedat Akdag, Al Magnuson and Armin Wulf
ICEM CFD Engineering
Berkeley, California 94705

ABSTRACT

In recent years, CFD has taken rapid strides through the development and application of unified, robust and efficient methods, and CFD grid generation codes have shown major improvements mainly due to stronger links to the underlying CAD geometry. However, many grid generation systems have focused on inadequate interfaces (e.g. IGES) for transferring CAD geometry into the grid generation environment. These interfaces have limited the utilization of advanced CAD features like parametric geometry definition by grid generation systems - as soon as the geometry is translated for grid generation, the associativity between the parametric geometry and the grid is no longer maintained. ICEM CFD's direct CAD interfaces maintain the associations between the CAD model and the grid generation process. Using ICEM CFD, unstructured grids can be directly remeshed on the modified geometry. For structured grids, once the initial topology is defined, changes in the CAD model cause the ICEM CFD grid generation system to produce corresponding changes in the computational grid. The capability of ICEM CFD operating in an integrated geometry and grid generation environment is demonstrated.

INTRODUCTION

Given the computational grid, today, flow solvers can simulate flow fields around very complicated geometries supporting complex physics. Geometry acquisition and grid generation, in an early design environment where geometry is continually updated can be very time consuming. The results are unacceptably long turnaround times for complex problems. In an ideal design environment, parametric models are used where evaluation of alternative designs can be implemented into the analysis environment effortlessly. The grid generation software used should provide automated, accurate tools that are directly linked to the parametric geometry model in the same design environment.

In a rapid design process, the geometry "thrown over the wall" approach from one discipline to another with no consideration for strong links between design and analysis increases design cycle time and cost. "Thrown over the wall" is the approach for all grid generation software including the early versions of ICEM CFD. Geometry was translated into a "third party" format (IGES, PDES, VDA, STEP etc.) and the grid generation system translated it back into it's own environment (including all the unnecessary information for CFD analysis). This was a time consuming effort because the geometries required an excessive amount of time for organization, clean up and geometry extraction from the translated geometry. In addition, users often ran into the well-known problems of "surfaces don't match", "holes in geometry", "overlaps in surfaces", and "missing surfaces". Currently few software tools are being developed to handle these problems effectively. Considering the features in today's CAD systems, the bothersome problem with a generic translator is the loss of parametric geometry information. As it translates to grid generation: if any parametric design changes occur, the translation process reruns, and the same problems have to be endured again.

The process for geometry acquisition in ICEM CFD through common translators is shown in figure 1. The ICEM CFD IGES translator translates NURBS surfaces, trimmed NURBS surfaces, and NURB curves into the ICEM CFD geometry module’s native format. The translation into ICEM CFD also has to maintain accuracy issues, but since the size of the problem is not known beforehand, translation is usually repeated a few times if the geometry has complex features. After the geometry is translated into ICEM CFD’s geometry module, the user has to organize geometry, clean up unneeded information, extract curves and points, and build surfaces to represent outer boundaries like inlet and exit faces. In order to produce an “Intelligent Geometry for Mesh Generation”, the geometry is organized using the family concept. The user defines a set of families (usually representing the CFD

analysis conditions) and groups the geometry into these families. During this process mesh size requirements and boundary conditions are attached to the family information. This geometry input is unified through all of ICEM CFD's mesh generation modules.

Data translation through a neutral format creates several problems for a grid generation system. With IGES, for example:

- The quality of data produced by the IGES pre-processors varies widely. To achieve robust translation, the receiving post-processor must be tuned or *flavored* for each specific pre-processor. Since an IGES post-processor is usually designed to handle generic IGES files, the specialization needed for a specific pre-processor is often difficult to achieve. In some cases, the data model of the sending CAD system is poorly matched to the IGES data model and the quality of the model is significantly degraded in its IGES representation.
- Limitations in the IGES interface impact the data flow between the CAD system and grid generation software. For example, in most CAD systems, it is possible to add the CFD family metadata using native features of the CAD system like entity naming or attribution. In some cases, the CAD system IGES pre-processor will not output this data and in no case is this data handled in any standard way. STEP will probably address this issue, but STEP translators are still immature and not yet widely supported.

These issues are not unique to grid generation. They apply to most downstream applications that make use of CAD geometry. Many U.S. companies have attempted to address data translation issues by requiring a single CAD system for the entire company. Integration of the grid generation system with the CAD system using a direct CAD interface significantly reduces the problems associated with data translation and has obvious advantages:

- Users organize the geometry in their primary CAD system using a familiar user interface.
- The geometry organization is maintained in the primary CAD model.
- There is no need for clean up (what you display is what you tag for grid generation).
- Geometries are as accurate as defined in their respective CAD system. Geometry degradation is significantly minimized by eliminating the translation through a neutral format and because the interface is designed specifically for the respective CAD system.
- If there are changes to the geometry there is no time consuming effort to re-acquire it for grid generation.

The ICEM CFD direct CAD interface module described in figure 2 provides this environment. The ICEM CFD direct CAD interface works with major CAD systems such as CATIA, ICEM Surf, Pro/ENGINEER, SDRC I-DEAS, and Unigraphics. The software provided executes inside the CAD system. The geometry is selected in the CAD system and tagged with information (made intelligent) for grid generation such as boundary conditions and grid sizes etc. This intelligent geometry information is saved with the master geometry. If there is a parametric change in the geometry, all the user has to do is a simple *file save* for grid generation. The user can immediately re-calculate for unstructured tetrahedral grids. The computational grid can be updated, since the topology information remains the same, by using a *replay file* for multi-block structured grids and hexahedral unstructured grids. This approach also maintains the geometry accuracy requirements.

ICEM CFD DIRECT CAD INTERFACES

For each CAD system supported, the direct CAD interface is implemented using the native application extension utilities of the CAD system. The interface is run as a *plugin* application within the CAD system's normal user interface and presents the CAD system's normal look and feel to the user. Within the direct CAD interface module, the user:

- Specifies tolerance and modal information required by the grid generation system.
- Defines CFD families and associates these families to point, curve, and surface geometry within the CAD model.

- Associates CFD boundary conditions to the families.
- Uses specialized features to visualize and edit the CFD families.

The geometry is transferred to the grid generation system through a save operation which writes an image of the collected information and the entities within the CFD families to a *tetin file,* the grid generation system's native geometry format. This file is read by the grid generation application in the initial steps of the actual grid generation process. It is important to note that the primary specifications of the CFD grid reside in the CAD model. In many cases, the CFD grid can be updated in response to parametric changes in the CAD model by rewriting the *tetin file* and rerunning the grid generator in batch mode.

SIMPLE WING-FUSELAGE GEOMETRY

The geometry shown in figure 3 was created using the Unigraphics V13.0 modeling module. This geometry was created using tools common to all the CAD systems with ICEM CFD direct CAD interfaces. Our objective here is to utilize the ICEM CFD direct CAD interface to create a computational grid with the initial configuration and then replay the grid generation after we increase the cord length of the root airfoil from 100" to 200".

This wing-fuselage with a cylindrical outer body is built using parametric solids. The geometry of the airfoil is sketched in a 2-D plane using simple conics and lines. The cord length is 100" and we will use this length as a parameter to change the airfoil shape thereby changing the whole wing-fuselage configuration. A sketch of the airfoil is created in the plane going through x=0, y=0 and z=0. This sketch is transferred in the z direction approximately 300" out and approximately 100" in x direction and scaled down by half. This produces a wing shape with a sweep angle of about seventy degrees. The solid wing geometry is built using simple extrusion. A curve mesh free form surface feature is created to complete the wing tip. A solid cylinder body from 0 to 180 degrees is created to represent the fuselage. Later the wing geometry and the fuselage are united to represent a single solid. Under free form surfaces, a fillet surface with a 5" radius is created at the root of the wing where it intersects with the fuselage and is added to the wing-fuselage solid. A second cylinder is created to represent the outer boundary. The solid made from the wing, fillet surfaces and the cylinder are subtracted from the outer boundary to create a single solid. Figure 4 shows the close-up of the initial wing geometry at the wing root area and the parameters, the chord length and the maximum height of the airfoil, all available for parametric changes.

After the geometry is created, the ICEM CFD direct CAD interface is called without leaving the CAD system. The extraction of the surfaces from the solid is done with a single selection. Using the *define families* option, the families INLET, OUTLET, OUTER, FUSELAGE, UPWING, LOWING, WTIP and FLUID are created. Appropriate surfaces, edges and points extracted from the surface edge curves are grouped into these families and mesh sizes are defined in the process. During the grouping, the direct CAD interfaces 's *blank entity* option is used to blank geometry from the display to simplify the entity selection operation. The ICEM CFD direct CAD interface writes a file, which can be utilized by ICEM CFD Hexa and ICEM CFD Tetra, to create a multi-block structured and a tetrahedral unstructured grid respectively. Figures 5 and 6 show the structured and unstructured grids created using ICEM CFD.

For multi-block structured grids the *replay file* is saved as the multi-block structure is created. It is later replayed on the geometry with the 200" chord length wing-fuselage configuration after the initial geometry is changed parametrically.

Using the *edit sketch* tool in Unigraphics, the wing root sketch is edited and the chord length is updated from 100" to 200". When the *geometry update* button is selected, the geometry shown in figure 7 is created. At this point all that is needed is to re-write the information into the file. ICEM CFD's grid generation modules are utilized to create the computational grids in figures 8 and 9. For the multi-block structured case, the replay file saved from the initial configuration is played back on the new geometry. The tetrahedral grid is simply recomputed.

ICEM CFD GRID GENERATION PROCESS

The ICEM CFD grid generation tools provide the capability to create grids from geometry in multi-block structured, unstructured hexahedral, tetrahedral, hybrid grids consisting of hexahedral, tetrahedral, pyramidal and prismatic cells; and Cartesian grid formats combined with boundary conditions. Translators for the over seventy flow solvers and structural analysis codes shown in figure 10 are provided.

Some of ICEM CFD's Modules are:

ICEM CFD Hexa - A mesh generation tool based on a global block topology providing a top-down approach to mesh generation. This semi-automated meshing module allows rapid generation of multi-block structured or unstructured hexahedral volume meshes. ICEM CFD Hexa represents a new approach to mesh generation. The operations most often performed by experts are automated and made easily available. Blocks can be adjusted interactively and body fitted internal or external O-Grids can be generated by the system automatically. Edge meshing is calculated based on the defined mesh parameters on the surfaces. Finally the mesh is projected to the underlying CAD geometry.

ICEM CFD Tetra - A tetrahedral mesher that takes full advantage of Octree meshing technology. No tedious up-front triangular surface meshing is needed to provide well-balanced tetrahedral volume grids. ICEM CFD Tetra works directly from CAD surfaces and fills the volume with tetrahedral elements using a top-down approach, providing triangular surface meshes on the object surfaces as well. Prescribed curves and points define positions of edges and vertices. A powerful smoothing algorithm provides good element quality. This automatic mesh generation tool is suitable to complex geometries and offers tools for local adaptive mesh refinement and coarsening.

ICEM CFD Prism - Hybrid tetrahedral grids consisting of layers of prism elements near the boundary surfaces and tetrahedral elements in the interior can be generated with ICEM CFD Prism automatically.

ICEM CFD Hybrid – This module allows combining of hexahedral and tetrahedral meshes. If two regions, one with a hexahedral grid and another with a tetrahedral grid, share surfaces, the two volume meshes can be merged into a single mesh. At the boundary, pyramidal cells are created automatically.

ICEM CFD COMAK - This module provides parametric geometry modeling for grid generation if the geometry is acquired using common translators.

ICEM CFD Visual3 - A new state of the art post-processing and visualization module provides the CFD professional with easy-to-use powerful result visualization features for both structured, unstructured, and hybrid grids. ICEM CFD Visual3 provides an in depth view of data with visualization tools such as cutting planes, contouring, iso-surfaces, streamlines, line plots, data probes and animation. Features such as a CFD function calculator and an intuitive based user interface make this module a powerful interpretation tool of computed results. ICEM CFD Visual3 provides an integrated environment for CAD geometry, ICEM CFD computational grids, and the flow solution.

CONCLUSIONS

The direct interfaces from major CAD systems to ICEM CFD's grid generation software provide a significant improvement over the problematic methods for transferring CAD geometry into the grid generation environment used in the past. More effective engineering in the design process should be possible with the elimination of the tedious step of data translation (and the resulting loss of geometry associativity) from a "third party" format into the grid generation environment.

REFERENCES

1. AKDAG, V and WULF, A. “Integrated Geometry and Grid Generation Systems for Complex Configurations,” *Proceedings of the Software Systems for Surface Modeling and Grid Generation Workshop*, R.E. Smith (Ed.), NASA Conference Publication 3143,. p. 161, NASA Langley Research Center, Hampton, VA, 1992.

2. KERR, P.A., SMITH, R.E. and PSENENAU, M.A., “GEOmetry LABoratory (GEOLAB) Surface Modeling and Grid Generation Technology Services,” *Proceedings of the Surface Modeling, Grid Generation and Related Issues in Computational Fluid Dynamics Workshop*, NASA Conference Publication 3291, p.69, NASA Lewis Research Center, Cleveland, OH, May 1995.

3. JONES, W.T. and SAMAREH-ABOLHASSANI, J., “Grid Generation Systems for Multi-Disciplinary Design Optimization,” AIAA-95-1689-CP, *Proceedings of the Surface Modeling, Grid Generation and Related Issues in Computational Fluid Dynamics Workshop*, NASA Conference Publication 3291, p.657, NASA Lewis Research Center, Cleveland, OH, May 1995.

4. BERTIN, D., CASTLES, C. and LORDON, J., “A new Automatic Grid Generation Environment for CFD Applications”, *AIAA CFD Applications meeting Proceedings*, AIAA-92-2720-CP Palo Alto, CA 1992.

5. COSNER, R.R, “Future Requirements in Surface Modeling and Grid Generation,” *Proceedings of the Surface Modeling, Grid Generation and Related Issues in Computational Fluid Dynamics Workshop*, NASA Conference Publication 3291, p.3, NASA Lewis Research Center, Cleveland, OH, May 1995.

6. THOMPSON, J. F., “A Reflection on Grid Generation in the 90s: Trends, Needs, and Influences,” *Proceedings of the 5th International conference on Numerical Grid Generation in Computational Field Simulations*, Mississippi State University, April 1996.

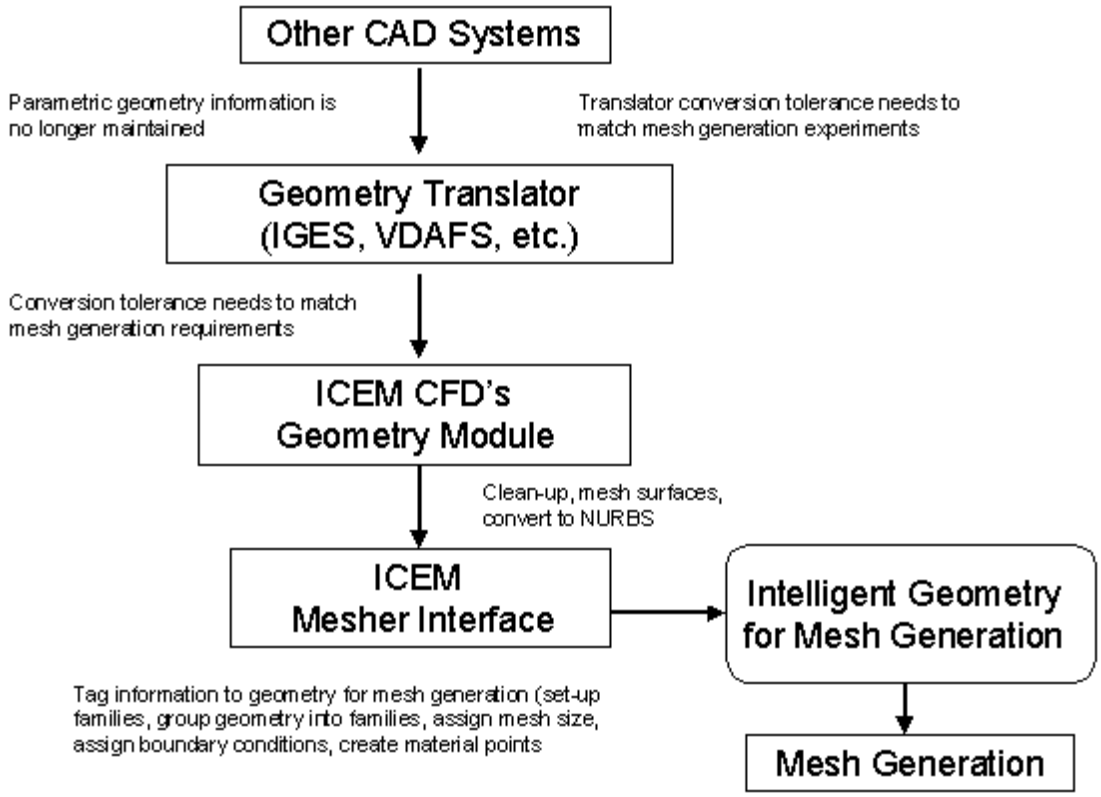

Figure 1: Common translator geometry into ICEM CFD.

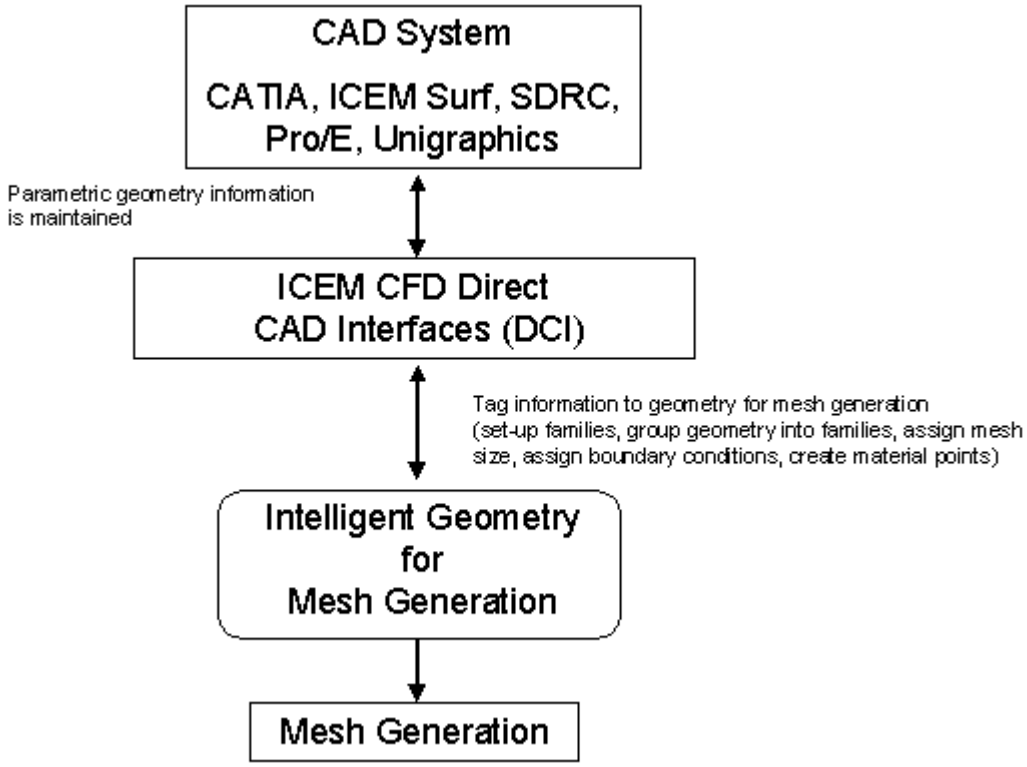

Figure 2: ICEM CFD direct CAD interfaces.

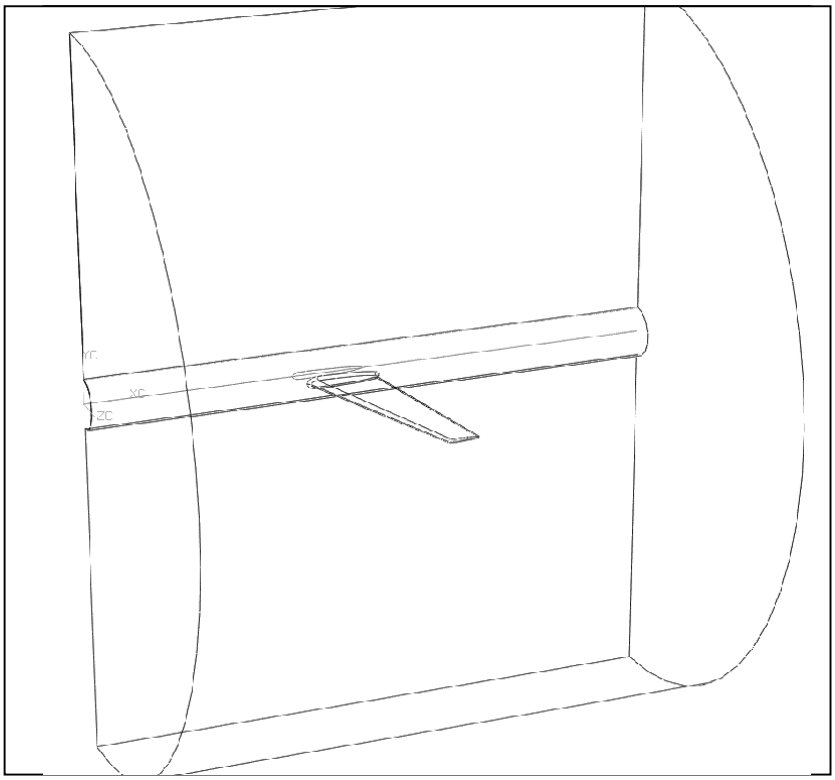

Figure 3: The wing-fuselage geometry model displayed in Unigraphics Version 13.0.

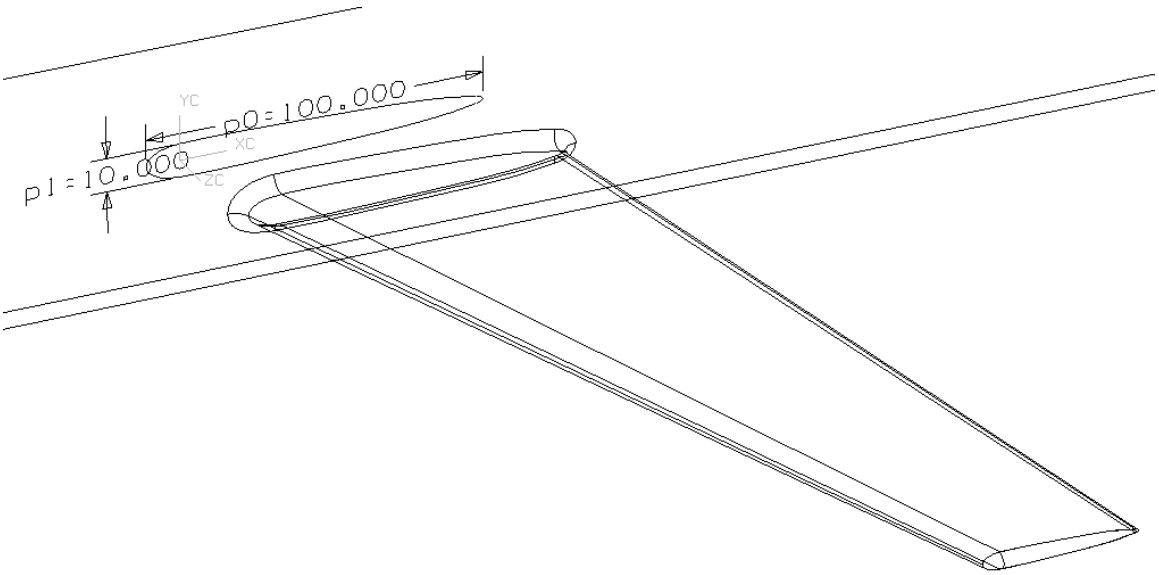

Figure 4: The wing root geometry with 100' chord.

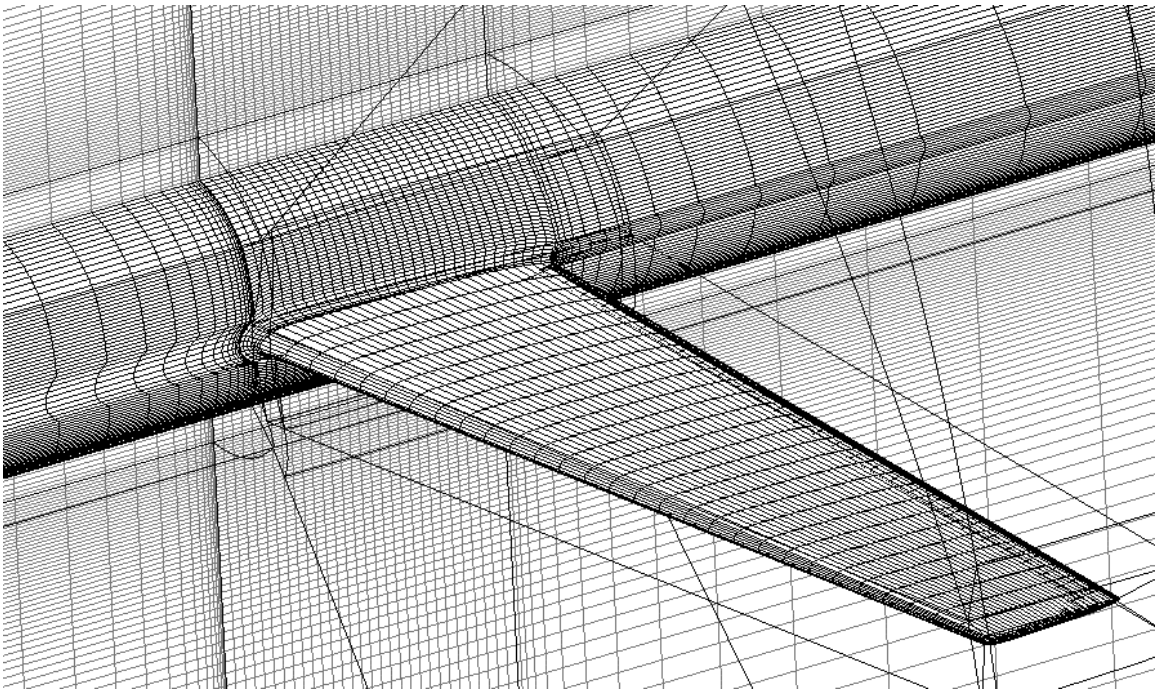

Figure 5: Multi-block grid created with ICEM CFD Hexa.

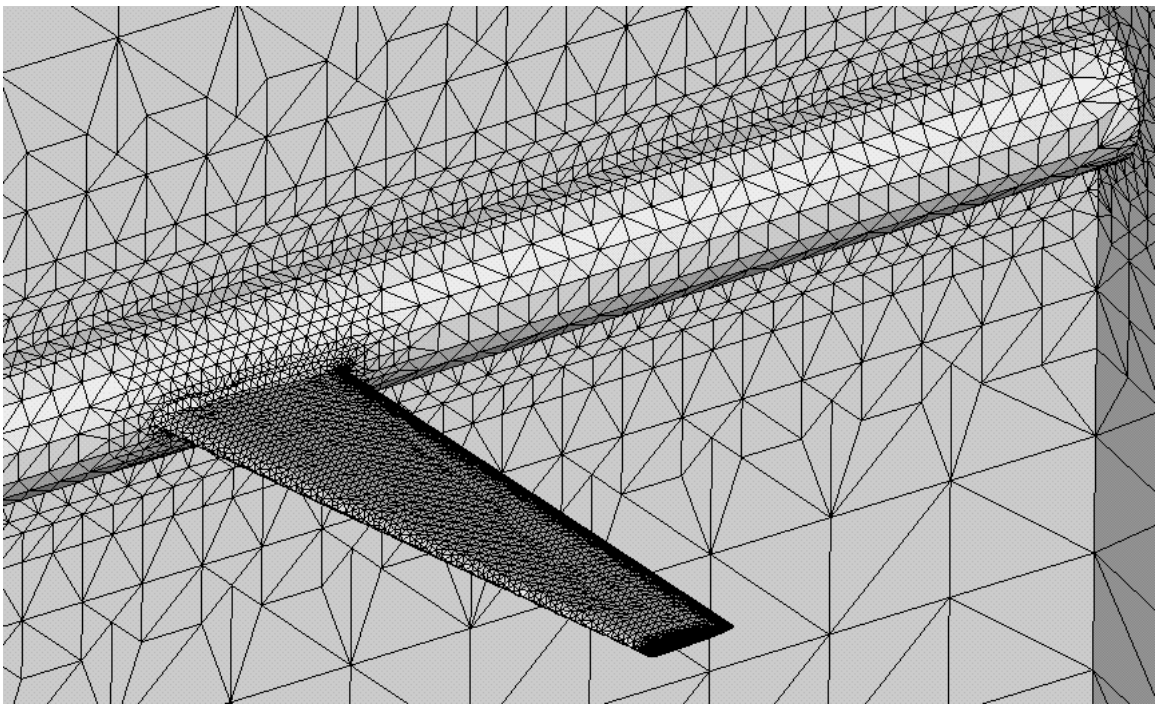

Figure 6: Unstructured grid created with ICEM CFD Tetra

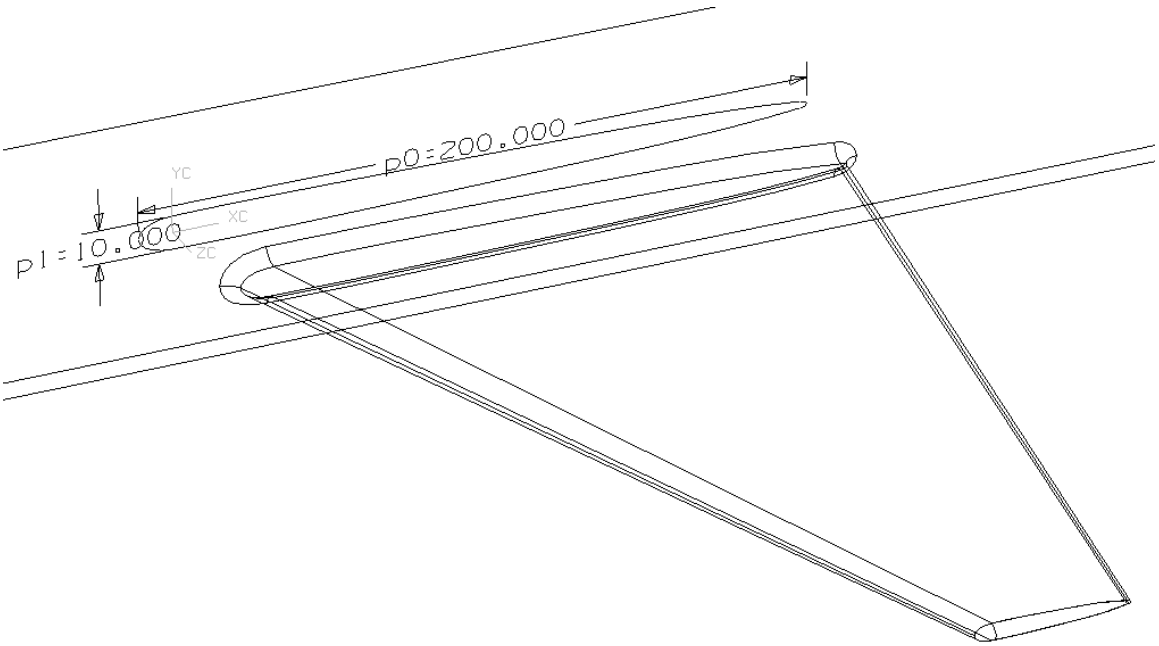

Figure 7: Changing the chord length of the wing.

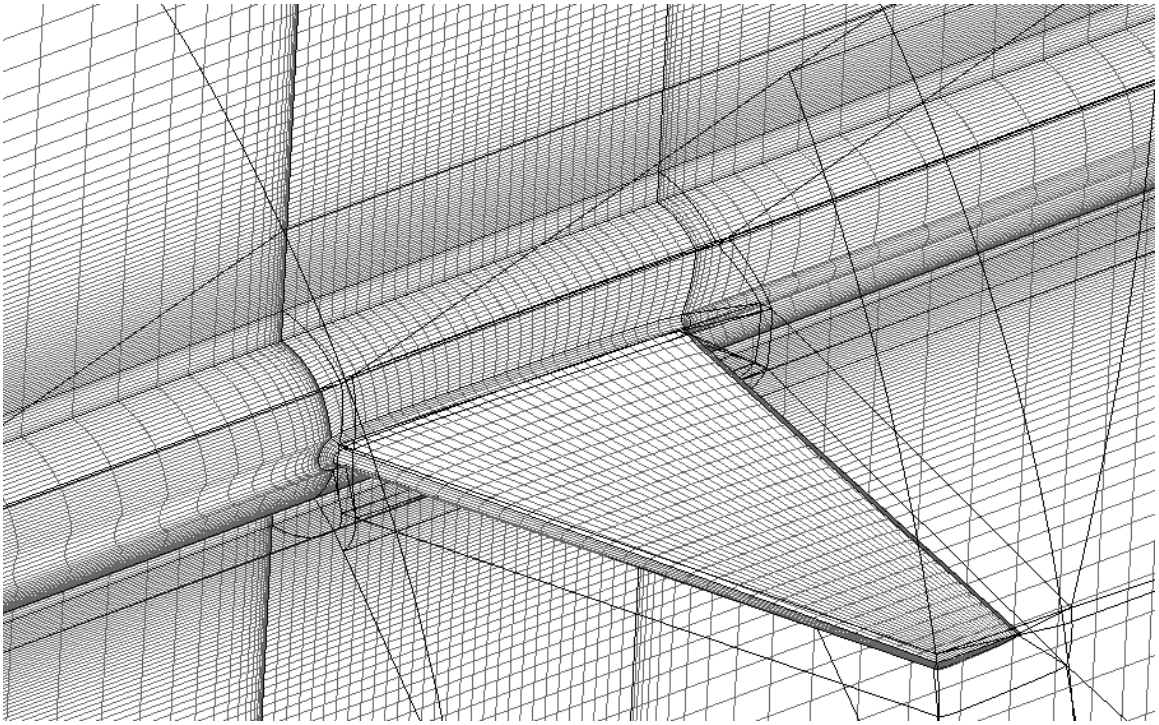

Figure 8: Structured grid calculated on the 200" root chord length wing.

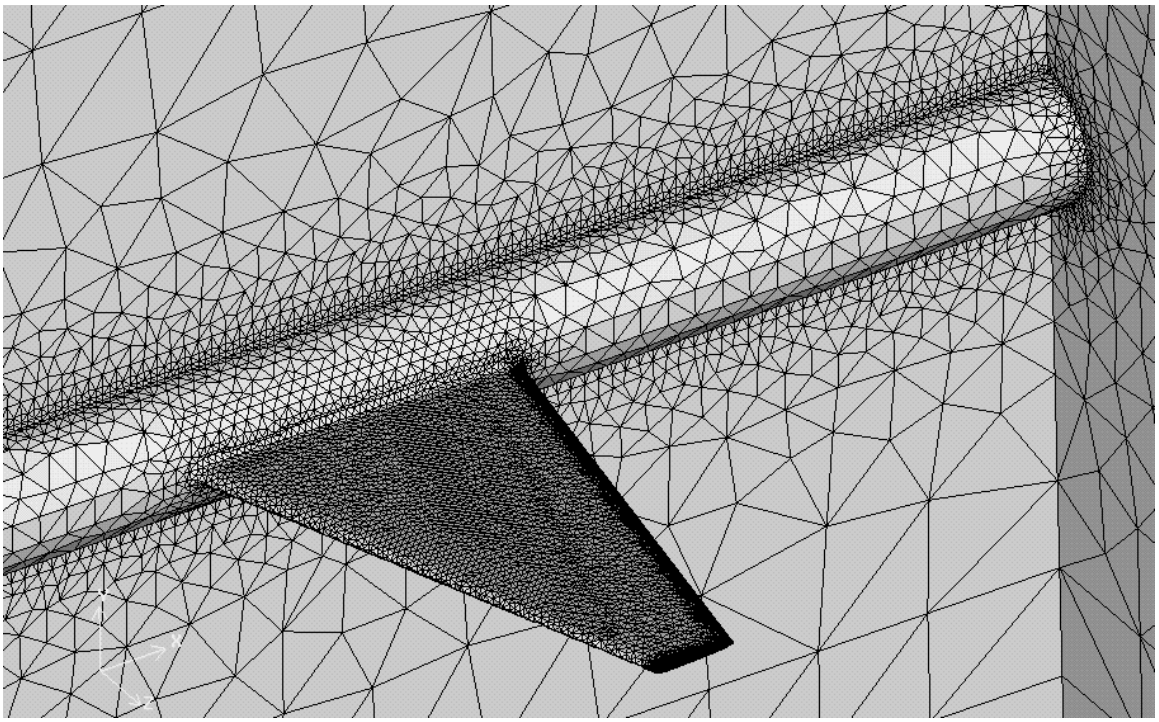

Figure 9: Unstructured grid on the 200" root chord length wing.

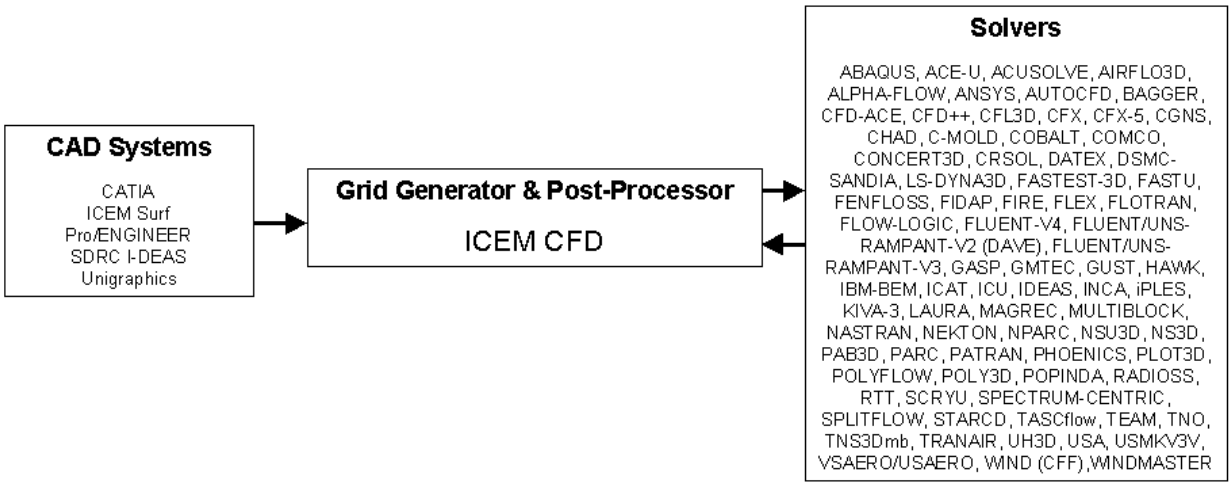

Figure 10: The direct path from the CAD system to ICEM CFD and the list of solvers.

COMPARISON OF INTEGRATED ANALYSIS METHODS FOR TWO MODEL SCENARIOS

Ruth M. Amundsen
National Aeronautics and Space Administration
Langley Research Center
Hampton, Virginia 23681-2199

SUMMARY

Integrated analysis methods have the potential to substantially decrease the time required for analysis modeling. Integration with computer aided design (CAD) software can also allow a model to be more accurate by facilitating import of exact design geometry. However, the integrated method utilized must sometimes be tailored to the specific modeling situation, in order to make the process most efficient. Two cases are presented here that illustrate different processes used for thermal analysis on two different models. These examples are used to illustrate how the requirements, available input, expected output, and tools available all affect the process selected by the analyst for the most efficient and effective analysis.

INTRODUCTION

Integrated analysis methods can substantially reduce the time and effort required to produce analytical results, and also potentially offer improved accuracy. By importing model geometry electronically, time spent in manual creation of geometry is eliminated, and the model created reflects the exact design. By sharing a model between the structural and thermal analysts, the time to develop a model can be cut in half. This also ensures that the analysts are working with the same version of the geometry. The direct access between thermal and structural models facilitates solution for problems that are driven by thermally induced stress. The exact methods and tools used in integrated analysis can vary depending on the type of analysis, the model geometry, and the expected variation in cases to be run. Shown here are two examples of integrated modeling approaches that differ based on the modeling requirements.

The first case discussed is the thermal analysis of a hypersonic wing. In this situation, there were several different proposed geometries to be analyzed, which meant that efficient import from the CAD software was important. The heating loads were provided from an independent aeroheating code. These loads went through several iterations and parametric studies, so that efficient import of those values significantly reduced the total analysis time. The grid used for the aeroheating calculation was much coarser than the grid used for the thermal analysis; therefore, the heat load distribution required interpolation to the thermal analysis mesh. The aeroheating parameters were interpolated in time from the aeroheating calculation time steps to the much finer solution time steps used in MSC/PATRAN THERMAL (ref. 1). The method was tailored in that the calculated aeroheating rates were used only on the wing flat sections, and stagnation point heating was calculated separately and applied to the swept leading edge only. Radiation analysis within the wing was performed using the VIEWFACTOR module internal to PATRAN. Radiative loss to the atmosphere was also included. The predicted temperature distribution was required for structural MSC/NASTRAN (ref. 2) runs to determine if the wing temperature gradient produced excessive stresses.

The second case is that of a large space-based antenna array. The array consisted of multiple composite antenna waveguides, each six meters in length with a small open rectangular cross-section, supported by a truss structure of tubular composite struts and metal joints. In this case, the geometry was such that direct import from the CAD software was neither effective nor efficient. The model was built manually, using selected import of parts from the CAD software. The large size of the model drove the use of beams for truss members in order to simplify the model. Orbital fluxes and radiation conductors were calculated using the TRASYS (ref. 3) solver. Because of

limitations with beam elements in both PATRAN and TRASYS, a separate TRASYS model was required, using cylindrical surfaces for the truss members to calculate correct orbital flux loads. The transient heat loads from TRASYS were applied to the PATRAN model using fields, with liberal use of text file import and automated session files to minimize modeling time. The limitations of the current PATRAN version (7.5) with respect to beam elements required the use of interesting workarounds to apply radiation and heating boundary conditions to the truss. In this situation, there were several parametric runs performed within TRASYS, so the heat load application method was selected to provide simple substitution of TRASYS result cases. The temperature distributions were again required for NASTRAN structural runs, this time to determine thermally induced deflections of the array. The driving requirement on the array was to maintain stability within certain deflection tolerances; thermal cases were applied as loads using both the differences around a single orbit as well as differences over a year.

The tools used in each of these two cases were tailored to the needs of that situation, and modifications to the methods were made as necessary. Customizing the integrated analysis methods on the fly optimized the speed and accuracy of the analysis performed in each case.

WING MODEL

Requirements

Requirements on the hypersonic wing modeling approach were as follows. The analysis was to be performed on the horizontal wing of a hypersonic vehicle that was under design by a contractor. Several geometry configurations and material combinations had been proposed and required analysis. Thus, it was important that the modeling approach simplify analyzing changes to the geometry and materials. The main thermal loads on the wing were aerodynamic heating loads from the hypersonic airflow, predicted by an independent aeroheating code. There were several different criteria used to predict aeroheating, and improvements in the design trajectory were continually being made, which resulted in a large number of different aerodynamic load cases to be evaluated. Thus, it was crucial that the model be able to rapidly evaluate updates to the aeroheating loads. The mesh used in the aeroheating model was much coarser than the thermal model would need. Also, the aeroheating loads were only put out at 18 time steps along the 127-second trajectory, which was a much larger time step than would be used in the thermal analysis. Thus, it was critical that the thermal analysis provide accurate interpolation of the heating data (both in space and time) onto the thermal model. A different method was required to calculate and apply the stagnation point heating at the leading edge, without compromising the heat values applied from the aeroheating code. The wing body contained internal open cavities. The radiation within these was a significant factor in equalizing the thermal distribution across the wing. Radiation from the wing surface to the atmosphere was also required to be included. The atmospheric temperature was a variable since the altitude change over the time period in question was substantial. The selected modeling method needed to include radiation within the geometry, as well as to an external variable temperature. Finally, the temperature prediction output was needed not only to determine if all materials would survive, but also for structural analysis. The temperature gradient was the main driver in creating stresses on the wing. Thus, a simple method for translating the thermal gradient to a structural model load was necessary.

Geometry Modeling

These requirements were satisfied by the methodology chosen, which included using MSC/PATRAN to model the wing. The geometry was imported electronically from the computer-aided design (CAD) software Pro/Engineer (ref. 4). After the geometry was imported into PATRAN, it existed as “trimmed solid” geometry. Using the current version of PATRAN (v. 7.5), it was only possible to mesh this with a tetrahedral mesh. For the structural model this was acceptable. For the thermal model, however, a more detailed hex mesh was desired near the leading edge where the extremely high heat loads and high gradients occurred. In the baseline design, the wing consisted of two parts, as shown in Figure 1. A tetrahedral mesh was acceptable on the aft or body portion of the

wing. For the leading edge portion, native PATRAN ("blue") solids were created from the imported trimmed solid, thus allowing an automated brick or hex mesh. Boundary conditions such as convection and radiation were applied only to the geometry faces. This allowed several different meshing densities to be evaluated without reapplying boundary conditions. When a new geometry was to be evaluated, a copy of the entire database was used that included material properties, boundary conditions, analysis parameters, boundary nodes and all fields. The original geometry and mesh were deleted, and the new geometry imported. Boundary conditions and properties then only needed to be modified rather than recreated. When a new geometry was brought in, it was possible to have the new model meshed and running in less than four hours. Most of the model sizes were in the range of 10000 to 30000 nodes. To compare geometries' performance, it was sometimes possible to use the trimmed solid geometry and a solely tetrahedral mesh. This did not allow the true curve of the leading edge to be represented. However, it was found that the difference in area between the curved leading edge and the flat edge presented by the tetrahedral mesh could be applied as a factor on the stagnation point heating. This was useful for qualitative comparisons of geometries; the thermal error it induced was determined to be less than 5%.

Boundary Conditions

The boundary conditions used were radiation within the cavities, radiation from the wing exterior, contact conductance, aeroheating convection to the top and bottom surfaces of the wing and stagnation point heating at the wing leading edge. Although temperature-dependent emissivity was an option, it was not used in this case since the emissivities were fairly constant with temperature, and the additional accuracy was not felt to be worth the sacrifice in solution speed. The internal PATRAN module VIEWFACTOR handled the radiation within the cavities. The viewfactors were run with several different tolerances and zero factors. Once the viewfactors had been run for a particular geometry, they could be re-used for subsequent runs of that geometry without recalculation. The radiation from the exterior surface of the wing to the atmosphere was done using the "between regions" radiation boundary condition. A boundary node for the atmosphere was created. The model was run initially with a constant temperature for the atmosphere; later this was revised to a variable temperature boundary condition to reflect the change in temperature with altitude.

Aeroheating Loads

FORTRAN subroutines were developed to perform the interpolation of aeroheating loads to the PATRAN model. The aeroheating model included all wing variables that changed as a function of time, such as wing angle of attack (AOA), altitude, mach number, etc. There are many routines built into PATRAN that allow the user to modify operation of the PATRAN THERMAL solver; four of these were utilized in this case. The first is a uinit.f routine, which is called once to initialize parameters before solution of the problem. Modification of this file allows the user to initialize files for later output. In this case, a file named uopen_trans.f was called within uinit.f. This file read in the aeroheating files and loaded them into arrays. Within the uopen_trans routine, the loads file values and co-ordinates were translated into the units and axes used in the PATRAN model. This is a valuable feature of this process – the units and coordinates in the loads file can differ from those used in the PATRAN model without interfering with the smooth transfer of data. A required uncertainty factor that was variable with time was applied to the values before loading them into the array. The next file, normally called by PATRAN at every solution iteration, is uhval.f. This file is activated by having a convective boundary condition ID greater than 1000 applied, and allows the user to define the desired convection configuration. The spatial interpolation requires only 2D interpolation since the location of any point on either the top or bottom surface of the wing is completely defined by the x and y location.

The interpolation of the loads incorporated some interesting features. The leading edge of the wing, where the highest gradients of heating and temperatures occurred, is highly swept (65° from normal). An example of the interpolated h_c (convective coefficient) values and their high gradients near the leading edge is shown in Figure 2. The aeroheating mesh was relatively coarse. Near the leading edge, both the aeroheating mesh and the PATRAN mesh followed the sweep angle of the leading edge. Due to the coarseness of the aeroheating mesh, the aeroheating grid spatially closest to a given PATRAN node was not always the best one to use for interpolation,

since it might be at a location substantially further from the leading edge. Thus, a method had to be developed to handle the interpolation correctly and weight the values using the distance from the leading edge.

The interpolation in time from the 18 time steps of the trajectory to the solution time steps used in PATRAN THERMAL was necessary since the average aeroheating time step was about 10 seconds, and the average PATRAN solution time step was about 0.1 seconds. The values used within PATRAN THERMAL were interpolated in a weighted fashion from the two closest points in time from the trajectory, with the heating at time zero assumed to be zero.

Another aspect of the aeroheating model that required modification was the leading edge heat flux. The h_c values over the curved leading edge portion had to be calculated outside of the aeroheating code. The stagnation point h_c values were calculated separately using FORTRAN software that used Fay-Riddell methods. These values were calculated over the same 18-point trajectory. The stagnation point values were placed in a mat.dat.apnd file and applied as a separate boundary condition. The node points on the tangent (between the curve of the leading edge and the flat wing section) received a combination of heating values. The leading edge curve elements had the stagnation point h_c applied, and the flat section elements had the aeroheating load file values applied. Nodes that joined these two elements received the stagnation point heat flux on the area associated with the element on the curved face, and the load file heat flux on the area associated with the flat section element. Thus the total heat applied to these nodes was an average correctly weighted by area.

Radiation

The radiation within the wing cavities was calculated by the internal PATRAN module VIEWFACTOR. Several runs were made with different zero tolerance values on the grey body factors. The optimum tolerance value was determined by taking the value at which there were no substantial changes in viewfactors due to a decrease in the tolerance. These calculated radiation conductors were then used in subsequent runs without the necessity for re-calculation.

Radiation from the wing exterior to the atmosphere is an important factor in controlling the wing temperature rise. The two materials on the exterior had relatively flat emissivity curves (little change in emissivity with temperature over the expected temperature range), so a constant emissivity was assumed. The radiation “between regions” boundary condition was used, with a radiation boundary node as the sink. The temperature of this node was originally approximated as a fixed temperature, and was later improved to reflect the change in atmospheric temperature with altitude over the trajectory. This small increase in model accuracy made very little difference in the model results.

Contact Conductance

Since several of the wing geometries evaluated consisted of two or more separate parts, and since there were high temperature differences between parts, the contact conductance between them was an important variable. The parts were in general attached via pinned connections, with little or no contact pressure. The gap between the parts would be dependent on machining tolerances, and would vary with temperature. No data on contact conductance between the candidate material types was found. For these reasons, the contact conductance problem was bounded by using minimum and maximum reasonable values to determine the worst-case. The minimum value was calculated by assuming no contact, with heat transfer via radiation and conduction through still air across the maximum gap distance. The maximum contact conductance value was determined by utilizing the maximum no-contact-pressure value found for dissimilar materials in the published data. Contact conductance between parts was simple to apply in PATRAN. After the parts were meshed, they were equivalanced individually, so that nodes on the boundary between the parts were not equivalanced together. The convection “between regions” boundary condition was used to simulate contact. This boundary condition was applied to the geometry, so that re-meshing operations would not force extensive model modification.

Results

The temperature output of the model was used for two purposes. First, the temperatures of each component in each geometry case were compared to the single-use temperature limits for that material. This allowed a determination of which design configurations would allow the materials to survive thermally. An example plot of the thermal distribution is shown in Figure 3. The gradients at the leading edge, apex and around the geometry pockets in the aft wing body are evident from the plot; these complex three-dimensional gradients are the main reason that this fully representational geometry model is necessary. This type of plot allowed the user to determine specifically what portions of each part were exceeding thermal limits, and at what solution times this was occurring. The thermal results are highly time-dependent, as shown in the example thermal transient chart (Figure 4). This illustrates why all time-varying features of the problem must be considered, such as Mach number, altitude, wing angle of attack, etc. The second use for the temperatures was translation to the structural model, which in some cases had a different mesh, to allow a structural analysis of the wing that combined thermal stresses and stresses induced by the air pressure loading. The temperature gradients on each design were the main drivers in producing large deflections and stresses. The deflections and stresses predicted for each design were the major factors utilized in selecting a final vehicle configuration. The use of a fully three-dimensional thermal gradient to predict the actual stress condition of the wing was found to be much more accurate than using two-dimensional cuts of the wing to approximate the thermal distribution.

ORBITING ANTENNA ARRAY MODEL

Requirements

The second modeling scenario is that of a large orbiting space-based antenna array. The modeling approach for this system had very different constraints than the hypersonic wing. Instead of being a single part with relatively small-scale geometry, the antenna array was a complex assembly with a large spatial extent, as shown in Figure 5. However, there was only one proposed geometry to be evaluated, so that variation of the assembly geometry was not a driving factor in the modeling approach. One factor in the geometry that was known in advance to be variable was the support strut diameter, so it was desirable to select a method that simplified this alteration. Several materials and several orbit conditions were to be evaluated, so facilitating the change of boundary conditions was important. Since this was an orbiting space-based array, correct radiation conductors and orbital fluxes for the surfaces were critical. Schedule constraints were an incentive to build a common model utilized by both the structural and thermal analysts. The main science requirement on the array was to minimize the on-orbit deflection of the waveguides with respect to each other. These deflections were mainly driven by the thermal gradients, since the array was orbiting in 0-g, and outside of atmospheric drag. Thus, similar to the wing model, an important factor in selecting the methodology was efficient transfer of temperatures to the structural analysis model.

Geometry Modeling Method

The constraints were efficiently met using a combined analysis methodology that utilized both PATRAN and TRASYS, as well as some “manual” model development. The array was composed of 16 waveguides, each 6 m in length with an open rectangular cross-section of 14.5 x 7 cm. This gave an inherent length ratio in the geometry of the thinnest face of 86:1. The waveguides were connected via a truss of tubular struts. The strut lengths varied from 0.1 to 1 meter, with a diameter of 2.5 cm, for a maximum length-to-diameter ratio of 40:1. The joints where struts were connected were extremely complex, involving a transition from composite truss to metallic joint, as well as rotational and locking capability within the joint. There were several dozen separate parts within each joint, and over 100 joints in the entire assembly. When this entire assembly was pulled in electronically from the CAD software Pro/Engineer, it created an extremely large PATRAN database, even prior to meshing. An entirely electronic imported geometry model would not have been reasonable in this case. The

model would have been too large to allow solution in a reasonable time, would not have allowed simple change of materials or orbital conditions, and would not have allowed simple application of rotational boundary conditions on the revolute joints. In addition, since the strut tubes were imported as trimmed solids, these extremely thin-walled struts would have been meshed with a tetrahedral solid mesh, which would not have been efficient or accurate. The diameters of the strut tubes could not have been modified in a simple way. In order to overcome these limitations, it was decided to build the model using PATRAN native shapes (plates and beams) with dimensions and positions from the Pro/Engineer geometry. The Pro/Engineer model was used to create an IGES file of the assembly parts' shapes and positions. This IGES file was imported into PATRAN and used to expedite geometry definition. The model was constructed using plates for the waveguide sides and beams for the struts. This gave the simplest model and facilitated the connection and application of boundary conditions in both the thermal and structural analysis. It also permitted simple force recovery in the struts. The joints were modeled as beams of the metallic material, with the correct cross-sectional area and length. This allowed the correct prediction of thermally-driven expansion and distortion, but simplified the modeling of joint connections. Since it had been determined that only a single geometry configuration would be evaluated, the time spent in manual model development was not as detrimental as it would have been for a system with continually changing geometry such as the wing.

Since the model geometry was developed manually, parts could be grouped as necessary so that alternate materials for struts, joints and waveguides could be easily analyzed. An additional benefit of using beams for the struts was that diameters different than the baseline design could be evaluated without re-meshing or re-applying boundary conditions. The model that was constructed only contained half the array (eight waveguides), since the two halves were relatively similar geometrically. The PATRAN model is shown in Figure 6. The meshed model contained roughly 13000 nodes.

Orbital Fluxes and Radiation

The most challenging part of the modeling for the thermal analyst was the application of orbital flux boundary conditions. The VIEWFACTOR module would not handle orbital flux calculations. A translator from PATRAN to the TRASYS radiation and orbital flux software existed, but included several severe limitations. None of the beams would be translated, and the rectangular plates would be translated as the "POLY" surface type. At first, this problem would seem to be tailor-made for application of the Thermal Synthesizer System (TSS), since that would allow simple calculation of the orbital flux heating loads. There were two reasons this software was not used. First, because of hardware limitations, there was not a running copy of TSS at NASA Langley at the time. Second, since the structural analysis would be performed from a PATRAN model, and the thermal analyst was to build that model, it saved a substantial amount of time to perform the thermal analysis using the same PATRAN model. The most efficient solution found was to re-build the geometry in TRASYS. The TRASYS model is shown in Figure 5. This allowed calculation of the transient orbital fluxes to each surface. Since the geometry was extremely sparse, most of the viewfactors of elements to space were unity. Viewfactors were calculated within TRASYS, but in most cases were averaged or rounded to unity when applying the radiation conductors within PATRAN. Only four distinct regions of different radiation-to-space factors were used in the PATRAN model, and these were applied via the "between regions" radiation boundary condition (which does not call the VIEWFACTOR module).

Much of the geometry information could be exported from the PATRAN model and used to place and size elements of the TRASYS model. However, there were several challenges inherent in the re-build of the geometry. First, in the TRASYS version used (version 2.7) the bar "ELEM" element type analogous to the PATRAN beam is not fully functional and does not provide accurate results. Thus, the strut and joint beams required construction as cylinders. Since they had fairly large length-to-diameter ratios, most of them were multiply noded, with the results averaged via correspondence data. Each surface area had a boundary condition applied for orbital flux, as well as a boundary condition for radiation to space. A completely integrated method for applying radiation-to-space to the PATRAN beam elements did not exist. Up through version 7.5 of PATRAN there is no way to convect or radiate from 1D conduction bars in 3D space. The workaround was to apply a boundary condition to the beams that was a variable nodal heat source on the bar nodes. The boundary condition template ID defined

the space node as the ambient node and called a straight-line microfunction that defined the heat as a workaround for radiation out. For radiation the independent variable was "Radiosity Difference," $\sigma*(T_1^4 - T_{amb}^4)$, where σ is the Stefan-Boltzmann constant, T_1 is the nodal temperature, and T_{amb} is the ambient radiation sink temperature. P1, the slope, was $-\varepsilon*A/2$, where ε was the emissivity of the bar and A was the total perimeter area of the bar (the negative was necessary to have the correct direction on heat flow). The value of P2, the intercept, was 0.0. A new microfunction was required for every beam element with a different area (ref. 5).

There were 460 regions in the TRASYS model that had different orbital heat flux transients to be applied to the PATRAN model, as well as 16 types of beams with different areas that required the radiation workaround heating boundary condition. There were two orbit extremes to be evaluated (solar $\beta = 90°$ and solar $\beta = 60°$). There were two halves of the array to be evaluated, one of which was extensively shaded by the spacecraft, and the other receiving direct sun in the $\beta=90°$ orbit. At first, the application of 460 boundary conditions for four different transient orbital conditions would seem an overwhelming task. However, the orbital flux values produced by TRASYS were in a text file, formatted in arrays of heat flux versus time. These could be manipulated in Microsoft Excel so that the format matched that required by PATRAN THERMAL in the micro.dat.apnd file. PATRAN THERMAL uses this file during execution to define time- and temperature-varying fields. The macros (command sequences) in Excel for performing this manipulation were saved so that they could be used on subsequent data sets. For the $\beta=60°$ orbit, there were 48 time steps in each orbit, and eight consecutive orbits were run to achieve stable repeating results. Using the micro.dat.apnd file, all of the fields could be constructed and applied via external text files. The template.dat.apnd file relating the boundary condition template ID to the appropriate microfunction was also simply generated in Excel. Most of the boundary conditions were applied to the PATRAN model in a repetitive manner, using editing of session files. Once a boundary condition had been applied to one portion of the model, that session file could be duplicated and edited to allow more automated application of boundary conditions. This substantially reduced the time required to apply all the boundary conditions. Evaluation of a different orbit condition was relatively simple -- none of the boundary conditions needed to be changed. The only alteration was to construct a new micro.dat.apnd file from the TRASYS output file, and use that file in the thermal analysis run. This facilitated switching between the two halves of the array, as well as evaluation of other orbital parameters and material properties. Once an analysis had been developed in this manner, alteration to evaluate another orbital condition could be done in less than an hour.

Another consideration in this model was the conflict between boundary conditions (BCs). Each of the beam elements had two heat source boundary conditions applied: the actual orbital heating, and the radiation workaround. If these were run in the same thermal load case, there was a choice between adding the conditions together, or setting an overwrite priority. Obviously, neither the radiation nor orbital heating should be overwritten. However, if "Add" was selected under the load case definition, then nodes at the intersection of two different beam heating BC's received double the correct amount of heating, because the beam heating BC did not weight heating by element area. The solution implemented for this problem was to use "Overwrite" in the load case definition, so that intersection nodes received the correct heating. Then two different load cases were run to create two different qmacro.dat files, one for radiation psuedo-heating, and one for true orbital heating. These qmacro.dat files were then manually combined and the full model was run using the combined qmacro file.

Results

The temperatures output from this analysis were quite easy to import into the structural model (in PATRAN, execute File…Import…Results), since the same mesh was used. Nodes used in thermal analysis but not in structural (such as the ambient space node) did not affect this transfer. The model was run for two array halves (one extensively shaded by the spacecraft, one with more direct solar flux) and for two different orbit conditions ($\beta=60°$ and $\beta=90°$). Each of these four conditions was evaluated for structural predictions. The predicted behavior of the array on initial entry into orbit (using several different assumptions for launch time), as well as the orbital and annual transients, were all determined in both the thermal and structural analyses. An example thermal distribution is shown in Figure 7. The predicted thermal distributions were also used to ensure that no material or component went outside its operational temperature range. Transient plots for each run were

constructed for selected nodes, using session files and the applicable routine in the patq executable. This enabled simple determination of whether the model had been run for a sufficient number of orbits to achieve stability. An animation of the transient distribution as a changing color map on the PATRAN model was constructed and transferred to video to enhance visualization of the thermal behavior. The animation was also placed on a Web page.

CONCLUSIONS

Unique integrated thermal analysis techniques using PATRAN, PATRAN THERMAL, TRASYS, and import from Pro/Engineer were applied to resolve potential thermal problems for an advanced hypersonic wing shape and a large orbiting antenna array. In each of these cases, the modeling approach was tailored to suit the modeling requirements and constraints. In the hypersonic wing case, the important parameters were to expedite alteration of geometry and materials, incorporate complex transient aeroheating gradients, and translate temperature distributions to the structural analysis. Extensive use of electronic import from Pro/Engineer into PATRAN, editing of PATRAN THERMAL subroutines, VIEWFACTOR radiation calculation, and boundary conditions applied to geometric entities were found to comprise the most efficient thermal analysis method for this case. In the orbiting array case, the critical factors were to provide a usable structural model, apply orbital heating, facilitate changes to certain geometry parameters, and translate temperature distributions to the structural analysis. This scenario required manual model development to minimize model size and increase usability, extensive text and session file use for boundary condition application, and novel workarounds for beam heating and radiation. Both cases effectively used integrated methods to decrease the time required for analysis and increase the accuracy of the final predictions.

ACKNOWLEDGEMENTS

The assistance of the structural analyst, Michael Lindell, in developing PATRAN models and providing modeling advice is gratefully acknowledged. The re-use of FORTRAN software developed and modified by Phil Yarrington is acknowledged with thanks. The assistance of Abel Torres and Chuck Leonard in providing aeroheating data and assistance is deeply appreciated.

ACRONYMS

AOA	Angle of Attack
BC	Boundary Condition
CAD	Computer Aided Design
CFD	Computational Fluid Dynamics
FEM	Finite Element Model
ID	Identification Number
IGES	Initial Graphics Exchange Specification
TSS	Thermal Synthesizer System

SYMBOLS

A	Area
ε	Emissivity
h_c	Convective Heat Transfer Coefficient
σ	Stefan-Boltzmann Constant
T_{amb}	Ambient Temperature

REFERENCES

1. MSC/PATRAN User Manual, MacNeal-Schwendler Corporation, Version 7.5 (August 1996).
2. Kilroy, K., MSC/NASTRAN, Quick Reference Guide, The MacNeal-Schwendler Corporation, June 1997.
3. Thermal Radiation Analyzer System (TRASYS) User's Manual, JSC-22964, April 1988.
4. Parametric Technology Corporation, Pro/Mechanica Reference Manual, 1997.
5. PATRAN Technical Note 3251, http://www.macsch.com/

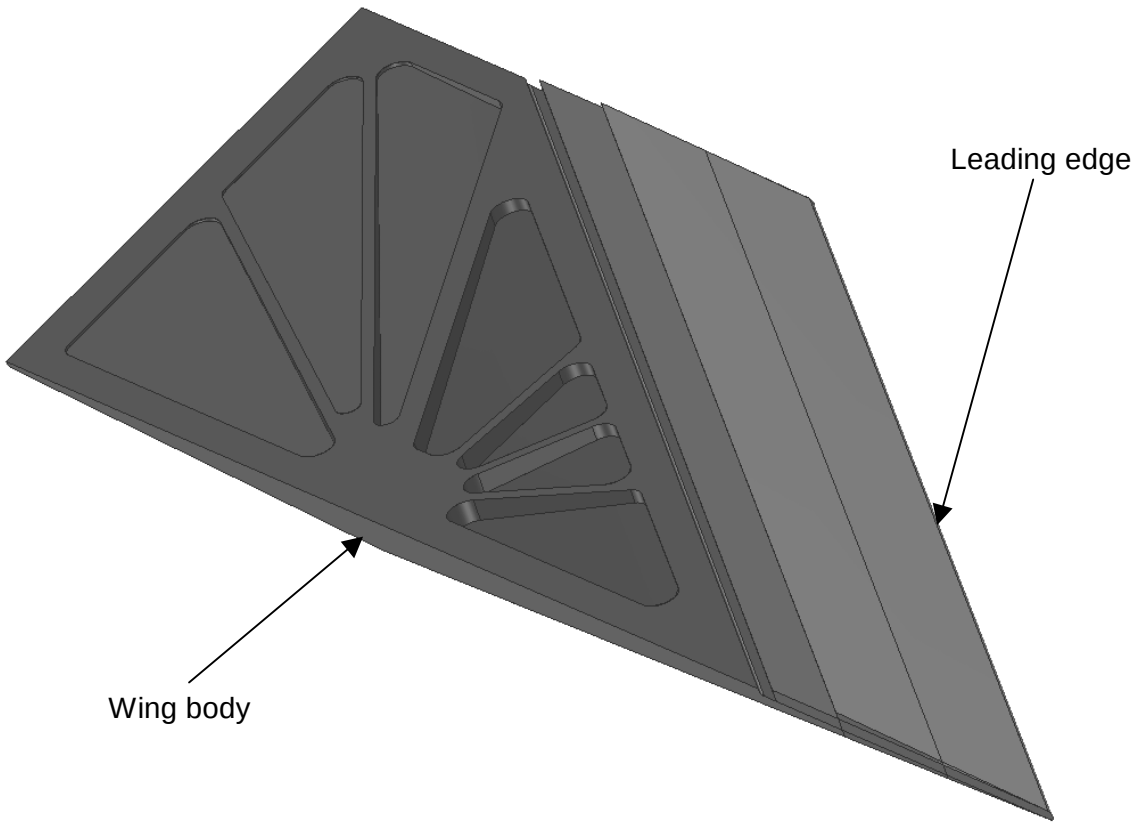

Figure 1. Hypersonic wing geometry (interior of wing body shown for illustration).

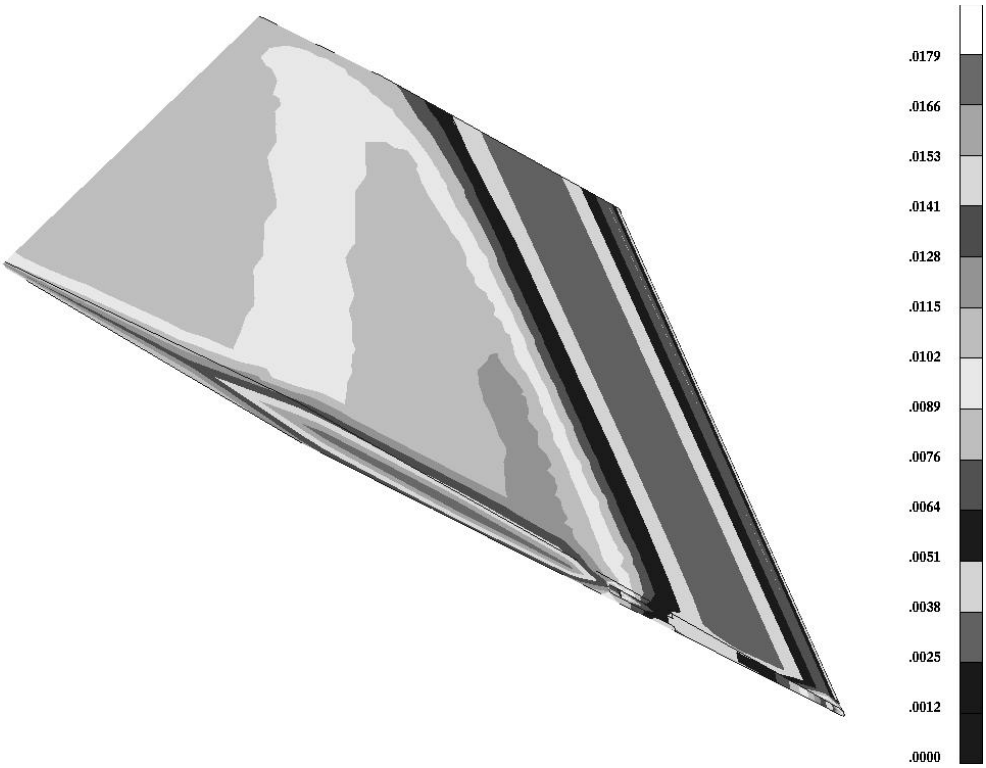

Figure 2. Example distribution of h_c values over wing at one time point (arbitrary units).

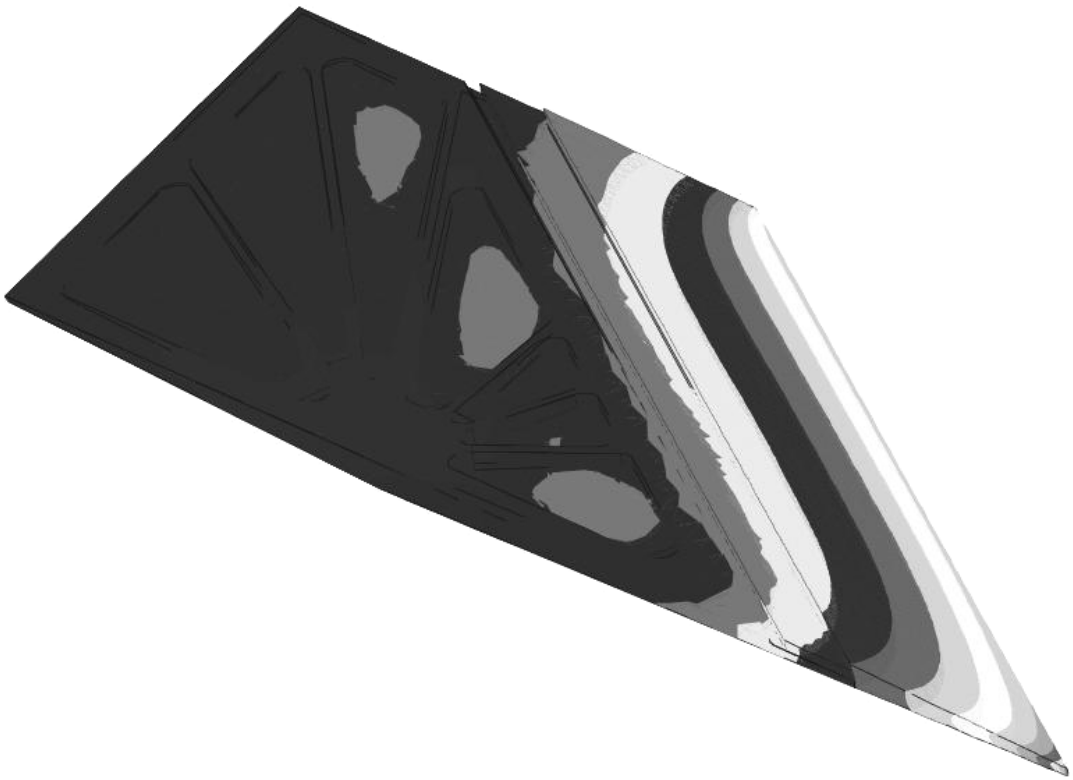

Figure 3. Example thermal distribution on hypersonic wing
(temperature values not disclosed due to information protection concerns).

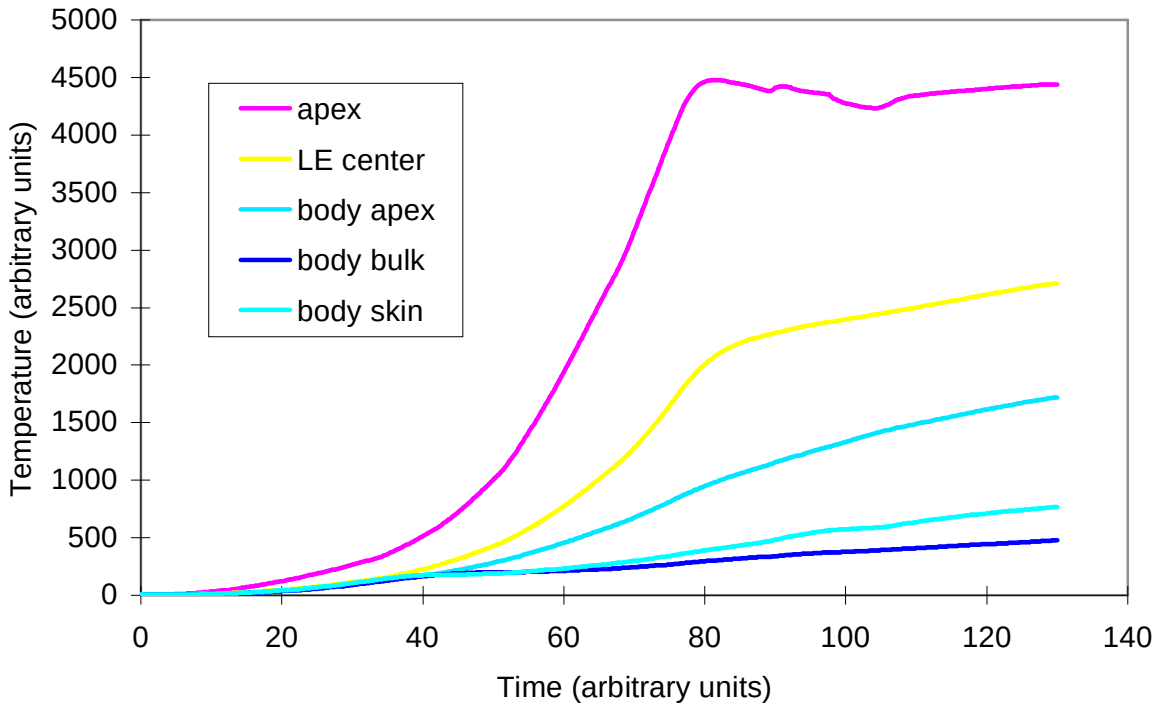

Figure 4. Thermal transient for several points on wing.

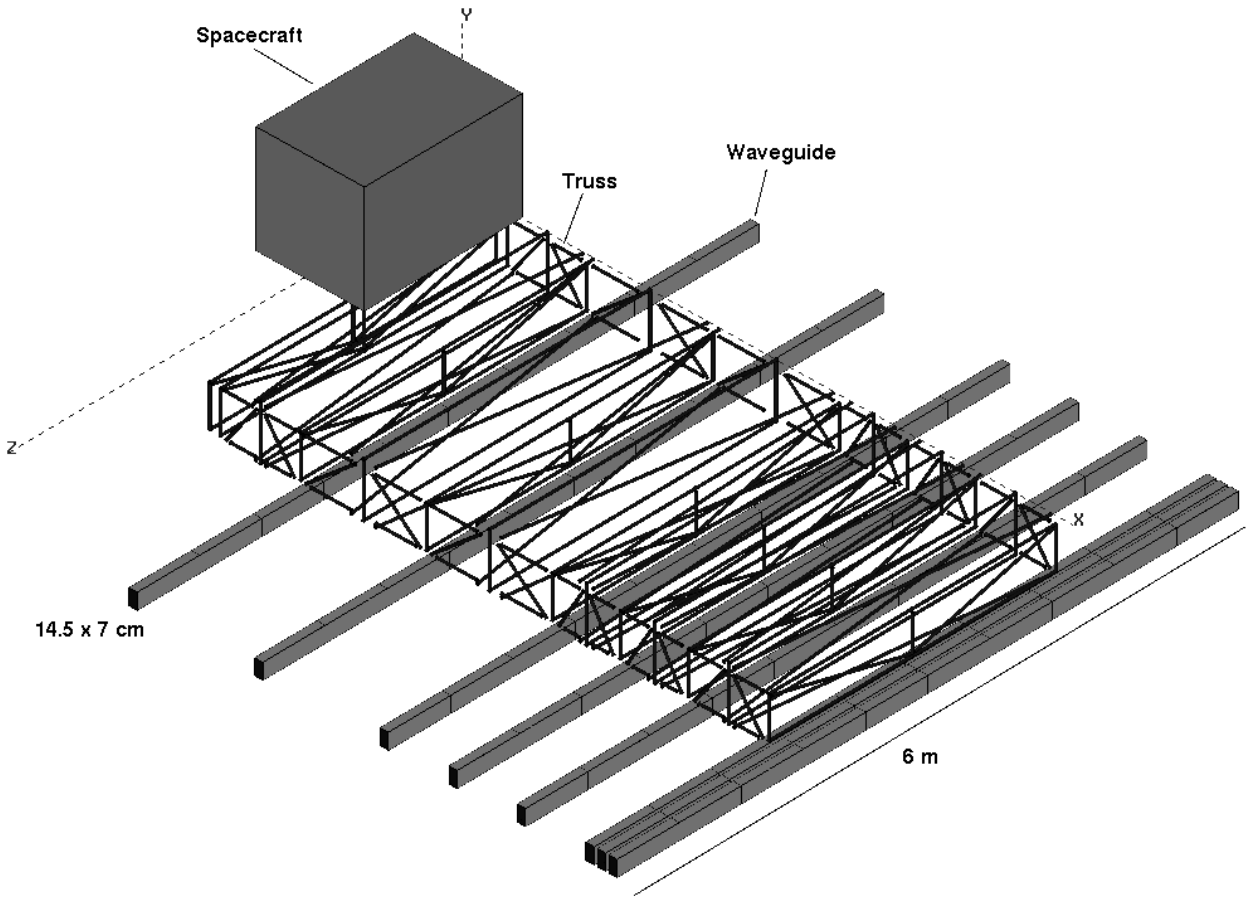

Figure 5. Antenna array geometry in TRASYS model.

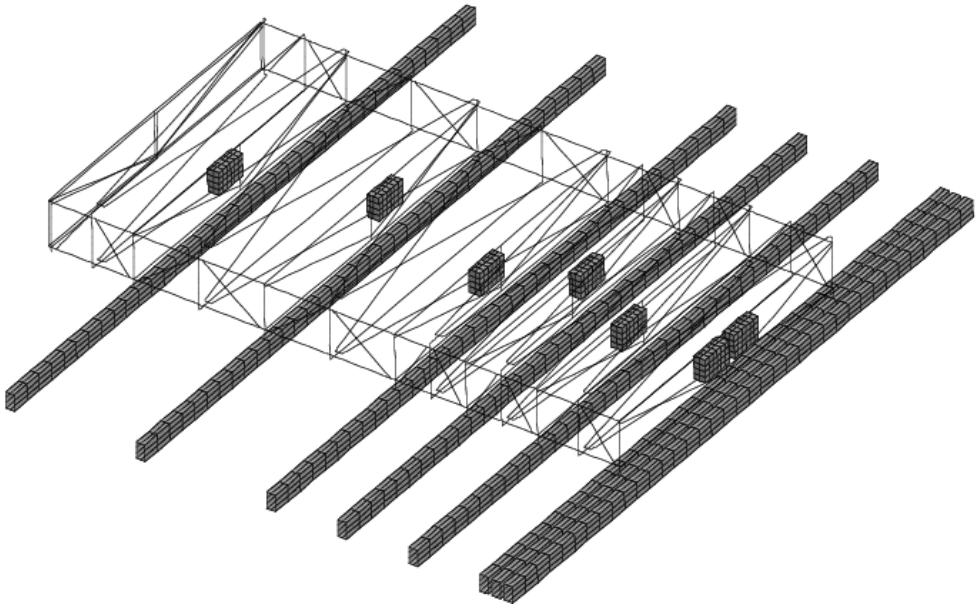

Figure 6. PATRAN model of array.

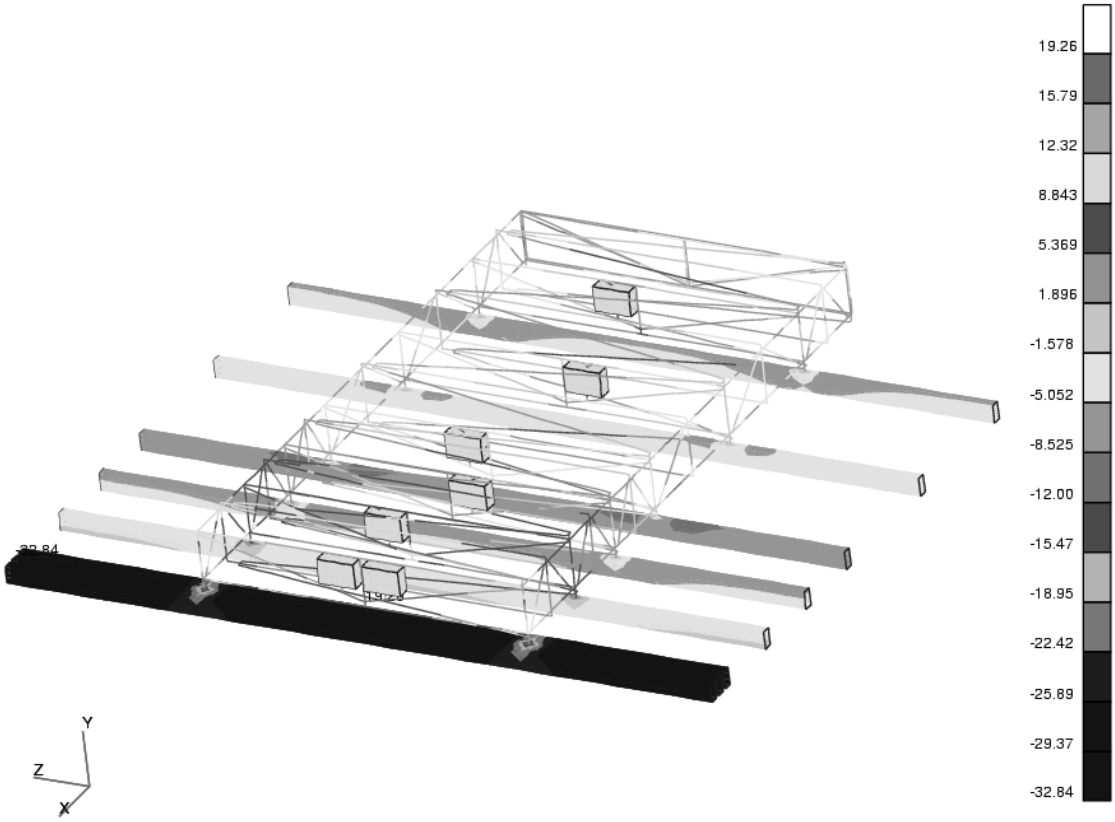

Figure 7. Predicted thermal distribution for β=60° orbit condition, at single orbit point (in °C).

COMPARATIVE ANALYSIS BETWEEN NEVADA AND TSS USING A JET ENGINE EXHAUST NOZZLE TEST RIG

Joseph F. Baumeister and James R. Yuko
National Aeronautics and Space Administration
Lewis Research Center
Cleveland, Ohio

Summary

Thermal analysis in both simple and complex models can require calculating the propagation of radiant energy to and from multiple surfaces. This can be accomplished through simple estimation techniques or complex computationally intense computer modeling simulations. Currently there are a variety of computer analysis techniques used to simulate the propagation of radiant energy, each having advantages and disadvantages. The major objective of this effort was to compare two ray tracing radiation propagation analysis programs (NEVADA and TSS) with experimental data. Results from a non-flowing, electrically heated test rig was used to verify the calculated radiant energy propagation from a nozzle geometry that represents an aircraft propulsion nozzle system. In general the programs produced comparable overall results, and results slightly higher then the experimental data. Upon inspection of individual radiation interchange factors, differences were evident and would have been magnified if a more radical model temperature profile was analyzed. Bidirectional reflectivity data (BRDF) was not used do to modeling limitations in TSS. For code comparison purposes, this nozzle geometry represents only one case for one set of analysis conditions. Since each computer code has advantages and disadvantages bases on scope, requirements, and desired accuracy, the usefulness of this single case study may be limiting.

Introduction

This paper describes the nozzle geometry used for comparing the predicted thermal radiation from the NEVADA (Net Energy Verification And Determination Analyzer) and TSS (Thermal Synthesizer System) computer codes to experimental data. To use an experimental test rig for code comparison purposes, required a geometry, measured surface temperatures, thermophysical properties, and a radiometer calibrated for the desired spectral wavelength band. For accuracy in predicting radiation propagation, extreme care was devoted to provide a direct correspondence between the test rig surfaces and the surfaces used within the thermal radiation codes. Selecting a nozzle for a code comparison provided the opportunity to study the level and path of multi bouncing radiation propagation.

Throughout this paper the term "model" will be used in two different applications. The term "model" will be applied when discussing the nozzle hardware geometry that is used in the test rig. The term "analytical model" is used to represent a data set that contains the information required to define the physical attributes of the test rig nozzle for analysis. The analytical model subdivides the nozzle geometry into a number of finite surfaces called nodes. The actual number of nodes and their geometry depends on the desired model representation, accuracy of results, structural design considerations, computer capabilities, and computer computational time requirements. Each nozzle node represents a uniform surface temperature over the entire node surface.

Axisymmetric Nozzle Test Rig Apparatus

A non-flowing, electrically heated rig was designed to verify calculated radiant energy propagation from a fixed axisymmetric convergent-divergent nozzle. The main components in the electrically heated rig are the nozzle model hardware, shields to mask unwanted radiant energy, and a radiometer. The nozzle model is heated and controlled using resistance wire which limits the maximum allowable temperature. A low temperature limit is set by the test rig operating conditions and the sensitivity of the radiometer. The axisymmetric convergent-divergent nozzle model used in the test rig is shown in Figure 1. Figure 2 shows the orientation of the 24 turbine exit guide vanes included in the model. The turbine rotor exit plane was represented by an electrically heated flat plate attached upstream of the vanes. A view of the nozzle in the electrically heated test rig is given in Figure 3. Two radiant energy shields between the nozzle model and the radiometer prevent background radiation from entering the radiometer. Both shields were cooled to 35 degrees Fahrenheit and painted with high emissivity paint. A Barnes Spectralmaster Infrared Research Radiometer measured the emitted nozzle radiant energy.

The nozzle model is constructed from .060" thick AISA 347 stainless steel with flanges of either spun or welded sheet metal. The model internal surfaces were grit blasted prior to final assembly. This grit blast operation provides the surface with diffuse reflecting characteristics. The nozzle model is mounted on a positioning system that provides dual axis azimuth and elevation orientation with respect to the radiometer. Extreme care was devoted to provide the required thermocouple instrumentation for determining nozzle model wall temperatures for use in the analytical model analysis. Thermocouples were required to record both axial and circumferential nozzle model temperature gradients. Axial temperature gradients were present through conduction between the model section flanges, while free convection inside the non-flowing model resulted in top-to-bottom temperature gradients from rising hot air. For this analysis comparison, a uniform temperature condition of 800 Degrees Fahrenheit was tested which resulted in a range of temperatures from 644 to 848 degrees.

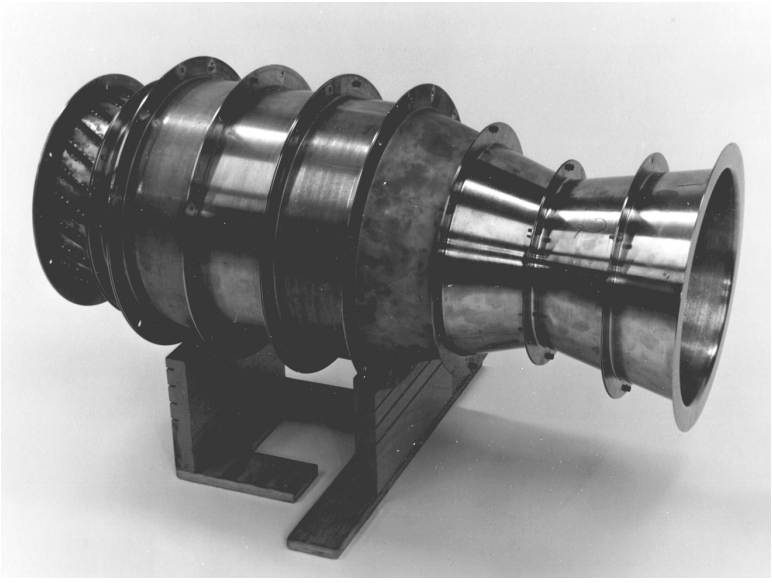

Figure 1. - Axisymmetric Nozzle Test Rig Model.

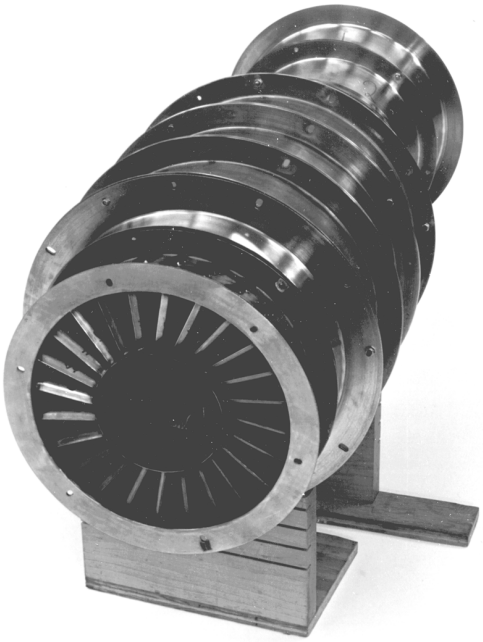

Figure 2. - View Of Nozzle Test Rig Model Vane Orientation.

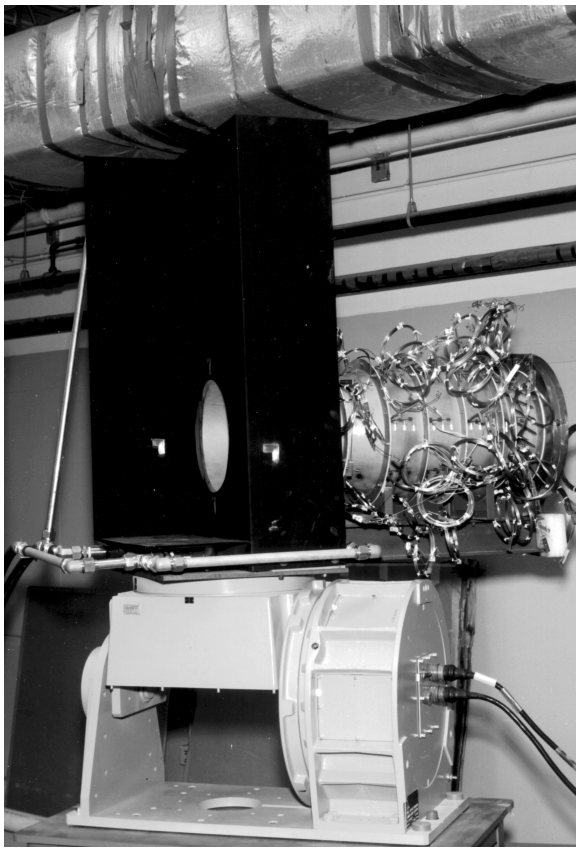

Figure 3. - Instrumented Nozzle Test Rig Model With Water Cooled Shield.

In the region between the divergent nozzle and the cooled radiant energy shield, a small separation gap exists to allow for nozzle thermal expansion. If the nozzle makes contact with the shield, the end of the divergent nozzle will experience some level of conductive cooling. If the nozzle does not expand to the shield, a small gap is possible. This gap or divergent nozzle cooling may present a boundary effect in the measured radiometer data. This boundary effect influence produces low-level changes in the radiometer data at off-axis angles.

Two radiant energy shields exist between the nozzle model and the radiometer. The first shield was installed at the nozzle exit plane to remove nozzle external surfaces, instrumentation, and various test rig apparatus from view of the radiometer. This shield provides an inside view of the nozzle, and is shown in Figure 3. A second, or foreground, shield was placed between the test rig and the radiometer. This shield was used to prevent background radiation from entering the radiometer. Both shields were cooled to 35 degrees Fahrenheit and painted with high emissivity paint. This high emissivity paint was added to absorb room radiation and prevent it from reflecting into the radiometer. The repositioning of the test rig nozzle model for different elevations and azimuths can require adjustments in the foreground shield and radiometer position. The placement and dimensions of the foreground shield were determined from the desired optical field of view of the radiometer. To maintain a radiometer response greater than 95%, an instrument incremental scan angle of five degrees was selected, based on a calibration with a small 1000 degree Centigrade blackbody source positioned at various angles from the radiometer centerline. This provided the shield center aperture dimensions.

A Barnes Spectralmaster Infrared Research Radiometer Model 12-550 Mark II was used to acquire the radiant energy. This spectral radiometer was positioned 36 feet from the axisymmetric nozzle. The radiometer optical head contains the following major components:

- A radiation telescope (Fore-Optics) for collecting radiation
- A 1000 Hz chopper for optically modulating the radiation
- A reference cavity (~56 degree's Centigrade) for comparison of target radiation with a standard reference radiation
- A cycling 340 position continuously variable spectral filter system for target wavelength determination from 1.306 to 14.536 microns
- A detector to convert the received radiation to electrical signal. An indium antimonide (InSb) sensor for wavelengths to approximately 5.5 microns, and mercury cadmium telluride (HgCdTe) sensor for wavelength above this level.

The precise wavelength band used in the test rig for code validation purposes was 2.9904 to 5.0201 microns.

Specimens of the nozzle surface material were tested to determine their optical surface properties. Normally bidirectional reflectivity data (BRDF) is use in these types of cavity analysis due to the influential relationship between multi bouncing radiation propagation and true surface absorption and reflectively characteristics. For this comparison, an integrated surface emissivity value was used for both emissions and reflections do to modeling limitations in TSS. For further information regarding the electrically heated test rig, see reference 1.

Radiation Analysis Computer Codes and Computer Operating Systems

The two thermal radiation analysis computer codes used in this comparison were NEVADA and TSS. Both programs are ray tracing programs. Each program has advantages and disadvantages based on its simulation of the fundamentals of radiation physics, analytical modeling requirements, computer requirements, solution convergence requirements, and accuracy and flexibility to solve both simple and complex problems. The following information introduces the computer codes and defines the computer systems used to run the programs.

NEVADA

The NEVADA 97 Software Package (Net Energy Verification And Determination Analyzer, ref. 3), is a series of computer programs which perform computer simulations of the Electro-Magnetic Theory of Radiation by means of advanced Monte Carlo techniques (statistical Ray Tracing). It is primary used in the thermal design and analysis of spacecraft, however, the broad capabilities of the software in modeling details associated with the laws of Optics, Physics & Light can and have been applied to a wide range of radiation heat transfer problems. NEVADA consists of 4 major programs:

RENO	Calculate View Factors (Fij's) and Interchange Factors (Bij's).
VEGAS	Calculate Solar Heat Inputs to an orbiting spacecraft.
SPARKS	3D visual modeling system of the NEVADA Software Package.
TNT	Automatic conversion of TRASYS models.

The programs can handle diffuse, specular, % specular reflectance, transmittance, refractance, translucence, and participating media. All surface properties can be dependent upon the angle of incidence and/or reflectance, or in accordance with a complete 2D, 3D, or 4D Bi-directional Reflectance Distribution Function (BRDF). There are 24 Surface Types available for defining your radiation geometry. TAC Technologies is the developer of the NEVADA Software Package.

Currently NEVADA runs on most computer systems (PC to CRAY Super Computer). The computer system used for the NEVADA analyses was a Pentium 100 MHZ. personal computer with 32.0 MB RAM, running Windows 95 operating systems (version 5.00.950a).

TSS

The Thermal Synthesizer System (TSS, ref. 4) is a user oriented thermal analysis tool that integrates geometric math model construction with Electro-Magnetic radiation simulation, thermal math model generation and the finite difference thermal analyzer, SINDA/FLUINT. The Monte Carlo Tracing and OCT-TREE surface intersection reduction algorithms are used to calculate radiation interchange factors and heating rates. TSS permits modeling of specularity, transparency, refraction, and angle of dependent properties in addition to the classical diffuse reflection modeling. The program uses 16 different surface types, six solid geometries and three CAD input elements to model the analysis geometry.

TSS runs on the Hewlett Packard workstation and on Personal Computers running a Unix emulator. The computer system used for the TSS analysis was a 90 MHZ. HP 735 workstation with 256 MB RAM running the HP-UX 10.20 operation system.

Background Analytical Modeling Information

There are a variety of analysis techniques used to simulate the propagation of radiant energy. Each analysis technique has advantages and disadvantages based on its simulation of the fundamentals of radiation physics, analytical modeling requirements, computer requirements, solution convergence requirements, accuracy and flexibility to solve both simple and complex problems. Since each computer code may have different operating efficiencies and computational tradeoffs, this nozzle analytical case was not optimized for any particular code, analysis conditions, or computational time minimizing techniques. So for code comparison purposes, this nozzle analytical model represents only one validation case for one set of analysis conditions. Since each computer code has advantages and disadvantages, the usefulness of this single nozzle baseline validation case can be limited or beneficial depending on the scope, requirements, and desired accuracy for code comparison purposes.

To simulate nozzle radiation propagation, typical analysis techniques calculate view factors and radiation interchange factors between the nozzle surfaces and outside environment. These results relate the percent of emitted surface energy that is incident and absorbed for each surface through direct and reflected radiant energy propagation. The percentages of absorbed energies can then be applied to energy balance equations. The influence of multi-reflecting radiation can lead to non-uniform incident and reflected radiant energy fluxes. Since some analysis techniques require uniform incident and reflected radiant energy fluxes on each surface node, smaller nozzle sectioning may be a requirement. See reference 2 for further information regarding limitations, advantages and disadvantages of analysis techniques. For this comparison case, the objective of the nozzle analytical model surface sectioning was to achieve the greatest possible accuracy in representing the test rig nozzle model. To accomplish this, the nozzle analytical model was sectioned to directly correspond with areas of uniform surface temperature in the test rig nozzle model. Thermocouples were required to record both axial and circumferential temperature gradients. Axial temperature gradients were present through conduction between the model section flanges, while free convection inside the model resulted in top-to-bottom temperature gradients from rising hot air.

Axisymmetric Nozzle Analytical Modeling Information

The nozzle analytical model geometry is defined by 288 surface nodes. The nozzle node sectioning and numbering sequence is shown in Figure 4. Figure 5 shows how the turbine rotor exit plane was modeled along with the vane support structure. The vane orientation sequence and surface numbering sequence are shown in Figure 6 and Figure 7. The complete nozzle analytical model is composed of four surface types: cylinder, disk, slant cone and polygon. Each of the 288 surface nodes represents surface areas of uniform temperature and surface thermophysical properties.

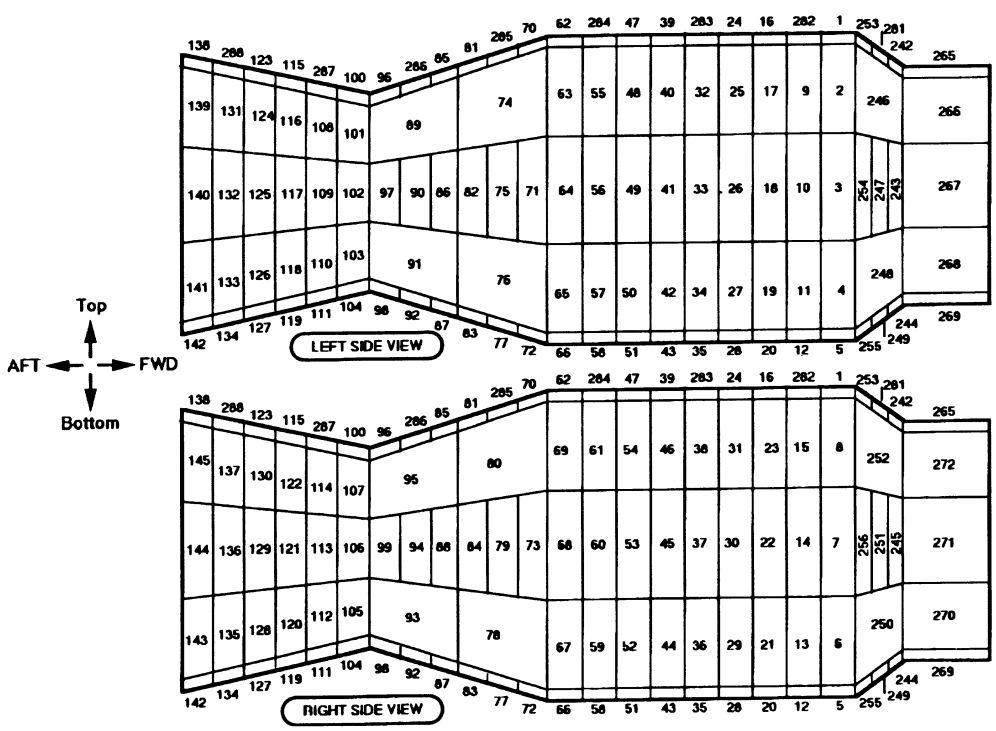

Figure 4. - Nozzle Surface Numbering Sequence.

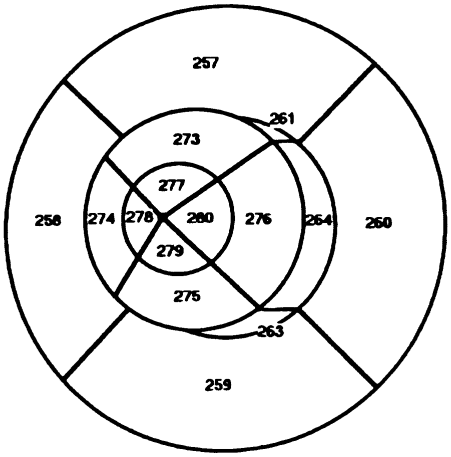

Figure 5. - Forward Turbine And Vane Support Surface Numbering Sequence.

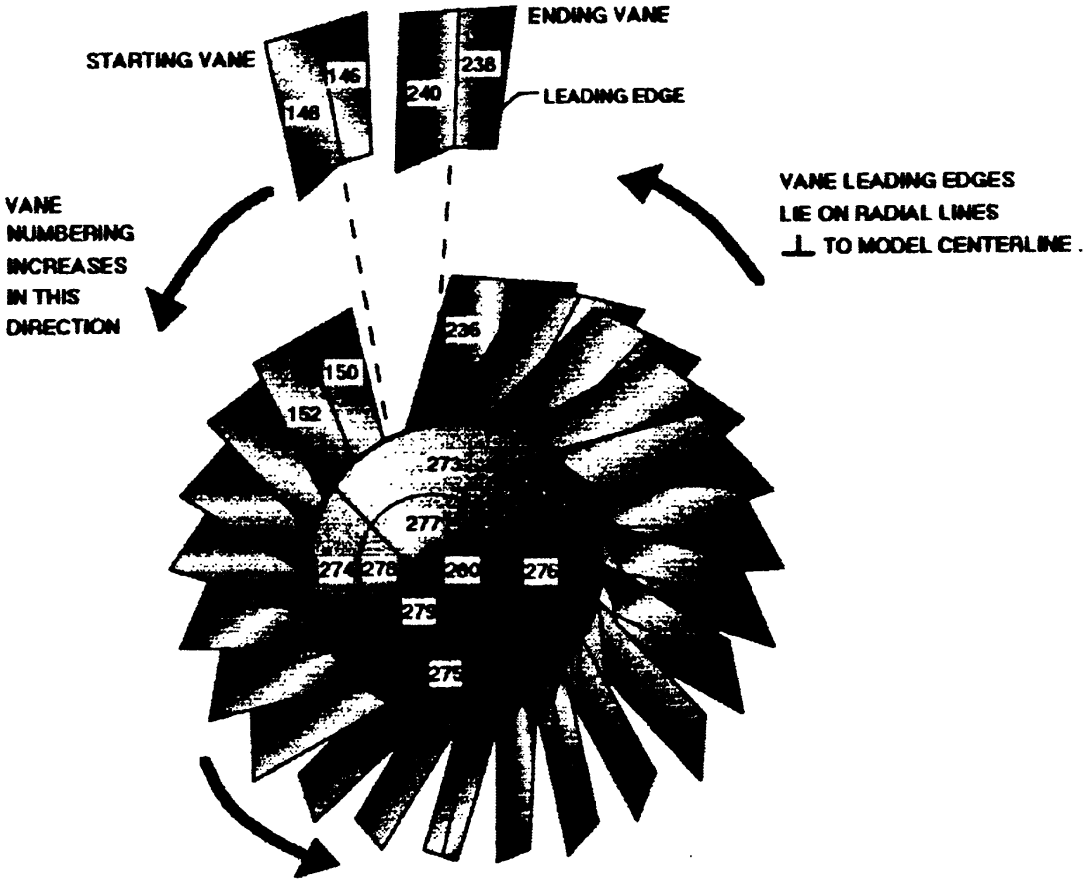

Figure 6. - Vane Orientation Sequence.

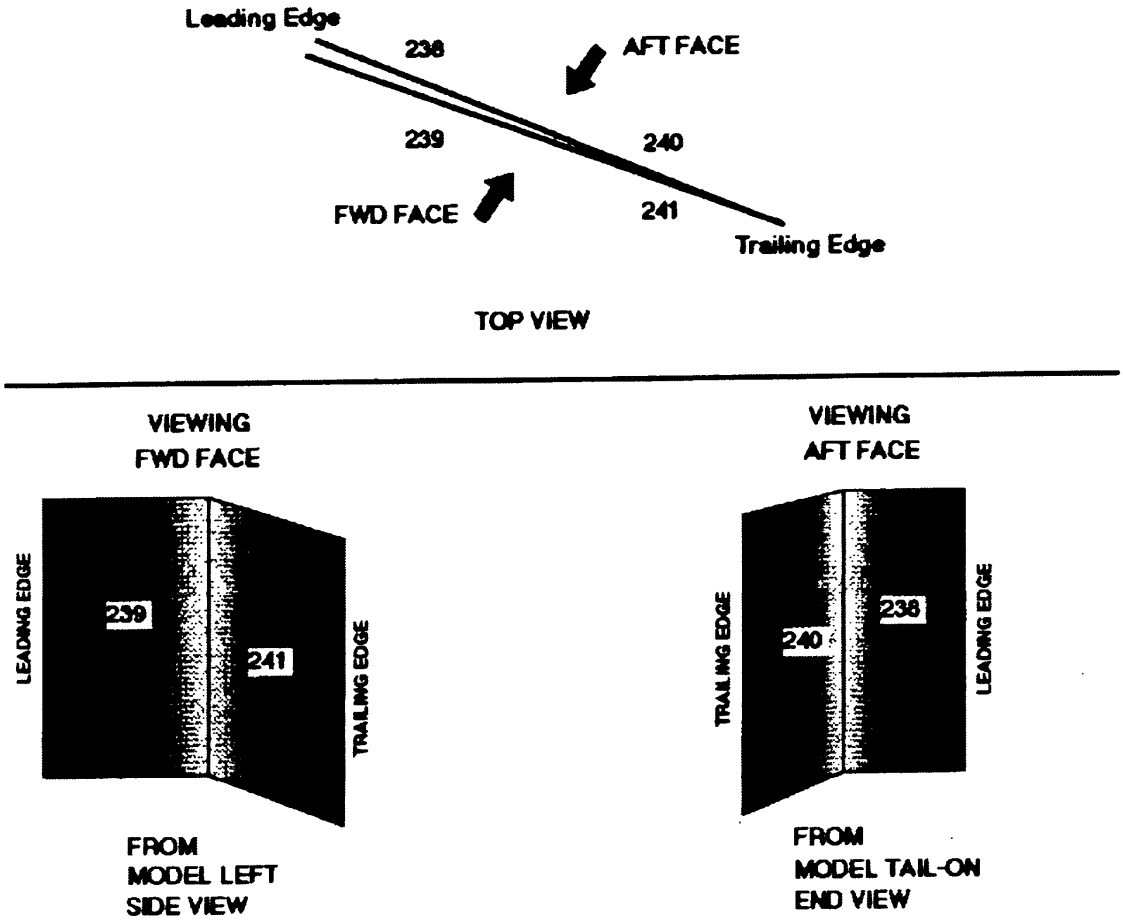

Figure 7. - Vane Surface Numbering Sequence.

Figure 8 displays a computer generated representation of the rig model used in both the NEVADA and TSS analysis. Figure 8 displays all 288 cavity emitting surfaces. An 18 node hemisphere, spherically sectioned, placed behind the cavity exit plane is used to absorb emitted cavity surface radiation, as shown in figure 9. The radiation interchange factors from the cavity surfaces to the hemisphere surfaces represent the radiation propagation path. The radiation interchange factors are then supplied to a program which applies the surface temperatures, surface emissivity values, and wavelength band factors. The program sums this radiation energy to the hemisphere sections and outputs the results in Watts per unit solid angle (Watts/steradian). The results are then modified to include atmosphere absorption along the path between the cavity and the hemisphere. The NEVADA and TSS results are then compared directly to the experiment rig mode results.

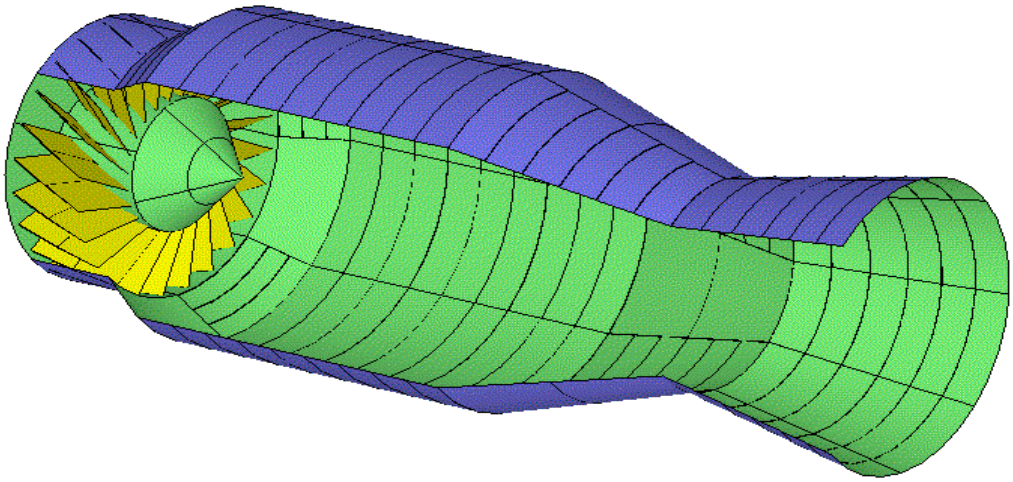

Figure 8. - Computer Cavity Model.

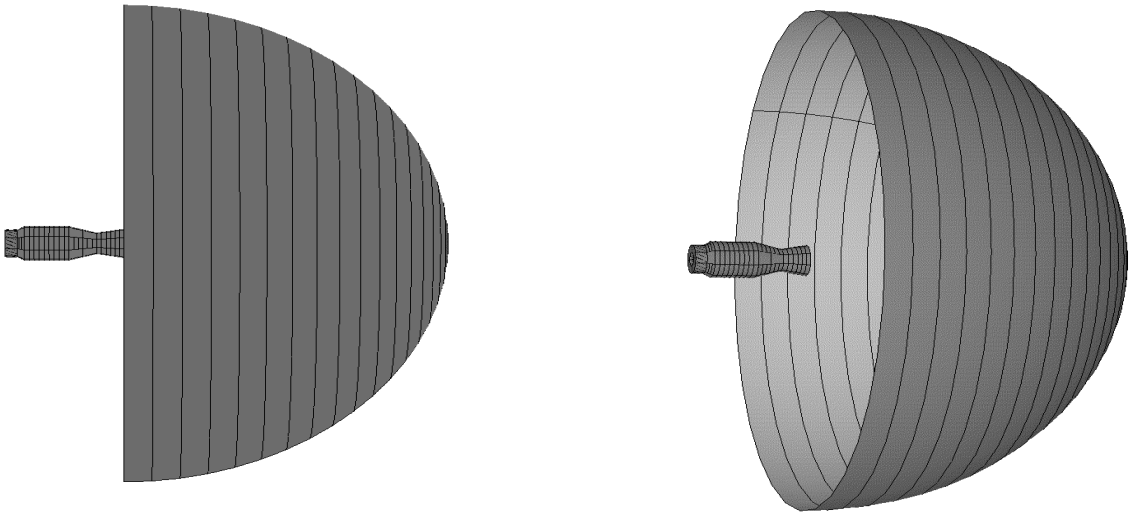

Figure 9. - Computer Hemisphere Model.

Surface thermophysical properties were experimentally measured for defining the nozzle surface emissivity and reflectively. For this comparison between NEVADA and TSS a specific case was select with a black coating to minimize the strong relationship between multi bouncing radiation propagation and true surface characteristics for nonblackbody surfaces. Bidirectional reflectivity data (BRDF) was measured for defining the nozzle surface emissivity absorption and reflection characteristics. This BRDF data was integrated over all angles to derive a uniform surface emissivity and reflectivity value. This was required due to the TSS program not having BRDF modeling capabilities. For this comparison a 0.6 hemispherical emissivity value in the 3 to 5 micron wavelength band of the IR spectrum was used.

The data from the test rig radiometer established the total nozzle emitted radiant energy propagation pattern for comparison to analytical code predictions at defined radiometer locations. The locations used to measure the nozzle emitted radiant energy are listed in table 1, all elevation angles were 0.0 degrees.

Table 1, Radiometer Positioning With Respect To The Nozzle Test Rig

AZIMUTH ANGLE (degrees)	0.0	2.5	5.0	10.0	15.0	20.0	30.0	40.0	50.0	60.0	70.0	80.0

The 0.0 degree azimuth and elevation location represents the axial direction, or angle normal to the nozzle exit plane. At these locations the radiometer measured total nozzle emitted radiant energy over the 3.0 to 5.0 micron wavelength band, in watts/steradian. The measured radiometer results including atmospheric radiant energy attenuation effects. Figure 10 shows the atmospheric radiation transmissivity data to simulate the atmosphere absorption effects between the model and the radiometer. This data represents the total radiation transmissivity for a tropical atmosphere at a range of 36 feet in the 3.0 to 5.0 micron wavelength band.

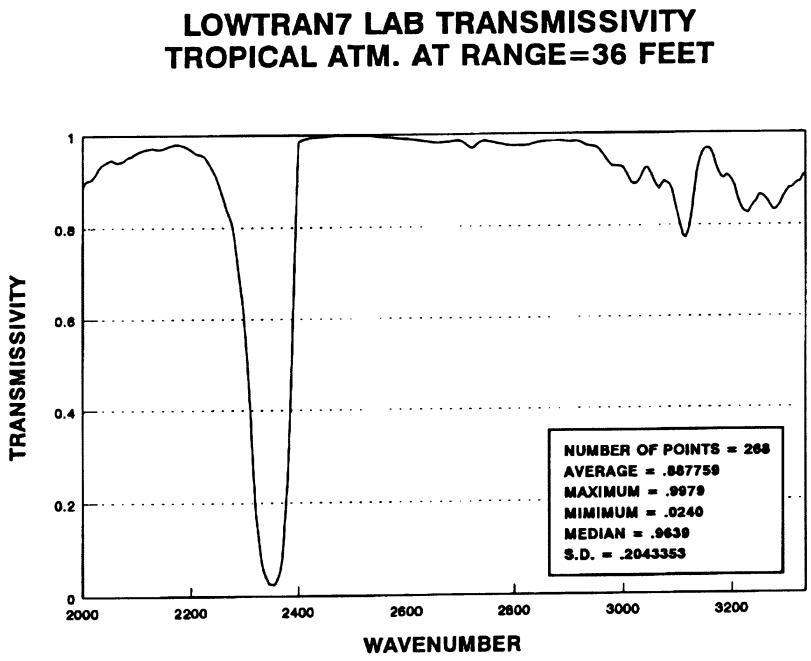

Figure 10. - Atmospheric Transmissivity Data From Model To Radiometer.

Nozzle Test Rig Experimental Data

The radiometer test data established the total nozzle emitted radiant energy propagation pattern for comparison to analytical code predictions. Table 2 gives the experimental measured total nozzle emitted radiant energy, in watts/steradian for the 3 to 5 micron wavelength band. This data includes atmospheric attenuation. The Data in table 2 will be used in comparing the NEVADA and TSS analytical predictions.

Table 2, Test Rig Nozzle Model Radiometer Results

AZIMUTH ANGLE (degrees)	0.0	2.5	5.0	10.0	15.0	20.0	30.0	40.0	50.0	60.0	70.0	80.0
ENERGY (Watts/ steradian)	65.4	63.9	61.8	59.2	57.9	56.3	49.2	40.1	30.1	20.0	12.0	3.0

Analytical Modeling Cases And Results

For this comparison between the NEVADA and TSS programs, no modeling optimizing techniques were applied to enhance code performance. The identical model was use in both NEVADA and TSS. The presented results are in the 3 to 5 micron wavelength band. The following parameters were applied to both computers codes:

- Random rays were emitted with a Lambertian distribution.
- Ray were terminated once energy level fell below .01.
- View factors and radiation interchange factors were calculated through ray tracing.
- Modeled in units of inches.
- Each cavity surface emitted the specified number of rays.

For this analysis comparison the term View Factors (Fij's) are defined as: the fraction of energy leaving blackbody i that is directly absorbed by blackbody j. Radiation Interchange Factors (Bij's) are defined as: the fraction of energy leaving graybody i that is absorbed by graybody j including ALL intervening reflections".

Three cases were analyzed by both the NEVADA and TSS programs. Table 3 list the cases defined by different thermophysical properties. The first case represents conditions identical to the experimental test rig. The second and third cases represent conditions where surface specularity can effect ray propagation path.

Table 3, Analytical Modeling Case Conditions

	Nozzle Surface Emissivity	Surface Reflectance
Case 1	0.6	Diffuse
Case 2	0.6	50% Specular
Case 3	0.3	50% Specular

The 50% specular condition represents approximately 50% of reflecting energy that obeys the laws of specular reflection and 50% diffuse reflection.

The results for the three case are presented in the following tables and graphs. For the Case 1 condition, the number of rays emitted from the surfaces were varied to evaluate the convergence of the results as well as the number of radiation interchange factors produced and run time. The run times only serve as a gauge for comparison. Running NEVADA on a Pentium 100 MHZ. personal computer provides easy adjustment to faster computer systems. Table 4 presents Case 1 code performance results in terms of CPU time and the number of radiation interchange factors produced.

Table 4, NEVADA and TSS Code Performance Results For Case 1

	Number of Rays	5,000	10,000	20,000	50,000
NEVADA	Run Time	1hr. 56min.	3hr. 48min.	7hr.36min.	19hr. 02min.
	Number of Radiation Interchange Factors Produced	85,422	86,579	87,340	87,819
TSS	Run Time	20min.	40min.	1hr. 20min.	3hr. 20min.
	Number of Radiation Interchange Factors Produced	86772	87747	88089	88126

Adjusting NEVADA to a Pentium 400 MHZ. personal computer would provide comparable CPU speed to the TSS runs. In Case 1, each modeled nozzle surface can see every other modeled nozzle surface. This results in 88128 possible radiation interchange factors. Table 4 shows that both NEVADA and TSS produced comparable numbers of radiation interchange factors. Figure 11 and 12 displays how the number of rays emitted from the surfaces effected NEVADA and TSS results convergence.

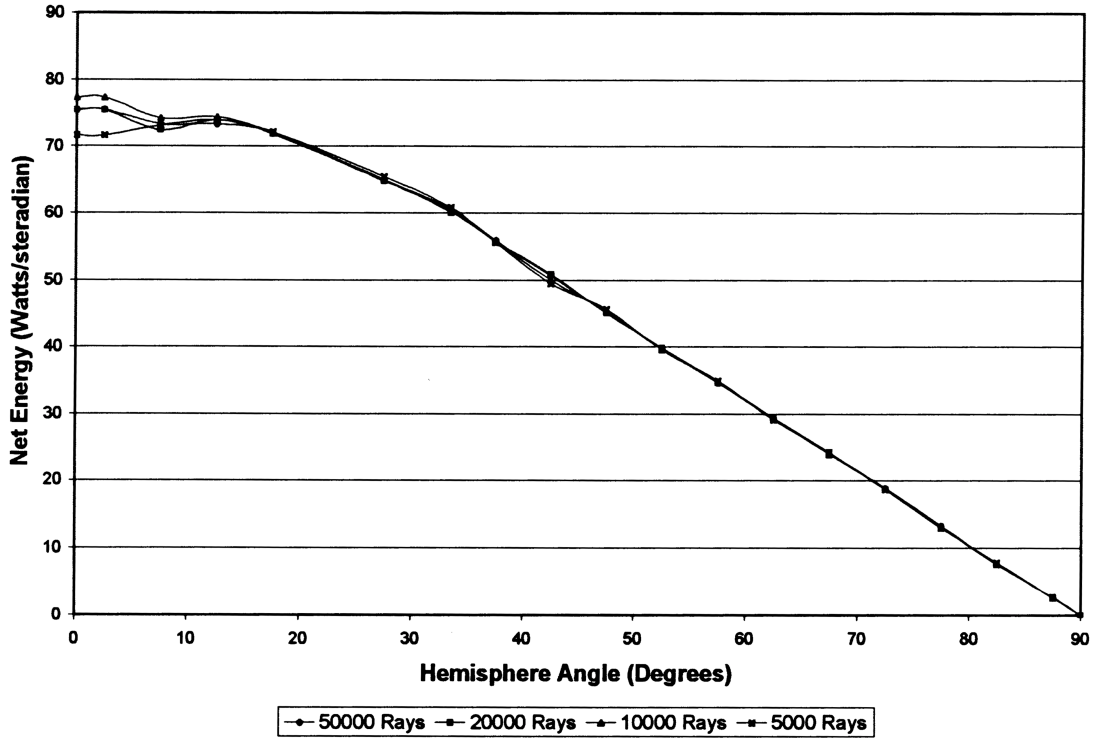

Figure 11. - Case 1 Net Hemisphere Absorbed Energy
Using NEVADA Radiation Interchange Factors.

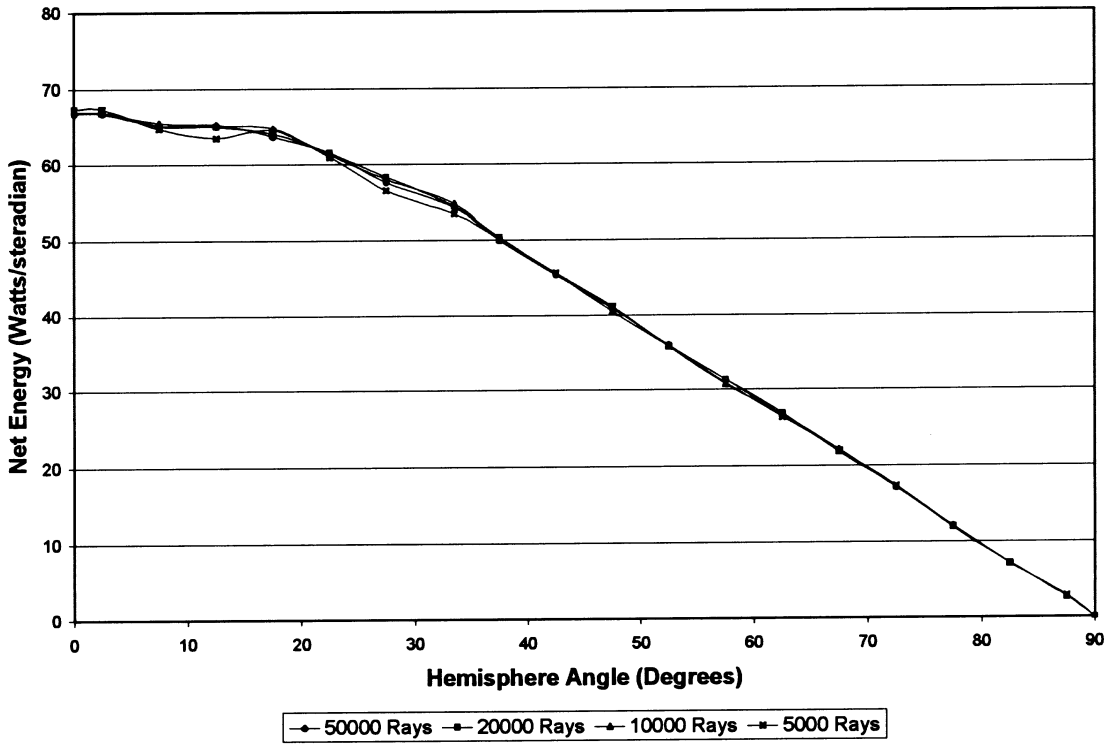

Figure 12. - Case 1 Net Hemisphere Absorbed Energy
Using TSS Radiation Interchange Factors.

Figure 13 compares the net hemisphere absorbed energy from NEVADA and TSS radiation interchange factors for Case 1. Both NEVADA and TSS produced comparable overall results for Case 1. To compare the differences between computer code predictions, individual nozzle component contributions to the total emitted radiant energy can be compared. Appendix A lists the radiation interchange factors for surface node 150 (vane surface) to the hemisphere surfaces. Upon inspection of individual radiation interchange factors, NEVADA and TSS can have large differences that are not evident from the total answers. These differences would be evident if a more radical model temperature profile was analyzed.

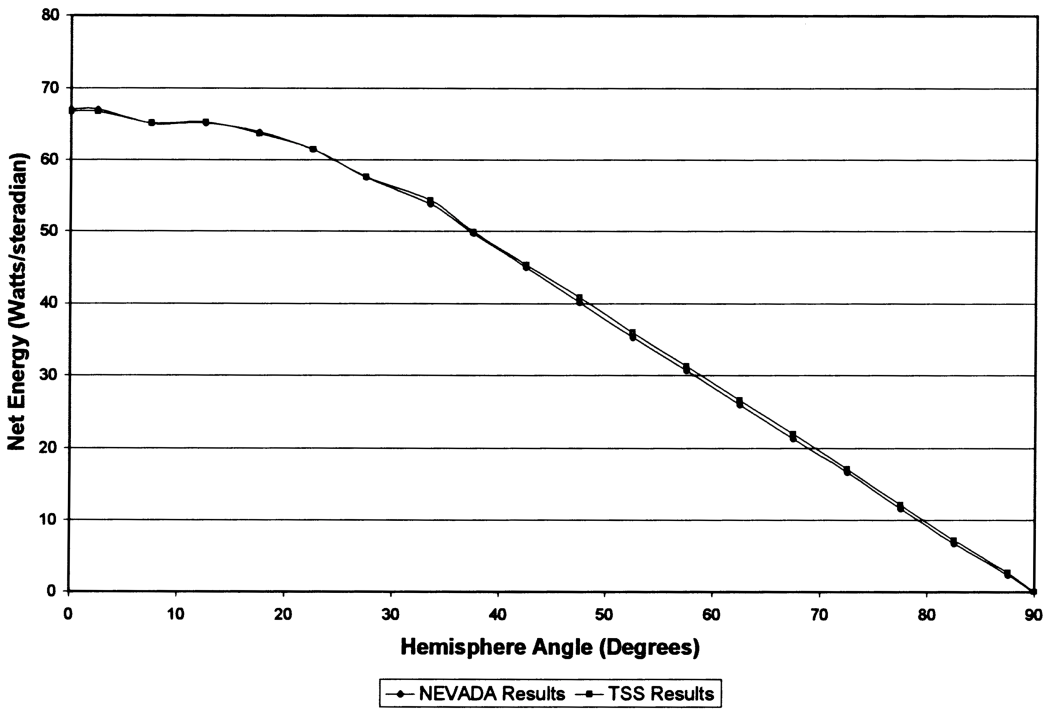

Figure 13. - Comparing Case 1 Net Hemisphere Absorbed Energy
Using NEVADA and TSS Radiation Interchange Factors
(50,000 Ray).

Table 5 presents Case 1, Case 2 and Case 3 code performance results. Comparing these cases will show surface specularity effects on the program solutions. Table 5 shows that surface specularity produces longer NEVADA CPU run times then TSS, and that both NEVADA and TSS produced comparable numbers of radiation interchange factors. Figure 14 displays that both NEVADA and TSS produced comparable overall results for Case 1, Case 2, and Case 3. Case 3 does point out potential code differences with surface specularity. Appendix A lists the radiation interchange factors for surface node 150 (vane surface) to the hemisphere surfaces. Upon inspection of individual radiation interchange factors, NEVADA and TSS can again have large differences that are not evident in the total answers. These differences would be evident if a more radical model temperature profile was analyzed.

Table 5, NEVADA and TSS Code Performance Results For Case 1, Case 2 and Case 3

	Number of Rays	Case 1 50,000	Case 2 50,000	Case 3 50,000
NEVADA	Run Time	1hr. 56min.	33hr. 50min.	57hr. 50min.
	Number of Radiation Interchange Factors Produced	85,422	87,959	88,128
TSS	Run Time	20min.	3hr. 7min.	5hr. 56min.
	Number of Radiation Interchange Factors Produced	86772	88127	88128

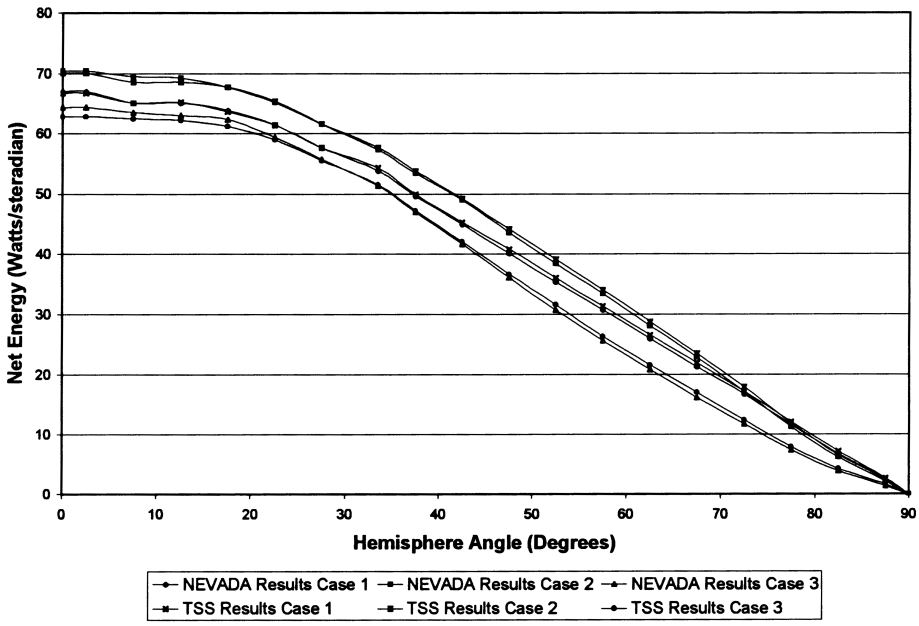

Figure 14. - Comparing Case 1, Case 2 And Case 3 Net Hemisphere Absorbed Energy Using NEVADA and TSS Radiation Interchange Factors (50,000 Rays).

Experimental Data and Analytical Model Results Comparison

Figure 15 compares the net hemisphere absorbed energy from NEVADA and TSS radiation interchange factors and the test rig data for the 50,000 ray case. The results are in the 3 to 5 micron wavelength band.

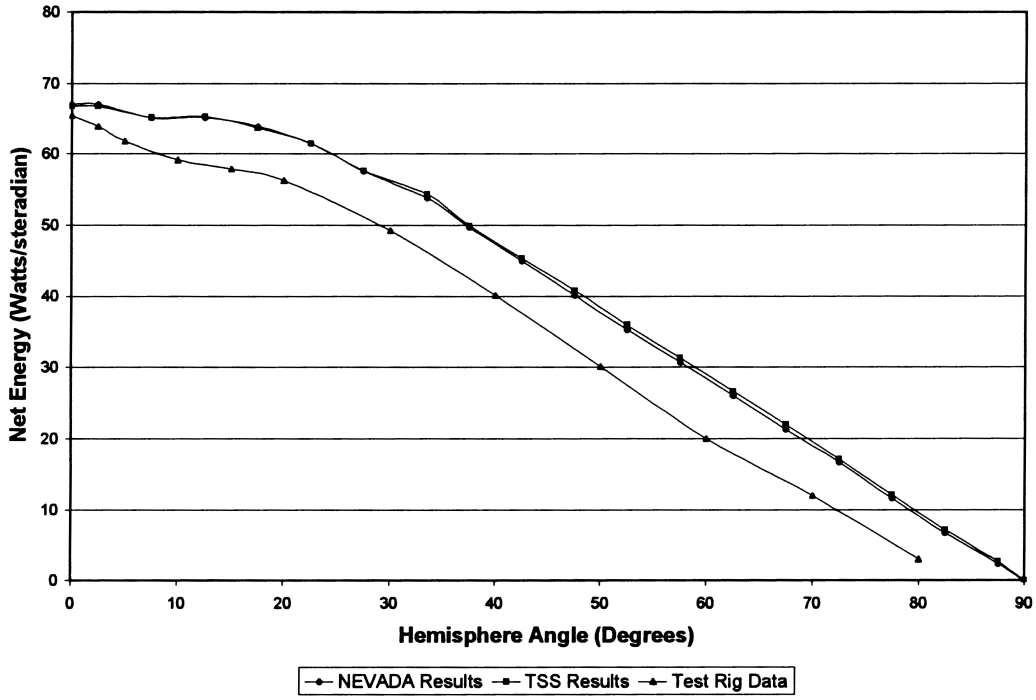

Figure 15. - Comparing Net Hemisphere Absorbed Energy From NEVADA and TSS Radiation Interchange Factors For Case 1 And The Test Rig Data (50,000 Ray)

The results in Figure 15 shows a separation between experimental and predicted results for angles greater then 0.0 degrees. For Case 1, direct cavity emission dominates at the 0.0 azimuth angle, while at off angles it is a function of both cavity emitting and reflecting characteristics. Because of this, NEVADA and TSS compare with the experimental data at the 0.0 azimuth angle. At other angles the cavity surface reflecting properties begin to effect overall results. Bidirectional reflectivity data (BRDF) is used in these types of cavity analysis due to the influential relationship between multi bouncing radiation propagation and true surface absorption and reflectively characteristics. For this comparison, an integrated surface emissivity value was used for both emissions and reflections do to modeling limitations in TSS. Using an integrated surface emissivity value can remove reflecting lobes that can greatly effect radiation propagation.

Concluding Remarks

Thermal analysis in both simple and complex models can require calculating the propagation of radiant energy to and from multiple surfaces. This can be accomplished through simple estimation techniques or complex computationally intense computer modeling simulations. Currently there are a variety of computer analysis techniques used to simulate the propagation of radiant energy, each having

advantages and disadvantages. The major objective of this effort was to compare two ray tracing radiation propagation analysis programs (NEVADA and TSS) with experimental data. Results from a non-flowing, electrically heated test rig was used to verify the calculated radiant energy propagation from a nozzle geometry that represents an aircraft propulsion nozzle system.

In general the programs produced comparable overall results, and results slightly higher then the experimental data. The results shows a separation between experimental and predicted results for angles greater then 0.0 degrees. Upon inspection of individual radiation interchange factors, differences were evident and would have been magnified if a more radical model temperature profile was analyzed. For this comparison, an integrated surface emissivity value was used for both emissions and reflections do to modeling limitations in TSS. Using an integrated surface emissivity value will remove reflecting lobes that can greatly effect radiation propagation. Bidirectional reflectivity data (BRDF) was not used do to modeling limitations in TSS. Modeling surface specularity did produce some differences in the analytical results.

Both NEVADA and TSS produced comparable numbers of radiation interchange factors for all analyzed cases. NEVADA had comparable CPU time to TSS for the diffuse cases and longer CPU time for specular cases.

For code comparison purposes, this nozzle geometry represents only one case for one set of analysis conditions. Since each computer code has advantages and disadvantages bases on scope, requirements, and desired accuracy, the usefulness of this single case study may be limiting.

References

1. Baumeister, J.F.: "Radiant Energy Measurements From a Scaled Jet Engine Axisymmetric Exhaust Nozzle For A Baseline Code Validation Case", NASA TM-106686, 1994.

2. Baumeister, J.F.: "Application of Ray Tracing in Radiation Heat Transfer", NASA TM-106206, 1993.

3. 1998, “NEVADA User’s Manual”, 13th Edition, Version 21, TAC Technologies.

4. 1997, “Thermal Synthesizer System User Manual”, Release 6.01, Lockheed Martin Space Mission Systems and Services under NASA contract NAS9-19100.

Appendix A - Radiation Interchange Factor Comparison For a Nozzle Surface

The following information is presented to show the differences in radiation interchange factors between the NEVADA and TSS programs. The results are for the 50,000 rays per surface cases. Node 150 represents a small vane surface (figure 6). Nodes 1001 to 1018 represent the hemisphere surfaces, where 1018 is the section directly behind the nozzle. The results are for the diffuse case, specular case with surface emissivity =.6, and specular case with surface emissivity =.3. The specular cases represents 50% diffuse and 50% specular surface reflections.

Diffuse Case

Node	Emiss.	Node	Emiss.	Bij (NEVADA)	Bij (TSS)
150	0.600	1001	1.000	0.00001	0.00001
150	0.600	1002	1.000	0.00001	0.00003
150	0.600	1003	1.000	0.00000	0.00001
150	0.600	1004	1.000	0.00000	0.00001
150	0.600	1005	1.000	0.00001	0.00002
150	0.600	1006	1.000	0.00001	0.00002
150	0.600	1007	1.000	0.00001	0.00002
150	0.600	1008	1.000	0.00002	0.00005
150	0.600	1009	1.000	0.00002	0.00003
150	0.600	1010	1.000	0.00003	0.00006
150	0.600	1011	1.000	0.00004	0.00014
150	0.600	1012	1.000	0.00008	0.00014
150	0.600	1013	1.000	0.00009	0.00010
150	0.600	1014	1.000	0.00015	0.00024
150	0.600	1015	1.000	0.00087	0.00109
150	0.600	1016	1.000	0.00098	0.00091
150	0.600	1017	1.000	0.00088	0.00098
150	0.600	1018	1.000	0.00049	0.00025

Specular Case (Emissivity =.6)

Node	Emiss.	Node	Emiss.	Bij (NEVADA)	Bij (TSS)
150	0.600	1001	1.000	0.00001	0.00002
150	0.600	1002	1.000	0.00001	0.00001
150	0.600	1003	1.000	0.00001	0.00001
150	0.600	1004	1.000	0.00003	0.00002
150	0.600	1005	1.000	0.00005	0.00003
150	0.600	1006	1.000	0.00004	0.00004
150	0.600	1007	1.000	0.00007	0.00004
150	0.600	1008	1.000	0.00009	0.00007
150	0.600	1009	1.000	0.00018	0.00013
150	0.600	1010	1.000	0.00046	0.00035
150	0.600	1011	1.000	0.00038	0.00044
150	0.600	1012	1.000	0.00034	0.00036
150	0.600	1013	1.000	0.00068	0.00068
150	0.600	1014	1.000	0.00092	0.00099
150	0.600	1015	1.000	0.00135	0.00165
150	0.600	1016	1.000	0.00119	0.00136
150	0.600	1017	1.000	0.00116	0.00101
150	0.600	1018	1.000	0.00063	0.00033

Specular Case (Emissivity =.3)

Node	Emiss.	Node	Emiss.	Bij (NEVADA)	Bij (TSS)
150	0.300	1001	1.000	0.00004	0.00007
150	0.300	1002	1.000	0.00008	0.00011
150	0.300	1003	1.000	0.00015	0.00020
150	0.300	1004	1.000	0.00024	0.00020
150	0.300	1005	1.000	0.00027	0.00033
150	0.300	1006	1.000	0.00031	0.00041
150	0.300	1007	1.000	0.00044	0.00055
150	0.300	1008	1.000	0.00066	0.00086
150	0.300	1009	1.000	0.00131	0.00124
150	0.300	1010	1.000	0.00223	0.00196
150	0.300	1011	1.000	0.00240	0.00268
150	0.300	1012	1.000	0.00214	0.00219
150	0.300	1013	1.000	0.00330	0.00327
150	0.300	1014	1.000	0.00369	0.00373
150	0.300	1015	1.000	0.00411	0.00478
150	0.300	1016	1.000	0.00340	0.00336
150	0.300	1017	1.000	0.00234	0.00235
150	0.300	1018	1.000	0.00100	0.00088

TWO-PHASE CENTRAL THERMAL CONTROL SYSTEM (TPS) OF INTERNATIONAL SPACE STATION «ALPHA» RUSSIAN SEGMENT

Y.I. Grigoriev, V.M. Cykhotsky, A.N. Sementsov, and Y.M. Prokhorov
Rocket-Space Corporation "ENERGIA"
Koroliov, Russia 141070

G.A. Gorbenko and C.A. Malukhin
Center of Technical Physics of Kharkov Aviation Institute
Kharkov, Ukraine 310070

ABSTRACT

International Space Station ALPHA Russian Segment (ISSA RS) will present an assembly of many modules with total heat load up to 30 kilowatts. Collection, transport and rejection of heat in outer space will be provided by Central Thermal Control System (TPS).

The TPS is being designed and built by Rocket-Space Corporation "ENERGIA" (Russia). The TPS design concept is commonly referred to as a "thermal bus" concept, when single-phase thermal control systems of individual modules are connected with central TPS through Evaporative Heat Exchangers (EHEX). Pump forces liquid coolant to pressure line, where it is fed to evaporative heat exchangers through actively controlled Flow Control Valves (FCV) if necessary. FCV maintains high ammonia vapor quality at the EHEX exit. Vapor gets condensed in condensers of heat pipe-based Central Heat Exchanger-Radiator (RAD). Then, heat is distributed all over the RAD due to heat pipes.

Heat Controlled Accumulator (HCA) maintains nearly constant pressure in vapor line. TPS has a number of auxiliary elements: Electric Heater (EH) in pressure line prevents the system from low temperatures under low heat loads, the Heat Exchanger-Regenerator (RHEX) heats up liquid ammonia entering the HCA, Separator (S), non-condensable gas trap, a number of flow control valves.

To maintain proper thermal regime of the station some control methods of the TPS elements have been suggested. Namely, how to control FCV operation, RAD panel rotation, Electric Heater on/off turning and bypass valves operation. Results of mathematical modeling and experimental investigations carried out in the Center of Technical Physics of Kharkov Aviation Institute (CEP KhAI) (Ukraine) are presented. It is proved the TPS Parameters Control System designed to be reliable.

ISSA CONCEPT DESCRIPTION

International Space Station ALPHA (ISSA) will present an assembly of many modules with total heat a few tens of kilowatts. The collection, transport and rejection of low-potential heat will be provided by Central Two-Phase Thermal Control System (TPS).

Current thermal control technology, using single-phase liquid coolant loops, proved itself to be acceptable for the individual Space Station "MIR" modules with heat load a few kilowatts. The operational conditions and parameters of the TPS of ISSA Russian Segment significantly differ from ones of individual modules.

The basic differences are the following:

- high heat load (tens of kilowatts);
- long heat transport distance (tens of meters);
- no radiator surface excess, partial radiator shadowing by Station structure elements;
- necessity to satisfy diverse requirements in heat load ranges and heat sink temperatures of the internal heat transport loops of the individual modules.

The collaborative research by RSC "ENERGIA" and KhAI (refs.1, 2) showed that under high heat loads and long heat transport distances two-phase thermal control system has the advantages over single-phase one in mass and in ability to satisfy users' requirements.

Numerous investigations on TPS were carried out since 1979 for "Freedom" Station (NASA) and for "Columbus" Station (ESA) (refs.3, 4). As a result, experts in USA, Western Europe, Russia and Ukraine arrived at a similar conclusion about TPS concept of design, which is being used now for ISSA Russian Segment. This concept is commonly referred to as a thermal bus concept, when single-phase thermal control systems of the individual modules are connected with central TPS through external evaporative heat exchangers. Thermal bus concept provides stable thermal regime at any number of attached modules and at variations in heat loads. Analysis of the thermophysical and operational properties of the various coolants has shown that ammonia is the most appropriate coolant for ISSA TPS and R-114 or R-113 are the most appropriate ones for test beds.

The accepted ISSA TPS concept contains the following basic elements:

- two-phase coolant (ammonia) is used;
- stable evaporative coolant temperature within heat collection sections is maintained according to a nearly constant pressure level in two-phase line due to Heat-Controlled Accumulator (HCA);
- insensitivity to heat load placement and value;
- the ammonia flow-rate through external heat exchangers is controlled by active flow control valves;
- high vapor quality at the evaporative heat exchangers exits and at the condensers inlets (x~0,8...1,0);
- nearly constant mechanical pump pressure head and flow control valve pressure drop;
- the system should be continuously able to accommodate heat loads of the modules;
- minimum use of the electromechanical control elements to provide proper TPS functioning and control;
- minimum thermal resistance across all the heat transport sections;
- prevention of the supercooling of the mechanical pump, flow control valves and evaporative heat exchangers under low heat loads;
- minimum volume of coolant space;
- on-orbit start-up, stop and restart capability;
- components and system ground testing capability;
- non-condensable gases blockage insensitivity;
- set point temperature variation capability within heat collection sections;
- maintenance and repair by crew;
- on-orbit repriming capability;
- serviceability of the system if some elements fails to operate;

The principal scheme of ISSA TPS is shown in figure 1. The system presents a branching thermal-hydraulic network including liquid ammonia pressure line 1, liquid ammonia bypass line 2 and two-phase ammonia line 3. Pump forces liquid ammonia to the pressure line, where it is fed to evaporative heat exchangers through flow control valves (FCV). In evaporative heat exchangers (EHEX) liquid ammonia collects heat loads of modules and vaporizes. The scheme includes an evaporative heat exchanger of one individual module only. In reality, the number of them can be more than seven.

Two-phase flow exiting evaporative heat exchangers passes through regenerative heat exchanger (RHEX), separators (S), rotary hydraulic joint (RHJ) and enters the radiator-heat exchangers (RAD). Here it gets condensed, mixed with bypass liquid, subcooled and through RHJ flows back to the pump inlet.

FCV provides variation of ammonia flow rate through EHEX in proportion with heat load thus maintaining high vapor quality of the EHEX exit. FCV is parallel assembly of three valves with graduated throttles. Various combinations of open and close valves provide 7 levels of ammonia flow rate through EHEX.

Heat-controlled accumulator (HCA) maintains constant pressure level in the system. HCA is a tank filled with ammonia liquid and vapor. Pressure and temperature control is based on variation of heat input (rejection) to (from) coolant in HCA. The maximum electric power of HCA is 200W but time-average one does not exceed 25W.

Electric Heater (EH) (Q=1.8 kW) heats the entering liquid coolant under low heat loads conditions, thus preventing the TPS basic elements from low temperatures.

Separator (S) removes liquid from vapor flow thus improving efficiency of condenser and reducing vapor line pressure loss under high heat loads.

Non-condensable Gas Trap (NGT) collects gases and removes them out of the loop.

The loop includes a number of throttles and valves providing optimal flow distribution at various heat loads. There are some repriming accumulators (not depicted on the scheme).

Figure 2 shows the principal schematic of the internal liquid loop of the individual module and connection with central TPS through EHEX.

Heat-rejection subsystem presents heat-pipe based Central Radiating Heat Exchanger (RAD) (Fig. 3). Such a design reduces a danger of puncture of RAD by micrometeoroids and improves uniformity of the RAD temperature field. RAD panel has a size 20x4 m and will be permanently oriented in parallel to solar radiation. The effective RAD radiating surface is 150 m^2. The basic heat rejection related element of RAD is 2 m length finned grooved heat pipe 5 attached to condenser 6 and subcooler 7. The number of heat pipes is 250. Vapor and bypassing liquid enter RAD through rotary hydraulic joint (RHJ) 11. RAD hydraulic network consists of 5 identical paths. Vapor flow is distributed in all paths with equal quality by special splitter 4. Vapor is condensed in condensers 6, then through throttles 10 enters subcooler 7 and mixes with bypassing liquid. At the exit of each path subcooler 9 is installed.

The basic design parameters of the system are the following:

- heat rejection up to 30 kW;
- maximum heat transport distance L=50 m;
- two-phase ammonia temperature in evaporative heat exchangers t=10±2,5°C (adjustable);
- heat load variation rate dQ/dt < 2kW/minute;
- pump design conditions ΔP=0.15 MPa, m=90gr/sec;
- liquid ammonia temperature at the radiator exit T>-65°C;
- pump positive suction head ΔP_{cav} > 0,8atm (ΔT > 4K);
- electric power consumption Q<200 W (without power of EH Q_{EH} = 1.8kW);
- volume of the coolant space (without HCA) V=40 litters;
- thermal resistance - temperature difference between evaporative heat exchangers boiling temperature and condensation temperature in condenser ΔT < 4°C at Q=30kW.

MATHEMATICAL MODELING OF THE TPS

The performances of two-phase loop depend basically upon system effects caused by mutual interaction between the elements under variable heat input and heat rejection conditions. Study of those effects, computation of steady and transient performances, choice of rational procedures of regulation, analysis of stability of the system and subsystems can be conducted most rationally with the use of adequate mathematical models. The approach and procedure of mathematical modeling of multicomponent two-phase heat transport systems developed in KhAI have the following basic features:

- presentation of multicomponent branching two-phase loops in the form of equivalent hydrodynamic and thermal networks;
- integration of hydrodynamic and thermal networks through heat transfer laws;
- modeling of the system real elements by idealized elements carrying fundamental real elements properties: coolant mass and energy accumulation, positive (mechanical pump) and negative (hydraulic resistance) momentum sources properties, coolant mechanical inertia, thermal capacitance of structure. The idealized elements describe a real heat transfer loop clearly.

All the idealized elements are divided into two groups:

1) elements intended to model hydrodynamic processes in coolant;
2) elements intended to model thermal processes in structure.

Basic idealized hydrodynamic processes related elements are control volumes and paths; thermal processes related elements are thermal nodes and thermal conductors (Fig. 4).

Control volume is being described by the basic mass and energy conservation laws equations in form of ordinary differential equations:

$$\frac{dM_k}{dt} = \sum m_j, \frac{dU_k}{dt} = \sum m_j \cdot i_j^* + q_{w-f,k} \cdot F_{w,k} + W_k.$$

Path is described by the momentum conservation law equation:

$$\frac{dm_j}{dt} = \frac{F_j}{L_j} \cdot \left(P_k - P_{k+1} + \Delta P_{fr} + \Delta P_a + \Delta P_p + \Delta P_g\right)$$

Thermal node is described by the energy conservation law equation in the following form:

$$\rho_{w,k} \cdot C_{w,k} \cdot \frac{dT_{w,k}}{dt} = q_k - \frac{q_{w-f,k}}{V_{w,k}} \cdot F_{w,k}.$$

Control volume and thermal node is connected due to thermal conductor:

$$q_{w\text{-}f,k} = \alpha_k \cdot F_{w,k} \cdot (T_{w,k} - T_{f,k}).$$

Where:

M - mass, kg; m - flow rate, kg/s; U - internal energy, J; i - specific enthalpy, J/kg; W - power, W; $q_{w\text{-}f}$ - heat flux density, W/m^2; q_k - heat source in the volume, W/m^3; t - time, sec; F - area, m^2; L - length, m; ρ - density, kg/m^3; C - specific heat capacity, J/kg•K; T - temperature, K; α_k - convective heat transfer coefficient between wall of structure, modeled with thermal node, and coolant in control volume;
k - index of control volume; j- index of path; w - wall; f - flow; fr - friction; a - acceleration; p - pump; g - gravity.

The mathematical models of the TPS heat transfer loop were developed on the basis of the approach described above. The computer programs are being used for computation of the TPS steady performances and for analysis of the following transient processes:

- variation of heat load;
- variation of heat rejection conditions;
- start of the loop from arbitrary thermal state;
- switching on (off) the pump and various regulating devices;
- emergency situations (for example, response on partial destruction of the radiating panels);
- regimes with excursive instabilities and self-excited oscillations.

The similar scenarios of the TPS performance during ISSA orbital flight have been simulated both in NASA/Johnson Space Center using SINDA-FLUINT code and in RSC "ENERGIA" using specially developed codes (refs. 5, 6). The results of both calculations are in good agreement. This fact proves the codes used to be adequate.

TRANSIENT CALCULATIONS

Numerical investigations of the TPS characteristics aimed to choose methods for prevention the TPS elements from low temperatures are given below as an example.

In fact, that reduction of the TPS element operation temperatures allows to increase the TPS elements reliability and their life-time. To fit the ISSA RS project specifications certain restrictions are imposed on the liquid ammonia temperature range at the RAD exit ($T_{RAD\ exit}$ = - 40 °C... 0 °C) and temperature range at the pressure line inlet ($T_{pres.\ line\ inlet}$ = - 20 °C ... 0 °C). Such a measure allows to prevent main TPS elements (pump, FCV, EHEX, valves etc.) from low temperatures. The set temperatures range can be provided due to the RAD panel rotation in a certain angle

increments, special electric heaters (EH) on/off turning in the pump line and variation of flow rates bypassed through throttles D_1 and D_2. High thermal inertia of the RAD panels and variation of heat rejection conditions during ISSA orbital flight are taken into consideration in the simultaneous control routine of the RAD panel rotation and EH on/off turning.

Low TPS coolant temperatures are most likely to occur while the early stages of ISSA assembling during ISSA "cold orbit" flight. That is why this paper describes methods for prevention the TPS from low temperatures considering heat loads from two modules of the ISSA RS only: Service Module (SM) and Scientific-Power Platform.

The "cold orbit" parameters were calculated in RSC "ENERGIA" Department 053. All the analyses were performed at an orbital altitude of 450 km. Figure 5 shows sink temperature T_∞ calculated using the "cold orbit" parameters with different RAD panels orientation respectively to solar radiation. The RAD panels surface has solar absorbtivity of 0,22 and infrared absorbtivity of 0,9; average T_∞ = - 87 °C (panels are oriented in parallel to solar radiation).

The following logic aimed at prevention of the TPS from low temperatures has been analyzed:

1. Liquid ammonia temperature at the RAD exit $T_{RAD\ Ex}$ is controlled due to the RAD panel rotation on angle $\varphi = 20°$ respectively to solar radiation.
2. Liquid ammonia temperature at the pressure line inlet $T_{pres.\ line\ inlet}$ is controlled due to the EH on/off turning in Q_{EH}=300 W increments (Q_{EH}^{max} = 1800W).
3. Bypass flow rate through the throttle D_1 can be set at a minimum value.
4. The throttle D_2 can be opened thus providing the set FCV pressure drop (0,1 ± 0.02 MPa).

The following is the scenario of the numerical experiment.

ISSA "cold orbit" flight was simulated by periodical T_∞ variation (Period = 90 min). The RAD panel is rotated on angle $\varphi = 20°$ respectively to solar radiation. Flow rate through the pump equaled ~ 140 g/s. Flow rate through the throttle D_1 equaled 1 g/s. FCV provided variation of ammonia flow rate through EHEX, proportionate to heat load. After each two periods heat load in modules was decreased on 1.8 kW beginning from Q = 9 kW down to 1.8 kW and the same way back.

The computer analysis has shown that both under decreasing and increasing heat load vapor temperature at the EHEX exit equaled 10 ± 1 °C. Electric heater EH actively maintained temperatures at the pump and at the pressure line exits within range -20 °C ... 0 °C. Temperature at the RAD exit was, in general, lower -40 °C. Figure 6 presents calculated TPS performances under decreasing heat load.

The following conclusions can be made:

To prevent the ISSA TPS from low temperatures during its "cold orbit" flight it's enough to close the liquid ammonia bypass line 2 and to regulate temperature in pressure line due to the EH on/off turning (Q_{EH}^{max} =1800 W). Requirement imposed by specification on the temperature $T_{RAD\ Ex}$ ($T_{RAD\ Ex}$ < -40 °C) cannot be met while ISSA flight under low heat loads. That is why it's possible to avoid the RAD rotation procedure. On the other hand this procedure doesn't yelled valves and EH to turn on/off frequently and is recommended as a fallback routine for prevention the TPS from low temperatures.

EXPERIMENTAL INVESTIGATIONS

A lot of experimental investigations of elements, subsystems, and whole system were conducted during the TPS designing period. Much of those experiments were carried out on KhAI experimental stand (ref. 7). As experiments were performed under gravity conditions main attention was paid to two-phase flow processes modeling. Working fluids were R-114, R-113. It has been proved that two-phase coolant hydrodynamics and heat exchange processes in heat exchangers, manifolds, separator, two-phase flow splitter can be considered self-similar in Froude number within TPS typical parameters range. Heat-Controlled Accumulator (HCA) is the most gravity sensitive element. The most conservative mathematical models and results of high-quality space experiments conducted by RSC

"ENERGIA" have been used while the HCA designing process. It is planned to test the HCA aboard cargo spacecraft "Progress".

The stand is intended for simulation of the system effects. The results of experimental investigations aimed at analysis of the Flow Control Valve regulation subsystem are given below.

The active Flow Control Valve (FCV) is used to maintain:
- liquid coolant (antifreeze) temperature T_a at the EHEX exit within set range $T_a = T_{a\ nom} \pm \Delta T$ ($T_{a\ nom}$ = 15 °C, ΔT = 2,5 °C);
- high ammonia quality (x > 0,8) at the EHEX exit.

The FCV will be controlled due to the antifreeze temperature T_a sensor signals. It is proposed the following FCV regulation logic:

1. Heat load increase (temperature T_{EHEX} increasing in time): FCV should be switched on to the next level of the flow rate after reaching $T_a \geq T_{a\ nom} + \Delta T$.
2. Heat load decrease (temperature T_{EHEX} decreasing in time): FCV should be switched on to the previous level of the flow rate if:

- $T_a \leq T_{a\ nom} - \Delta T$;
- T_a is within the set range, but prescribed time $\Delta\tau$ = 20...30 min has passed. Such a measure will provoke the temperature T_a and ammonia vapor quality x increase at the EHEX exit.

Proposed regulation method has been tested on ground-based functional analog of the ISSA TPS (ref. 7). The working fluids were R-113 and transformer oil. Figure 7 shows graph of parameters variation in time (1RUN = 10 sec.) under arbitrary heat loads. When liquid coolant temperature T_a was out of the set range FCV was switched on to the proper level of flow rate (RUN=200, 240, 270, 320, 600, 645, 685) thus maintaining T_a within the set range $T_a = 56 \pm 2$ °C. Vapor quality at the EHEX exit was ≈ 1. R-113 saturation temperature T_{sat} in EHEX was stabilized by HCA in appropriate way during period RUN = 200...520 (T_{sat} =50 ± 2 °C).

Conclusions are the following: experimental investigations have proved the FCV regulation logic proposed to maintain antifreeze temperature within set range and to provide high ammonia vapor quality at the Evaporative Heat Exchanger exit.

At the present time experimental investigations of the TPS subsystem using ammonia as a working fluid are being conducted in Celdish Research Center.

REFERENCES

1. Nikonov A.A., Gorbenko G.A., Blinkov V.N., "The Two-Phase Space-Craft Thermal-Control Systems", Moscow, Series: Rocket-Space and Mechanical Engineering, 1991, P. 302.
2. Nikonov A.A, Gorbenko G.A., Blinkov V.N., "Hydromechanics and Heat Transfer in Components of the Two-Phase Heat Transport Loops for Space-Craft", First International Conference on Aerospace Heat Exchanger Technology, Palo Alto, CA, USA, 15-17 February 1993. P. 57-74.
3.Tandler J.J., Bilardo V.J., "An Integrated Model of the Space Station Freedom Active Thermal Control System", AIAA-89-0319.
4. Supper W., "Two-Phase Heat-Transport Systems for Space-Craft", ESA Bulletin N 66, 1991. P. 64-70.
5. K. Ungar, T.D. Mai, "The Russian Two-Phase Thermal Control System for the International Space Station: Description and Analysis", National Heat Transfer Conference. August 3-5, Houston TX, 1996, P. 19-24.
6. Grigoriev Y.I, Cykhotsky, Prokhorov Y.M, Surguchev, Gorbenko G.A., Blinkov V.N., Brus N.A., Ganja E.P. "Prediction of Parameters of the International Space Station ALPHA Russian Segment Two-Phase Thermal Control System Under Various Orbit Environmental Conditions", National Heat Transfer Conference, August 3-5, Houston TX, 1996, P. 25-31.
7. Grigoriev Y.I, Grigorov E.I., Cykhotsky V.M., Prokhorov Y.M, Gorbenko G.A., Blinkov V.N., Teniakov I.E., Malukhin C.A., "Two-Phase Heat Transfer Loop of Central Thermal Control System of the International Space Station ALPHA Russian Segment", National Heat Transfer Conference, August 3-5, Houston TX, 1996, P. 9-18.

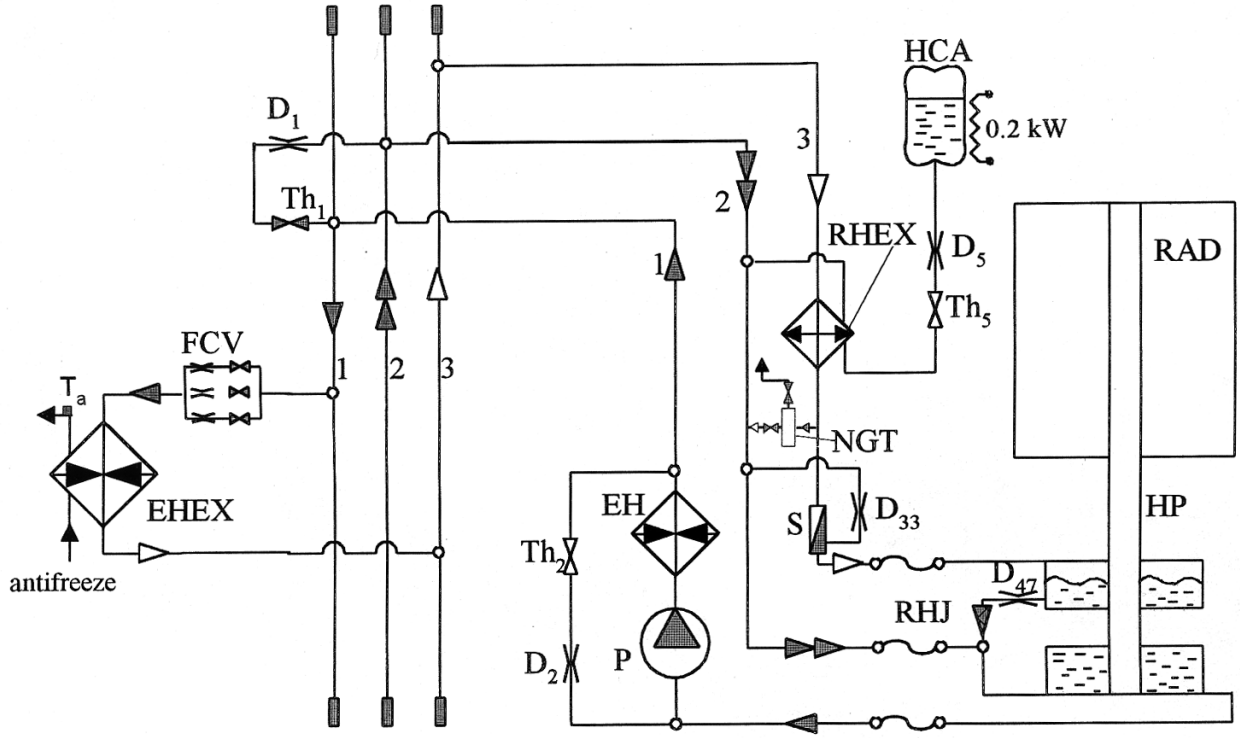

HCA - heat controlled accumulator; RAD - central radiating heat exchanger ; P - pump; RHJ - rotary hydraulic joint; RHEX - heat exchanger-regenerator; S- separator; EH - electric heater; NGT - non-condensable gas trap; FCV - flow control valve; HP - heat pipe.

- vapor line; - bypas line;

hydraulic joint; valve; - throttle;

- heat exchanger; - pressure line.

Figure 1. - Principal schematic of "ALPHA" Russian Segment Two-Phase Heat Transport Loop

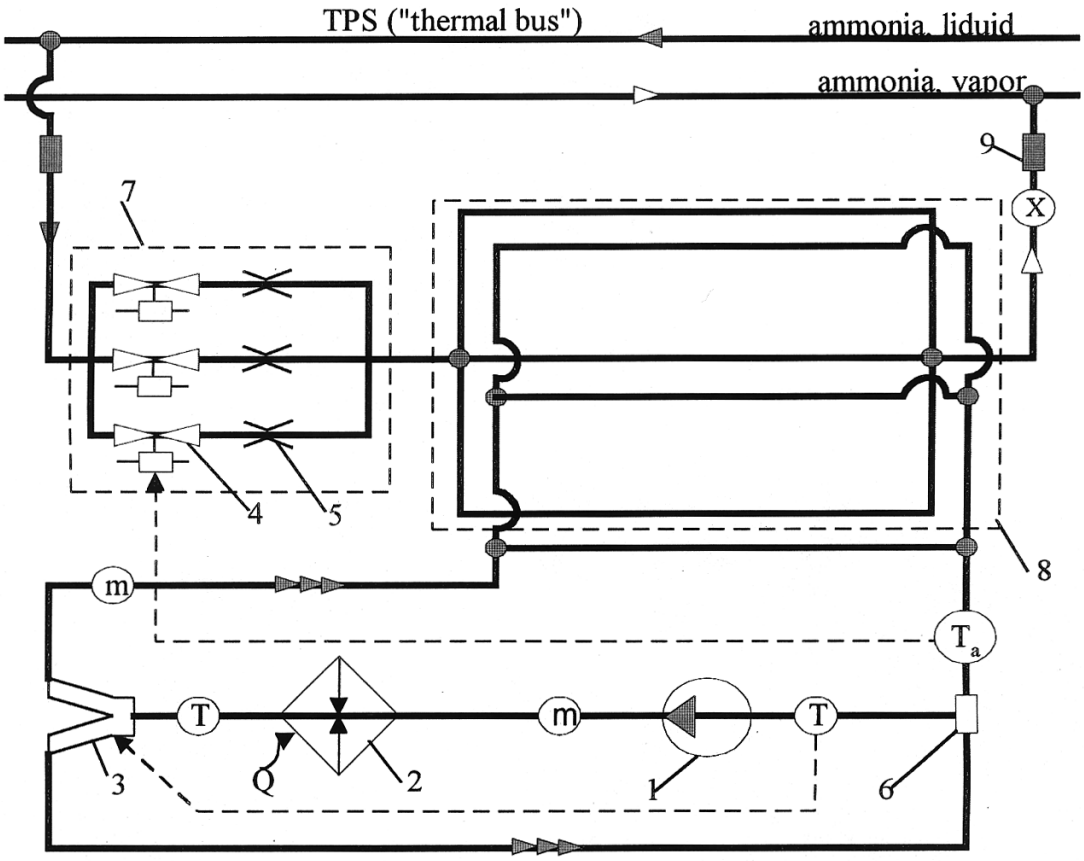

1 - antifreeze pump; 2-heat loads of individual modules; 3-flow control valve; 4 - valve; 5 - throttle; 6 - mixer; 7 - flow control facility; 8 - evaporative heat exchanger; 9 - rotary hydraulic joint; (X) - vapor quality sensor;
(T) - temperature sensor; - vapor ammonia; (m) - flow rate meter
- liquid ammonia antifreeze (internal loop)

Figure 2. Principal schematic of the internal liquid loop of the individual module

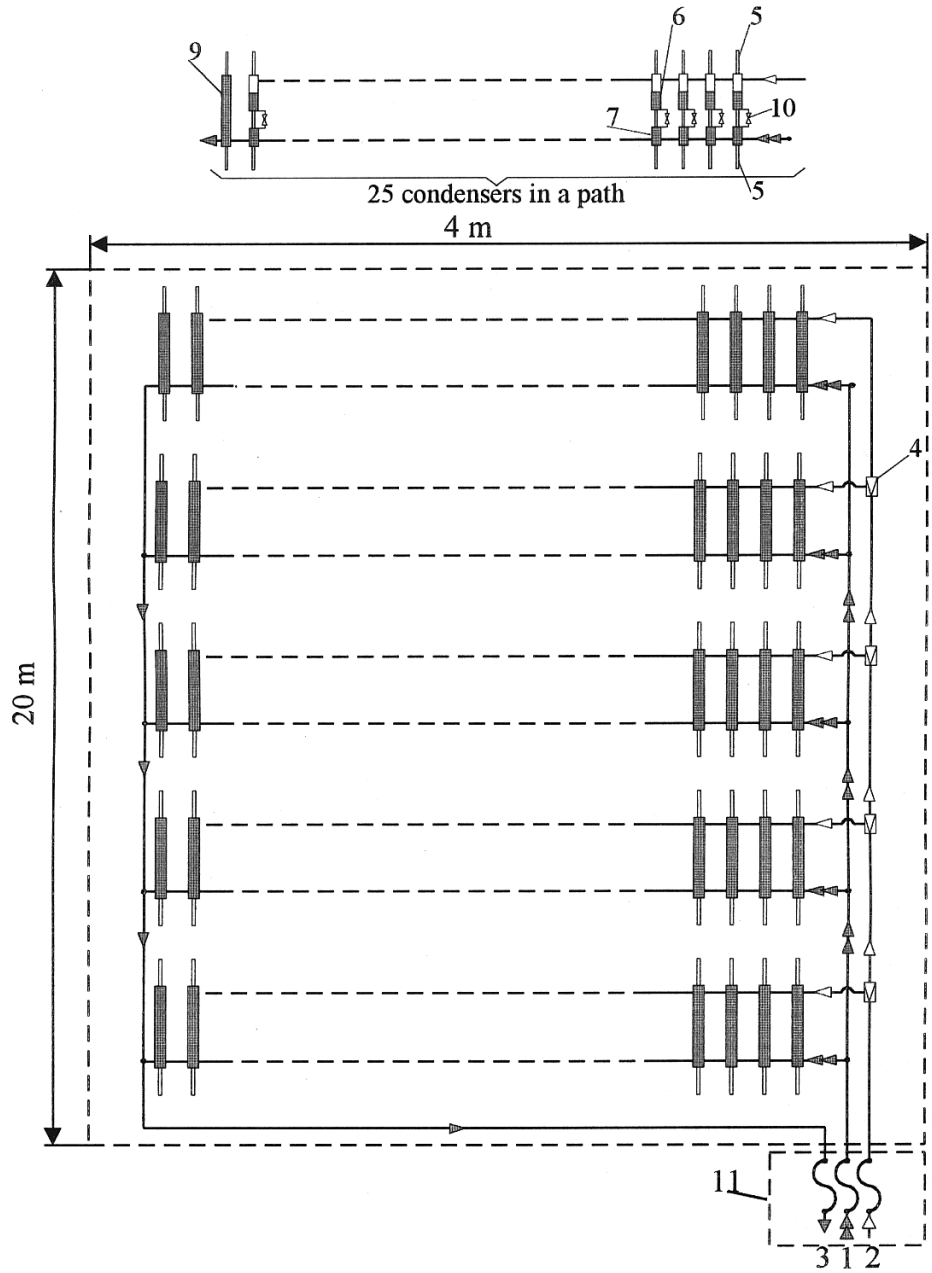

1-liquid inlet; 2-vapor inlet; 3-liquid exit; 4-two-phase flow splitter; 5-heat pipe; 6-condenser; 7-subcooler attached to the condenser; 9-separate subcooler; 10-throttle; 11-rotary hydraulic joint (RHJ).

Figure 3. Principal schematic of the heat-rejection subsystem (central radiating heat -exchanger)

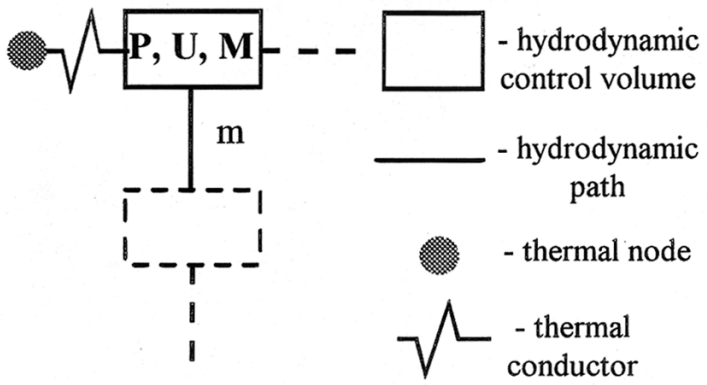

Figure 4.- Basic elements of equivalent thermalhydraulic network

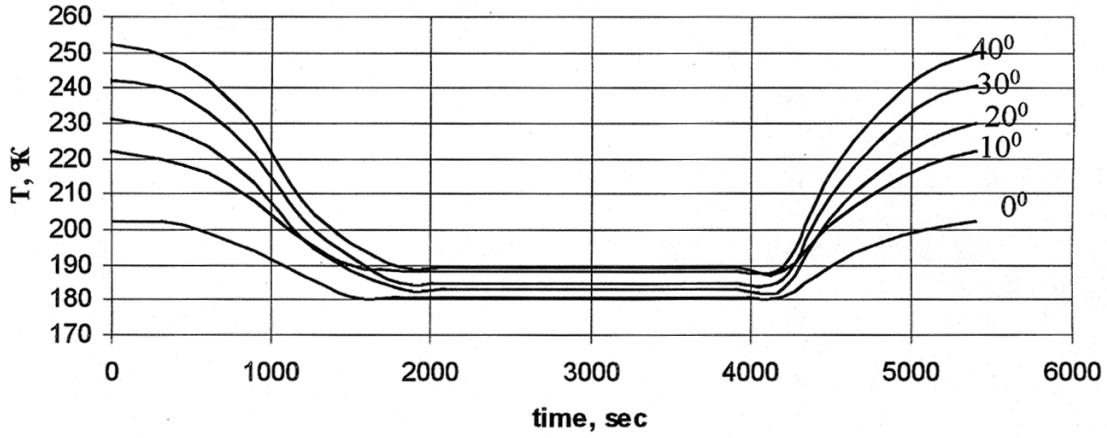

Figure 5. - Sink temperature T_∞ in dependence from RAD panel rotation respectively to solar radiation (cold orbit)

a) Heat load

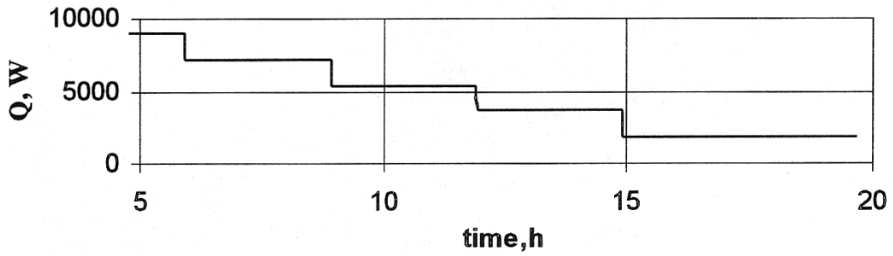

b) Heat Load of Electric Heater (EH) in the pump line

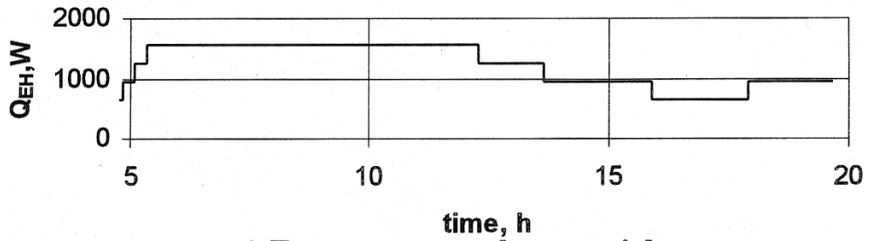

c) Temperature at the pump inlet

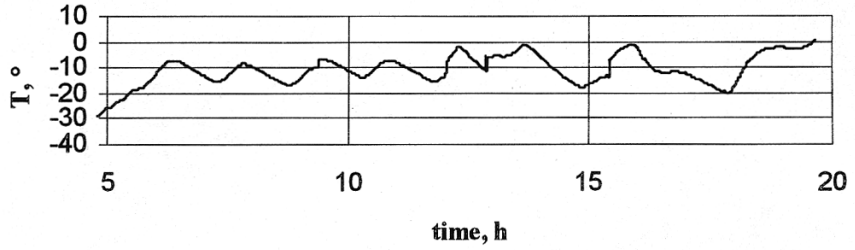

d) Temperatures at the pump exit and at the RAD exit

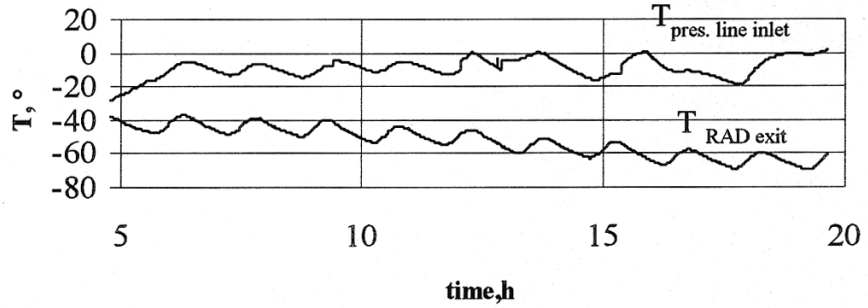

e) mass flow rates

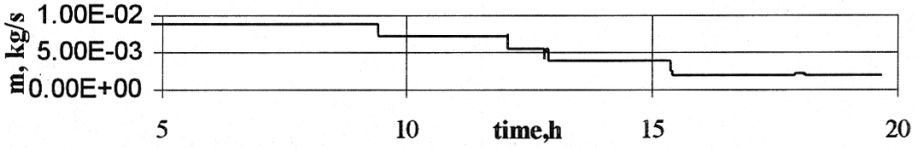

Figure 6. - ISSA TPS "cold" orbit performances

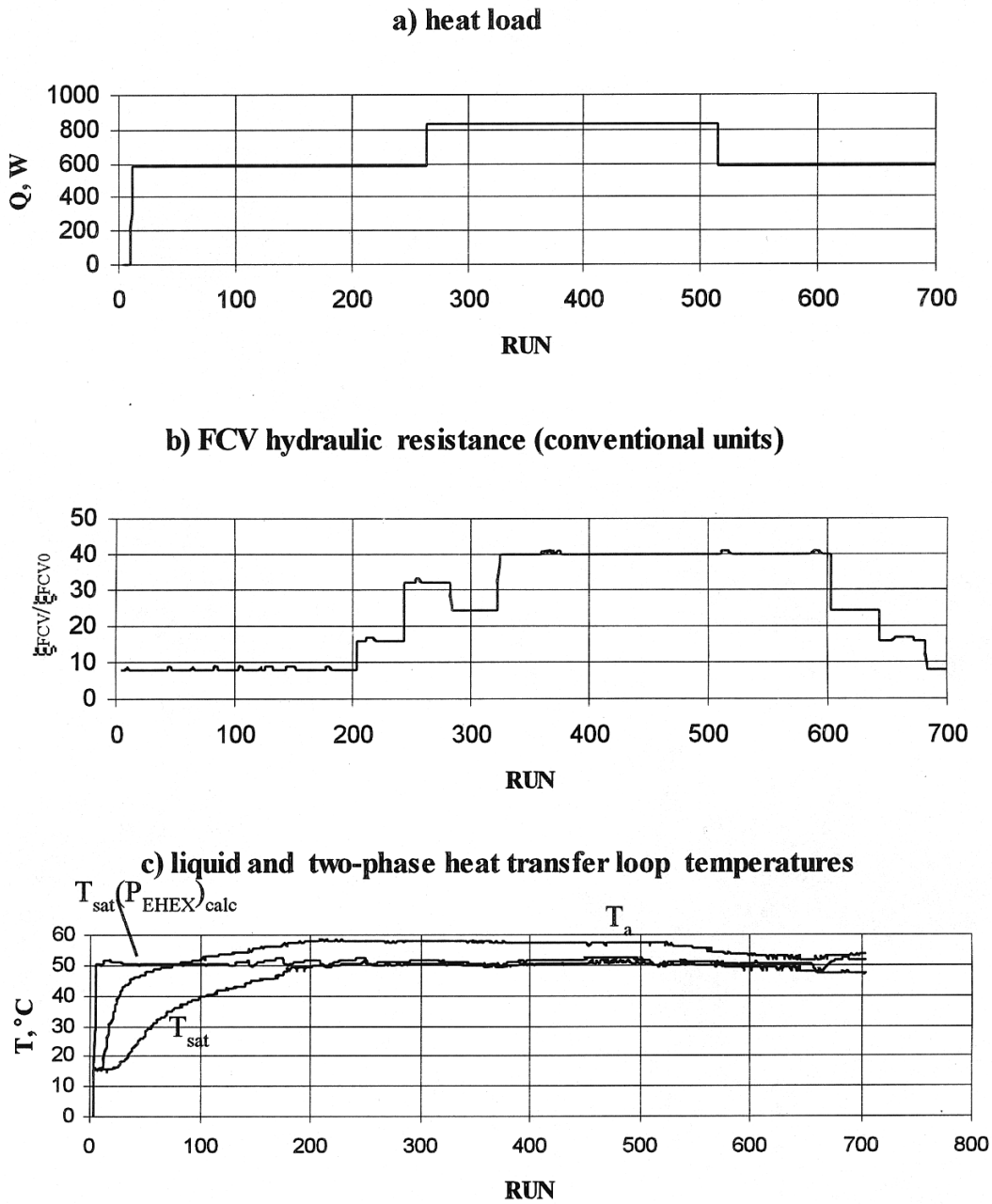

Figure 7.- Experimental ISSA TPS prototype performances

THERMAL CONTROL OF A 195 KELVIN IR DETECTOR ON A SMALL LOW-EARTH ORBIT SATELLITE

H. Craig Heffner and George Firstbrook
Northrop Grumman Corporation
Baltimore, Maryland 21043

SUMMARY

A practical solution is described for cooling an IR detector to 195K on a small satellite in a low-Earth orbit where size constraints preclude a passive approach using radiation shades. The most important design feature is a Peltier thermo-electric cooler, though the design of all of the components was found to be critical as the temperature requirements approached the limits of what could be achieved using this method. Discussions of the primary design drivers and the results of sensitivity studies of various design parameters are included.

SYSTEM DESCRIPTION

The spacecraft is depicted in Fig. 1. The six surfaces that form the hexagonal portion of the bus each measure 20" by 40" and serve as the heat radiating areas. Solar arrays having nearly the same shape as these six sides deploy in a flower pedal fashion as shown. The orbit is circular with a Beta angle varying from 11° to 33° and an altitude of 470km. The satellite flies in a solar inertial orientation with the solar array end toward the Sun when not in eclipse, and with the Z-axis nadir pointing and the solar arrays away from Earth during eclipse. A TSS plot of the orbit is shown in Fig. 2. During the 5-minute imaging period the satellite Z-axis will turn up to 45° off nadir. This satellite hosts several Focal Plane detectors covering a bandwidth of .45 to 4.9 microns though this paper will only address the SWIR/VIS/NIR system.

The principal elements of the SWIR thermal control system are a two-stage Peltier thermo-electric cooler (TEC), a Beryllium thermal storage unit, a flexible thermal link, an ammonia axial groove heat pipe and a silver/FEP-coated aluminum radiator. An illustration of the system is given in Fig. 3. As the heart of the system, the TEC provides not only sub-cooling below the available radiator temperature, but also temperature control of the detector chip to within +/-0.2°C of its set point via a PI controller. The Beryllium storage unit serves to reduce the peak temperature of the TEC hot side, allowing the TEC to operate more efficiently, and reduces the rate of change of the TEC hot side during imaging facilitating the necessary fine control of the detector temperature. The purpose of the flexible thermal link is to isolate the detectors and optical system from distortions and vibrations emanating from the spacecraft structure.

Two other detectors, the VIS and NIR, also share the same radiator and heat pipe as the SWIR. As these devices have higher operating temperatures they are simply cold biased by sinking to the heat pipe using flexible metal straps and then actively heated to the appropriate temperature. They are also shown in Fig. 3.

The predicted performance of the system for the worst-case hot condition is given in Fig. 4. The temperature profiles of the Be storage unit and the VIS and NIR focal planes are plotted for one full orbit. The critical design point is the maximum Be temperature of 243K, which is nearly the highest temperature at which the TEC can maintain a detector temperature of 195K. As the TEC is operated throughout the orbit rather than just during imaging to limit temperature cycling of the detector chip, TEC hot side temperatures much higher than 243K will result in a runaway-like situation if the TEC power is not limited below the 6.7W allowed by the control circuitry. The design has margin against this condition and a fix if it does occur, as will be described further, but there is no danger of any equipment overheating at any time. The VIS and NIR focal planes are heated to their operating temperature of 257K for the imaging period and then allowed to drift for the remainder of the orbit.

Listed below are the more important quantities in the system representing either requirements or performance of particular components. The actual TEC cold side set point is 192K to accommodate the additional temperature rise through the detector chip assembly as well as control tolerances.

SWIR

- TEC Set point = 192K
- Control Tolerance = +/-0.2K
- Thermal mass on TEC Cold Side = 2.3 Joules/K
- Active Load on TEC from Detector = 120 mw
- Linearized TEC Cold Side Parasitic = 4.5 mW/K
- TEC performance per Table 1. (assuming active load + linearized parasitic)
- Beryllium Storage Unit = 800 Joules/K (~1 lb.)
- Flexible Thermal Link: Conductance = 1.0 W/K
- Coaxial Fiberglass tube (Be isolator) conductance to bench = 3 mW/K
- Coaxial Fiberglass tube MLI emissivity to bench = 0.03
- Bench Temperature Range: 273K to 293K
- Radiator = 300 sq. in., 0.08" thick Al w/ 10 mil silver/FEP, conductance to bench = 18 mW/K, emissivity to bench = 0.03
- Heat pipe: 3/8" OD axial groove ammonia, conductance to bench = 8 mW/K, emissivity to bench = 0.05

VIS/NIR

- Thermal mass of Focal Plane: 30 Joules/K
- Thermal Strap to Heat Pipe: Copper "litz" wire with Conductance = 30 mW/K
- Linearized Conductance to Bench: 8.8 mW/K
- Active Load from Detector = 120 mw
- Maximum warm-up time = 10 minutes
- Set point = 257K
- Control Tolerance: VIS = +2K/-4K; NIR = +/-0.5K
- Maximum Heater Power = 3.0 Watts

Operational Alternative

The original operational concept for the system was to cool the chip only for the 5 minutes the system images each orbit. However, due to concerns about fatigue from temperature cycling on the detector chip, the operation was changed to have the TEC maintain control continuously. This obviously had a large impact on the thermal control system. The optimized system for the cycled concept had a 100in^2 radiator rather than the 300in^2 required for continuous operation. With this small of a radiator the Be storage unit was a much more critical element, and there was a much stronger inter-dependency between radiator area and Be storage unit mass.

If a runaway situation is encountered on orbit, one solution would be to revert to a cycled mode of operation for the TEC. As any runaway would likely occur only at the extremes of seasonal variations in orbital fluxes and Beta angles, the number of additional temperature cycles on the detector would be relatively small.

SWIR Assembly Design

The SWIR design was driven not only by thermal performance but also by dimensional stability, detector reliability and EMI requirements and hence these items warrant some discussion here. The resulting design is seen in Fig. 5.

The key area of importance was the design of the TEC. The current 2-stage design yields the performance summarized in Table 1. The input power the TEC requires is affected by hot side temperature in two ways. The cold side parasitics, and thus the load on the TEC, vary with hot side temperature; and the thermodynamic efficiency, or Coefficient of Performance, of the device is temperature dependent. This COP is achieved only by careful selection of the Peltier material by the TEC supplier. The physical size of he cooler was also a consideration in the design since it was required to support a rather substantial detector. The large area CdZnTe detector / multiplexer chip is mounted to a molybdenum spacer (0.05" thick) with a full face bond of an alumina-filled

adhesive. This assembly is then mounted to the TEC cold side BeO ceramic substrate using the same adhesive applied in such a way to create a pedestal-like mount. This alleviates bowing due to CTE mismatches. The Mo spacer serves to isothermalize the assembly, provide a flex cable interface point and provides a good CTE match to the MUX chip to minimize induced stress in the detector bump bonds. The detector assembly has a 5 second settling time with a 0.05K final gradient with the 120mW detector load.

BeO was chosen for the custom TEC top substrate to minimize gradients caused by the pedestal mount. The cooler is soldered to a Beryllium support plate that is bolted to the mass storage unit using a thermal RTV in the interface. The support plate simplifies the mounting and testing of the TEC detector and flex interconnect cable. A cold shield heat sunk to the same support plate reduces the background radiation on the SWIR detector to meet NEI requirements.

This entire assembly is thermally isolated from the warm interface mount using 3 inch diameter 0.032" thick folded fiberglass tubes with gold plating to keep the conductance to the bench to 0.003 W/K. This design also provides for a structurally stiff (k > 50,000 lb/in) symmetrical assembly thereby improving its dimensional stability which is important for achieving the inter-FPA co-registration requirements. Thermal parasitics are also limited by low emissivity coatings on all Be surfaces, the internal surfaces of the enclosure and a low thermal conductance flex cable supplying the electrical interconnect from the detectors to the processing electronics located external to the assembly.

An aluminum can surrounding the entire assembly provides two major functions. The first is to provide an EMI enclosure. The enclosure is sealed with an EMI gasket at the wall of the optical housing into which it is later mounted. The cold finger penetration for the connection to the thermal flexible link requires a unique design. It incorporates a ferrite core to increase impedance at higher frequencies thereby limiting conducted EMI from external sources onto the Be thermal mass via the flexible link. A ground path of lower electrical impedance that also provides high thermal impedance is provided by a SST bellows configuration. The bellows accommodates manufacturing tolerances between the inner Be storage unit and the enclosure which could otherwise structurally load the fiberglass isolators to unacceptable levels for dimensional stability. The second function the enclosure performs is to provide a containment shroud during the dry Nitrogen purge required when performing ambient testing, a requirement for camera and spacecraft testing. The TEC hot side requires external cooling to 213K maximum in order for it to achieve the 192K cold side with the additional convective thermal load. Having a hermetically sealed container was considered to make ground testing easier but this benefit was outweighed by the simplicity and cost effectiveness of the purged assembly.

PARAMETRIC TRADE STUDIES

2-Stage vs. 3-Stage TEC

A trade between 2- and 3-stage devices was performed by the TEC vendor and it was found that the 3-stage device would be about 10-20% more efficient. This was somewhat unexpected as the usual trend is for efficiency to drop as stages are added, but is explained by the fact that our temperature differential pushes the performance envelope for the 2-stage device. The downside is that the optimization required to increase the 3-stage efficiency also reduces its maximum capacity. This would impact cooldown time and reduces margin against unexpected parasitic or active power increases. On the other hand the maximum temperature differential, is improved by about 2K, which would provide additional margin against higher than expected orbital fluxes. In the final analysis the differences were small, and because choosing a 3-stage would have increased cost and delayed schedule, and would have been slightly riskier, the 2-stage TEC was selected.

It can also be inferred from this study that a break point is being approached in terms of TEC usage in this environment with this kind of load. The only way to achieve a significantly lower cold side temperature would be to use a 4-stage device, for which the usual trends would dictate a significant increase in power. This increase, after rippling through the system, would have required an increase in radiator area that would be difficult to accommodate.

Radiator Area

The curves in Fig. 6 illustrate the relationship between radiator area and the maximum Be storage unit temperature. The bus side designated "2000" is the one being used and is the most favorable side (along with its mirror image "6000") except for "1000" which was reserved for cooling of the spacecraft batteries. All the other surfaces would have environmental heat fluxes too high to allow the TEC to maintain control. The plot clearly shows a point of diminishing returns near 400in^2, with the temperature actually increasing as further radiator area is added. This behavior is due to the fact that as more radiator area is added, the additional radiating surface becomes incrementally closer to the solar arrays, which are somewhat warmer than the radiator.

Sensitivity to Other Design Aspects

The sensitivities of the Be storage unit temperature to variations in performance of the four other primary classes of components of the design were studied. These parameters were the conductance of the flex-link, the mass of Be storage unit, and separately the conductive and radiative parasitics from the spacecraft. The results of these studies are summarized in Figures 7 & 8. The performance of each element was varied from 50% to 150% of the design value, representing a "Figure of Merit" for that component. The temperatures in the first set of curves are the orbital peaks of the Be unit while the second set shows the maximum Be unit temperature during the period when the imaging may occur. Both plots assume that the TEC power is limited by some means when the Be temperature exceeds the control limit of –27°C. The first plot represents a more stringent constraint on the design as it gives the threshold at which TEC power limiting must be implemented. The second plot provides the threshold at which imaging control would not be possible even if such power limiting is in place.

The first set of curves indicates there is about 15-20% of margin in each design component, with the exception of the Be unit which has significantly less impact. Margins of 35% or more are indicated in the second chart as the criterion is applied only to the imaging period, with the Be unit again exhibiting less sensitivity.

These sensitivity studies indicate the design is fairly well balanced in terms of margin in each element of the design. They do point out, however, a slightly higher sensitivity to radiation parasitics than the other aspects. This may warrant additional scrutiny of the detailed design and fabrication to ensure the performance of the Multi-layer blankets and surface plating. The margins, though adequate, are not excessive and indicate the limit of this type of cooling scheme is being approached. It also should be noted that this system used materials and fabrication techniques that tended more toward the typical rather than the exotic to keep costs down. Some additional performance could be gained by using "high-performance" blankets and more refined mechanical mount.

In summary, Thermo Electric Coolers when incorporated into the mechanical design with an integrated approach can provide a relatively inexpensive and reliable cooling alternative for low-Earth orbit focal plane cooling.

Table 1 – TEC Performance

TEC Hot Side Temperature (K)	Current (amps)	Voltage (volts)	Power (watts)	Cold Side Load (mW)	COP
246.8	2.17	3.08	6.7	366	0.0548
246	2.11	3.00	6.3	364	0.0574
245	2.02	2.88	5.8	359	0.0617
244	1.95	2.76	5.4	355	0.0660
243	1.88	2.66	5.0	350	0.0702
242	1.81	2.57	4.6	346	0.0744
241	1.75	2.48	4.3	341	0.0786
240	1.70	2.39	4.1	337	0.0828
239	1.65	2.32	3.8	332	0.0872
238	1.60	2.24	3.6	328	0.0917
237	1.55	2.17	3.4	323	0.0963
233	1.37	1.91	2.6	305	0.1167
228	1.18	1.61	1.9	283	0.1484
223	1.00	1.35	1.4	260	0.1917
218	0.84	1.11	0.9	238	0.2545
213	0.69	0.89	0.6	215	0.3537

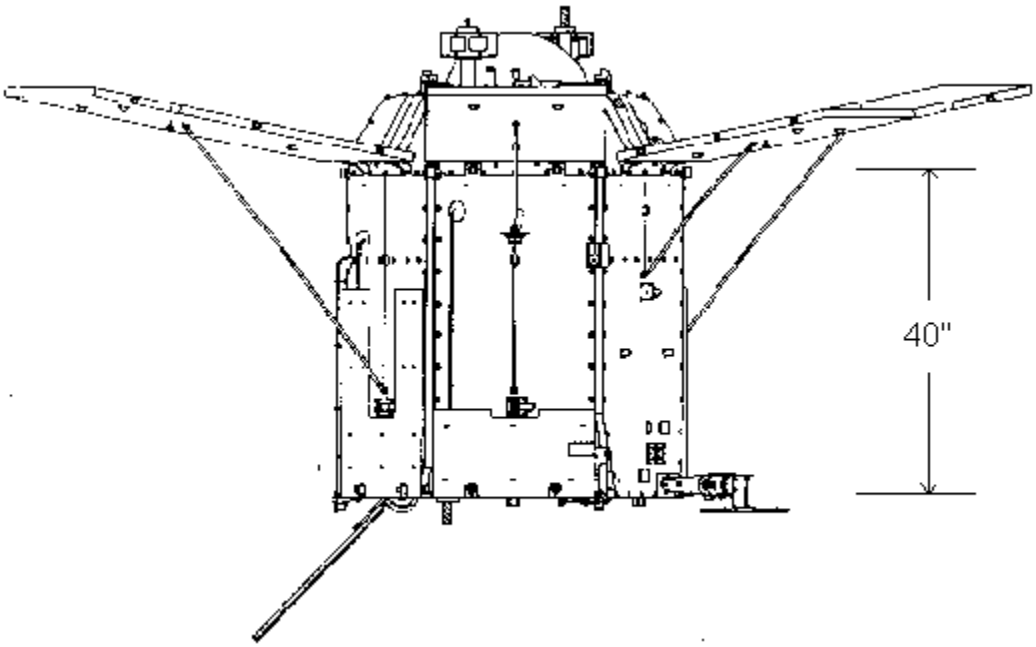

Figure 1 – Spacecraft

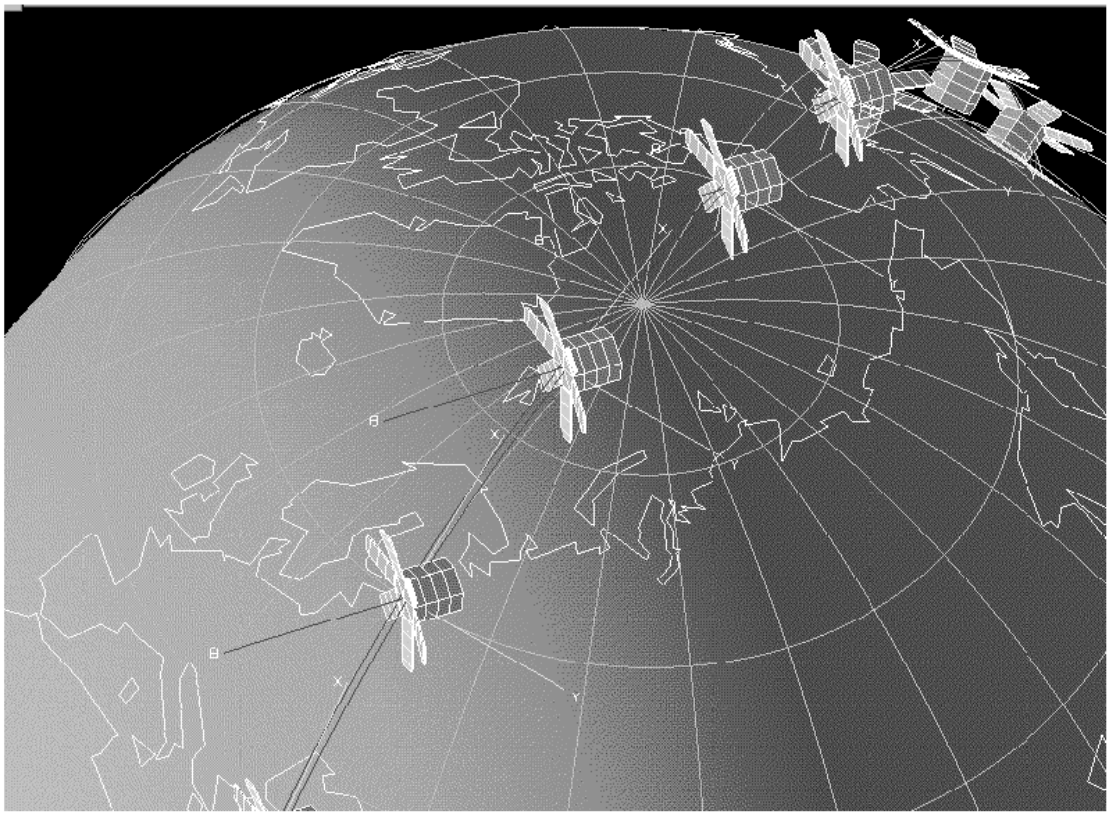

Figure 2 – Beta 33 Orbit Showing Orientation Change at Eclipse

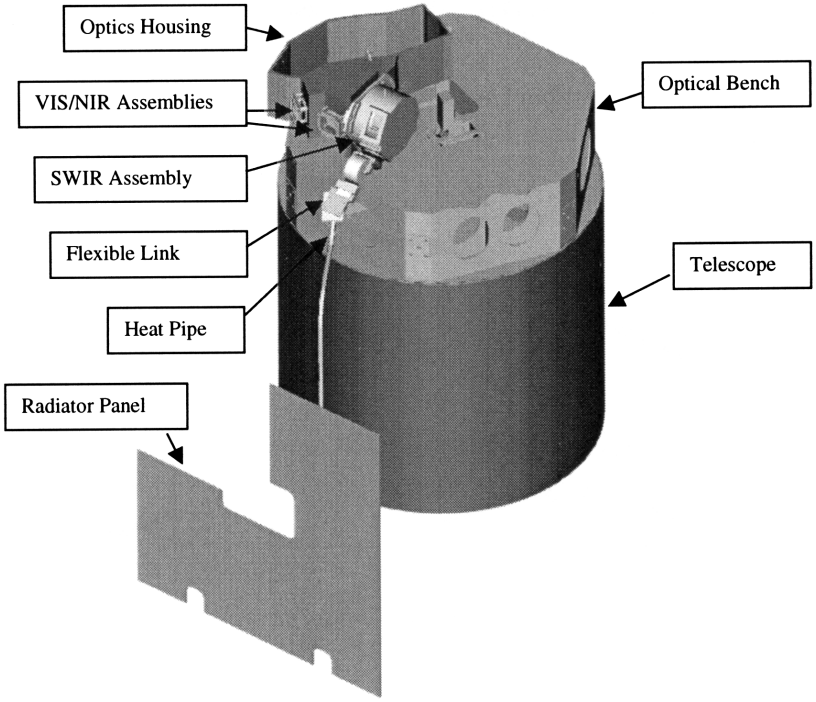

Figure 3 - SWIR Thermal Control System

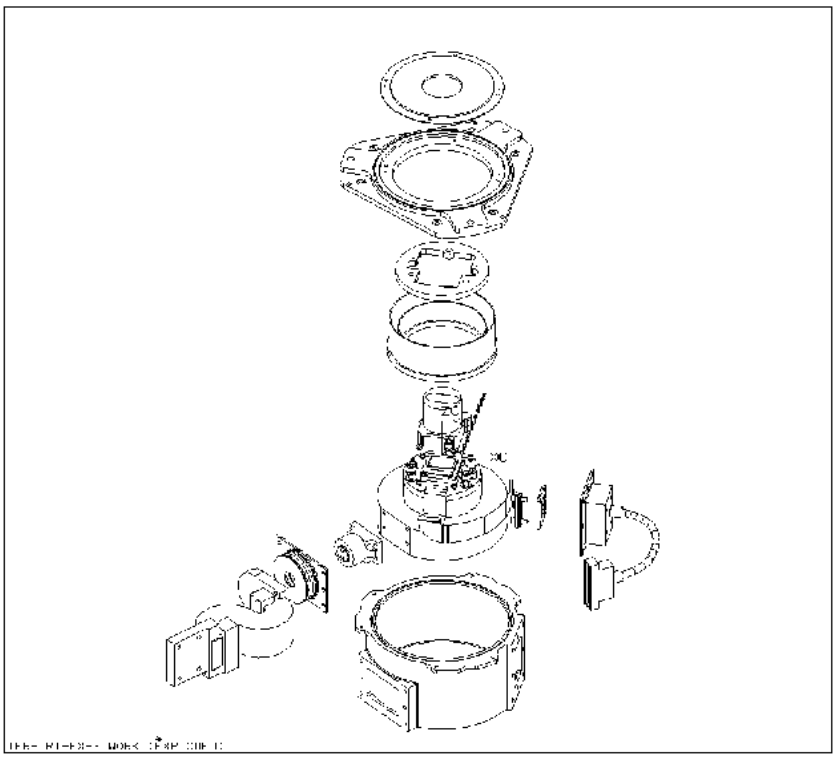

Figure 4 – SWIR Focal Plane Assembly Exploded View

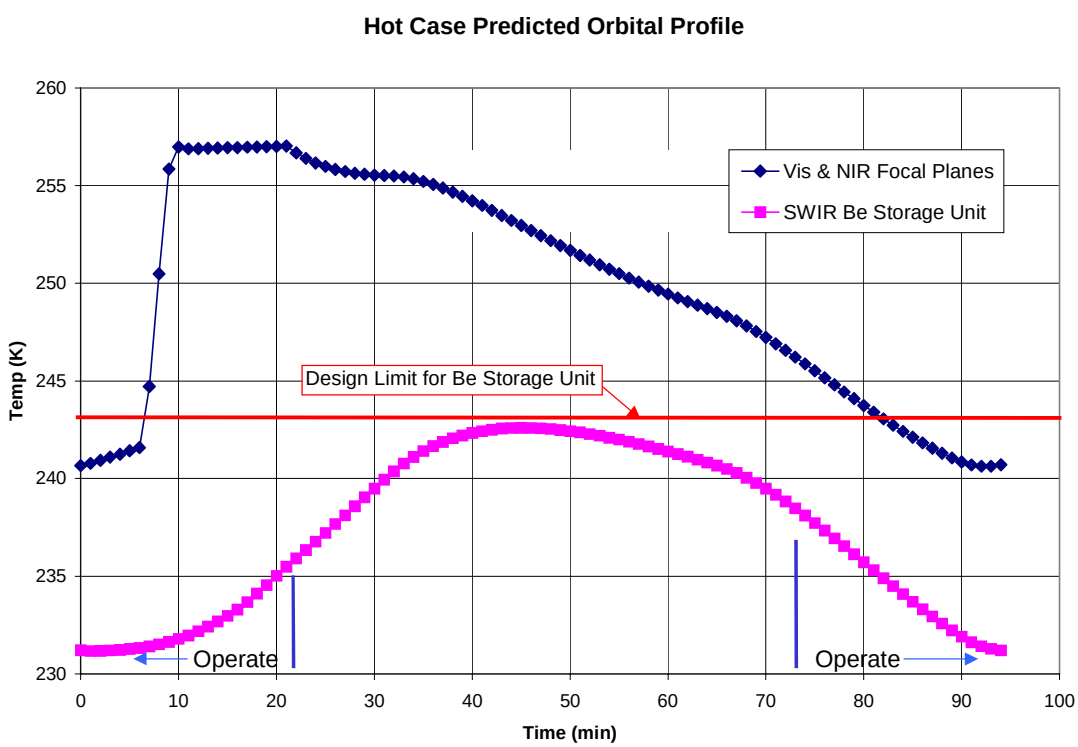

Figure 5 – Hot Case Predictions for SWIR/VIS/NIR System

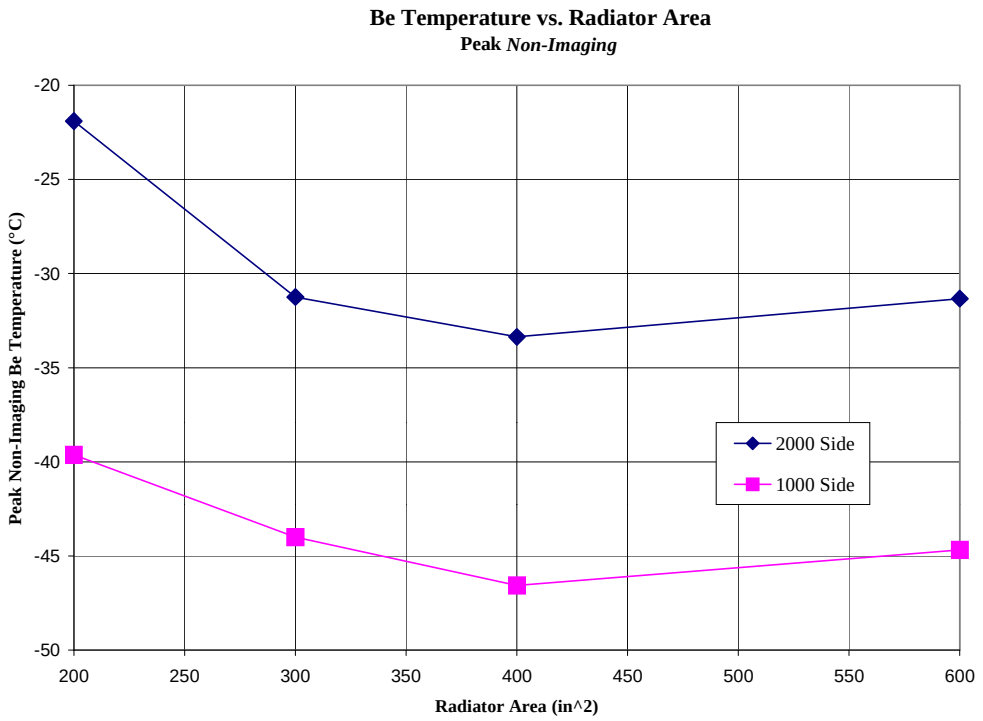

Figure 6 – Radiator Area Sensitivity

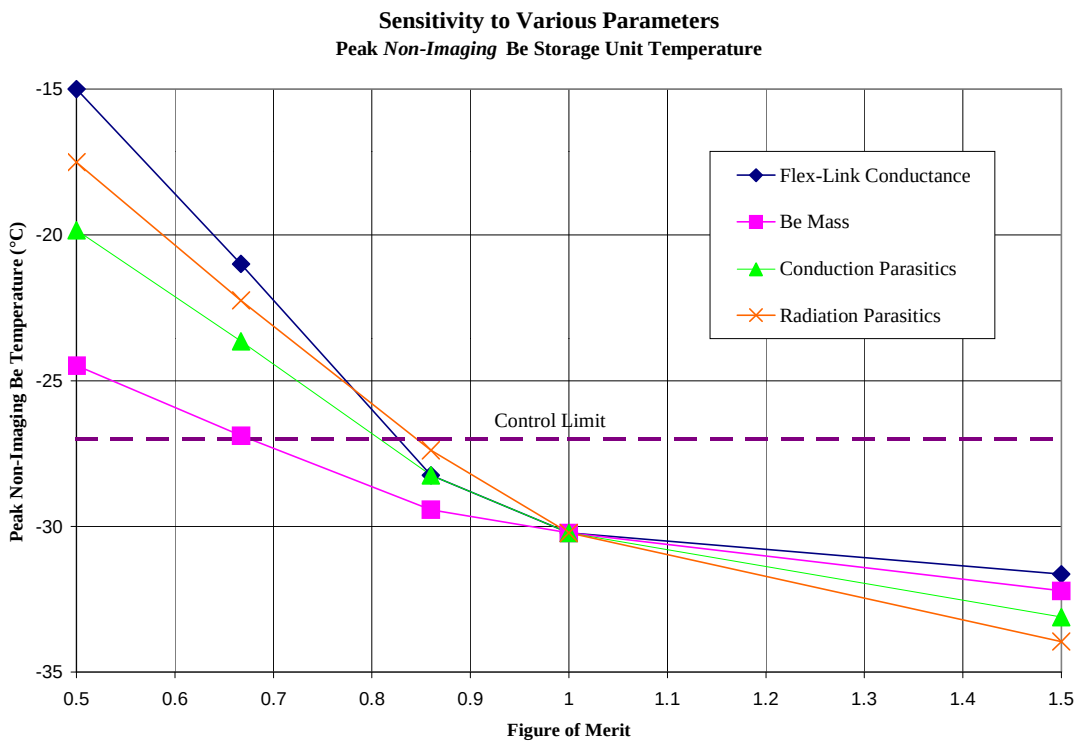

Figure 7 – Non-Imaging Sensitivity to Various Parameters

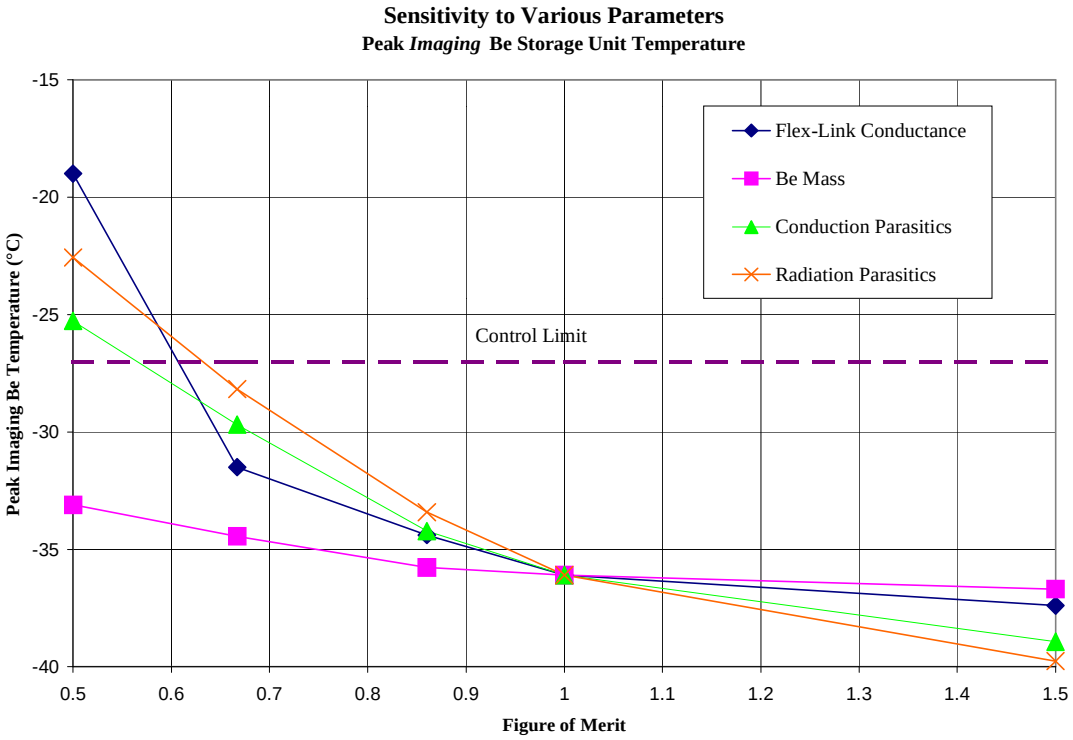

Figure 8 – Imaging Sensitivity to Various Parameters

Thermal Analysis of the X-38 Aft Fin During Re-entry

Andrew E. Hong
National Aeronautics and Space Administration
Johnson Space Center
Houston, Texas 77058

SUMMARY

This document contains the details of the thermal analysis of the X-38 aft fin during re-entry. Figure 1 shows an artist's depiction of the X-38. This analysis was performed in order to calculate temperature response of the aft fin components. This would be provided as input to a structural analysis and would also define the operating environment for the electromechanical actuator (EMA). The calculated structural temperature response would verify the performance of the thermal protection system (TPS). The geometric representation of the aft fin was derived from an I-DEAS finite element model that was used for structural analysis (ref 1). The thermal mass network model was derived from the geometric representation.

INTRODUCTION

The X-38 is an experimental spacecraft that will demonstrate a spacecraft design that could be used as a low-cost emergency Crew Return Vehicle (CRV) for the International Space Station. The X-38 will be carried as a payload by the Space Shuttle in the year 2000. During the mission, the X-38 will be deployed and will return to Earth through re-entry without a crew. The success of the X-38 will lead to the design of the CRV that will become an operational spacecraft.

MODEL

The model originated from a set of points from a I-DEAS generated finite element model shown in Figures 2 and 3. The nodes of the I-DEAS finite element model were used as points to simplify the model into larger elements shown in Figure 4. This simplified finite element model was exported to a NASTRAN model. This was then translated to a Thermal Synthesizer System (TSS) Geometry format. The resulting surfaces of the NASTRAN to TSS translation were used as guides to create a series of triangles and rectangles. These surfaces shown in Figures 5 and 6 were used to define the internal and external radiation environments.

For the external radiation environment, the areas of the skin (colored orange in the figures) were used to calculate radiation conductors to the sink temperature. These radiation conductors were not from the skin to the sink temperature but were from the most external node to the sink temperature. On the inboard side, radiation conductor calculations used optical properties for the outside of the flexible reusable surface insulation (FRSI) TPS. On the outboard side, the leading edge, and the aft surface, these calculations assumed the reaction cured glass (RCG) coating of the alumina enhanced thermal barrier (AETB-8) tile. In these calculations, the view factors to the sink boundary condition were assumed to be 1.0 without any view to any other surfaces. The hinge lines and rudder gap (blue excluding aft surface) were considered adiabatic and therefore no external radiation conductors were calculated for these surfaces.

The internal radiation conductors were calculated from the same model using the Monte-Carlo ray tracing method. The infrared emittance of the internal surfaces was assumed to be 0.74, and the conductors were considered to be between the inner most nodes (i.e. the aluminum skin). All internal surfaces were considered in the calculations including the internal frames.

This model was also used to calculate a thermal mass network using the TSS Conductance/Capacitance application. Rectangles representing the internal frame were added to the geometry under the skin as shown in Figure 7 in red. The internal frames were modeled as 0.15 " aluminum. The skin, shown in orange in Figures 5 and 6, was assumed to be 0.09 " thick for thermal mass calculations and 0.06 " for thermal conduction calculations. This was done to account for the stringers on the inside of the aluminum structure. However, the panels alone are 0.06 " thick. The blue areas shown in Figures 5 through 7 were considered 0.125 " thick. Conduction paths were defined where the rectangles were adjacent to each other. Arithmetic nodes were defined at the junctions so that more than two nodes could contact to a single junction (e.g., where internal frames and skin met).

Although not defined in the geometry, a 65 pound mass of stainless steel was defined as the electrical mechanical actuator (EMA) for the rudder. Four conduction paths were defined from the EMA to the aft fin structure. Two were to the aft rudder gap surface, and two were to the aft folding hinge line structure. These conduction paths were defined as areas that were 4" x 0.125" and were 6" long. This was derived from dimensions from aluminum C-clamps. The EMA generated 700 Watts of power from 0 to 1800 seconds.

The outboard side, the leading edge, and the aft side uses AETB-8 as TPS. Figure 8 shows the tile thicknesses for the tile TPS locations. The conduction paths from the external through the internal nodes for these areas are depicted in Figure 9. The external node is represented by an arithmetic node of RCG. Below the RCG, the tile is modeled as ten nodes which in turn conducts to a strain isolation pad (SIP) node through an arithmetic node. The SIP node, which incorporates the thermal mass of the adhesive, conducts to the aluminum structure. The leading edge tile is an exception to this modeling scheme. In this case, twenty nodes represent the leading edge AETB-8 tile.

The inboard side, the rudder gap, and the rudder hinge line uses one inch thick FRSI as TPS. The FRSI is modeled as ten nodes as shown in Figure 10. The FRSI conducts directly to the aluminum structure.

The total number of nodes is 4268, and the mass of the nodes adds to 147.2 pounds. This weight is approximately 60% of the designed weight. This is mostly due to the lack of detailed modeling in the internal structure. Because of this, the thermal mass network model would be expected to calculate higher temperature rise rates for the re-entry temperature transients.

Heat fluxes are applied directly to the external nodes with the exception of the hinge lines and the rudder gap. These heat fluxes were supplied from a computation fluids dynamics analysis documented in Reference 2.

RESULTS

Figure 11 depicts the hottest surface temperature at each time step which reaches approximately 2100 F on the outboard side. The hottest skin temperature at each time step reaches approximately 320 F as shown in Figure 12. The location of the hottest skin temperature is color mapped onto the geometry in Figure 13. Figure 14 shows that the EMA temperature is at about 200 F after one hour, and the EMA temperature is still slightly rising due to soakback heating.

CONCLUSIONS AND RECOMMENDATIONS

The X-38 aft fin thermal analysis is an example of a methodology of using an I-DEAS finite element model to create a geometry model that can be used to perform thermal radiation calculations. In turn, the geometry can be used to create a thermal mass network model. Though this method was effective, multiple translators were needed, and renodalization was performed twice. Future analyses should study variations on this method as well as look at other tools and methods to solve the issue of using design models and structural analysis models for the development of thermal geometries and thermal mass networks.

The results of this thermal analysis should be used for preliminary sizing of thermal protection systems and should be used to derive requirements for the EMA. As heating rate calculations and aft fin design increase in fidelity, the X-38 aft fin thermal geometry and thermal mass network models should be modified to incorporate the latest and most accurate boundary conditions.

REFEFERENCES

1. X-38 Structures and Mechanics Design Team, X-38 Aft Fin Finite Element Model, May, 1998.

2. Fitzgerald, Steve M., X-38 Aft Fin Inboard and Outboard Heating Rates by electronic transfer, May, 1998.

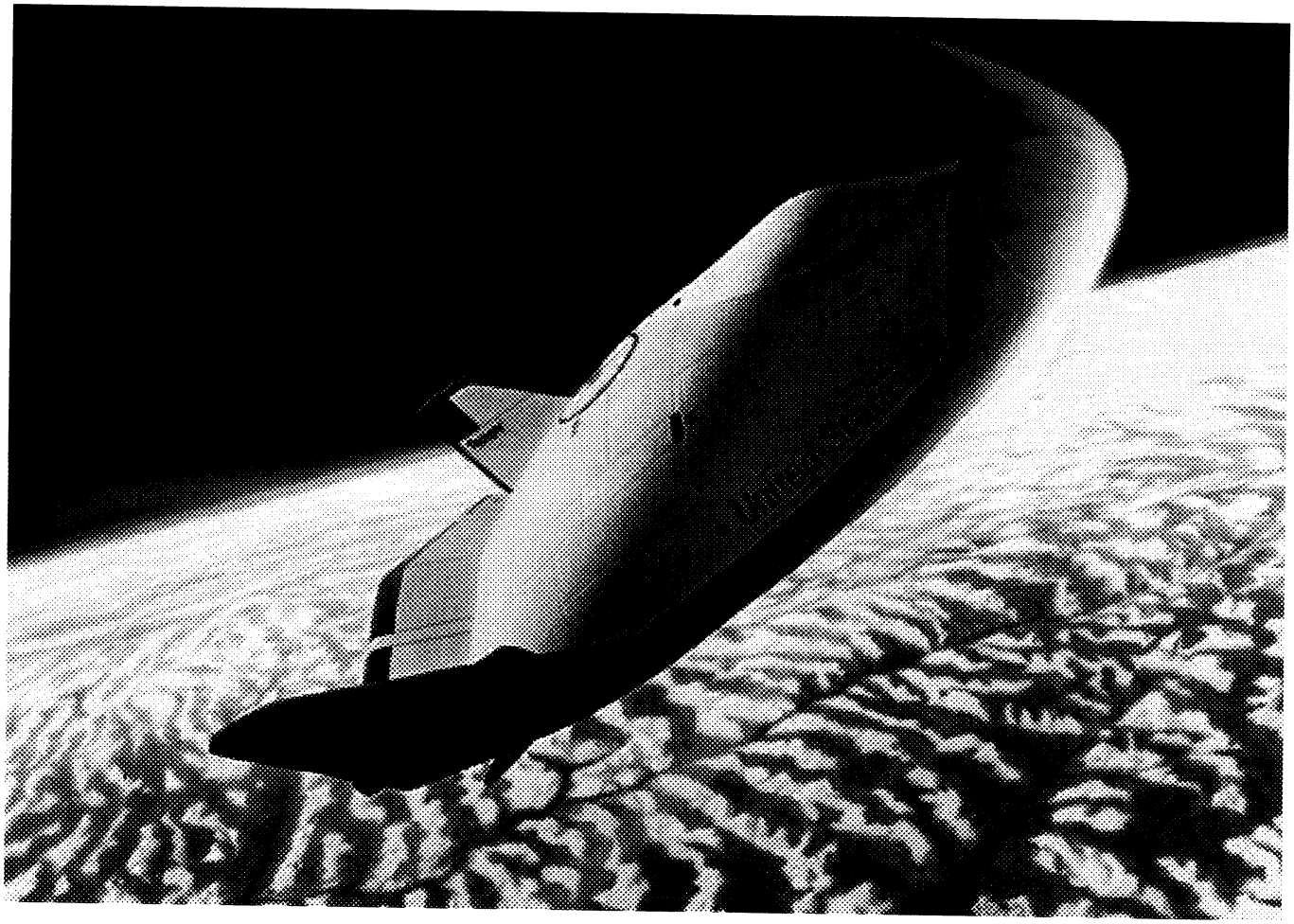

FIGURE 1. X-38 DURING RE-ENTRY

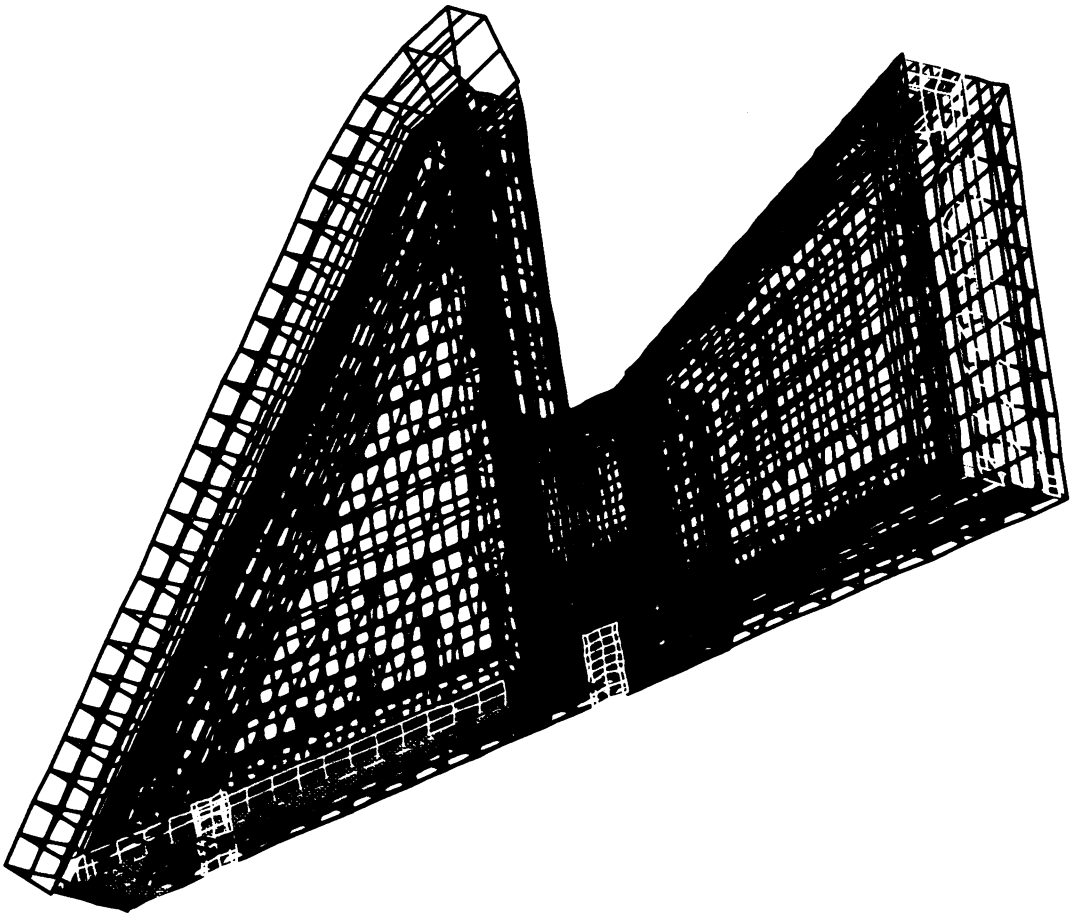

FIGURE 2. AFT FIN I-DEAS FINITE ELEMENT MODEL (WIREFRAME)

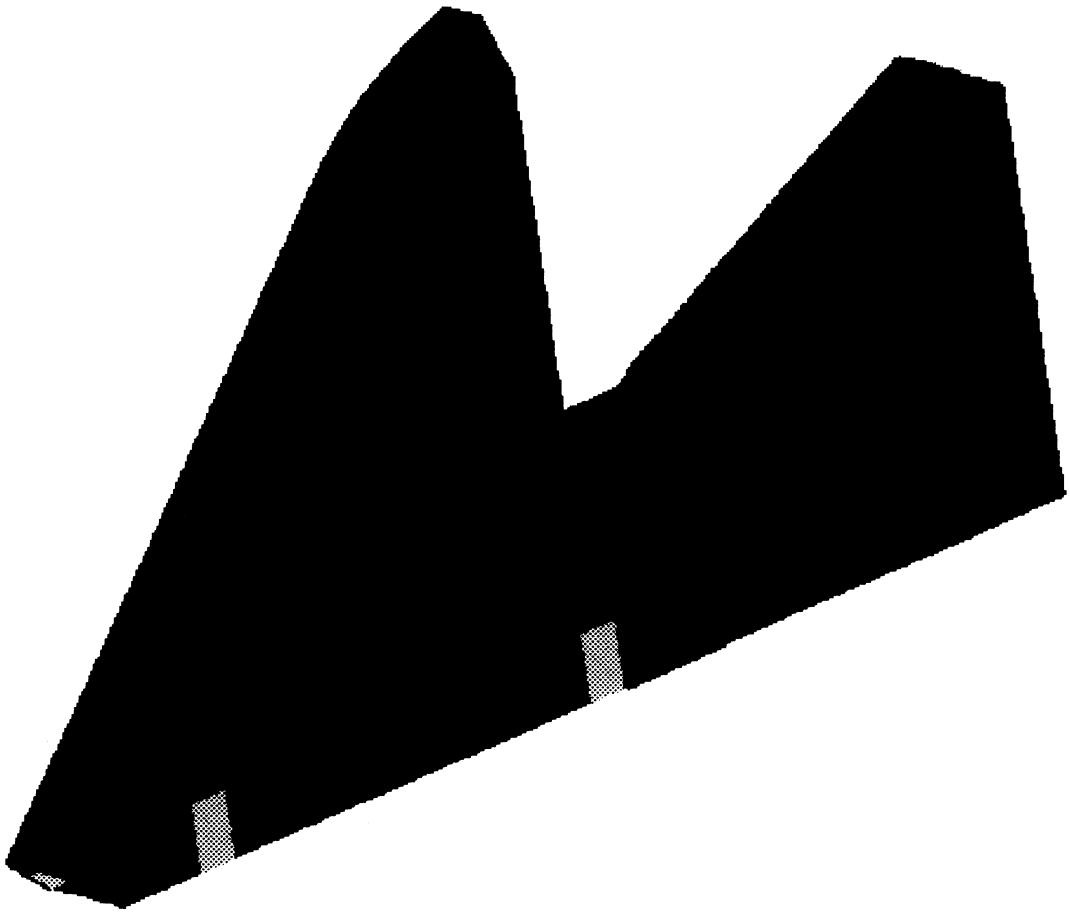

FIGURE 3. AFT FIN I-DEAS FINITE ELEMENT MODEL (SOLID)

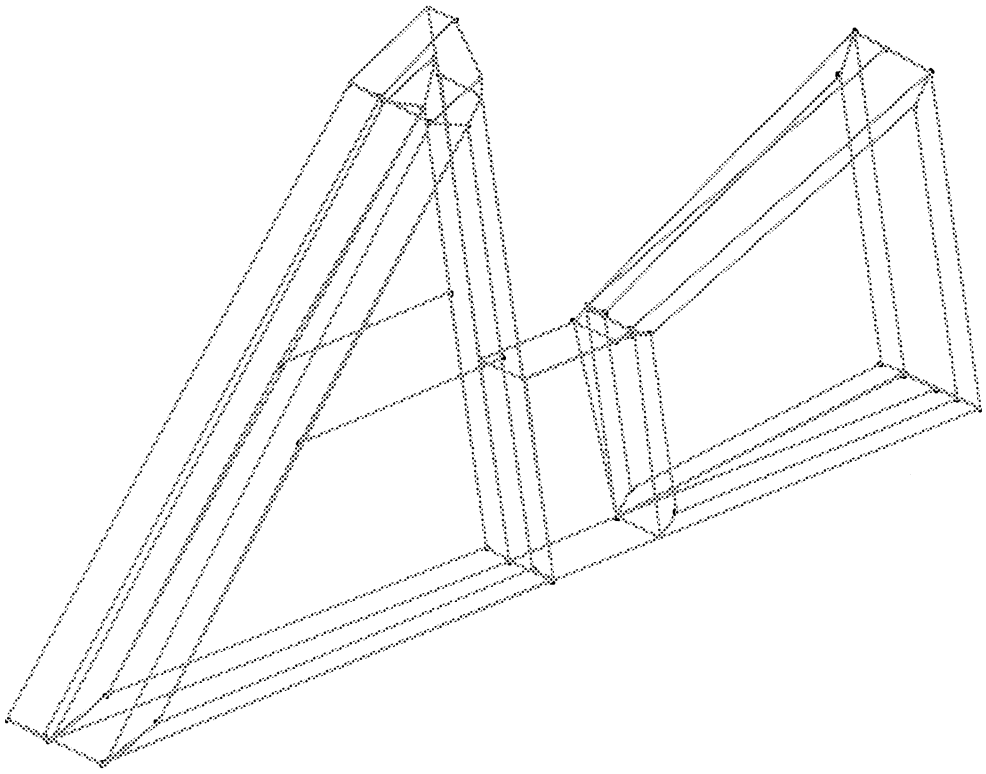

FIGURE 4. SIMPLIFIED AFT FIN I-DEAS MODEL

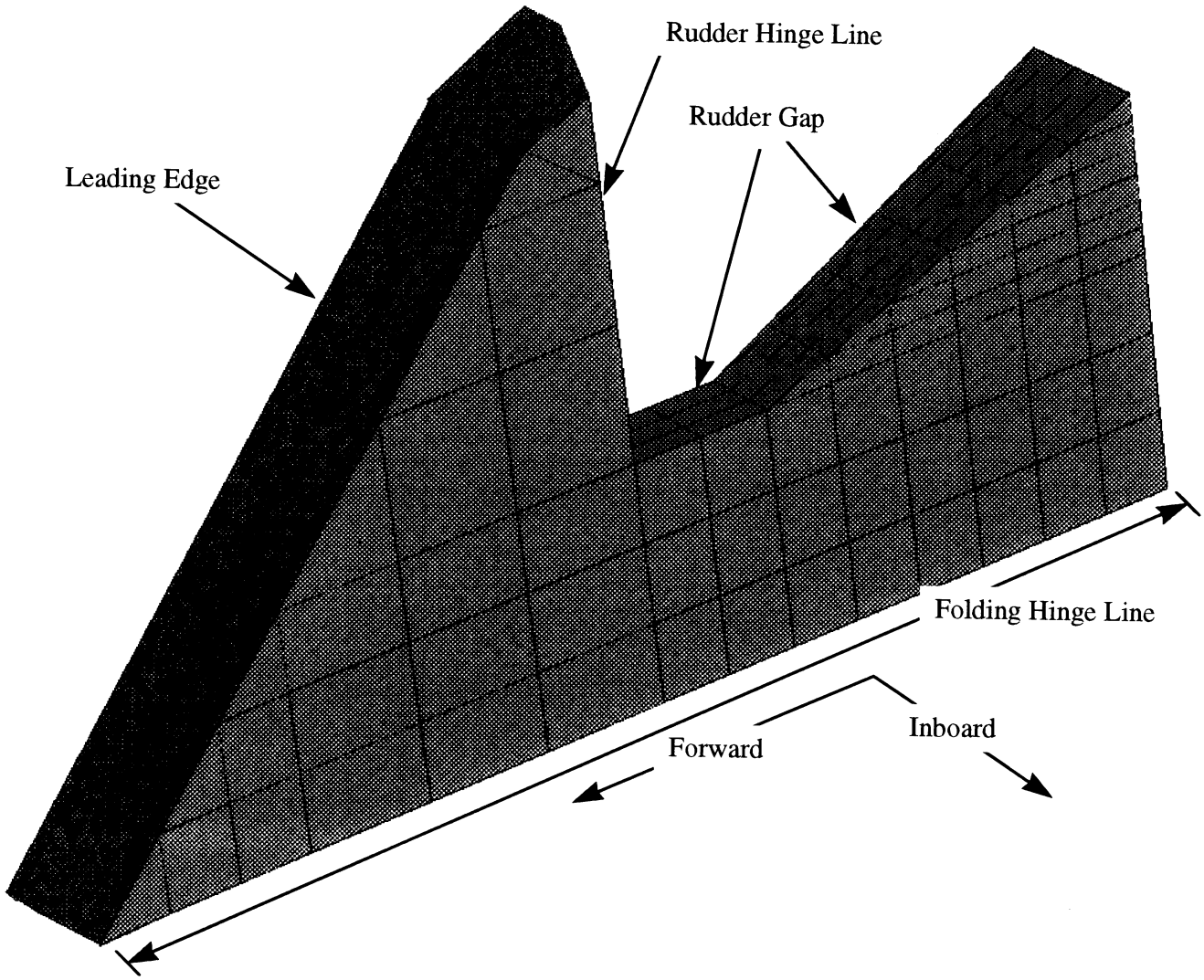

FIGURE 5. INBOARD VIEW OF TSS THERMAL RADIATION MODEL

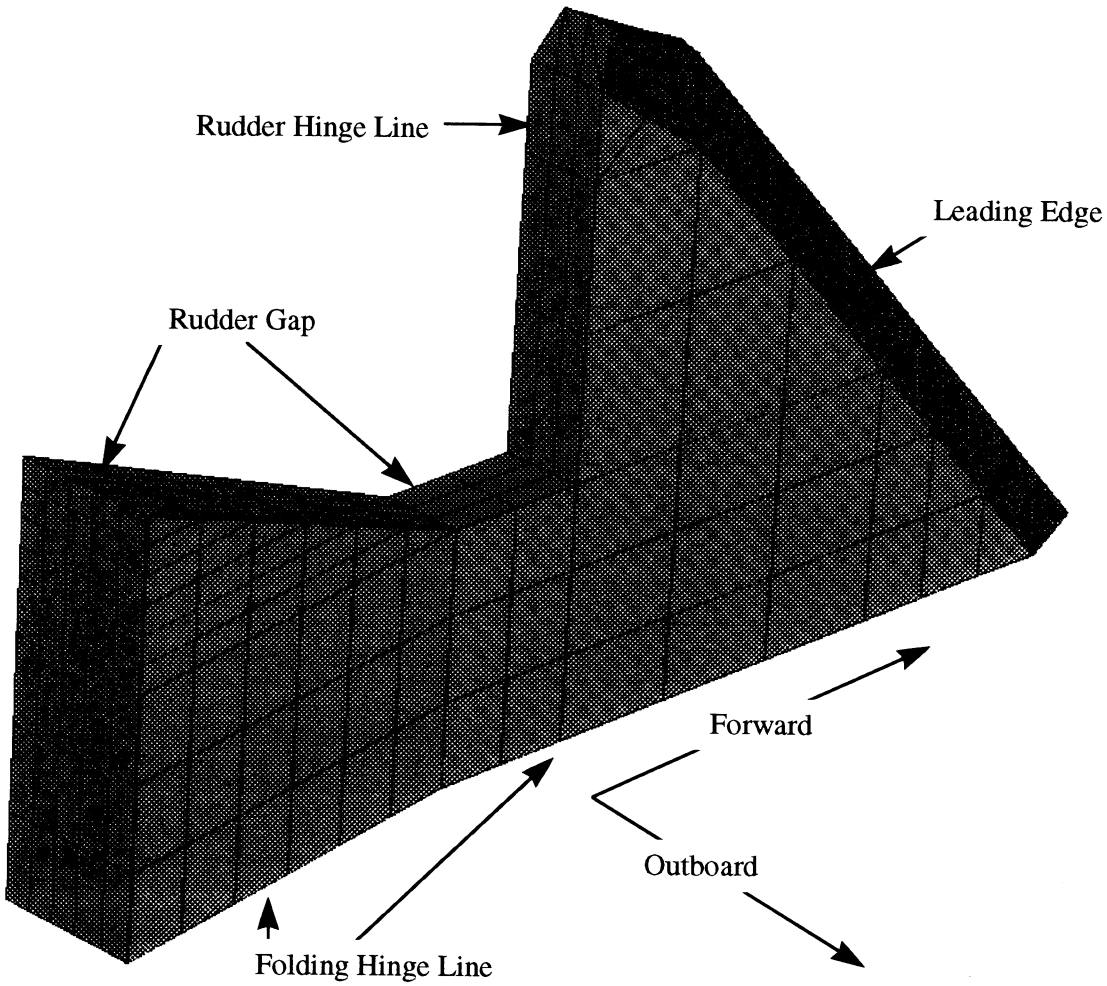

FIGURE 6. OUTBOARD VIEW OF TSS THERMAL RADIATION MODEL

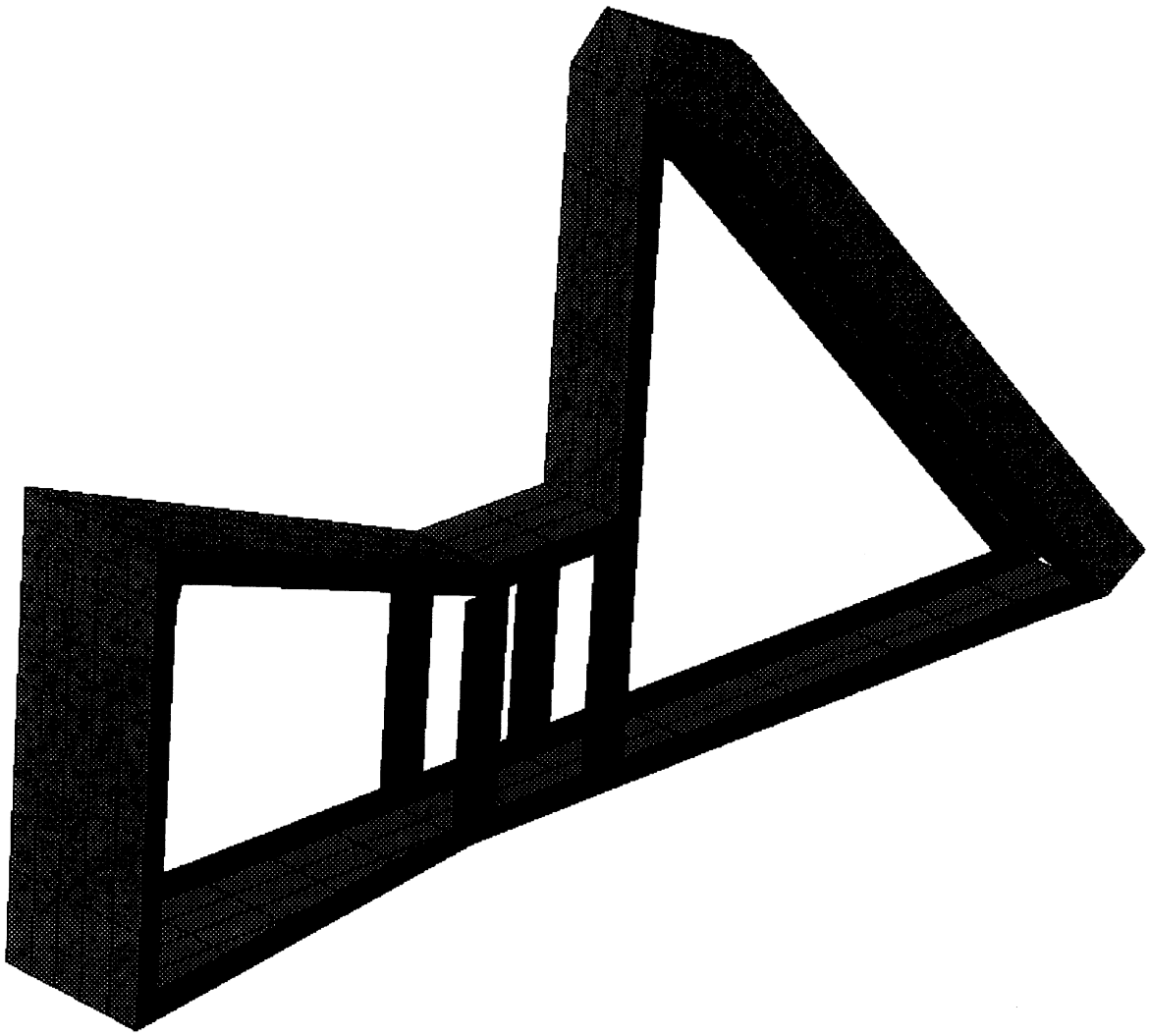

FIGURE 7. VIEW OF TSS GEOMETRY WITHOUT SKIN

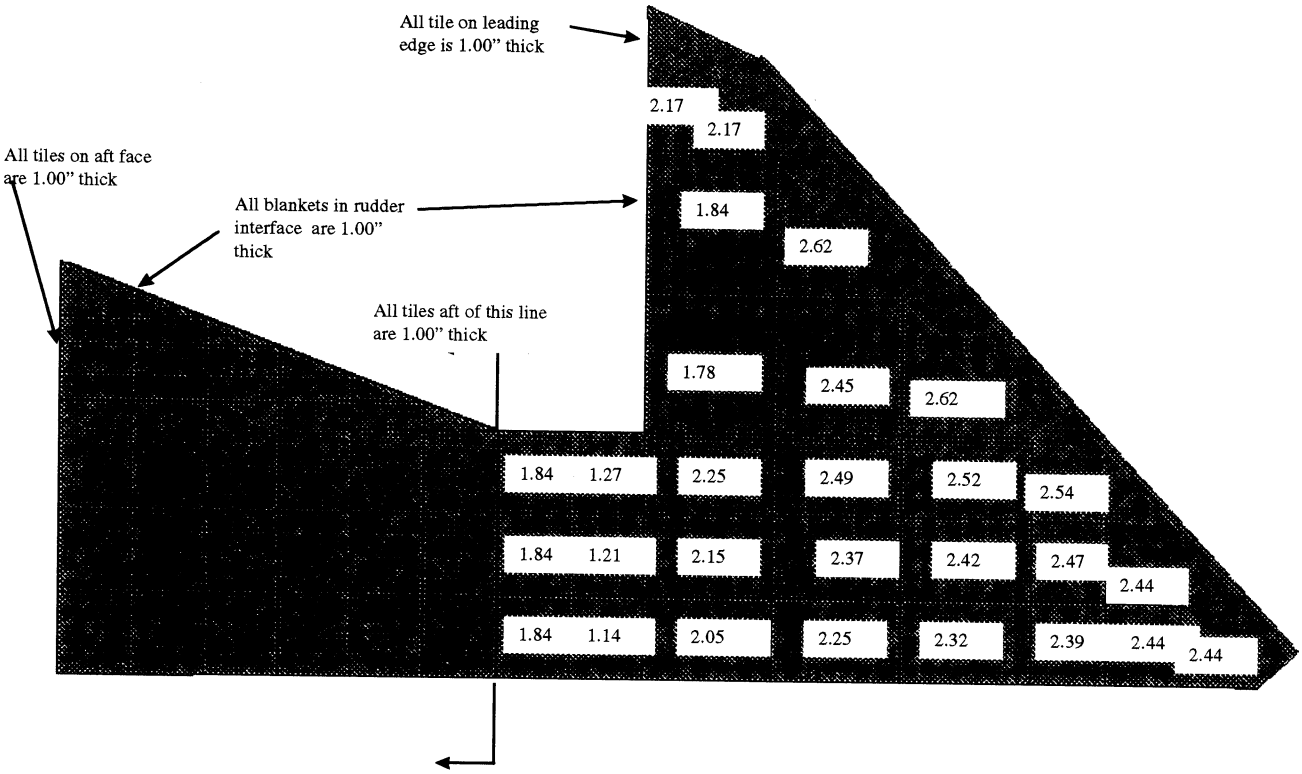

FIGURE 8. TILE THICKNESSES

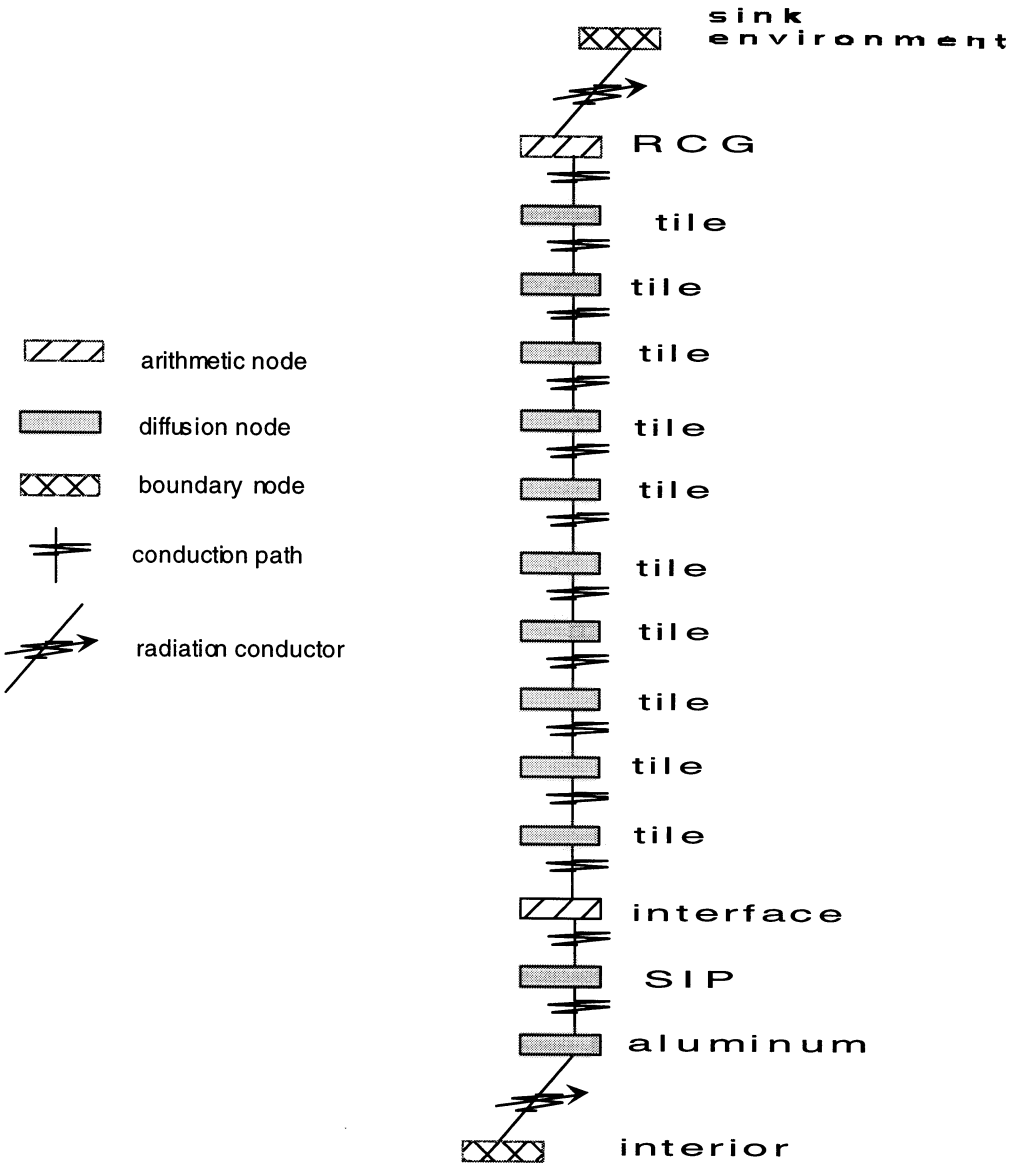

FIGURE 9. LOCAL TILE NODALIZATION

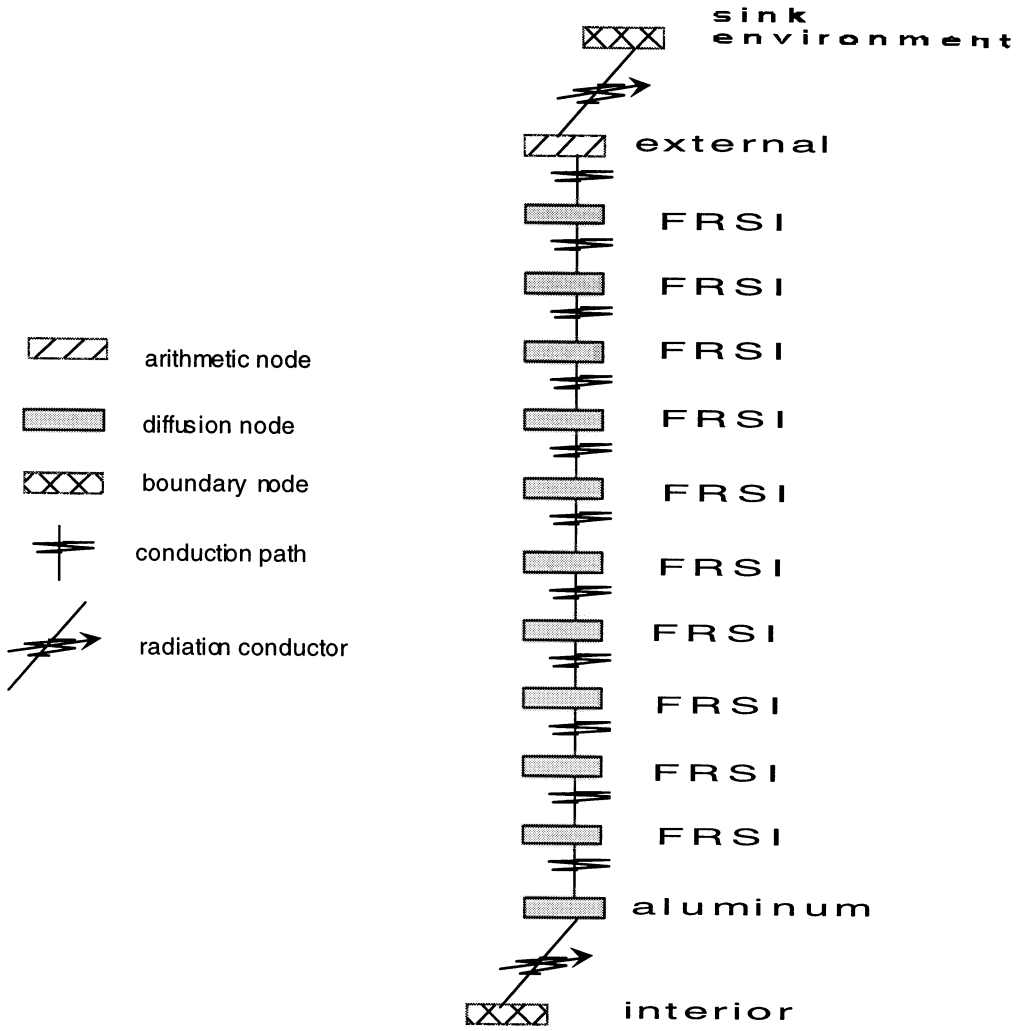

FIGURE 10. LOCAL BLANKET NODALIZATION

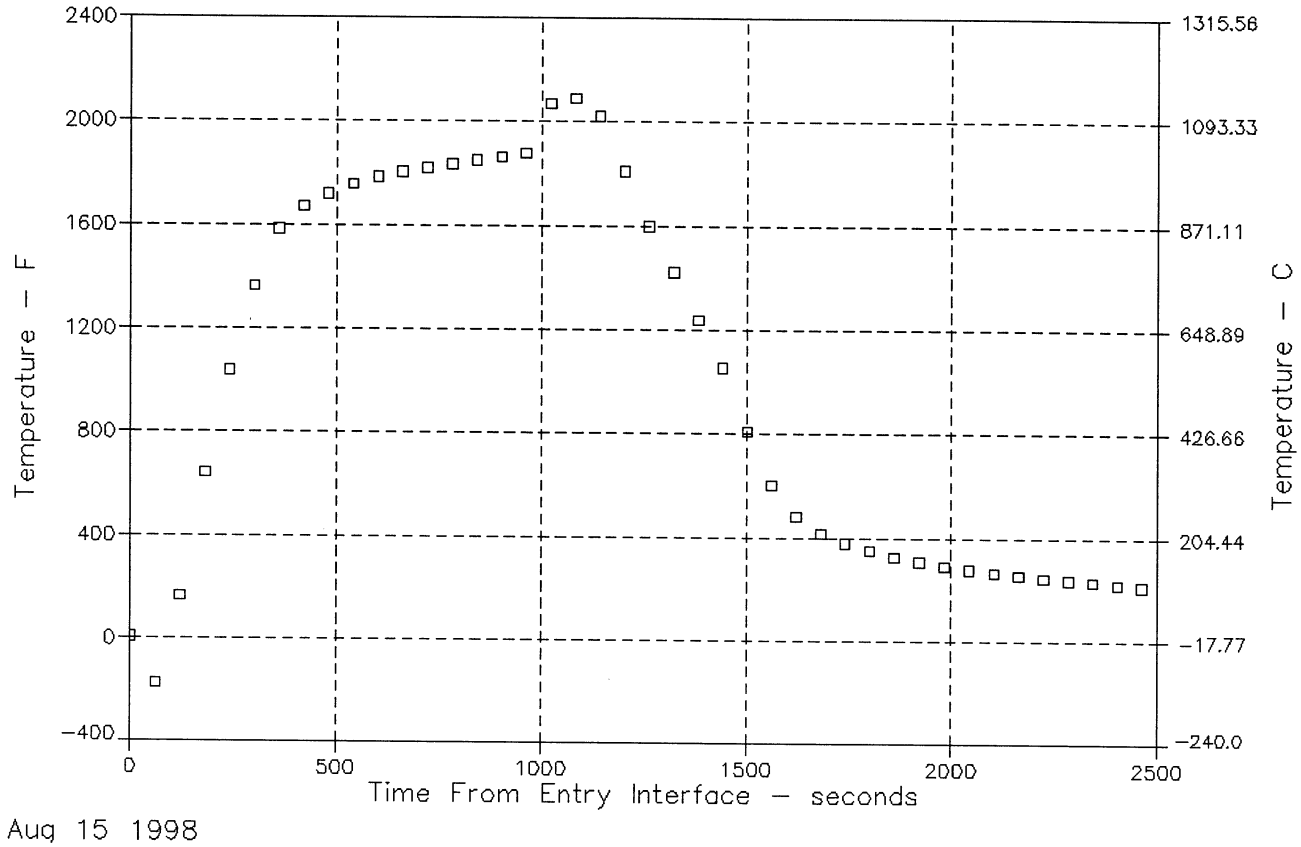

FIGURE 11. PEAK SURFACE TEMPERATURE AT EACH TIME STEP

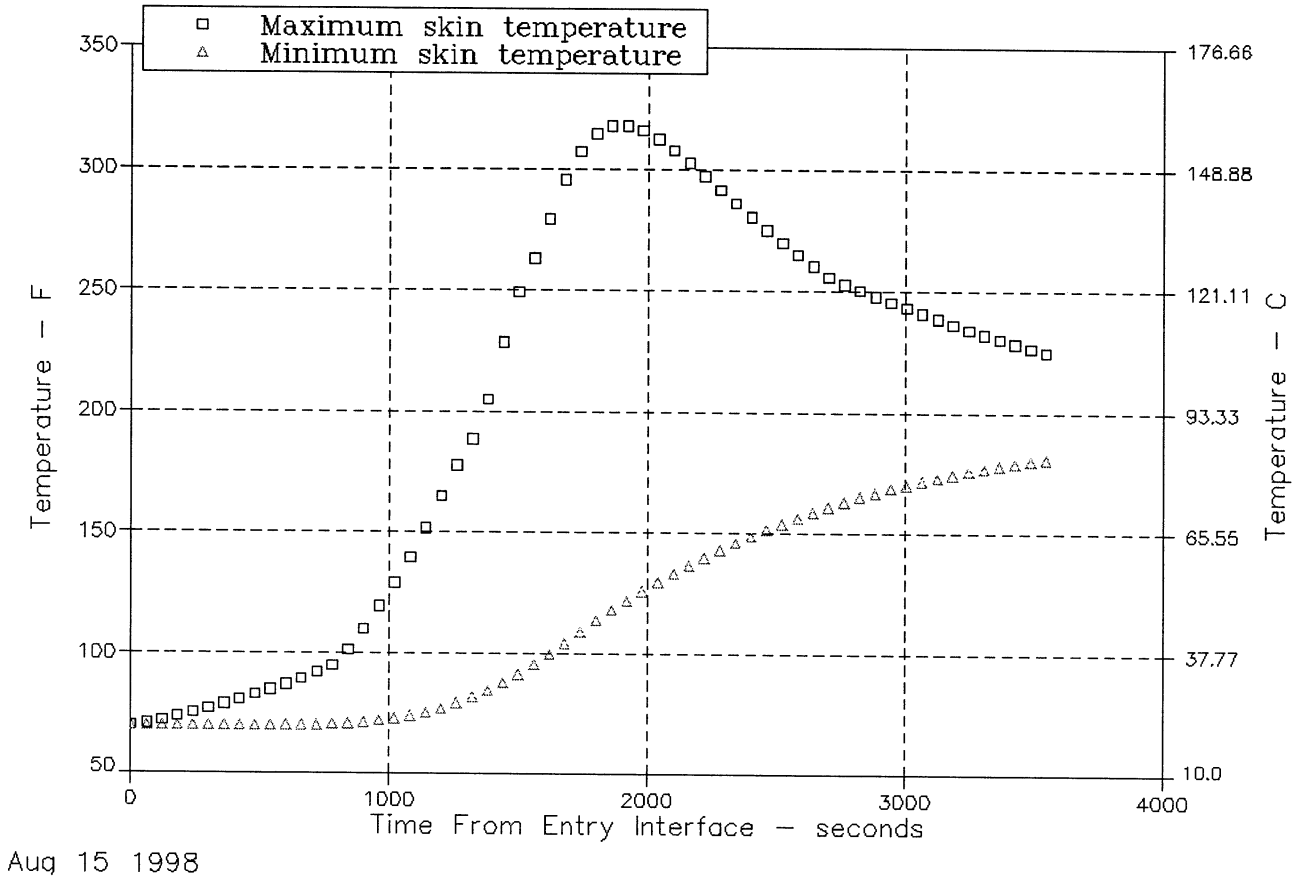

FIGURE 12. HIGHEST AND LOWEST SKIN TEMPERATURES

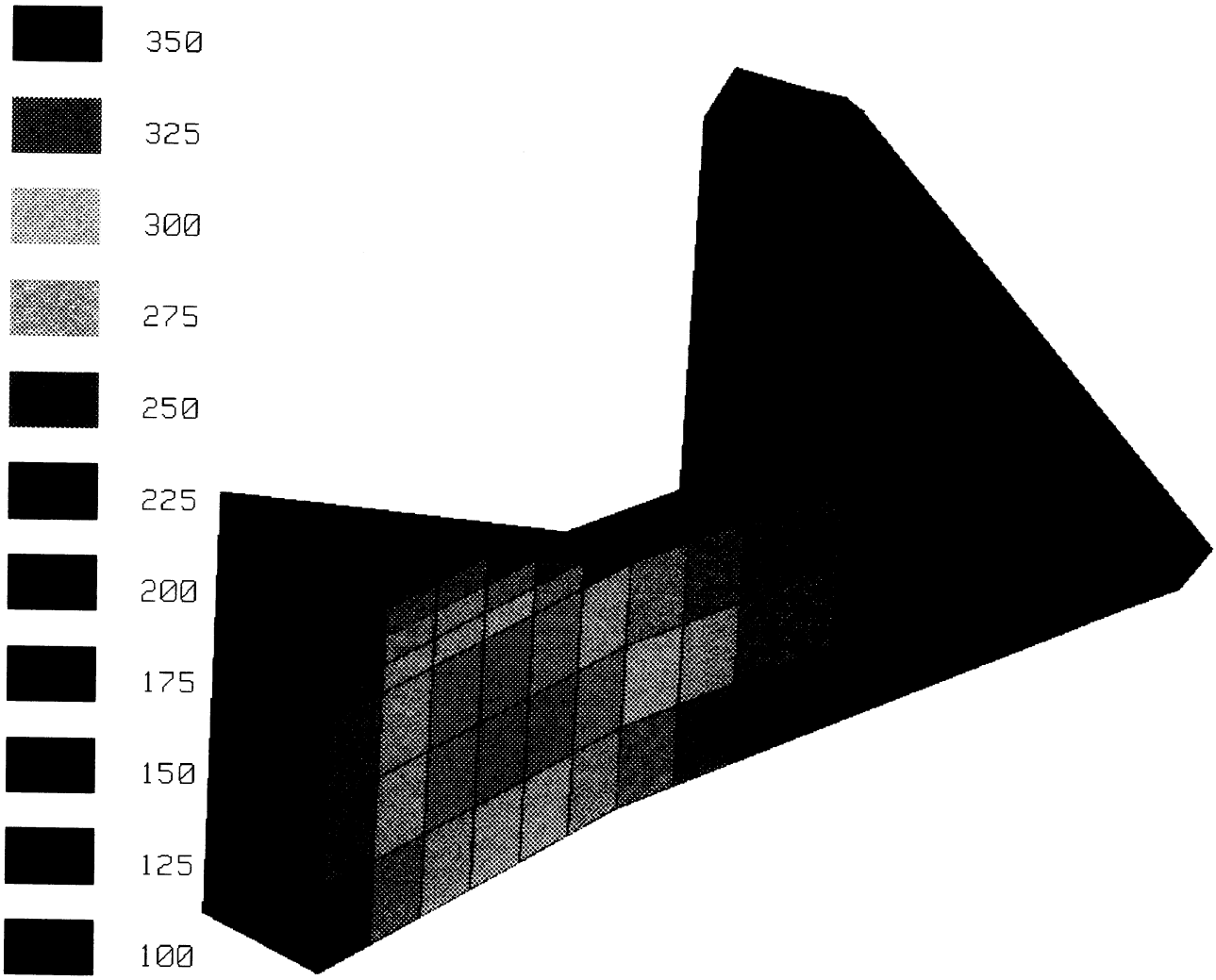

FIGURE 13. OUTBOARD SKIN TEMPERATURES AT 2000 SECONDS
(ALL TEMPERATURES IN DEGREES F)

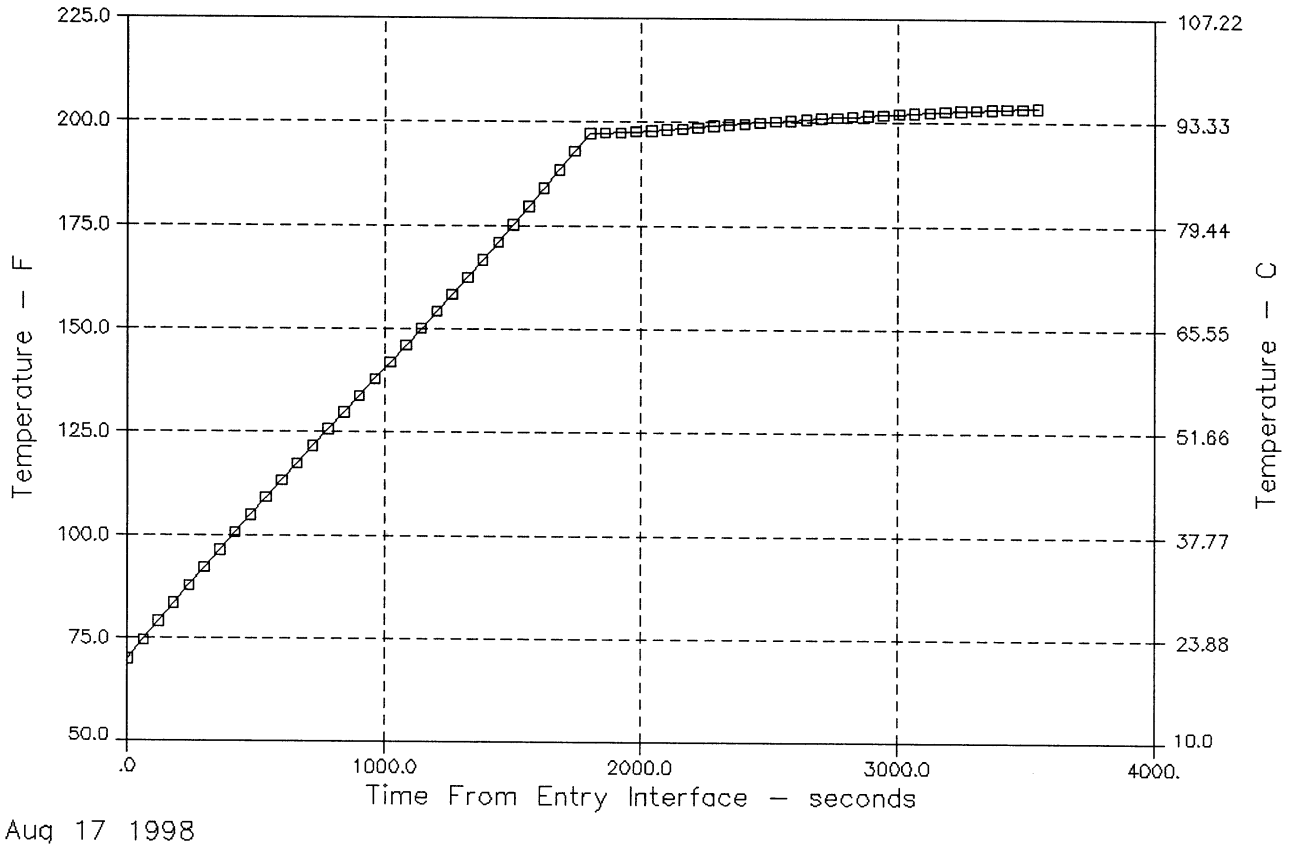

FIGURE 14. ELECTROMECHANICAL ACTUATOR TEMPERATURE RESPONSE

CONCEPT OF THE LOCAL THERMO-CHEMICAL SIMULATION FOR RE-ENTRY PROBLEM: VALIDATION & APPLICATIONS

Anatoliy F. Kolesnikov
The Institute for Problems in Mechanics in Russian Academy of Sciences
Moscow, Russia 117526

SUMMARY

The concept of the local thermo-chemical simulation (LTS) of the high-enthalpy flow action on a vehicle stagnation point formulated in references 1 and 2 is based on the requirement to locally provide in a ground test the same boundary layer on the model as at the re-entry conditions. The validation of this concept is carried out through the comparative analysis of computed heat transfer rates and profiles of gas temperature and atoms fractions within boundary layers near the model in the subsonic high-enthalpy air flow and near the blunt body in the hypersonic air flow whose parameters are extrapolated from the inductively heated plasma experiment. It is established that the LTS provides a very good accuracy if air temperatures at the outer edges of both boundary layers near a model and a body are close to equilibrium value or surface catalycity is high enough. An example of the LTS concept application is shown through a prediction of the plasmatron subsonic test parameters for the simulation of heat transfer to the Mars Pathfinder aeroshell at the peak-heating conditions in the Martian atmosphere. The computed stagnation point heat flux range for the model in the subsonic dissociated carbon dioxide flow in the whole range of surface catalycity is found in good agreement with the viscous-shock layer analysis carried out in reference 3 for the aeroshell without the surface ablation.

INTRODUCTION

In fact, only partial heat transfer simulation could be achieved by using high-enthalpy wind tunnels. The stagnation point configuration is mostly important for TPM testing and surface catalycity rebuilding (refs. 4 to 11) In particular, the catalytic properties of TPM for the Buran space vehicle were studied by using the inductive plasmatron IPG-2 on cylindrical models with a flat face and 30 mm in diameter (ref. 6). In subsonic high-enthalpy flows of dissociated nitrogen, oxygen and air, the effective probabilities of the catalytic recombination of *N* and *O* atoms on the tile coating and on the antioxidation coating of carbon-carbon material were determined at the enthalpy 20-22MJ/kg in the pressure range 0.1-0.3atm and the surface temperature up to 1700K: for the tile surface $\gamma_{wN,O} \leq 3 \cdot 10^{-3}$, for the antioxidation coating of C-C material $\gamma_{wN,O} \approx 7 \cdot 10^{-3}$ (refs. 2 and 6). These data were confirmed by the Bor and Buran space vehicles flight experiments (ref. 12).

It is almost obvious now that requirements to provide in tests only full-scale values of stagnation pressure and surface temperature (ref.8) or total enthalpy (ref.9) are not sufficient for the complete simulation of heat transfer and oxidation and we still need to answer the question: for what hypersonic flight conditions can we use substantiatenly the data on TPM catalytic properties or thermo-chemical resistance obtained in ground tests for the prediction of full-scale heat transfer or vehicle surface aging?

For a stagnation point this question can be solved on the base of the concept of the local thermo-chemical simulation (LTS) formulated in references 1 and 2. This concept includes the requirements to provide in high-enthalpy tests the same values of total enthalpy, stagnation pressure and velocity gradient in the stagnation point of the model as in a hypersonic flow around the vehicle at the given re-entry trajectory point. By means of this nearly simple theory ground test data could be extrapolated to flight conditions if we know effective radii of a model and a body nose. But an accuracy of such extrapolation should be estimated.

In this paper some results of validation of this concept are presented. The validation is carried out through the direct comparison of computations of the 1D boundary layer problem for the high-enthalpy experiment and corresponding 1D thin shock layer problem for the extrapolated flight parameters. The well documented experimental and numerical results for subsonic high-enthalpy flow parameters in the induction plasmatron IPG-2 (ref.2) have been

used. By means of the LTS theory the test parameters were recalculated to hypersonic flight conditions. After that the nonequilibrium boundary layer near the model and the shock layer near the body along the stagnation line have been computed for a 5-species dissociated air. Then stagnation point heat fluxes, temperature and species fractions profiles within two boundary layers were compared. It is shown that the surface catalycity and the displacement of air temperature from the equilibrium value at the outer edges of boundary layers are the factors in the actual accuracy of the presented test-to-flight extrapolation.

Another example of application of the LTS concept is demonstrated through an analysis of the test parameters required for the stagnation point heat transfer simulation for the Mars Pathfinder aeroshell at the peak-heating point of the trajectory in the Martian atmosphere (ref.3) by using the induction plasmatron of 100 kW power (refs. 10, 11 and 13) and the standard European model configuration (refs. 8, 10 and 11). The numerically predicted heat transfer range for the experiment in a subsonic high-enthalpy carbon dioxide flow is found in good agreement with computations from reference 3 in the whole range of surface catalycity.

CONCEPT OF THE LOCAL THERMO-CHEMICAL SIMULATION

Our way to study the problem of the ground test-to-flight extrapolation lies in the use of the theory of the local heat transfer simulation formulated in references 1 and 2. At least for the case of a stagnation point heat transfer we can point out the hypersonic flow parameters and a blunt body radius which are in direct correspondence with high-enthalpy subsonic flow parameters and a model radius if both surfaces have the same catalycity and emissivity and also the same heat transfer boundary conditions (for example, radiative-equilibrium walls). For an axisymmetric subsonic flow past a blunted model of radius R_m the conditions of simulation of the heat transfer to the stagnation point on a blunted body of radius R_w in a hypersonic flow with velocity V_∞ and density ρ_∞, in the case when $R_m << R_w$, are expressed in the form (ref. 1)

$$P_w = \rho_\infty V_\infty^2, \quad H_e = \frac{1}{2} V_\infty^2 \tag{1}$$

$$\frac{V_s}{R^*(R_c, R_m)} = \left(\frac{8}{3} \frac{\rho_\infty}{\rho_e} \right)^{\frac{1}{2}} \frac{V_\infty}{R_w} \tag{2}$$

Here P_w is the stagnation point pressure on a body and a model, H_e is the enthalpy at the outer edges of boundary layers near a body and a model, V_s is the velocity of the subsonic jet at the center of the plasmatron channel exit section, R^* is the model effective radius that depends on the channel radius R_c and the model radius R_m..

The conditions (1) are simple, but the condition (2) is not trivial and contains a geometrical parameter R^* which should be computed for the test configuration by using CFD. For subsonic jets over cylindrical models with a flat face we obtained the following approximation for R^* from numerical solutions of Navier-Stokes equations

$$R_m^* = \begin{cases} R_m \left[2 - l - 1{,}68(l-1)^2 - 1{,}28(l-1)^3 \right], & l \le 1 \\ R_c, \ l > 1 \ \ (l = R_m / R_c) \end{cases} \tag{3}$$

RECALCULATION OF EXPERIMENT CONDITIONS TO FLIGHT PARAMETERS

In accordance with (1), (2) there is one-to-one correspondence between subsonic jet parameters H_e,, P_o $(\approx P_w)$, V_s and the given dimensions R_c, R_m, on the one hand, and parameters of the hypersonic flow and the nose radius of a blunt body, on the other

$$V_\infty = \sqrt{2H_e}, \quad \rho_\infty = \frac{P_o}{2H_e}, \quad R_w = \left(\frac{8}{3} \frac{\rho_\infty}{\rho_e} \right)^{\frac{1}{2}} \frac{V_\infty}{V_s} R^* \tag{4}$$

In order to estimate the accuracy of the correspondence between the heat fluxes and nonequilibrium boundary layers structures near the stagnation points on the model and the body, whose parameters are linked by the conditions (4), we will analyze the well characterized IPG-2 plasmatron subsonic regime for air at the pressure 0.1atm , the generator anode power 37.4kW and the mass flow rate through the discharge channel 2.8g/s (ref.2). At the distance of 30mm from the plasmatron exit section, the enthalpy H_e = $2.19\cdot10^7 m^2/s^2$, the velocity V_s = 180m/s,the density ρ_s = 3.86 10^{-3} kg/m^3, Reynolds number $Re_s = \rho_s V_s R_m / \mu_s \cong 58.6$, Mach number M_S = 0.14. For the VGU-2 plasmatron channel of radius $R_c = 3\cdot10^{-2}$ m and the cylindrical model radius $R_m = 1.5\cdot10^{-2}$m we have, in accordance with (3), $R^* = 1.2R_m = 1.8\cdot10^{-2}$ m.

Using these subsonic air flow parameters, from expressions (4) we have determined the parameters of the hypersonic air flow past the blunt body : V_∞= 6620 m/s, $\rho_\infty = 2.28\cdot10^{-4}$ kg/m^3, R_w = 0.265m. This value of density corresponds to the altitude of 62.4km in the Earth atmosphere. Correspondingly the flight Reynolds number Re_∞ = 1750 and Mach number M_∞ = 20. We see, that Reynolds and Mach numbers are quite different for these ground test and hypothetical flight regimes. That means that these numbers are not the similarity parameters for a stagnation point heat transfer.

METHOD OF VALIDATION

The proposed method of validation of the LTS concept consists of comparing the calculated heat transfer rates and also the profiles of the temperature and species fractions within the boundary layers near the stagnation points of the model and the body for subsonic and hypersonic flows conditions linked by the correlations (4). Such a comparison is carried out below.

A method for calculation of heat transfer rates at the stagnation point of a model with a flat face exposed to a subsonic jet of a viscous multicomponent reacting gas was developed in references 2, 6 and 14. Here we also use the concept of a boundary layer of finite thickness in the neighborhood of the stagnation point with the numerical solution of the Navier-Stokes equations as the outer solution. In particular, the thickness δ of the boundary layer and the hydrodynamic parameters at its outer edge, including the flow vorticity, which are given below in the formulation of the problem, are determined from this Navier-Stokes equations solution.

In the case of a one-temperature multicomponent mixture of atoms and molecules in the equilibrium excitation of the vibrational degrees of freedom, the system of ordinary differential equations describing the flow within the boundary layer near the stagnation point of the model has the following form

$$
\begin{aligned}
&\left(l u'_\eta\right)'_\eta + f u'_\eta - \frac{u^2}{2} + \frac{1+\alpha_e}{2\rho} = 0, \\
&\left(\frac{l}{Pr} H'_\eta\right)'_\eta + f H'_\eta + \left[\frac{l}{Pr}\sum_{i=1}^{N}(h_i - h_i)^*(Le_i - 1)c'_{i_\eta}\right]'_\eta = 0, \\
&\left(\frac{l}{Sc_i} c'_{i_\eta}\right)'_\eta + f c'_{i_\eta} + w_i = 0 (i=1,...<N-N_e), \\
&f'_\eta = u, y'_\eta = \Delta_\rho^{-1}\chi^{-1}, \\
&1/\rho = T/m, c_j^\bullet \equiv c_{j_e}^\bullet, J_j^\bullet \equiv 0 (j=1,...,N_e), H = \sum_{i=1}^{N} c_i h_i, \\
&l = \mu\rho/\eta_e^2, \eta_e = \Delta\sqrt{2Re u_{1e}}/\chi, \chi = \int_0^1 \frac{d\eta}{\rho}, Re = \rho_s V_s R_m/\mu_e, \\
&\Delta = \delta/R_m, u = u_1/u_{1e}, u_1 = \partial u/\partial x, \upsilon = -V^0/V_s, \\
&\alpha_e = -\upsilon_e(\partial u_1/\partial y)_e/u_{1e}^2, U = U^0/V_s, x = x^0/R_m, \\
&y = y^0/R_m, \rho = \rho^0/\rho_e, T = T^0/T_e, h_i = h_i^0/H_e.
\end{aligned}
\tag{5}
$$

The boundary conditions at the outer edge of the boundary layer and on the surface of the model are:

$$\eta=1: u=H=1, c_i=c_{i_e}\ (i=1,...,N-N_e) \tag{6}$$

$$\eta=0: u=f=0, T=T_w, y=0$$

$$\frac{\mu}{Sc_i\eta_e}c'_{i_\eta}=\frac{K_{w_i}}{V_s u_{1e}}\sqrt{\frac{Re u_{1e}}{2}}c_i\left(K_{w_i}=\frac{2\gamma_i}{2-\gamma_i}\sqrt{\frac{kT_w}{2\pi m_i}}\right) \tag{7}$$

$$i=1,\ldots,N-N_e$$

In (5)-(7) U^o,V^o are the velocity components in the cylindrical coordinate system x^o, y^o which is related with flat face, ρ is the density, c_i is the mass concentration, h_i is the enthalpy, h_i^* is the energy of formation of the species j; c_j^*, J_j^* are the mass concentration and the diffusive flux of the chemical element j; H is the enthalpy of the gas mixture, T is the temperature, m is the molecular weight, Pr, Sc_i and Le_i are the Prandtl, Schmidt and Lewis numbers; $K_{w\,i}$ and γ_i are the effective heterogeneous recombination rate constant and catalytic efficiency; k is the Boltzmann constant, m_i is the molecular weight of the species i, N is the number of species, N_e is the number of chemical elements, and η is the Dorodnitsyn's variable. The circle superscript denotes dimensional quantities, and the subscripts s and e correspond to the dimensional parameters at the channel exit and at the outer edge of the boundary layer on the axis of symmetry of the flow.

In the momentum equation the parameter α_e=const takes into account the vorticity of the flow at the outer edge of a boundary layer of thickness δ. Parameters α_e , U_e and u_{1e} are determined from the profiles of the velocity components obtained from the numerical solution of the Navier-Stokes problem for a viscous reacting gas jet flow past a cylinder with the flat face at M <<1 (refs.2, 6 and 14). For our case $\Delta = \delta/R_m = 0.4$, $\upsilon_e = 0.52$, $u_{1e} = 0.445$, α_e=2.626. It was assumed in calculation that $Pr = 0.71$, Sc=0.65 and $\mu \sim T^{0.77}$.

We assume that the following gas-phase reactions in a 5-species air occur within the boundary layer: *1)* $O_2 + M \leftrightarrow O + O + M$, *2)* $N_2 + M \leftrightarrow N + N + M$, *3)* $NO + M \leftrightarrow N + O + M$, *4)* $O + N_2 \leftrightarrow N + NO$, *5)* $O + NO \leftrightarrow N + O_2$
The chemical equilibrium is supposed to be at the outer edge of the boundary layer: P = 0.1 atm, $H_e = 2.19\cdot10^7$ m^2/s^2, T_e = 5960K, C_{N2} = 0.4576, C_{O2} = $0.3513\cdot10^{-3}$, C_{N2} = $0.2922\cdot10^{-2}$, C_N = 0.3091, C_O = 0.2304.

The thin viscous shock layer model has been used independently for the computation of the hypersonic air flow (V_∞= 6620 m/s, ρ_∞= $2{,}28\cdot10^{-4}$ kg/m^3) past a sphere of the radius R_w =0,265 m. At the formulation of this problem the same boundary conditions at the wall and the same chemical reactions rates, as for the subsonic flow, have been used. For the numerical solutions of the problem (5)-(7) and the viscous shock layer problem the same fourth-order-accurate finite-difference scheme was used. All computations were made for the surface temperature T_w=1500K.

RESULTS OF VALIDATION FOR AIR FLOWS AND DISCUSSION

Figure 1 shows the calculated dependencies of the heat fluxes q_w to the stagnation points of the model (M<<1) and the body (M>>1) as the functions of the heterogeneous recombination rate constant K_w for the case $K_w = K_{wo} = K_{wN}$. For a highly catalytic surface the difference in the heat fluxes q_w under corresponding conditions of the subsonic and the supersonic flow is only about 5%. As K_w decreases, this difference increases and on a noncatalytic surface in the subsonic jet the heat flux is 30% less then the heat flux in the hypersonic flow. So, we see, that the accuracy of the heat transfer simulation on the base of the theory LTS developed in references 1 and 2 depends on the surface catalytic efficiency. It is quite good for a highly catalytic surface and it does not look good for a noncatalytic one. Nevertheless, both curves in figure 1 are functionally similar and they have the common interval $10^{-1} < K_W < 10^2$, where the heat transfer rates drastically depend on wall catalycity. From here we can conclude that the data on the effective catalytic rates for atomic oxygen and nitrogen recombination on the Buran's TPM obtained in subsonic jets (refs. 2, 6 and 14) are quite applicable to hypersonic re-entry conditions with flight parameters of the same orders of magnitude that calculated above.

For clearer understanding of the LTS capabilities we will compare the profiles of air temperature, *N* and *O* atoms fractions across the boundary layer and the shock layer at the same conditions for two limiting cases: fully and noncatalytic surfaces. Figure 2 shows the temperature profiles within the boundary layer near the model and within the shock layer near the blunt body for a fully catalytic wall case. We see that temperature profiles are rather different at the outer edges of two boundary layers. For the hypersonic flow the temperature T_e considerably (~ by 2000K) exceeds the equilibrium value because the shock layer is fully nonequilibrium in this case, but temperature profiles are quite close to each other near the walls. This leads to a good agreement between thermal conductive parts of the heat fluxes to fully catalytic surfaces of the body and the model.

Within a hypersonic shock layer we can see the displacement of mass fraction of *N* atoms from the equilibrium value at the outer edge of the boundary layer (see figure 3): the mass fraction of C_N is significantly less then the equilibrium value in the subsonic case. On the other hand, close to fully catalytic surfaces, the profiles of *N* atoms fractions for considered subsonic and hypersonic air flows are quite similar including fine details of different behavior in comparison with *O* atoms profiles due to exchange reactions in dissociated air 4) and 5) mentioned above. In fact, the contributions in the heat fluxes due to nitrogen atoms diffusion are insignificant in this case. Also we can see on figure 3 that the excellent simulation accuracy is achieved for the atomic oxygen fraction profile within the whole boundary layer because oxygen is almost completely dissociated at the outer edges of both boundary layers. As a result the parts of the heat fluxes due to the atomic oxygen diffusion for both flows are equal within 5%. The same is correct for the total heat fluxes to the fully catalytic wall.

For the noncatalytic wall case the situation is more dramatic as we can see from figures 4 and 5. The temperature profiles across boundary layers are different exterior to nearest vicinities of stagnation points and the heat flux due to thermal conductivity is much higher in the supersonic flow. Both boundary layers are almost frozen and diffusion does not influence heat transfer. The atomic nitrogen fraction near the surface of the model is significantly higher in the plasmatron test, but the atomic oxygen fraction profiles within boundary layers are quite close in experiment and hypothetical flight. That means the formulae (4) for ground test-to-flight extrapolation should provide a complete simulation of the diffusion flux and the partial pressure of atomic oxygen and, therefore, surface catalysis and oxidation processes. These are the arguments for using here the term “thermo-chemical” simulation.

We can conclude that the displacement of air temperature from the equilibrium value at the outer edges of boundary layers in high-enthalpy tests or in flight is a factor in actual accuracy of the LTS concept. One should expect that an agreement between the heat fluxes and two boundary layer structures will be improved when the air temperatures outside boundary layers will be closer to equilibrium. For example, for higher values of the pressure P_W , as have already been predicted for the high-enthalpy nitrogen experiment in reference 15.

PREDICTION OF SUBSONIC TEST CONDITIONS FOR MARS PATHFINDER AEROSHELL

Let us consider another application of the LTS concept to a problem of determination of high-enthalpy test conditions for precise simulation of the stagnation point heating for the Mars Pathfinder aeroshell which is a 70-deg sphere cone with a nose radius of 0.6625m (ref.3). In accordance with reference 3 the maximum of the heat flux is achieved at the altitude 40.7km and the following freestream conditions in the Martian atmosphere (C_{CO2} = 0.97, and C_{N2} = 0.03) : V_∞= 6590m/s and ρ_∞= 3.23 $\cdot 10^{-4}$ kg/m^3 .

Desired test conditions are determined for a subsonic dissociated carbon dioxide flow around the cylindrical model of 50 mm in diameter with a flat face and the rounded edge of 11 mm in radius exposed for testing in the IPG-4 plasmatron of 100kW power with the quartz discharge channel of 80mm in diameter (refs. 10 and 11). For such flow configuration on the base of previous numerical solution of Navier-Stokes equations (ref.11) we have the following approximation for the effective radius of this model : R^* = 1.28 R_m = 3.2$\cdot 10^{-2}$ m. Now we can recalculate the entry parameters prescribed above to plasmatron test conditions by using formulae (1) and (2). This simple technique (when we know the effective radius R^*) gives the following test conditions : the enthalpy H_e = 21.73MJ/kg, the static pressure P_s = 0.14atm, the flow velocity V_s = 184 m/s. For considered test configuration the calculated dimensionless parameters in equations (5) are: Δ= 0.4, u_{1e} = 0.39, α_e = 2.10 (ref.11).

For these flow parameters and test geometry prescribed above the stagnation point heat transfer rates have been calculated as a function of the surface temperature T_w and the effective catalytic efficiency γ_w from the numerical solution of the 1D boundary layer problem (5) - (7) for a 5-species dissociated carbon dioxide mixture (CO_2, O_2, CO, O, and C). The next assumptions have been made. 1) The following reactions are running in the mixture: $CO_2 + M \leftrightarrow CO + O + M$, $O_2 + M \leftrightarrow O + O + M$, $CO + M \leftrightarrow C + O + M$, $CO + O \leftrightarrow C + O_2$, $CO_2 + O \leftrightarrow CO + O_2$. 2) Surface catalytic recombination of CO molecules in reaction $CO + O \rightarrow CO_2$ and O atoms in reaction $O + O \rightarrow O_2$ are of the first order and have equal efficiencies γ_w, and C atoms are not involved in surface reactions. The same finite difference scheme was exploited for the numerical solution of the boundary layer problem (5) - (7).

Computed stagnation point heat flux envelope for the predicted subsonic test is shown on figure 6. The upper border of this envelope (the curve 1) corresponds to the fully catalytic surface ($\gamma_w = 1$), the lower border (the curve 7) - to the noncatalytic surface ($\gamma_w = 0$). The solid curves 2-6 correspond to the constant values of γ_w, the dash line 9 corresponds to the theoretical minimum of the heat flux from the frozen boundary layer to the noncatalytic wall. The heat flux envelope is limited from the right side by the curve $q_w = \varepsilon_{th}\, \sigma\, T_W{}^4$, where ε_{th} is the total hemispherical emissivity, σ is the Stefan - Boltzmann constant. The curves 9 and 10 correspond to radiative-equilibrium walls with $\varepsilon_{th} = 1$ and 0.78. Now it is very easy to determine the heat flux and the radiative-equilibrium surface temperature for the given values of ε_{th} and γ_w : q_w and T_w are just the coordinates of the intersection point for two curves: $q_w = q_w$ (T_w, γ_w = const) and $q_w = \varepsilon_{th}\, \sigma\, T_w{}^4$. Thus, in the predicted test at $\varepsilon_{th} = 0.78$ for the fully catalytic wall we have q_w = 142W/cm^2 and T_W = 2380K, for the noncatalytic wall - q_w = 47W/cm^2 and T_w = 1800K.

For the heat transfer rates at the stagnation point of the Mars Pathfinder aeroshell and the radiative-equilibrium wall from reference 11 we have maximum values q_w = 127W/cm^2 and T_w = 2315K at the wall condition of fully recombined CO_2 and q_w = 42W/cm^2 and T_w = 1755K in the noncatalytic wall case. So, we observe a good agreement between numerically predicted heat flux ranges for the Mars Pathfinder aeroshell at the trajectory peak-heating point and for the euromodel overflowed by the subsonic high-enthalpy carbon dioxide jet in the inductive coupled plasma torch in the case when ground test parameters are determined on the base of our LTS concept. It is practically important that the above determined enthalpy and pressure values belong to the operating envelope of the IPG-4 plasmatron in a subsonic mode (refs. 11 and 13) and the maximum of the thermo-chemical load on the stagnation point of the Pathfinder aeroshell could be simulated precisely enough.

This analysis was performed without taking into account surface ablation, but in general the concept of the local thermo-chemical simulation validated here can be applicable to a heat transfer problem with ablation effects if the influence of injection into the incoming flow is not very strong. The accuracy of prediction of ground test parameters or extrapolation to flight could be improved if the velocity gradient for flight conditions is calculated more accurately directly from numerical solution of a hypersonic shock layer problem.

CONCLUSIONS

The LTS concept reveals the new capabilities in the planning of a high-enthalpy experiment and the new approach in the extrapolation from ground to flight. For the complete stagnation point thermo-chemical simulation, the conditions of a hypersonic flow past a blunt body and a ground test could be easy linked on the base of the LTS concept if one knows or can calculate an effective model radius by using CFD for a test configuration. The accuracy of such prediction of dissociated air thermo-chemical action for a hypersonic flight depends on surface catalycity and deviations of air temperatures from the equilibrium value at the outer edges of the boundary layers on a body and a model. For a highly catalytic surface the satisfaction of conditions (1), (2) or (4) ensures the accurate simulation of the convective heat fluxes and the diffusive fluxes of atoms in subsonic high-enthalpy jets. If the state of the dissociated air flow at the edge of the boundary layer at the test or hypersonic flow conditions is significantly nonequilibrium, ground test parameters predicted by using the LTS concept in order to simulate the heat transfer to a low catalytic surface may be applied as support values. In this more dramatic case for the prediction of the well-founded test conditions we have to solve numerically not only the nonequilibrium shock layer problem, but also to compute the nonequilibrium plasma flow within a plasmatron discharge channel and a subsonic reacting air flow past a model.

The computed heat flux range for simulation of the stagnation point heat transfer rate to the Mars Pathfinder aeroshell at the trajectory peak-heating conditions in the subsonic high-enthalpy carbon dioxide flow is in a good agreement with the study presented in reference 3. That means that maximum thermo-chemical load on this aeroshell and TPM behavior can be directly simulated by using the IPG-4 plasmatron in the subsonic regime.

ACKNOWLEDGMENTS

The author would like to thank V. Shchelin for providing the shock layer parameters from his own code and S. Vasil'evskii for help in figures design. This research was supported by the INTAS-RFBR grant 95-1329 and in part by ISTC project 036.

REFERENCES

1. Kolesnikov, A.F., "Conditions of Simulation of Stagnation Point Heat Transfer from a High-Enthalpy Flow," Fluid Mechanics, Plenum, (tr. from Russian), 28, 1, 1993, pp. 131-137.
2. Kolesnikov, A.F., "The Aerothermodynamic Simulation in Sub- and Supersonic High-Enthalpy Jets: Experiment and Theory," Proc. of the Second European Symposium on Aerothermodynamics for Space Vehicles, ESTEC, Noordwijk, The Netherlands, November 1994, ESA SP-367, pp. 583-590.
3. Gupta, R.N., Lee, K.P., Scott, C.D., "Aerothermal Study of Mars Pathfinder Aeroshell," J. of Spacecraft and Rockets, 33, 1, 1996, pp. 61-69.
4. Anderson, L.A., "Effect of Surface Catalytic Activity on Stagnation-Point Heat Transfer Rates," AIAA J., 11, 1973, pp. 649-656.
5. Scott, C.D., "Catalytic Recombination of Nitrogen and Oxygen on High Temperature Reusable Surface Insulation," Progress in Astronautics and Aeronautics, Vol. 77, edited by A.L. Crosbie, AIAA, New York, 1981, pp. 192-212.
6. Vasil'evskii, S.A., Kolesnikov, A.F., Yakushin, M.I., "Determination of the Effective Probabilities of the Heterogeneous Recombination of Atoms When Heat Flow is Influenced by Gas-Phase Reactions," High Temperature, Plenum, (tr. from Russian), 29, 3, 1991, pp. 411-419.
7. Stewart, D.A., Chen, Y., Bamford, D.J., Romanovsky, A.B., "Predicting Material Surface Catalytic Efficiency Using Arc-Jet Tests," AIAA -95-2013.
8. Gulhan, A., Vennemann, D., Yakushin, M., Zhestkov, B., "Comparative Oxidation Tests on Reference Material in Two Induction Heated Facilities," presented at the 46th International Astronautical Congress, Oslo, Norway, October 1995.
9. Eitelberg, G., Krek, R., Beck, W., "Stagnation Point Heat Transfer Testing in Non-Equilibrium Flow Produced by the HEG," AIAA-96-4504.
10. Bykova, N.G., Vasil'evskii, S.A., Gordeev, A.N., Kolesnikov, A.F., Pershin, I.S., Yakushin, M.I., "Determination of the Effective Probabilities of Catalytic Reactions on the Surfaces of Heat Shield Materials in Dissociated Carbon Dioxide Flows," Fluid Mechanics, Plenum, (tr. from Russian), 32, 6, 1997, pp. 876-886.
11. Kolesnikov, A.F., Pershin, I.S., Vasil'evskii, S.A., Yakushin, M.I., "Study of Quartz Surface Catalycity in Dissociated Carbon Dioxide Subsonic Flows," AIAA-98-2847.
12. Voinov, L.P., Zalogin, G.N., Lunev, V.V., Timoshenko, V.P., "Comparative Analysis of Laboratory and Full-Scale Data Concerning "Bor" and "Buran" Space Vehicles Thermal Protection Material Catalycity," Cosmonautics and Rocket Engineering, TSNIIMASH, (in Russian), 2, 1994, pp. 51-57.
13. Bykova, N.G., Vasil'evskii, S.A., Gordeev, A.N., Kolesnikov, A.F., Pershin, I.S., Yakushin, M.I., "An Induction Plasmatron Application for Simulation of Entry into Martian Atmosphere," Proc. of the Third International Symposium on Environmental Testing for Space Programmes, ESTEC, Noordwijk, The Netherlands, June 1997, ESA SP-408, pp. 195-200.
14. Vasil'evskii, S.A., Kolesnikov, A.F., Yakushin, M.I., "Mathematical Models for Plasma and Gas Flows in Induction Plasmatrons," Molecular Physics and Hypersonic Flows, ed. by M.Capitelli, NATO ASI Series, Vol. 482, Kluwer, 1996, pp. 495-504.
15. Kolesnikov, A.F., Shchelin, V.S., "Numerical Analysis of Simulation Accuracy for Hypersonic Heat Transfer in Subsonic Jets of Dissociated Nitrogen," Fluid Dynamics, Plenum, (tr. from Russian), 25, 2, 1990, pp.278-286.

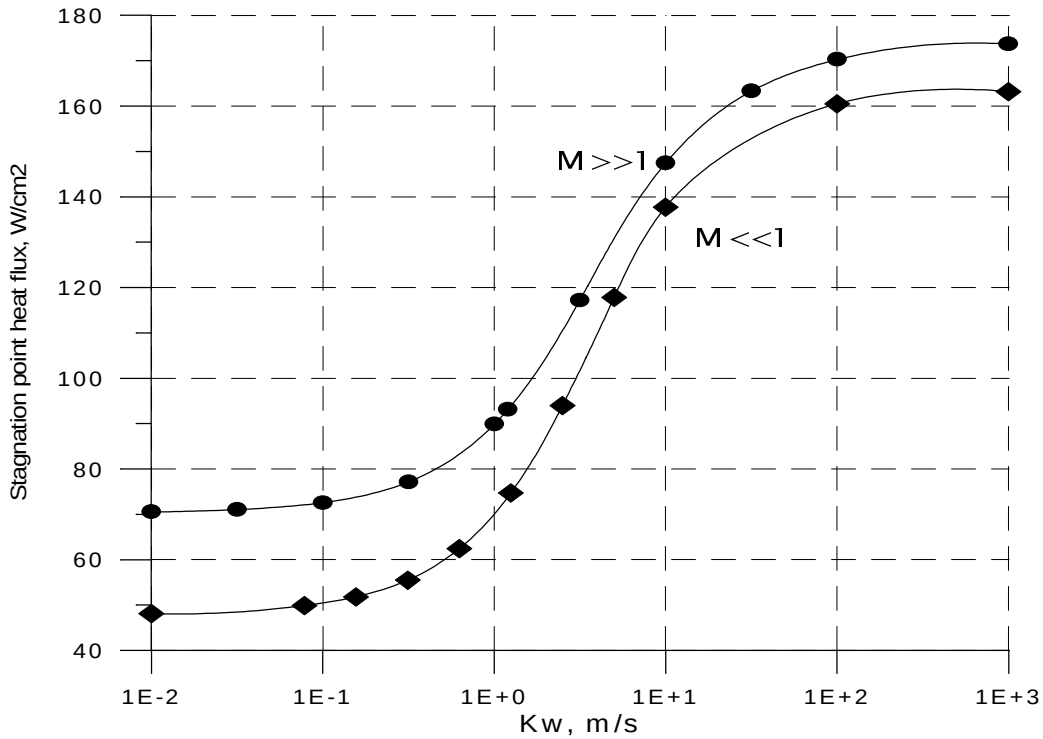

Figure 1. - Heat flux to stagnation point versus effective rate constant Kw of surface atom recombination

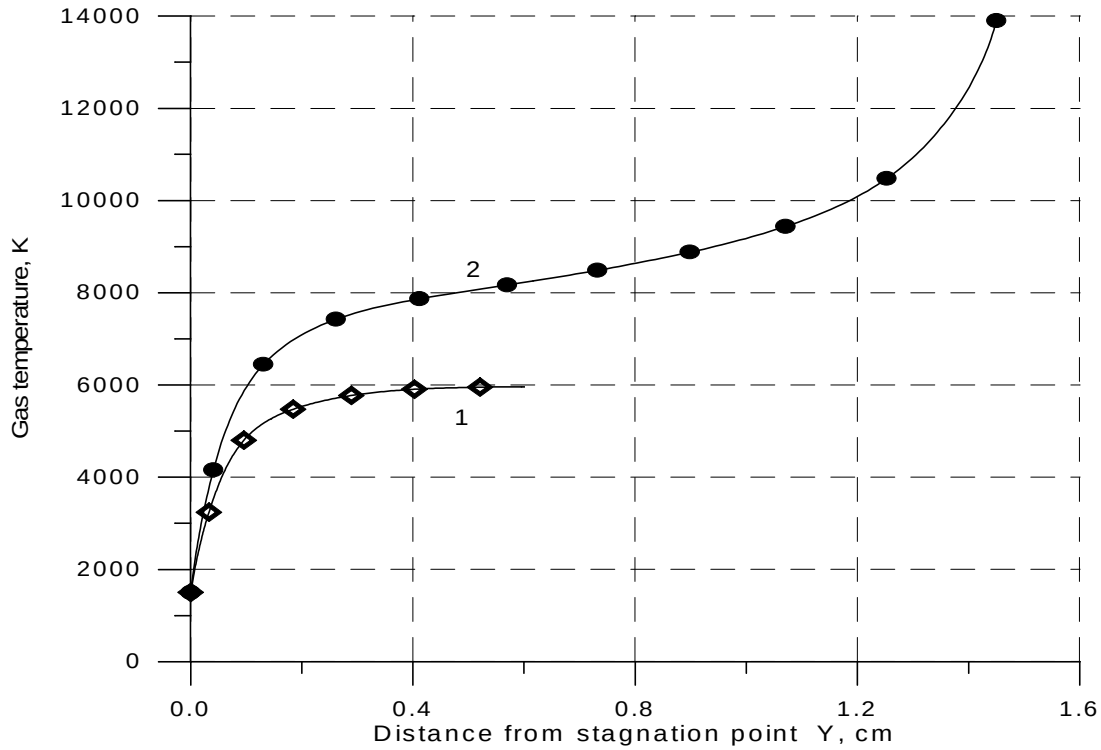

Figure 2. - Temperature profiles along stagnation line (fully catalytic wall): 1- the boundary layer near the model; 2 - the shock layer near the body.

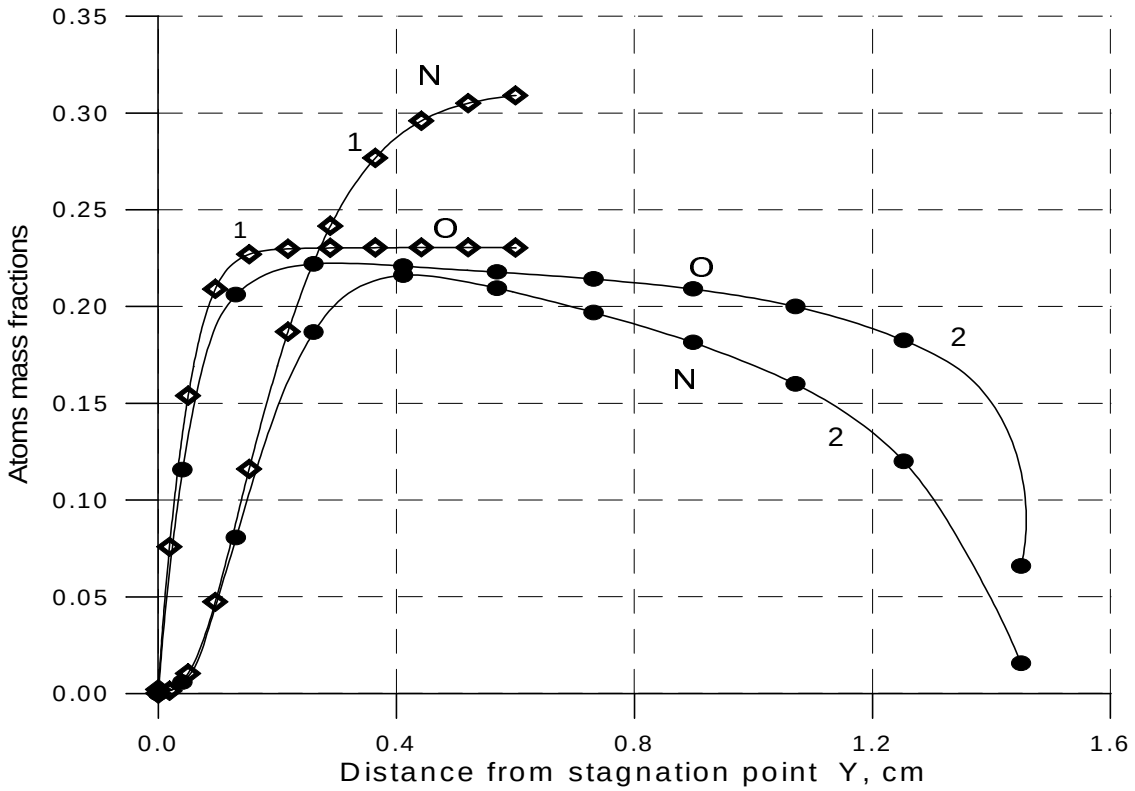

Figure 3. - Profiles of mass fractions of N and O atoms along stagnation line (fully catalytic wall):

1 - boundary layer near the model ; 2 - shock layer near the body

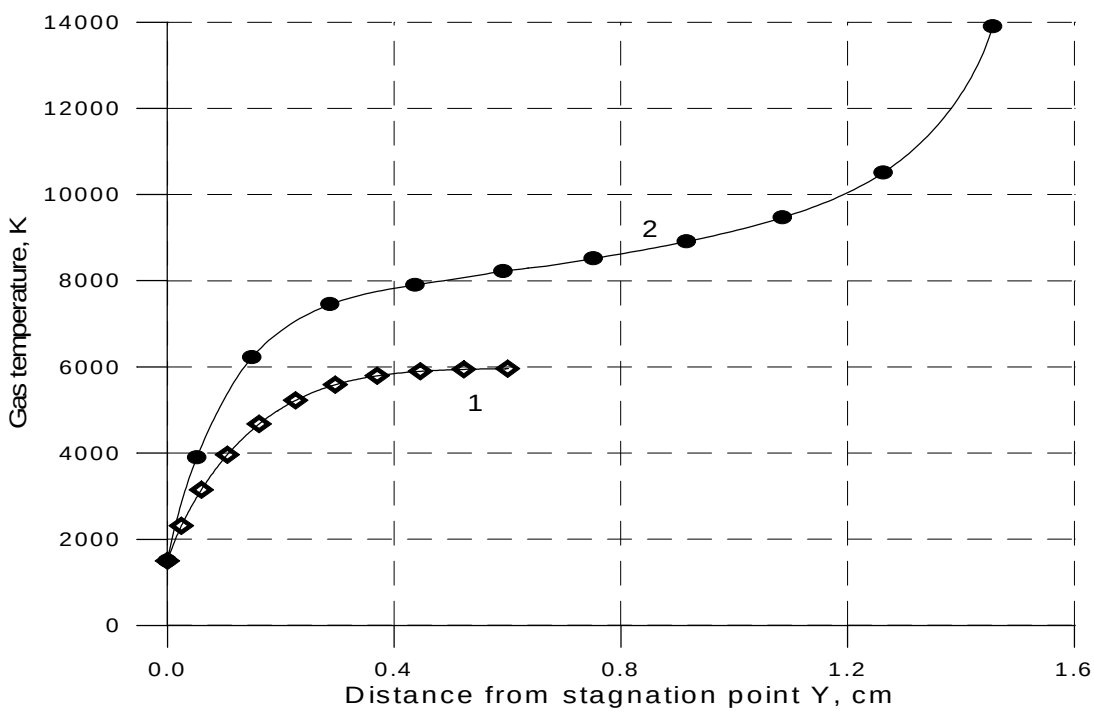

Figure 4. - Temperature profiles along stagnation line (non-catalytic wall):

1 - the boundary layer near the model; 2 - the shock layer near the body.

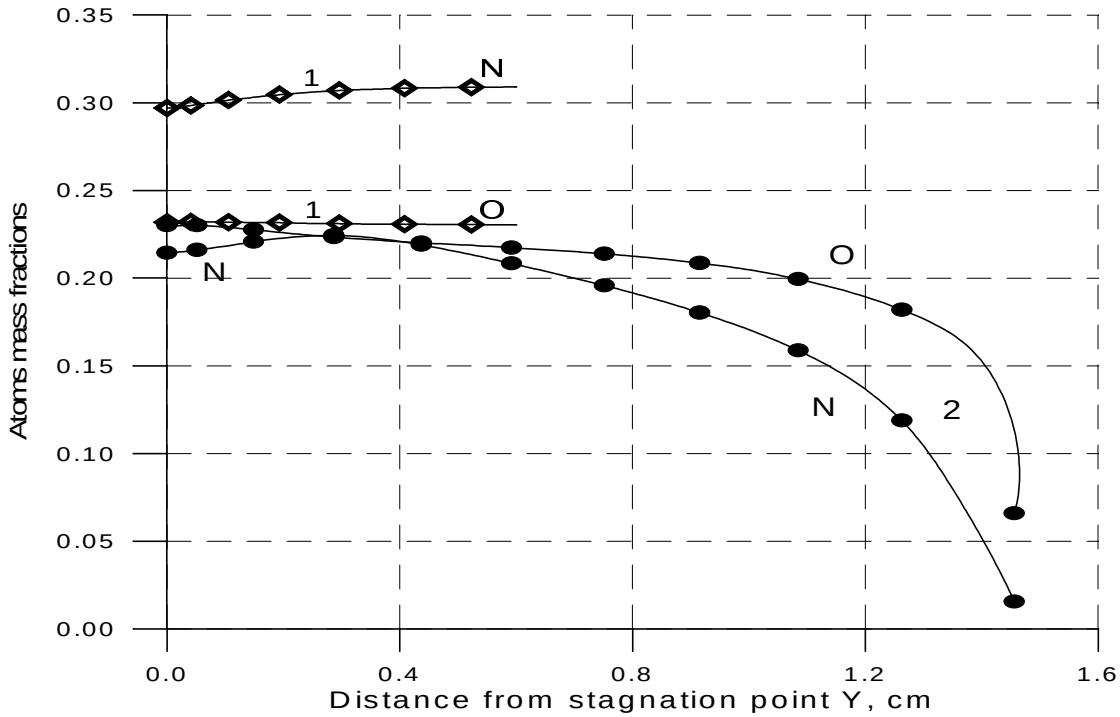

Figure 5. - Profiles of mass fractions of N and O atoms along stagnation line (non-catalytic wall):

1 - the boundary layer near the model; 2 - the shock layer near the body

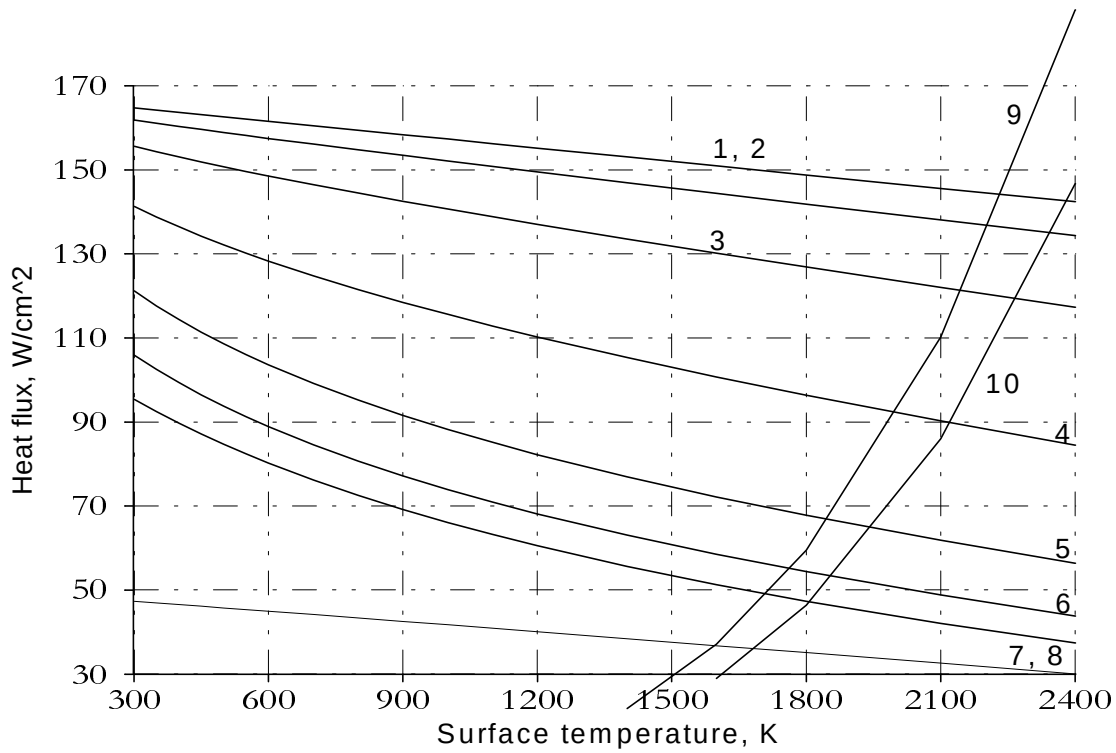

Figure 6. - Heat flux envelope for modeling of heat transfer to Mars Pathfinder aeroshell

1 - 7: Gamma=1; 0.1; 3.2e-2; 1e-2; 3.2e-3; 1e-3; 3.2e-4; 0 ; 8 - frozen boundary layer, Gamma=0

9,10: heat transfer to radiative-equilibrium wall at Epsilon=1 and 0.78

A STOCHASTIC APPROACH TO SPACECRAFTS THERMAL ANALYSIS

Félix Lamela Herrera
Construcciones Aeronaúticas S.A.
Madrid, Spain 28022

Ana Laverón Simavilla
Instituto Universitario "Ignacio da Riva"
Madrid, Spain 28040

SUMMARY

Thermal design of spacecraft's is commonly undertaken by means of analysis tools based on deterministic methodology. However great benefits can be obtained when Stochastic Analysis, and Monte Carlo Simulation in particular, is implemented in an integral approach with the existing codes used to run conventional spacecraft thermal analysis.

Scatter, or uncertainty, is present everywhere in engineering so that it is essential not only to build up a detailed physically representative model, but also consider one additional important component, which is the scatter in parameter governing the analytical response.

In this light, a European Consortium under the leadership of CASA-Space Division has developed the PROMENVIR code which is an advanced Meta-Computing tool for performing stochastic analysis of generic physical systems. PROMENVIR is the result of a research project partially founded by the European Commission within the Fourth Framework of the ESPRIT program. Several Companies coming from different industrial areas (automotive, aerospace, energy) has participated in its development and have actively contributed to present a final product which meets the main performances required by the end industrial users of different disciplines.

PROMENVIR is a code based in Montecarlo Simulation what imply numerous advantages when compared to other classical approaches, e.g. no limitation as to the type of analysis (linear, non-linear, etc.), no limitation as to the amount of scatter in the parameters, any solver may be used, learning new codes is not needed since Montecarlo Simulation allows practically painless accommodation to any solver in the market. It must also be emphasized that PROMENVIR is not a product conceived for a specific engineering application, but it can be used in different areas, such as Structural Analysis, Thermal Control and Fluid Mechanics.

A non-exhaustive list of potential applications for thermal space engineering could be as follows,

- Analysis of the impact of the control attitude scatter for satellites Sun or Earth pointed.
- Sensitivity and uncertainties analyses of any data of spacecraft, like multi-layer insulation conductances, radiator areas or thermal properties.
- Interface conductive couplings scatter and washers/ interfillers design limits.
- Correlation of flight data, from thermo-optical properties to variation of albedo and Earth radiation data depending on the orbit, season and lifetime.
- Any other data input variable or manufacturing scatter, especially applicable to fluid loops, pipes or active thermal control elements.

This paper presents some examples of analysis performed using stochastic method in the field of Thermal Control applications using the code PROMENVIR. In particular three typical topics of a standard development are discussed, based on real analyses performed in two satellites under CASA responsibility:

- Sensitivity analysis.
- Temperature qualification limits evaluation.
- Correlation between analysis and tests.

Finally, a discussion on how the use of a Stochastic Analysis approach can modify the classical methodology based on Deterministic Analysis is discussed. Since scatter in the properties of materials, design parameters and input loads are impossible to avoid, it appears to be highly recommended to take into account this fact from the beginning in the development of a new product. Benefits of such decision will be noted in both technical performances and development costs.

HOW PROMENVIR WORKS?

PROMENVIR is basically a generic tool for:

- Setting-up a stochastic analysis problem (FEM, CFD, QCD, MBD, etc.)
- Defining and managing either a LAN or WAN Meta-Computer (called the Parallel Virtual Computer).
- Running the Monte Carlo Simulation.
- Processing statistically the results.

Modern stochastic analysis is based in the Monte Carlo Simulation technique which requires the execution of series of typically hundreds of deterministic analyses, all of which are clones or replications of a nominal *mother* model. The idea of Monte Carlo Simulation is basically very simple:

1. Take a reference (nominal) model of the system.
2. Select a set of variables that we know to scatter within a certain range of tolerance (e.g. conductivity and capacitance).
3. For each variable pick *randomly* a value from the above range.
4. Replace the nominal value of each variable with the random one and execute an analysis.
5. Extract and store the value of the response parameters of interest (e.g. temperature).

POTENCIAL APPLICATIONS IN S/C THERMAL DESIGN

To have the possibility of hundreds of cases and a very friendly statistical analysis can help in different jobs along the S/ thermal design and analysis.

Really, in the thermal design of S/C there are two main jobs that can be purely called “stochastic events”. The first one is referenced as uncertainty analysis. In this analysis the thermal control specialist selects different variables, like the material thermo-optical properties, the conductivities of the materials,...), and performs some run varying them between the extreme values, but one by one. After it performs root mean square of the differences between these sensitive cases and the nominal one. The resulting value is call uncertainty margin to be added to the nominal solution. This analysis approach implies that all the phenomena are independent. With PROMENVIR all the variables to be modified are selected at once, to apply to each one a probabilistic profile, and to run with the Montecarlo Method many cases. The results of the analysis can be studied, seeing the impact of each variable and one special curve that represents for example the temperature of one units in the hundred of cases. With this figure you see the worst combination and the temperature margins with level of confidence of 90, 95 and 99 percent. The information supplied with this method is several order of magnitude that the present obtained with the RMS method.

The second case is to determine the large number of design cases generated by the AOCS. For example, for a satellite in low orbit and pointing to the sun, the Attitude Control can maintain the pointing inside a determined cone, and thermal radiators can receive sun in a non-known probability. This problem increases if around that axis the satellite can reach any position of the other two with different external radiation on the radiators due to the attitude. With Promenvir is feasible to run hundred of cases and to reach very good confidence on the thermal performances.

For design of S/C, but considering that the use of Promenvir is not for probabilistic variation of parameters, Promenvir can be a very nice tool. Some examples could be:

- Selection of a thermal design in a preliminary phase of a project. As example, the design of a flat antenna in low orbit with high conductive coupling to a large mass. In this case hand calculations are very difficult because is a transient case, with impact in the temperatures derived from the conductance and thermal capacitances that generates out-of-phase response of the temperatures and external heat inputs. This particular case will be outlined in a dedicated point of this paper.
- Limits of the design. An example of this case could be the conductive coupling in a thermal interface with washers. When the isolation increases many times the temperatures varies and the heat flux reaches asymptotic values where the design cannot be improved.
- Sensitive response of thermal performances when the design parameters can be combined but the appears a global variation of the performances because one change affects to the rest. This means that input variables are not independent. One S/C thermal example corresponds to the design of heating lines applied to propulsion subsystem components. The heating power dissipated in one particular element selecting the resistance of the heater affects to the rest of components which are connected in serial. For a quick knowledge of a feasible design it is possible with Promenvir to modify any heater of the chain and to see the response of all the elements to this change
- Thermal testing. For thermal testing, a nominal test predictions and sensitivity analysis of the most significant parameters that affects to the heat balance are normally generated. With Promenvir, instead of a simple table with extreme expected variations, it is possible to generate curves with continuous results varying the desired parameters. Thus, an important knowledge is supplied during the test reviews. This sensitivity analysis is also important for correlation purpose, because in Promenvir, the response profile versus the parameter variation is obtained. This kind of analysis will also be outlined in a particular paragraph of this paper.
- Flight Data Correlation. Flight data are continuously recorded and depend on many parameters which are changing in different periods. This changes are related to the planet radiation factor, season, mission time, power dissipation profiles. All these cases requires a large data base or to run the modifications during the mission. The Promenvir allows to generate the data base anticipating correlation of flight recorded data and actions to be taken in case of mission problems.

In all these cases it is assumed that the variation of the parameters can be the expected one with an associated probability, or are only parameters for which you select a large range to evaluate the impact in the expected response.

THERMAL ANALYSIS OF AN ANTENNA IN LOW ORBIT

This is a real case of analysis performed with Promenvir to select a thermal design and to demonstrate the feasibility of that proposed design. This was a waveguide antenna panel supported by aluminium bracket to a rigid platform, with very high mass in comparison with the one of the radiating panel. This antenna was mounted on a low orbit satellite with descending node at 10h. The external environment varies due to the terrestrial, albedo and direct solar radiation close to the eclipse entry and exit. Due to the tight pointing requirements, this antenna needs to work between –20º and +60ºC along the mission and with a temperature variation along one orbit of 35ºC. These temperatures and the orbit variation depend on the selected thermal coating of the radiating surface. Analysis with the trial and error method is very long and difficult to extract conclusions. With Promenvir it has been selected a large range of thermo-optical properties, from metals to black paint, as independent input variables. As results it has been selected the maximum and minimum temperatures along the orbit and the difference between these two values. The results of the analysis are shown in figures 1 to 6.

In the figure 1, it is possible to determine that the thermal absorptivity must be lower than 0.8 to reach a maximum temperature lower than 60ºC . In the figure 2 the emissivity must be higher than 0.22 to get temperatures lower than 60ºC . Thus, with the first two curves of the maximum temperature function of the absorptivity and emissivity are obtained limits of both characteristics.

For the curves of minimum temperatures (figures 3 and 4) same conclusions than the ones of the maximum temperatures are obtained. In all the cases the temperatures are over –20ºC.

The tightest requirement of the mission is the temperature variation along the orbit. The requirement is 35 degrees. In the figure 5, it is clearly outlined that the orbital temperature variations are linearly dependant on the thermal absorptivity. To reach a temperature variation lower than 35 degrees the absorptivity must be lower than 0.62. The dependence of the temperature variations with the emissivity has not a clear curve. This means that is not possible to define a direct relation between the temperature variation and this variable.

As summary, the Absorptivity must be in the range of 0.0 and 0.62, and the emissivity higher than 0.22. This preliminary analysis was confirmed with a detailed mathematical model. The final coating selection is a pattern of silver paint and VDA kapton foil with end of life thermo-optical properties: absorptivity 0.52 and emissivity 0.28.

This analysis has been performed in a simplified model but it shows the response of the system to different variables in a coupled analysis. This analysis assesses the performances of the system to the engineers working in the problem but also to justify the selection of a thermal design with clear improvement in the schedule and confidence of the customer.

SENSITIVITY THERMAL ANALYSIS OF XMM SATELLITE

The sensitivity analysis of a satellite is of utmost importance to predict flight temperatures. This sensitivity analysis is requested due to the large uncertainties of flight characteristics, and low predictability of some parameters that also in ground thermal test cannot be correlated. The final uncertainties are added to the nominal flight predictions and, therefore, define the margin in which the thermal control is going to guarantee the performances in orbit.

Also, the sensitivity analysis for thermal test is a very important tool to determine the possible deviations and assesses in time changes during the “Test Review Boards”. The satellite heat balance is clearly affected by a short number of parameters. In some cases the radiator areas, the efficiency of multi-layer insulations, the thermo-optical properties and the dissipated power of the units. As example of a thermal sensitivity analysis for a thermal test it has been selected a “mirror platform” of this satellite. This platform requires that the temperature must be controlled in a very narrow range, between 19 and 21ºC . This range can be obtained if the heat exchanges of the platform and the power dissipated are very well known. This is a very nice example of differences using Promenvir and the classical analysis using extreme values of some parameters. The difference is the amount of results obtained with Promenvir in which is easy to verify the range of influence of one parameter in the response, when results are asymptotic, or how affect a combination of some parameters in the response (compensating or generating systematic deviations).

The XMM satellite (figure 7) is a Scientific Satellite to determine the X-rays radiation generated in the universe. The satellite due to the large focal length is divided in two modules. The Lower Module that includes the Service Module, the Mirror Support Platform and a half of the Telescope Tube that connects physically both modules. The Upper Module includes the Focal Plane Assembly and the other half of the Telescope Tube.

The problem of the Mirror Support Platform is the one treated here. The temperature of this platform, sandwich in carbon fiber with distributed heating lines, is dependant on several parameters. The most important are the heat leaks by radiation at the top and at the bottom face, and the conductive heat leaks in the perimeter (mechanical interface with the Service Module). These heat balance elements have been referenced in the analysis considering four variables in the mathematical model. The heat leaks at the bottom of the platform are dependant on the emissivity of a foil that closes the bottom side of the satellite. The emissivity of the foil can vary between 0.05 and 0.25, with a measured value in a sample of 0.15. This foil is Kapton VDA but reinforced with glass fiber wires that affect to this parameter.

The second parameter that affects to the temperatures is the conductance at the perimeter between the platform and the service module. This conductance is the results of a serial connectivity’s with high uncertainty like the contact conductances and the mathematical discretization that clearly produces an uncertainty in the performances. The

conductance per node was analyzed in the range of 0.25 to 3. A value close to 0.4 was predicted before test. After test correlation this parameter was assumed close to 2. This is pointed out to outline this kind of uncertainties analysis.

For the heat leaks upwards, that is a heat exchange by radiation, two parameters were selected. Both parameters are related to the Telescope Tube temperatures. The first one is the heat leaks from the “cold plate” that simulates the upper module during test. This cold plate temperature was dependant on the Multi-layer insulation performances that covers it. The second parameter is the performances of the multi-layer insulation that wraps the Telescope Tube. The efficiency of the MLI depends on the design and manufacturing and it has an uncertainty in the performances with influence in the telescope temperatures. For the “cold plate has been considered the whole range in the emissivity, 0.03 to 0.9, and for the telescope tube MLI from 1 to 4 in the factor between the ideal and real value.

The results of the analysis with the 4 variables are shown in figures 8 to11. For the figures are selected the nodes of the telescope tube 108 to 117, the nodes of the platform 213 to 234, the nodes of two units, located in the platform, 176 to 284 and the service module nodes 701 to 708.

The first parameter (emissivity of the bottom foil) affects to the platform in about 5 degrees which are followed by the service module cone. In the units this parameter is very important and variations are about 30 degrees. This data is very important in the correlation because these units can be use as checking value.

With the second parameter is clearly obtained in figure 9 that the conductance platform to service module has two compensating behaviors between the platform and the service module cone. Differences in the test in both results can be correlated by this parameter in both (cone and platform) results. Also in this figure appears the asymptotic behavior when a high value in conductance is considered.

The third parameter (emissivity of cold plate to chamber) has not a high influence, but is a systematic error because affects in the same sense in all the results.

The forth parameter (conductance through the MLI of the Telescope tube) produces expected results. Half of the MLI has direct solar radiation the other is in shadow. With higher factor, the sunny face increases the temperatures and the shadowed face decreases. The rest of nodes in the same sense follow this response. The ones, close to the sunny face, increase the temperatures, decreasing the ones at the opposite sides.

CONCLUSIONS

Thermal design and analysis of satellites requires detailed model but also a good knowledge of the thermal response that requires tools that provides statistical analysis of the performances, a large number of runs with small effort coming from engineers. Promenvir is a software and working philosophy that has been applied to other engineering fields. Now it can work for thermal design and other thermal disciplines like life support or fluid dynamics.
Many space responses are stochastic with scattering in the input parameters. A full data-base will help in all the analysis phases, from the preliminary design, testing and flight data correlation.

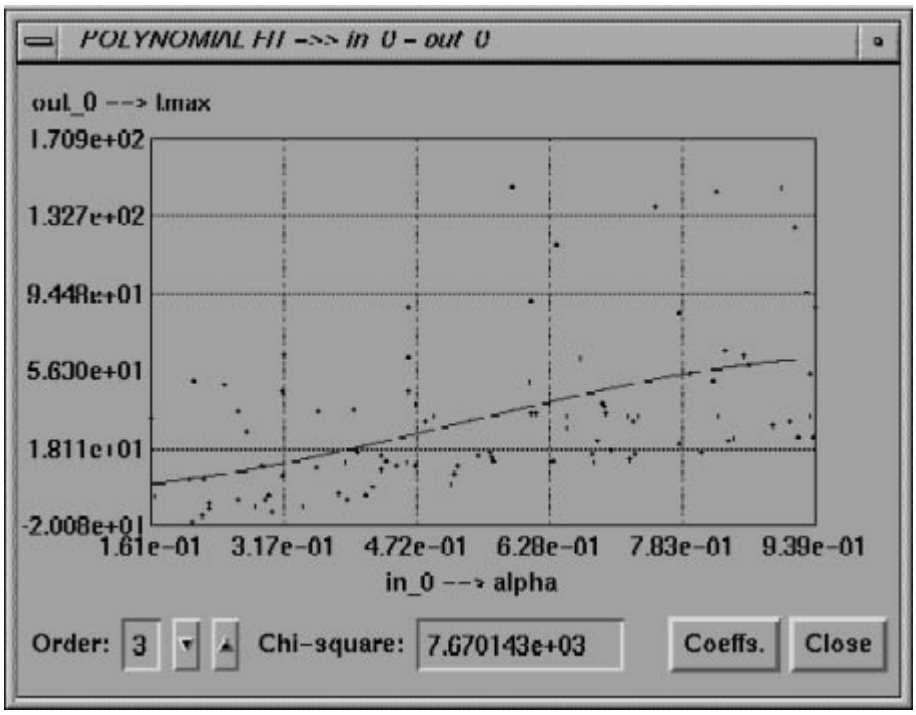

Figure 1. Maximum temperature versus absorptivity

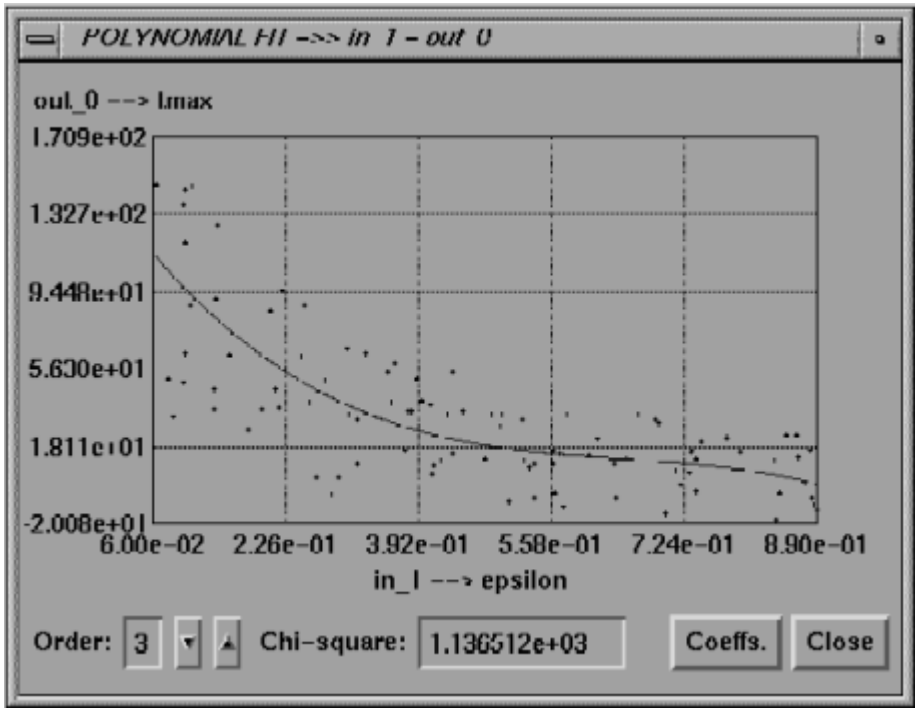

Figure 2. Maximum temperature versus emissivity

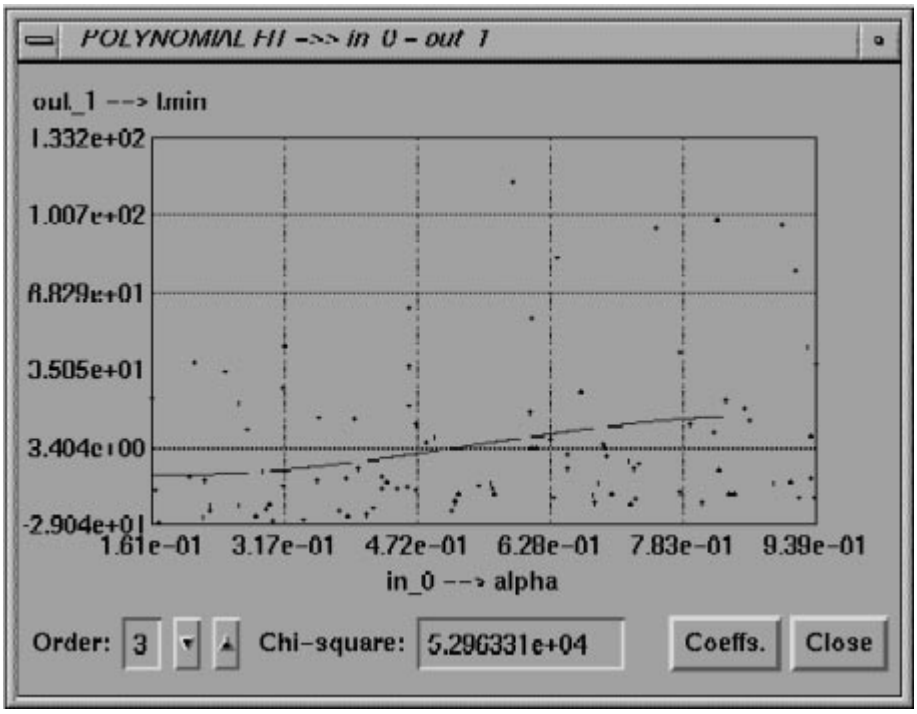

Figure 3. Minimum temperature versus absorptivity

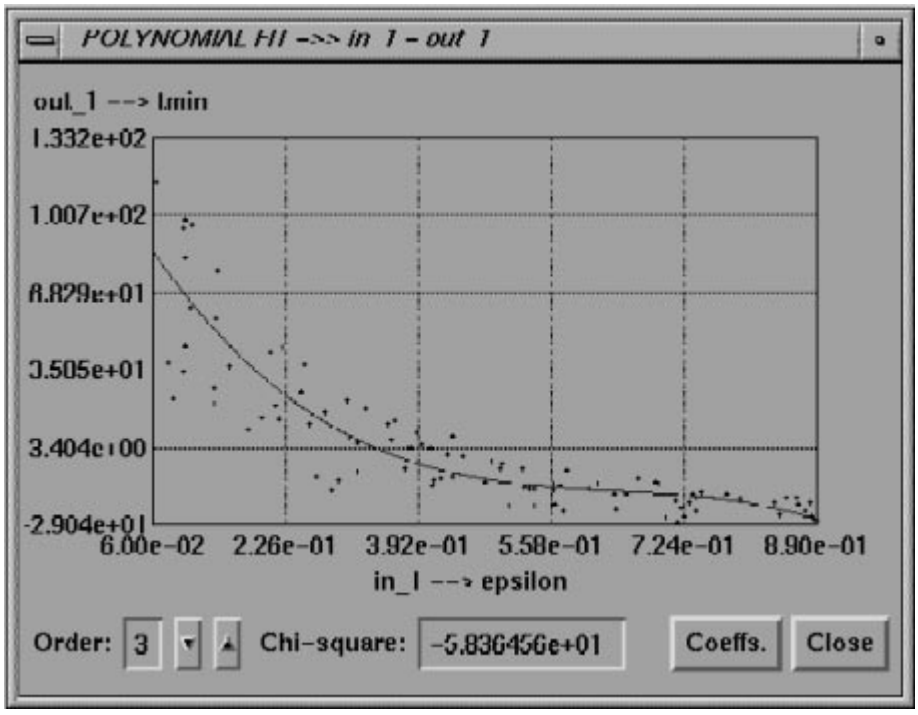

Figure 4. Minimum temperature versus emissivity

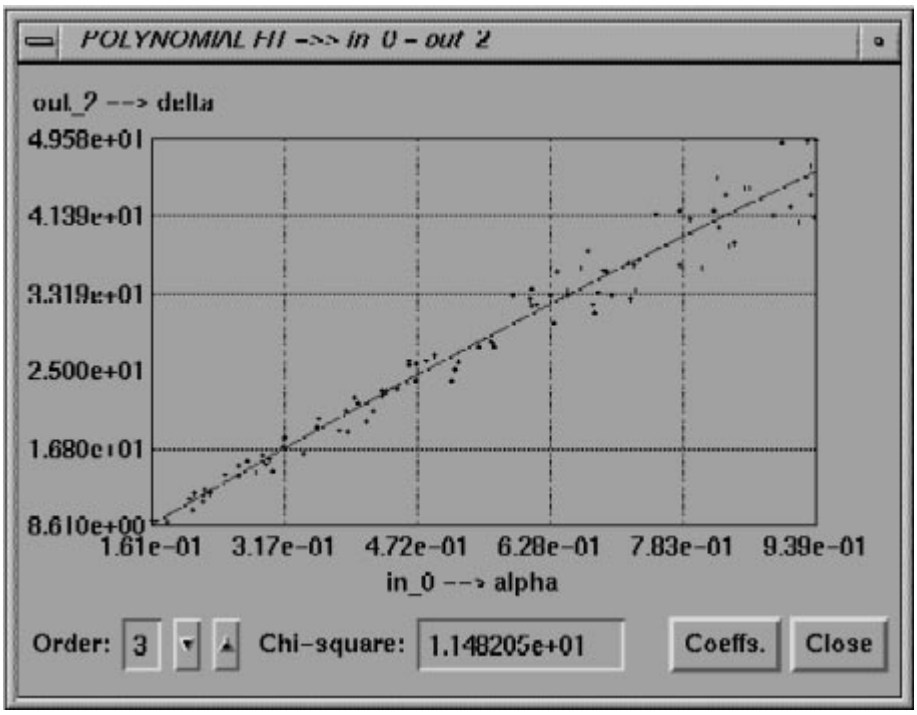

Figure 5. Maximum orbital temperature variation versus absorptivity

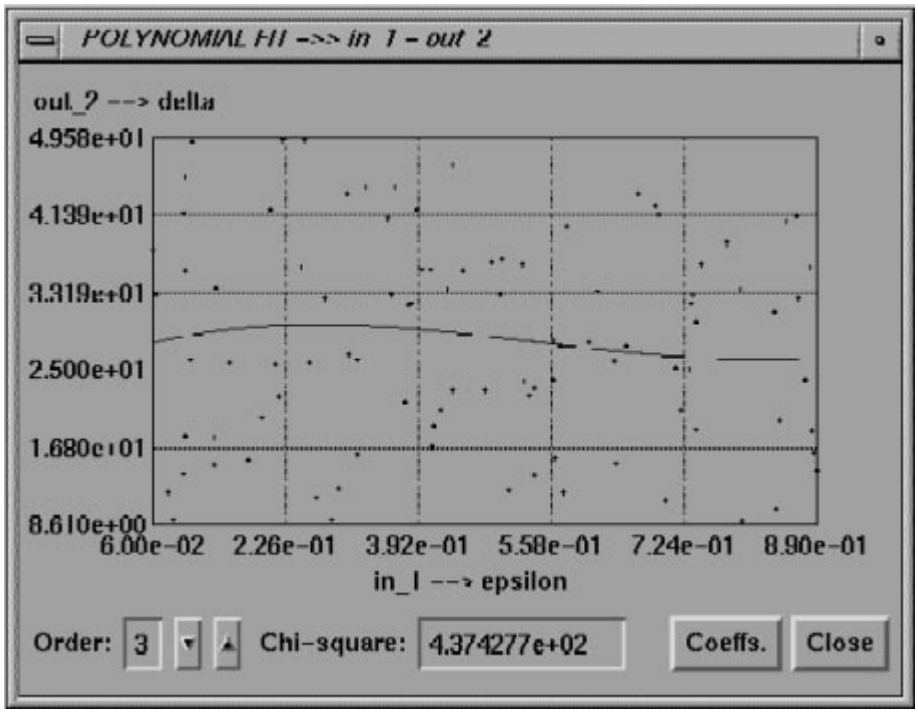

Figure 6. Maximum orbital temperature variation versus emissivity

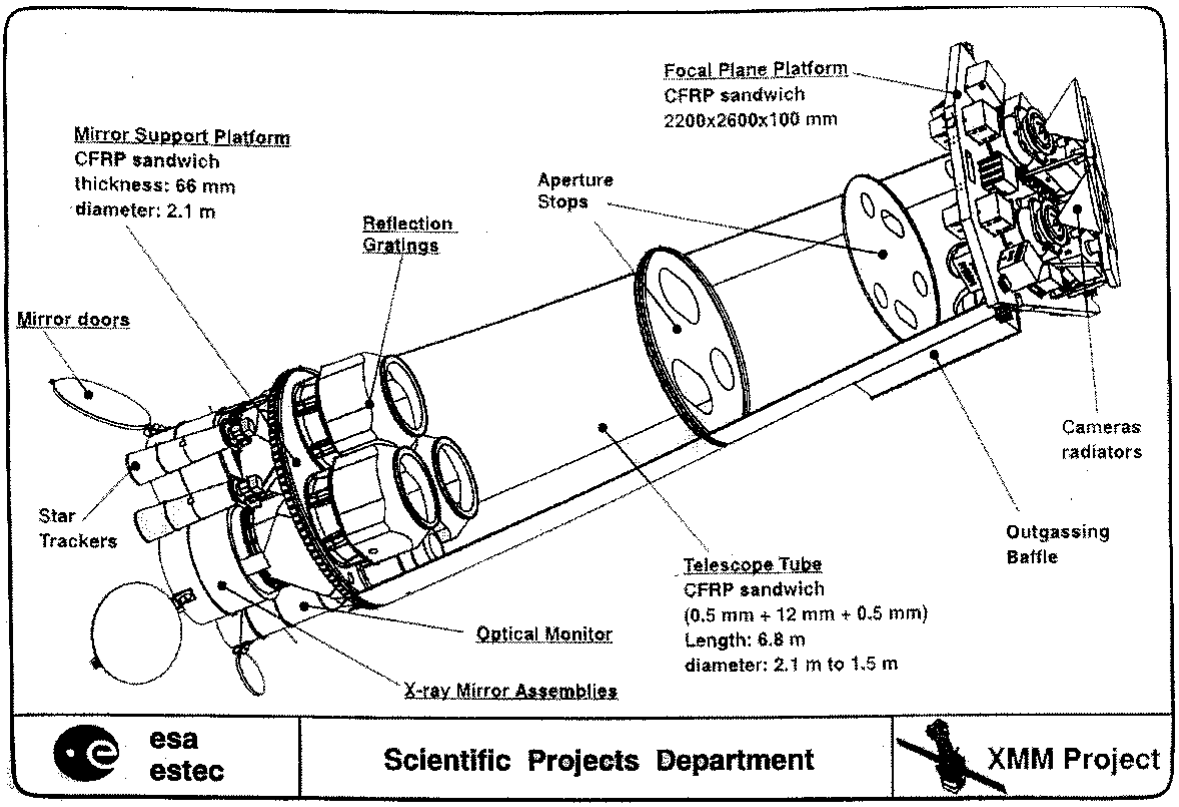

Figure 7. XMMSATELLITE

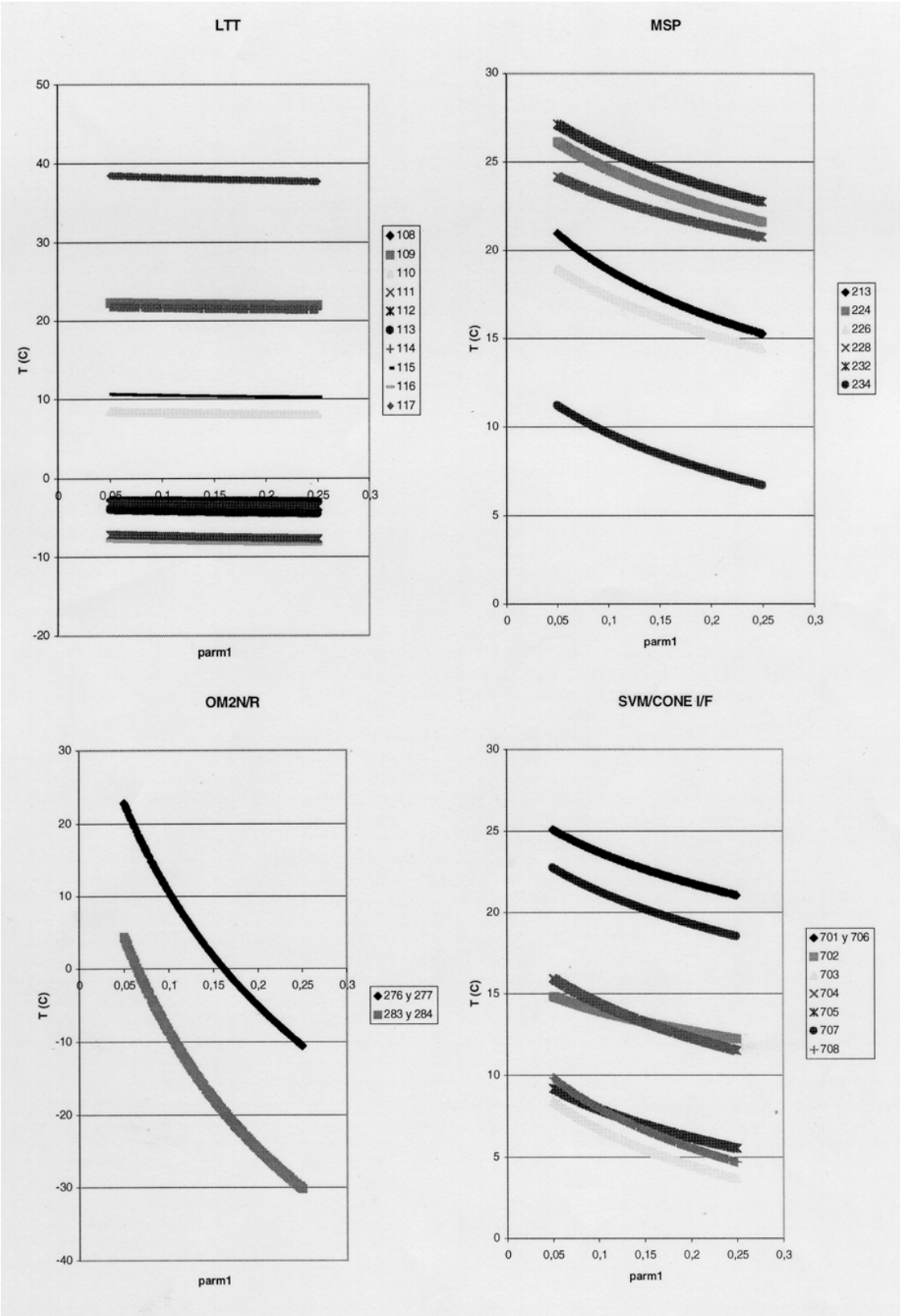

Figure 8. Sensitivity analysis with *param 1*

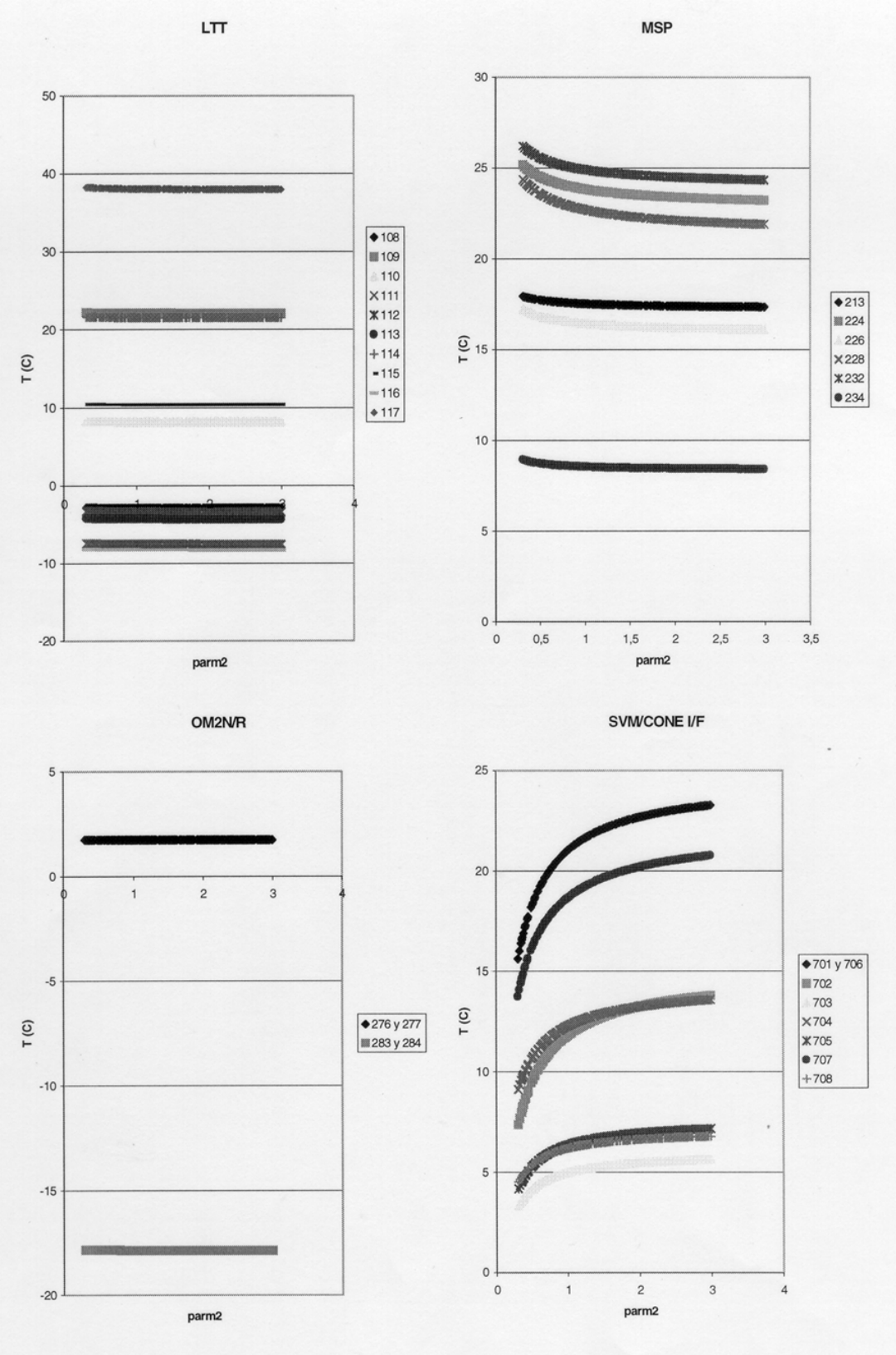

Figure 9. Sensitivity analysis with *param 2*

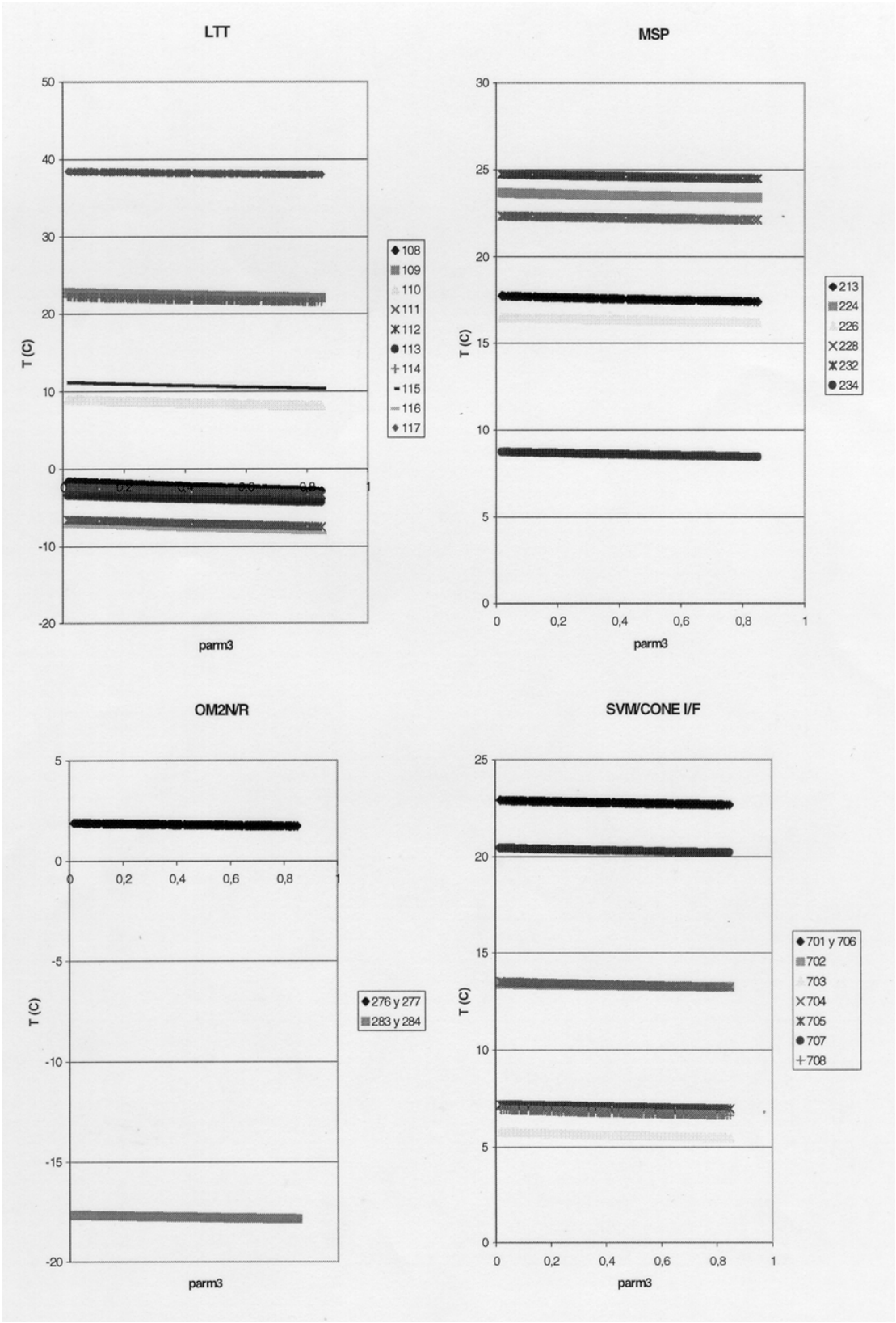

Figure 10. Sensitivity analysis with *param 3*

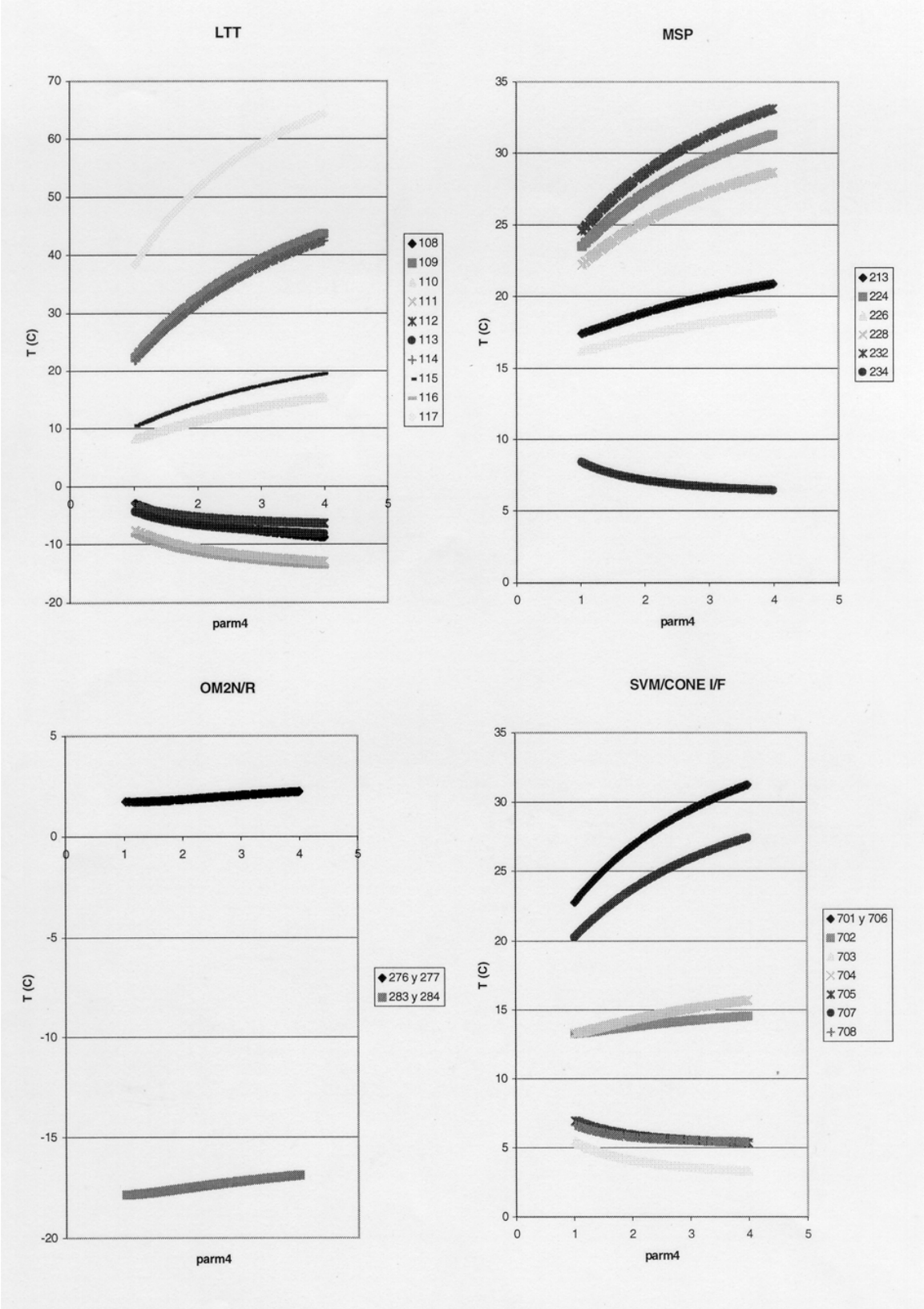

Figure 11. Sensitivity analysis with *param 4*

THERMAL MANAGEMENT OF AERO AND SPACE ELECTRONIC BOARDS

Greg Lazzaro
Dynamic Soft Analysis, Inc.
Pittsburgh, Pennsylvania 15213

Tom Andrikowich
AlliedSignal Aerospace
Tucson, Arizona 85737

INTRODUCTION

The thermal management of electronic boards for aero and space applications must conform to severe requirements between limited heat removal options and limited weight tolerance. With the trend toward higher packaging density in chips and faster clock speeds, the power dissipation of each component has increased over the last few decades (ref. 1). Also, the condensed system packaging has led to an increase in power per unit area on electronic boards. Thus, the most severe thermal management challenges occur in aerospace electronics where reliability issues are high and the means for heat removal are limited.

As a result of these conditions, thermal analysis software must be an integrated step along with component placement, routing, electronic simulation, mechanical analysis, and reliability prediction. The use of thermal analysis software helps to identify thermal problems during the early stages of design. It also provides various options to resolve possible thermal problems during the design process. This process will reduce expensive corrections to prototypes by predicting the thermal performance before the first prototype is constructed.

In routine product design, engineers generally use thermal analysis software along with other CAE software. A specific example of an aircraft engine control unit from AlliedSignal Aerospace is provided as an example. Modeling specifics and temperature comparisons between the software and test data will be presented in the following pages.

AEROSPACE THERMAL MANAGEMENT

For aero and space environments, the major heat transfer mechanisms are conduction, radiation, and minor or negligible conductive cooling. The major concern in the conduction design is to reduce the thermal resistance between the heat sources and the heat sink.

Conduction

The conduction from the components to the board, and in turn through the board to the heat sink, can be enhanced by many methods. Components interact with the board through the individual leads as well as the through the gap beneath the component. In order to reduce the thermal resistance between the components and the board, thermal conductive pads can be inserted into the gap between the board and the components to provide a better conductive path. There are many forms of conductive epoxy that are also used for this same purpose.

Metal frames are frequently used to channel the conductive heat from the board to the ultimate heat sink. These frames strengthen the board and provide rigidity for vibration considerations. They help to suppress the vibration during take off and flight, while also removing heat effectively. Metal frames are frequently used rather than solid planes so that components can be placed on the same side as the frame.

Thermal vias have proven effective in displacing heat through the thickness of the board for surface mount components. The thermal vias are scattered in an array beneath the components and are generally used to displace heat from the front side to the back, where it can be effectively carried to the heat sink or metal frame.

Alternate cooling strategies include the use of wedge locks along the edges of the board and thermal screws attached from the board to the heat sink. Along with this practice comes the use of heavy copper ground planes or aluminum cores to increase the lateral conductivity of the board.

Radiation

Another major consideration in aerospace thermal management is the radiative heat transfer. Each component may have different power dissipation, temperature, emissivity and configuration.

A conformal coating is sometimes applied to the total board for environmental protection as well as for emissivity control. When a board faces a case wall or an adjacent board, the thermal emissivity of the boundaries also becomes important. The wall temperature could be very high if it is subject to solar radiation, and it may require chrome plating to reduce the emissivity. Also, adjacent boards may be extremely hot, depending on their power dissipation. When an adjacent board or wall temperature becomes very high, radiation begins to play an important role in the heat transfer.

Convection

In most space applications and in many aircraft applications with sealed compartments, the convective heat transfer is negligible. For some aircraft applications there may be cardcages at forced or natural convection. Pin and extruded fin heat sinks may be used to cool the high powered parts. Component heights play an important role in flow divergence and downstream wake effects.

INTEGRATED THERMAL ANALYSIS

To conduct an accurate thermal analysis, software must be used to take into account all mechanisms of heat transfer. This software must also be integrated with many other software packages. The board configuration and component placement are transferred directly from ECAD placement and routing programs through a seamless interface to BETAsoft-Board. The power of the components can be derived from electronic simulation programs and then entered into the thermal software for accurate power modeling. Since the power dissipation is directly related to the clock speed, the same board may generate different power for different operating conditions.

The thermal designs should be cross checked with the mechanical designs for compatibility with the vibration and configuration limitations. Another important aspect is to use the predicted thermal results as input for reliability analysis of the total board and system. BETAsoft-Board interfaces directly with several well known reliability software packages. The junction temperatures predicted by BETAsoft-Board are used in the reliability analysis. Iterations among electrical, thermal, mechanical, and reliability analysis tools may occur frequently to achieve the total design requirements. For aerospace applications the electronic, thermal, vibration, reliability, and weight constraints should be compromised to achieve the overall design goal.

EXAMPLE CASE: ALLIEDSIGNAL ENGINE CONTROLLER

An example case selected to illustrate the modeling techniques in aerospace thermal design is an engine controller design by AlliedSignal Aerospace (See Figure 1). The engine controller is subjected to severe environmental constraints. External cooling is provided by natural convection and radiation to the ambient air. The ambient air temperature can range from -40C to 70C. Inside the engine controller are two boards, an Input/Output CCA (Circuit Card Assembly) and a CPU/Power Supply CCA (See Figure 2). Each board is bonded to an aluminum frame heat

sink. The heat sink assembly is screwed to the chassis to maximize conduction cooling of the boards. The total power dissipation for both boards is 18 Watts. When modeling the design, AlliedSignal used several CAE packages in conjunction with a rigorous design process to simulate the final component temperatures.

System Level Simulation

The analysis of this design began with an initial system level model of the engine controller created in a finite difference based software. A mesh was generated to simulating the various layers throughout the engine controller. The power was assigned accordingly to the board layers, and the design was analyzed at natural convection and an ambient of 71C. A surface temperature profile was generated for the engine controller to identify the boundary conditions for each board. The maximum surface temperature was used as the boundary to ensure a greater level of safety.

Board Level Simulation

BETAsoft-Board, a commonly used thermal analysis software application was used for the thermal design of each board in the engine controller. The software uses a finite difference scheme that incorporates locally adaptive grids for mesh generation within the analysis. These adaptive grids are generated where grid refinement is necessary to model the conduction through the pins into the board. The program considers conduction, convection, and radiation based on a set of semi-empirical correlations and theoretical modeling.

The board analysis began by exporting the board placement designs from Mentor Graphics where all the layout was performed. BETAsoft-Board provides an interface which extracts the components placement, geometry, partnames, and board dimensions from the Mentor files. The power of the components, which was derived from simulation, was entered into the BETAsoft library. Board properties, such as the placement of thermal vias beneath the higher power dissipating components, along with the board metal and non-metal material properties and ratios were modeled in the software.

The metal frame used to carry heat from the PCB to the chassis was modeled by creating several screw type components in the BETAsoft library. The frame was selected rather than a solid plate because of the need to place components on the back side of the board. To model the frame, several components were created and placed on the board to match the frame size and positioning. The screw components allow for proper connection between the PCB and the chassis. They were given the appropriate resistance and end temperature or sink temperature. The maximum case temperature predicted by the system level simulation was used as the boards' sink temperature.

The board analysis took very little time to set up and run. The output from BETAsoft-Board included the isothermal temperature map of the board as well as the case and junction temperatures of each component. The component junction temperatures were imported from BETAsoft-Board into a reliability software to ensure fulfillment of reliability concerns.

COMPARISON OF PREDICTIONS WITH DATA

After all the simulation and any design iterations were completed on the engine controller, an initial prototype was developed and tested. Controlled testing was conducted on the design, and data was collected for the many components with significant power dissipation. The test was conducted in a temperature chamber with a 71C ambient, and thermocouples were used to record the temperature rise of the components. The Input/Output CCA showed a small temperature rise since it dissipated much less power than the second board (See Figure 3). The CPU/Power Supply CCA core board showed the most significant temperature rise (See Figure 4). A table of the BETAsoft-Board predictions versus the actual test results is included as (See Table I). The results compare favorably, and the design met its criteria.

CONCLUSION

With the trend of higher clock speeds and decreasing package sizes, the power density of aero and space boards has increased dramatically in the last decade. Higher power densities generally lead to higher junction temperatures. Since the failure rates of components increase exponentially with their temperatures (ref. 2), thermal control becomes critical in achieving acceptable product reliability. Among the thermal management of electronic systems, the most demanding requirements continue to be in the aerospace industry where environments continue to be demanding and heat removal options are limited.

The integration of thermal analysis software with other CAE tools becomes necessary to conduct an accurate simulation. Iterative design and compromise are necessary due to the various constraints presented by the operating conditions. In the case of the AlliedSignal engine controller, the BETAsoft-Board software was integrated effectively into the design process to ensure superior product quality and performance.

REFERENCES

1. Oktay, S.; Hannemann, R.; and Bar-Cohen, A.: "High Heat from a Small Package," Mechanical Engineering, March 1986, pp. 36-42.

2. MIL-HDBK-217, Naval Publications and Form Center, Philadelphia.

Table I. Test Data vs. BETAsoft-Predictions

	Test Data	BETAsoft-Prediction
Ref. Des	Junction Temp (C)	Junction Temp (C)
cr9	97.20	98.90
cr14	91.70	92.00
cr20	85.23	86.30
g15	85.99	84.70
u12	88.40	87.70
u24	88.37	88.90
u25	86.67	88.40
u31	89.50	87.60
u32	87.90	89.40
u34	89.90	92.70
u44	87.75	88.30
u50	88.11	89.40
u53	86.05	87.30
u54	85.95	86.30
u56	88.05	88.60

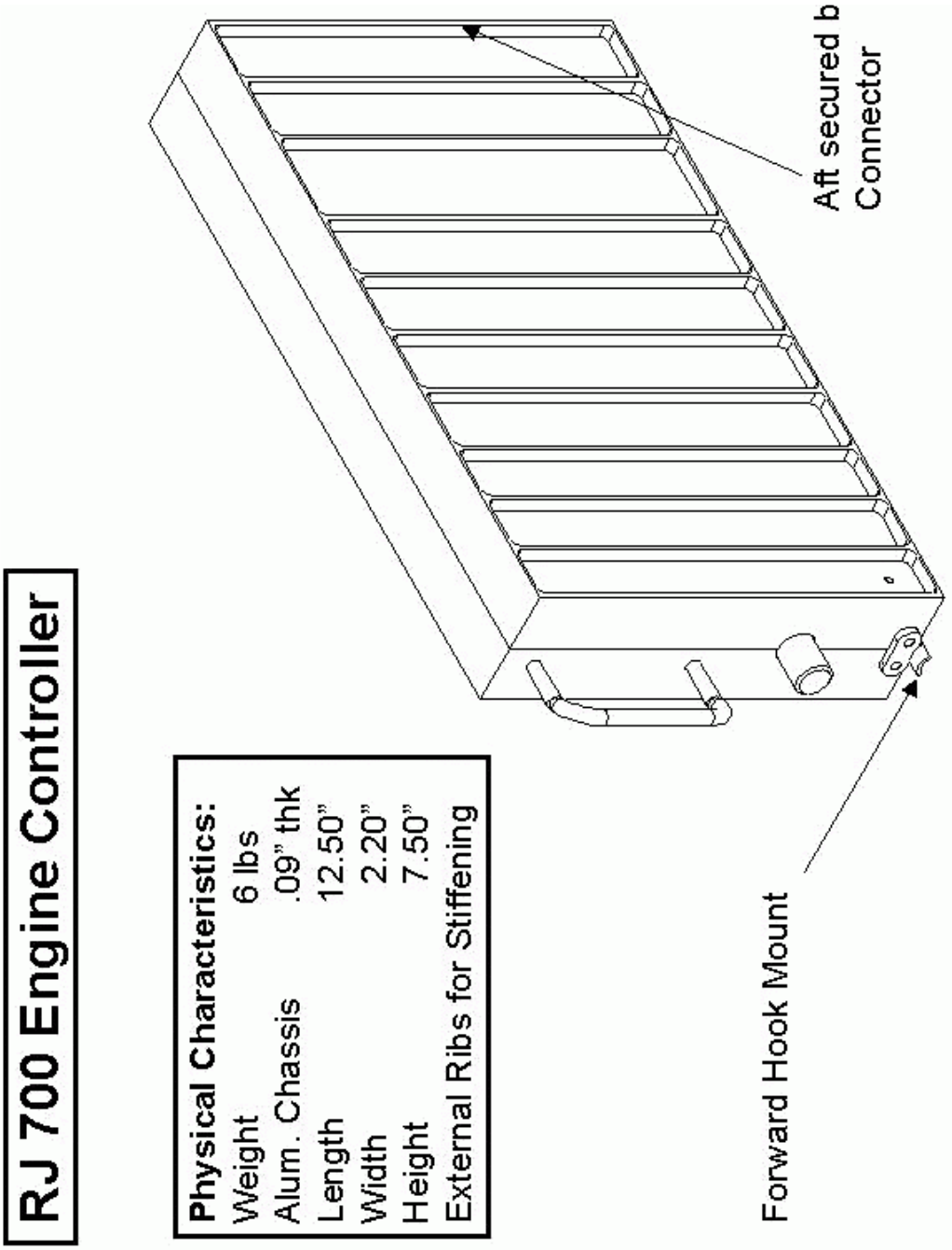
RJ 700 Engine Controller
Physical Characteristics:
Weight 6 lbs
Alum. Chassis .09" thk
Length 12.50"
Width 2.20"
Height 7.50"
External Ribs for Stiffening
Forward Hook Mount
Aft secured b
Connector

Figure 1.

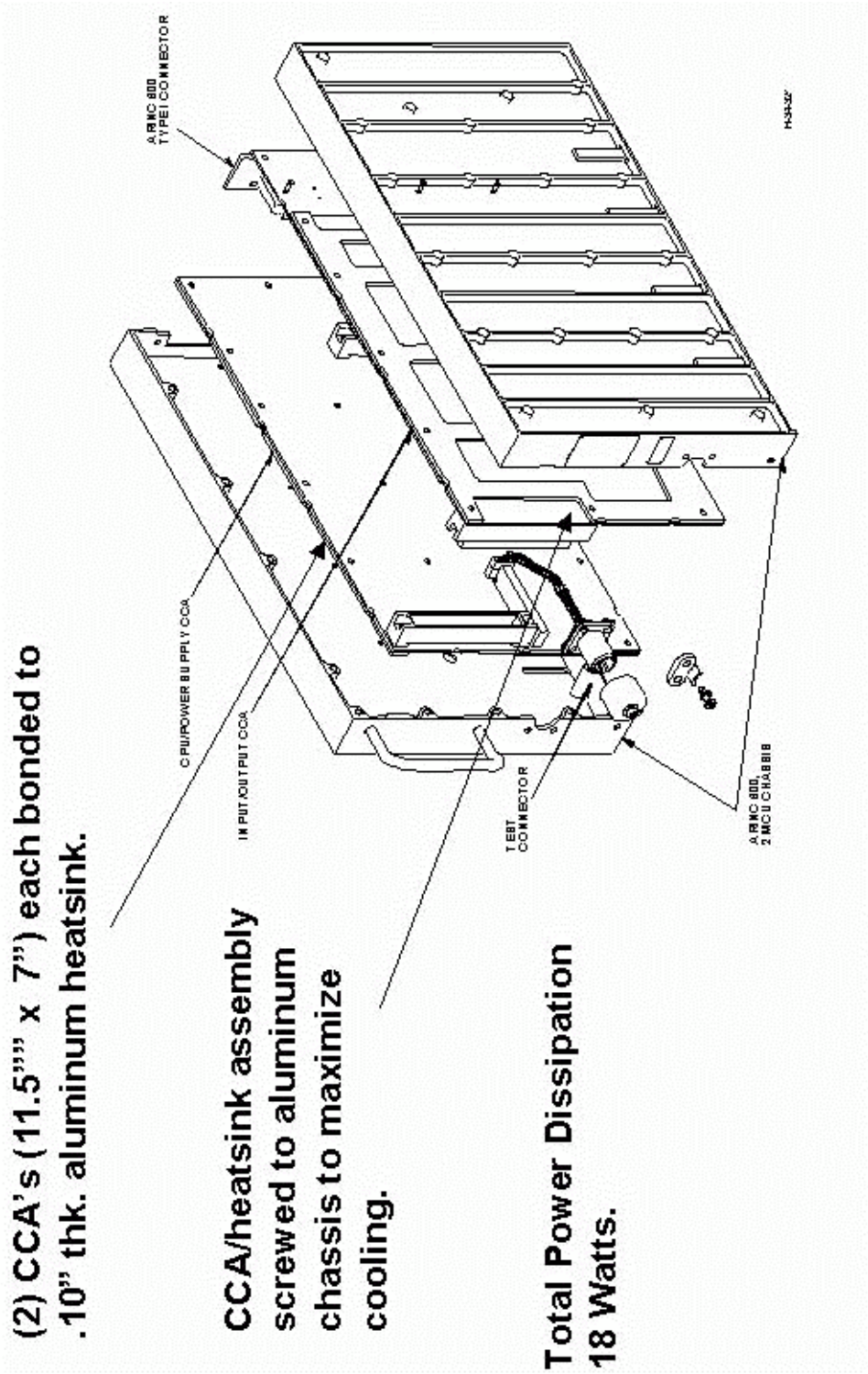
(2) CCA's (11.5"" x 7") each bonded to
.10" thk. aluminum heatsink.
CCA/heatsink assembly
screwed to aluminum
chassis to maximize
cooling.
Total Power Dissipation
18 Watts.
CPU/POWER SUPPLY CCA
I/O PUT/OUTPUT CCA
TEST
CONNECTOR
ARINC 600
TYPE I CONNECTOR
ARINC 600
2 MCU CHASSIS

Figure 2.

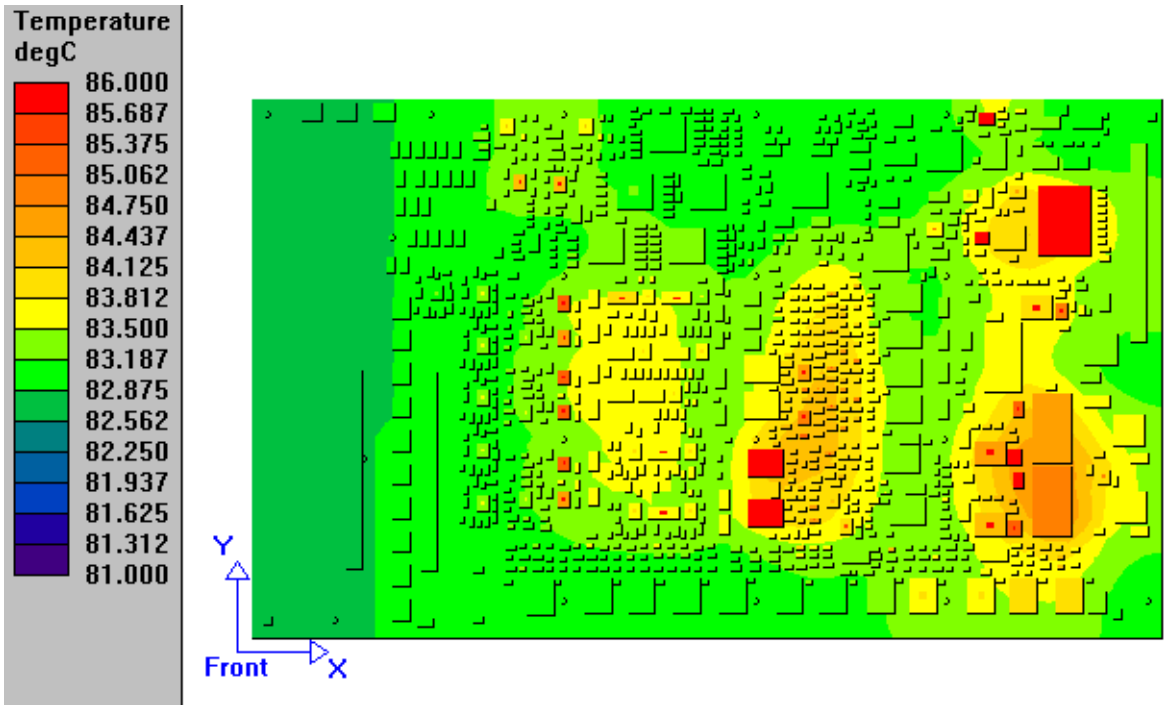

Figure 3.

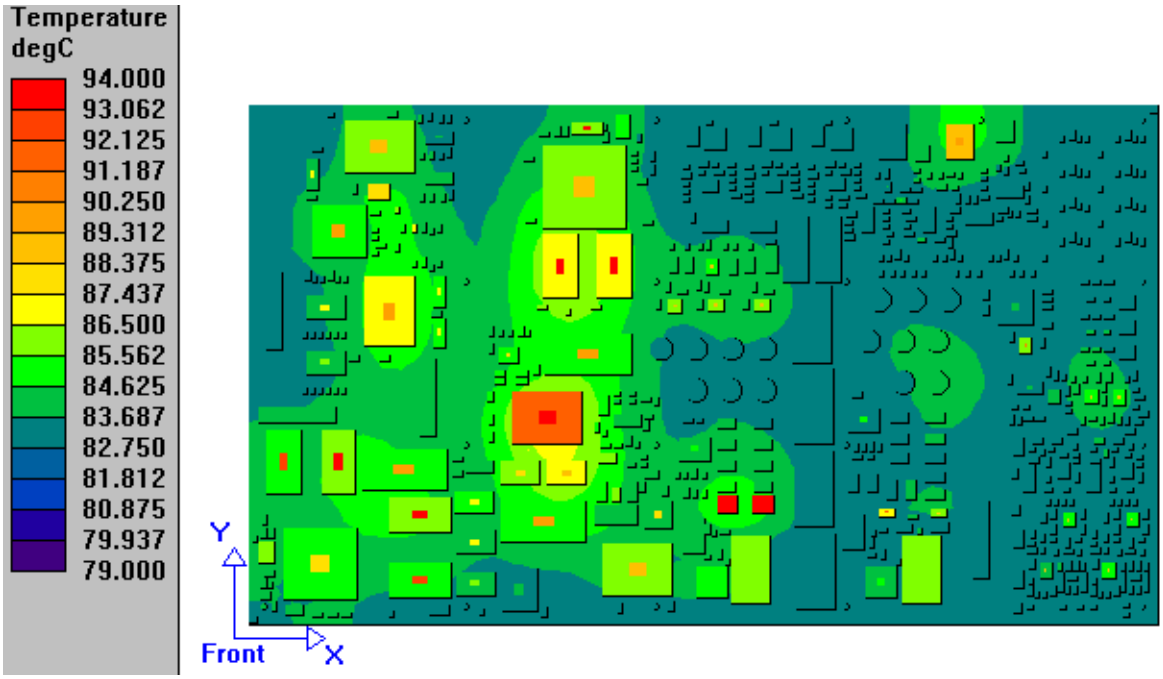

Figure 4.

MULTI-DISCIPLINARY ANALYSIS IN ENGINE DESIGN[1]

Kamel G. Mahmoud and Andreas Ennemoser
AVL-LIST GmbH
HANS-LIST PLATZ 1
A-8020 Graz
Austria

SUMMARY

Automobile manufacturers are faced with a strong requirement today for developing high quality vehicles in a short period of time. Since the coolant system is playing a key role in vehicle performance, it is particularly important to be able to optimize the cooling cycle. Experimentally optimizing the complex three dimensional coolant system geometry has proven to be extremely difficult. Simulation tools provide engineering values that can be incorporated in the early stages of the design process where they complement the conventional experiment by virtual prototyping. Engine virtual prototyping has been the goal of AVL-Advanced Simulation Technologies business area for a couple of years.

To improve the quality of the cooling system simulation results and to speed-up the simulation process, a multi-disciplinary (MD) analysis method has been developed by AVL in the frame work of the Multi-disciplinary Engineering Design via Unitary Software Applications MEDUSA[2] project. In this MD analysis methodology, three different disciplines have been addressed to simulate the cooling of the cylinder head/block compound. The physical phenomena which are considered in simulating this cooling process are: the combustion in the combustion chamber, conduction in the engine structure, and convection and fluid flow in the cooling water jacket.

Regarding the combustion, cycle-averaged gas temperature and convective heat transfer coefficient in the combustion chamber are calculated using a thermodynamic program, BOOST. Finite Element (FE) code, MSC/NASTRAN is used to calculate the temperature distribution in the structure where a Computational Fluid Dynamic (CFD) program, FIRE is used to calculate the flow field, and the fluid temperature and heat transfer coefficient in the water jacket. The cycle-averaged gas temperature and heat transfer coefficient in the combustion chamber are assumed to be wall temperature independent and coupling is carried out between the FE and CFD codes. Two approaches have been facilitated to perform the coupling. In the first approach a loose coupling is used, where the fluid-structure thermal interaction information are exchanged between the CFD and FE programs via file transfer. In the second approach, a tight coupling between the CFD and FE codes has been achieved, where the object libraries of FIRE and MSC/NASTRAN are linked and a single executable is generated.

A 6 cylinders engine is used to demonstrate the MD coupling where the high performance computing facilities at AVL are used to carry out the calculations. Manually generated cooling water jacket mesh as well as a mesh generated using AVL **F**lexible **A**utomatic **M**eshing **E**nvironment, FAME had been used for the CFD calculations. The simulation results have been checked against the experimental data and have shown to be comparable. It. has been show that the current status of the high performance computing facilities makes it possible to carry out the MD simulation procedures within a reasonable time.

INTRODUCTION

Recent engine design trend toward higher output, lower emission, more passenger comfort and safety; initiated the interest to develop accurate analytical tools for a more rapid engine design process. Understanding and quantifying aspects of the thermal behavior of engine components and systems has been the subject of a number of heat transfer investigations over recent years (refs. 1 to 6). The finite element method (FEM) is a versatile and powerful tool used by engineers on a routine basis for the analysis of a wide range of engine components (refs. 1, 7). The development of the finite element method for the prediction of the temperature in the engine components, has

[1] This work is done during the participation of AVL in ESPRIT HPCN MEDUSA project (EP 22746).
[2] Medusa consortium comprises: British Aerospace (Operations) Ltd., ABB Teknologi AS, AVL List GmbH, Genias Software GmbH, Computational Dynamics Research, MacNeal-Schwendler GmbH, University of Wales, Swansea.

led to a growing need for reliable tools to derive accurate spatially varying thermal boundary conditions. The Computational Fluid Dynamics (CFD) shows to be highly promising tools for the calculation of these thermal boundary conditions on the structure surface.

Performing isothermal (refs. 1,2,5), adiabatic (ref. 4) CFD simulation or resistor-capacitor (R-C) thermal network of the fluid interactions throughout the engine (ref. 6) gives a general (qualitative) idea about the temperature distribution in the engine but it does not tell anything about the absolute (quantitative) values. It informs the engine developer whether there is a homogenous cooling of all the cylinders or – more likely – a rather non-uniform temperature distribution in the structure. In additional to the visualisation of the temperature distribution in the structure, the distribution of the convective heat transfer coefficient between the structure and the coolant and the velocity distribution in the cooling water jacket may be presented and the places at which the cooling water velocity is too high (cavitation tendency) and the stagnation zones (places of poor cooling response) may be visualised. The overall velocity distribution gives a fairly good indication in which way the cooling jacket and/or the cylinder-head gasket can be optimised. The pressure distribution which is one of the variables evaluated in the CFD calculations, shows the locations of the big pressure drops. Being able to detect the pressure distribution, helps in minimising the pressure losses which reduces the size of the water pump and consequently decreases the fuel consumption.

From this short introduction about the isothermal CFD simulation of the engine cooling water jacket, one can see that the simplified simulation process (isothermal or adiabatic wall temperature) gives comprehensive information about the cooling cycle characteristic. However, the calculation misses the accurate wall temperature (CFD boundary conditions) which influences the fluid physical properties (e.g. mass density, viscosity, etc). These physical properties have a significant effect on Reynolds number which dominates the value of the convective heat transfer coefficient and affects also the flow pattern. From the finite element side, it is necessary to obtain detailed information regarding the coolant side heat transfer distribution. The distribution is a function of the local flow velocity, the local turbulence level, the metal surface geometry and the metal surface temperature.

Ennemoser, Petrin and Dilgen (ref. 8) have taken into consideration the effect of the wall temperature on the CFD results, where the temperature of the structure calculated by an FE program is used as CFD thermal boundary conditions. The convective heat transfer coefficient calculated by the CFD program is copied to the FE model to be used as structure thermal analysis boundary conditions. These procedures are carried out manually 2 or 3 times. This approach has the disadvantage that all the data exchanges are done manually as well as only the heat transfer coefficient is transferred from the CFD model to the FE thermal analysis model. The temperature of the coolant which is calculated in the CFD is not used and an assumed temperature is applied in stead. The assumed temperature is selected from the experience of the FE engineer and the local changes in the coolant temperature are not considered.

Till recently, the 3D mesh required for the MD analysis and the CPU demanded by the CFD are the main obstacles toward an efficient integration of the MD analysis into the development process. The advances in computer hardware and software technology will have a strong impact on the MD analysis. The high performance computers (HPC) will substantially expedite the engine design process by allowing the designer to carry out various analysis and design tasks in parallel. The tasks can belong to individual discipline as well as to other disciplines (such as in multi-disciplinary optimization problems).

For complex geometries (e. g. Internal combustion engines) the time spent in the analysis program is still much less than the time and amount of work spent in the pre-processing. Due to the fact that in the pre-processing today still the man-work playing the major role, the development projects are facing a high time and economical pressure. The time here plays not only economical role but also play a big role in the development cycle. The costs/hour of an engineer can be estimated as being 10-20 times higher than for a fast computer. So it is rather worthwhile to spend all man power mainly on results analysis and optimization tasks and to perform the routine and most time consuming work by the computer. With the **F**lexible **A**utomatic **M**eshing **E**nvironment (FAME) (ref. 9), AVL introduces a tool for automatic mesh generation which dramatically reduces the mesh generation time and convincingly satisfies the requirements for accurate CFD simulations (ref. 10-11).

The objectives of this work went in two directions. From one side, to enhance the coupling methodology developed by the authors (ref. 12) and from the other side to expedite the use of the cooling jacket mesh generated by FAME and the use of the HPC facilities in multi-disciplinary analysis.

MULTI-DISCIPLINARY ANALYSIS

To improve the quality of the simulation results and to speed-up the simulation procedures, an automation of the multi-disciplinary analysis process is initiated by AVL in the MEDUSA project, where three different disciplines have been addressed in order to simulate the cooling process in the cylinder head/block compound. The thermal behavior of the engine is governed by the heat released by combustion which transfers from the combustion chamber to the structure by convection. This heat transfers in the engine body by conduction and it must be removed from the structure via cooling fluid which flows through the cooling jacket. On the gas side, BOOST (ref. 12) is used to calculate the cycle-averaged gas temperature and convective heat transfer coefficient in the combustion chamber, T_g and h_g , respectively. These cycle-averaged values are used to replace the time varying temperature and heat transfer coefficient. Using the cycle-average values calculated by BOOST and the boundary conditions on the coolant side, MSC/NASTRAN (ref. 13) is used to calculate the temperature distribution in the structure. The coolant temperature and heat transfer coefficient in the water jacket are calculated using FIRE (ref. 14). It is assumed that the cycle-averaged temperature and heat transfer coefficient do not change with the combustion chamber wall temperature. Therefore, BOOST is used only once to calculate these cycle-averaged variables in the combustion chamber and coupling is done between the CFD and FE codes only.

Two modes have been facilitated in this MD coupling methodology, see Fig. 1. In the first mode, the coolant temperature and convective heat transfer coefficient are assumed and used to be the structure thermal boundary conditions. MSC/NASTRAN is started using the assumed boundary conditions to calculate the temperature distribution in the structure. Having calculated the temperature distribution in the structure, FIRE uses this temperature vector to calculate, among the other well known CFD variables, the convective heat transfer coefficient and the near wall coolant temperature. These two variables (convective heat transfer coefficient and near wall coolant temperature) are required as structure thermal analysis boundary conditions. An interpolation program maps the CFD results to the FE mesh and generate new structure boundary conditions in the form of MSC/NASTRAN input format. Starting from the second coupling iteration, a test for convergence program is used to check the CFD-FE coupling convergence. The convergence criteria depends on the change in the temperature vector, T_s of the structure. The coupling iterations are stopped when the change in temperature vector becomes insignificant. The convergence test is expressed by the ratio of the norm of the temperature difference of two consecutive iterations over the norm of the temperature vector at the current iteration. Mathematically this can be expressed as follows.

$$\frac{\left| T_s^{\,i} - T_s^{\,i-1} \right|}{\left| T_s^{\,i} \right|} \leq \varepsilon \tag{1}$$

where i is the iteration number and ε is a tolerance value.

The same procedures are carried out in the second coupling mode, but the order of execution is different. The order of the programs execution is: FIRE ⇒ the interpolation and data format translation program ⇒ MSC/NASTRAN ⇒ a program to check for CFD-FE coupling convergence. Like the first coupling mode, the iterations are repeated until the previously mentioned ratio becomes less than or equal to a given tolerance value, ε .

FIRE–MSC/NASTRAN Coupling Methods

FIRE and MSC/NASTRAN have been coupled using two different methods, namely indirect and direct coupling. The previously mentioned coupling modes are applicable in both of the direct and indirect coupling approaches.

i. FIRE–MSC/NASTRAN Coupling Via File Transfer

In the indirect coupling approach (loose coupling), the data are exchanged between the MSC/NASTRAN and FIRE via file transfer. The first coupling mode is used here to explain the coupling procedures. Assuming a constant convective heat transfer coefficient, h_f, and a constant water temperature T_f, MSC/NASTRAN is used to calculate the temperature distribution in the cylinder head/block compound, T_s. Having calculated T_s, it is read together with the FE mesh by an interpolation routine which maps it from the FE-mesh to the CFD-mesh. FIRE uses this temperature vector to calculate the coolant near wall temperature, T_f and the new convective heat transfer coefficient h_f.

In the second coupling mode, the structure wall temperature is assumed and used as boundary condition for the CFD calculations and the procedures shown in Fig. 1 for coupling mode 2 are performed.

A script shell is written to automate both of the previously mentioned MD indirect coupling modes.

ii. FIRE–MSC/NASTRAN Direct Coupling

In the second MD coupling method, a dynamic linkage between FIRE and MSC/NASTRAN has been developed. This results in a single executable program in which both FIRE and MSC/NASTRAN run simultaneously and exchange boundary data at every coupling iteration. MSC/NASTRAN user's modifiable version (ref. 16) is used for this tight (direct) coupling. Figure 2 presents a schematic of this approach.

As a first step of the direct coupling approach, MSC/NASTRAN Module Property List (MPL) is modified where three modules are added to the standard MSC/NASTRAN MPL. The first module is a driving module for FIRE. This module reads the input matrices and data blocks and passes them to FIRE main program which in turn interpolates the structure temperatures vector and maps it to the CFD mesh using the interpolation methods which are described under interpolation between the CFD & FE meshes subsection. FIRE main program uses this mapped temperature as wall temperature, perform the CFD calculations and provide new values for the convective heat transfer coefficient and the near wall coolant temperature. The input to this module are the FE mesh geometry, the data of the heat transfer boundary elements and the FE thermal analysis results. The data are passed to the FIRE driving module in standard MSC/NASTRAN matrices and data blocks. The second module is convergence test module and it is used to compare between the results of two consecutive FE-CFD coupling iterations. The convergence criteria used in this module is described in equation (1). In the third module the results at each iteration is saved to be used for post-processing. Otherwise, only the results of the last iteration will be by the time of job termination available for post-processing.

Having modified MSC/NASTRAN MPL to include the new coupling modules, FIRE object code as well as the objects of the other two modules are linked to MSC/NASTRAN library to generate one executable which includes the CFD, FE, convergence test as well as the interpolation codes.

The last step is to invoke the new modules by modifying the MSC/NASTRAN thermal analysis solution sequence. Therefore, a new MSC/NASTRAN thermal analysis solution has been developed to perform the MD analysis in MSC/NASTRAN environment.

MD COUPLING EMBEDDED WITHIN PSUE

The previously mentioned FIRE & MSC/NASTRAN direct and indirect coupling approaches, have been embedded within PSUE (ref. 18). The functionality of the coupling approaches in PSUE can be summarised as follows:

Direct Coupling **:** By submitting the job using PSUE GUI, a program called DIGRESS is started. This program is used to monitor the CFD residuals during the execution. The decision of terminating FIRE execution depends on the behaviour of these residuals. This termination is done either automatically or manually.

The automatic termination depends on two convergence criteria. The first one depends on the change in the fluid temperature which is expressed as the norm of the difference between the temperature vectors in two consecutive time steps, (time step i and time step i-1) over the norm of the coolant temperature vector at the time step i. The ratio between the two norms should be less than a tolerance value ε_1 given by the user as a PARAM in MSC/NASTRAN input deck or in a file used as an input, if indirect coupling is used. The second convergence criteria depends on the change in the turbulence kinetic energy. This change is checked against a tolerance value ε_2 which is also given as a parameter by the user in MSC/NASTRAN input deck or in the previously mentioned file. These tests can be expressed as follows:

Temperature convergence test

$$\left| \frac{T_f^{\,i} - T_f^{\,i-1}}{T_f^{\,i}} \right| \le \varepsilon_1 \tag{3}$$

Turbulence kinetic energy convergence test

$$\left| \frac{E^i - E^{i-1}}{E^i} \right| \le \varepsilon_2 \tag{4}$$

where:

$T_f^{\,i}$ & $T_f^{\,i-1}$	are the cooling water temperature vectors at time steps i and i-1, respectively.
E^i & E^{i-1}	are the turbulence kinetic energy vectors at time steps i and i-1, respectively.
ε_1 & ε_2	are tolerance values for the change in the cooling water temperature and turbulence kinetic energy.

The manual termination depends on the results visualisation which is facilitated by PSUE. If the user is satisfied with the behaviour of the temperature and the turbulence kinetic energy, he/she may interrupt the calculations by editing the contents of a file called *flag.conv* and modifying the convergence flag in this file to "Y" to signify satisfactory convergence behaviour. This file is read at every CFD time step and on recognising this flag, the execution of the CFD calculation will be stopped and the other calculations will be started.

Indirect Coupling : The script shell written by AVL to be used for MSC/NASTRAN indirect coupling is invoked and the PSUE-DIGRESS program which monitors the progress in the CFD results is activated. The same monitoring and termination features mentioned in the direct coupling are made available here at the loose coupling approach. The variables which are given in MSC/NASTRAN input deck as parameters are entered here as script shell input arguments.

INTERPOLATION BETWEEN THE CFD & FE MESHES

Due to the fact that the CFD and FE meshes have different resolutions, interpolation between the results of the two codes must be done. In this work, two methods are used for exchanging the data between the CFD mesh and FE meshes. In the first method, no interpolation is done. Values of the nearest structure grid point to each CFD gird is assigned to that point or vice versa.

In the second approach, the 4 closest structural nodes to each CFD node are used to calculate the value of the state variable at that node. The CFD node is assigned a weighted average of the value at the 4 structural nodes. The weights are the inverse of the distance between the two nodes:

$$u_j = \frac{\sum_{i=1}^{4} \frac{u_i}{d_i}}{\sum_{i=1}^{4} \frac{1}{d_i}} \tag{2}$$

in which u_j represents any variable to be interpolated (temperature or/and convective heat transfer coefficient) and d_i is the distance between the CFD and FE grid points.

RESULTS

The previously mentioned MD analysis techniques have been tested on a 6 cylinders engine where two water jacket meshes are used. One mesh is generated using FAME and the other CFD mesh is generated manually. Short statistics about these CFD meshes can be summarized as follows:

	Manual mesh	FAME mesh
Number of Nodes	872 853	1 550 021
Number of cells	737 516	421 231
Number of cell faces	2 384 807	5 099 045

From the statistics, one can see that FAME leads to more cells. A comparison between the time used in generating both meshes will be given later together with the CPU required for MD simulation process. The manually and automatically generated CFD meshes are shown in figures 4 &5. Detailed comparison between the two meshes is given in figure 6. From this figure one can see FAME generates tetrahedron as well as hexahedron elements.

The operating conditions of the engine at which the measurements and simulation have been carried out can be summarised as follows:

Engine speed	2000 RPM
Inlet temperature of the coolant	79 °C
Engine coolant mixture	50% water & 50% anti freeze
Volume flow rate	478 l/min

In the experimentation, the cooling cycle part which connects between the thermostat and the water pump is removed and replaced by a cooling system such that it keeps the coolant temperature at the inlet of the water pump constant, 79 °C.

The time varying heat transfer coefficient and temperature in the combustion chamber are replaced by cycle-averaged values. The cycle-averaged heat transfer coefficient and temperature are calculated using AVL combustion cycle simulation program, BOOST (ref. 13). It is assumed that at the engine previously mentioned operating conditions, the cycle averaged temperature and the heat transfer coefficient are independent of the combustion chamber wall temperature. This assumption is justified by the cyclic measurements done by Stone et al. (ref. 17) which showed that the combustion process reaches its steady-state condition in less than 10 cycles after the engine first firing.

Using the cycle-averaged heat transfer coefficient and temperature calculated using BOOST, an internal program developed at AVL is used to read these averaged values and generate the gas-side surface element cards required for MSC/NASTRAN.

The CFD calculations based on both of the manual and FAME meshes converged with no major problems. A comparison between both meshes based on the time used in mesh generation and CPU is given in the following table.

	Mesh Hours	MD analysis (Fujitsu) Hours
Hand	240	20
FAME	50-60	30

Table 1. Time and CPU used for Pre-processing and MD simulation for FAME and manual Mesh

Due to the fact that the FAME mesh is much bigger than the manually generated mesh, leads to higher CPU required for CFD calculations. Although the CPU required by MD analysis based on the FAME mesh is much more than that based on the manual mesh, the reduction in the man power and time required for pre-processing is substantial. And this is much more expensive than the CPU which is getting cheaper and cheaper.

Both the direct and indirect MD coupling approaches have been tested on the manual mesh, using an SGI 8, MIPS R10000 processors power challenge machine. Although there are much faster machines available at AVL, SGI has been used for the direct coupling. This is because for direct coupling, the machine must have both FIRE and MSC/NASTRAN licences. At AVL, SGI is the only HPC machine which has both licences. The indirect MD coupling has been tested on both the manual and FAME meshes using a Fujitsu VX machine and the previously mentioned SGI power challenge. The CFD calculations has been carried out on the Fujitsu VX machine which is much faster than the power challenge and the FE calculations have been carried out on the SGI machine.

Figure 7 shows the temperature distribution in the engine block/head compound with a maximum temperature of about 340.0 ºC by the exhaust port of the first cylinder. The convective heat transfer coefficient as it is calculated using FIRE is presented in figure 8. This figure gives some engineering data for the engine designer about the cooling process in the cylinder head/block compound. One can see that the first two cylinders are cooled less than the other 4 cylinders.

To validate the MD simulation procedures, the simulation results have compared with the experimental data. Figure 9 shows the measurement points. The measured and calculated temperatures of these points are given in table (2). One can see from this table, that the measured and calculated results are qualitatively and quantitatively comparable. The differences at some places are all within a reasonable bandwidth of the engineering target.

Each of the previously mentioned MD coupling approaches has its advantages and disadvantages. According to the experience gained so far, the direct approach has the limitation that, not all the companies who have FIRE have and like to work with the MSC/NASTRAN user's modifiable version which is used in this approach. The other disadvantage of the direct approach caused by the single executable which is generated in this case. The machine on which this single executable is installed must have both FIRE and MSC/NASTRAN licences. The direct coupling method has the advantage that it is more efficient, stable (network independent) and no disk space is required to save the data to be transferred between the CFD and FE programs. The indirect method has the advantage of using the standard MSC/NASTRAN version which makes it usable for all the customers who have FIRE and MSC/NASTRAN standard versions. The indirect coupling approach is more flexible, where each peace of software may be executed on different computer.

CONCLUSION

A description has been made of the state-of-the art of multi-disciplinary analysis tools which is developed and used at AVL GmbH for analysing and/or optimising the cooling cycle in automotive engines. These tools have been developed, refined and validated through extensive analysis works and experimental investigations.

An automatic mesh generator has been used to generate a detailed 3D unstructured mesh for the CFD calculations of the cooling water jacket of a 6 cylinders engine. The mesh has been tested using the MD simulation procedure developed at AVL for coupling FIRE as CFD program and MSC/NASTRAN as FE thermal analysis software. The results have been validated against manually generated mesh and experimental data. The results are qualitatively and quantitatively comparable. The differences at some places are all within a reasonable bandwidth of the engineering target.

REFERENCES

1. Lowe, S. H., Morel, T. "A New Generation of Tools for Accurate Thermo-Mechanical Finite Element Analyses of Engine Components," SAE 920681, 1992.
2. W. Stütz, Kratochwill, H. "Cylinder Head Development using Numerical Methods," MTZ, Heft 5, 1993 (German).
3. Sakai, T., Ishiguro S., Sudoh, Y. "The Optimum Design of Engine Cooling System by Computer Simulation," SAE 942270, 1994.
4. Blümcke, E., Stenzel, M. "Validation and Applications Procedure for Calculating The Isothermal Fluid Flow in Water Cooling Cycle of Vehicle Engines," VDI Berichte Nr. 1283, 1996 (German).
5. Stenzel, M., Uhl W., Marzy, R. "Structural Optimization of Cylinder Head-Block Compound Using FE-Methods," Vienna Motor Symposium, pp. 234, 1997 (German).
6. Baker, D. M., Assanis, D. N. "A Coupled Methodology for Modeling the Transient Thermal Response of SI Engines Subject to Time-Varying Operating Conditions," SAE 920681, 1992.
7. Dan Deitz, "FEA for the real world", ASME Journal, Vol. 119, No. 5, pp. 78, 1997.
8. Ennemoser, A., Petrin, H., Dilgen, P. "Optimisation of a Cooling Jacket by Coupled CFD-FEM Analysis, 3rd International FIRE Users Meeting, Graz, June, 16-17. 1997.
9. Putz, N., Rebhandl. H, Sampl, P., " FAME-Flexible Automatic Meshing Environment," 4th World Conf. In Applied Fluid Dynamics (WUA-CFD 1998), Freibug, Germany, June 7-11, 1998.
10. Wieser, K., Ennemoser, A., Plimon, A., "Automatic Mesh Generation – The Key to Successful Integration of CFD in The Development Process," MTZ, Heft 5, 1998.
11. Schober, P. Hofhaus, J., Zemsch, S., "Experimental and Numerical Analysis of Ventilation Ducts in Passenger Cars," Haus der Technik e.v. Numerical Fluid Dynamics in Automobile Construction, Essen, Germany, March 25-26, 1998 (German).
12. Mahmoud, K. G., Ennemoser, "Applications of Multi-Disciplinary Engineering in Engine Design," 1st Inter. Symposium on Concurrent Multidiscplinary Engineering (CME), Bremen, Germany, June 17-19, 1998.
13. NN, AVL BOOST, User Manual Version 3, s. l., AVL LIST GmbH., Graz, Austria, 1997.
14. MSC/NASTRAN User's Quick Reference Guide, V. 70, Ed. Kevin Kilroy, MacNeal –Schwendler Corporation, Los Angles, CA, 1997.
15. FIRE™ User Manual Version 6, AVL LIST GmbH., Graz, Austria, 1997.
16. MSC/NASTRAN User's Modifiable Version User Guide, Ed. Dale Layield, The MacNeal –Schwendler Corporation, Los Angles, CA, 1997.
17. Stone, C. R., Sorrel A. J., Biddulph T. W, Marshall, R. A., " Analysis of Spark-Ignition Performance After a Cold Start, with Thermal and Cyclic Measurements," ImechE, C 394/007, 1990.
18. Parallel Simulation User Environment (PSUE), User Manual V1.5, University of Wales, Swansea, January 1998.

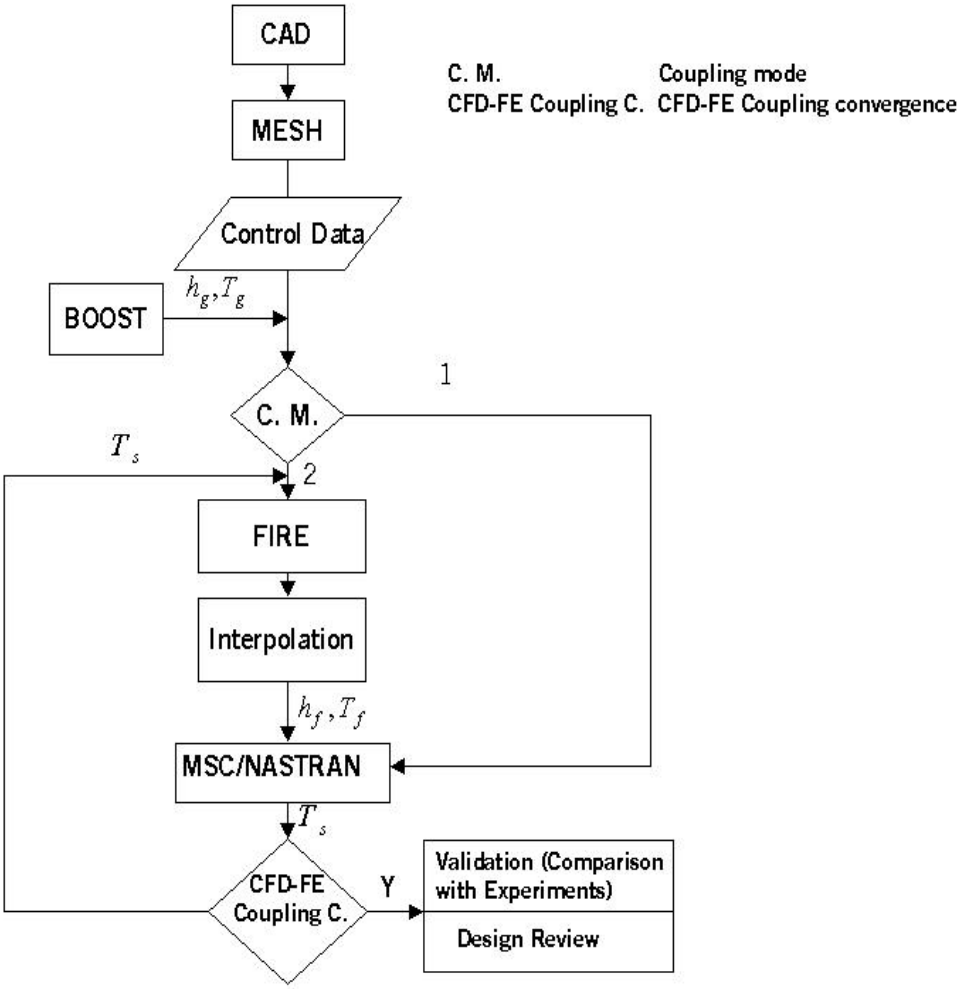

Figure 1. FIRE-MSC/NASTRAN coupling

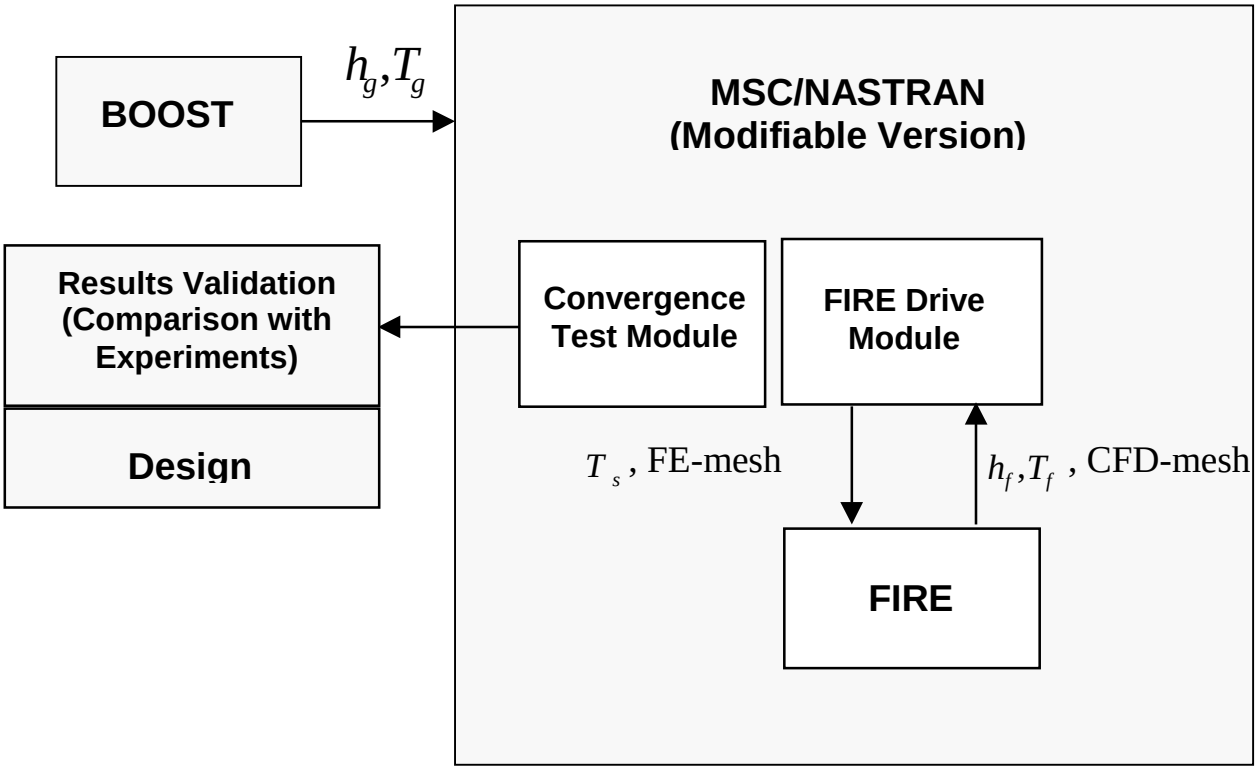

Figure 2. FIRE-MSC/NASTRAN embedded within MSC/NASTRAN

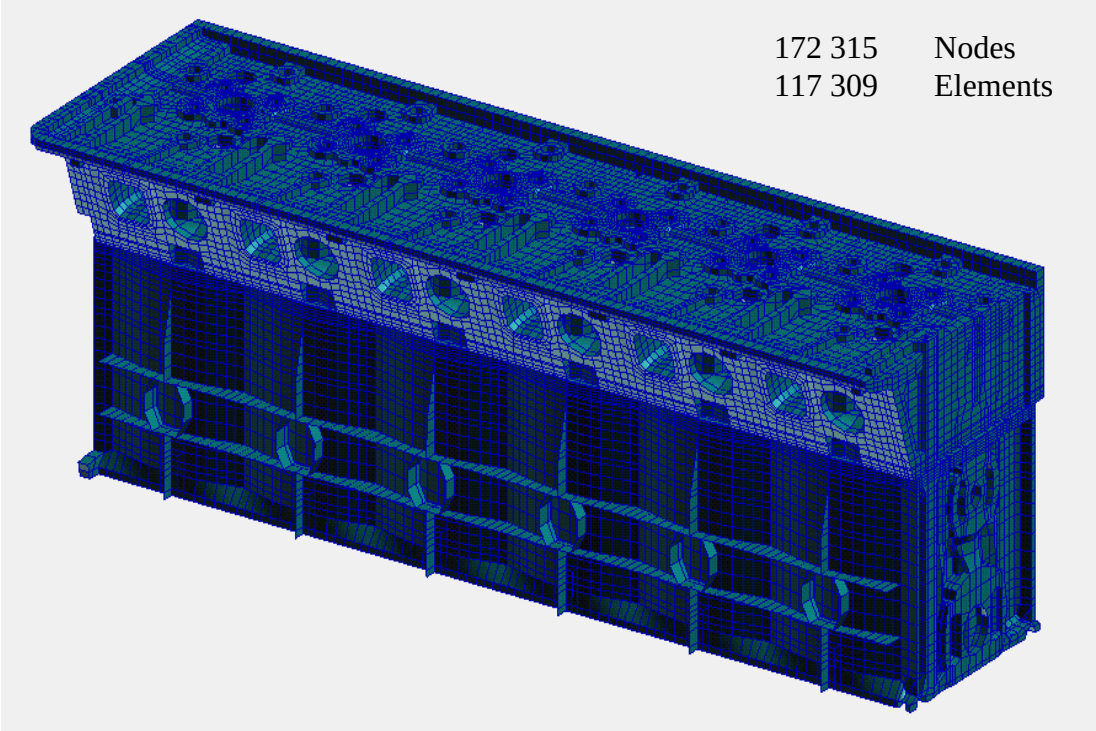

Figure 3. Finite element model

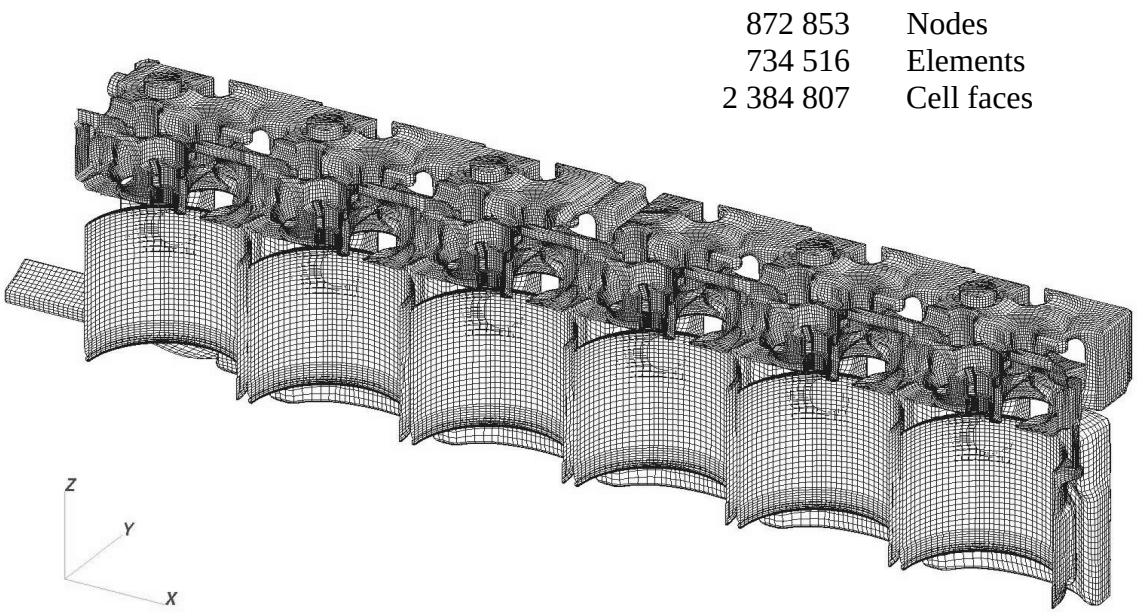

Figure 4. Water jacked CFD mesh (manually generated)

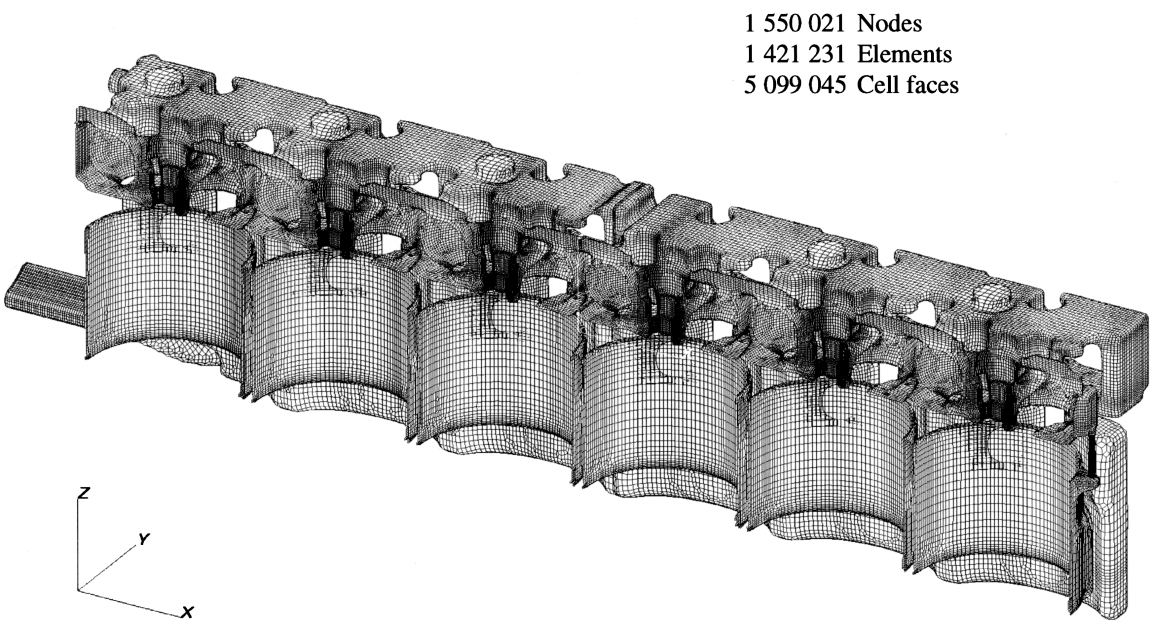

Figure 5. Water jacked CFD mesh (FAME mesh)

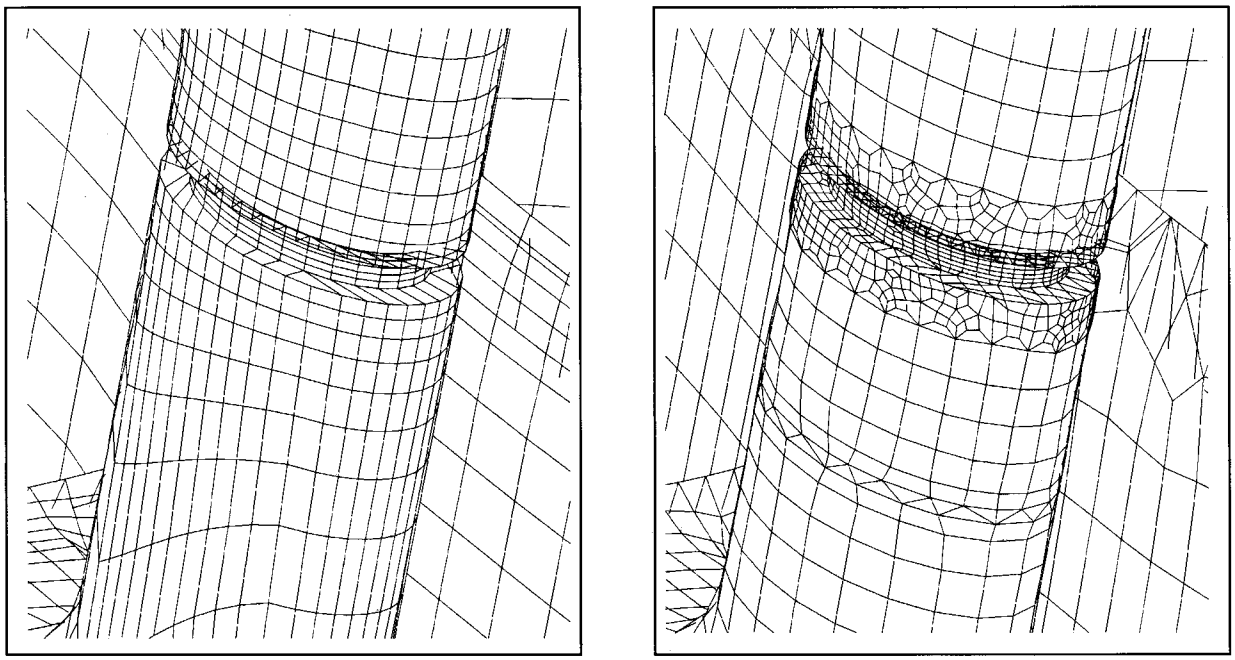

Manual FAME

Figure 6a. Comparison between manually and FAME generated meshes

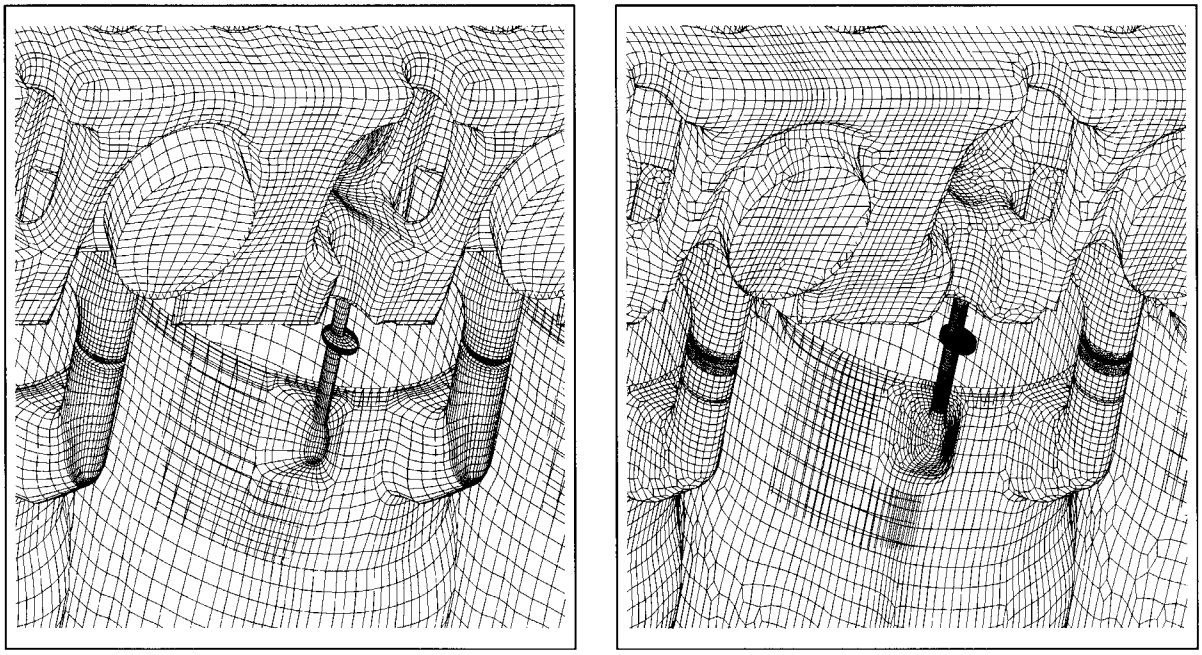

Manual FAME

Figure 6b. Comparison between manually and FAME generated meshes

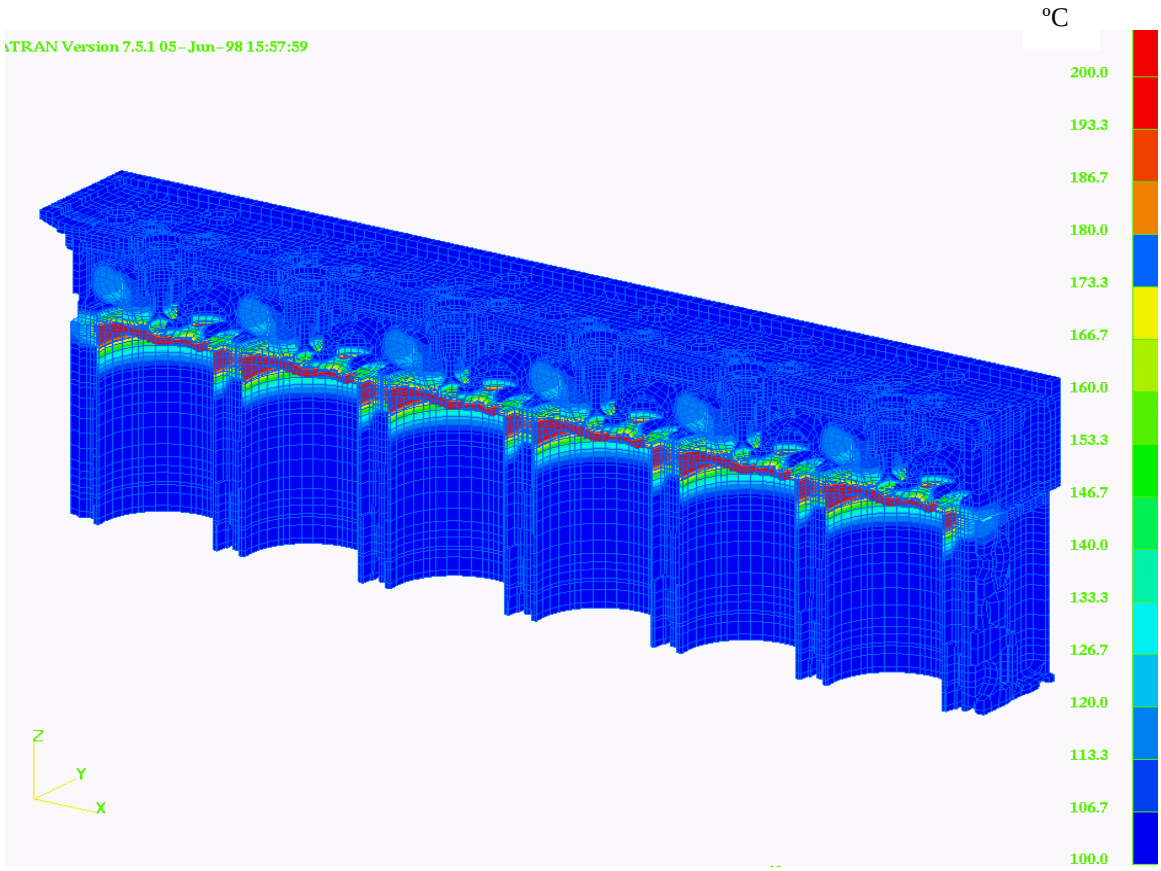

Figure 7. Temperature distribution in the structure

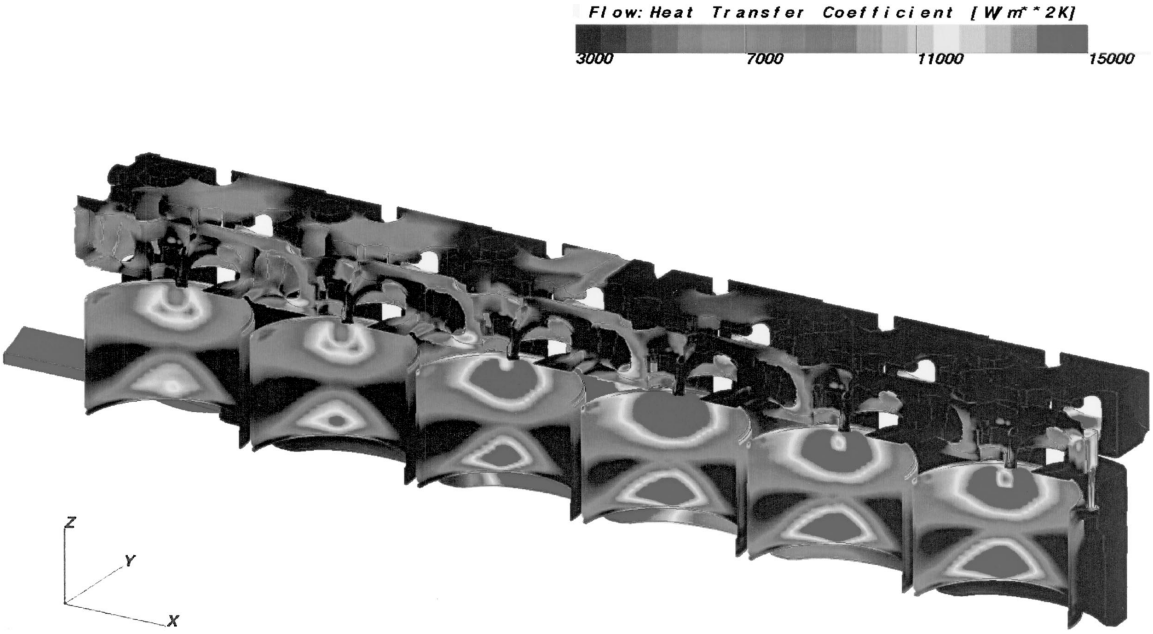

Figure 8. Distribution of the convective heat transfer coefficient

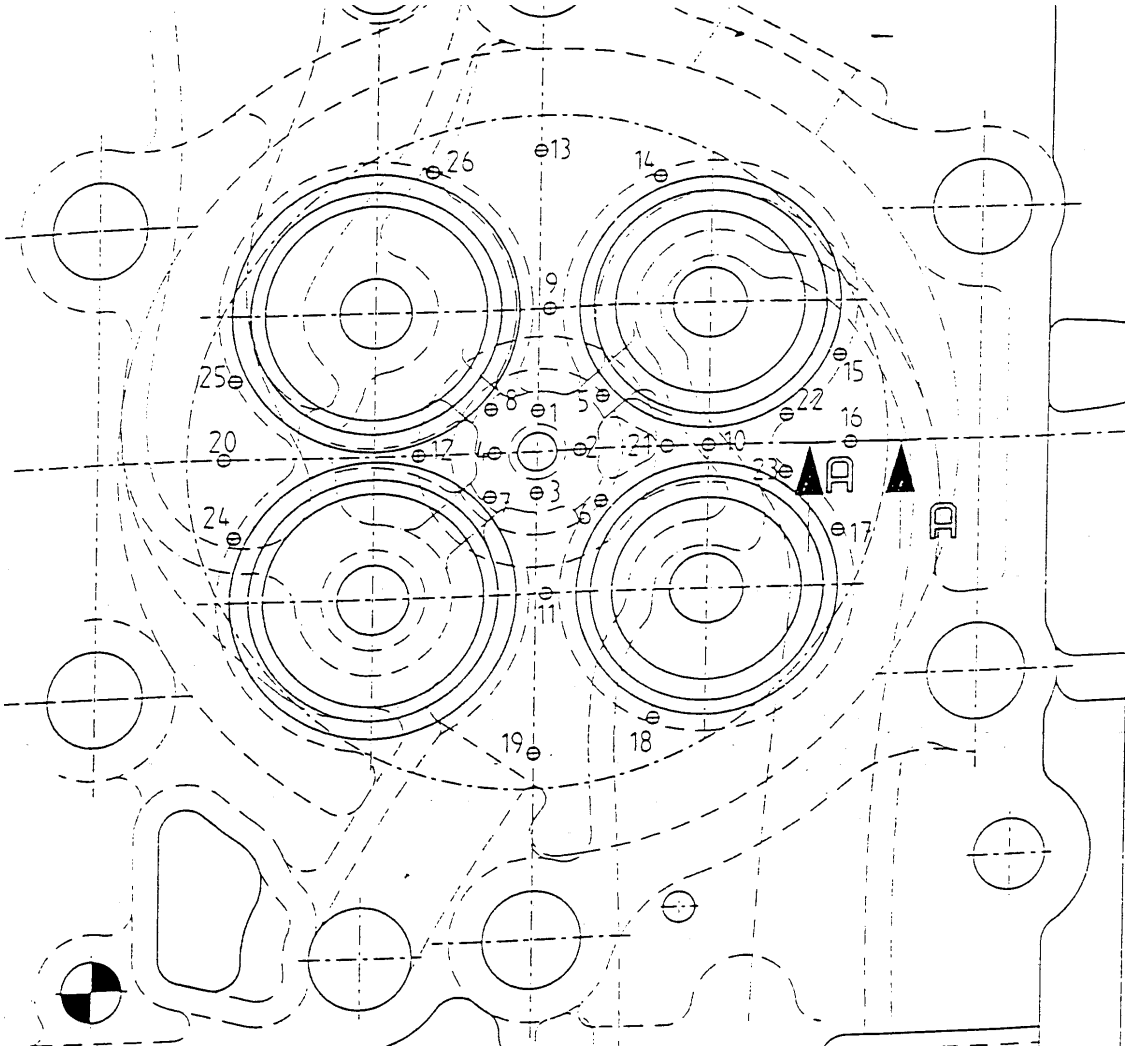

Figure 9. Places of temperature measurement points

THERMAL ANALYSIS AND DESIGN OF A PHASED ARRAY ANTENNA

James E. Marthinuss, Jr.
Northrop Grumman Corporation
Electronic Sensors and Systems Division
Baltimore, Maryland 21203

ABSTRACT

This paper will address the thermal analysis and design process for a generic phased array antenna that is liquid cooled. Much of the information is based on the knowledge and experience gained during the thermal design of advanced phased array antennas done at Northrop Grumman. Design and analysis procedures from the GaAs chip heat source to the entire array will be discussed. Computational finite difference using Northrop Grumman developed Direct Numerical Simulation (DNS) to solve complex geometric shapes will be shown. Lessons learned and critical issues in the design process will be shown and their impact on design. This paper will allow an inexperienced thermal engineer to understand the important issues in the design and thermal analysis of a phased array antenna. The same techniques can also be applied for thermal analysis of many different electronic packages because many of the same items are critical to the design.

INTRODUCTION

Phased Array Antennas are the up and coming technology for antennas with applications on many airborne or space development programs. With this the thermal design is becoming more difficult because these antennas are tightly spaced with very high power densities. A typical older technology antenna might have a power density of 0.02 W/cm^3. A liquid cooled phased array antenna could have power densities as high as 1.0 W/cm^3. New techniques must be developed in order to design the antenna efficiently and effectively.

A typical liquid cooled phased array antenna consists of Transmit/Receive (T/R) Modules, the liquid cooled heat exchangers and the housing that holds the heat exchangers. As shown in figure 1 there are many heat exchangers which hold even more T/R Modules. There may be anywhere from 10 to 70 heat exchangers with each heat exchanger having anywhere from 5 to 50 T/R modules. The T/R modules are where the heat is generated. The total power on a liquid cooled phased array antenna could be as low as 5 kw and as high as 40 kw. With power levels this high and the small size of the system, cooling of the parts is critical.

GALLIUM ARSENIDE CHIP ANALYSIS

The thermal analysis and design of the Gallium Arsenide (GaAs) chip is critical to predicting RF performance and reliability. On most T/R modules the Power Amplifier design and analysis is the most important because it is typically the hottest part. A typical Power Amplifier is shown in Figure 2. The heat sources are very small and require a large number of nodes to accurately predict the junction temperatures. A steady state analysis of the chip using Direct Numerical Simulation (DNS) and approximately two to three million nodes is typically used to generate an accurate temperature prediction. A node sensitivity study should be done by varying the number of nodes in the model until the temperature predication stops changing from one number of nodes to the next. This is critical to predicting the junction temperature. From past experience running a model without the proper amount of nodes could under predict the temperature rise in the GaAs chip by three times or more. As an example, a model is run with 200,000 nodes and predicts a temperature rise of 30°C. The same model is run with the correct number of nodes needed of 700,000. The actual temperature rise will actually be 70°C. This could cause serious problems to reliability and performance by under predicting the junction temperature by 40°C. Output from the DNS model is shown in figure 3 after the node sensitivity study was completed.

The steady state output is used to develop a simple transient model that predicts the junction temperatures of the chip accurately so that trade studies can be done quickly. The transient results of a typical chip are shown in figure 4. This GaAs chip was pulsed with a 20 percent duty and for a 10-microsecond pulse. This means that the chip was on for 10 microseconds and off for 40 microseconds. The pulse is repeated until the peak temperature reaches the same temperature for every on pulse. The top layer of the GaAs reacts to the input power very quickly as shown in figure 4. The other layers below the top of the GaAs react much slower than the top layers because the heat is spreading. More area is available so therefore more volume is available as the heat spreads. This additional volume can store more heat and will not react as fast as the top layers. The bottom layers change very little to the changes from the heat load. It is important to note that the transient response of the GaAs Chip is not exponential. There is not a time constant that can be associated with the response because of the large temperature gradients through the GaAs. Many chip manufacturers will try to use a time constant. This is not valid and will give erroneous results.

The output from the transient analysis can be used to examine the effects on the pulse width and duty cycle of the GaAs chip as shown in figure 5. As the duty cycle increases from a low duty cycle of approximately 15 percent the temperature of the chip increases rapidly. At higher duty cycles the temperature of the GaAs chip is less dependent on the pulse width. Output from the GaAs chip thermal analysis is used as input for the T/R module thermal analysis.

TRANSMIT AND RECEIVE MODULE ANALYSIS

The T/R Module thermal analysis includes all of the electrical components in the module. This module is generally bolted or bonded to the subarray coldplate. Many considerations are involved in the design of the T/R module such as junction temperatures, ease of removal of non-functioning parts and manufacturing time and cost. A cross section of a typical mounting scheme is shown in figure 6. Spreaders can be added to reduce the junction temperature of the chips. Particular attention must be paid to any interfaces or bonded joints when adding spreaders. A poor bond could increase the junction temperature and negate any possible decrease in temperature from the spreader. Figure 7 shows how a poor bond can increase the junction even though an additional spreader is added to the stack up of materials.

Many different materials can be used in the design of the T/R module that the thermal engineer must use in the thermal analysis. Property information such as conductivity, specific heat and density are needed to perform an accurate thermal analysis. A partial listing of typical materials is shown in Table I. Once a steady state analysis is done and the junction temperatures of the electrical components are under the maximum allowed the output is used as input to the coldplate design. Due to the fact that the coldplate does not require the same number of nodes and node size the information must be reduced in order to use as input to the coldplate model. Using the temperature gradient through the last layer of the module and calculating the area that was used to obtain this gradient is then used as input to the coldplate model. This is shown in the calculation below.

$$A = Lq/\Delta Tk = (0.000075\text{m})(6.0 \text{ watts})/(1.3\text{W/mC})(5.0 \text{ C}) = 0.0000692 \text{ sq meters}$$

Where:

ΔT = Temperature gradient = 5.0 C
L = Length or thickness of Layer = .000075 m
q = Power dissipated = 6 Watts
k = Conductivity = 1.3 W/m C

The calculated area of 0.0000692 square meters can be input into the coldplate thermal model as a source that is 8.3 mm by 8.3 mm.

FLUID FLOW ANALYSIS

Steady State Flow Distribution

Once the conduction part of the model is completed the fluid flow must be modeled and integrated into the system model. The flow path must first be defined so that the temperatures of the Phased Array Antenna are within a certain temperature range. Typically all of the T/R Modules need to be within +/- 5 C of each other for proper performance. It is also important that the temperature distribution across the antenna is of a smooth pattern as shown in Figure 8. There are several ways to accomplish this temperature distribution but it was decided that a dual path two-pass flow design would be used as shown in the figure 9. The fluid is supplied to the subarray at each end and is also returned at the same end. A vacuum brazed coldplate with finstock is used to efficiently remove the heat from the T/R Modules.

Due to the fact that the antenna is elliptical the subarrays in the center are longer and have more power to be dissipated to the fluid. More flow will have to go through the center subarrays in order to maintain the same inlet to outlet temperature rise. The outside subarrays will also need to be orificed so that flow is distributed properly. The flow rates to the antenna were tested and varied so that the flow distribution at different total flow could be determined. It is important to note that when the flow rate is varied to the Array, the flow distribution changes. By increasing the flow rate a higher percentage of flow goes to the subarrays in the center of the Array. With a lower flow rate a lower percentage of flow goes to the subarrays in the center. This is explained by the fact that the center subarrays have more viscous pressure loss than the subarrays on the ends. The subarrays on the ends have more non-viscous pressure loss because more orifice drop is required to balance the Array. As the flow rate is increased the viscous loss increases linearly with the flow rate. The non-viscous loss increases by the square of the flow rate. This is important so that the flow distribution is known under different conditions and different flow rates. This flow distribution is shown in figure 10 for various flow rates.

The pressure drop of the Antenna was also measured under different fluid temperatures ranging from -20°C to 40°C. These conditions are important because of the cold start and hot start requirements. The flow rate must be determined for these transient conditions so that temperatures can be accurately predicted based on the flow rate and pressure drop. The pressure drop of the Antenna increases significantly as the fluid temperature decreases. This is due to the fact that the viscosity increases rapidly as the temperature decreases. At temperatures above 0°C the pressure drop is still reasonably low as compared to the high pressure drop below 0°C. The measured pressure drop curves at different fluid temperatures are shown in figure 11. A curve fit equation of the measured data is shown below and is valid for a temperature range between -40°C and 71°C.

$$\Delta P = 110936 m^2/\rho + 18189 \mu m/\rho$$

where:

m = mass flow rate (kg/s)
ρ = density (kg/m^3)
μ = viscosity (Centipoise)
ΔP = pressure drop (kPa)

This equation is very useful in determining the pressure drop of the antenna under different flow rates and temperatures. It is also useful in understanding how much pressure drop is viscous loss and much is non-viscous loss. This point is critical when designing for cold start conditions.

Cold Start Analysis

A cold start on a Phased Array Antenna is very different from most electronic cold starts. The time required to heat up a phased array antenna is dependent on the fluid temperature into the antenna. If the fluid into the antenna rises at a fast rate according the coolant supply system the antenna will also rise in temperature very quickly. A typical cold start for a phased array antenna is shown in figure 12.

The antenna follows the temperature of the inlet fluid closely until the antenna is powered. Cold start considerations are important early in the design phase. Creating a design that under cold conditions the more critical parts warm up faster can be done by intentional increasing the minor-loss pressure drop and reducing the viscous pressure drop in a parallel flow path. This is done at cold temperatures when the viscosity of the fluid is high compared to that at normal operating conditions. More flow will go through the flow path with the lower viscous losses. A typical fluid viscosity and density with temperature are shown in figures 13 and 14. By using the curve fit pressure drop curve at 25 C the ratio of viscous loss to non-viscous loss is 2/1 with at total pressure drop of 276 kPa at .68 kg/s. At -40 C the ratio of viscous loss to non-viscous loss is 30/1 with a total pressure drop of 276 kPa at 0.0075 kg/s. If the ratio at 25 C is changed to 1/1 by adding an orifice type loss and reducing the viscous loss at the same pressure drop and flow rate the corresponding flow rate is 0.03 kg/s at 276 kPa at -40 C.

Thermal overload or an overheat condition is of great concern. The antenna changes temperature rapidly and can overheat in a less than a minute without adequate cooling. Most systems require that the antenna operator receive information that the system is overheating. The operator then can decide if they want to allow the system to continue to operate in this condition. The next level of overheating is when the antenna will be permanently damaged and the system will shut down. The time between overheat and shut down is small due to the extremely low thermal resistance between the Chips and fluid. This leaves the operator very little time to decide what to do before the system shuts down. As an example a typical thermal time constant for a liquid cooled phased array antenna is shown below.

$$\tau_t = (L/kA)(\rho V C_\rho) = RC \qquad (1)$$

Where:

R = Thermal resistance (C/Watt)
R = ΔTemp/Power
R = 30 C/25,000watts= 0.0012 C/W

C = Capacitance
C = 100 kg x 1068 J/kg-K = 106,800 J/K

RC = Time Constant = R x C
RC= 0.0012 C/W x 106,800 J/K = **128.2 seconds**

With a time constant of only 2 minutes the array will react very quickly to any changes in power or boundary conditions. Cold start is very critical to the RF performance of the antenna because most electronics are calibrated at temperatures around room temperatures. When the temperatures in the antenna are changing this rapidly it is important to know these temperatures accurately so if temperature compensation is needed it can be done.

Hot Start Analysis

The Hot start analysis for a phased array antenna is much easier to design for than a cold start condition. With the fluid at a high temperature the viscosity of the fluid is low so the flow is developed quickly. The system can be turned on when the fluid reaches an acceptable operating temperature. A plot showing the hot start of a phased array antenna is shown in figure 15. How soon the antenna can be turned on is completely dependant on the response time of the liquid cooling system. A fast response allows the antenna to be turned on in a short period of time with very little cool down time required. This is a big advantage to a liquid cooled phased array antenna.

SYMBOLS

m = mass flow rate (kg/s)
ρ = density (kg/m^3)
μ = viscosity (centipoise)
ΔP = pressure drop (kPa)
τ_t = thermal time constant (seconds)
L = Length of Conduction Path (m)
k = conductivity (W/m-K)
A = Area of conduction path (sq meters)
V = Volume (cubic meters)
C_ρ = Specific heat (J/kg-K)
R = Thermal resistance (C/Watt)
C = Capacitance (J/K)
RC = Time Constant (seconds)
ΔT = Temperature gradient = (C)
q = Power dissipated = (Watts)

REFERENCES

1. Incropera, F.P., DeWitt, D.P., “Fundamentals of Heat and Mass Transfer”, Second Edition, John Wiley and Sons Inc., 1985.
2. Gerhart, P.M., Gross, R.J., “Fundamentals of Fluid Mechanics”, Addison-Wesley Publishing Company, 1985.
3. Kays, W.M., London, A.L., “Compact Heat Exchangers”, Second Edition, McGraw Hill Book Company, 1964.
4. Holman, J.P., “Experimental Methods for Engineers”, Fourth Edition, McGraw Hill Book Company, 1984.
5. Cristou, A., “Reliability of Gallium Arsenide MMICs”, John Wiley and Sons Inc., 1992.
6. Gilmore, D.G., “Satellite Thermal Control Handbook”, The Aerospace Corporation Press, 1994.

Table I Typical Materials used in T/R Modules and Conductivity.

NAME	CONDUCTIVITY (W/m K)
3M A10	0.16
ABLEBOND 36-2	1.73
ABLEBOND 564A	0.20
ABLEBOND 84-1 LMINB1	1.97
ABLEBOND 84-1 LMIT	5.87
ABLEBOND 8700E	2.04
ABLEBOND 971-1	2.10
ABLEBOND ECF564	3.80
ABLEFILM 550MTV	0.31
ABLEFILM 561K	0.96
ABLEFILM ECF550	0.28
ABLEFILM ECF561	1.49
ABLEFILM ECF563	1.73
ABLESTICK 8175	3.20
ABLESTICK 958-7	2.00
ABLESTIK 5025E	3.39
ABLESTIK 8175	3.20
ABLESTIK 958-7	2.00
ABLSTIK ECF561E	1.60
AI TECH-DIAMOND ESP 7359	11.54
AI TECH-SILVER TC 8750	6.50
AI TECH-SILVER ESP 8350	6.50
AI TECH. ESP8350-SS	6.50
AI TECH. ESP9353	1.71
AI TECH.-AL NIT ESP 7358	3.62
AI TECH.-AL2O3 ESP 7355	1.73
AI TECH.-GOLD ZME 8155	3.62
AI TECH.-SILVER RE 8155	3.62
AI TECH.-SILVER ME 8412-A	7.92
ALNI	125.29
ALUMINA 91%	16.71
ALUMINA 99.5%	25.14
BEO	429.46
BERYLLIA	230.46
FERRITE	6.23
GERMANIUM	43.34
LTCC	1.97
SiC	25.02
ZIN SELENIDE	18.03
ZNSE	18.01
80W/20CU	246.41
85W/15CU	229.70
90W/10CU	204.64
SIC/ALUMINUM	181.24
CHOTHERM 1671	4.33
CHOTHERM 1664	1.73
CHOTHERM 1661	4.33
DIAMOND	553.96
Q-PAD I	1.58
Q-PAD II	2.36
SILPAD	0.71
SILPAD-1000	1.10

NAME	CONDUCTIVITY (W/m K)
THERMAL GREASE	0.75
THERMSTRATE	3.03
ALUMINUM 6063	217.94
ALUMINUM 6061T6	166.05
ALUMINUM 2024T6X	150.48
ALUMINUM 1100	221.40
ALUMINUM 6061T4	155.67
BE CU C17200	107.17
BERYLLIUM C2600 CART	200.15
CM-15	184.37
CM-20	197.00
COPPER CDA 11000	387.44
COPPER CDA 17200	107.24
COPPER-MOLY 70%M	145.11
COPPER-MOLY 65%M	135.10
COPPER-TUNG 25%C	190.14
COPPER-TUNG 20%C	180.14
COPPER-TUNG 15%C	167.13
COPPER-TUNG 10%C	157.13
GOLD PURE	297.47
GOLD PASTE	49.25
INCONEL 617	13.47
INDIUM	70.92
IRON ASTM-A-48	48.46
KOVAR	16.71
LEAD COMMON	35.34
MAGNESIUM PURE	156.02
MAGNESIUM ALLOY Z31	76.04
MOLYBDENUM	159.23
MONEL 400	21.67
PLATINUM PURE	71.71
SILVER PURE	412.91
STAINLESS STEEL AISI 302	15.13
STAINLESS STEEL AISI 316	16.15
STAINLESS STEEL	15.60
STAINLESS STEEL AAIS 347	14.22
THERMLCON 83 75%Tu/25%Cu	189.12
TIN GRADE A	69.34
TUNGSTEN	167.61
ZINC	116.62
DUROID	0.24
POLYAMIDE	0.51
TEFLON	0.45
GAAS	45.03
SILICON	86.68
AGSN 62	50.04
AUGE 88/12	44.44
AUSB 75/25	224.58
AUSI 94/6	283.68
AUSN 80/20	57.33
INPB 70/30	63.83
PBSN 60/40	50.04

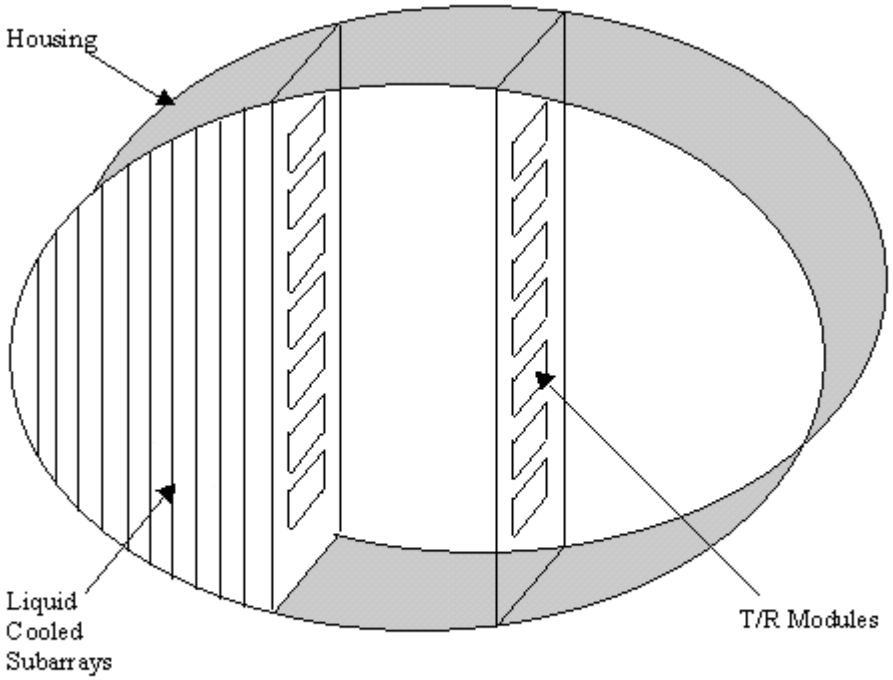

Figure 1 - Components of a Typical Phased Array Antenna

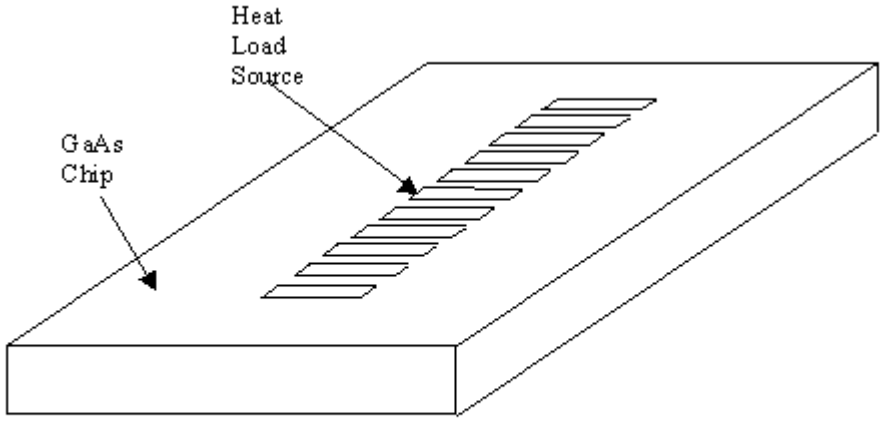

Figure 2 - Typical GaAs Chip

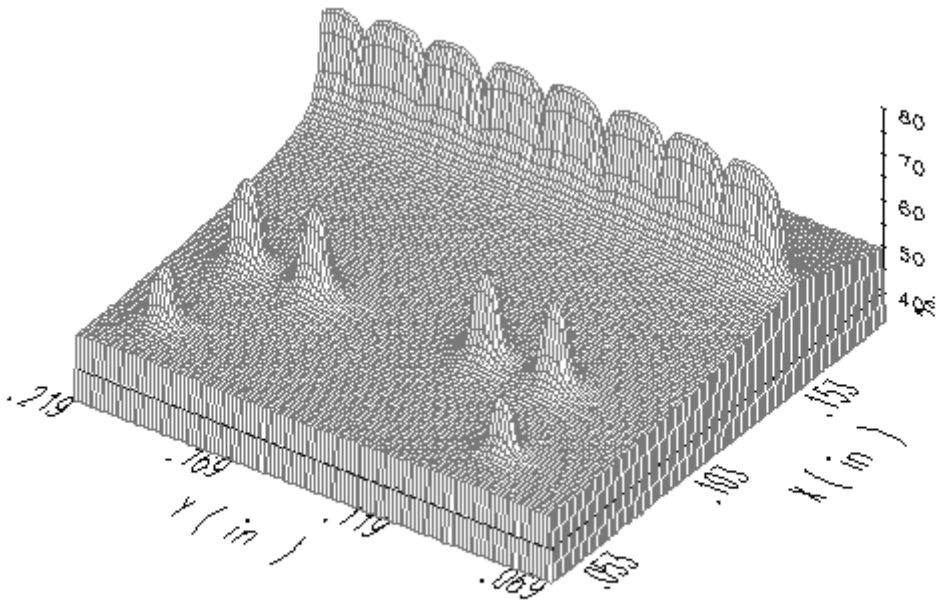

Figure 3 Temperature Output From DNS

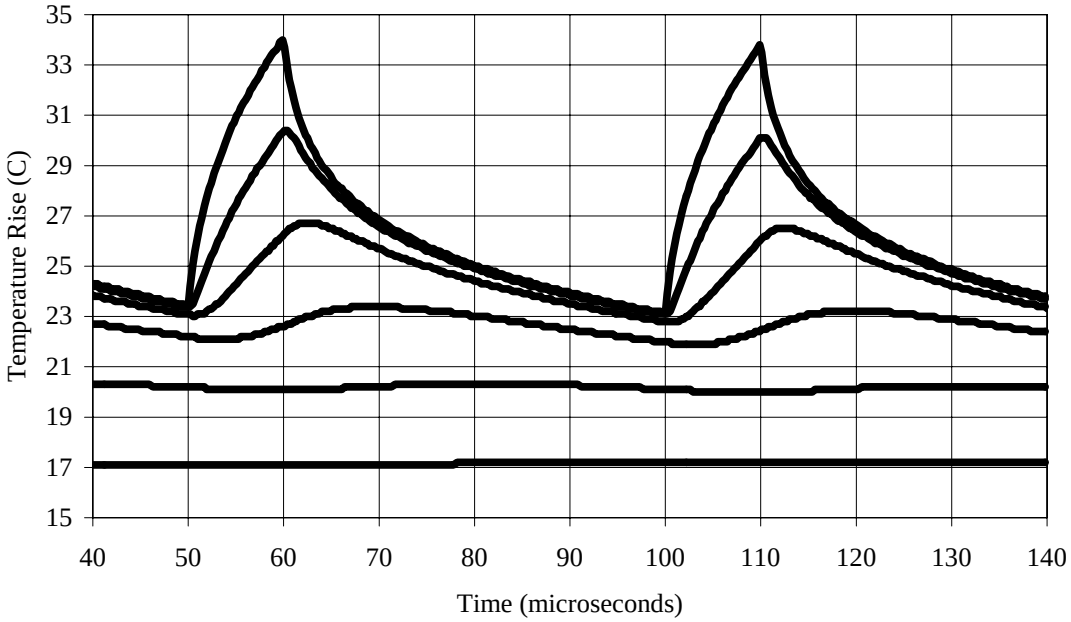

Figure 4 - Transient Response of GaAs Chip with 20 % Duty and 10 Microsecond Pulse

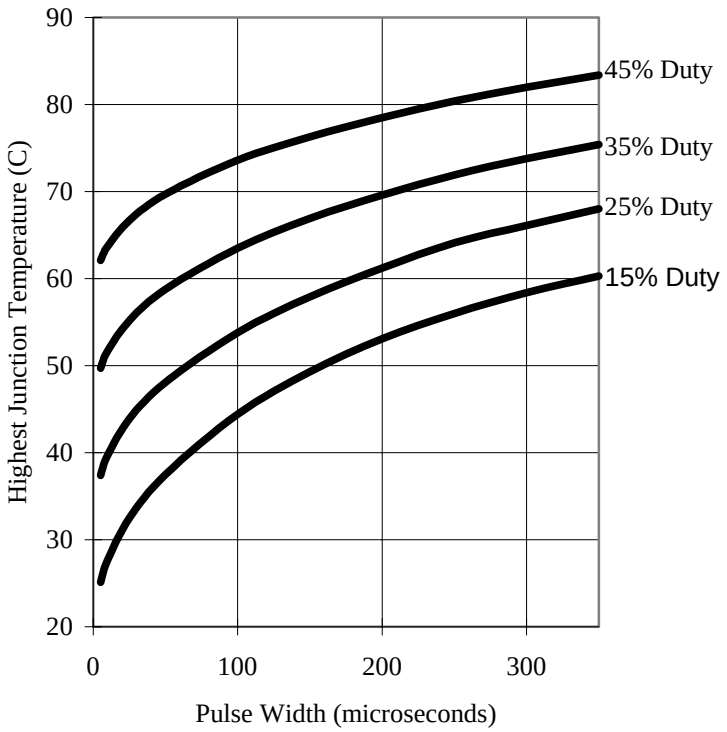

Figure 5 - Trade Study Pulse Width and Duty Cycle

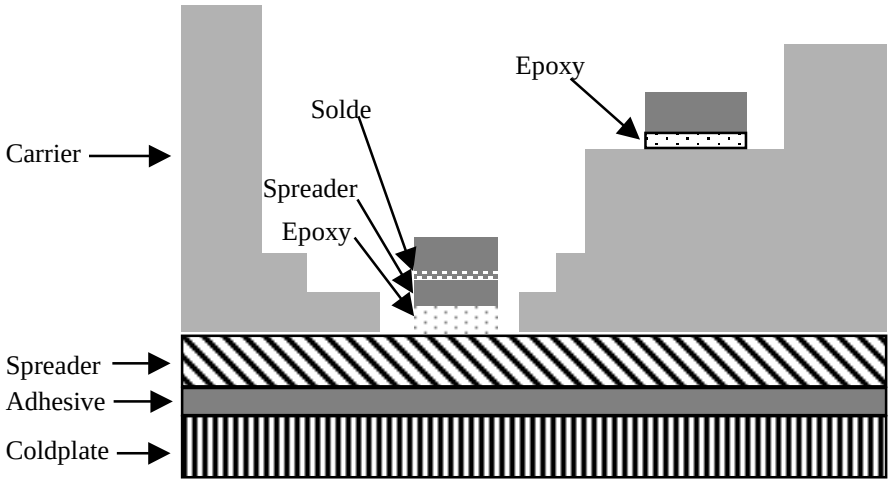

Figure 6 - Cross section of T/R Module mounting

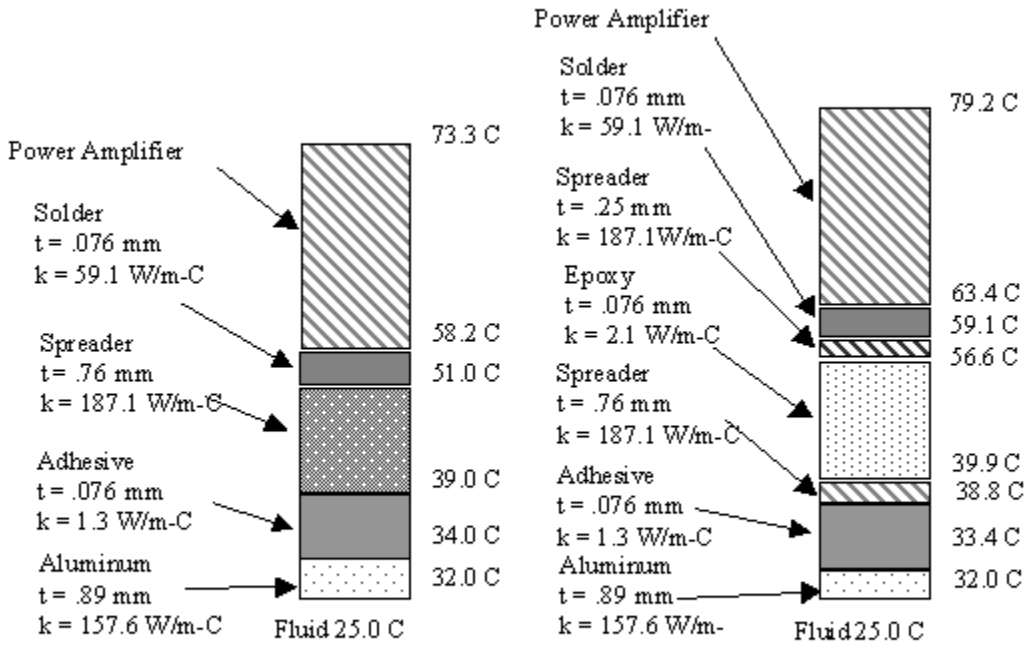

Figure 7 - Temperature Rise of Chip in T/R Module

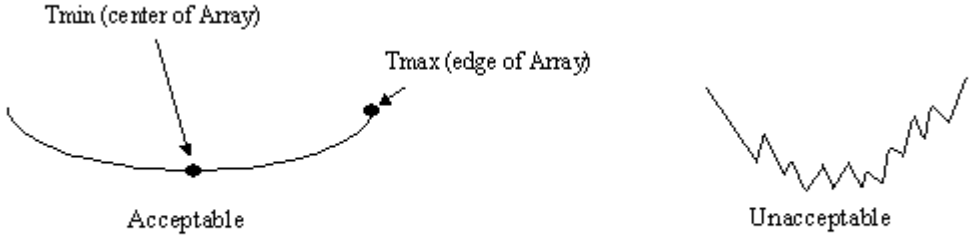

Figure 8 - Antenna Temperature Distribution

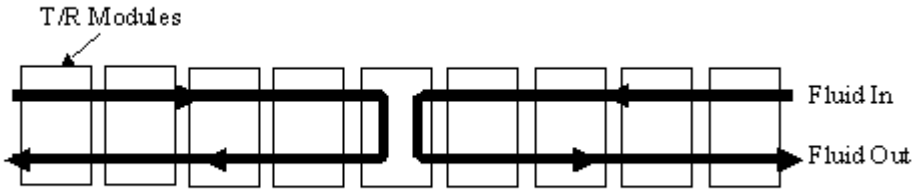

Figure 9 - Flow path of a subarray

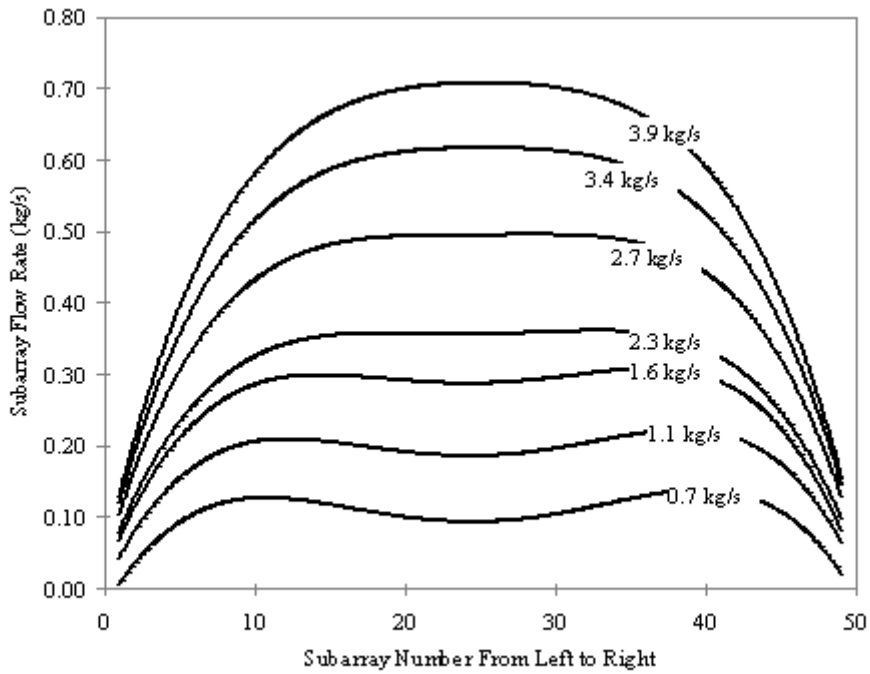

Figure 10 - Subarray Flow Distribution

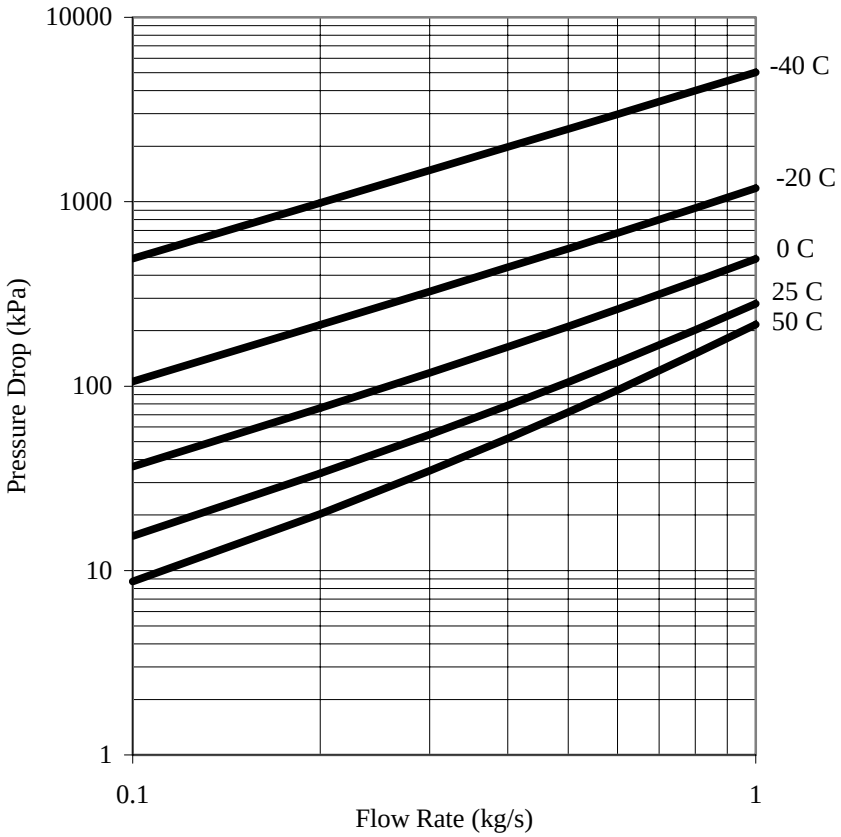

Figure 11 - Pressure Drop at Various Fluid Temperatures

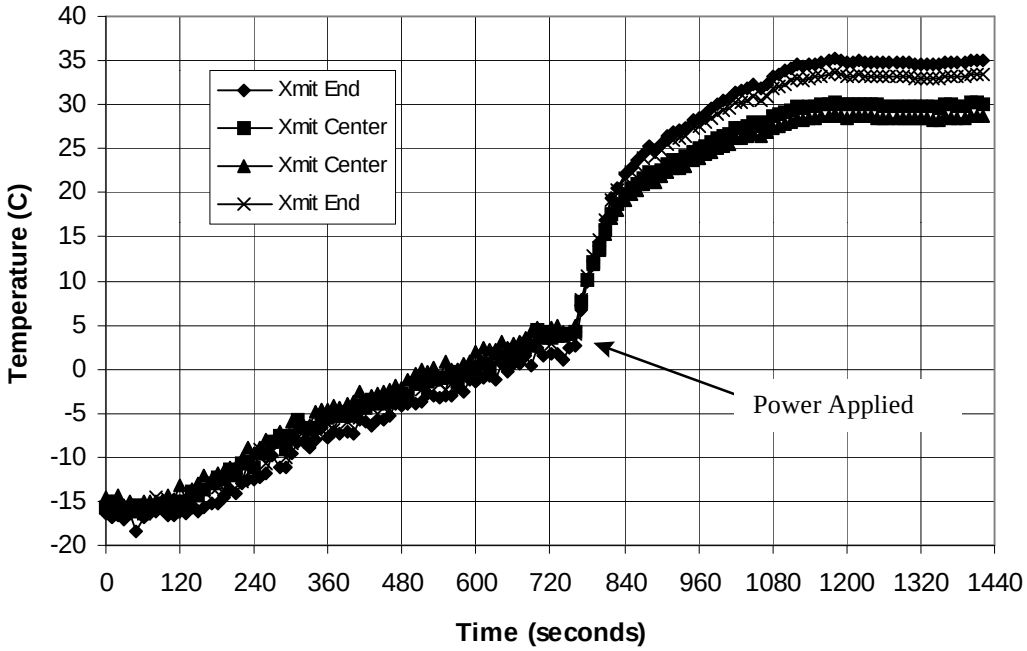

Figure 12 Typical Coldstart Measured Data

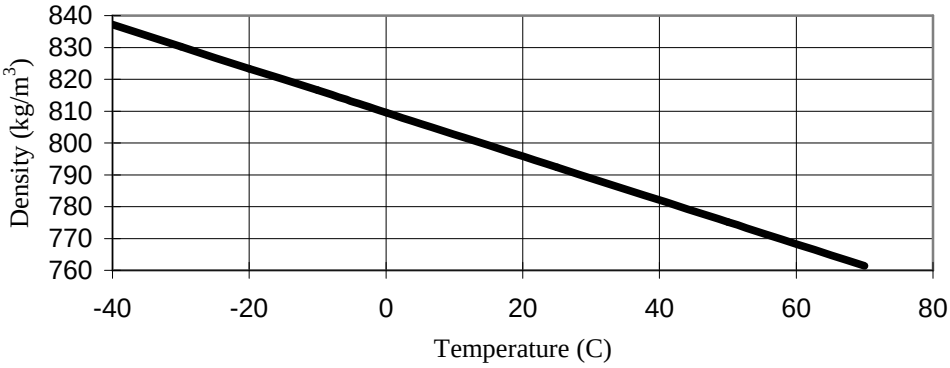

Figure 13 - Typical Fluid Density with Temperature

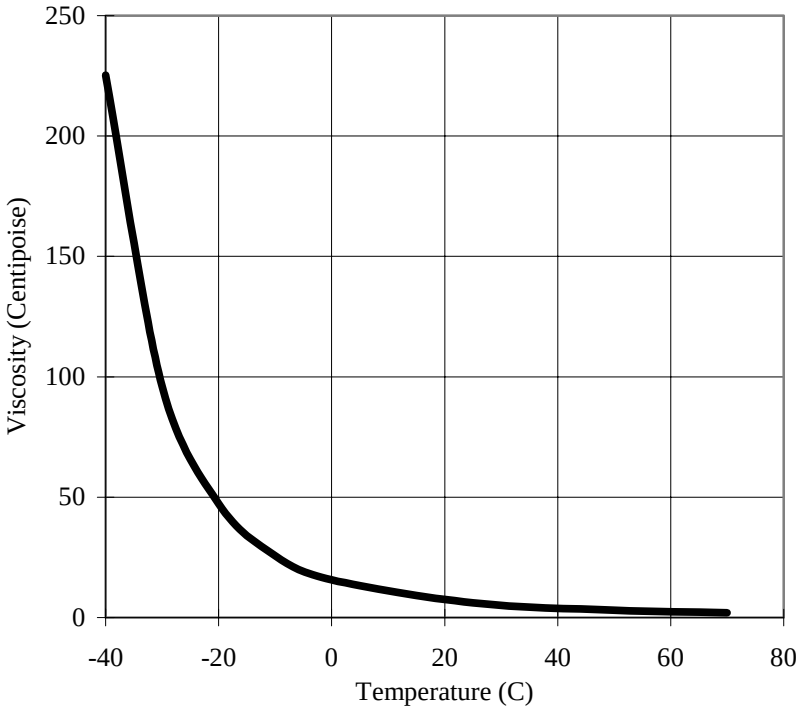

Figure 14 - Typical Fluid Viscosity with Temperature

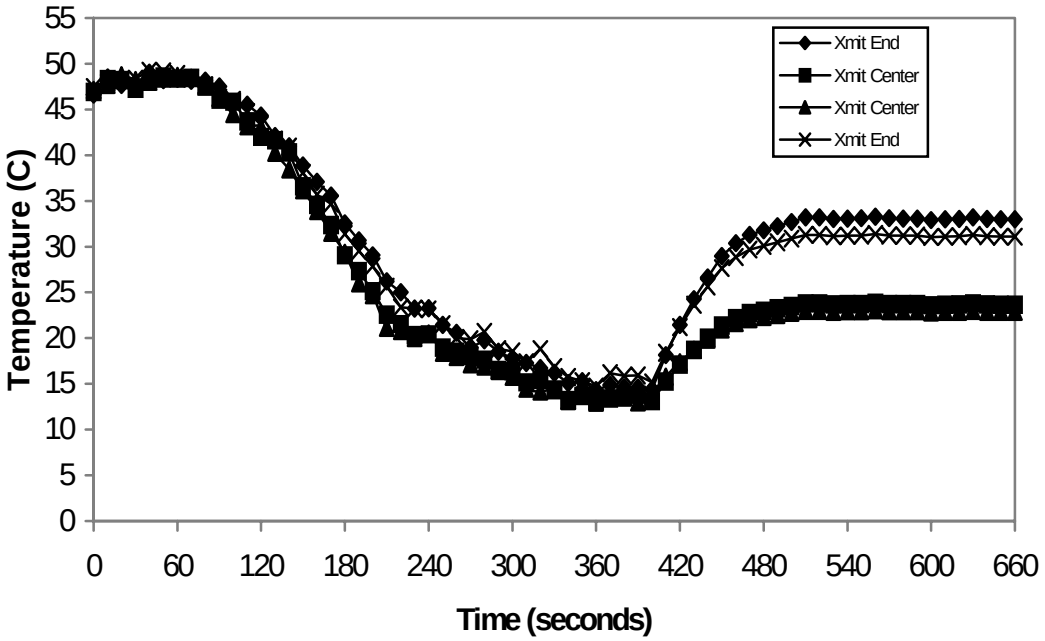

Figure 15 - Hot Start

INTEGRATED MODELING TOOLS FOR THERMAL ANALYSIS AND APPLICATIONS

Mark H. Milman, Laura Needels, and Miltiadis Papalexandris
Jet Propulsion Laboratory
California Institute of Technology
Pasadena, California 91109

INTRODUCTION

Integrated modeling of spacecraft systems is a rapidly evolving area in which multidisciplinary models are developed to design and analyze spacecraft configurations. These models are especially important in the early design stages where rapid trades between subsystems can substantially impact design decisions. Integrated modeling is one of the cornerstones of two of NASA's planned missions in the Origins Program -- the Next Generation Space Telescope (NGST) and the Space Interferometry Mission (SIM).

Common modeling tools for control design and opto-mechanical analysis have recently emerged and are becoming increasingly widely used. A discipline that has been somewhat less integrated, but is nevertheless of critical concern for high precision optical instruments, is thermal analysis and design. A major factor contributing to this mild estrangement is that the modeling philosophies and objectives for structural and thermal systems typically do not coincide. Consequently the tools that are used in these discplines suffer a degree of incompatibility, each having developed along their own evolutionary path. Although standard thermal tools have worked relatively well in the past, integration with other disciplines requires revisiting modeling assumptions and solution methods.

Over the past several years we have been developing a MATLAB [1] based integrated modeling tool called IMOS (Integrated Modeling of Optical Systems) [2] which integrates many aspects of structural, optical, control and dynamical analysis disciplines. Recent efforts have included developing a thermal modeling and analysis capability, which is the subject of this article.

Currently, the IMOS thermal suite contains steady state and transient heat equation solvers, and the ability to set up the linear conduction network from an IMOS finite element model. The IMOS code generates linear conduction elements associated with plates and beams/rods of the thermal network directly from the finite element structural model. Conductances for temperature varying materials are accommodated. This capability both streamlines the process of developing the thermal model from the finite element model, and also makes the structural and thermal models compatible in the sense that each structural node is associated with a thermal node. This is particularly useful when the purpose of the analysis is to predict structural deformations due to thermal loads. The steady state solver uses a restricted step size Newton method, and the transient solver is an adaptive step size implicit method applicable to general differential algebraic systems. Temperature dependent conductances and capacitances are accommodated by the solvers.

In addition to discussing the modeling and solution methods, applications where the thermal modeling is ``in the loop'' with sensitivity analysis, optimization and optical performance drawn from our experiences with the Space Interferometry Mission (SIM), and the Next Generation Space Telescope (NGST) are presented.

IMOS CONDUCTION ELEMENTS

Thermal systems are typically modeled via a network approach, and most of the existing thermal analysis tools are set up to accommodate this formulation. On the other hand, finite elements have dominated the structural and dynamics analysis communities for decades, and the corresponding software reflects this approach. There has been a great deal of preprocessing and post-processing software developed for automating much of the finite element analysis process. These developments have probably played favorably into the integration of finite element tools with other disciplines. However, there are compelling reasons to retain the network formulation. The more intuitive formulation of the problem gives the analyst greater flexibility in modeling the system. For example, complicated geometric surfaces that are nearly isothermal can be adequately modeled as a single thermal node as opposed to

some large model with intricate mesh (e.g. an engineer may choose a single node to model an electronics box or a cryogenically cooled component of a spacecraft).

IMOS takes something of a middle ground between finite elements and finite differences. Currently, conduction elements for 1–D and 2–D conduction can be automatically generated from a finite element model consisting of beam (rod) and triangular plate elements. Conduction elements are obtained by integrating the heat equation over an appropriate control volume. When the triangular elements are restricted to have interior angles that are less than or equal to 90° the resulting thermal network consists of only positive conduction elements. These elements have the same values as would be obtained by the finite element method with piecewise linear trial functions. The control volume, which is used for calculating capacitances (and defining the radiation surface elements), makes the IMOS formulation equivalent to a certain lumped mass finite element approximation, although formulated as a purely finite difference approximation. IMOS also allows the user to define thermal nodes that are not a part of the finite element geometry, and to define arbitrary conduction elements between nodes.

The finite volume integral approach to generating finite differences is very much akin in spirit to the network approach -- they both are derived by approximate flux calculations. Consider the heat equation

$$\nabla \cdot (k \nabla u) = f, \tag{1.1}$$

and note that for any region V with smooth boundary ∂V in which (1.1) holds, we have the identity

$$\int_V \nabla \cdot (k \nabla u) d\upsilon = \int_V f d\upsilon. \tag{1.2}$$

Here k denotes the thermal conductivity, f is the heat generation within the region and u is the temperature. An application of Green's theorem yields

$$\int_V \nabla \cdot (k \nabla u)\, dv = \int_{\partial V} k \nabla u \cdot n d\sigma\,, \tag{1.3}$$

where n is the outward normal vector and $d\sigma$ is the surface differential. The finite volume method approximates the surface integral above. We show how this approximation is performed on a triangular plate element below.

Consider the element in Figure 1. Let Q, R, and P denote the midpoints of the segments AC, AB, and BC, respectively, and let O denote the unique point within the triangle ΔABC where the perpendicular bisectors of these segments intersect. Let V_0 denote the region bounded by the polygon $AQOR$. We assume A is an interior point of the entire region, so that it is the vertex of additional triangles, say $\Delta_1, \ldots \Delta_r$, and we write $V = \cup V_i$ where the regions V_i are constructed in an analogous manner to V_0. Then we compute as before using Green's theorem

$$\int_V \Delta u = \sum_i \int_{\partial V_i} \nabla u \cdot n. \tag{1.4}$$

Let O_1 denote the midpoint of the triangle Δ_1 adjacent to ΔABC as shown in Fig. 1. Since AB is normal to OO_1 we approximate the contribution of the segment OO_1 to the boundary integral on the right side of (1.4) by

$$\int_{OO_1} \nabla u \cdot n \approx \frac{u(B) - u(A)}{|AB|} \left[|OR| + |RO_1| \right]. \tag{1.5}$$

The first term in the product in (1.5) is the central difference approximation to the normal derivative through OO_1, and the second term is the length of the segment OO_1. We will next show that

$$\frac{|OR|}{|AB|} = \cot C/2, \tag{1.6}$$

so that the conductance between nodes A and B contributed by ΔABC is $k\tau \cot C/2$, where k is the material conductance and τ is the thickness through the plate (both of which are assumed constant over the element).

This geometric fact is deduced from Figure 2. Let $\theta = \angle AOQ$, $\phi = \angle COP$, $\psi = \angle AOR$. Since $\Delta AOR \cong \Delta BOR$, $\psi = \angle BOR$. And in turn we have $\angle COQ = \theta$ and $\angle BOP = \phi$. Now note that $\theta + \psi + \angle A = \pi$, and $\phi + \psi + \angle B = \pi$. Then since $2\pi - (\theta + \phi) = \phi + \psi + \theta + \psi = \pi - \angle B + \pi - \angle A$, it follows that

$$\phi + \theta = \angle A + \angle B \tag{1.7}$$

Arguing in a similar manner we obtain

$$\psi + \theta = \angle C + \angle B;\ \phi + \psi = \angle A + \angle C, \tag{1.8}$$

which imply that $\angle A = \phi$, $\angle B = \theta$, and $\angle C = \psi$, so that (1.6) follows.

It is also easy to compute the total volume associated with node A since $V = \cup V_i$. In particular the volume of V_0 is computed as

$$V_0 = \frac{\tau\left[|AC|^2 \cot B + |AB|^2 \cot C\right]}{8}. \tag{1.9}$$

From this formula the capacitance associated with the node is easily computed. Also observe that the total conductance and capacitance for each node is summed element by element just as with the finite element method.

These formulae for the conductance and capacitance were earlier derived by Dusinberre [3] using geometric arguments; however the first use of the finite volume method apparently goes back to MacNeal [4] and was subsequently popularized by Varga [5].

It is easy to convince oneself that on a uniform rectangular mesh the standard 5-point approximation of the Laplacian results when using these formulas. When the mesh is not uniform it is well known that accuracy is lost. For arbitrary meshes conforming to the interior angle constraint on the triangular elements, the resulting discretization is equivalent to a finite element discretization with piecewise linear trial functions. The angular restriction on the elements is necessary in our interpretation of the control volume, but the formula for the conductances holds even for obtuse elements (although negative conduction elements result). This restriction, nevertheless, is useful for two reasons. The first being that the discretized system obeys the discrete maximum principle, and thus enabling superior convergence properties than would be obtained otherwise [6]. The second reason is that the conduction matrix is *diagonally dominant*, a property that happens to be quite useful in solving the nonlinear steady state problem with radiation elements. The general discussion of solving the network equations is taken up next.

IMOS INTERNAL SOLVERS

IMOS has internal solvers for both steady state and transient problems. The IMOS lumped mass approximation leads to the system of ode's

$$M_i \frac{dT}{dt} = Q_i + \sum_{j=1}^{N} C_{ij}\left(T_j - T_i\right) + \sum_{j=1}^{N} R_{ij}\left(T_j^4 - T_i^4\right), \quad i = 1, \ldots, N \tag{2.1}$$

as the governing equations of the thermal network. Here C_{ij} are linear conduction coefficients arising from conduction and convection, R_{ij} are radiation exchange coefficients characterizing radiative heat transfer within the system, and Q_i are heat sources and sinks. The associated steady state thermal network equation has the form

$$Q_i + \sum_{j=1}^{N} C_{ij}\left(T_j - T_i\right) + \sum_{j=1}^{N} R_{ij}\left(T_j^4 - T_i^4\right) = 0, \quad i = 1, \ldots, N \tag{2.2}$$

The Steady State Solver

Although (2.2) is a very commonly occurring problem in the aerospace industry, there does not appear to be any general proof of the existence of positive solutions to this system of equations, even for the constant coefficient problem. We will give a brief outline of a proof of this result which will also serve to motivate the solution method used in IMOS.

After reindexing and eliminating the equations associated with the (known) boundary nodes (so that the first n nodes contain all of the unknown interior nodes), (2.2) can be written in matrix form as

$$F(T) = 0; \;\; F(T) = CT + RD(T) + Q. \tag{2.3}$$

Here T is the n vector of unknown temperatures, C = (c_{ij}) and R = (r_{ij}) are the matrices defined by

$$c_{ij} = \begin{cases} C_{ij} & \text{if} \quad i \neq j \\ -\sum_{j=1}^{N} C_{ij} & \text{if} \quad i = j, \end{cases} \tag{2.4a}$$

and

$$r_{ij} = \begin{cases} R_{ij} & \text{if} \quad i \neq j \\ -\sum_{j=1}^{N} R_{ij} & \text{if} \quad i = j, \end{cases} \tag{2.4b}$$

$D(T) = \left[T_1^4, \ldots, T_n^4\right]^T$, and Q is the n vector consisting of heat sources and sinks together with the contributions of the boundary terms. Because the conducatnces c_{ij} and R_{ij} are all nonnegative, C and R are *diagonally dominant* matrices, although not necessarily strictly diagonally dominant. (A matrix $A = (a_{ij})$ is diagonally dominant $\sum_{i \neq j} \left|a_{ij}\right| \leq \left|a_{ii}\right|$. Strict diagonal dominance holds when strict inequality holds for all i.)

An important assumption we make is that the matrix $C + R$ is *irreducible*. An n x n matrix $A = (a_{ij})$ is irreducible if its directed graph $G(A)$ is strongly connected, that is, for any pair of indices i, j there is a sequence of nonzero entries of the form (a_{ir}, a_{rs}, a_{st}, ..., a_{uj}) [5]. This condition has a simple physical interpretation for the sum of the conduction and radiation interchange matrices $C + R$: Given a pair of nodes i, j there is a sequence of nodes $r, s, t, ..., u$ connecting i and j such that the interchange factors between each successive pair is nonzero. Thus each node can transfer energy to any other node through a sequence of nodes connected by a combination of conductors or radiators. Under these physical assumptions, the hypothesis $C + R$ is irreducible is satisfied. Furthermore, if at least one node is connected to a boundary node with nonzero interchange factor, then $C + R$ has strict diagonal dominance in the row corresponding to this node. In this case $C + R$ is an *irreducibly dominant* matrix, and irreducibly dominant matrices are invertible [5].

The existence result for solutions to the system (2.2) is established by a simple homotopy argument using the facts about C and R, and can be briefly summarized as below.

Let $T_0 > 0$ denote an initial estimate of the solution, and define Q_0 by

$$Q_0 = -CT_0 - RD(T_0).$$

Let $\lambda \in [0, 1]$ consider the function

$$H(T, \lambda) = CT + RD(T) + Q_0 + \lambda(Q - Q_0). \tag{2.5}$$

Note that $H(T_0, 0) = 0$, while the original problem is to solve $H(T, 1) = 0$. The homotopy idea is to show that solution curve to

$$H(T, \lambda) = 0 \tag{2.6}$$

can be continued from $\lambda = 0$ to $\lambda = 1$. Demonstrating this involved properties of the differential of H, so we first note that

$$\frac{\partial H}{\partial T} = \frac{dF}{dT},$$

where

$$\frac{dF}{dT} : h \to Ch + RD_T h, \quad \text{where} \quad D_T(h) = \left[4T_1^3 h_1, \ \ldots, \ 4T_n^3 h_n\right]^T. \tag{2.7}$$

(Thus the differential D_T is the diagonal matrix with i^{th} entry $4T_i^3$.) The irreducibility properties of $C + R$ can be used to show that $\frac{dF}{dT}$ is invertible so long as $T > 0$. The implicit function theorem then guarantees that (2.5) has a solution in a neghborhood of $(T_0, 0)$ so that $H(T(\lambda), \lambda) = 0$, and can be determined via the differential equation

$$\frac{dT}{d\lambda} = -\frac{dF}{dT}^{-1}\left(Q - Q_0\right), \tag{2.8}$$

with initial condition $T(0) = T_0$. The solution to the steady state problem corresponds to T_1. The relevant question then is whether (2.8) has a solution over the interval [0, 1]. As is well known, solutions can be continued so long as they remain bounded. The irreducibility properties of $C + R$ can be used to show that $\frac{dF}{dT}$ is invertible along the solution and that the solution remains bounded on any finite interval. In particular the solution can be continued to $\lambda = 1$ so that the steady state problem has a solution. It can also be shown that this solution is unique.

Although homotopy methods generally offer a robust technique for solving difficult problems, they are typically inferior to quasi–Newton methods, when these latter methods are convergent. We turn to these next.

IMOS uses an algorithm that is motivated by the nonlinear least squares problem,

$$\min_{T \geq 0} J(T) = \left|F(T)\right|^2. \tag{2.9}$$

J has a unique stationary point for $T > 0$ corresponding to $F(T) = 0$ since $F(T) = 0$ has a unique solution for $T > 0$ and F' is invertible for $T > 0$. Thus the minimization problem above consists of simple bound constraints, and for this class of problems trust region methods enjoy, under standard assumptions, that are satisfied here, global convergence to a Kuhn–Tucker point of the inequality constrained problem above [7,8,9]. Furthermore, under mild restrictions, the Kuhn–Tucker point is unique for (2.9). A restricted stepsize Newton algorithm similar in spirit to the globally convergent box constraint algorithm described in [8] has been implemented in IMOS. The standard Newton step has the form:

$$T_{n+1} = T_n - F'(T_n)^{-1} F(T_n) \tag{2.10}$$

A globally convergent algorithm is developed from the observation that the Newton direction

$$d_n = F'(T_n)^{-1} F(T_n)$$

is a descent direction for J in (2.9). The algorithm we implemented uses this direction coupled with a line search algorithm (see for example, [10]) to obtain a sufficient decrease in J. Hence, the actual step taken in the algorithm has the form

$$T_{n+1} = T_n - s_n d_n \tag{2.11}$$

where the scalar s_n is determined via the linesearch algorithm. Near the actual solution, the algorithm will typically use the full Newton step, and quadratic convergence is achieved locally.

For moderately and larger sized problems efficient calculation of the function F, and the inverse of its derivative, F'^{-1}, are desired. As C and R are typically sparse matrices, these features are inherited by F and F', and are thus easily exploited.

Transient Solver

A frequently used technique for solving the transient equations (2.1) is to introduce "arithmetic" nodes, i.e. nodes that have zero capacitance. Once aritmetic nodes have been introduced the ode is transformed into a Differential Algebraic Equation (DAE) because of the presence of purely algebraic equations in (2.1). Due to the stiffness of the equations an implicit solver is necessary to achieve stability of the computation with a reasonable number of time steps. IMOS uses the DAE solver DASSL, developed by Petzold [11] for DAE's of the general form:

$$F(t,T,T') = 0;\ T(t_0) = T_0,\ T'(t_0) = T'_0 \tag{2.12}$$

DASSL approximates the time derivative $\frac{dT_i}{dt} = T_i'$ by $\frac{\Delta_k T_n}{\Delta t_n}$, a k–th order backward difference operator, where k ranges from one to five. The resulting equations at the current time t_n,

$$F\left(t_n, T_n, \frac{\Delta_k T_n}{\Delta t_n}\right) = 0, \tag{2.13}$$

are then solved using Newton's method,

$$T_n^{m+1} = T_n^m - \left[\frac{\partial F}{\partial T} + \frac{1}{\Delta t_n}\frac{\partial F}{\partial T}\right]^{-1} F\left(t_n, T_n^m, \frac{\Delta_k T_n^m}{\Delta t_n}\right), \tag{2.14}$$

where m denotes the iteration index.

The system of equations above can either be dense or have a banded structure. The program automatically determines the nature of the system and selects the appropriate storage type for the thermal data.

To solve the system numerically it is necessary to compute the iteration matrix

$$J = \frac{\partial F}{\partial T} + \alpha \frac{\partial F}{\partial T}, \tag{2.15}$$

where α is a constant selected by the code that changes whenever the step–size or the order of the method changes.) This computation uses the analytic expression for the derivatives in (2.15) instead of numerical evaluation via finite differences; this improves the speed and convergence properties of the method.

The rate of convergence, ρ, is estimated whenever two or more iterations have been taken. ρ is estimated by

$$\rho = \left[\frac{\left| T^{m+1} - T^{m} \right|}{\left| T^{1} - T^{0} \right|} \right]^{1/m} .$$

The iteration has converged when

$$\frac{\rho}{1-\rho} = \left| T^{m+1} - T^{m} \right| > .3$$

If ρ >.9 or m >4, the step size is reduced and the step is attempted again. After the iteration has converged, an error test is made to verify that the solution satisfies a local error tolerance set by the user. The test is verified when

$$C \left| T_n - T_n^0 \right| \leq 1.$$

C is a constant determined by the code that controls both the truncation error and interpolation error. On each step the order k and the time step Δt_n are evaluated based on the behavior of the solution and are adaptively adjusted (see [11]).

The initial conditions of the DAE are obtained in two different manners depending on whether the node is a diffusion or arithmetic node. For diffusion nodes the initial temperatures are supplied b the user, and the derivatives are calculated directly from the heat equation (2.1). For arithmetic nodes (nodes with zero heat capacitance), the initial temperatures are obtained by *solving* the associated steady state equations while keeping the temperature of the diffusion nodes constant. The IMOS steady state solver is used to make this calculation. The initial time derivatives of the set of arithmetic nodes is set to zero.

EXAMPLES

In this section we will give examples of the internal solvers, integrated analysis and optimization. The first two examples demonstrate the internal solvers of IMOS.

The first example illustrates the convergence properties of the steady state solver on a thermal model of the Next Generation Space Telescope. This model contains 1802 nodes, more than 160,000 radiation conductors, and approximately 5800 linear conductors. The convergence history is shown in Figure 3. The error tolerance was set at 1.0e-8. This means that the global energy balance must be satisfied to 1.0e-8, and the change in temperatures between successive iterations must also be less than this quantity. Convergence was achieved after 7 iterations, which required approximately 10 minutes on an Ultra Sparc workstation.

The next example uses the transient solver to compute the evolving temperature distribution of a small asteroid rotating about itself and being heated by a star. The period of the asteroid's rotation is 48 hours. The thermal model of the star consists of 48 nodes, 16 of which are external and subject to radiation. There is also one boundary node that models the surrounding space. There are 33 linear conductance coefficients in the model, and 16 radiation coefficients, one for each external node. Figure 4 shows the time-dependent temperatures of four external nodes of the thermal model, located at different sides of the asteroid.

The error tolerance for this problem (difference between successive approximations of the temperature of each node via the Newton iteration procedure) was set to 1e-5 K. The results produced by IMOS compare well with those obtained by SINDA [12]; the maximum difference between the two results at any node and throughout the simulation was 0.016 K. The SINDA results were obtained with a constant timestep δt = 15 mins, and error tolerance of 1e-3.

The next two examples concern applications of the IMOS thermal tools. First we will set up the general form for opto–mechanical sensitivity analysis that is commonly used in IMOS. IMOS has a sister program MACOS which generates optical sensitivity matrices that map perturbations of structural degrees of freedom to perturbations in optical ray states. This sensitivity matrix is called the C matrix. (The nomenclature is adapted from control theory where C is commonly used to denote the state to output map.) For example, if x denotes the generalized coordinates of a finite element model and y represents an optical path difference due to motions of the elements comprising an optical train, the matrix C provides this relationship via

$$y = Cx.$$

IMOS develops sensitivities of optical metrics such as mean optical pathlength difference between two arms of an interferometer or the strehl ratio of a telescope (quantities that can be expressed in terms of functions of y) to changes in temperature as follows. The IMOS finite element code generates a temperature (strain) to force map F where $FT = f$, T = vector of temperatures and f = force vector. When used in conjunction with the pseudoinverse of the structural stiffness matrix, $K^{\dagger}$, the temperature to displacement map results:

$$K^{\dagger} FT = x.$$

Concatenating this with the C matrix yields the temperature to optical path difference sensitivty matrix

$$CK^{\dagger} F.$$

This sensitivity matrix is illustrated with the following application to the Space Interferometry Mission (SIM). SIM requires a very stable thermal environment to prevent distortions of the optical train and optical surfaces during an astrometric observation sequence. The duration of such a sequence is about 1 hr. Of particular concern is the change in the mean optical pathlength traversed by the starlight, which illuminates a large annular region of each optical element, versus the mean pathlength traversed by a metrology beam, which illuminates only the central core of each element. Small temperature changes are produced when a collecting aperture is slewed to view a new star. These changes in turn cause a deformation to the mirror surface, which then leads to deviations in the mean optical pathlengths of the starlight and metrology beam. Figure 5 shows the effect of the temperature variation on the mirror surface and pathlength. The sensitivity matrix $CK^{\dagger} F$ corresponding to the mean pathlength difference for this problem is actually a single vector since the mean pathlength difference is a scalar quantity. The components of the vector that have large magnitude represent the thermal nodes that contribute most to the pathlength difference error. These nodes are candidates for thermal control. Not surprisingly, this analysis indicates that controlling the temperature at the middle of the optic is most important.

We next take up how IMOS can be used in a thermal control problem. Consider the problem of determining a heat load Q applied to a specified node set to maintain a desired temperature. To set up this general problem, first let us write

$$G(x) = -Cx - RD(x).$$

The equation $G(x) = Q$ has a unique solution x ($x > 0$) for each $Q \geq 0$. Let $R_+^n = \left\{x \in R^n : x \geq 0\right\}$, and let $G^{-1}: R_+^n \to R_+^n$, denote the solution map so that

$$G(G^{-1}(Q)) = Q, \ \{Q : Q \bullet \ 0\}.$$

Let x^* represent a desired temperature vector at some subset of nodes of the system, $J \subset \{1, ..., n\}$, and let P denote the matrix that picks off the J components of a vector in R^n. Let $J \subset \{1, ..., n\}$, denote the set of nodes to which heat can be applied. The temperature control problem can be formulated as the constrained nonlinear least squares problem

$$\min_{Q} \left| x^* - PG^{-1}(Q) \right|^2 \text{ such that } 0 \le Q_i \le Q_{max}, Q_i = 0 \quad \text{if} \quad i \notin L,$$

where Q_{max} is the maximum heat that can be applied to a node. The numerical perspective of the previous section is useful for solving this optimization problem. Specifically, the gradient of the objective functional is essentially calculated "analytically" in the process of computing $G^{-1}(Q)$. (This accelerates the computation time for the optimization enormously as it is not necessary to develop the gradient numerically.) To see why this is so, observe that the only quantity that is difficult to calculate in computing this gradient is the Jacobian of G^{-1}. But by the inverse function theorem

$$G^{-1\prime} = (G')^{-1}.$$

Therefore a good approximation of $G^{-1\prime}$ (which is exact when the conductors are temperature invariant) is

$$G^{-1\prime} = (C + RD_x)^{-1}.$$

which is calculated in the process of computing the solution map G^{-1}.

Using this approach, a thermal optimization problem was posed using the model in Figure 6. The goal is to control all of the nodal temperatures of the glass, except for nodes 9 and 13, which are very difficult to control because of their proximity to the boundary nodes. The controlling agent is heat that can be applied to the middle nodes of the metal frame. These are nodes 2, 4, 6, and 8. A maximum of 10 watts can be applied to each node. The controller is not allowed to remove heat from the system. The desired temperature for nodes 10, 11, 12, 14, 15, 16, and 17 is 310°. Let T^* denote this vector of desired temperature values. Let J =[10 11 12 14 15 16 17] denote the set of temperature nodes of interest, and let L =[2 4 6 8] denote the set of nodes where heat may be applied to the system.

The solution to the control problem obtained in this fashion using the sequential quadratic programming solver in MATLAB is

Q^* = [1.313 .3622 .3622 1.313],

and the temperatures were controlled to

T_{opt} = [310.2 310.2 310.4 310.4 310.4 310.2 310.2 308.0],

where T_{opt} denotes the steady state temperature associated with the optimal heat input Q^*.

CONCLUDING REMARKS

The idea of creating end–to–end models for the purpose of design and analysis has begun to take hold in the spacecraft/instrument design community. This has spawned new opportunities to establish connections between previously disparate disciplines. IMOS is a multidisciplinary tool that was initially developed as a response to a growing need to improve the hand--off between the structural and control analysis disciplines. IMOS has grown to incorporate optical modeling, and more recently thermal modeling and analysis. Future work in IMOS development will continue to tighten connections between thermal analysis and design and other disciplines, particularly in structural analysis, control, and optimization.

Acknowledgement

This publication was prepared by the Jet Propulsion Laboratory, California Institute of Technology, under a contract with the National Aeronautics and Space Administration. Thanks are due to Andy Kissil, Scott Basinger and Walt Petrick for providing their results on the thermal opto–mechanical modeling of SIM.

REFERENCES

1. MATLAB, Mathworks, Inc., 1992.
2. Needels, L., *Integrated Modeling of Optical Systems User's Manual*, Jet Propulsion Laboratory Publication D–13040, January, 1998.
3. Dusinberre, G.M., *Heat Transfer Calculations by Finite Differences*, Internation Textbook Company, Scranton, PA, 1961.
4. MacNeal, R.H., *An Asymmetrical Finite Difference Network*, Qar. Appl. Math, Vol. 11, pp. 295–310.
5. Varga, R., *Matrix Iterative Analysis*, Prentice–Hall, Englewood Cliffs, N. J., 1962.
6. Ciarlet, P.G., *The Finite Element Method for Elliptic Problems*, North–Holland, Amsterdam, 1978.
7. Conn, A., Gould, N., and Toint, P., *Global Convergence of a Class of Trust Region Algorithms for Optimization With Simple Bounds*, SIAM J. Numer. Anal, 25 (1988), pp. 433-460.
8. Facchinei, F., Judice, J., and Soares, J., *An active set Newton Algorithm for Large–scale nonlinear Programs with Box Constraints*, SIAM J. Opt., 8, February, 1998, pp. 158–186.
9. Fletcher, R., *Practical Methods of Optimization, Second Edition*, John Wiley and Sons, New York, 1987.
10. Dennis, J.E. Jr., and Schnabel, R.B., *Numerical Methods for Unconstrained Optimization and Nonlinear Equations*, SIAM, Philadelphia, PA, 1996.
11. Petzold, L., *A Description of DASSL: A Differential Algebraic Equations Solver*, Tenth IMACS World Congress, Montreal, Canada, 1982, pp. 430–432.
12. Cullimore, B.A., *SINDA '85/FLUINT System Improved Numerical Differencing Analyzer and Fluid Integrator*, Version 2.3, Martin Marietta, 1990.

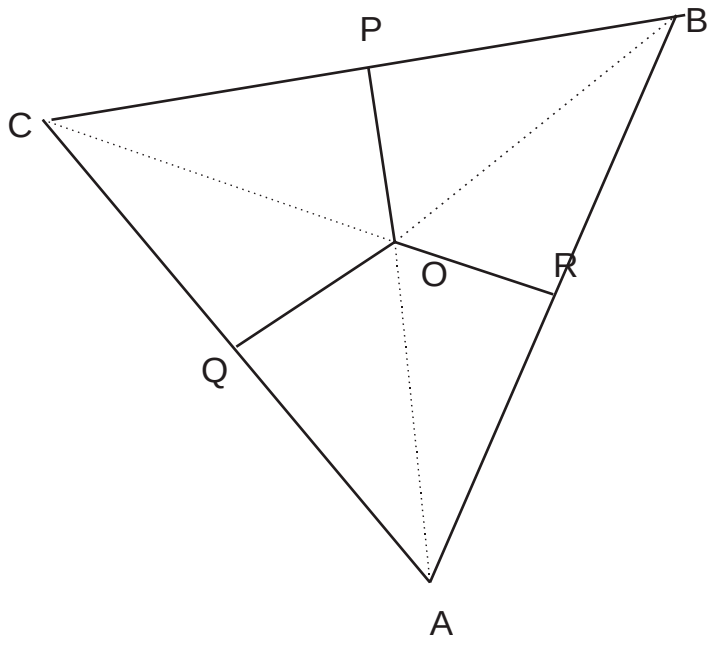

Figure 1. Control Volume Associated with Triangular Element

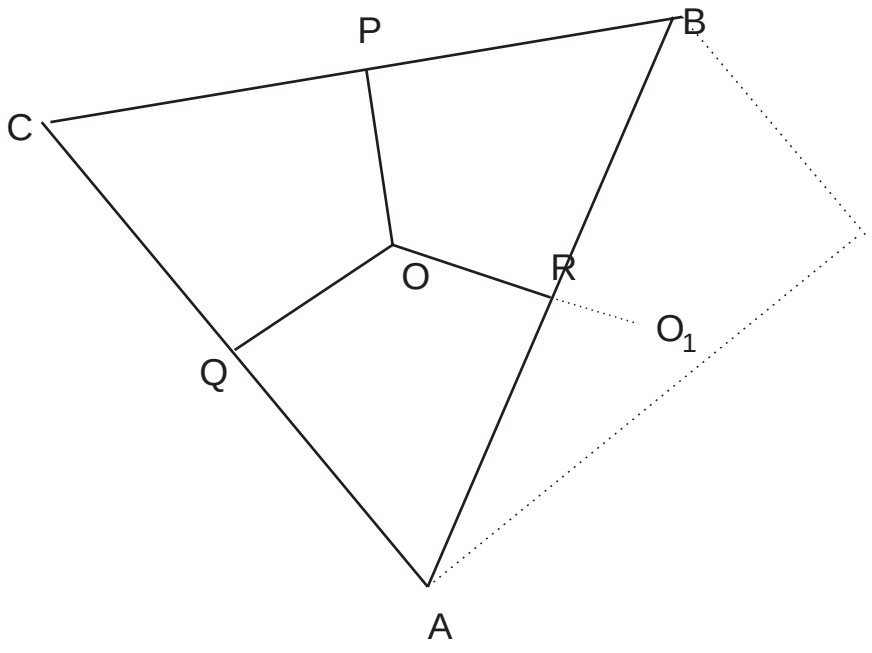

Figure 2. A Helpful Geometric Figure

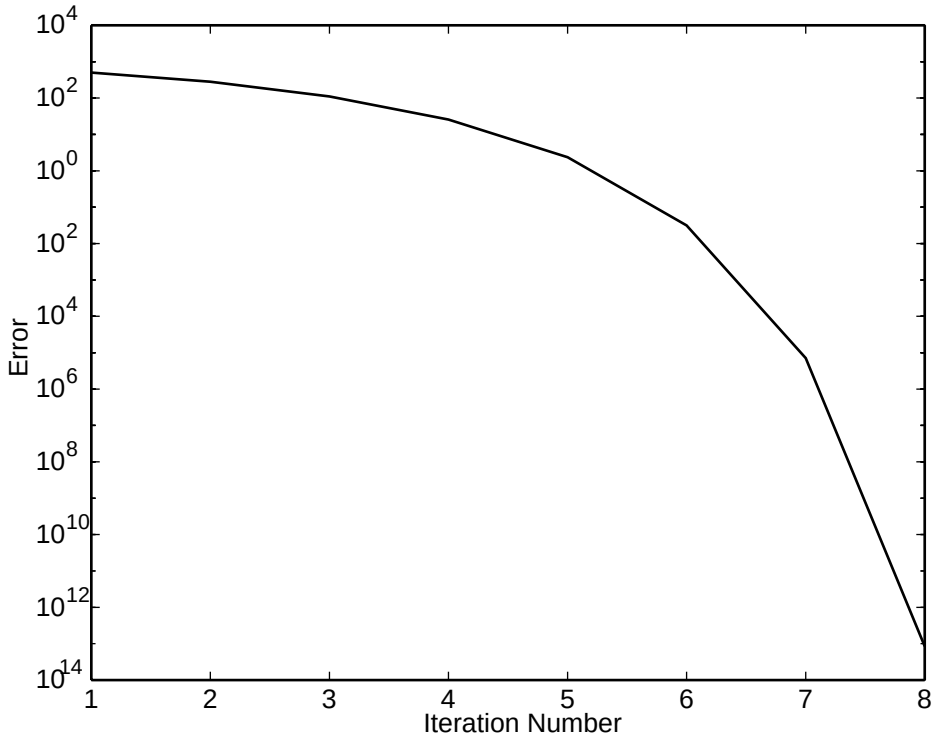

Figure 3. NGST Example Steady State Solver Convergence

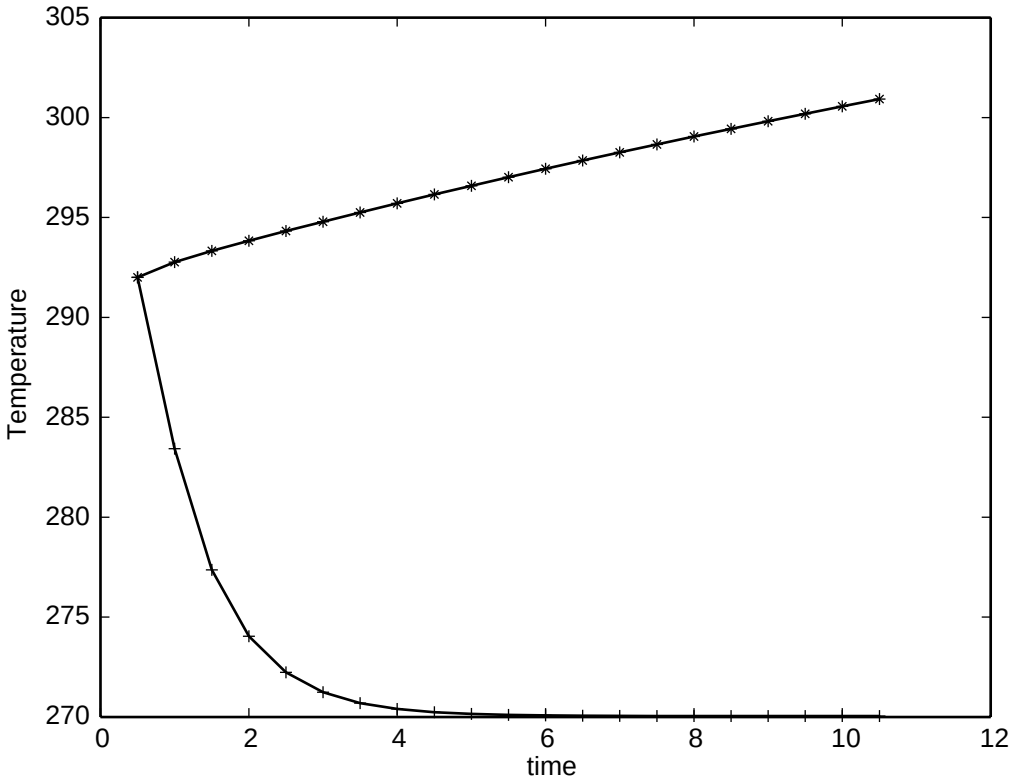

Figure 4. Transient Solver Example

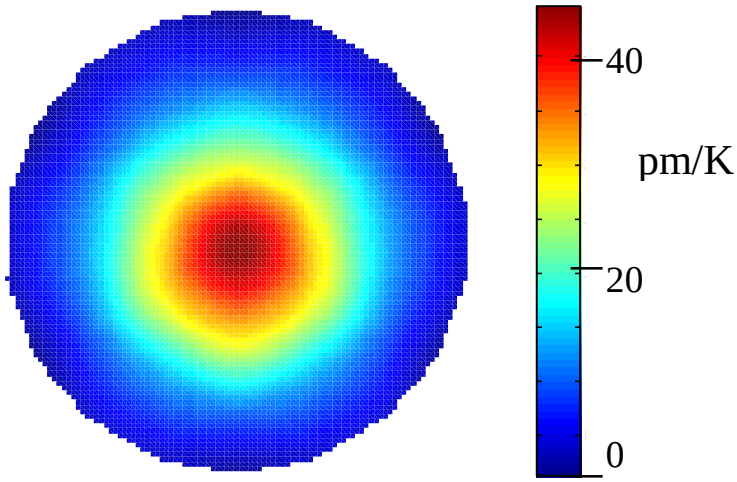

- ΔOPD = starlight *OPD* - metrology *OPD*
- ΔG= changes in temperature gradient thru the primary thickness
- $C_{\Delta G}$ = *Sensitivity* matrix

$$\Delta OPD = C_{\Delta G} * \Delta G$$

Figure 5. Contour Map of Sensitivity Matrix

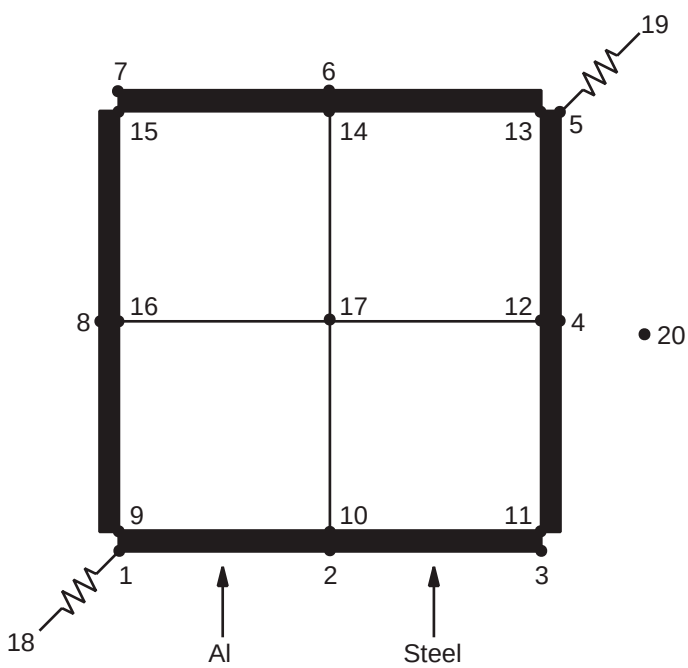

Figure 6. Frame Network Problem

CATALYTIC EFFECTS OF HEAT SHIELD MATERIALS IN DISSOCIATED AIR

Masahito Mizuno and Yoshiki Morino
National Space Development Agency of Japan (NASDA)
Office of Research and Development
Tsukuba-shi, Ibaraki-ken, Japan 305-8505

Yasuo Watanabe
National Aerospace Laboratory (NAL)
Fluid Science Research Center
Choufu-shi, Tokyo, Japan 182-8522

SUMMARY

Catalysis of the heat shield materials was preliminarily evaluated by use of arc heated wind tunnel test data and approximate solution on heating rates. Test specimens are C/C materials with Chemical Vapor Deposition(CVD)-SiC coating. Evaluation of the material catalysis was conducted using aerodynamic heating test data obtained by both a 750 kW arc heated wind tunnel of the National Space Development Agency of Japan (NASDA) and a 1 MW arc wind tunnel of the Institut für Raumfahrtsysteme of the Universität Stuttgart (IRS). Aerodynamic heating rates on the surface of the specimen were calculated based on the surface temperature distribution. On the other hand, fully catalytic heating rate was calculated by use of the data of heat flux measurements. The ratio of these values are compared with the theoretical values (based on Goulard's theory) and recombination rate constant was estimated to be 5-6 m/s. The difference between NASDA test and IRS test is also discussed in order to verify the proposed estimation process. Dissociated flow diagnostic in arc wind tunnels would be the most important research issue in the next step.

NOMENCLATURE

c_e	: mass fraction
c_w	: mass fraction at the surface
$c_w \rho_w$	: atom density at the surface $[\mathrm{kg/m^3}]$
h	: enthalpy $[J/kg]$

h_D	: dissociation energy $[J/kg]$
h_R	: coupling reaction heat $[J/kg]$
j_w	: mass flux of atoms diffusing towards the material surface $[kg/m^2 \cdot s]$
k_w	: reaction rate constant of the material surface $[m/s]$
Le	: Lewis number
M_A	: molecular weight of air $[kg/\mathrm{mol}]$
p	: pressure $[Pa]$
Pr	: Prandtl number
q	: heat transfer rate $[W/m^2]$
R_c	: radius of a cylinder $[m]$
R_{eff}	: effective radius $[m]$
R_u	: universal gas constant $[J/mol\ K]$
Sc	: Schmidt number
T	: temperature $[K]$
u	: flow velocity $[m/s]$
x	: distance from the stagnation point along the surface $[m]$
β	: velocity gradient $[1/s]$
ϕ	: correction factor for catalytic effects
γ	: recombination efficiency
λ_w	: ratio of heat transfer rate $\left(= \dfrac{q_w}{q_{FCW}}\right)$
μ	: viscosity $[kg/m\ s]$
ρ	: density $[kg/m^3]$

Subscript

cw	: cold wall
e	: outer edge of boundary layer
FCW	: Fully Catalytic Wall
hw	: hot wall
s	: stagnation point
w	: wall
∞	: free stream

INTRODUCTION

In aerodynamic heating by hypersonic rarefied gas flows through an atmospheric re-entry, high temperature air heated by an intensive shock wave and containing dissociated oxygen atoms or nitrogen atoms in part will reach a spacecraft body (Fig.1). Such dissociated gases will couple each other partially or wholly due to the catalytic effect of a spacecraft body surface and reaction energy discharged then will heat the spacecraft body surface.

It is considered that the gases in the shock layer is high-temperature air consisting of $N_2, O_2, N, O, NO, N_2^+, O_2^+, N^+, O^+, NO^+, e^-$. The nitrogen atoms (N) and the oxygen atoms (O) re-combine into nitrogen (N_2) and oxygen (O_2) by the reaction of (1) and (2) on the body surface with the catalyst of heat shield material.

$$N + N \rightarrow N_2 \tag{1}$$

$$O + O \rightarrow O_2 \tag{2}$$

The percentage of a heating rate attributable to dissociated gas coupling in the overall heating rate will vary by the state of gas flows and the surface characteristics of material, and it could reach more than a half of the overall heating rate, if the degree of dissociation gases in gas flows is high and the catalytic efficiency of a body material is also high.

It is well known that the degree of this surface reaction influences thermal heating rates at the wall. In the past, many researches have been performed about the effects of wall catalysis, evaluation, modeling and the reaction mechanisms of catalysis. Reference [1]-[4] studied the recombination coefficients of the nitrogen and oxygen atoms at the surface of the heat shield materials.

Scott [1] measured heat flux to the high-temperature reusable insulation materials covered with reaction cured glass with a finite catalytic recombination coefficient and heat flux to nickel by the arc heated wind tunnel. By using this data and the theoretical solution of Goulard [5] of heat flux to catalytic wall, he obtained the wall recombination coefficient of the materials.

Stewart et al. obtained the wall recombination coefficients of reaction cured glass [3], glass coated blanket, borosilicate glass, and silicon carbide cloth[4]. They measured heat flux of heat shield material and the conditions of an arc heated flow in an arc heated wind tunnel. They obtained the wall recombination coefficient, by using the Goulard's heat flux formula directly.

Clark et al. [6] used the approach of Goulard [5] for computing catalytic effects with the stagnation-point laminar-boundary-layer heat-transfer technique of Fay and Riddell. The approach used experimental results from arc-jet tests

with an analysis to determine the efficiency for the recombination of atomic species present in the boundary layer. The discussions are based on experimental data and calculations for arc-jet tests of the titanium alloy $Ti-14$-aluminum-21Nb with a borosilicate-like glass coating that has a recombination efficiency of about 0.006 to 0.01.

The ratio of recombination heating rate to the total heating rate is different for flow conditions and characteristics of the material surface. When the degree of dissociation of air is large and the catalytic efficiency of the material surface is high, the latter could occupy the major part of the heating rate.

However, procedure to estimate the aerodynamic heating rates around spacecraft including such catalytic effect has not been established, nor data on the catalytic efficiency of materials have been clarified to date yet; it seems that there are still many problems which should be solved in order to establish the evaluation method available for a catalytic effects that can be used in the early design phase of reentry vehicles.

This paper tries to evaluate catalytic characteristics of the heat shield materials using experimental data obtained in the aerodynamic heating test conducted with the arc heated wind tunnel (both NASDA and IRS tests) designed for evaluating the heat resistant of the materials [7]. Test specimens are Carbon / Carbon (C/C) materials covered with thin layer of the Chemical Vapor Deposition (CVD) – SiC which was sealed with thin SiO_2 / B_2O_3 layer.

EVALUATION METHOD OF CATALYSIS

Definition of catalysis

Catalytic effects discussed in this paper means recombination phenomena of high temperature dissociated air at the surface of Thermal Protection System (TPS) materials. Components of high temperature air are mostly molecular oxygen/nitrogen and atomic oxygen/nitrogen. The fundamental parameter of catalysis is recombination efficiency γ which is defined as a ratio of recombined atoms to total atoms arriving at the surface. This ratio is determined with respect to species of gas and solid surface, temperature of surface.

On the other hand, catalysis can also be evaluated by rate constant k_w of chemical reaction at the surface. k_w is defined by the following formula, assuming first-order reaction.

$$j_w = k_w(c_w \rho_w) \tag{3}$$

That is, j_w means recombination reaction rate at the surface. The unit of k_w is $[m/s]$ based on the above definition.

Following relationship exists between recombination efficiency γ and rate constant k_w.

$$\gamma = k_w \sqrt{\frac{2\pi M_A}{R_u T}} \tag{4}$$

It is desirable for this research to express catalysis of the materials by γ or k_w based on experimental measurements of surface heating rates. For this purpose, the relationship between surface catalysis and surface heating rate should be clarified.

Fully catalytic heating rate

In this research, fully catalytic heating rates are estimated from heat flux measurements by use of a Gardon gauge type heat flux module which geometry was identical to the specimen/holder system. This heating condition was assumed as fully catalytic because the surface of gauge and module are made of copper, although influence of oxidation of the surface must be studied in future investigation. The module was water-cooled and the surface temperatures were kept at around room temperature. In this research, the ratio of partially catalytic heating rate to fully catalytic heating rate is compared with the theoretical value. Therefore, conversion of the heating rates from low temperature to high temperature is needed. This conversion is performed by use of the approximate theory of fully catalytic heating rate for a sphere given by Fay and Riddell in the case of equilibrium flow as follows.

$$q = 0.763 Pr^{-0.6} (\rho_w \mu_w)^{0.1} (\rho_s \mu_s)^{0.4} \left\{ 1 + \left(Le^{0.52} - 1 \right) \frac{h_s}{h_w} \right\} (h_s - h_w) \sqrt{\left(\frac{du_e}{dx} \right)_e} \tag{5}$$

From this equation, it is found that the most significant term influenced by temperature difference is the enthalpy related term $(h_s - h_w)$. Accordingly, the ratio of heating rate at a high temperature to at a low temperature is estimated by the following equation.

$$\frac{q_{hw}}{q_{cw}} = \frac{h_s - h_{hw}}{h_s - h_{cw}} \tag{6}$$

This is based on the assumption that only h_{cw} is changed when wall temperature decreases and other parameters in equation (5) are unchanged.

On the other hand, total enthalpy H_∞ of the free stream can be estimated by fully catalytic heating rates of sphere as follows[8][9].

$$q = K\sqrt{\frac{p_s}{R_{eff}}}\left(H_\infty - h_w\right) \tag{7}$$

where

$$K = 117$$

$$[q] = kW/m^2, \quad [p_s] = \text{atm}, \quad [R] = m, \quad [H,h] = MJ/kg$$

Using this equation, total enthalpy H_∞ can be calculated from measured heat flux and pressure of the sensor module. Effective radius R_{eff} is introduced to account for the actual geometry of the module (flat head cylinder). R_{eff} was obtained based on investigation of Boison [12] as follows.

$$R_{eff} = 2.9R_c \quad \text{for} \quad M_\infty = 2.01$$

$$R_{eff} = 3.7R_c \quad \text{for} \quad M_\infty = 4.76$$

where R_c is the radius of a cylinder.

In the case of experiment conducted by NASDA/NAL (National Aerospace Laboratory) the latter value is considered appropriate because estimated Mach number at NASDA wind tunnel is around 4.8. This conversion is used in equation (10). Fully catalytic heating rate at high wall temperature is finally estimated from equation (6) by assuming H_∞ nearly equal to h_s.

Partially catalytic heating rate

The influence of material catalysis on the heating rate was investigated by Goulard [5] and the following λ_w was given assuming a frozen boundary layer.

$$\lambda_w = \frac{q_w}{q_{FCW}} = \frac{1 + \left(Le^{\frac{2}{3}}\phi - 1\right)\frac{h_R c_e}{h_s}}{1 + \left(Le^{\frac{2}{3}} - 1\right)\frac{h_R c_e}{h_s}} \tag{8}$$

where

$$\phi = \frac{1}{1 + \frac{0.47Sc^{-\frac{2}{3}}\left(2\beta\mu_s\rho_s\right)^{\frac{1}{2}}}{\rho_w k_w}}$$

and

$$\beta = \frac{2u_\infty}{d}\left[\frac{\rho_\infty}{\rho_s}\left(2-\frac{\rho_\infty}{\rho_s}\right)\right]^{\frac{1}{2}} \tag{9}$$

Using this equation λ_w is calculated with respect to rate constant k_w. In equation (8) c_e is atom mass fraction outside the boundary layer.

The parameters of a free stream included in the velocity gradient β is difficult to calculate in an arc heated wind tunnel test because it include a high temperature dissociated flow parameter. For this reason, the following equation, in which β can be calculated from the stagnation condition, was used [10].

$$\beta = \frac{du_e}{dx} = \frac{1.54}{R_{eff}}\sqrt{\frac{p_s - p_\infty}{\rho_s}} \tag{10}$$

In this equation, R_{eff} means the radius of a sphere. $R_{eff} = 3.7R_c$ was assumed by following the Boison's conversion formula [12] as described above.

By comparing this theoretical ratio with experimentally obtained value using the result of section "Fully catalytic heating rate" and "Thermal analysis of specimen holder", we can estimate the rate constant k_w as shown later in section "RESULT AND DISCUSSION".

Thermal analysis of the specimen holder

In order to evaluate the heat flux onto specimen, the thermal analysis was conducted by use of a specimen/holder assembly model. Temperature responses to a surface heating input was calculated. General-purpose finite element method program "ANSYS" was used in this analysis. A specimen/holder assembly is shown in Fig. 2. The support system for the samples at NASDA and IRS is very similar. Although the samples are of different size, their geometry and the fastening mechanism is the same. Finite element division is shown in Fig. 3. Two-dimensional axisymmetrical model was used. Although the back of the specimen was supported by four pins, they are not modeled in analysis. The element used for the main-part of the model is the 2-dimensional element PLANE55 with four nodes. Radiation heat dissipation was modeled by the 2-dimensional surface effect element SURF19 for the external surface. In order to take into consideration mutual heat exchange in internal space, radiation matrix generation routine AUX12 was used. The physical-properties of each constituent material is shown in Table 1. Especially about large specific heat ratio, the change by temperature inputted as a function of temperature (related with C/C material, and holder material). Temperature dependent characteristics are provided for specific heat values of the specimen and holder cap materials.

EXPERIMENT

The experimental data described in this paper were obtained through plasma wind test series for the purpose of investigation on erosion characteristics of SiC coated C/C materials. For this research program two different plasma wind tunnels - the NASDA and the IRS facilities - were used. The facility of NASDA is equipped with a thermal plasma generator (TPG) for the simulation of the interim re-entry phase with moderate specific enthalpies and high stagnation pressures. The wind tunnel PWK1 of the IRS is equipped with a magnetoplasmadynamic generator (MPG) and capable of simulating the first phase of a re-entry flight, where the specific enthalpies are high and the stagnation pressure is low. Both facilities have a small overlapping region with respect to stagnation pressure and heat flux.

Thermal Plasma Wind Tunnel of NASDA

The arc-heated plasma wind tunnel of NASDA located at the National Aerospace Laboratory (NAL) consists of a plasma generator, different nozzle designs, the test chamber with model injection system, a diffuser and a heat exchanger. It is connected with a 750 $[kW]$ DC power supply. The plasma generator is a thermal plasma generator of constrictor type. The constrictor assembly may have up to three constrictor packs. A diagrammatic view of NASDA arc heated wind tunnel is shown in Fig. 4. Both anode and cathode are made of copper and are water-cooled. The facility is equipped with a conical nozzle and a channel nozzle for different tasks. The conical nozzle with a throat diameter of 115 $[mm]$ and a cone half angle of 15 degrees is used for stagnation tests. Its nominal Mach number is 4.8. The facility is limited to a maximum power input of 750 $[kW]$. Mass flow rates of up to 20 $[g/s]$ have been realized. Test objectives are introduced into the plasma jet by rotating a turrethead capable of holding three probes at a time (120 degrees arrangement). This set-up yields a distance of 100 $[mm]$ to the nozzle exit. For more details of the NASDA facilities see Reference [13].

Magnetoplasmadynamic Wind Tunnel at IRS

The magnetoplasmadynamic wind tunnel PWK1 at IRS consists of a stainless steel tank 6 $[m]$ in length and 2 $[m]$ in diameter, which is connected to a vacuum system with a suction power of 250,000 $[m^3/h]$ at 10 $[Pa]$ and a power supply with the capacity of 6 $[MW]$. The tank is equipped with a four axis positioning system for material of measurement probes. For the test reported in this research the wind tunnel (Fig, 5 (a)) was equipped with the magnetroplasmadynamic generator (MPG) RD5 which is shown in Fig. 5 (b). This plasma generator consists of two coaxial electrodes, separated by neutral, water-cooled copper segments. The nozzle exit, which is also a water-cooled

copper segment forms the anode. The cathode, made of 2% thoriated tungsten, is mounted in the plenum chamber. Current passes through the expansion nozzle from the tip of the cathode to the end of the nozzle. The test gas is dissociated and partially ionized. In order to avoid oxidation only the nitrogen part of the test gas is fed in along the cathode into the heating chamber, heated up by the arc and accelerated partly by the thermal expansion and partly by the electromagnetic forces due to the self-induced magnetic field in the nozzle. With this MPG the oxygen needed for the duplication of high enthalpy air flow is fed in radially at a high velocity at the supersonic part of the nozzle, but still within the arc region. The various gas injection points enable the operation of the MPG with different gas mixture. For more details of the IRS facilities see Reference [14].

RESULT AND DISCUSSION

Estimation of heat input

The purpose of heat analysis is to estimate the actual aerodynamic heating rates into the material based on the measured surface temperature data at the wind-tunnel experiments.

Heat flux measured by a calibration module was assumed to be fully catalytic heat flux at the condition of low temperature wall. The calibration module has seven heat flux gauges along its surface and its geometry is the same as the specimen / holder system. The distribution of the heat flux along the surface is shown in Fig. 6.

The modification to a high-temperature wall heating rate from a low-temperature wall heating rate is performed as follows. From equation (6), the compensation coefficient of $\frac{q_{hw}}{q_{cw}} = 0.90$ was applied. And heating rate distribution around the holder was calculated in the same way. Where following data was used from the experiment data.

$$R_{eff} = 20 \times 3.7 = 74\,[mm], \quad p_s = 3500\,[Pa], \quad q = 2479\,[kW/m^2]$$
$$H_\infty = 31.6\,[MJ/kg]$$
$$h_{cw} = 0.6\,[MJ/kg], \quad h_{hw} = 3.7\,[MJ/kg]$$

If this heating rate is applied to the thermal model as it is, material surface temperature reaches very high value, and does not in agree with the experiment. Therefore, we considered that the finite catalytic nature of specimen decreases the heating rate. On the contrary, side wall of the holder showed a temperature which was very close to calculated temperature at the condition of fully catalytic surface. Therefore full catalysis was assumed on the side wall. For the front surface of specimen, λ_w (ratio of partial catalytic heating rate to fully catalytic heating rate) which agrees with

measured temperature distribution was searched by trial-and-error calculation. Finally, it was found that $\lambda_w = 0.33$ at the front surface of the specimen/holder assembly. In this condition surface temperature distribution become fairly close to the experiment value. Temperature distribution and heat flux at this condition is shown in Fig. 7 (a) and 7 (b), respectively. This is at 500 seconds after the heating started. According to this, heat flow is blocked by the internal thermal insulation. It was found that the main heat flows are generated through the gap between the C/C specimen and holder. Especially the largest heat flux is generated at the shoulder of the holder. The difference of heat flow between surface net heating and radiation heat dissipation is considered to go to the side of the holder cap and to be radiated there.

Evaluation of catalysis

Estimation of k_w is conducted through following steps (Flow chart of this steps is shown in Fig. 8).

① In the arc wind tunnel test, high-temperature gas was blown to the front surface of a specimen shown in Fig. 2. Typical conditions of gas flows are shown in Table 2. The heating efficiency at the stagnation point and the stagnation pressure in the table were measured with a copper calibration module, which had the same geometry with the specimen holder. For the heating efficiency at the stagnation point , correction (multiplied by 0.9) was made for a high-temperature wall. The stagnation enthalpy was estimated by use of equation (7), while the ambient pressure was a measured value in the vacuum chamber that contains a specimen, and the Mach number was an estimated value from a nozzle contour.

② With these gas flow conditions, $\frac{q_w}{q_{FCW}}$ in the right hand side of the equation (8) can be calculated by using k_w as a parameter. The result of calculation is shown by the solid line (NASDA test) in Fig.9. In this calculation, the value of equilibrium air that had an enthalpy of h_s was used as $h_R c_e$. k_w for nitrogen and oxygen were assumed to be the same value.

③ Meanwhile, as the surface temperature of a specimen including the specimen holder was measured by a radiation thermometer in the test, an actual heat inflow to a specimen can be estimated from the temperature data and a heat model of a specimen / specimen holder. The proportion of the estimated value to the value after high-temperature correction of the copper calibration module measurement (assumed to be a complete catalytic heating rate) was 0.33 for NASDA test and 0.43 for IRS test A (high pressure and low temperature condition), respectively. In IRS case, this value was calculated assuming 15% heat loss from the specimen instead of conducting thermal FEM analysis as in the case of NASDA test. By comparing these values with the curve in Fig.9, the reaction rate constant of the specimen used was estimated to be about 5 m/s. To verify the appropriateness of this estimation, a similar reaction rate constant must be obtained in tests that different gas flow conditions.

However, in a low pressure condition, a large difference is seen when compared with Goulard's theoretical value if

the same value of k_w was assumed (see curve of IRS test B in Fig. 9). One possible explanation for this discrepancy is that the surface of material was changed from glass (SiO_2) to SiC. Due to the lower pressure and higher temperature, the oxidation mode was changed from passive to active [11]. At such high temperature, the surface of material is in the process of oxidation and erosion. Therefore, more consideration needs to be paid with respect to the physical phenomenon and state on the surface. In addition, with respect to the dissociated flow in the arc heated wind tunnel, reliability of data should be improved by accumulation of experimental data since there is many parameters depending on presumption or assumption.

CONCLUSIONS

In this research, a process to estimate catalytic efficiencies of heat shield materials was proposed. This process requires data obtained from arc heated wind-tunnel experiment.

The major conclusions of the present study are summarized as follows:

(1) From the data of the surface temperature at the wind-tunnel experiment, temperature response analysis to a surface heating input was performed in order to estimate the amount of aerodynamic heating to specimen. As a result, it was found that if $\lambda_w = 0.33$ at the front surface of specimen / holder, surface temperature distribution become fairly close to the experiment value.

(2) Reaction rate constant of the heat shield material was evaluated by use of Goulard's equation.

(3) At high stagnation pressure and low surface temperature case, the rate constant is around 5 $[m/s]$ for both NASDA and IRS experiment.

(4) However, when stagnation point pressure is low and surface temperature is high, a large difference is found between experiment and theory if k_w is the same value. Possible explanation would be oxidation which changes surface material from SiO_2 to SiC in low pressure and high temperature condition.

ACKNOWLEDGMENTS

The authors are grateful to Professor M. Nishida, Kyushu University, and Professor H. Kubota, University of Tokyo for valuable discussions and suggestions. Special acknowledgement is given to Professor M. Auwerter-Kurtz, University of Stuttgart who guided the PWT testing at IRS and gave us valuable suggestions on catalysis.

REFERENCES

[1] Scott,C.D. : "Catalytic Recombination of Nitrogen and Oxygen on High Temperature Reusable Surface Insulation", AIAA Progress in Astronautics and Aeronautics: Aerothermodynamics and Planetary Entry, Vol.77(1981),pp.192-212.

[2] Stewart,D.A., Rakich,J.V. and Lanfranco,M.J. : "Catalytic Surface Effects Experiment on the Space Shuttle, AIAA Progress in Astronautics and Aeronautics: Thermophysics and Atmospheric Entry, Vol.82(1982), pp.248-272.

[3] Stewart,D.A., Chen,Y.K., Bamford,D.J. and Romanovsky,A.B. : "Predicting Material Surface Catalytic Efficiency Using Arc-Jet Tests", AIAA-95-2013(1995).

[4] Stewart,D.A. : "Determination of Surface Catalytic Efficiency for Thermal Protection Materials - Room Temperature to Their Upper Use Limit", AIAA-96-1863(1996).

[5] R. Goulard, "On Catalytic Recombination Rates in Hypersonic Stagnation Heat Transfer", Jet Propulsion, Vol.28,No.11. November, 1958, pp.737-745.

[6] R.K.Clark, G.R.Cunnington Jr. and K.E.Wiedemann. : "Determination of the Recombination Efficiency of Thermal Control Coating for Hypersonic Vehicles", Journal of Spacecraft and Rockets, Vol.32, No.1. 1995, pp.89-96.

[7] Yoshiki Morino, Toshinari Yoshinaka, Kozo Yudate, Seiichi Matsuoka, Yasuo Watanabe, Takashi Matsuzaki. : "Heat Resistant Characteristics of C/C Materials with Oxidation Resistant Coating", the 4th International Symposium on Ultra-high Temperature Material , November,1994, pp.44-57.

[8] J.G.Marvin, R.B.Pope. : "Laminar Convective Heating and Ablation in the Mars Atmosphere", AIAA Journal, Vol. 5, No. 2. 1967, pp.240-248.

[9] R.B.Pope : "Measurement of Enthalpy in Low-Density Arc-Heated Flows", AIAA Journal, Vol. 6, No.1,1968,pp. 103-110.

[10] Jiro Kondo: " High Speed Aerodynamics", Corona Co. Ltd.,1977, p. 531 (in Japanese).

[11] Y. Morino, T.Yoshinaka, M.Auweter-Kurtz, G.Hilfer, H.-D.Speckmann and A. Sakai. : "Erosion characteristics of SiC Coated C/C Materials in Arc Heated High Enthalpy Air Flow", IAF-97-I.4.02,1997.

[12] J.C.Boison and H.A.Curtiss : "An Experimental Investigation of Blunt Body Stagnation Point Velocity Gradient", ARS Journal, 1952, pp.130-135.

[13] M.Auweter-Kurtz, G.Hilfer, H.Habiger, K. Yamawaki, T.Yoshinaka, H.D.Speckmann. : "Investigation of Oxidation Protected C/C Heat Shield Material in Different Plasma Wind Tunnels", IAF-96-1.3.06, October,1996.

[14] M.Auweter-Kurtz, H.Habiger, G.Hilfer, H.Früholz, T.Stöckle. : "Comparison of a magnetoplasmadynamic and a thermal plasma wind tunnel as tools for the investigation of heatshield materials for space transportation systems",IRS-95-P10, December,1995.

TABLE 1. THE PHYSICAL PROPERTIES VALUE OF EACH COMPOSITION MATERIAL

1. Specimen material

Material	: C/C material with SiC + glass coating
Density	: $1650\,[kg/m^3]$
Heat conduction	: Inside the surface $36[W/mK]$, Outside the surface $11\,[W/mK]$
Surface emissivity	: 0.87

2. Holder

Material	: Conversion SiC treatment graphite material (SOLSIX-N)
Density	: $3146\,[kg/m^3]$
Heat conduction	: $55\,[W/mK]$
Surface emissivity	: 0.87

3. Insulation

Material	: Aluminum-silica sintered material
Density	: $480\,[kg/m^3]$
Heat conduction	: $0.49\,[W/mK]$
Specific heat	: $1004\,[J/kg \cdot K]$
Surface emissivity	: 0.70

4. Specimen-holder filler

Material	: Glass disposition
Density	: $1807\,[kg/m^3]$
Heat conduction	: $0.6\,[W/mK]$
Specific heat	: $1920\,[J/kg \cdot K]$
Surface emissivity	: N/A

<PTO>

5. Temperature dependence of specific heat

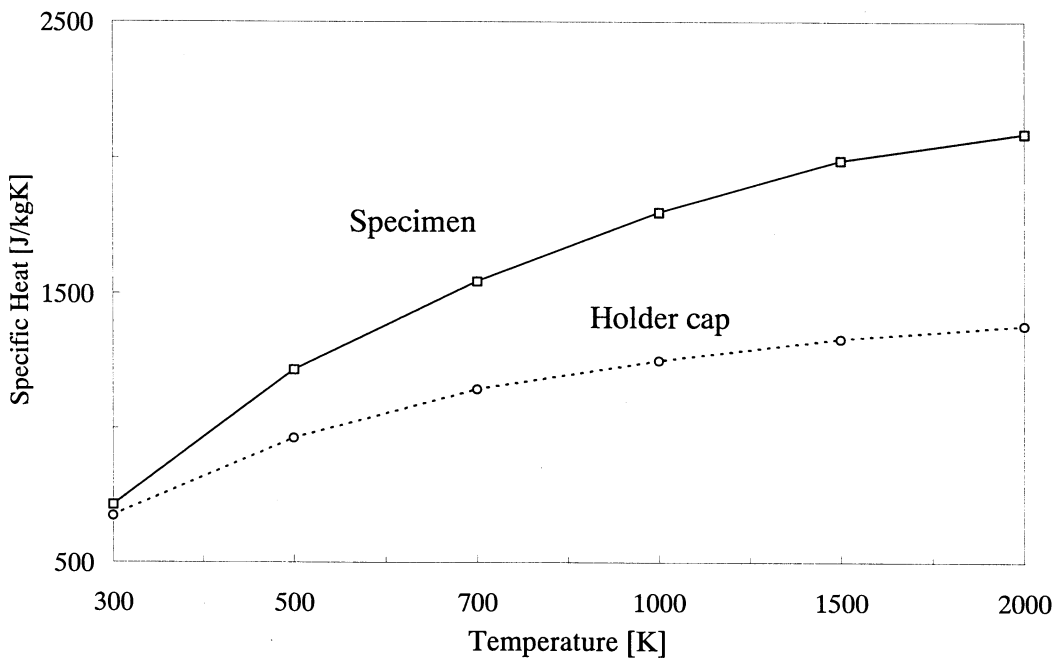

TABLE 2. TYPICAL ARC HEATED WIND TUNNEL TEST CONDITIONS

	NASDA	IRS	
		test A	test B
stagnation pressure	3500 $[Pa]$	3570 $[Pa]$	780 $[Pa]$
free stream pressure	170 $[Pa]$	2700 $[Pa]$	490 $[Pa]$
stagnation heating rate	2480 $[kW/m^2]$	1.54 $[MW/m^2]$	1.29 $[MW/m^2]$
stagnation enthalpy	31.6 $[MJ/kg]$	22.7 $[MJ/kg]$	39.25 $[MJ/kg]$
stagnation wall temperature	1853 $[K]$	1853 $[K]$	1973 $[K]$
effective radius	0.074 $[m]$	0.0725 $[m]$	0.0725 $[m]$
Mach number	4.8	subsonic speed	subsonic speed

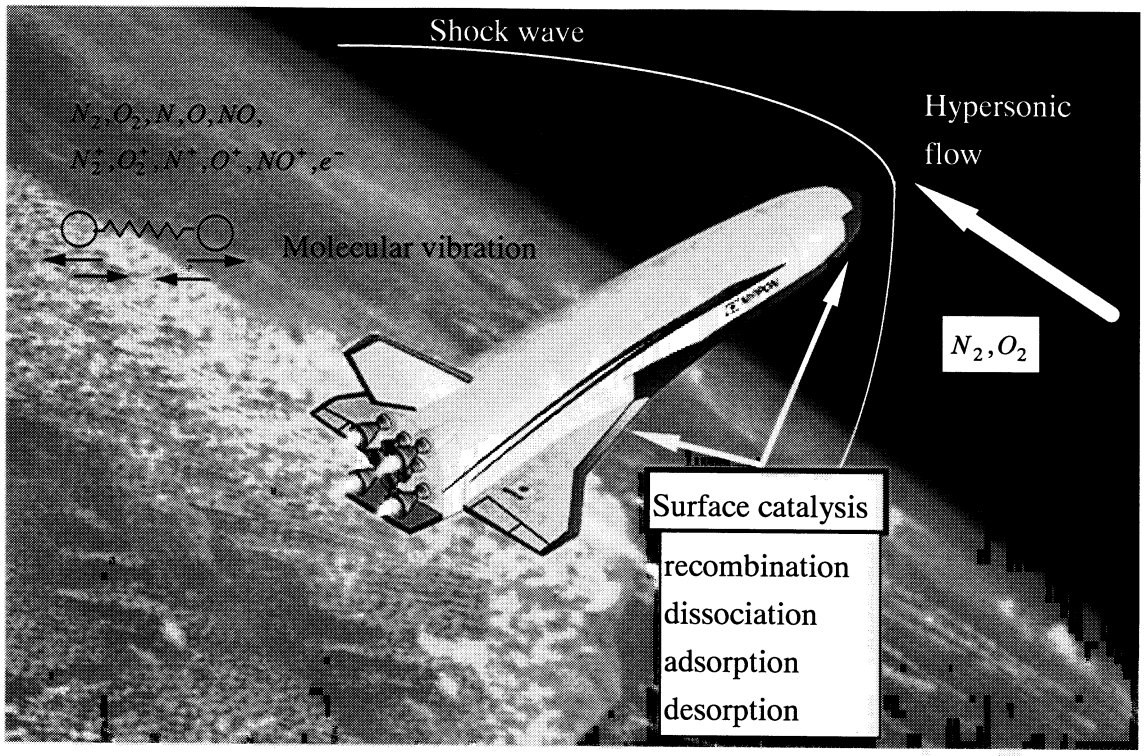

Fig. 1. Re-usable type rocket plane proposed by National Space Development Agency of Japan.

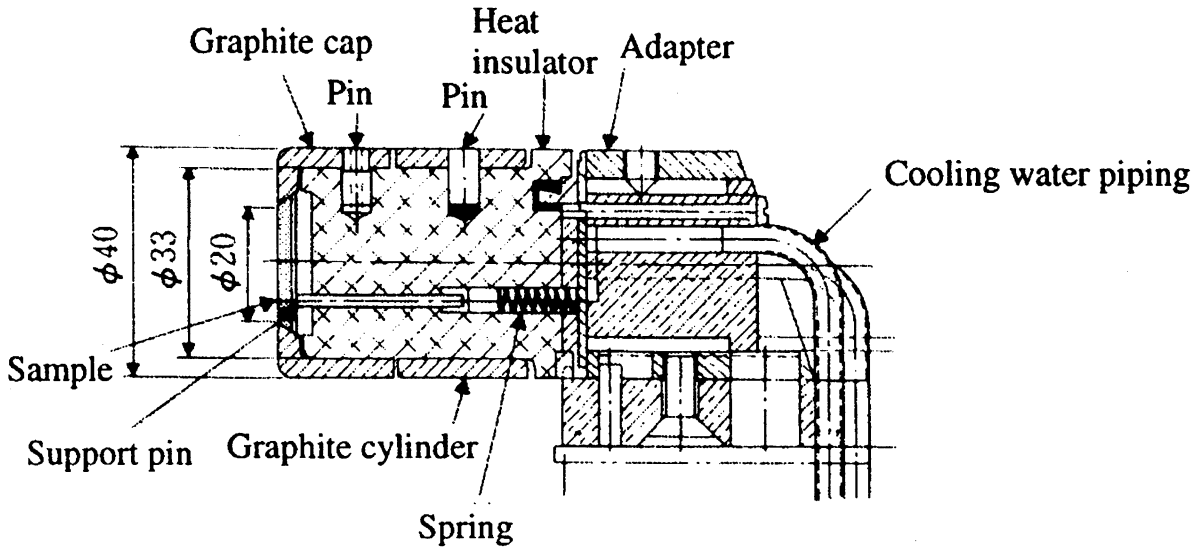

(a) Specimen / holder assembly structure at NASDA test

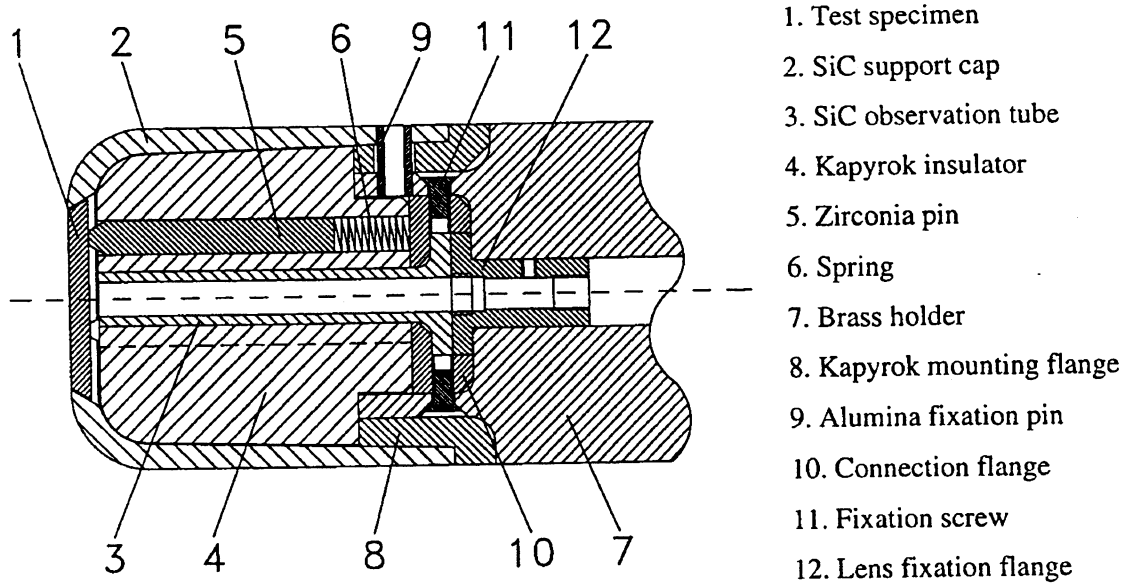

(b) Specimen / holder assembly structure at IRS test

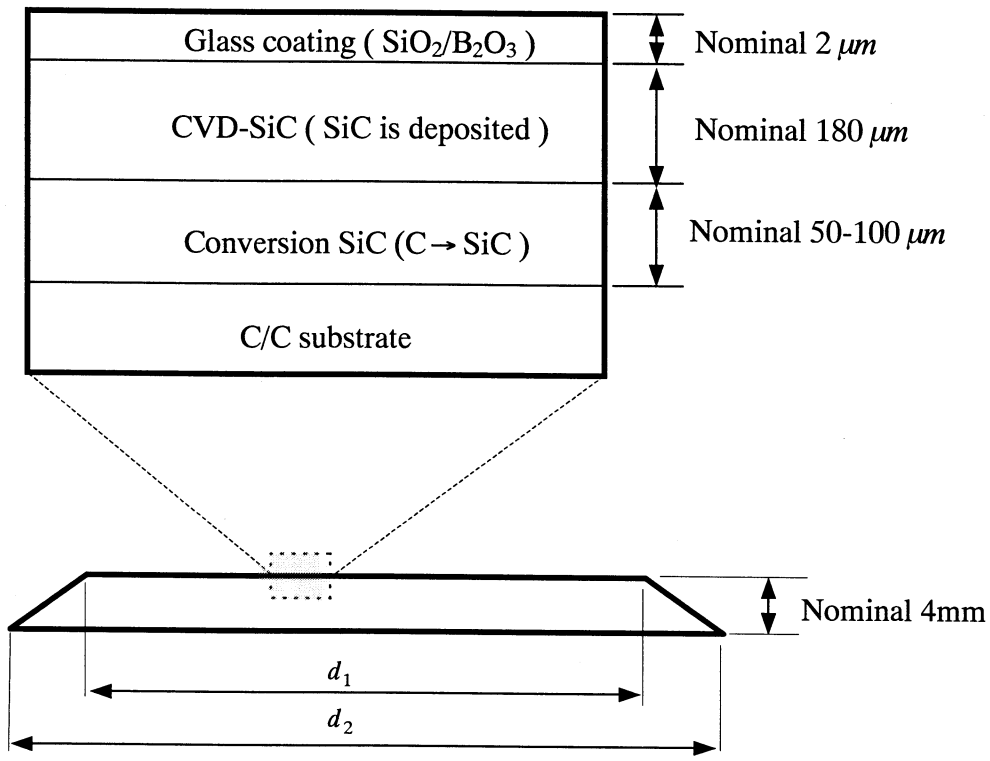

$$d_1 = \begin{cases} 20[mm] & \text{for NASDA test} \\ 26.5[mm] & \text{for IRS test} \end{cases}$$

$$d_2 = \begin{cases} 33.8[mm] & \text{for NASDA test} \\ 30[mm] & \text{for IRS test} \end{cases}$$

* The material used in this research is made up of a C/C-substrate to which several coatings are applied. The SiO_2/B_2O_3 coating on top is designed to allow for sealing of cracks developed during the manufacturing process as well as during the working cycles of the material.

(c) Specimen dimensions

Fig. 2 Specimen / holder assembly structure and specimen dimensions

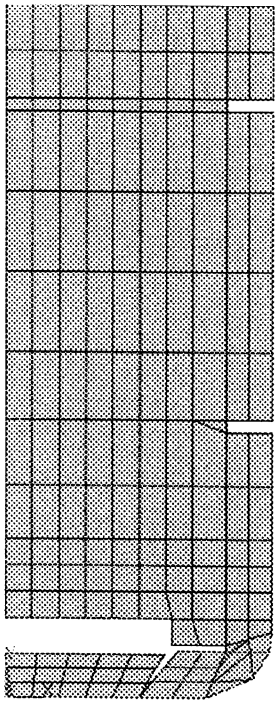

Fig.3 Finite Element Division

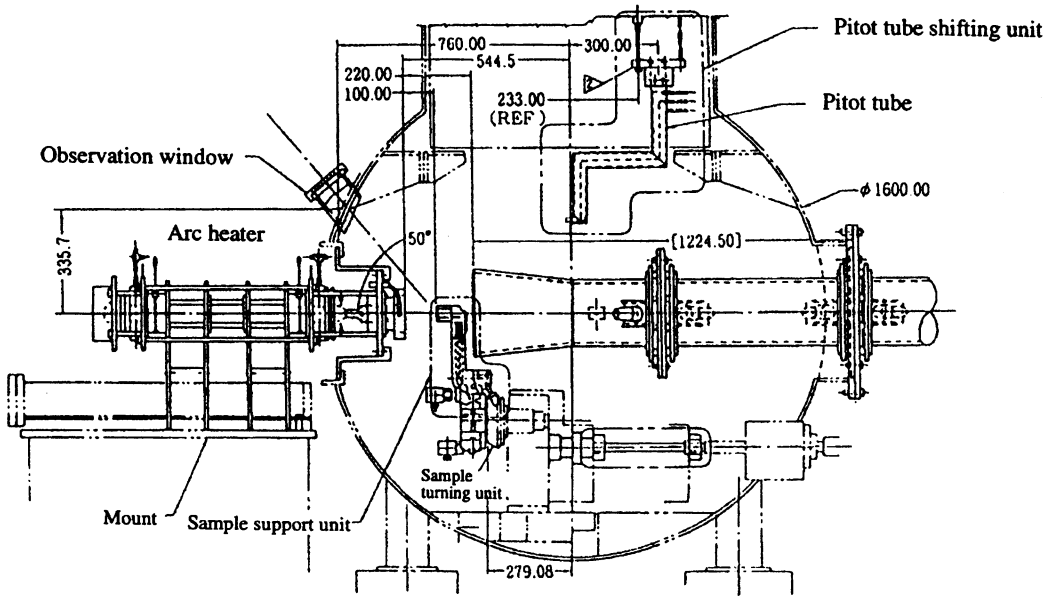

(a) Diagrammatic sketch of the NASDA arc-heated wind tunnel

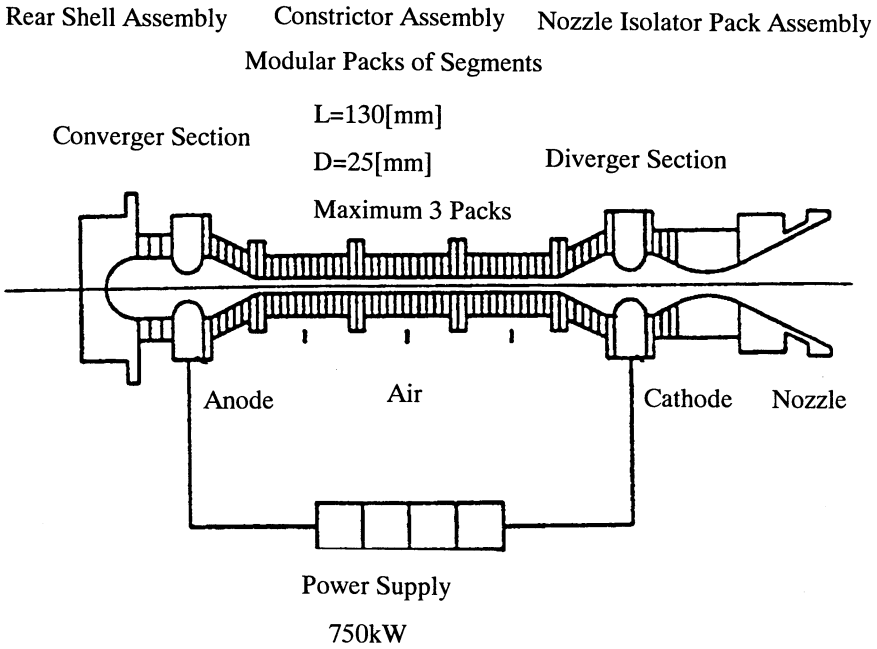

(b) Schematic view of the constrictor type plasma generator of NASDA

Fig.4 NASDA arc heated wind tunnel

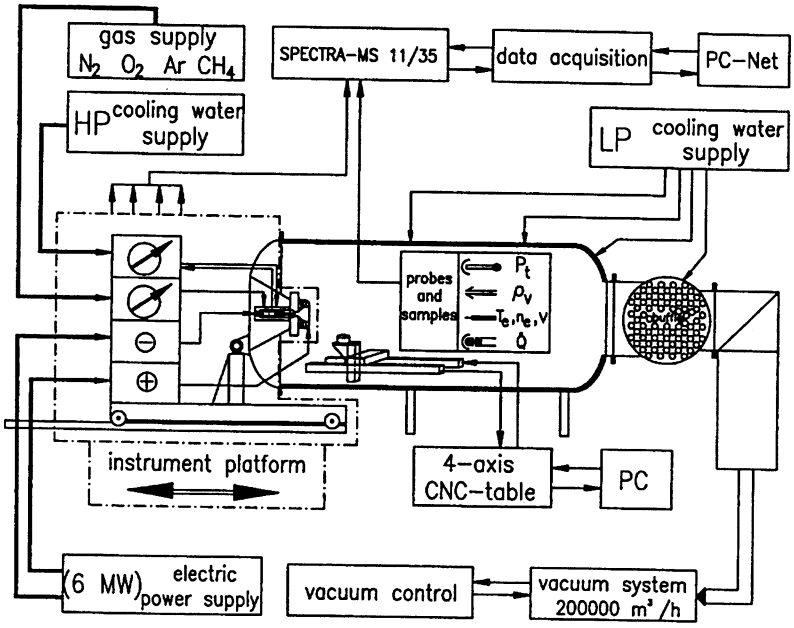

(a) Scheme of PWK1

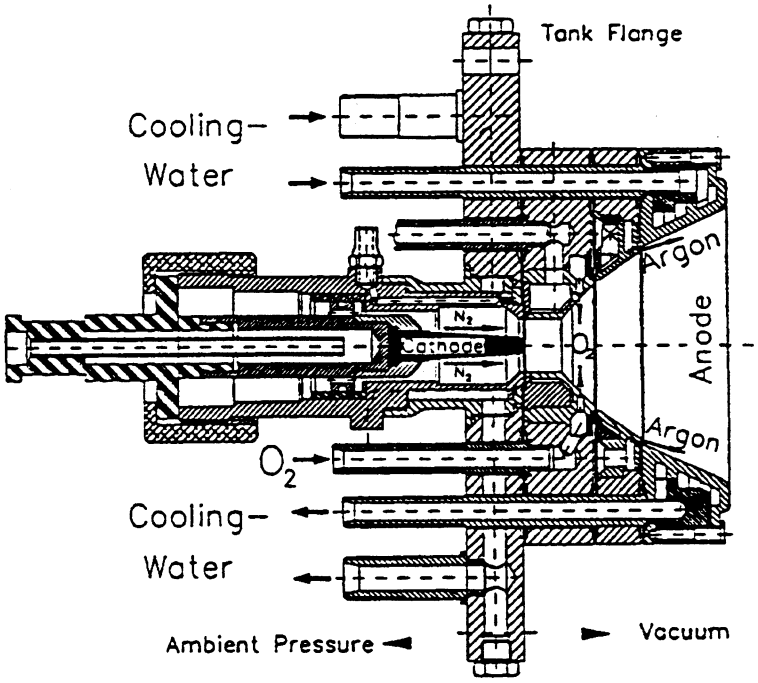

(b) Plasma Generator RD5 of IRS

Fig.5 IRS arc heated wind tunnel

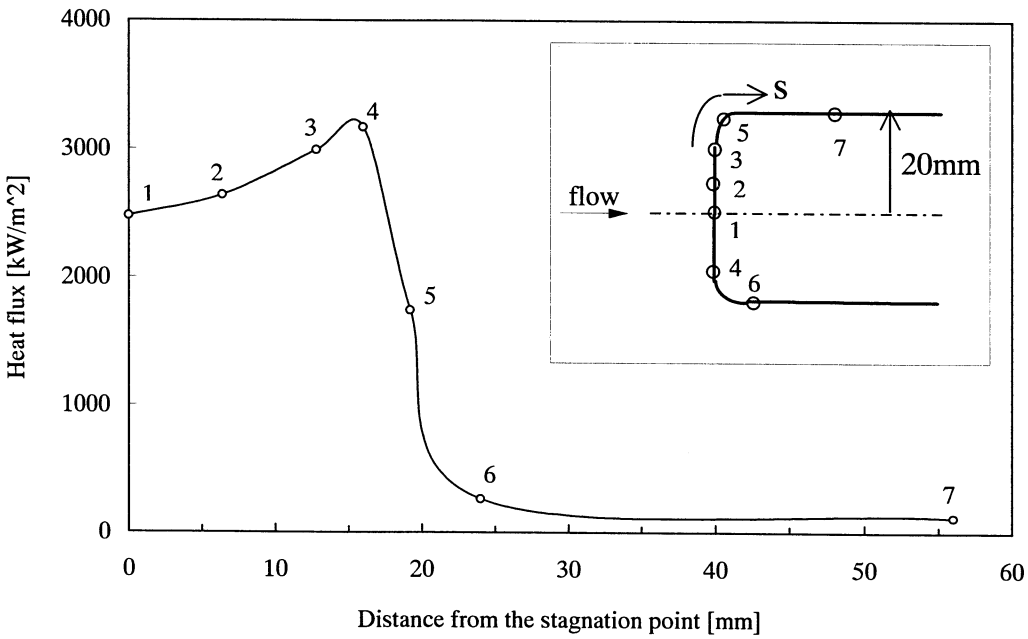

Fig.6. Heat flux measurement flow into the calibration module

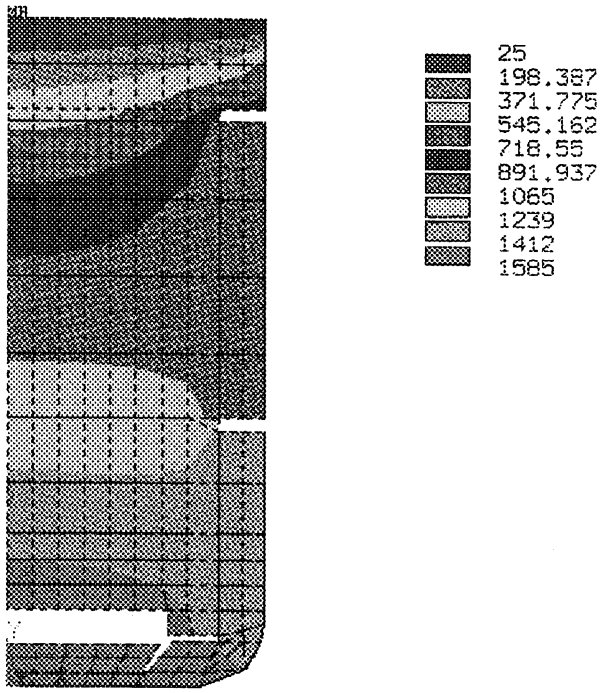

(a) Specimen / holder temperature distribution

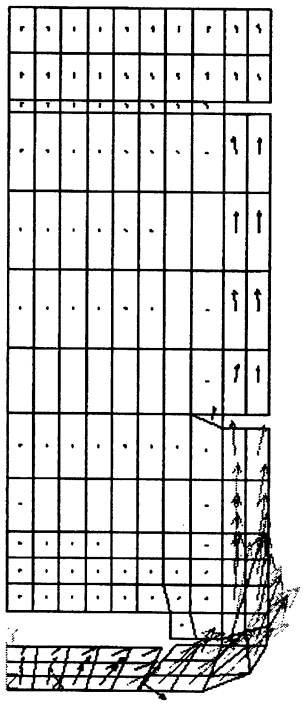

(b) Specimen/ holder heat flux distribution

Fig.7 ANSYS analysis results

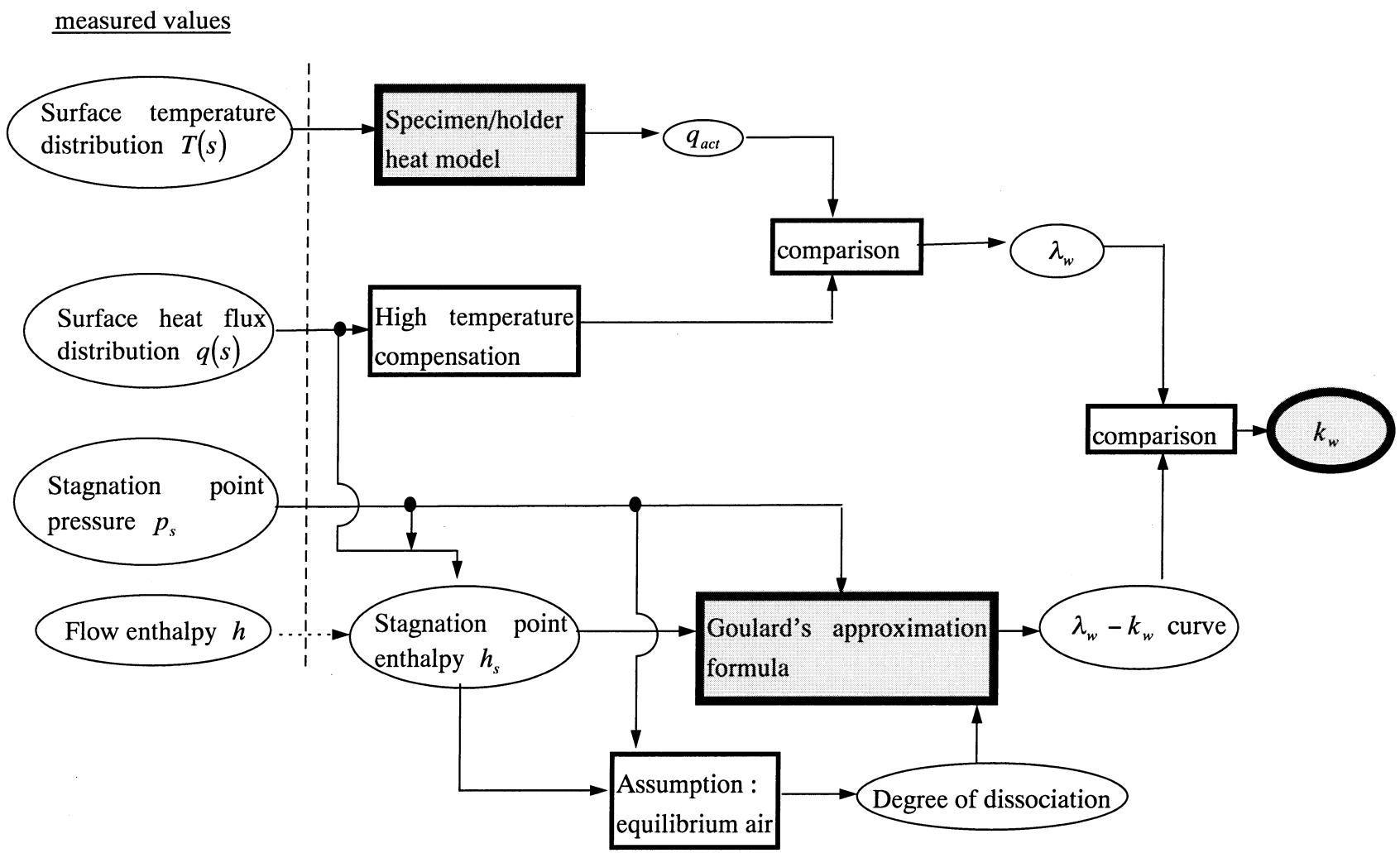

Fig. 8 Flow chart of estimation method for reaction rate constant

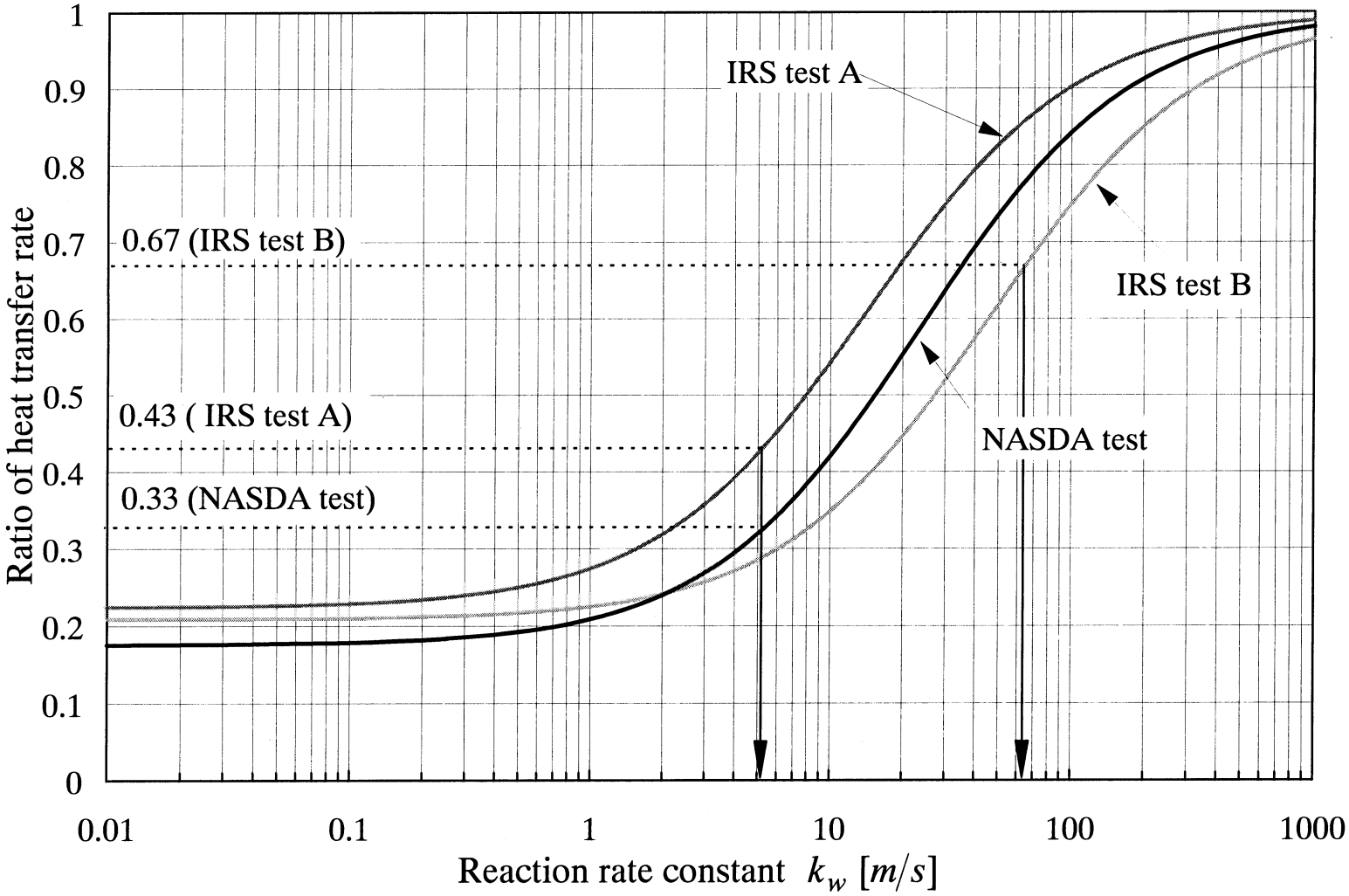

Fig.9 Estimation of reaction rate constant

A Concurrent Design Environment for Designing Space Instruments

Knut I. Oxnevad
Jet Propulsion Laboratory
California Institute of Technology
Pasadena, CA 91109-8099

ABSTRACT

At the Project Design Center at the Jet Propulsion Laboratory, a concurrent design environment is under development for supporting development and analyses of space instruments in the early, conceptual design phases. This environment is being utilized by a Team I, a multidisciplinary group of experts. Team I is providing study and proposal support. To provide the required support, the Team I concurrent design environment features effectively interconnected high-end optics, CAD, and thermal design and analysis tools. Innovative approaches for linking tools, and for transferring files between applications have been implemented. These approaches together with effective sharing of geometry between the optics, CAD, and thermal tools are already showing significant timesavings. Further timesavings are expected.

1. INTRODUCTION

At the Jet Propulsion Laboratory (JPL), large resources are put into efforts aiming at improving and changing the organization to effectively deal with developing smaller missions in the hundred million, rather than in the billion dollar range. A large number of these missions are won based on competitive proposals in response to Announcement of Opportunities (AO's) from NASA headquarters. Writing and developing proposals is, therefore, becoming increasingly important for JPL.

To support the high number of proposals, this year about 50, a proposal support infrastructure has been developed. The Project Design Center (PDC) which has been developed over some 3 years forms the core of this support. The initial aim (refs. 1, 2) of the PDC was to support various projects and proposals with early conceptual mission design analysis capabilities. These conceptual mission designs are developed in a couple of weeks by a multidisciplinary team of specialists that work concurrently, in the same room, together with their customers on a set of computers (stations) and tools that are linked. The team, called Team X, utilizes Macintosh computers, Excel spreadsheets, and publish and subscribe for linking these spreadsheets together. This provides a very powerful environment for conceptual mission design studies.

In late 1996, it was decided that there was also a need for a team that could provide early conceptual design analysis support for instrument development and instrument proposal work. This led to the development and implementation of Team I. Team I builds on the same general principles as Team X, but different customer requirements led to a different implementation. Typically, an instrument proposal requires a higher degree of detail in both the optical, radiometric, and thermal analyses. Team I is, therefore, utilizing what is considered high-end tools, rather than spreadsheets for its development and analysis work.

The initial version of Team I was set up to primarily support optical instrument work. The Team I set of tools, consequently, includes tools such as Code V, ZeMax, TracePro, Mechanical Desk Top (MDT), and RadCAD/SINDA (ref. 3). Most of the Team I tools are running on PC NT platforms. The plan is to modify the Team I composition and tool set to also support other types of instruments. Integrating these high-end tools in a user friendly way, and making the passing of data between them effective and happen in near real time required the Team I development

group, headed by the author, to employ some innovative approaches (ref. 4). The development of executives, utilizing a graphical programming language, represents one such approach. This language makes code generation as well as code modification relatively easy. The latter is especially important in an environment requiring rapid adaptation to new customer needs.

Team I includes experts from the areas of optical analysis and design, mechanical and CAD design, thermal analysis, costing, radiometry, and electronics analysis and design. Each of these experts man a computer with the appropriate tools. During the development phase these experts worked very closely with the development group. These experts are also playing an active role together with Team I customers in the continuous development and improvements taking place as more operational experience is being gained.

This paper starts with a description of the Team I environment and ends with a discussion about some of the approaches utilized in this environment that are showing great potential for time savings, inside as well as outside the Team I environment. The Team I environment is described in section 2, its stations in section 2.1, its tools in section 2.2, and its process in section 2.3. Team I unique approaches for saving time within the Team I environment are discussed in section 3. Some of these approaches are the computerizing of preliminary calculations, section 3.1; the automating of data transfers between tools, section 3.2; and the sharing of common geometry between applications, section 3.3. How these approaches are creating potential time savings also in the later design stages is discussed in section 4. A glossary is provided in section 7.

2. THE TEAM I ENVIRONMENT

2.1 The Stations

In its current configuration, Team I includes a mechanical/CAD station, an optics station, a radiometry station, a thermal station, a cost station, a system station, a documentation station, and an electronics station.

The current Team I configuration is primarily set up to support the design and analysis of optical instruments. However, the Team I environment was made to be flexible and be able to change with changing customer needs. Changes may effect both the station and tools mix. The electronics and documentation stations are still under development, and they will, therefore, not be discussed any further. The visualization statión, also called the orbital analysis station, is for now incorporated into the system station and will briefly be discussed under that station. To improve group interactions, any station's display can be shown on the large projection screen in front of the Team I room, shown in Figure 1.

At the **optics station,** an optical designer and analyst uses variables such as number of wavelengths, aperture diameter, F#, field of view (degrees), temperature, mirror/lens surface types, and type of mirror material for designing the right optics configuration. The tools Code V and ZeMax are used for this part of the design and analysis work. The geometric representation of the surfaces of the selected optics configuration, together with the geometric representation of the resulting rays, are provided as an IGES file. Additionally, the optics configurations itself can be ported to TracePro (ACIS based), also on the optics station, and turned into ACIS based solids and provided as SAT files. These SAT files can be exchanged between any ACIS based programs. MDT is one such program. Cost and mass estimates of the developed optics configuration can also be provided. The ACIS engine is developed by Spatial Technology.

At the **radiometry station**, variables such as required temperature, quantum efficiency, dark current level and readout noise of the detectors, #bits/pixel, aperture diameter, F#, spectral resolution, target scene reflectivity, altitude, number of bands, and observed wavelengths are used for ensuring that minimum signal to raise (S/N) ratios are achieved, and for calculating noise equivalent temperature (NEΔT) curves. The tools used for these calculations was developed by the radiometry analyst in Excel spreadsheets.

The mechanical designer sits at the **mechanical/CAD station**. His/her job is to design support structures (holders for lenses, mirrors, and detectors) and enclosures around the optics configuration provided as output from the optics station. The geometry of these set ups is provided in IGES and SAT formats. MDT, which is also built on the ACIS engine is currently being used as the Team I CAD tool. The station also provides preliminary mass, volume, and area estimates of the developed instrument design. The mechanical/CAD work can be time-consuming, and it is, therefore, mostly done before or after a concurrent session. More about this in section 2.3, The Process.

At the **thermal station,** a combination of RadCAD and SINDA tools are used. RadCAD uses the geometry developed on the mechanical/CAD station together with orbital parameters, for calculating orbital heating rates, and for producing radiation interchange factors. SINDA, a thermal analysis program, utilizes these results for calculating detector and optics temperatures for the given orbital environments. This information is then used for discussions about radiator placing, and about whether active or passive cooling is required.

The **cost station** is manned by a cost expert that will perform either grassroots costing (costing by analogy) or parametric costing. The parametric cost models take into account factors such as mass, type of technology, development time, and complexity of instrument part. Output from the cost station is fed into the system station.

At the **system station**, the high level mission parameters (inputs) are defined at the beginning of the session. The main output variables are also sent to and displayed on this station. Some of the high level mission parameters are type of mission; type of orbit; the classical orbital parameters, semi major axis, orbital inclination (calculated for Sun synchronous orbits), right ascension of ascending node, argument of periapsis, true anomaly, and observation time and date; orbital time (calculated), orbital velocity calculated (rad/s, and km/s); orbiting body (Earth, Mars, etc.); surface temperature, reflectivity of orbiting body; wavelengths to be observed at; and number of bands. The main output variables are instrument mass and cost, and the power required by the instrument. Preliminary estimations of instrument datarates and communication downlink data rates will also be calculated and displayed on the system station. The system station was put in place primarily to ensure that all applications would be using the same high level system parameters at all points in the design cycle. This is achieved by the system station making these high level parameters available to the various Team I applications in a format that they can read. In the same way, data from the various applications are extracted from their output files and displayed on the system station. This work is under development. LabVIEW has been used for developing file data extraction routines, file building routines, and routines for exchanging data between the team I applications and the system station. Collectively these routines or programs are called executives. The Team I satellite orbital analysis and display software (SOAP) is also located on the system station, so is the electronic white board used in some Team I sessions.

2.2 The Tools

Mechanical Desktop (ref. 5) **(MDT)** is a parametric, ACIS 3.0 and feature-based 3-D solid modeling engine. The program supports blended NURBS surface features, and non constrained and constrained design approaches. Dimensions and annotations are automatically displayed in drawing view. The program can be used for calculating surface area, mass, moments of inertia, and volume of parts and assemblies. Files can be imported and exported utilizing file formats such as STEP (STandard for the Exchange of Product model data), IGES Version 5.3, STL (stereolithography), DWF, DWG, DXF, IDF, VRML, SAT (ACIS), 3DS (3D Studio®), WMF (Windows Metafile), EPS (Encapsulated Post Script), and BMP. MDT supports the AutoLISP® programming language, and application programming interfaces (API's) provide C language access to MDT features, functions, and attributes.

CODE V® (ref. 6) is a non sequential optical design, analysis, illumination calculations, and fabrication support program, that features optimization, various analyses types, and tolerancing.

Optimization routines include , transverse ray errors for pre-stored ray patterns, wavefront variance for pre-stored ray patterns, modulation transfer function (MTF) at user-selected spatial frequencies, and Global Synthesis®.

Supported analysis capabilities include, geometric performance analysis, diffraction analysis, illumination analysis, spectral analysis, and environmental analysis. In the geometric performance analysis, the program utilizes, third-order aberration analysis, real ray tracing, MTF and square-wave responses, radial energy distribution, line spread distributions, detector energy analysis, scanned quadrant detector analysis, cat's eye diagrams, and footprint analyses. Diffraction analysis is provided through root mean square (RMS) wavefront error and Strehl definition, the polychromatic point spread function, encircled energy, and MTF. The illumination analysis features Monte Carlo simulation, and includes analysis of undesired radiation, location and evaluation of ghost images, narcissus calculation for calculating equivalent differential temperature of integrated surface/detector retro-reflections. In the spectral analysis, based on a specified detector, black body, or filter, the system spectral response curve is calculated together with appropriate sampling wavelengths and weights for polychromatic computations. In the environmental analysis, changes in ambient temperature and pressure in the optical system, including expansion of lens spacers, are simulated.

Semi-automatic tolerancing is provided based on RMS wavefront error, diffraction MTF, or chief ray distortion. The program also has capabilities for calculating system weight and center of mass, and it supports the export of files in the IGES format.

ZeMax (ref. 7) is a non sequential optical design analysis program that features optimization routines, various analyses types, and tolerancing.

Optimization routines include actively damped least squares, minimization of peak-to-valley or RMS of either spot radius, x, y, x+y, or wavefront error, referenced to either the chief ray or the centroid, and MTF response and encircled energy. Equality, inequality, and Lagrange multiplier constraints are all supported with arbitrary weighting. The program can optimize most of the parameters in a optical system, including radii, thicknesses, glasses, conics, aspheric coefficients, grating spacings, apertures, wavelengths, and fields.

Analysis types include spot diagram analysis, diffraction analysis, and encircled energy analysis. Spot diagrams include, standard field-by-field, through focus, full field, matrix (spot diagrams separated by field and wavelength). Diffraction analysis functions supported include, MTF, square wave MTF, through focus MTF (sine or square), point spread function, point spread function cross section, surface 3D MTF, geometric transfer function (GTF), and through focus GTF. As for the encircled energy analyses, diffraction radial, geometric radial, x, y, and line and edge response analyses are supported. The program also features analysis of grid distortion, longitudinal aberration, lateral color field curvature and distortion, RMS vs. field, RMS vs. focus, extended source imaging capability, interferograms, chromatic focal shift, glass internal transmittance vs. wavelength, and relative illumination.

The program utilizes both sensitivity analysis, and Monte Carlo simulations for performing tolerancing, and RMS spot size, RMS wavefront error, MTF, as well as user defined criteria are supported. Tolerancing can be performed on radii, thickness, lens position, tilt, decenter, irregularity, and wedge. Inverse tolerances, giving maximum acceptable increase in performance are also given. The IGES export file format is supported.

TracePro (ref. 8) accounts for absorption, specular reflection and refraction, scattering, and aperture diffraction of light propagating through a solid model. TracePro can be used for stray light analysis, non-imaging analysis, radiometry analysis, or any application where the accurate determination of distributions and intensities of light is required. The program includes features for importing lens design data from most lens design applications for creating accurate solid models of lenses with no loss of information. Being based on the ACIS geometric modeling engine, the program can effectively share solid model data with other ACIS based applications. For non ACIS based CAD and analysis programs, data can be exchanged via IGES and STEP files.

RadCAD (ref. 9) is PC based radiation analysis system that combines the analysis capabilities of programs such as TRASYS with CAD techniques and integrates CAD generated surfaces with parameter-based (TRASYS-like) surfaces. The program works within MDT. From a MDT supplied geometric description of a set of surfaces along with optical property data or from a TRASYS input file, the program can produce form factors and radiation conductors ("RADKs") ready for import into SINDA. The program supports the TRASYS ORBIT1 or ORBIT2 conventions, defines and displays the S/C orbit and orientation, and calculates the orbital heating rates. Support for

the creation and manipulation of optical property databases is also provided. CAD 3D faces, regular MxN meshes, and arbitrary polyface meshes are supported by the program.

SINDA (ref. 10) is a user-extensible finite-difference, lumped parameter (circuit or network analogy) software tool for analyzing complex thermal systems. The program deals with radiation, conduction, and convection, and it includes system performance simulation capabilities, steady state and transient solution capabilities, goal seeking capabilities, optimization capabilities (multiple variables), time and temperature-varying properties, user-determined solution techniques, solution sequences, accuracy levels, and outputs, and spreadsheet-like expressions and user variables (registers).

LabVIEW (ref. 11) is a cross-platform (UNIX, PC, Mac, and PowerPC) program development tool similar to, for example, C. It uses a graphical programming language called G rather than a text-based programming language for creating code. A LabVIEW program will appear in a block diagram form. The boxes in the block diagram can represent user defined programs, subroutines, or subsystems, or built in functions and subroutines. These boxes are recognized through their icons. For user-defined subroutines, the icons are drawn by the user. Functions or subroutines are, in the LabVIEW vocabulary, called virtual instruments (VI's), because they imitate the appearance and operations of an actual instrument. A VI includes a front panel and a (block) diagram. The front panel is the VI's interactive user interface. In the front panel, the model developer will define all input (controls) and output (indicator) variables. The relationships between these input and output variables are defined in the block diagram.

2.3 The Process

The Team I process is under development, and the process that is being described here is what the Team I development group is working towards. The process, which is shown in Figure 2, starts with Team I sending a potential customer a list of input parameters required by the team prior to a Team I session. The list can be accessed and filled in from the Team I Home-Page. About a week after the list has been sent to the customer, Team I and the customer meet to discuss the input list and plan the Team I sessions. At this meeting, the customer will also be briefed on the workings of Team I. Based on the input from this meeting, the Team I members and developers will prepare the session. These preparations will vary in volume and complexity depending on the type of support the customer requires, complexity of instrument, and inheritance from other instruments.

The radiometry expert may have to modify his models to make them work with the specified number of bands, the spectrum being analyzed, and the number of detectors required. The optics expert will have to do preliminary design and analysis on an optics (lenses, or mirrors) configuration that meets customer requirements on orbital altitude, ground resolution (instantaneous field of view: IFOV), swath width, and aperture size. This work easily takes a week. The optics expert will use Code V or ZeMax for this work. At the mechanical/CAD station, a preliminary model of the instrument will be put together. This will be used for visualizing the design and helping the Team I members better understand issues, such as orientation towards the sun, direction of the orbital velocity vector, and direction to the orbiting object. On the system station, the main input parameters will be set up, and calculations of variables such as inclination, orbital time, and orbital velocity will be performed. Possible modifications to the system front page will also be performed to meet special requests from the customer. The orbital parameters from the system station will be used for setting up SOAP for visualizing and analyzing the selected orbit. The thermal expert will also utilize these parameters for setting up RadCAD.

The aim of all of these preparations, is to have the tools prepared to a point where, it becomes possible to perform changes and trades, in a concurrent fashion.

On about day 14, the customer and the Team I members meet to conduct a concurrent design session. The main flows and interactions between the Team I stations are illustrated in Figure 3. These sessions are lead by the Team I Study Lead.

Encircled numbers (1...5) show the main steps in the design process. These are discussed below. Dotted lines indicate that electronic transfer of data between applications on the shown stations is under development or under consideration for development. Complete lines indicate that electronic data currently can be transferred and used by applications on the station at the end of the arrow. Connections being regarded as important, especially from a timesavings perspective, are marked with thick complete lines. These connections are discussed in more detail in section 3.3, Sharing Common Geometry.

The Team I session would start (1) with the Team, together, furnishing the high level mission parameters for the system station. At this point the system station display would be shown on the large projection screen. Ref. Figure 1. Having the team do this together, helps getting it on the same page from the very beginning of the session. The system station serves both as a placeholder, as well as a point of distribution for these common high level parameters. Preliminary calculations of orbital time, velocity, inclination are also performed. Next, for visualizing the mission, the six orbital parameters are fed automatically through a routine into a SOAP .orb file. This file is then automatically opened and displayed on the system station and on the large projection screen. As the dotted arrows in Figure 3, indicate, there also are plans for electronically transferring high level parameters to other applications. After the high level mission parameters are established, typically work starts in parallel, and interactively, on the optics station, and on the radiometry station (2). Aperture diameter, detector placing, and focal length, are defined on the radiometry station, and utilized by the optics station, using Code V, or ZeMax, for setting up, and analyzing initial, and prepared optics configurations. After some back and forth between these stations, a recommended optics configuration should emerge. The geometric representation of this configuration is transferred to TracePro and turned into ACIS solids. These are saved in a SAT file format. In parallel, the same geometry plus the resulting rays are saved as an IGES file. The two files are read into MDT (3), on the mechanical/CAD station. Next, the geometries in these two files are aligned, ensuring that the surfaces from the IGES file, exactly match the corresponding surfaces of the TracePro developed solids lenses, mirrors, and detectors. This process also perfectly aligns the rays. At the mech/CAD station, support structure, an enclosure, radiators, and electronics are added. Some of these parts may have been prepared before the session or during the time the time of the optics analysis. As part of the Team I development effort, we are looking into effective ways of parameterizing key dimensions of the support structures, making it possible to modify and use them for a variety of mirror and lens shapes, and sizes. The final CAD drawing will in most cases be finished after the concurrent session. However, after an initial geometry, including lenses, and support structures has been developed, it will be used directly by RadCAD (4) for calculating orbital heating rates and for producing radiation conductors. For this purpose, a very detailed geometric representation of the instrument is not required. Prior to getting the geometry from the mech/CAD station, preliminary orbital heating rates can, therefore, be calculated based on the simple geometry of a box dimensioned as the final instrument and the orbital parameters provided from the system station. From the RadCAD analysis, a file containing form factors and radiation conductors is imported to SINDA for calculating detector and optics temperatures. The MDT developed solids geometry (lenses, support structures, and detectors) may be saved as a SAT file, and transferred back to TracePro for stray light analyses.

After all these analyses have been performed, and there is agreement that the resulting design meets the set design criteria, mass and cost will be calculated and displayed on the system station (5) together with other main output variables such as data rate and power. Datarate calculations will initially be performed on the system station. Mass will be calculated in two ways, one based on volume and densities as defined in MDT and Code V (lenses and mirrors), and one based on mass relationships derived from expert knowledge from the Team I members. For mass estimates provided by MDT, a routine has been developed for automatically extracting this information from the MDT mass file, and displaying it on the system station. The instrument costing process is still under development.

Most likely, issues will arise during this first session that may require more detailed analysis that should be done off line. A likely scenario is, therefore, that after the first concurrent session the team and the customer take a break for about 10 days. This should give the customer time to consider the initial results, and the team members time to do required off-line design and analysis work. Any changes coming from the customer should be conveyed to the team members in good time for them to prepare for the second concurrent session at day 24.

The design and analysis process for this session will be similar to that of the first session, with the exception that a report has to be generated at the end of it. Currently, this report is generated jointly by the Team I members during

the session. The final report will be delivered to the customer a couple of days later. If no design has been reached that satisfies the customer requirements or if the instrument is too complex for just two concurrent sessions, the report will be postponed to the last concurrent session between the customer and Team I.

3. REDUCING DEVELOPMENT AND ANALYSIS TIME

3.1 Computerizing Preliminary Calculations

After having gone through some concurrent sessions, utilizing parts of the Team I process, it seems that time can be saved by reducing the number of reoccurring manual calculations done on pieces of paper at the beginning of these sessions. Typically, these calculations range from orbital time, to estimates of aperture diameter. It was assumed that time could be saved by making these calculations and their results electronically available.

The Team I development group, therefore, is looking into using G-code developed by National Instruments, for developing small programs, above called executives, that will perform these calculations. These programs or virtual instruments (VI) will be linked directly to the high level parameters on the system station, also developed in G-code. This will make it possible to perform effective and numerous trade-off analysis based on those parameters. Both input and output variable values from those trade-off analyses will be stored in a file for later retrieval and analysis. This file is set up on the system station and termed the history file. The calculations to be performed in this way are primarily mission related and high level calculations, not performed on any of the other stations. So far, VI's for calculating orbital time, velocity, inclination of Sun synchronous orbits, aperture diameter, F#, have been implemented in the Team I environment. More VI's will be added. The benefit of using G-code is that it is simple to learn, easy to develop in, and easy to modify. These features enables rapid development and modifications of VI's to make them fit any new customer's demands. Additionally, these features make it possible to involve the system experts in the model (VI) development process (refs. 12, 13). The approach and methodology utilized in this work was developed and demonstrated in earlier research by the author (ref. 14).

3.2 Automating the Transfer of Data between Applications

Very early in the Team I development effort it was recognized that to have high-end tools with unique file formats work together in a near real-time fashion, there was a need for developing effective ways of transferring data between them. Without this capability, too much time would be spent on duplicating manual data entries, and manually searching through and possibly modifying input and output files.

The Team I development group solved this problem by developing routines, (VI's) in G-code, for extracting information from, as well as for inserting code and values into any file type by the press of a button. For example, a routine has been built for automatically extracting mass data from a summary mass file from MDT, transferring it to, and displaying it on the system station. An associated routine transfers this mass data from a system station file into assigned cells in the parametric cost model spreadsheet. Another routine has been developed for inserting orbital elements and other variables from the system station into a unique SOAP formatted orb. file. Through the push of a button on the system station, SOAP opens up this file and displays visually the orbit of the instrument, its ground track, and any other parameters defined from the system station. The latter routine shows how G-code can be used for opening applications and files, a capability that will be useful for performing semi-automatic trade studies, with people in the loop, across a number of tools. These types of trade studies will be looked into in later phases of the Team I development effort.

3.3 Sharing Common Geometry

The largest time savings seem to come as a result of the optics, the CAD, and the thermal tools being able to utilize the same geometric data. These time savings can be attributed to progress made by the developers of these tools, and

the mix and the utilization these tools in the Team I environment. In many ways, the requirements of Team I forced an effective integration of the optics, CAD, and thermal tools. The process changes that lead to these time savings are discussed below and illustrated in Figure 4. In the figure, rectangles and thick lines symbolize the Team I process. The crossed over, rounded rectangles illustrate the manual steps eliminated through the introduction of this process.

According to mechanical designers who have been designing support structures, fasteners, etc. for space instruments for a number of years, the Team I approach, typically, saves them 7-10 days worth of work. Up to recently, they had to manually translate the dimensions and positions (x, y, z) of lenses, mirrors, and detectors from, for example, a Code V output file, into a 2D CAD drawing. Often, such output files would be provided as print outs. In the Team I environment, these steps are eliminated, and the geometry of the optics configuration (dimensions and positions) is transferred automatically without any human intervention, except for opening, and saving files, from the optics tools to the CAD tools. The details of how this is done is discussed in section 2.3 The Process.

On the thermal side, the situation was similar. Dimensions and positions (x,y,z) of surfaces had to manually be read from a CAD drawing and then typed into, for example, TRASYS or NEVADA formatted ASCII files. This procedure required that the analyst knew how to set up these file formats, and that he/she also knew which commands to use for inserting dimension and position values. By using RadCAD instead, CAD geometry from MDT is utilized directly in the RadCAD environment. RadCAD, which works within MDT, provides a visual representation of the geometry, and surfaces to be analyzed, and provides the analyst with a graphical user interface. These features, according to thermal experts, may reduce the time for calculating, radiation interchange factors and orbital heat inputs by a factor of 5.

4. IMPACTS BEYOND THE TEAM I ENVIRONMENT

The utilization of interconnected, high-end optical, mechanical and thermal analysis tools in the concurrent Team I environment has made it possible to generate designs of such quality and fidelity that they can be used directly as starting points for the detailed design and analysis required for converting these designs into real hardware. The resulting time savings can be substantial. The Team I development group, therefore, is developing procedures for transferring the final geometry and data generated in the Team I environment to the next phases in the design process. So far, successful transfers of Team I generated geometry have been made from MDT to Pro-E using commercially available STEP translators. Data will initially be transferred as text files.

Today, in the instrument design process, most data and geometry information is handed over from the conceptual design phases to the later design phases in the form of print outs. Consequently, it may be quicker for the designers and analysts in the later design stages to start from ground zero rather than having to recreate the geometry and data in these print-outs. The difference between the current data hand over process and the Team I based data transfer process is illustrated on the left side in Figure 4.

5. CONCLUSIONS

The Team I development is very much at its early stages. However, both team members and customers are starting to see the benefits of utilizing this concurrent and multidisciplinary design and analysis environment. Much good work has been done in interconnecting and making the Team I tools effectively work together. There is still much work to do in this area, especially in transferring high level system parameters to the various applications. More work is also needed in developing high level preliminary analyses capabilities. Later, as more operational experience is gained, the Team I concept will be expanded to include design and analysis capabilities for non optical space instruments and in-situ instruments. From this perspective, the Team I environment can be seen as a laboratory for developing effective early conceptual design environments for demanding types of space instruments. Taking into consideration the impact the Team I processes and procedure s may have on the instrument design process, the Team I environment may also be regarded as laboratory for developing more effective instrument design processes JPL.

6. ACKNOWLEDGMENTS

During the Team I development effort, the author has benefited from discussions with numerous people at JPL, especially, listed alphabetically, Apostolis Deslis, Edward C. Hagerott, Randall C. Hein, Pantazis Mouroulis, David D. Norris, Stanley W. Petrick, James F. Schmidling, George Siebes, Jeffrey L. Smith, Harold R. Sobel, and Fred Vescelus.

The research described in this paper was carried out by the Jet Propulsion Laboratory, California Institute of Technology, under a contract with the National Aeronautics and Space Administration. Reference herein to any specific commercial product, process, or service by trade name, trademark, manufacturer, or otherwise, does not constitute or imply its endorsement by the United States Government or the Jet Propulsion Laboratory, California Institute of Technology.

7. GLOSSARY

Aperture diameter: The diameter of the opening through which light passes to reach the optics and the detectors in an optical or photographic instrument

Argument of Periapsis: Angle from the ascending node to periapsis measured in the direction of a satellite's motion.

F#: Defined as the focal length of the instrument (f) divided by the aperture diameter (D).

Field of View (FOV): Angular extent of field which can be observed by a spacecraft or an instrument.

Focal Length: The distance from a lens or a mirror to the point on the optical axis where parallel rays of light converge (the Focal Point).

IGES: Initial Graphics Exchange Specification is a standard file format for exchange of CAD data. IGES 1.0 was accepted as an American National Standards Institute (ANSI) standard in 1981.

Noise Equivalent Temperature (NEΔT): Defined as a the minimum ΔT within a scene element required to produce a change in the electrical signal level numerically equal to the root mean square (RMS) of the electrical system noise. Used as a figure of merit for Infrared (IR) systems.

Orbital Inclination: The angle between the angular momentum vector, perpendicular to the orbital plane of a satellite, and the spin axis of the body being orbited.

Radiometry: A specialist field dealing with issues related to the measurement of the intensity or force of different types of radiation.

Right Ascension of Ascending Node: Angle from the Vernal Equinox to the ascending node. Ascending node is defined as the point where a satellite passes through the equatorial plane from south to north. Right ascension is defined as a right-handed rotation about the pole.

Semi Major Axis: Half the distance between the apoapsis and periapsis points of an elliptical orbit

Spectral resolution: Number of bands that a given spectral range can be divided into

True Anomaly: The angle from the eccentricity vector to the position vector of the satellite. The angle is measured in the direction of the satellite motion.

REFERENCES

1. Casani, K. Thomas, N., "FST - Faster, Better, Cheaper", SPIE-94, Conference.
2. Project Design Center, Jet Propulsion Laboratory (JPL), Brochure JPL 400-533, July 1994.
3 Oxnevad, K. I., "A Concurrent Design Approach for Designing Space Telescopes and Instruments", Paper 3356-131, Proceedings from the Space Telescopes and Instruments V Section of the SPIE Astronomical Telescopes & Instrumentation Conference, Kona, Hawaii, March 20-28, 1998.
4. Oxnevad, K. I., *A Total Systems Analysis Method, for The Conceptual Design of Spacecraft: An Application to Remote Sensing Imager Systems*, Old Dominion University, Ph.D. Dissertation, May 1996, pp. 13-22.
5. AutoDesk, WWW: http://www.autodesk.com/prodsol/mech/products/desktop/techspec/index.htm.
6. Optical Research Associates, WWW: http://www.opticalres.com/cv/cvtechds.html, 1998.
7. Focus Software, WWW: http://www.focus-software.com/zemax/, 1998
8. Lambda Research, WWW: http://www.lambdares.com/PRODUCTS/products.html, 1998.
9. Cullimore and Ring Technologies, WWW: http://www.webcom.com/crtech/radcad.html, 1998.
10. Cullimore and Ring Technologies, WWW: http://www.webcom.com/crtech/sfcap.html, 1998.
11. LabVIEW for Macintosh, User Manual, National Instruments, Part Number 320591-01, December 1993 Edition.
12. Wise, R.M., "LabVIEW our Choice for Cardiothoracic Research", Instrumentation Newsletter, Technical News from National Instruments, Vol. 7, Autumn 1995, p. A-5.
13. Clarkson, M., "Tools on the Fly: Virtual Instruments Take Off", Desktop Engineering, September/October 1995, pp. 20-28.
14. Oxnevad, K. I., pp. 1-96.

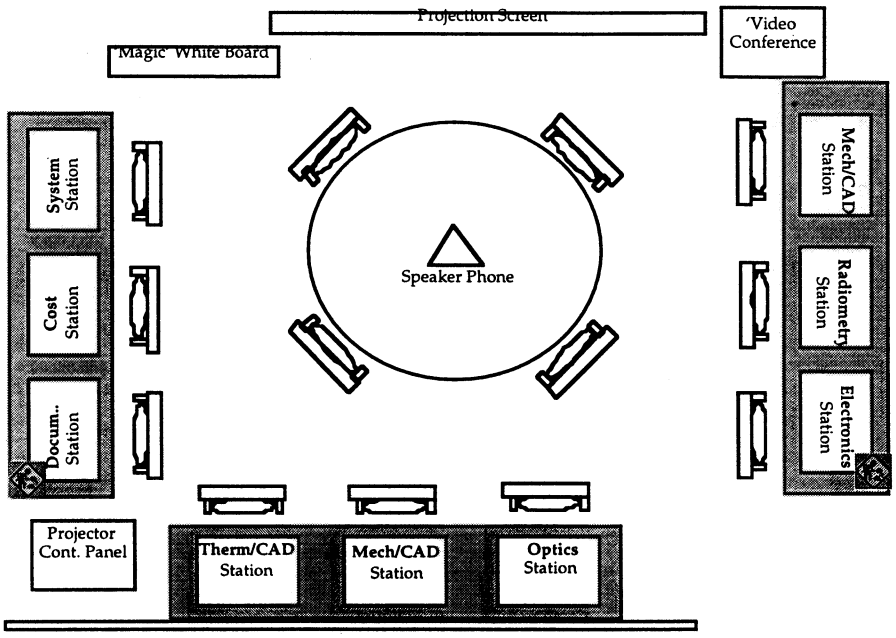

Figure 1: The Team I Room

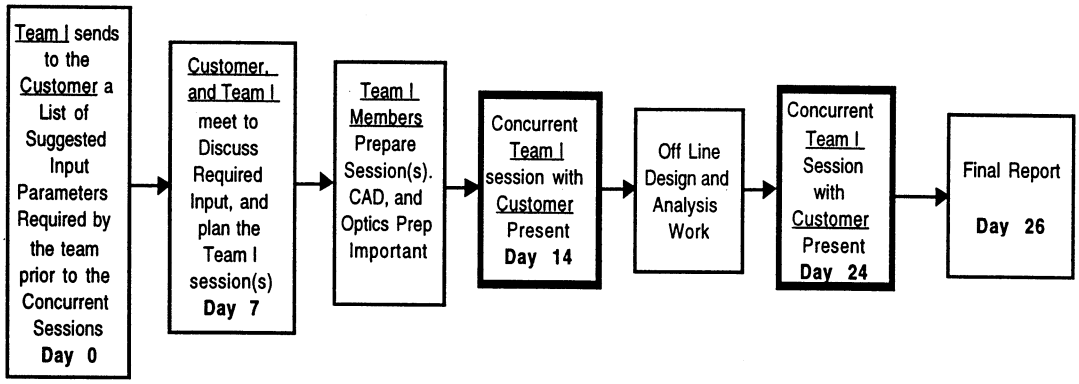

Figure 2: The Design Process

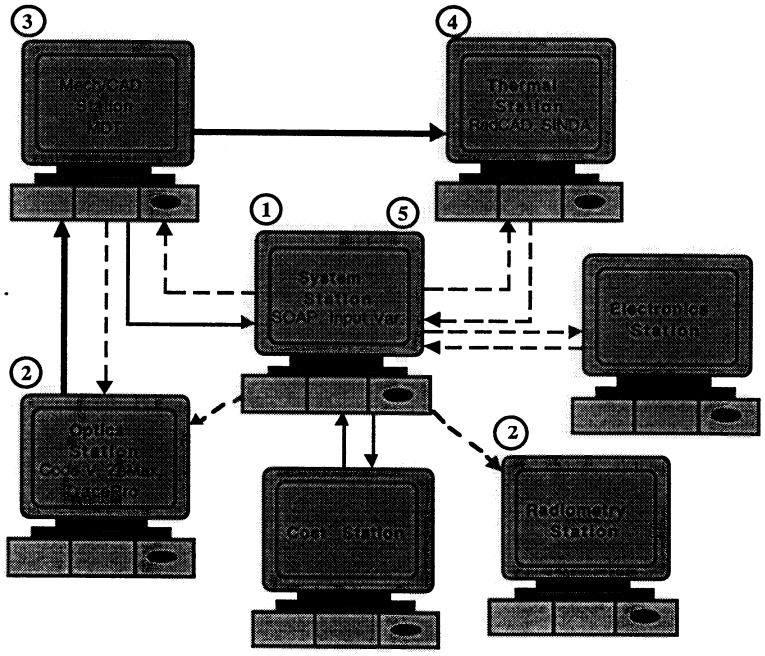

Figure 3: Interconnected, High-End Analysis, and Design Tools

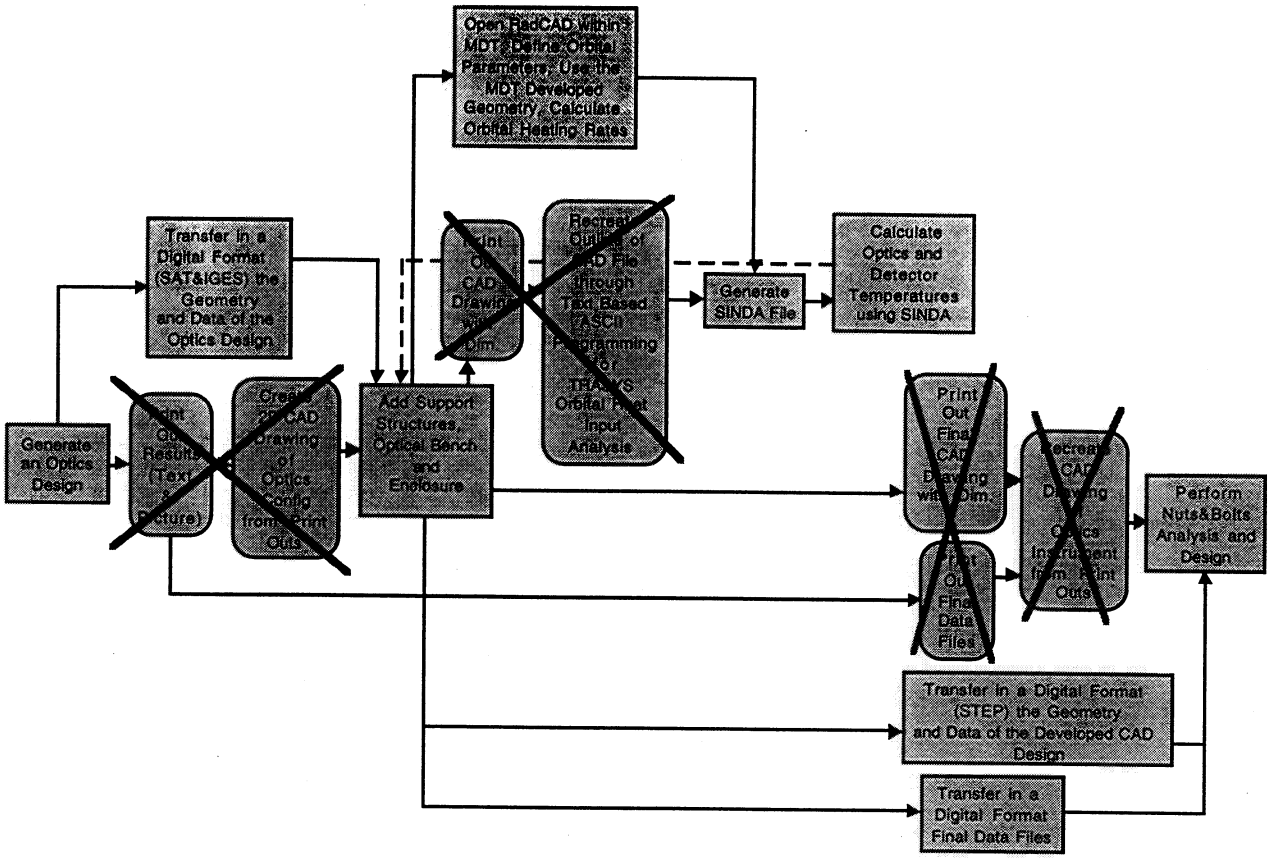

Figure 4: The Team I Based Instrument Design Process

TRUE CONCURRENT THERMAL ENGINEERING INTEGRATING CAD MODEL BUILDING WITH FINITE ELEMENT AND FINITE DIFFERENCE METHODS

Tim Panczak, Steve Ring, and Mark Welch
Cullimore and Ring Technologies
9 Red Fox Lane
Littleton, Colorado 80127-5710 USA
CRTECH@NETCOM.COM

ABSTRACT

Thermal engineering has long been left out of the concurrent engineering environment dominated by CAD (computer aided design) and FEM (finite element method) software. Current tools attempt to force the thermal design process into an environment primarily created to support structural analysis, which results in inappropriate thermal models. As a result, many thermal engineers either build models "by hand" or use geometric user interfaces that are separate from and have little useful connection, if any, to CAD and FEM systems.

This paper describes the development of a new thermal design environment called the Thermal Desktop. This system, while fully integrated into a neutral, low cost CAD system, and which utilizes both FEM and FD methods, does not compromise the needs of the thermal engineer. Rather, the features needed for concurrent thermal analysis are specifically addressed by combining traditional parametric surface based radiation and FD based conduction modeling with CAD and FEM methods. The use of flexible and familiar temperature solvers such as SINDA/FLUINT is retained.

INTRODUCTION

Thermal engineering (especially in aerospace) has been performed with tools that have had a long heritage, before CAD systems and graphical FEM systems even existed. Finite difference based conduction and capacitance models were built by hand, and solved with programs such as CINDA (Chrysler Improved Numeric Difference Analyzer). Radiation analysis was performed by constructing geometric models consisting of conic primitives (cones, spheres, discs, etc.) using a text editor and solved using programs such as TRASYS[1]. Early radiation tools did not have the ability to graphically verify model geometry.

Improvements continued over the years, with CINDA ultimately being superceded by SINDA/FLUINT[2]. Progress was made in improving radiation analysis tools from TRASYS with the development the graphical based TSS[3]. However, the basic analysis process remained the same, independent of advances being made in CAD and FEM systems.

Part of the reason that thermal engineering has been outside of the concurrent fold is the entrenchment of current FD based analysis processes, but also because alternative FEM based systems have failed to address important thermal analysis requirements. Current FEM based systems facilitate only one aspect of thermal modeling: generating conduction and capacitance data directly from a geometric description.

Other, equally important aspects are addressed poorly or not at all. Not all thermal modeling is derived from detailed geometric specifications. Often thermal models are represented more abstractly with a conduction capacitance network generated using basic first law principles (for example, to simulate an interface for a vendor or customer).

Many geometrically complex components can be reduced to a simple and efficient network representation using an engineering estimate of the heat flow paths and basic finite difference methods. These techniques are used to develop fast executing thermal models, which have a significant advantage over brute-forced FEM models when many thermal simulations must be performed under different scenarios, or a number of design trades must be considered.

Many thermal control components are not represented by a network at all, but must be simulated procedurally. Examples are heaters, thermostats, and variable conductance heatpipes. This type of modeling is not found in FEM based thermal tools, which have usually been based on a program originally designed for structural analysis.

More specifically, support for radiation analysis in FEM based systems has been traditionally weak. In addition, the standard types of finite elements result in model nodal densities greatly exceeding thermal requirements. Coupled with inefficient radiation analyzers, models quickly become intractable.

For example, with radiation analyzers such as TRASYS, a cylinder may be modeled with one node around the circumference. With current FEM based tools, a cylinder must be represented by a sufficient number of flat facets (each of which contributes one or more nodes) to approximate the geometric shape. Model size is governed by geometric fidelity rather than by thermal requirements. In addition, ray-surface intersection tests employed by radiation codes must be performed on a large collection of facets, rather than a single mathematical cylinder, which greatly increases run times.

Complex radiation phenomena such as angular dependent optical properties, transparency, refraction, and specularity are not well supported in the FEM world. More specific aerospace needs such as articulating geometry that tracks the sun, planet, or other satellites are not well supported, if at all.

Until now, the thermal engineer has had to choose between two undesirable solutions: (1) use current analysis tools that efficiently satisfy thermal modeling requirements but have no connectivity to the CAD design database or other engineering disciplines, or (2) use tools that support concurrency but sacrifice thermal modeling functionality.

The Thermal Desktop was designed from the ground up with both the requirements for concurrent engineering and for thermal analysis as key design drivers. This paper discusses the design approach and features of the Thermal Desktop that enable it to successfully integrate CAD and FEM with traditional analysis approaches.

OVERVIEW OF THERMAL DESKTOP

The Thermal Desktop is implemented as a single application that:
1) Integrates CAD, FEM, FD, radiation, and procedural modeling into a single low-cost environment. The environment simultaneously supports both “design geometry” used for the exact specification of hardware and “analysis geometry” which may (or may not) be a simplified abstraction of the design geometry used for thermal analysis.
2) Allows analysis geometry to be constructed using CAD operations: booleans, sweeping, blending, ruling, revolving, etc…
3) Allows design geometry to be imported from other CAD systems using IGES and/or DXF formats.
4) Permits design geometry to be used “as is” for analysis geometry, or used as “scaffolding” on which to construct suitable analysis geometry using interactive graphics operations.
5) Provides familiar types of thermal modeling surfaces such as cones, paraboloids, discs, rectangles, and cylinders using true mathematically precise representations (rather than as a collection of facets). These surfaces provide all of the functionality associated with TRASYS type surfaces but are directly integrated within the CAD environment.
6) Integrates CAD methods for generating, resizing, and positioning surface types.
7) Integrates conduction/capacitance generation, surface insulation, radiation analysis, and contact conductance calculations.
8) Provides graphical construction of arbitrary nodes and conductors for abstract thermal network modeling.
9) Allows FE models to be created natively, or imported from popular FE programs.
10) Provides efficient radiation analysis for common types of finite elements plus implements new types of curved finite elements for even faster radiation analysis.
11) Implements a new thermal super element that simplifies a collection of complex finite elements into one or more SINDA/FLUINT nodes.
12) Provides graphical construction of procedural thermal model entities such heatpipes, heaters, and thermostats.
The main screen of the Thermal Desktop is shown in Figure 1. The figure shows the design geometry for an optical assembly. Commands may be typed at the command line, selected from pull-down menus or from user customizable tool bars.

The Thermal Desktop is implemented as an embedded application integrated with Autodesk's AutoCAD™ or Mechanical Desktop™ product. Integrating the application directly with the CAD environment provides the necessary link with the CAD world and provides viewing and model building functions at a very low cost.

An example of thermal analysis geometry constructed from design geometry is shown in Figure 2. The four views show the analysis geometry created from the solid model design geometry shown in Figure 1. These modeling entities were easily constructed by picking on key points in the design model. Sample results for the calculation of radiation exchange factors are shown in Figure 3.

Thermal Desktop's layering feature allows design and analysis geometry to be viewed independently. Geometry may be placed on as many different layers as desired. The visibility of each layer may be controlled to aid in model building and postprocessing.

Thermal analysis geometry may be constructed and modified using two complementary methods. The first technique is to use dialogs invoked by the pull-down menu or tool bar icons. The editing dialogs contain fields to enter shape parameters and other thermal information. For example, the shape of a paraboloid may be modified by specifying the minimum and maximum radius, angular span and height. The second method takes advantage of the unique CAD features incorporated into the Thermal Desktop.

Thermal analysis geometry is easily constructed from design geometry using two powerful features of the Thermal Desktop: snap points and grip points. Snap points are defined for all graphical objects and may be used whenever a point location is required for input. Snap points are located at key locations on an object such as the ends, middle, center, and intersections.

For example, the move command requires selecting the objects to be moved, and then inputting a "from" point and a "to" point. This point can be entered directly on the command line as an (x,y,z) triple, or the snap feature may be used to interactively select a location directly on the geometry. As the cursor is moved around the screen, snap points automatically highlight to show the user the available snap locations. An advanced expression utility may also be used to generate points not at snap locations (such as half way between two snaps).

Grips are used to modify a geometric object interactively. When an object is selected, the grip points appear, as shown by the small squares in Figure 4. Each grip point controls some aspect of the geometric object's location, shape, or size. When a grip is selected, the object will change dynamically as the cursor is moved about the graphics screen.

Figure 4 shows a Thermal Desktop (TD) cone surface. The cone is divided into three nodes in the height direction and two nodes in the angular direction. Solid lines show the nodal boundaries, and dotted lines pass through the nodal centers. The grip point at the base controls the base radius, and likewise, the grip at the top controls the top radius. Other grips are available for setting the angular span, height, location, and orientation of the surface.

If the base radius grip is selected, the cone will dynamically change size as the grip point is moved. The new location of the grip point may be entered at the command line, arbitrarily placed on the current workplane with the mouse, or placed by selecting a snap point. For example, the radius of the cone can be made to precisely match a cylinder that it is on top of by selecting the cone radius grip, then moving the cursor over the cylinder until a suitable snap point is highlighted. Selecting the snap point completes the operation.

CONCURRENT ENGINEERING

A primary goal of the Thermal Desktop is to bring thermal analysis into the concurrent engineering fold. Two key areas must be satisfied for a successful concurrent engineering environment: integration with the design database, and exchange of analysis models and data between engineering disciplines.

Integration with the design database means the ability to generate analysis models directly from design geometry, and to react quickly to the inevitable changes in the design. Integration with other engineering disciplines means the

ability to perform multi-discipline analysis from the same analysis model, or the tight coupling of data from one analysis model to another.

INTEGRATION WITH THE DESIGN DATABASE - The Thermal Desktop satisfies integration with the design database through its direct implementation in the CAD environment. Engineering shops using Autodesk's AutoCAD or Mechanical Desktop share the same drawing files that are generated by the designer. These design drawings can be linked externally to analysis files so that they are updated automatically when changes are made.

The Thermal Desktop was also designed to work with UNIX based CAD packages such as I-Deas or Pro/E. Thermal Desktop's IGES import capability allows analysis geometry to be constructed directly from the CAD design database. Design geometry is easily imported to form the basis for generating analysis models.

Geometry suitable for analysis may be directly converted to thermal analysis geometry. And, as is the usual case, a simplified representation of the design geometry for analysis is easily constructed using Thermal Desktop's snap/grip methods. Generating models by hand from 2D paper drawings, ruler, and calculator are replaced by efficient interactive graphical operations performed directly on the 3D design geometry.

The low cost of AutoCAD running on today's inexpensive and powerful PC's is an attractive alternative to costly high-end UNIX systems. AutoCAD does not compare to higher end solutions in terms of the functionality for the designer, but provides all of the needed viewing, IGES import, and CAD building methods for constructing analysis models. In addition, the evolution of the PC platform from a 16-bit DOS environment to a true 32-bit multitasking system has allowed AutoCAD to significantly expand its performance and functionality compared to previous versions.

The user interface and modeling features specifically designed for thermal engineers and AutoCAD's relative simplicity makes for a much faster learning curve compared to training engineers as designers on more expensive CAD platforms. AutoCAD is included as part of the Thermal Desktop.

INTEGRATION WITH OTHER ENGINEERING DISCIPLINES - A typical scenario in engineering organizations is the use of a CAD package that includes an integrated tool for constructing Finite Element Method (FEM) models. Some FEM modelers have the capability of basing meshes on design geometry and have the ability to automatically remesh based on design changes, a useful capability for rapidly responding to design changes.

Engineers use the FEM tool bundled with their in-house CAD system for model building and postprocessing. A typical pattern of usage is to export the FEM model for use with discipline specific "solvers" and then import results from their solver for postprocessing and data exchange.

The Thermal Desktop has solved the problems that have lead to the resistance of thermal analysts to adopt this engineering analysis approach. The Thermal Desktop may import and analyze FEM models directly, without the typical ad-hoc "element centroid" conversion process. FD and FEM methods are supported simultaneously, within the same thermal model, and temperatures are predicted using the industry standard thermal analyzer, SINDA/FLUINT. Thus, Thermal Desktop integrates into the CAD-based engineering process in the same way as tools that support analysis for other engineering disciplines.

The Thermal Desktop may be used as the engineering organization's thermal "solver", importing FEM meshes and performing radiation, orbital heating, and conduction and capacitance calculations. This data is then used by SINDA/FLUINT for steady state and transient temperature analysis. SINDA/FLUINT routines for producing appropriate input files to FEM packages are bundled with the Thermal Desktop so that temperature data may be transferred to other engineering discipline's models.

However, integrating with the standard in-house FEM package is only one mode of usage of the Thermal Desktop. Thermal Desktop contains the ability to generate FEM meshes directly, perform model-to-model data translation, and provides full postprocessing operations. A unique feature of Thermal Desktop is that it supports both traditional types of FD modeling primitives (conic surfaces, arbitrary nodes, and arbitrary conductors) and FEM modeling primitives simultaneously. This can often lead to advantages in system level modeling.

A full system level model constructed from a detailed FEM model will consist of many more nodes than a model constructed using traditional approaches. With the Thermal Desktop, specific areas of the hardware to be analyzed may be modeled using FEM, and other areas modeled using FD methods. For example, in an integrated thermal-structural-optical analysis of a telescope, the optical components can be modeled using FEM so that data may be transferred for thermal distortion analysis and optical performance predictions. The surrounding enclosure and spacecraft may be modeled using more CPU efficient FD methods. The geometric basis for the model may come from both design geometry and other engineering discipline's FEM models.

Despite pressures from the need to integrate tighter with other engineering disciplines, FE methods have been resisted by the thermal analysis community. One of the reasons is a perception that FE methods are not as physically based as traditional FD approaches (in part because of the generation of "negative conductors", which are viewed as physically unrealistic). The other reason is simply that current FE codes do not satisfy all of the requirements for performing system level thermal analysis. However, a failure on the part of FE *codes* to supply needed functionality does not negate the advantages of the finite element *method*.

Integrating FEM into current thermal analysis approaches, including a new first law formulation of the method was presented in detail in reference [4]. The derivation and approach will not be repeated here, but a few of the extensions to the finite element method implemented in the Thermal Desktop that make its application appropriate for thermal analysis are presented in the following section.

THERMAL SPECIFIC EXTENSIONS TO FEM

A common complaint against FEM is that an excessive number of nodes are generated. Nodalization is often driven more by geometric fidelity to the actual hardware rather than by thermal accuracy concerns. For example, a curved surface must be approximated by many flat elements. Traditional modeling primitives such as cylinders and cones allow nodal regions to be curved, permitting only the number of nodes as necessary for thermal accuracy to be used, while retaining geometric fidelity.

Typical FEM meshing utilities operate on detailed solid model representations of the design, leading to meshes that capture unnecessary detail for thermal analysis. Details of interest to a structural engineer calculating stress in a part may not be important thermally.

The Thermal Desktop employs two unique features to reduce the complexity of models generated using FEM. One is the formulation of a new set of thermal specific linear elements on curved surfaces. The other is a new thermal super element formulation.

THERMAL SUPER ELEMENTS - Thermal super elements may be constructed from any set of ordinary finite elements. A subset of ordinary nodes in the super element may be specified to be super nodes. The Thermal Desktop will compute conductance and capacitance data for the super nodes on the super element for use in SINDA/FLUINT. Correspondence between the super nodes and the sub nodes on the super element is maintained so that temperatures may be assigned to the sub nodes for post processing and for mapping data to other analysis models.

An example may illustrate the process. Consider the bracket shown in Figure 5, which contains holes to reduce weight. Suppose that the bracket is thermally attached only at the four end points.

Thermally, only the conduction paths between the four mounting points are of interest. Using the traditional approach, the temperature distribution within the part is deduced, and equivalent conduction areas and lengths are calculated. Such estimation often requires considerable skill and experience to arrive at an accurate approximation.

Using thermal super elements, the part is first discretized with enough elements to capture the geometric detail and the set of elements is labeled as a super element. Next, super nodes are assigned to selected sub nodes of the mesh, which in this case are the four mounting locations. Conduction and capacitance data for the four super nodes are calculated automatically by Thermal Desktop. The super node data is then used by SINDA/FLUINT for temperature calculations.

Super elements work by numerically calculating the form of the temperature distribution over the super element. A Numerically computed shape function for each super node is used for the calculation of conduction and capacitance terms using a first law apportioning method[4].

In a regular finite element, the temperature distribution over the domain of element is assumed to have some simple mathematical form, such as a bilinear interpolation for a quadrilateral element. In a super element, the temperature distribution is not approximated by simple interpolation, but rather by a temperature solution calculated using the entire super element mesh.

The shape function for each super node is derived in turn by performing a steady state solution with the super node set to unity and the remaining super nodes set to zero. Because the problem is linear, superposition holds and the resulting shape functions can be used to compute the steady state temperature distribution for any set of super node temperatures.

Figure 6 shows the temperature distribution computed using super element shape functions compared to the temperature distribution performed using the full mesh. As can be seen, the temperature distributions are exact. The shape function for one of the super nodes is shown as a height plot in Figure 7.

In this example, the nodes along each flat edge were specified as super nodes, reducing the part down to three SINDA/FLUINT nodes. The choice of super nodes gives Thermal Desktop additional knowledge of the temperature distribution in the super element, which is used to reduce the complexity of the part. Specifying that all of the nodes along an edge are a single super node tells Thermal Desktop that the temperature distribution is isothermal in this area. The remaining edges are assumed to be adiabatic.

If this region were incorporated into a larger surface, the assumption of an adiabatic edge may not be correct. The Thermal Desktop also allows sub nodes to be specified as being interpolated from super nodes. For example, the temperature distribution along a curved edge can be specified to be linearly interpolated from the end points, which are specified to be super nodes.

This allows the computer to perform the work that is normally done by hand. The specification of super elements and super nodes provides Thermal Desktop with additional knowledge about the form of the resulting solution, which is used to reduce the number degrees of freedom in the problem.

The choice of super elements and super nodes is governed by the same considerations that the engineer uses in nodalizing any thermal problem. In a macro sense, energy is always conserved, and “bulk” properties of the region are accurate regardless of the size of the super element. Like FD nodes and regular finite elements, larger regions trade local fidelity for faster run times.

LINEAR CURVED FINITE ELEMENTS - The Thermal Desktop has integrated finite element meshes with finite difference based modeling. Thermal Desktop’s first law based formulation of FEM shows that nodes represent control volumes and can be used in conjunction with traditional modeling methods. The lines that connect the element centroids delimit the control volume for a node. Direct radiation analysis of FEM meshes also avoids problems associated with ad-hoc conversion of valid FEM meshes to element-centroid networks.

Radiation analysis is performed using the shape functions to weight ray energy. When a ray is emitted from an element, its energy is determined by the shape functions for each of the nodes on the element. When a ray strikes an element, the energy is distributed to each of the nodes on the element using the receiving element’s shape functions[5]. Thus, radiation is modeled *non-isothermally*, providing better accuracy for the same nodal density as codes that are restricted to isothermal radiative exchange.

The problem remains; however, of the need to use many flat elements to approximate curved surfaces. Curved element formulations do exist, implemented with higher order shape functions. However, these parabolic elements are still more complicated than necessary for thermal concerns.

Nodal densities are greatly increased compared to using familiar TRASYS surfaces. In a radiation dominated problem, this can quickly lead to intractable models. The obvious solution is to implement curved, linear finite elements. The advantages for postprocessing, model-to-model data mapping, and conduction and capacitance generation are gained without sacrificing radiation performance.

Imagine a conduction problem in which a flat region subjected to some boundary conditions produces a temperature distribution. This temperature distribution does not change if the flat surface is somehow made into a curved surface (without stretching). Topologically, the problems are equivalent. As another example, conduction terms calculated by hand for a cylinder are identical to conductors calculated for a flat plate.

However, the problem is entirely different when one considers the stress problem. A flat plate subjected to external forces responds considerably different than a cylindrical section. This is the reason this simple solution has not been implemented in present FE based tools.

Most FE codes have their origins in solving structural problems. To implement a custom type of element that satisfies a narrow market of radiation dominated thermal problems has not been a priority among providers of FEM based tools.

The Thermal Desktop implements curved finite element based surfaces in the same manner as traditional conic FD based surfaces. From a modeling standpoint, the only difference is that nodal points span the entire surface, rather than just lying in interior regions. Each node is still viewed as being the center of a control volume, to which any other types of conduction, convection, and radiation connections may be made.

The main advantage of FEM conic surfaces over regular TRASYS-like surfaces becomes apparent when these surfaces are to be coupled together conductively. Conduction modeling based on FD surfaces requires artificial nodes to be generated at the boundaries of the surface. Sometimes these artificial intermediate nodes may be eliminated from the model, other times they may not. FEM based surfaces eliminate many ambiguous conditions and provide a simpler interface since intermediate nodes do not have to be created. For surfaces that share a common edge, or solids that share a common face, nodes occupying the same location can be merged into the same node, or connected together through a contact conductance.

For compatibility with existing models and for those that prefer the familiar FD approach, Thermal Desktop also supports full conduction and capacitance generation for FD based radiation surfaces.

INTEGRATING THERMAL MODELING APPROACHES

The Thermal Desktop simultaneously supports FD, FEM, arbitrary network, and procedural modeling methods. An advanced radiation analysis tool, RadCAD, is integrated within the Thermal Desktop. RadCAD works with both FD and FEM based geometry. The use of the industry standard thermal analyzer, SINDA/FLUINT is retained, allowing complete user control and simulation capabilities along with advanced fluid flow modeling.

An example analysis of a fictitious spacecraft is presented to illustrate the combined use of these modeling methods simultaneously in a thermal analysis model. Figure 8 shows a simple box shaped spacecraft with two solar panels. Inside the box is a battery, mounted in a sleeve that is attached to a radiator panel at the base.

The battery was converted into a two node super element using the top and bottom edges of the cylindrical section as the super nodes. The battery was placed into the sleeve with the battery mesh and the sleeve mesh nodes non-aligned.

The interior of the sleeve and the base of the sleeve were specified as having a contact conductance. The Thermal Desktop performed the calculations to connect the sleeve to the battery and the sleeve to the radiator panel through these contact surfaces. A heatpipe on each side of sleeve connects the outside of the sleeve to the radiator panel. The heatpipe was connected using FD calculated conductors.

The edges of the four long rectangles of the enclosing box were coupled together with a high contact conductance. The square ends were coupled to the long section with a thermally poor contact conductance. A single network type conductor modeled the conduction between the solar panel and the spacecraft body.

Radiation conductors were computed for both the interior and exterior of the spacecraft. Orbital heating rates were computed and the temperatures predicted using SINDA/FLUINT. Contour plots of the analysis results are shown Figures 9-10.

The radiation exchange with the warm battery and the enclosure can be seen, as well as the interaction between the solar panels and the ends of the box. The effects of the heatpipe on the battery sleeve and radiator panel are also apparent.

CONDUCTION/CAPACITANCE GENERATION

An overview of the user's interaction with the Thermal Desktop has been presented in previous sections. This section presents a few of the user interface dialog forms and techniques for controlling the generation of conduction/capacitance data.

Analysis geometry is edited by selecting the geometry with the mouse and choosing the edit command from the pull-down menu or by clicking the edit icon on the toolbar. A single entity may be modified, or a group of entities may be edited together.

The edit command invokes the tabbed dialog shown in Figures 11-13. This form contains tabs for setting the nodal breakdown, numbering, optical properties, and active sides for radiation analysis. The "Surface" tab allows parameters to be input for the shape of the surface. The "Cond/Cap", "Contact", and "Insulation" pages are used for conductor and capacitance generation.

Nodal capacitances and intra-entity conduction hookups are controlled by the "Cond/Cap" page, as shown in Figure 11. Node-to-node conductors for nodes on the solid or shell entities will be generated using the data input on this page.

Surfaces have the additional capability of being modeling as a simple thin shell, or as two shells separated by a small distance coupled with a "through" conductivity. For example, the conduction and capacitance terms for a honeycomb panel constructed from two face sheets and a core material may be modeled by a single graphical entity. Orientation angles may be specified for anisotropic materials.

Figure 12 shows the input page to control contact conductance. Contact boundary conditions may be applied to faces or edges of thermal modeling entities. For example, the base of an electronic box on a panel may be specified to have a certain contact conductance. Likewise, the edges of surfaces used to represent computer cards that attach to the panel may also be specified as having a contact conductance. Thermal Desktop will integrate along the faces and edges of these entities, searching the other entities in the model, and generate the appropriate connections to adjoining nodes. The nodal meshes do not have to be aligned.

Insulation is often used in spacecraft and cryogenic applications. Multi Layer Insulation (MLI) is commonly used for spacecraft, relying on reducing the radiative coupling to the environment. Foam type insulations are often used in cryogenic applications. The input form permits insulation to be placed on the top or bottom sides of a surface, or selected sides of a solid. The insulation can be characterized by a combination of effective radiative emissivity and effective conductivity.

Conduction and capacitance data along with analysis results may be graphically displayed, as shown in Figure 14. Spheres are drawn at the nodal centers, and tubes are drawn to represent node-to-node heat flow paths.

Both size and color are used to represent nodal and heat flow data. Five different quantities may be displayed simultaneously using the color of the nodal surface, the color and size of the nodal sphere, and the color and size of the nodal heat flow path.

RADIATION MODELING

Thermal Desktop may be used for conduction and capacitance generation and results postprocessing. An advanced radiation analysis module, RadCAD, is optionally available for calculation of radks and orbital heating rates. RadCAD works with both traditional conic surfaces and with FEM generated meshes. Import and Export of TRASYS models is supported.

RadCAD employs both raytracing and a unique progressive radiosity algorithm. Specular, angular dependent and refractive optical properties are supported. Articulating geometry including star, sun, and planet tracking are provided. An overview of RadCAD and its unique computational algorithms are described in reference [6].

SUMMARY

A new thermal analysis system has been presented that addresses the problems associated with integrating thermal engineering into the concurrent engineering environment. Present radiation modeling techniques are preserved and directly integrated into a CAD environment.

Conduction and capacitance generation from these surfaces along with full support for FE models expands the set of modeling tools available to the thermal engineer and permits closer coupling with other engineering disciplines.

New types of custom finite elements have been developed to address specific thermal needs, as well as a unique super element formulation to reduce complicated meshes into a simpler SINDA/FLUINT network. Thermal Desktop along with SINDA/FLUINT forms a complete thermal analysis and fluid flow solution, that also integrates with existing in-house CAD systems and FE based tools.

The most up to date information regarding the release and availability of Thermal Desktop can be found at http://www.webcom.com/crtech.

ACKNOWLEDGMENTS

Development of Thermal Desktop is made possible by the continued support of NASA Marshall Space Flight Center, with Mr. Bill Till serving as contract monitor.

REFERENCES

1. Lockheed Engineering and Management Services Company, “Thermal Radiation Analysis System Users Manual,” JSC 22964, Contract NAS 917900, October 1991.
2. Cullimore, B., “Optimization, Data Correlation, and Parametric Analysis Features in SINDA/FLUINT Version 4.0”, SAE paper 981547, 28th ICES Conference, July 1998.
3. Panczak, T., et al., “Thermal Synthesizer System: An Integrated Approach to Spacecraft Thermal Analysis,” SAE paper 911582, 22nd ICES Conference, July 1992.
4. Panczak, T., “The Failure of Finite Element Codes for Spacecraft Thermal Analysis,” SAE paper 961450, 26th ICES Conference, July 1996.
5. Chin, J. H., Panczak, T. D., and Fried, L., “Finite Element and Raytracing in Coupled Thermal Problems,” *Proceedings of the Sixth International Conference on Numerical Methods in Thermal Problems*, pp. 683-791, Pineridge Press, Swansea, U.K. 1989.
6. Panczak, T. and Ring, S., “RadCAD: Next Generation Thermal Radiation Analyzer”, SAE paper 972241, 27th ICES Conference, July 1997.

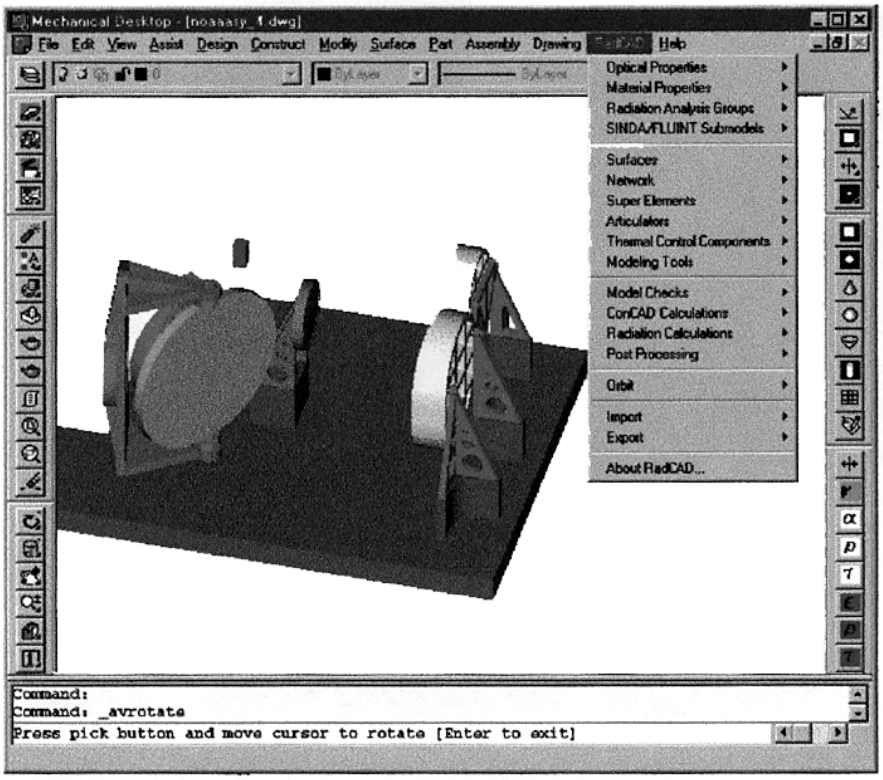

Figure 1. Thermal Desktop main screen

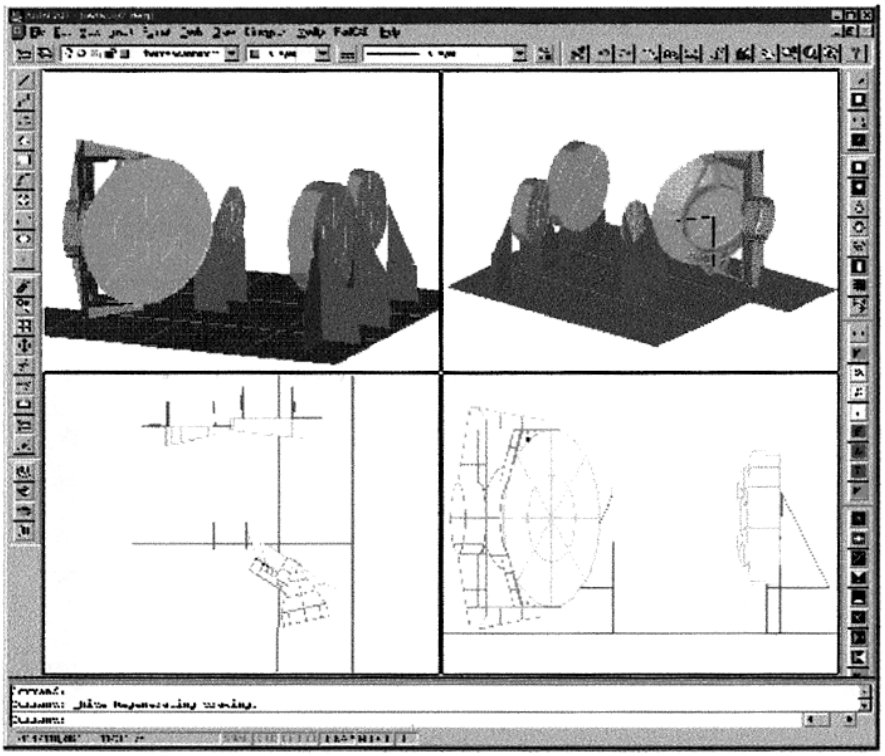

Figure 2. Analysis geometry for example model

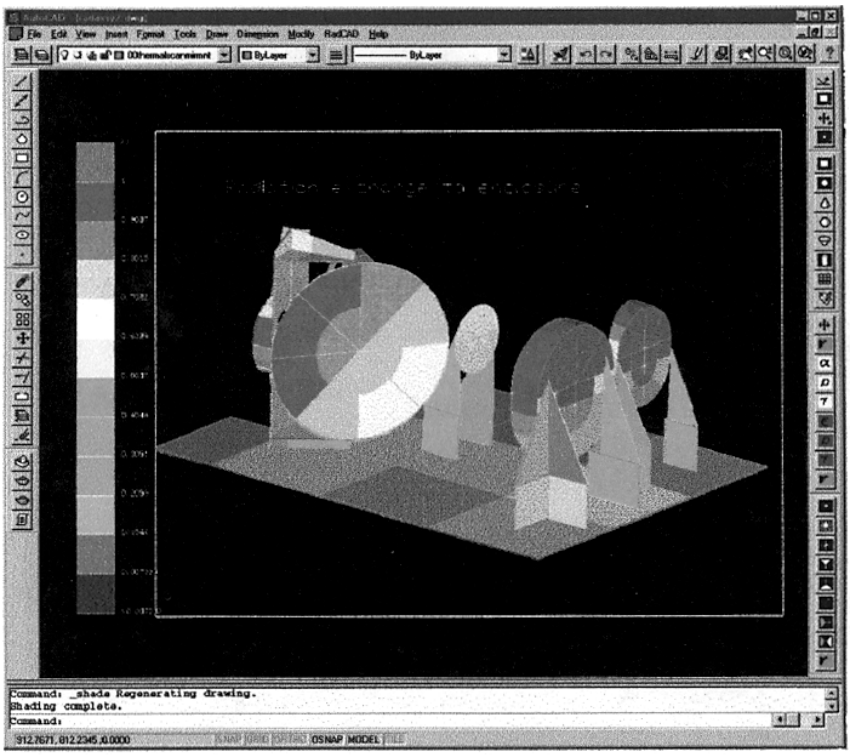

Figure 3. Thermal results for example model

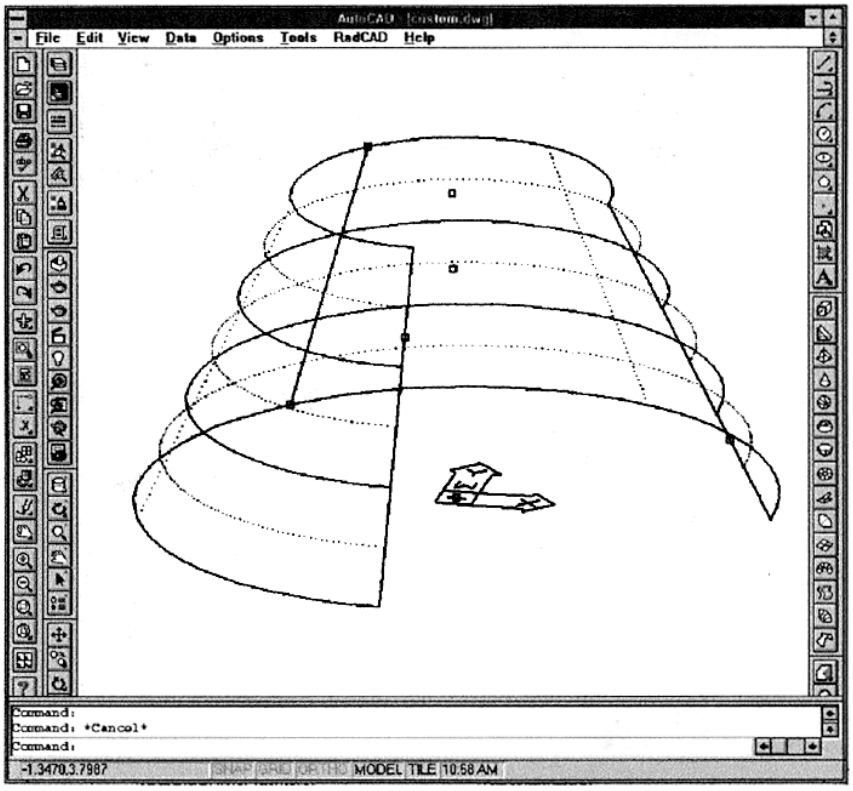

Figure 4. Snap points for TD cone

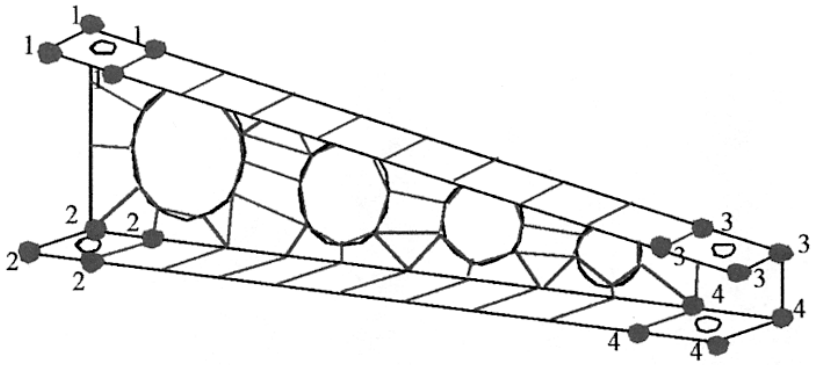

Figure 5. Detailed mesh simplified with super element

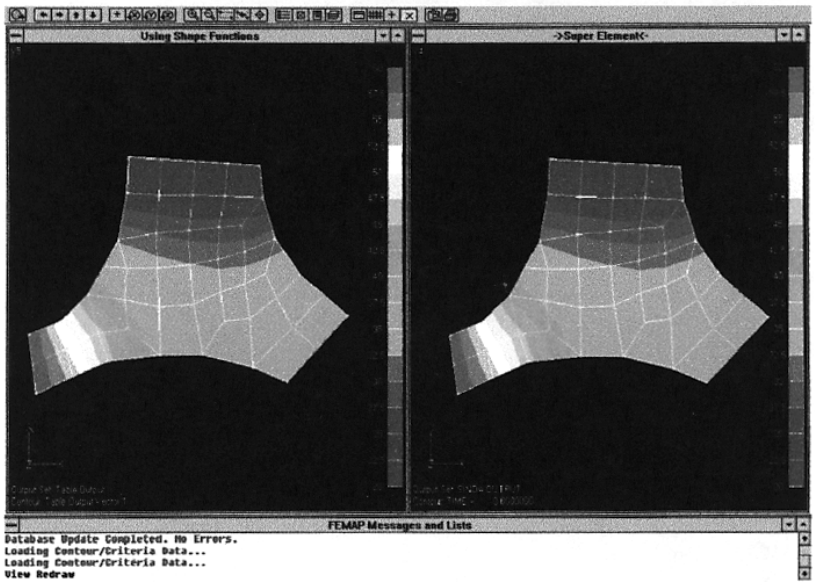

Figure 6. Comparison of super element solution

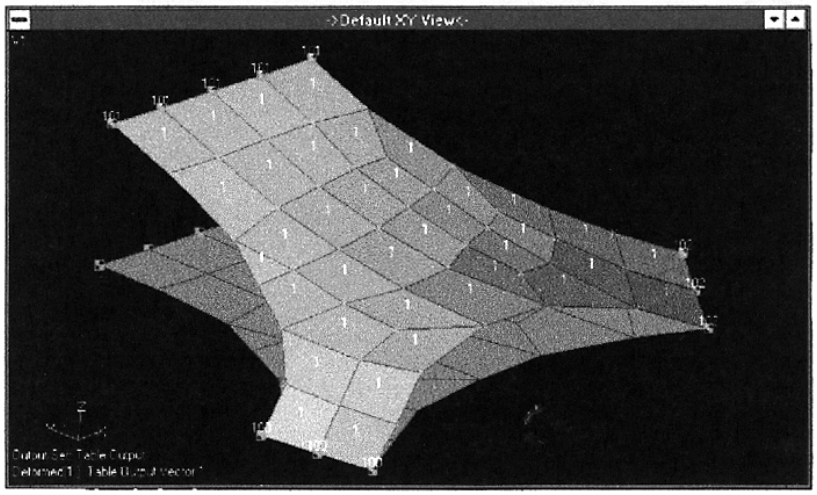

Figure 7. Numerically computed shape function

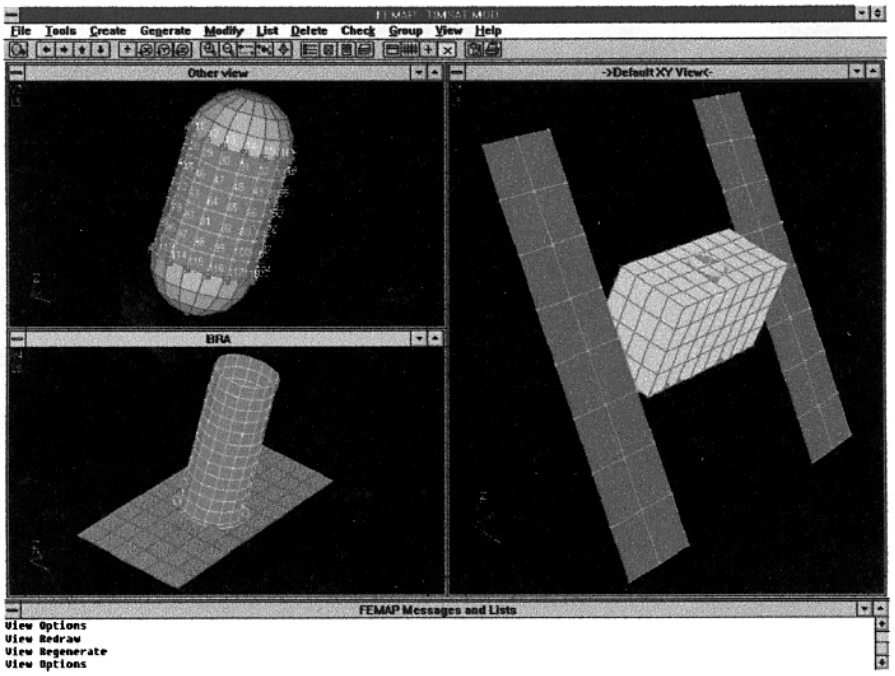

Figure 8. Simple FD/FEM test model

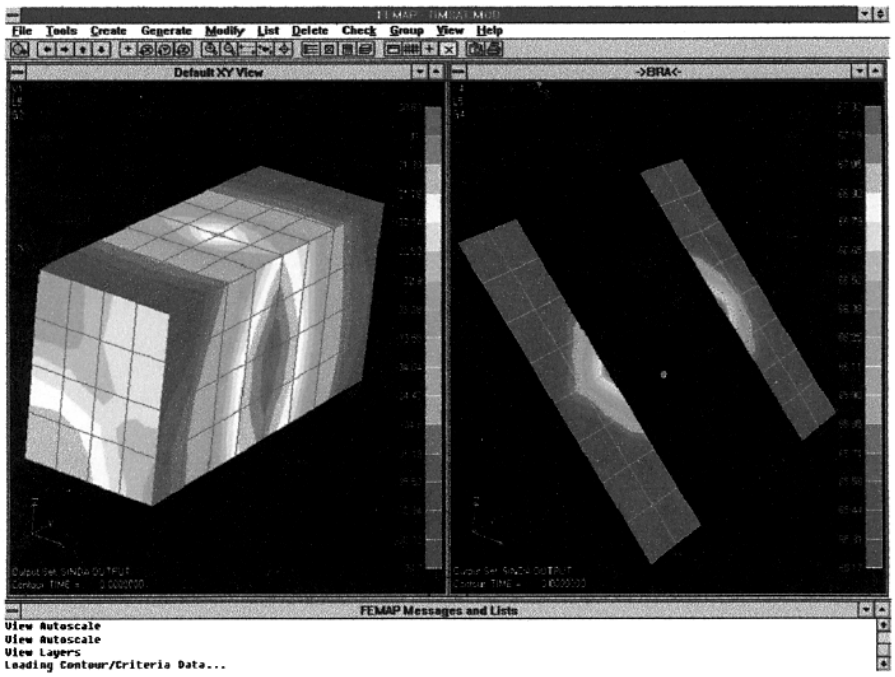

Figure 9. Temperature results for exterior of model

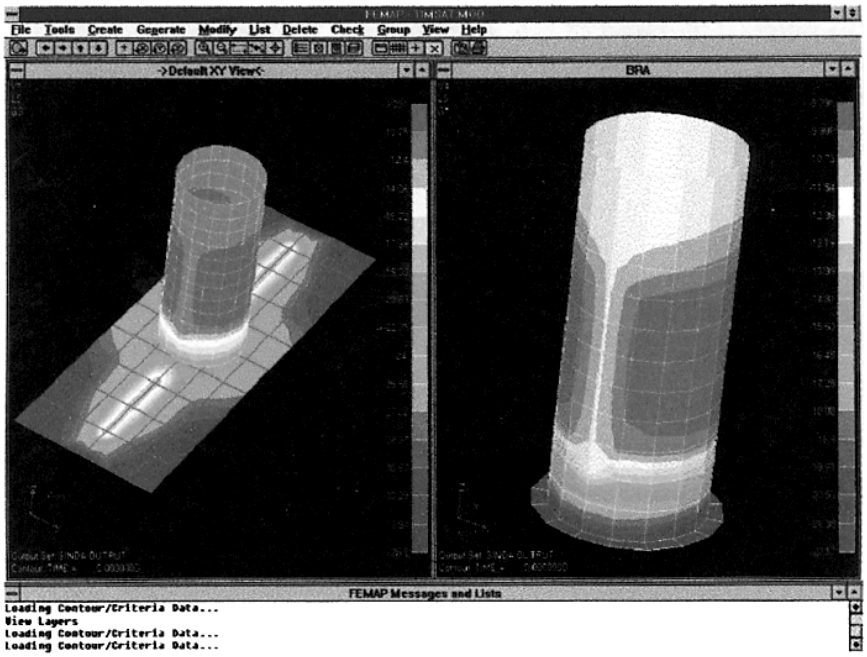

Figure 10. Temperature results for interior of model

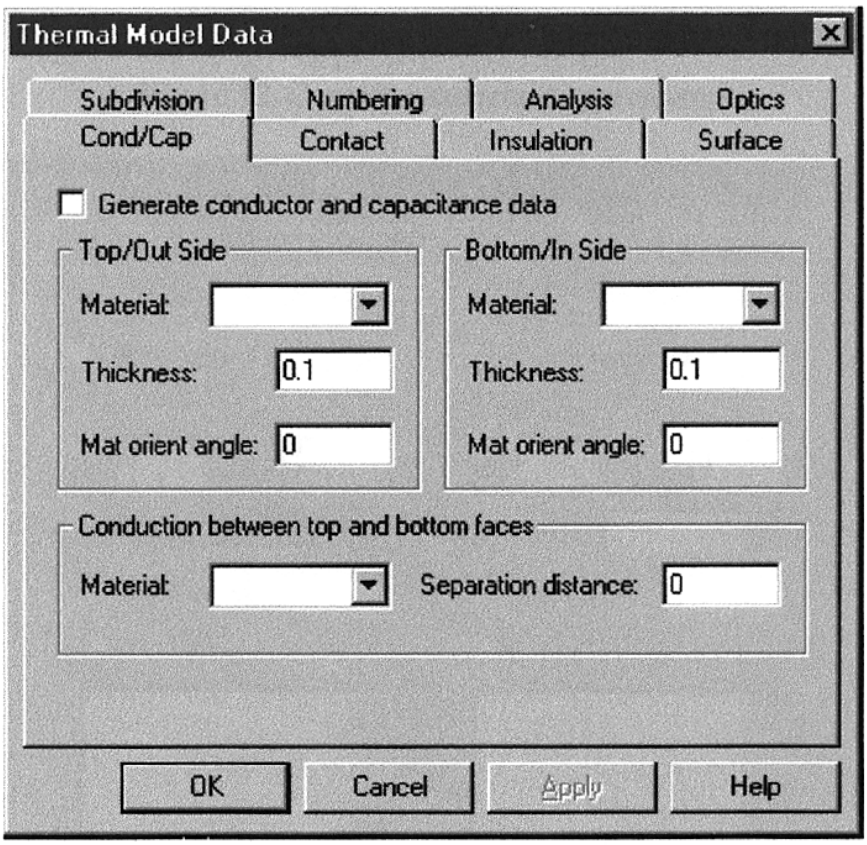

Figure 11. Conduction/Capacitance parameters

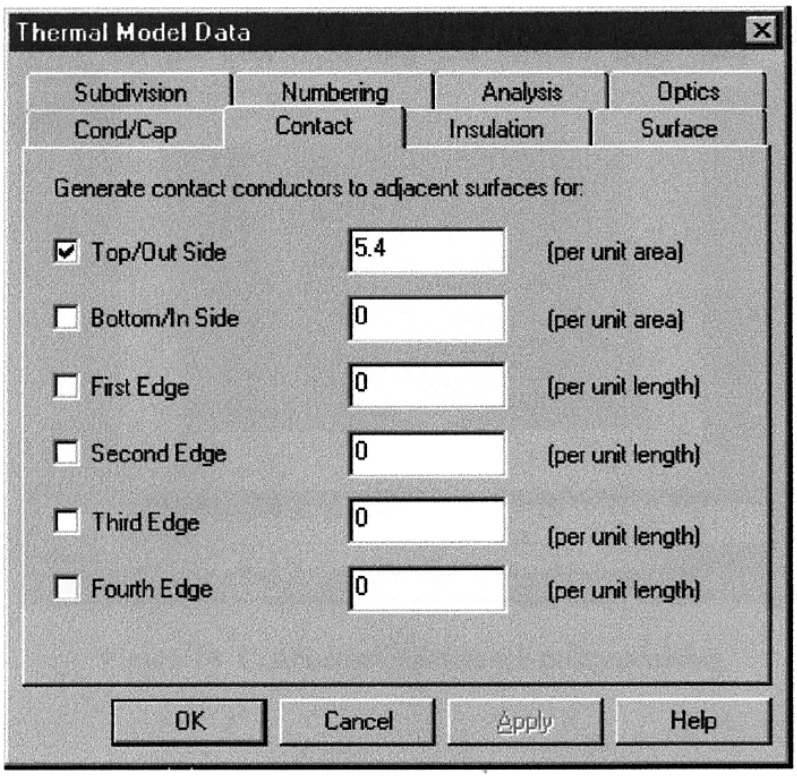

Figure 12. Contact conductance parameters

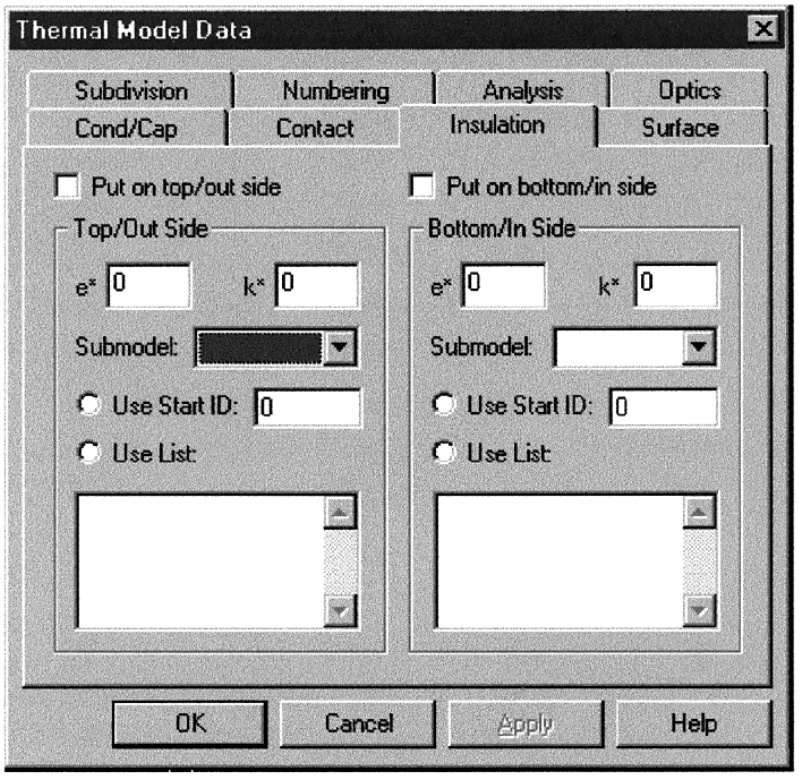

Figure 13. Surface insulation parameters

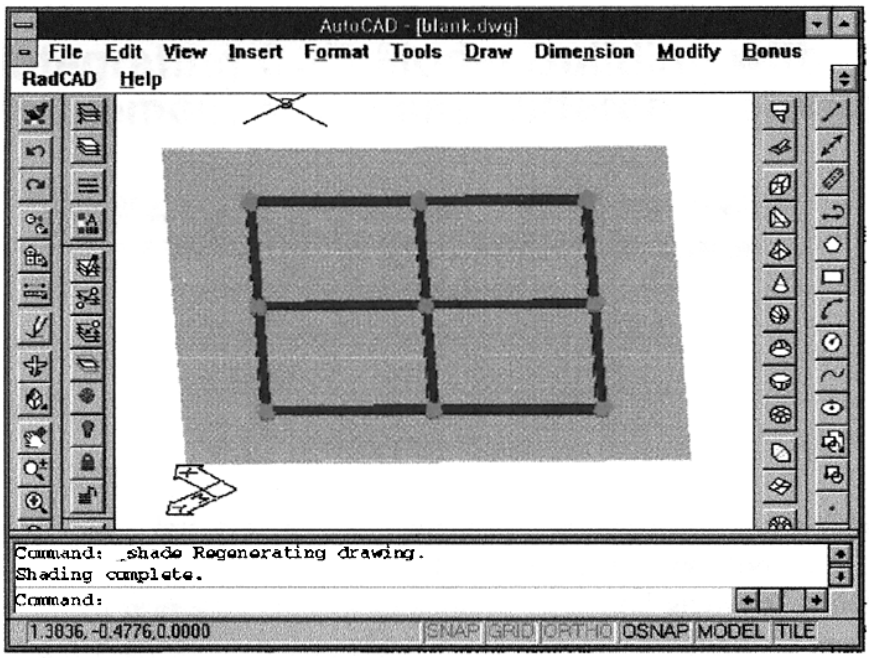

Figure 14. Conductor/Capacitance postprocessing

MODELING OF A DEPLOYABLE RADIATOR/LOOP HEAT PIPE SYSTEM

Michelle L. Parker and Bruce L. Drolen
Hughes Space and Communications
Los Angeles, California 90009

P.S. Ayyaswamy
The University of Pennsylvania
Philadelphia, Pennsylvania 19104

ABSTRACT

The commercial satellite industry is booming, and the demand for increased-capability spacecraft has presented thermal engineers with an interesting challenge. Higher and higher power levels create a need for more efficient heat rejection systems. The size of future satellites, however, does not provide for sufficient "fixed" radiator area to remove the heat generated by the increasing number of high-power units. A way had to be found to increase the heat rejection area, and to efficiently transport heat to this additional area. Over the past few years, Hughes has developed a system which utilizes deployable radiators to increase the heat rejection area, and Loop Heat Pipes (LHPs) to transport heat from inside the spacecraft to the deployable radiators whence it is rejected to space. This combination has made it possible for Hughes to greatly increase transponder capacity on its commercial satellites. The ability to accurately model this system has therefore become critical to the design and integration of high powered spacecraft. This paper presents the modeling methodology, and the correlation of the model to ground tests performed at Hughes. In the modeling, SINDA/FLUINT has been used to model both the thermal and fluid aspects of the system.

One of the keys to modeling this system is an understanding of the Russian developed Loop Heat Pipe (LHP). A brief description of the characteristics of the LHP and the approach taken in modeling it are also included in this paper. Accurate modeling of the LHP has been verified by correlation with ground test data.

A ground test was performed with a simulated deployable radiator having two LHPs creating an upper zone and a lower zone. Results have been correlated and are presented for an upper LHP input power of 828 W. The lower zone provides the boundary temperature. The effects from parasitic heat leaks from the lower zone are apparent in the test results and are reproduced by the SINDA/FLUINT model. It may be noted that this is the first time that interactions between two LHPs mounted on a radiator have been systematically analyzed. The ground test has proved that these interactions are important, and the correlated model now gives us the ability to predict the effects of parasitic heat leaks. This enhanced modeling capability enables a better understanding of the deployable radiator/LHP system, and will aid in the design of more efficient systems in the future.

INTRODUCTION

The loop heat pipe (LHP) was developed in Russia (the former Soviet Union), and is experiencing increasing acceptance and utilization in the United States. Like a conventional heat pipe, the LHP is totally passive and allows the transport of large amounts of heat with a low ΔT (high conductance). It accomplishes this by the continuous evaporation and condensation of its working fluid, taking advantage of the latent heat of the working fluid to transport large amounts of heat. The conventional heat pipe and the LHP both have an evaporator section, a condenser section, and possibly an adiabatic or transport section (Figures 1 & 2). Once liquid is formed at the condenser, it must be returned to the evaporator and this is accomplished via a capillary structure. The capillary structure develops capillary forces that pump the liquid back to the evaporator. Among the disadvantages of the conventional heat pipe are sensitivity to adverse tilt, inflexibility in layout, and the possibility of liquid entrainment in the vapor flow (since the liquid and vapor are not separated by any barrier). The biggest limiter for the heat pipe is liquid drag in the grooves. These disadvantages are all overcome by the LHP.

The LHP consists of five components: evaporator, vapor transport line, condenser, liquid transport line, and compensation chamber (reservoir). The wick in the LHP is confined to the evaporator which allows a wick with very fine pore size and associated low permeability to be used. This small pore wick generates a greater pumping capacity than that experienced with the conventional heat pipe. The maximum pumping capacity may be related to the pore size of the wick:

$$\left(\Delta p_{cap}\right)_{\max} = \frac{2\sigma}{r_{pore}} \tag{1}$$

This increased pumping capability allows the loop to overcome large adverse elevations between the evaporator and condenser under unit gravity conditions. Confining the wick to the evaporator allows the condenser and transport lines to be smooth walled tubes permitting greater flexibility in layout and simplicity in manufacture; it also limits the Δp for liquid flow which is a big limiter for a conventional heat pipe. The separation of the liquid and vapor lines prevents liquid entrainment.

In order to become more familiar and confident with the performance of the LHP, a ground test was conducted at the Hughes Space & Communications facilities in El Segundo, CA. The test lasted for six days and was intended, among other things, to prove the feasibility of a deployable radiator using two LHPs and to determine the interaction present between the radiator zones of the two LHPs. Tests were performed at various power levels and at hot and cold sink temperatures. Start-ups were performed and rapid power changes were investigated. Both LHPs performed flawlessly during all aspects of the test.

This paper focuses on steady state testing with input power of 828 W, and on the development of a SINDA/FLUINT model which accurately predicts the performance of the LHP including the interaction between zones and the effect of parasitic heat leaks from the portions of the condenser to the subcooled liquid return line. The interaction between zones, mainly conduction from the upper zone to the lower zone, or vice versa, was observed during testing to play a role in LHP performance, e.g. operating temperature of the loop. Also, the parasitic heat leaks from the condenser bends to the cooler liquid return line due to the nature of the layout on the deployable radiator tended to reduce the subcooling present in the loop and thereby impact the operational characteristics of the loop. Models used to make pre-test predictions did not take these effects into account and it was determined that a more detailed model would more accurately predict the behavior of the LHP as observed in testing. The model described in this paper was developed with this in mind.

EXPERIMENTAL

Ground testing on the deployable radiator/LHP system was conducted in a thermal vacuum chamber at the Hughes facilities in El Segundo, CA. The ground test consisted of a simulated spacecraft enclosure, a simulated deployable radiator (aluminum facesheet), and two Loop Heat Pipes whose evaporators were located within the spacecraft enclosure and whose condensers were mounted in serpentine fashion to the deployable radiator. The condensers were mounted one above the other to create two distinct zones, the upper and the lower. Heat was supplied to the evaporators of the LHPs via dual bore heat pipes equipped with heaters (upper LHP), or by heaters placed directly on the evaporator (lower LHP). The frontside of the deployable radiator was painted with black primer and had an emittance of 0.93. The backside of the deployable radiator was blanketed with 11 layer multi-layer insulation (MLI). The simulated spacecraft structure was closed out with 10 layer MLI. Calrod arrays were used to set effective sink temperatures.

The test setup was instrumented with 180 thermocouples to provide temperature data. The upper and lower zones on the radiator were not isolated from each other, and therefore interactions between the zones were evident. Also of importance to note are the interactions between the rungs of the same condenser, and between the condenser and the liquid return line. Successful modeling of these interactions is important for accurate prediction of LHP performance.

The test setup is shown in Figure 3.

Temperature and power data were recorded using Hughes Space & Communications Lab's data acquisition system.

Tests were performed at power input levels ranging from 50 W to 900 W with various step sizes. Three different sink temperatures were achieved 20°C, -27°C, and -120°C. Startup responses, rapid power step responses, and steady state operation were all recorded. Different combinations of input power on each zone (e.g. upper zone high power, lower zone low power and vice versa) was also investigated.

As noted earlier, ground testing revealed impacts to the performance of the system caused by interactions between the zones and by parasitic heat leaks to the subcooled liquid return line. Predictions made before the test were produced by a model not capable of delineating such effects and therefore a more detailed model was developed.

FORMULATION OF MODEL

The model for the LHP is based on a prebuilt SINDA/FLUINT model provided by Cullimore & Ring Technologies, Inc. [Cullimore, et al]. The prebuilt model was modified to fit the parameters of the tested LHP and also to include a finely nodalized radiator to better simulate conductive interactions. Nodalization was also increased along the condenser. The steady state SINDA/FLUINT model consists of 64 fluid lumps and 3000+ thermal nodes, with many of the nodes serving to make up the radiator. The upper LHP is modeled in detail while the lower zone serves as a boundary condition. The upper loop heat pipe is represented by its five main components: evaporator, compensation chamber, condenser, vapor line, and liquid transport line. The vapor line, liquid line, and condenser are all nodalized so that appropriate gradients are resolved.

Evaporator

The LHP's evaporator serves as the heat input region and also the location of the wick which provides the pumping capability for the device. The evaporator is modeled as a wick, vapor removal grooves, and a thermal node where heat is input. The wick is modeled as a CAPPMP macro in SINDA/FLUINT. The CAPPMP macro is basically a CAPIL with a junction in the middle. The junction is tied to a thermal node with a user defined heat transfer coefficient. The thermal node represents the shell of the evaporator and the heat input occurs in this location. One CAPPMP serves as the entire wick. Parameters required for the evaporator include wick conductivity, permeability, length, inner and outer diameters. There are also vapor removal grooves on the external surface of the wick which are represented by tube in the SINDA/FLUINT model.

Compensation Chamber

The compensation chamber is modeled as a tank tied to a thermal node. The thermal node is able to radiate to the environment. The compensation chamber tank serves as the reference pressure for the loop.

Vapor and Liquid Lines

Both the vapor line and the liquid line are represented as macros containing five junctions tied to five thermal nodes via heat transfer coefficients calculated by SINDA/FLUINT. The nodes are not permitted to radiate to the environment since they were blanketed in the test.

Condenser

The condenser consists of forty-eight tanks tied to forty-eight thermal nodes. The condenser was converted from the annular cross section, which was in the prebuilt, to a circular cross section. The convective heat transfer between the fluid and the walls is modeled as flow through a duct and appropriate heat transfer coefficients are calculated by SINDA/FLUINT.

Radiator

The radiator consists of 2982 nodes. The nodes are coupled together using simple conduction calculations. The radiator is also coupled to the condenser by a previously determined per inch conductance. One side of the radiator is coupled to a sink temperature using an emissivity of 0.93. The other side of the radiator in the test was blanketed with an 11-layer blanket and this is represented by an effective emissivity of 0.025. Parasitic heat leaks and interactions between the zones are represented by conductances from the liquid return line to the condenser in the region and conductances from the upper radiator zone to boundary temperatures representing the lower zone. These conductances can be zeroed out to remove the effect of parasitics for comparison.

In the present study, the solution is arrived at employing the process suggested by Cullimore & Ring in their LHP prebuilt model. The compensation chamber is modeled as a tank whose state is maintained at each solution step. The system pressure is adjusted to arrive at an energy balance through the loop. The logic to do this exists in the prebuilt.

A steady state 828 W case has been analyzed. The sink temperature was –27°C while the spacecraft environment temperature was 23°C.

RESULTS AND DISCUSSION

Results are presented for an 828 W steady state case. This power is input to the upper LHP while the lower LHP zone serves as boundary temperatures. Figure 4 shows the temperature predictions and test results around the loop. Two different model results are presented, one with all parasitic heat leaks accounted for, the other with such heat leaks zeroed out as described above. It is readily apparent from examination of the results that these parasitic effects are necessary for proper correlation. As noted earlier, the ground testing showed effects caused by parasitics and zone interactions which could not be sufficiently predicted with the previously existing models. Since these interactions impact the operational characteristics of the deployable radiator/LHP system they are important, and the correlated model now gives us the ability to predict the effects of such interactions and parasitic heat leaks. This enhanced modeling capability enables a better understanding of the deployable radiator/LHP system, and will aid in the design of more efficient systems in the future primarily by layout of the lines on the deployable radiator and sizing of the radiator.

Future work will include incorporating increased detail in the evaporator section in order to better understand the processes occurring in this critical section. Also, transient correlation to the power steps and start-ups will be handled along with correlation of microgravity data obtained from a space shuttle experiment.

CONCLUSION

A ground based test of a LHP-deployable radiator system consisting of two LHPs mounted on the same radiator was conducted at the Hughes Space & Communications thermal vacuum facilities. The test results were successfully correlated using a SINDA/FLUINT model. The LHP prebuilt model provided by Cullimore & Ring served as a good basis for this model, and with some modifications was able to accurately predict the test results. The finely nodalized radiator was important in attaining the correct interactions occurring between various zones which were evident in the test. Inclusion of the parasitic heat leaks present between portions of the condenser and the subcooled liquid return line also lead to improved correlation. The ability to model the effects of these interactions and parasitics on LHP performance will lead to more robust designs for future deployable radiator/LHP systems.

ACKNOWLEDGMENTS

The authors would like to express their thanks to Mr. Dave Esposto who put much time and effort into the Loop Heat Pipe ground test at Hughes.

REFERENCES

Cullimore & Ring Technologies, “Loop Heat Pipe Prebuilt Model, User Documentation, Rev. 2.” May 1998.

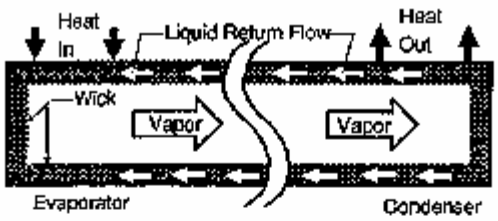

FIGURE 1. CONVENTIONAL HEAT PIPE

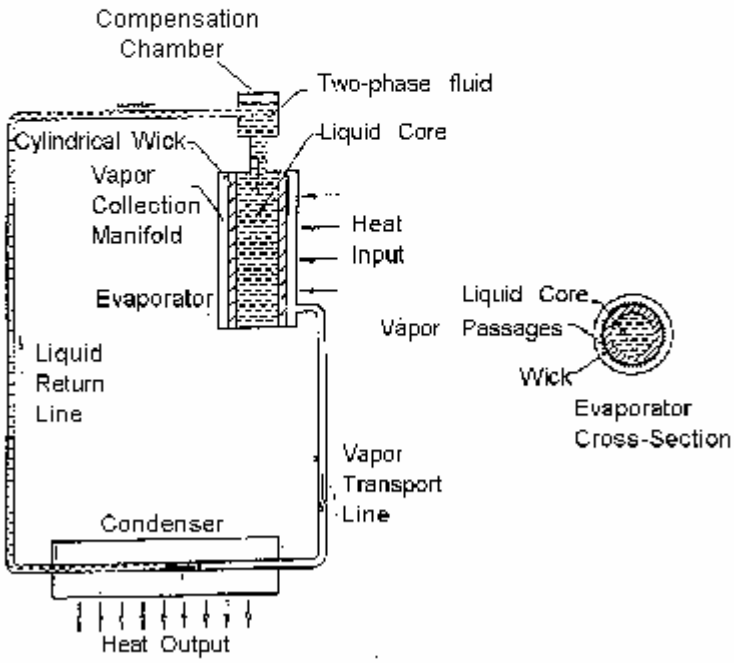

FIGURE 2. LOOP HEAT PIPE

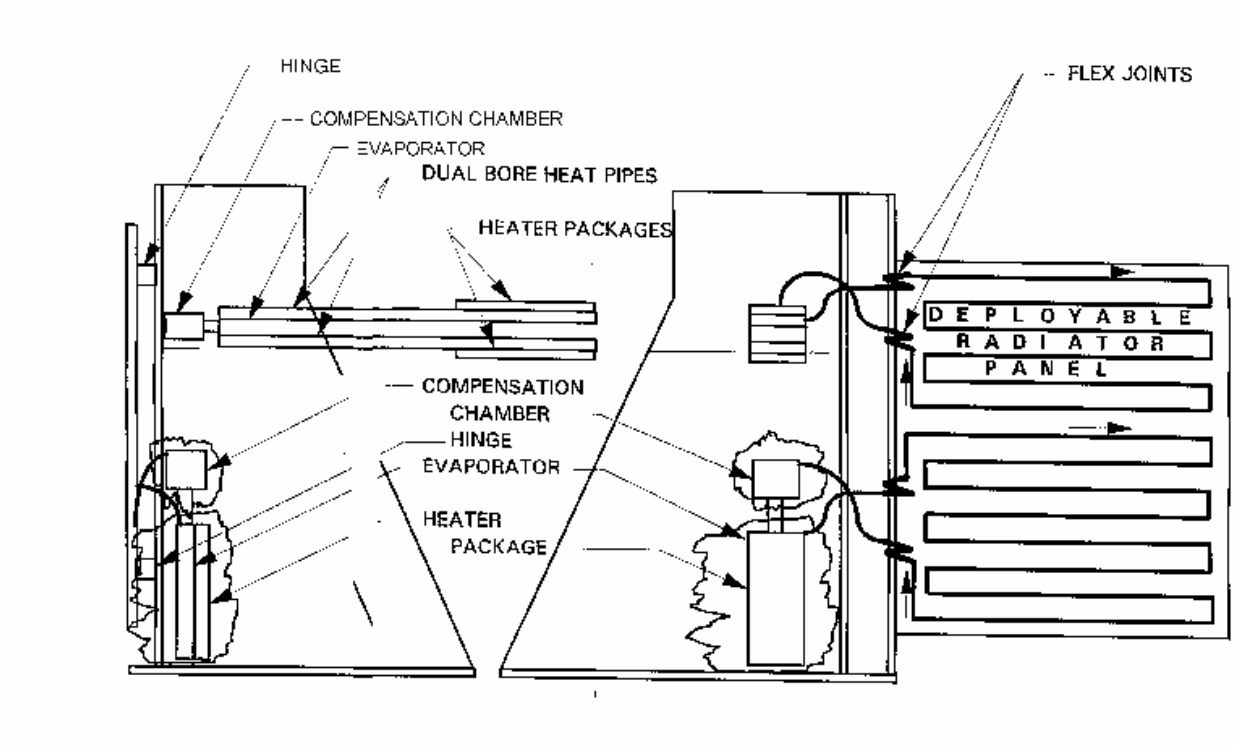

FIGURE 3. TEST SETUP

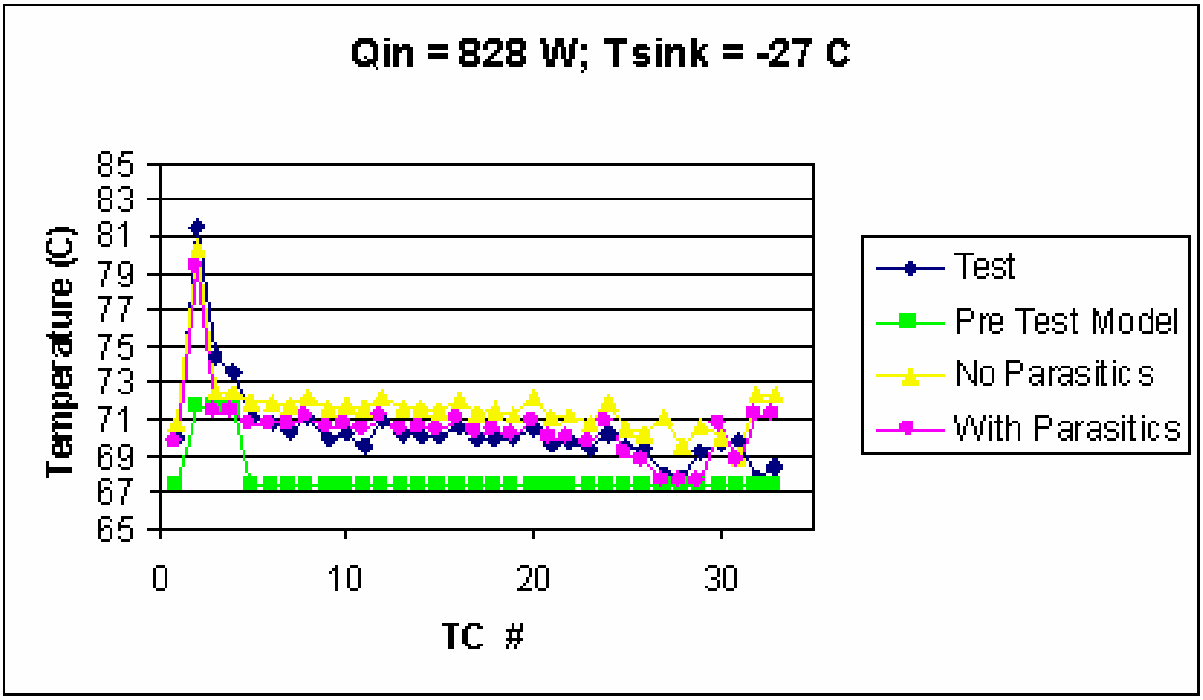

FIGURE 4. MODEL RESULTS

INTEGRATING THERMAL TOOLS INTO THE MECHANICAL DESIGN PROCESS

Glenn T. Tsuyuki, Georg Siebes, Keith S. Novak, and Gary M. Kinsella
California Institute of Technology
Jet Propulsion Laboratory
Pasadena, California 91109

SUMMARY

The intent of mechanical design is to deliver a hardware product that meets or exceeds customer expectations, while reducing cycle time and cost. To this end, an integrated mechanical design process enables the idea of parallel development (concurrent engineering). This represents a shift from the traditional mechanical design process. With such a concurrent process, there are significant issues that have to be identified and addressed before re-engineering the mechanical design process to facilitate concurrent engineering. These issues also assist in the integration and re-engineering of the thermal design sub-process since it resides within the entire mechanical design process. With these issues in mind, a thermal design sub-process can be re-defined in a manner that has a higher probability of acceptance, thus enabling an integrated mechanical design process. However, the actual implementation is not always problem-free. Experience in applying the thermal design sub-process to actual situations provides the evidence for improvement, but more importantly, for judging the viability and feasibility of the sub-process.

INTRODUCTION

Integration of engineering analysis tools into computer-aided design/computer-aided engineering (CAD/CAE) environments is highly attractive since it holds the promise that the entire mechanical design process becomes concurrent. Such an integrated process enables the efficient overall evolution of a particular design. While design and analysis are conducted, machining paths for manufacturing, strategies for assembly, and plans for inspection can be developed. Automated finite-element modeling tools have supported this vision for quite some time. The ability to link finite-element modeling tools with (CAD/CAE) tools has been demonstrated for many applications, such as Auto Desktop, Pro Engineer, and I-DEAS Master Series. On the other hand, space-borne system-level thermal design (i.e., design beyond the part level) has not been available in an integrated environment without compromise or the penalty of a significant training effort.

The entire mechanical design process is composed of sub-processes such as configurational design, structural design, and thermal design. With increasing pressures on competitiveness and reduction in cycle time, it is necessary to redefine the system-level thermal design sub-process. The thermal design sub-process must strive to maximize the design activity and to minimize mundane, but necessary activities such as analytical model development. With the “big picture” in mind, re-engineering the thermal design sub-process should strive to globally optimize the overall mechanical design process.

The desired future state is an integrated mechanical design tool that has CAD/CAE, analysis, manufacturing, assembly, and inspection modules. CAD/CAE packages such as Pro Engineer and I-DEAS are striving to approach this ideal. However, it is fair to say that such an ideal for system-level aerospace applications is still several years into the future. The purpose of this paper is to describe the primary issues surrounding the integration of the thermal design sub-process into the entire mechanical design process, to suggest an integration approach that affords a higher probability of success, and to present lessons learned in exercising this integrated approach.

CONCURRENT ENGINEERING

First of all, it is necessary to clarify some terminology. Producing the “mechanical design” (from art to part) is the whole *process*. This process is composed of *sub-processes* such as design or analysis. Specific *activities* such as design assessment or testing are performed within each sub-process. The relationships between process, sub-process, and activity are shown in Figure 1.

The intent of a mechanical design is to deliver products that meet or exceed customer expectations, while reducing cycle time and cost. In reality, the final product is a mechanical system, where its compliance with requirements is measured against its system-level performance. However, in more traditional approaches the mechanical design has been developed by serial iteration with the various sub-processes (e.g., structural design, thermal design, and optical design). The demonstration of end-to-end system performance through analysis has been formidable in scope and protracted in time. In the face of budgetary (time and money) constraints, the ability to remain competitive is severely hampered with a traditional approach. Additionally, other sub-processes such as manufacturing, assembly, and inspection are deferred until the design matures. Again, this further increases the protracted lifecycle of a mechanical design.

In order to facilitate the mechanical design process, preliminary designs are analyzed with several idealizations. As the design matures, some of these idealizations are removed so that a more realistic representation of the actual performance can be obtained through analysis. There have been instances where serious design inadequacies have been uncovered late in the design life cycle. Such deficiencies could have been discovered earlier if the mechanical design process was more streamlined. The system-level nature of the thermal design sub-process is self-evident since thermal design issues permeate through most flight hardware. Compliance with thermal requirements is not the sole responsibility of the thermal engineer. From a system-level perspective, one of the primary thermal design objectives is to minimize consumption of system-level resources (mass, power, cost, schedule, etc.) within the given constraints. The ability to discover mechanical design deficiencies as early as possible increases the likelihood of developing a robust thermal design. Mechanical design deficiencies can be discovered not only in design development, but also in other sub-process such as manufacturing, assembly, and test. Lastly, today's competitive environment dictates that more design development be performed with less cost and schedule. Evolution of the thermal design sub-process is imperative since the traditional thermal design sub-process probably cannot meet more demanding cost and schedule constraints..

AN INTEGRATED MECHANICAL DESIGN PROCESS

An integrated mechanical design process permits the parallel development of the design, manufacturing, assembly, and inspection sub-processes. The emphasis of the design is at a system-level since each sub-process is concerned with the entire mechanical system. Obviously, a tool that assists an integrated mechanical design process is practically a prerequisite. Most importantly, the system-level performance can be more easily assessed, because problematic data interfaces between sub-processes would be seamless. Additionally, this would free the engineer from mundane or repetitive activities such as analytical model development or product database management to concentrate more on the creative design activity. To this end, CAD/CAE tools have incorporated many of the pertinent sub-processes such as analysis, manufacturing, and inspection. Some of the more familiar integrated CAD/CAE tools are AutoDesk, Pro Engineer, and I-DEAS Master Series.

Typically, engineers and designers spend an inordinate amount of time searching for and compiling product data. The cornerstone of the integrated mechanical design process is the product parameter database. This database is the complete mechanical description of the hardware product, which includes information such as the mechanical configuration, materials, mission design (orbital trajectory), and electrical power dissipation. A salient feature of this database is its comprehensive nature. Newly assigned personnel would have a single source for product information. The control of this database is typically a single authority, be it a single individual or a single organization. Database access is usually provided by a product database management system within the highly integrated tool. For ISO 9001 registered organizations, the documentation of design control would be very straightforward. Engineers and designers would have immediate access to the most current product data, virtually eliminating the need for local product databases.

As shown in Figure 2, the product database resides at the center of the mechanical design process. Sub-processes have ready access to the product database, and this permits each individual sub-process to be conducted in parallel. In the natural course of design, each sub-process may identify mechanical design revisions. If approved by the governing product database manager, each other sub-process owner is notified of the change and requested to assess the impact of the change on their sub-process. As stated earlier, sub-processes such as manufacturing and assembly can take a proactive stance by initiating their activities concurrently with the design and analysis sub-processes. Additionally, the design process lifecycle can be significantly reduced.

From a cursory glance, this proposed ideal process seems best suited for the detailed design phase, commonly referred to a "Phase C/D." However, this process can and should be used for earlier design development phases. The product database will lack some maturity, but an early assessment of system-level performance, especially with optical or radio frequency systems, should be established. This performance assessment also should include the ease of manufacturing, assembly, test, and inspection, sub-processes that are not usually addressed early in the design cycle.

Focusing on the thermal design sub-process, the most noticeable benefits are: 1) better access and control of most of the crucial thermal product data, 2) more widespread use of automated analytical model development, and 3) improved data interfacing with other sub-processes or sub-process activities. The underlying theme is improvement of sub-process efficiency which enables the thermal engineer to accomplish more design trade studies in a given time period (or to accomplish a given activity in a shorter time).

INTEGRATED MECHANICAL DESIGN ISSUES

While the benefits of an integrated mechanical design process are alluring, there are some major stumbling blocks that must be overcome. Even prior to exercising an integrated mechanical process task, some of these issues are readily apparent. For convenience, the issues are categorized as logistical and psychological. The logistical issues can be easily stated, and potentially solved with some definition of a process or procedure (similar to ISO 9001 documentation). However, the psychological issues are not easily resolved since humans are involved. The key to developing a solution to the psychological issues lies with understanding the mindset of the workgroup. One solution is to develop approaches that have a higher probability of being accepted and, ultimately, adopted. This concept is known as "ownership" or "buy-in."

Logistical Issues

1) Product parameter database accommodation for thermal design – a CAD/CAE configuration database tends to include a great deal of detail since it represents the actual hardware product. On the other hand, analytical thermal models are usually simplified, but faithful representations of the configuration. Configuration details such as number of fasteners or chamfered corners are typically inconsequential to thermal engineers. In addition, a plethora of such details makes the database unwieldy, difficult to work with, and hard to modify. Therefore, the CAD/CAE product database for the thermal design sub-process should include a simplified geometric representation of the hardware. It is this simplified geometry that will be the genesis of analytical models. The simplified geometric representation will be tailored specifically to the thermal design sub-process. Some coordination between the specific sub-processes (e.g., thermal and structural design) is required so that there are no technical data interface gaps (e.g., temperatures can be specified for all structural grid points).

The biggest issue is the development of a simplified geometric representation (sometimes referred as a "skeleton model"). One logical approach is to start with the detailed configuration and then modify it by removing and simplifying thermally unnecessary geometry. This requires proficiency with the CAD/CAE tool that the mechanical designer (not the thermal design engineer) usually possesses. However, the thermal engineer determines the degree of geometric simplification that is necessary and appropriate. The question is: "Who should develop the simplified geometric representation?" In an ideal situation, the thermal engineer would be skilled with the CAD/CAE tool, but in practice, the mechanical designer and the thermal engineer must work together to develop the simplified geometry. As both the designer and engineer cycle through the mechanical design process, they will begin to cross-train in the deficient areas

2) Data transfer to other sub-processes – It is highly likely that the thermal and structural analytical models will not be of the same fidelity. Mapping of temperatures from a relatively coarse thermal model onto a finer structural model has been a longstanding issue. There are some stand-alone mapping routines (refs. 1-3). In recognition of this issue, the integrated CAD/CAE tool should have provisions to handle this mapping procedure by integrating existing routines or by developing better ones.

3) Analytical thermal model size – The temperature mapping issue can be avoided by using the same fidelity as the structural finite-element model (FEM). Such models typically have many more nodes than the thermal model, sometimes approaching a few thousand nodes. Finite-difference solvers such as SINDA (refs. 4 and 5) have node

and conductor limitations that are less than FEM solvers. Evolution of traditional thermal tools (e.g., SINDA) will be required to accommodate larger model sizes. If this does not occur, an opportunity for new FEM thermal solvers such as IMOS (ref. 6) may emerge. Troubleshooting and understanding results from large models have always been difficult. A portion of this issue is addressed by incorporating the ability to display temperature results graphically. Isotherms, themselves, do not provide the entire picture. Temperatures are merely the consequences of heat flow. Incorporating the ability to display the heat flow field is a necessity for interpretation of model results. The heat flow visualization option is not readily available from common FEM tools.

4) Analytical thermal modeling – With the use of FEM for thermal analysis, the modeling of thermal hardware such as louvers and closed-looped heater control become more difficult, if not impossible. The shear number of FEM grid points (or thermal nodes) will complicate the identification and simulation of thermal hardware.

5) Populating the product parameter database –Information is power, and this is very much the truth with the mechanical design process. The centralized product parameter database is a formidable body of knowledge. Constructing this database is huge task in itself, and facilitating the population the database is imperative so that the mechanical design process can be responsive. The issue of collecting and controlling product information is fundamental to this process.

In recognition of this problem, a procedure has been developed to expedite the collection of thermal-related product data (ref. 7). The procedure relies upon an intensive initial collaborative effort between senior thermal and systems engineers. The centerpiece of this procedure is comprehensive set of thermal design questions whose answers provide the basic structure for the thermal-related product data. Prior to the initiation of the pure thermal design sub-process, senior thermal and systems engineers complete the thermal engineering data survey to the best of their ability. It is expected that this procedure would take four to eight weeks depending on the system design maturity. Once the thermal design sub-process begins, the thermal design team will have an excellent point of departure. This procedure can be replicated for other sub-process so that the entire product parameter database can be assembled.

Psychological Issues

1) Sub-process “buy-in”— The integrated mechanical design process represents a major change in conducting business. People have a natural resistance to change. While it is quite easy to focus on the positive aspects, the real issue is at the working level. The engineers who will be implementing the integrated processes and sub-processes must be convinced that this change is sensible, appropriate, and necessary. To ignore a negative mindset is analogous to ignoring a design flaw until after the hardware is delivered. In this analogy, a tremendous amount of time and workforce is expended to fix the hardware. In the same manner, a tremendous amount of time and management energy late in the schedule will be expended if the integrated process is forced upon resistant working-level engineers. An integrated mechanical design process that is entirely new and abruptly adopted will probably meet a large wave of resistance, and ultimately its acceptance as a standard process will probably fail. Replacing an existing process with one that has no pedigree with the past casts doubt upon whether the previous process was appropriate at all. Additionally, a challenging burden is placed on the working-level engineers to quickly learn the new process and to produce real results. A more enlightened approach to change involves linking new processes with positive attributes from the previous processes. The working-level engineers should be involved in many of the aspects of the transition from the existing process to the new process. The idea is to obtain “buy-in” at the initiation of a new process rather than somewhere downstream.

2) Training engineers to become proficient with the process – Although this issue can be categorized under logistics, training is intimately related to “buy-in.” It is very reasonable to expect a regimen of training. However, it rarely occurs in an effective fashion or in a sufficient amount. Again, involving working-level engineers in the planning and scheduling of training will help to define an effective regimen. Once initial training has commenced, a strategy for introducing the process into a production mode is required. The benefits of changing the process probably will not be realized in the short-term. In fact, the process change can result in higher cost and longer schedules which should be understood and accepted by management. Management needs to provide tangible evidence of endorsement. The strongest form of endorsement is to become familiar with the process by participating in the same training. Other indications of management endorsement include providing separate labor funding for training, accommodating work schedule to facilitate training, and taking a long-term return-on-investment perspective.

THE THERMAL DESIGN SUB-PROCESS

Previous discussion has been centered on an ideal integrated mechanical design process. This ideal is far from standard practice in the current aerospace industry. Currently, there is no one CAD/CAE tool that may serve as an aerospace standard to support the integrated mechanical design process. Hence, the change from the traditional to the ideal mechanical design process should be a metered approach, using a series of steps to achieve the integrated mechanical design process. By understanding the gap between the traditional and ideal process and by taking stock in the identified issues, some decisions surrounding the integration of the thermal design sub-process can be established. Similarly, the thermal design sub-process will change commensurately with the mechanical design process (i.e., in carefully planned steps). Therefore, the first wave of change will align the thermal design sub-process with the ideal state. It is the first step in the thermal design sub-process evolution. While the ultimate goal is an integrated mechanical design process, the first objective is to develop a thermal design sub-process, which initiates integration and is likely to be adopted.

By examining the issues with the ideal mechanical design process, a great deal of insight can be extracted about the first step for the thermal design sub-process. The psychological issues are the most important ones. Even the most technically rigorous tool will be doomed for abandonment if the working level engineers do not truly believe that it is the "right" tool. Change is a self-realization process, and it would be highly arrogant to force-feed a new sub-process. Training is next in priority, and a sub-process that attempts to maintain some heritage with the previous sub-process will have a higher probability of acceptance (and ultimately gain "buy-in"). Most engineers would like to build on previous knowledge and experience, and recognition of this mindset is very important to defining an integrated thermal design sub-process. The logistical issues follow behind the psychological ones with regard to priority. This is not to belittle their seriousness or stature. Logistical issues can be defined in concrete terms, and so their solutions are more tractable than psychological issues. The top logistical issue is the development of the thermal "skeleton" database (geometry and other thermal-related product data). This is critical to the success of the integrated mechanical design process.

The proposed first wave of change for the thermal design sub-process spans the gap between traditional thermal tools and CAD/CAE tools. The "bridges" are translators that take a skeleton geometry and transform them into an analytical thermal model. Commercially-supported translators were selected to avoid any unnecessary tool development, and to relieve the burden of troubleshooting translator bugs. The foremost reason for such an approach is centered on the psychological issues. On the top of most thermal engineer's wish list is the automated development of an analytical thermal model. A thermal design sub-process that enables automated model generation and is still linked with traditional thermal tools has a high probability of acceptance. The training associated with this sub-process is focused on the automated model development. Obviously, there is no training involved with the thermal tools. Again, the training is not as formidable or protracted as an entirely new tool such as I-DEAS Master Series, and the possibility of sub-process use is higher than a totally new tool. Another salient feature with this sub-process is its independence from the specific type of CAD/CAE tool. The aerospace industry has yet to unanimously adopt a single CAD/CAE tool standard. Being independent from any specific CAD/CAE tool provides a great deal of flexibility in applying this sub-process in conjunction with other CAD/CAE tools. Emphasis on data exchange formats rather than "tools" provides the necessary flexibility to develop an integrated design process. The skeleton geometry is preferably formatted using the IGES standard. However, other neutral formats such as DXF or NASTRAN can be accommodated. A future format is the promising Standard for the Exchange of Product Model Data (STEP, ref. 8). This reduces the amount of CAD/CAE tool proficiency that a typical thermal engineer requires. It should be noted that some basic CAD/CAE tool proficiency is required so that thermal-specific items such as thermal blanketing can be added to the "skeleton" geometry.

Figure 3 schematically depicts the thermal design sub-process. The product data is queried through a product data manager within the CAD/CAE tool. It is tacitly assumed that thermal-specific information such as the thermal blanket configuration has been added to the product data. The thermal skeleton database is extracted from the CAD/CAE tool and imported into a commercially-available, finite-element modeler, FEMAP (ref. 9). FEMAP was initially developed as pre- and post-processor for structural FEMs. With a graphical user interface (GUI), the user can construct an FEM, and after conducting the analysis elsewhere, the results can be graphically shown within FEMAP. Recently, upgrades were incorporated into FEMAP to permit the development of FEMs for thermal analysis. FEMAP is the workhorse tool of the thermal design sub-process. It is used to develop the FEM from the simplified geometry within the skeleton database. The FEM is developed using specific two- and three-dimensional

elements (e.g., plates, laminates, membranes, bricks, and tetrahedra). FEMAP is not a "true shape" modeler; items such as cylindrical or spherical shells are approximated with plates. Additionally, the thermophysical properties such as thermal conductivity and specific heat as well as mechanical properties such as density are prescribed. Variable thermal conductivity and/or specific heat can be accommodated by FEMAP. Heat loads from internal power dissipation may also be assigned. These attributes assist in the determination of the thermal math model (TMM). The thermo-optical properties are assigned and doubly-active geometry is identified for the development of the geometric math model (GMM).

From FEMAP, TCON (ref. 3) can be used to develop the input files for the traditional thermal tools. This commercially-available tool was developed under a small business innovation research grant with the Goddard Space Flight Center. TCON is a translator that imports the FEMAP data and creates a TMM and a GMM based on the finite-element grid. This usually includes node and conductor definition, array specifications if there are variable thermophysical properties, and SINDA execution control constants such as absolute temperature scale, solution routine, and convergence criteria. The user must incorporate any variable logic and output options. There is flexibility to create a SINDA/G (ref. 4) or a SINDA/FLUINT (ref. 5) formatted TMM.

In most space-borne thermal designs, it is necessary to develop a GMM to determine overall radiation interchange within the TMM and to calculate absorbed environmental heating (i.e., direct solar, planetary albedo, and planetary emissive). Once the FEMAP data has been imported into TCON, a GMM that contains the entire geometry can be generated. At this time, it is not possible to distinguish "internal" geometry from "external" geometry. Separation of internal and external geometries must be performed manually. TCON can generate a TRASYS (ref. 10) or a TSS (ref. 11) formatted GMM. In this particular thermal design sub-process, TSS is the preferred thermal radiation tool because of its use of the Monte Carlo ray-tracing and GUI features.

Once the GMM and the TMM have been generated, the specific thermal tools (i.e. SINDA/G or SINDA/FLUINT and TSS) are used to perform the analysis. TCON generates output logic to create an ASCII temperature output file that may be imported into FEMAP. Within FEMAP, the isotherms are graphically presented. The MAPBACK routine within TCON permits the mapping of temperature results onto the structural FEM. The thermal and structural FEM grids do not need to be equivalent. The mapped temperature file can be readily used by a structural analysis tool such as NASTRAN.

LESSONS LEARNED

The Goddard Space Flight Center developed the path between FEMAP and the traditional thermal tools. The work described herein has linked FEMAP and the product data. This proposed thermal design sub-process has been used for a few thermal design activities, and the experience has been invaluable in identifying the capabilities and limitations of this sub-process.

The initial roll-out of the thermal design sub-process was hastily prepared. While there was buy-in at the management level, the sub-process was imposed on the working-level engineers without sufficient training. As one can imagine, there was a sundry of problems. Because the thermal skeleton geometry had not been developed, importing the product data into the FEM tool was arduous and frustrating. The working-level thermal engineer struggled with the FEM meshing, because of the lack of training. Additionally, the resulting TMM was too large for the capability of SINDA/G. When the thermal skeleton geometry started development, the CAD/CAE designer was distracted with other activities, and the skeleton geometry was never completed to the satisfaction of the thermal engineer. In short, the initial roll-out was a dismal failure since implementation of the thermal design sub-process was not well-thought out.

Shortly afterward, a small thermal team was formed to receive some training and to put the sub-process through some trial cases. This team was formed with thermal engineers with a keen interest in this sub-process. At the same time, an upgrade to FEMAP was released, which had improved IGES translation capability. Some classroom training for FEMAP and TCON was conducted, and the link between FEMAP and the traditional thermal tools was established for the first time on a working level. Rudimentary thermal analysis problems (e.g. insulated flat plate in Earth orbit) were undertaken and were validated with hand-calculations. The team generated a preliminary thermal design sub-process primer (ref. 12) for other thermal engineers to consult.

The next usage of the sub-process demonstrated some success. An avionics support structure (X2000 Integrated Avionics Structure) was analyzed to assess the benefit of using composite materials versus aluminum. The product data was imported into FEMAP, and the geometry was translated as "solids." The working-level thermal engineer did not have the proficiency to mesh the solid geometry. At this point, it is not clear whether solid geometry can be meshed for thermal modeling purposes. However, there were discrete geometry points, and these were utilized to create the thermal FEM within FEMAP. In turn, the SINDA/G model was easily created. This model was a conduction only TMM, and a GMM was not required. The results for the aluminum structure are shown in Figure 4. As noted previously, the development of the thermal skeleton geometry is a must for this sub-process. Additionally, the need for the CAD/CAE designer and thermal engineer to interact in the definition of thermal pertinent product data was shown clearly in this case.

During the same time the avionics support structure analysis were underway, an inflatable radio interferometry antenna (the Advanced Radio Interferometry Between Space and Earth, ARISE) thermal analysis was being conducted. This was the first full use of the thermal design sub-process since the analytical determination of the interferometric performance was derived from thermostructural distortion analysis. Due to the preliminary stage of the project, the product data had not been formally established. However, a structural FEM had been developed. Through discussions with the structural engineer, the applicability of the structural FEM for thermal modeling was established. It was determined that small modifications such as ignoring the vacuum-deposited aluminum layers on the reflector were required. These changes were implemented with FEMAP and SINDA/FLUINT TMM was easily created. However, the structural and thermal FEMs maintained a one-to-one grid point correspondence. One salient feature of TCON is its ability to always generate positive conductance values. When triangular elements are generated, negative thermal conductance will result when one of the triangular interior angle is greater than ninety degrees. However, TCON recognizes this situation and employs a different, but rigorous method to determine the thermal conductances.

The generation of the antenna GMM proved to be more difficult. A number of TCON bugs were uncovered when translating the FEM to a TSS GMM. Most of them were minor, for example the declaration of the initial conductor, an option not used for the GMM, but required for completeness, was not specified. The most serious bug was the incorrect translation of a trapezoid. The TCON vendor eventually solved all the identified bugs, but the GMM development took longer than expected. The size of the TSS GMM was at the maximum capability of TSS. System memory was nearly depleted during a TSS calculation, and the size of temporary files nearly depleted available hard disk space. The oversight occurred in the assessment of the structural FEM for thermal analysis use. Even though, the number of FEM grid points was modest (~500), the number of GMM surfaces created could increase by an order of magnitude. This is because a thermal node (i.e., FEM grid point) is made up of portions of all surrounding elements (e.g. in a rectangular mesh, each node can be surrounded by four element, implying four separate GMM surfaces). The resulting TSS GMM for this antenna had nearly 3600 surfaces. Fortunately, radiation interchange factors and absorbed environmental heating were computed successfully.

The antenna system isotherms when positioned at the sub-solar are shown in Figure 5. FEMAP was used to transport these results to the structural model. The thermostructural distortions were determined and subsequently so was the interferometric performance.

CONCLUSIONS

This proposed thermal design sub-process is the first step in evolving toward a truly integrated mechanical design process. As demonstrated previous, the proposed sub-process is still in the incipient stages of usage, and some pitfalls have been uncovered. At the same time, this sub-process has shown promise for its use on component- and system-level. Over its short life span, there has been many lessons learned. The key to its subsistence is buy-in from the working-level engineers. Since FEMAP has its heritage with structural design and analysis, most thermal engineers indicated that FEMAP is not organized from a thermal design and analysis perspective. The FEMAP, TCON, and SINDA/G vendors are currently considering a collaborative effort to integrate this tool suite. The development of the thermal skeleton geometry remains a major open issue.

This proposed thermal design sub-process was developed by understanding the underlying logistical and psychological issues of an ideal mechanical design process. It is likely that the ideal mechanical design process will continue to evolve with time, so the thermal design sub-process will need to evolve as well. The identification of

the ideal mechanical design process issues will dictate how the thermal design sub-process evolves. Integrated mechanical design tools that were presently dismissed should be monitored so their future benefit may be known. Other efforts such as STEP should be closely watched for its possible incorporation into the integrated mechanical design process.

ACKNOWLEDGEMENTS

The authors would like to acknowledge the Develop New Products Domain at the Jet Propulsion Laboratory (JPL) for providing the funding and oversight of the work described in this paper. The domain process owner is Dr. William Weber. Recognition is due to the Design, Build, Assemble, and Test Sub-Domain at JPL, with Mr. Phillip Garrison as sub-domain process owner. The Mechanical Design Build, Assemble, and Test Process effort is responsible for the re-engineering of the mechanical design process, with Mr. Michael Mangano as sub-process owner. Mr. Arthur Fanzon was the initial sub-process owner. Mr. Richard Helms and Dr. Paul McElroy helped define and develop the initial thermal design sub-process. The authors are indebted to Dr. Robert Norton and Mr. Anthony Melak for conducting FEMAP and TCON training. Finally, the authors would like to acknowledge the support of their line management, Mr. Brian McGlinchey, Mr. Wesley Menard, and Mr. Timothy O'Donnell, for the accomplishment of this work

The work described in this paper was carried out by the Jet Propulsion Laboratory, California Institute of Technology, under a contract with the National Aeronautics and Space Administration. Reference herein to any specific commercial product, process, or service by trade name, trademark, manufacturer, or otherwise, does not constitute of imply its endorsement by the United States Government or the Jet Propulsion Laboratory, California Institute of Technology.

REFERENCES

1. Crouthamel, M. "PATSIN Interface Guide," PATRAN Division, PDA Engineering, March 1990.
2. Anonymous. "SNIP – SINDA to NASTRAN Interface Program," COSMIC, University of Georgia, Athens, GA, 1997.
3. Costello, F. "TCON Rapid Thermal Modeler User's Manual," FAC, Inc. Herndon, VA, 1997.
4. Anonymous. "SINDA/G User's Guide," First Edition, Network Analysis Associates, Inc., Fountain Valley, CA, 1994.
5. Cullimore, B.A., Ring, S.G., Lucas, S.L., Goble, R.G., and Jensen, C.L. "SINDA/FLUINT, Systems Improved Numerical Differencing Analyzer and Fluid Integrator, Version 4.0, User's Manual," Cullimore and Ring Technologies, Inc., Littleton, CO, October 1997.
6. "Milman, M., Needels, L., and Papalexandris, M. "Integrated Modeling Tools for Thermal Analysis and Applications," Proceedings of the Ninth Thermal and Fluids Analysis Workshop, NASA Lewis Research Center, Cleveland, OH, August 1997.
7. Kinsella, G. "Fast Track Engineering, Thermal Engineering Data Survey," JPL Internal Document 3534-REN-97-003, Jet Propulsion Laboratory, Pasadena, CA, November 12, 1997.
8. Hunten, K.A. "CAD/FEA Integration with STEP AP209 Technology and Implementation," Virtual Product Development Initiative, Lockheed Martin Tactical Aircraft Systems, Forth Worth, TX, 1997.
9. Anonymous. "FEMAP Version 5.0 User Guide," Enterprise Software Products, Inc., Exton, PA, 1997.
10. Anonymous. "Thermal Radiation Analyzer System (TRASYS) User's Manual," LEMSCO-22641, Lockheed Engineering and Management Services Company, Houston, TX, December 1987
11. Welch, M.J., Fogerson, P.E., and Lepore, J.M. "User Manual, Thermal Synthesizer System, Release 3.01," LESC-31078, Lockheed Engineering & Sciences Company, Houston, TX, September 1994.
12. Thermal Reengineering Team. "Concurrent Engineering Process: Thermal Reengineering Instructional Primer," JPL Internal Document 3534-REN-97-004, Jet Propulsion Laboratory, Pasadena, CA, December 25, 1997.

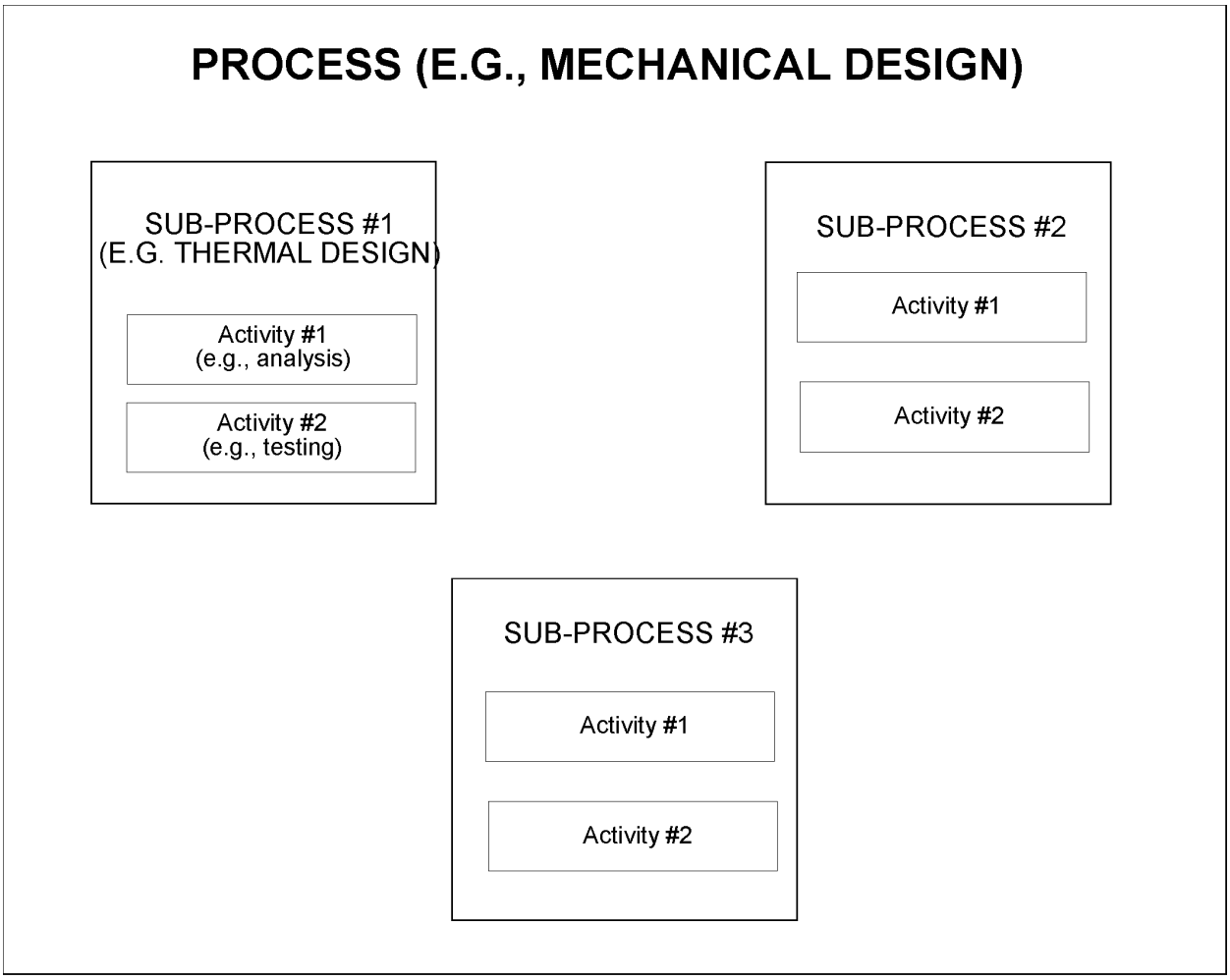

Figure 1—Relationships between process, sub-process, and activity.

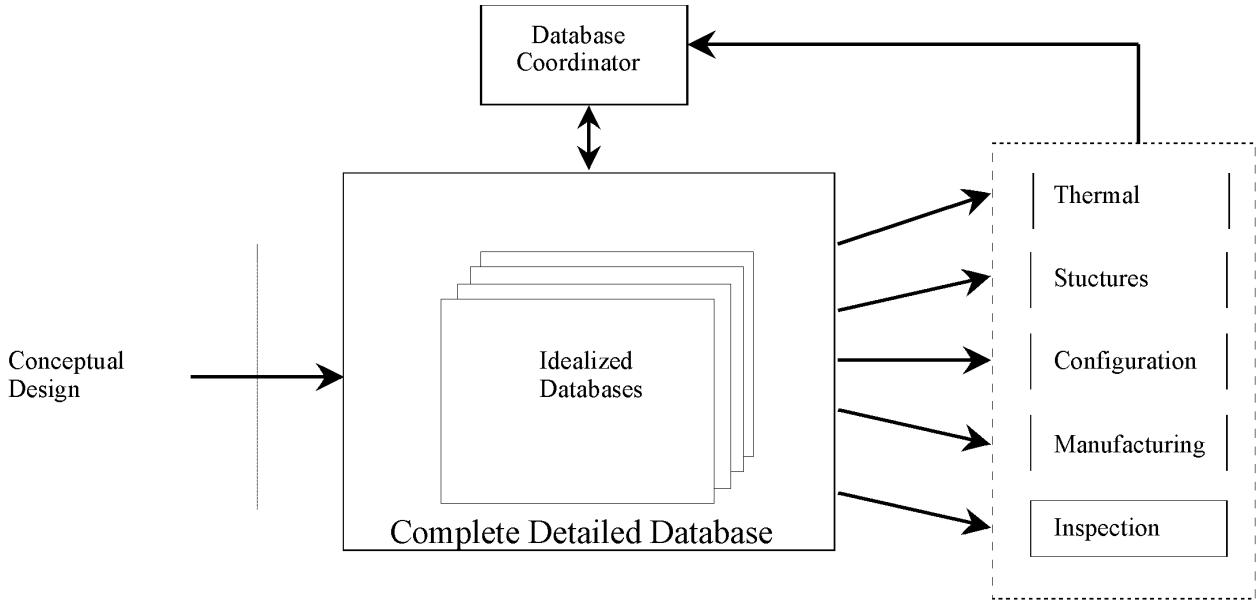

Figure 2—The product database and its relationship to other sub-processes.

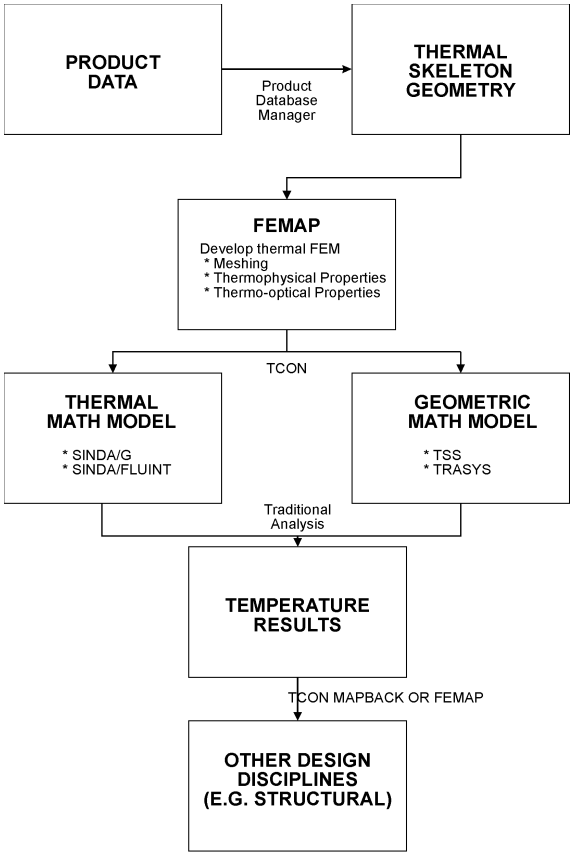

Figure 3—Integrated thermal design sub-process flow diagram.

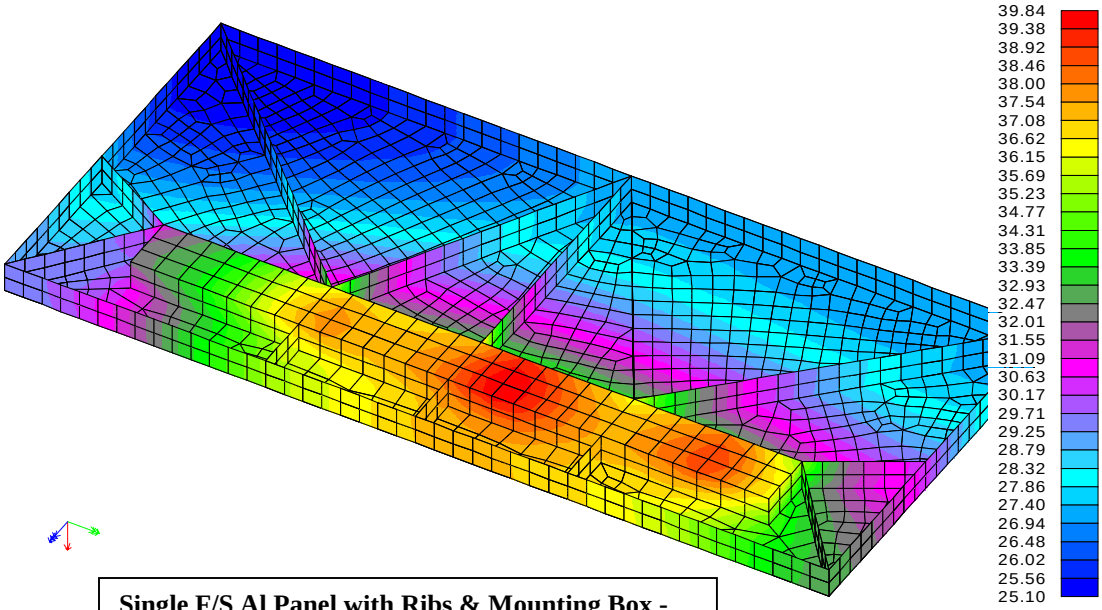

Single F/S Al Panel with Ribs & Mounting Box -

- Design #5, mass = 2.00 kg
- Max Boss Temp = 39.8C at Q = 49.5W
- Max Heat Rejection = 52.5W at Tmax = 45C
- 89% efficient

Figure 4—X2000 IAS all-aluminum temperature results.

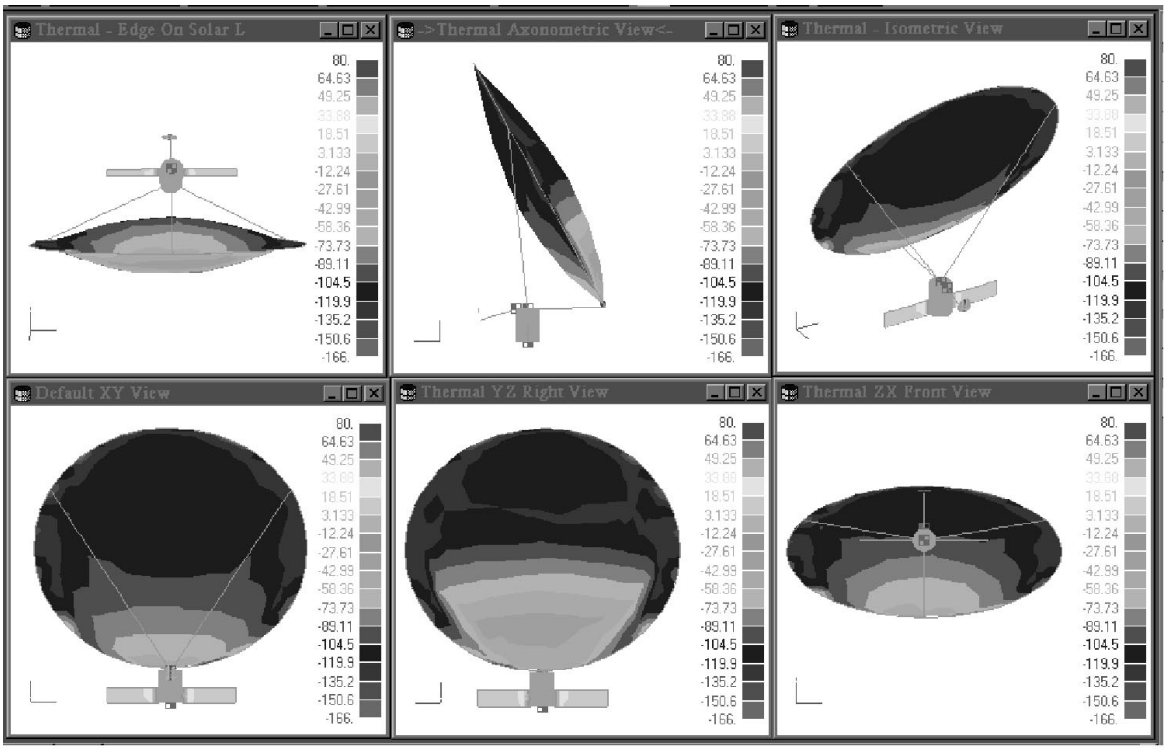

Figure 5—ARISE on-orbit temperatures (in degrees Celsius).

NUMERICAL THERMAL MODEL OF A 30-CM NSTAR ION THRUSTER

Jon Van Noord and Alec Gallimore
University of Michigan
Ann Arbor, Michigan 48109-2118

Vincent K. Rawlin
National Aeronautics and Space Administration
Lewis Research Center
Cleveland, Ohio 44135

ABSTRACT

A thermal computer model of the NSTAR xenon ion thruster has been produced using a lumped parameter thermal nodal network scheme. This model contains 104 nodes on the thruster and was implemented using SINDA and TRASYS on various UNIX workstations. The model includes radiation and conduction heat transfer, the effect of plasma interaction on the thruster, and an account for finely perforated surfaces. The model was developed in conjunction with an NSTAR thruster outfitted with approximately 20 thermocouples for thermal testing at the NASA Lewis Research Center. The results of these experiments were used to calibrate and confirm the computer model first without and then with the plasma interaction. The calibrated model was able to predict discharge chamber temperatures to within 10°C of measured temperatures. To demonstrate the ability of the model under various circumstances the heat flux was examined for a thruster operating in the environment of space.

NOMENCLATURE

A_I = area of Ith element, m^2
A_J = area of Jth element, m^2
C_i = thermal capacitance at node i, cal/g · K
F_{ij} = form (view) factor
G_{ji} = linear conductor attaching node j to node i, W/K
H_{ji} = radiation conductor attaching node j to node i, W/K^4
J_A = ion current hitting grid, A
J_B = ion beam current, A
N = number of nodes
Q_i = heat source or sink for node i, W
r_{ij} = distance between the ith and j^{th} element, m
T_j^k = temperature of node j for the kth iteration, K
T_i^{k+1} = temperature of node i for the k+1 iteration , K
T_j^n = temperature of node j at time t, K
T_i^{n+1} = temperature of node i at time t+Δt, K
U_+ = ionization energy, eV
V_P = plasma potential, V
Φ_{sh} = energy deposited in the form of heat, W
Φ_T = total thruster power, W
Φ_N = neutralizer power, W
θ_i = angle between normal of ith element and the line connecting the ith and j^{th} element, radians
θ_j = angle between normal of jth element and the line connecting the ith and j^{th} element, radians

INTRODUCTION

The 30-cm-diameter ring cusp NSTAR ion thruster represents the state-of-the-art in ion thruster technology. Ion thrusters have long been known to have the highest efficiency at high specific impulse of all electric propulsion devices. The combination of high power utilization efficiency at specific impulses in excess of 3,000 seconds has made the ion engine an attractive candidate for high delta-V planetary missions.

Despite these advantages, however, application of ion propulsion to scientific, military, and commercial spacecraft was hampered in the past by perceived high engine development costs and the inability of spacecraft manufacturers to reliably identify potential integration and thruster lifetime issues. The primary concerns that spacecraft manufacturers had in regards to using ion propulsion included the likely impact of thruster operation on spacecraft design and operations, electromagnetic compatibility, spacecraft contamination from thruster efflux, spacecraft damage from the plume, thruster reliability, and thermal loading of the spacecraft from the thruster. Ion propulsion became (and will continue to become) more attractive once tools were developed (e.g., plume PIC codes) (ref. 1) which helped spacecraft manufacturers identify potential spacecraft integration issues associated with this technology.

Given the wide range of thermal environments an ion thruster on a deep-mission will likely encounter, it is essential that computer tools be developed to predict the temperatures of thruster components over the expected range of operating and thermal conditions. Some critical areas of concern include the degaussing of permanent magnets from excess heating, freezing of xenon in propellant lines (ref. 2), distortion of the ion optics from thermal gradients (ref. 3), and spacecraft integration issues in general (e.g., thermal soakback). Although work has been done in the past to model the thermal behavior of 20-cm-diameter (ref. 4) and 30-cm-diameter (ref. 5) divergent-field ion thrusters utilizing mercury propellant, no such model has been developed for modern ring-cusp xenon thrusters like the NSTAR engine. The most recent approaches used to develop the thermal models started with analytical models to determine thruster self-heating from the plasma but then relied on data from experiments to adjust the numerical model to fit measured thruster temperatures. This same approach was used to determine the self-heating terms on the NSTAR thruster. The tests used for calibrating this model were based on experiments performed at NASA Lewis Research Center in June and July of 1996.

Once adjusted to match experiments, the model can then be used to investigate other operating conditions. It has already been used to alert of the possible dangers of overheating the magnets at certain thruster settings. Other issues investigated but not presented here include enclosing the thruster in an adiabatic surface, changing materials on the thruster, and the influence of ambient conditions in space on the thruster.

MODEL DESCRIPTION

Thermal Model

There are two major modes of heat transfer which take place in the NSTAR thruster. The dominant process is radiation heat transfer, but conduction still plays a major role in establishing thruster component temperatures. The interaction of the plasma with the thruster will be discussed later. In order to handle a model of significant size and to study the thermal response of the thruster to various steady-state and periodic external radiation loads over its full range of operating conditions, a computer model was utilized using two well-used codes.

SINDA (Systems Improved Numerical Differencing Analyzer) analyzes thermal systems represented in electrical analogy, lumped parameter form. The "conductors" based on the conductive and radiative properties of the system are calculated between nodes and then included in the SINDA input file. The equation used for steady-state analysis in SINDA is:

$$0 = Q_i + \sum_{j=1}^{i-1}\left[G_{ji}\left(T_j^{k+1} - T_i^{k+1}\right) + H_{ji}\left\{\left(T_j^{k+1}\right)^4 - \left(T_i^{k+1}\right)^4\right\}\right] + \sum_{j=1}^{N}\left[G_{ji}\left(T_j^{k} - T_i^{k+1}\right) + H_{ji}\left\{\left(T_j^{k}\right)^4 - \left(T_i^{k+1}\right)^4\right\}\right] \quad (1)$$

which is solved by a "successive point" iterative method (ref. 6). The transient equation used is based on an implicit forward-backward differencing method:

$$\frac{2C_i}{\Delta t}\left(T_i^{n+1}-T_i^{n}\right)=2Q_i+\sum_{j=1}^{N}\left[G_{ji}\left(T_j^{n}-T_i^{n}\right)+H_{ji}\left\{\left(T_j^{n}\right)^4-\left(T_i^{n}\right)^4\right\}\right]$$
$$+\sum_{j=1}^{N}\left[G_{ji}\left(T_j^{n+1}-T_i^{n+1}\right)+H_{ji}\left\{\left(T_j^{n+1}\right)^4-\left(T_i^{n+1}\right)^4\right\}\right] \qquad (2)$$

For Equations (1) and (2) the radiation terms are linearized before solution routines are initiated.

The second piece of software used is TRASYS (Thermal Radiation Analyzer SYStem). TRASYS uses geometry and surface characteristics to provide radiation conductors for SINDA. TRASYS computes the radiation view factors using the Nusselt Sphere and double summation techniques (ref. 7). Both of these calculation methods are based on the equation:

$$F_{ij}=\frac{1}{A_I}\int_{A_I}\int_{A_J}\frac{\cos\theta_i\,\cos\theta_j}{\pi\, r_{ij}^2}\,dA_J\,dA_I \qquad (3)$$

which gives the view factor for two finite areas.

The NSTAR model contains 104 thruster nodes with conductors connecting the nodes for conduction and radiation heat transfer. The thruster is essentially broken up into 4 quadrants. However, two of the quadrants are further subdivided in half to accommodate the gimbal pads. Since the neutralizer has been shown to be insignificant in its thermal impact to the thruster (ref. 5), a simplified model of it was used. Figure 1 shows the nodal layout of the thruster. The nodal numbering scheme in this figure for off-axis nodes starts with the lowest number on the bottom (in the quadrant of the neutralizer) and then increases by one for each quadrant in a counterclockwise manner when viewed from the optics end of the thruster. This scheme is true for all the nodes except those on the neutralizer (400's), which are contained only in the one quadrant.

The tests which were used to calibrate the NSTAR model took place at the NASA Lewis Research Center (LeRC) (ref. 8). The experimental setup at LeRC included the thruster enclosed within a 116 cm-diameter liquid nitrogen cooled shroud contained in a 4.6-m-diameter by 19.5-m-long vacuum chamber. The model used temperature measurements along the shroud and tank walls to establish boundary conditions. These boundary nodes consisted of 37 nodes making up the shroud and experimental setup, and 6 nodes for the tank wall. The thruster was modeled as being isolated from the shroud and its test stand. The model does not include feed lines, electrical lines, or the isolator box as those are predicted to have minimal impact on the thermal characteristics of the thruster. Figure 2 shows the shroud/thruster setup in the model.

Since radiation is the major form of heat transfer within the thruster, accurate surface property values are very important. Changing materials or surface properties could modify the thermal characteristics of the thruster significantly. These properties could also change over the life of the thruster further complicating matters. For this model the emissivities of materials were assumed to be constant throughout the temperature range examined; a valid assumption for the conditions experienced by the thruster. Emissivities in the infrared surface temperature regime were obtained from published sources and also from experiments conducted with components of the NSTAR thruster (Table I). Joint conductances were modeled with a constant conductivity of 0.0057 W/cm^2 °C on the basis of experiments (ref. 5). All other material properties used in the model are listed in Table I.

Another surface characteristic which had to be modeled were the perforated surfaces, which TRASYS was not designed to model. To approximate these surfaces, transmissive values were assigned to allow the appropriate percentage of incident energy to pass through. The value used for the transmissivity corresponded to the open area fraction of the perforated surface. However, it is not clear how accurate this assumption is for modeling these surfaces. For example, transmissive surfaces in series will artificially block radiation which would normally travel through the aligned open areas of two perforated surfaces. Another approach in treating perforated surfaces is to model them as checkered surfaces. In this approach the amount of open area in the checkered surface corresponded

to the same amount of open area present in the perforated surface. The grids of the engine were modeled both as transmissive surfaces and as course checkered surfaces (Figure 3).

To determine the accuracy of these various thermophysical properties in the model, comparisons were done between the model and cold soak experiments with the non-operating thruster in the shroud.

Self-Heating due to Plasma Interaction

One of the more complex aspects of the thruster model is ascertaining the amount of thruster self-heating from the plasma interaction with surfaces. In order to determine analytically the amount of heat that is produced by the plasma, several characteristics must be well understood. One of which is the precise location of the deposition of charged particles on the various surfaces. The current produced by these particles and their corresponding temperatures are also relevant. Work is underway to model this process.

However, for this model, a method which was used in past work was applied (refs. 4,5). This method entailed using previous heat flux data from past work and then adjusting the values until the temperatures in the model agreed with the experimental data. Once the self-heating values were adjusted to correlate the temperatures from the model to the experiment, the total amount of energy used in self-heating was compared to the analytically derived amount. The total heat applied was determined analytically by taking the total energy added to the system and subtracting out the energy which exited the thruster in the beam. Equation 4 shows this energy balance.

$$\Phi_{sh} = \Phi_T - \Phi_N - (J_B - J_A)(V_P + U_+) \qquad (4)$$

The adjusted values of self-heating are shown in Figure 4 for the NSTAR thruster operating at 2.3 kW. Other operating levels were investigated, but only the 2.3 kW case is examined here since it was the highest operating power in the experiments and it would yield the highest temperatures to which the thruster would be exposed to.

RESULTS AND DISCUSSION

The computer model was first compared to the cold soak test which was done at LeRC. The shroud or enclosure which is shown in Figure 2 was cooled by liquid nitrogen. The open end of the shroud was closed off by a door which was cooled by the rest of the shroud through radiation. A ring piece was located close to the front (optics end) of the thruster face and was cooled through conduction with the cylindrical part of the shroud. It was used to minimize the amount of the thruster which interacted with the room temperature vacuum chamber wall. The shroud was painted with a commercial, high temperature, fireplace flat black paint which has a measured emissivity of 0.9.

The temperatures for the boundary conditions in the model consisted of monitored shroud temperatures. A total of 37 nodes were used in modeling the shroud and other experimental features such as the test stand.

Figure 5 shows a cross sectional view of the NSTAR thruster with the temperatures determined experimentally and by the SINDA computer model. There are two temperatures derived from the computer model which correspond to different approaches to modeling the optics (checkered vs. transmissive).

The SINDA model accurately predicted all thermocouple values within 5 °C except at three nodes. One of those three, the neutralizer tip, is within 6 °C. The other two, on the edge of the mask and front edge of the thruster, are within 15 °C and are shown in Figure 5 with the temperatures enclosed in a double-lined box.

The application of the model to the cold soak experiment is necessary to determine the accuracy of the thermophysical properties of the thruster (radiative and conductive) independent of the self-heating from plasma. It is difficult to determine the discrepancy of the temperatures in the mask area. This may reflect the difficulty in determining the contact resistance between the mask and the rest of the thruster.

The effect of changing the method of modeling the optics appears to be minimal in this case. Most of the temperatures changed by only a degree or two Celsius. The most drastic change in temperature was in the optics, (2-3 °C). This would indicate that modeling the surface as transmissive is sufficient for the conditions considered in the cold soak test simulation.

The NSTAR thruster has also been modeled in SINDA to predict its transient behavior. Figure 6 and 7 show a comparison between experimentally determined data on February 28, 1996 and the SINDA model with the optics modeled as transmissive surfaces.

The predicted results from SINDA agree to within 10 °C for all of the nodes except 112 (mask), 400 (neutralizer rear), 102 and 104 (plasma screen). The areas of greatest discrepancy tend to be along the plasma screen and mask. Again, this represents the difficulty in determining some of the contact resistances in the system and in modeling perforated surfaces. In Figure 6 the nodes corresponding to the plasma screen (1xx) increase in temperature from 300 to 400 minutes. This is due to an increase in the shroud temperatures. The modeled plasma screen surfaces in SINDA are more sensitive to the shroud temperatures than the actual plasma screen surfaces in the experiment. This sensitivity could be due to a difference in thermal capacitance between the modeled and the actual plasma screen surfaces and it could also be affected by the method of modeling the perforated surface.

Figure 7 shows that the agreement of temperatures in the discharge chamber area is very good. The temperatures follow within 5 °C throughout the test with the exception of the neutralizer tip (node 404). The accuracy in the discharge chamber temperatures is crucial since most of the components in the thruster of concern are on or near this surface. The model also shows that the discharge chamber is interacting with its surroundings (the shroud) as in the experiment. The energy exchange between the plasma screen and the discharge chamber is of less influence than between the shroud and the discharge chamber since the plasma screen is perforated and hence only a portion of its surface interacts with the discharge chamber, and because the emissivity of the screen (0.1) is considerably lower than that of the shroud (0.9). Thus, even though the temperatures of some outer components such as the plasma screen may be less accurate, their impact on the discharge chamber is minimal.

The next step is to examine an operating thruster. Figure 8 gives the temperatures on the NSTAR thruster when it was operating at 2.3 kW as well as the temperatures for the SINDA model for both types of optic surface representations.

As mentioned, prior initial values of self-heating were used and then adjusted to correspond to the experimental data. Those adjusted values were given in Figure 4. This method resulted in 331.5 W being applied to the thruster. After subtracting 28 W used by the neutralizer, the thruster has 303.5 W of applied heat.

Using Equation 4 where Φ_T=2274 W, Φ_N=23 W, J_B=1.75 A, J_A=0.01 A, V_P=1100 V, and U_+=12.13 A results in the applied heat being 316 W. The 303.5 W derived from the model is within 4% of the calculated value.

Although the temperatures in the discharge chamber are within 5 °C of the experimental data, the temperatures along the plasma screen and mask are off by considerably more. The discrepancy is most likely caused again by the difficulty in modeling a finely perforated surface and modeling contact resistances. The coupling between the discharge chamber and the plasma screen is through isolators which have a high number of contact points. But as shown earlier, the interaction between the discharge chamber and the environment is accurate. Therefore, this model will give an accurate prediction of the discharge chamber and its components under varying conditions. This is supported by the good agreement between the amount of self-heating energy supplied for the model and that derived analytically.

Once the model is calibrated it can be used to predict various thruster operating scenarios. One of the major concerns is knowing the direction heat is flowing out of the thruster and in particular, the amount of heat which will be directed toward a satellite in space. To estimate the directional heat fluxes, the thruster was modeled in a box maintained at a temperature of -273 °C and an emissivity of 1.0 (Figure 9). The thruster was then given the heat distribution corresponding to the 2.3 kW throttle point.

It can be seen on Figure 9 that a majority of the heat is expelled through the optics of the engine. It should be noted that the effect of the plasma is only included as the heat applied to thruster components and the power through the grids does not include the ion beam power. The sides of the thruster are uniform in power distribution with a slight

variation caused by the neutralizer with the rear having the lowest amount of heat flux. However, these values would change if an object of different temperature were on a given side. If a satellite was behind the thruster at a much higher temperature than absolute zero, the amount of heat flux in that direction would be drastically reduced.

CONCLUSIONS

The SINDA thermal model developed accurately models the NSTAR thruster discharge chamber and components to within 10 °C. There is a larger discrepancy with the temperatures on the plasma screen and mask. However, it has been shown that this has minimal effect on the temperatures of the discharge chamber and its components. There is still an accurate representation of the interaction between the inner surfaces and the environment. Changing the discharge chamber whether by a material change or a change in its layout will have the greatest effect on the thruster temperatures. The plasma screen and neutralizer were shown to be of lesser importance to the thruster thermal environment.

Limitations of the model include approximating perforated surfaces. There are no thermal tools currently available to model finely perforated surfaces. Not only is the determination of radiation view factors more difficult, calculating the conduction along the material is also more challenging. Some work has been done to further approximate the perforated surface. The methods used here included modeling the surface as having a transmissivity equal to the open area fraction, and creating a coarse checkered pattern of appropriate open area. Other limitations include modeling the contact resistance between parts. While the dominant form of heat transfer is radiation, it was shown that contact resistance plays a significant role in the connection of the discharge chamber to the plasma screen via conduction.

The self-heating terms were developed from experimental data. Further work is being done to determine these terms analytically for various cases. The model is now capable of being integrated into various environments. It can be used to investigate spacecraft integration issues and evaluate proposed design changes from a thermal impact point-of-view.

ACKNOWLEDGMENTS

This work was supported by a research grant from the NASA Lewis Research Center (NAG3-1572). Mr. James Sovey is the contract monitor.

REFERENCES

1. Gatsonis, N.A., Samanta Roy, R.I., and Hastings, D.E., "Numerical Investigation of Ion Thruster Plume BackFlow," AIAA 94-3140,30th Joint Propulsion Conference, 1994
2. Lide, D.R., "CRC Handbook of Chemistry and Physics," 71st ed.,CRCPress Inc., Boca Raton, 1990, p4-37.
3. MacRae, G.S., Zavesky, R.J., Gooder, S.T., "Structural and Thermal Response of 30 cm Diameter Ion Thruster Optics," AIAA Paper 89-2719, July 1989.
4. Wen, L., Crotty, J.D., Pawlik, E.V., "Ion Thruster Thermal Characteristics and Performance," Journal of Spacecraft and Rockets, Vol 10, No. 1, Jan. 1973, pp 35-41.
5. Oglebay, J.C., "Thermal Analytical Model of a 30 cm Engineering Model Mercury Ion Thruster," NASA Technical Memorandum, NASA TM X-71680.
6. Cullimore, B. A., Goble, R. G., Jensen, C. L., Ring, S. G., "Systems Improved Numerical Differencing Analyzer and Fluid Integrator; User's Manual," Contract NAS9-17448, March 1990, Martin Marietta Corporation, Denver, Colorado; also MCR-90-512, 1990, NASA.
7. Anderson, G. E., Garcia, D., "Thermal Radiation Analyzer System (TRASYS); User's Manual," Contract NAS9-17900, April 1988, Lockheed Engineering and Management Services Company, Houston, Texas; also JSC-22964, 1988, NASA.
8. Rawlin, V., Patterson, M., Becker, R., " Thermal Environment Testing of NSTAR Engineering Model Ion Thrusters," IEPC paper 97-051, August 1997.

TABLE I – ASSUMED PHYSICAL PROPERTIES OF ION THRUSTER MATERIALS

Material	Density g/cm^3	Capacitance cal/g °C	Conductivity W/cm °C	Emissivity
Aluminum 5052	2.68	0.20	1.37	0.14 0.30*
Pure Titanium	4.43	0.15	0.2	0.23 0.4*
Carbon Steel	7.81	0.13	0.60	Not Needed
304 Stainless	7.92	0.125	0.20	0.11 0.27* 0.5**
Molybdenum	10.19	0.20	1.20	0.2
Tantalum	16.16	0.035	0.60	0.1
Tungsten	19.38	0.035	1.50	0.1
Alumina	3.79	0.20	0.17	0.3
Kovar	8.36	0.105	0.15	0.1
6Al-4V Titanium	4.43	0.15	0.10	0.15

*Grit blasted surface
**Meshed surface

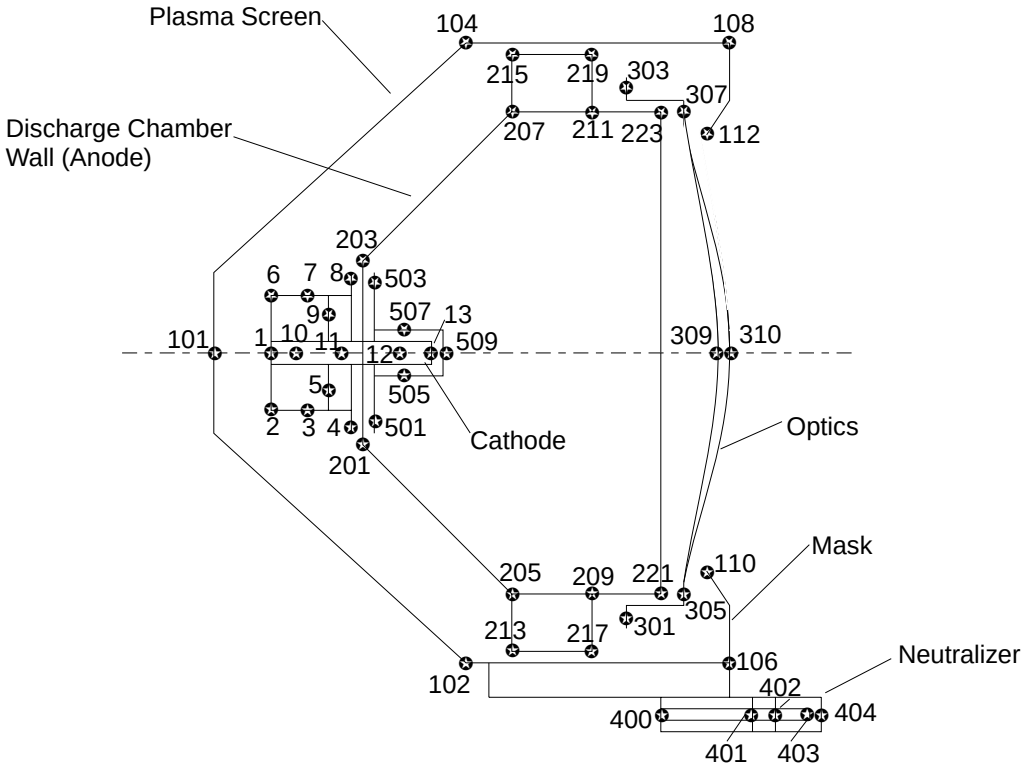

FIGURE 1 – NSTAR ION THRUSTER LAYOUT

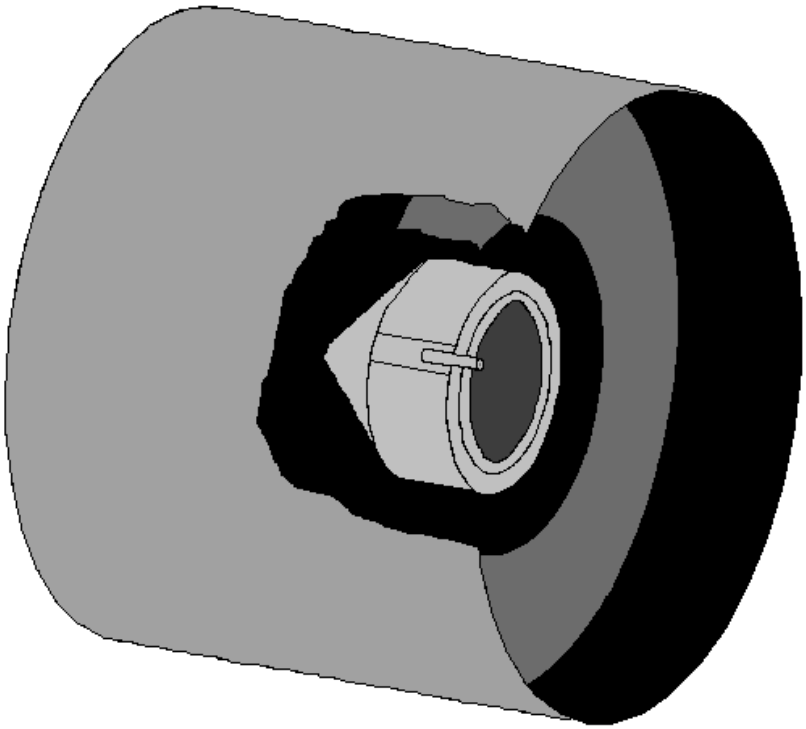

FIGURE 2 – MODEL LAYOUT OF THE NSTAR THRUSTER IN EXPERIMENTAL SHROUD

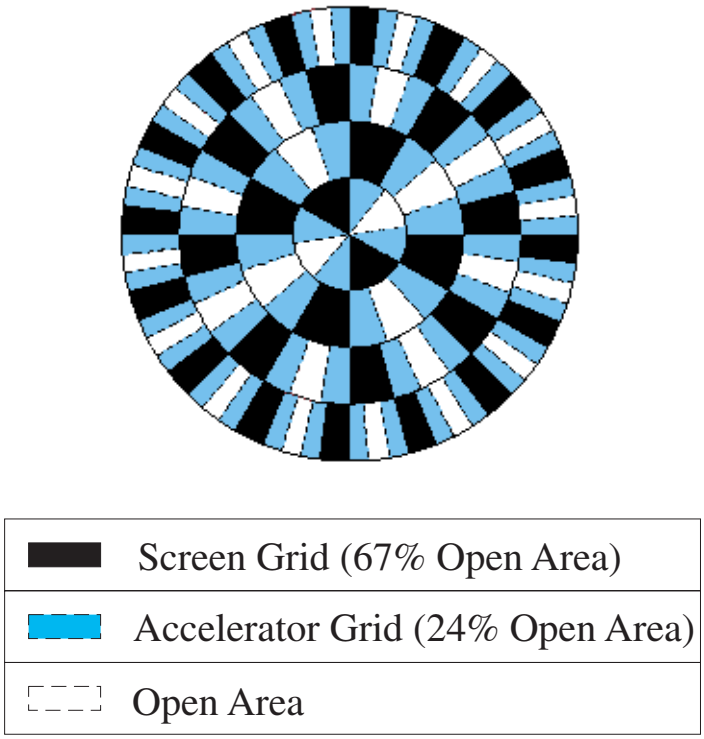

FIGURE 3 – CHECKERED PATTERN USED TO MODEL ION OPTICS IN TRASYS

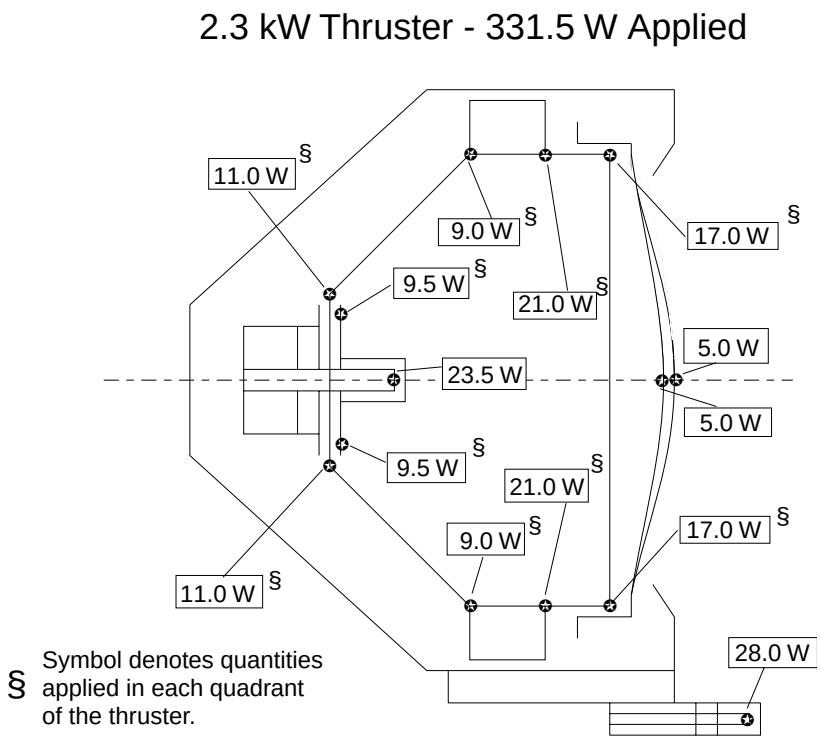

FIGURE 4 – SELF-HEATING VALUES FOR NSTAR THRUSTER

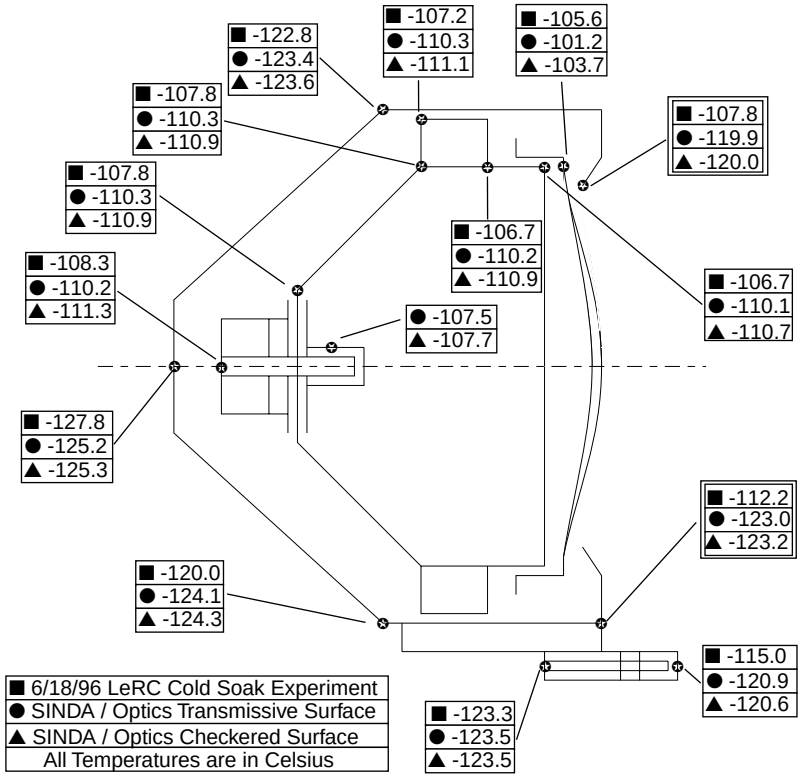

FIGURE 5 – NSTAR THRUSTER TEMPERATURES UDER COLD SOAK CONDITIONS

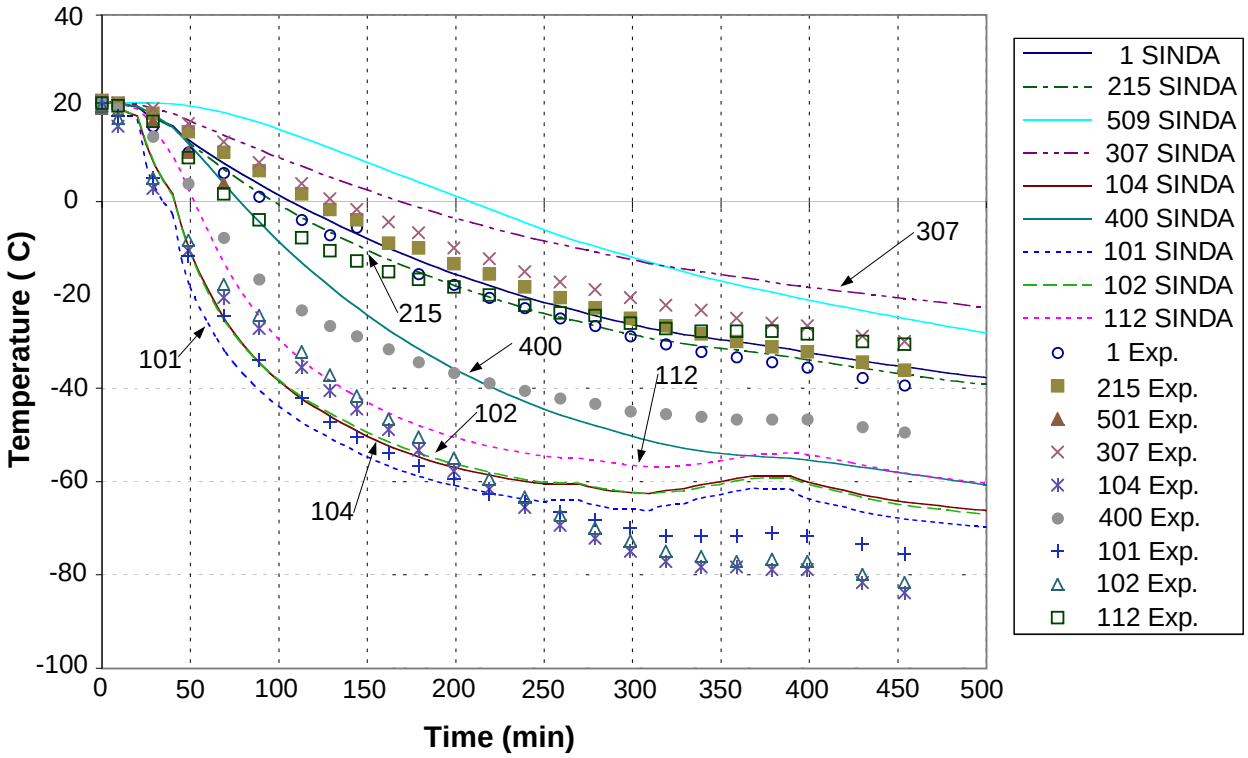

FIGURE 6 – TRANSIENT COLD SOAK EXPERIMENT (2/28/96) COMPARED TO SINDA MODEL OF NSTAR THRUSTER

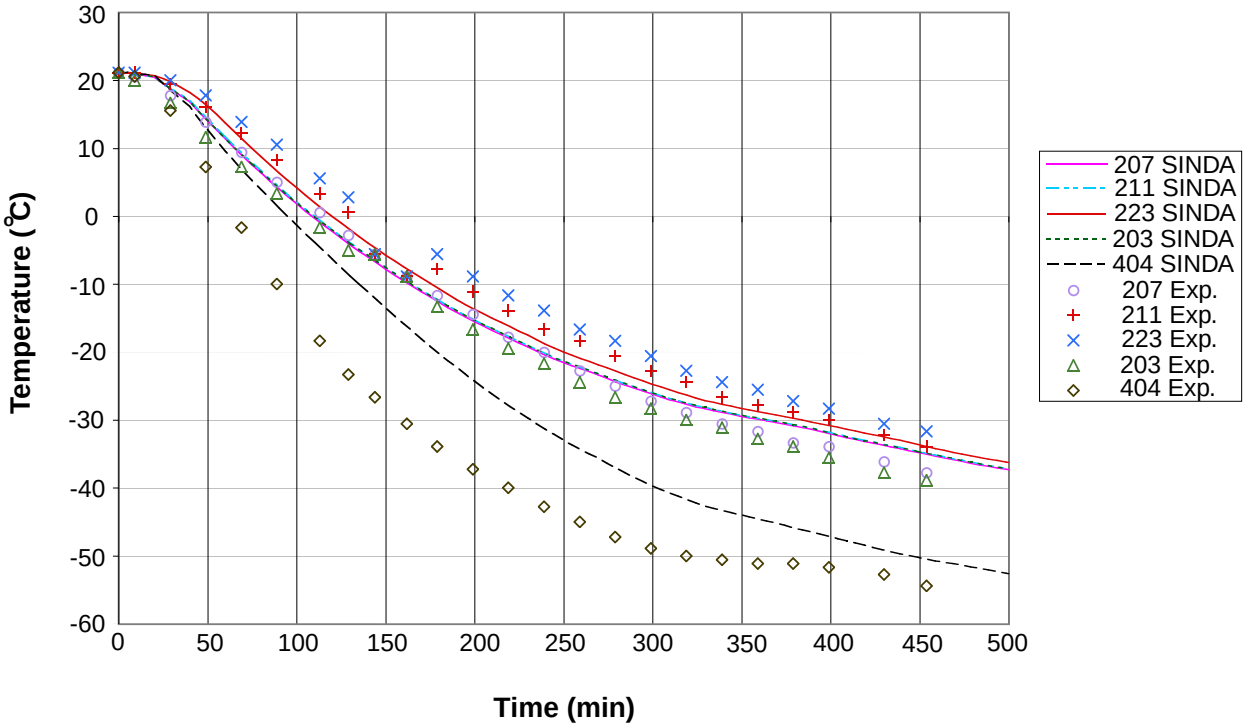

FIGURE 7 – TRANSIENT COLD SOAK EXPERIMENT (2/28/99) COMPARED TO SINDA MODEL OF NSTAR THRUSTER DISCHARGE CHAMBER

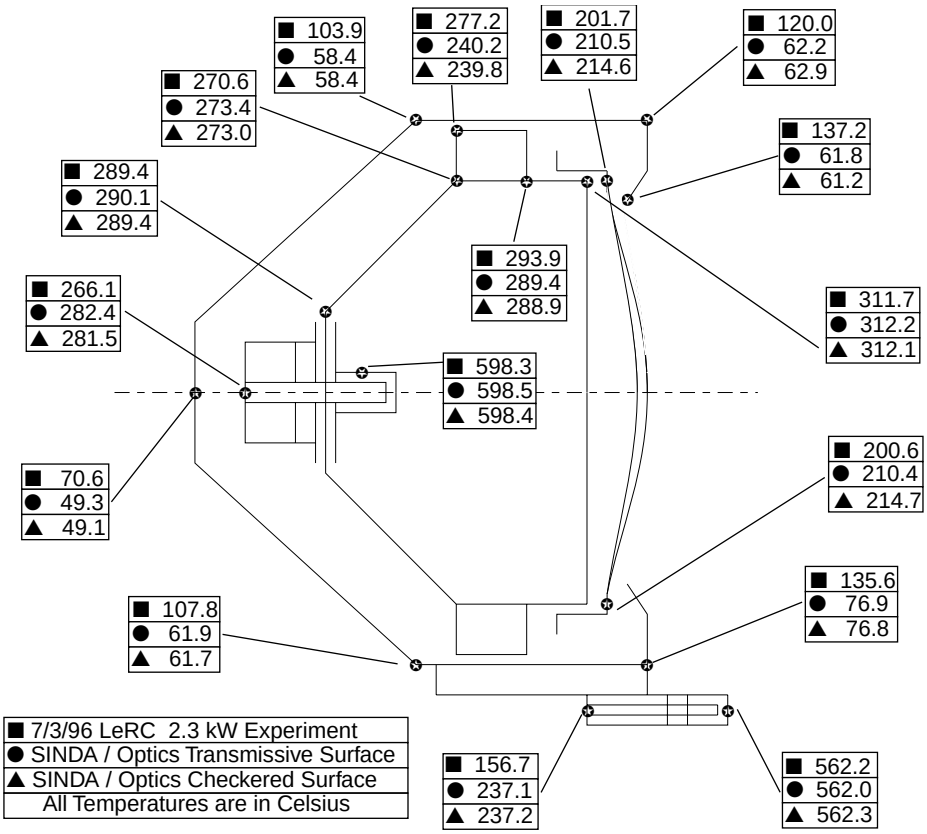

FIGURE 8 – NSTAR THRUSTER TEMPERATURES WHEN OPERATING AT 2.3 KW

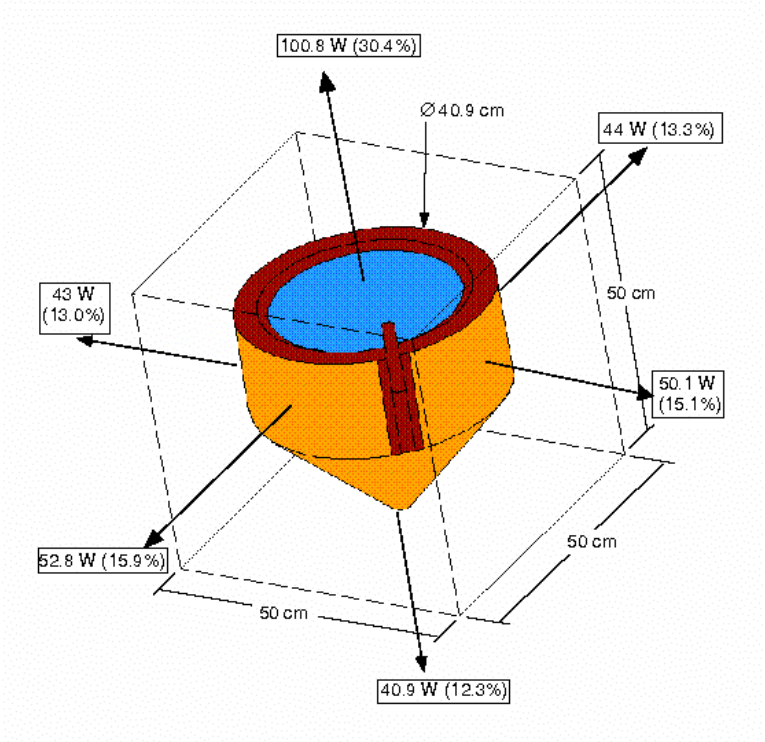

FIGURE 9 – HEAT FLUX FROM NSTAR THUSTER TO BOX WITH SPACE CONDITIONS

A SHORT HISTORY AND A BRIGHT FUTURE FOR OPTO-MECHANICAL INTERFACE

Timothy D. Wise
Opto-Mech Interface Organization
6106 Old Brompton Road
Boulder, Colorado 80301-3142
(303) 530-9342
twise@csn.net

SUMMARY

Just thirteen years ago several key aerospace companies, among them Hughes Aircraft, recognized the need to pass data between the optical and mechanical design environments more efficiently. Up to that time it was common to wheel a stack of computer printout, two feet deep, into the mechanical designer's office for the purpose of describing the clear aperture requirements along the optical train and the connecting ray-path volumes that were not to be invaded by mechanical mounts. The contents of the "stack" were page after page of ray-surface intersection coordinates that the mechanical designer had to meticulously load into his CAD model. No wonder the relations between optical and mechanical designers were strained, at best.

The change that occurred around 1985 was the development of the first few translators that automated the transfer of optical ray data. In particular, Hughes Aircraft presented a key paper at the 1986 SPIE conference in Innsbruck/Austria, which described a translator that wrote optics/ray-data from the CODE-V™ optical design program to IGES format, for input to the ANVIL™ mechanical drafting program. This touchstone accomplishment represented the first of a whole stable of translators that were created to provide fast and accurate interfaces among many CAD programs. Unfortunately, therein lay the problem with this approach: the possible permutations of interfaces among, say, a half dozen CAD software packages multiplied out to 36 individual translators, all of which have to be updated as the CAD packages are revised. And this was just within one company. The number of possible permutations becomes even more ridiculous if one attempts to share data between companies.

Therefore, it became clear as early as 1988 that a simpler approach was needed to port optical data into a variety of CAD environments. Starting in that year was an effort to create an international standard called NODIF, the Neutral Optical Data Interchange Format, which was to be implemented in the pre- and post-processors of a variety of CAD packages. By 1993 it was decided that NODIF should become part of the *much* larger STandard for the Exchange of Product model data (STEP). Then in 1995 a working group within the International Organization for Standardization (ISO) was formed to "make it so". Now 3 years later, it is appropriate that we review where we stand in this effort, demonstrate what we've accomplished so far and describe the bright future that awaits us. As we carry this out in the remainder of this paper, there may be some useful concepts for those of you working in the myriad of fields that may be tangent to optics and mechanics.

INTRODUCTION

The increasingly pervasive effect of computer software in the disciplines of optical design, engineering, and manufacturing, makes the standardization of digital exchange of data defining optical systems increasingly desirable to optical engineering practitioners from both quality and time to market perspectives. The “bottom-line” is that, while it may be easy for the optical designer to generate a two foot stack of data, no one has the time to read it, scan it, interpret it or incorporate it into a tangent design discipline. Even if paper is not the preferred, or necessary, medium of exchange, all those megabytes of information have to be processed somehow and no one has the time to write the ad-hoc software to service all of the possible engineering interfaces. The reasons for this situation are that:

- systems are becoming more complex
- performance specifications are becoming harder to meet … even unreasonable
- budgets are tighter
- systems are supposed to work right the first time, without the benefit of engineering model units

At the same, optical designs are finding their way into an ever growing constellation of applications. Did you know that it is increasingly ***less likely*** that you can:

- visit a doctor
- go to a hospital
- place a phone call
- watch a TV program
- go out onto the Internet
- drive your car
- operate your computer
- learn more about the universe
- buy food at the supermarket
- receive police and FBI protection

without the intervention of beneficial optical systems?

Most people aren't aware of this because optical systems tend to be absorbed into the products that they make possible. People know about the products and services, but not about the optical systems that enable them.[1] No, optics are ***not*** just binoculars and microscopes anymore. Optical systems now include:

- optical fibers and lasers in medicine and communications
- optically recorded and guided drives in computers
- heads-up displays and Forward Looking Infrared (FLIR) systems in both airplanes and automobiles
- optical scanners in supermarket checkout and inventory systems
- optical night vision systems used by your local police as well as the military
- and a whole new generation of sophisticated telescopes probing the cosmos

Since 1995, an international task group has worked on defining an information model for a generic optical system, guided by the technical content of the 10110 series of "optical drawing" standards, generated by ISO. Its goal is to make the integration and analysis of optical systems in the systems that ***you*** use far easier.

STATEMENT OF THE PROBLEM

The goal is to completely describe an optical system digitally so that an arbitrary designer or end-user receiving the description may make use of it unambiguously. An optical system can be specified via three categories of information:

1. context or descriptive information
2. a physical system description
3. an optical system description

The contextual information consists of various identifying information, such as the company or organization responsible for the optical system, descriptive information and/or part numbers, the designer's name and the software producing the exchange file. The physical system description of the system is comprised of data conveying the geometrical shape of the optical parts, grouping information relating to subassemblies, material specifications, geometrical tolerances on shape and location, and kinematic data such as for zoom and scanning mechanisms. Finally, the optical system description includes such information as ray paths, beam footprints or other light bundle defining information, usage specifications such as relative aperture, focal length, transverse magnification, wavelength band and image format.

With respect to these categories an optical system (product) has much in common with a mechanical product, but with some important additional characteristics peculiar to optical systems being taken into account. Examples of these characteristics include:

- the extraordinary precision required by the fabrication of optical systems, as evidenced by the error in the Hubble Space Telescope's primary ... less than the breadth of a human hair
- minuteness of some features of optical systems, such as multi-layer coatings
- the description of aspherical optical surfaces via the conic constant, which is a truly alien parameter in the world of mechanical design

APPROACH TO STANDARDIZATION

Initially work was carried out by task group #2 under task committee #172, subcommittee #1; in ISO parlance, that's "ISO TC172/SC1/TG2." It was given the charge to achieve "data transfer without optical drawings and tables." The effort has required the specification of both the data to be transferred as well as the file format, known as NODIF - the Neutral Optical Data Interchange Format. The first official working session, held October 1988 in Oberkochen FRG, has been followed by a total of eleven working sessions, prior to the last general ISO meeting in Paris in May 1993. Throughout this period our group leader was Mr. Eckart Wieder of Carl Zeiss.

In the same timeframe, a separate and much larger international standardization effort was underway to provide neutral data exchange and sharing for product data in general. Recent efforts by the task group have therefore been aimed at expressing the optical system information model outlined above using the infrastructure developed by the STandard for the Exchange of Product model data (STEP). STEP has already been used as the standard exchange protocol by a variety of industries:

- architectural
- electrical
- automotive
- shipbuilding
- aircraft
- a variety of product life cycle areas

STEP is being developed as a "follow-on" to the US Initial Graphics Exchange Standard (IGES). (You may visit their website at http://www.cme.nist.gov/sc4/) Building on experience gained with IGES, STEP standards are developed using more advanced tools and guidelines than were involved in IGES development. Shown here contributing to STEP, in addition to IGES, are:

- SET from the French standard agency, AFNOR
- the German DIN standardization institute
- ESPRIT, a European standards organization embracing the CAD language

Formal methods for information modeling, embodied in the EXPRESS language, are used to define the data to be exchanged. Implementation methods, e.g. ASCII files and DataBase Management System (DBMS) interfaces, are defined independently of the content of the information models. Standards for different applications and industries all use a common set of generic entity definitions. Finally, requirements that an implementation of a STEP standard must meet in order to conform to the standard are explicitly codified. These all contribute to the goal of exchanging and archiving product model data without loss of information throughout the entire product life cycle.

SHAPE OF A NODIF APPLICATION PROTOCOL

In the case of optical system information models, a STEP-compliant standard would consist of an Application Protocol (AP). All context information and much of the physical system description would be defined using existing or planned STEP entity definitions. Functioning as a "toolbox" to be used to support a variety of APs, the availability of this toolbox maximizes the inter-operability between data generated for optical applications and those of related mechanical CAD/CAM/CAE disciplines. It is expected that, by the end of this century, STEP will be the standard for the exchange of all design data.

The NODIF optical system description is data specific to the optical industry and contains representations of the quantities defined in the optical drawings standards, among other information, e.g., defining ray bundles. This information model will be defined using the STEP-EXPRESS language, which in turn permits a range of standard tools to be used to implement data exchange and/or sharing, such as reading and writing ASCII (American Standard Code for Information Interchange) files and database interfaces. Table I contains a sample of a NODIF entity using the syntax of the EXPRESS language for their expression.

The physical or geometric description of the mechanical aspects of a product such as an optical system have been exhaustively defined by STEP. For example, the descriptive information section would be largely represented by entities from Part 41, "Fundamentals of Product Description and Support." A number of sets of Generic Resources are being defined in the following areas: geometry and topology of products (Part 42), grouping information relating to subassemblies (Part 43, 44), material specifications (Part 45), geometrical tolerances on shape and location (Part 47), and kinematic data such as for zoom and scanning mechanisms (Part 105). In the case of geometry and topology, it became apparent to STEP developers that there were a number of major geometric subsystems such as trimmed surface modeling, faceted Boundary Representation (BREP) solid modeling, elementary BREP modeling using analytic surfaces and advanced BREP modeling using sculptured surfaces defined by B-splines, each defined using entities from Part 42, that could be reused in different application areas. These resulting information models are referred to as Application Interpreted Constructs (AICs). AICs provide a means of reusing information models that are common across many application areas.

There is a considerable "variation in bandwidth" of the physical description of an optical system that can be produced and exchanged by software. Some software may only be able to provide surface geometry and locations for the optically active surfaces in the optical system. Others can model non-optically active surfaces as well. Some optical modeling capabilities based on BREP solid modeling are beginning to become available. Thus a NODIF AP would specify several different conformance levels (one for each geometric AIC) to accommodate the different capabilities of optical software. Those who would implement the NODIF AP could support any or all of the conformance levels to be in compliance with the standard.

Finally, information specific to optical systems would be specified. Here the information content of ISO 10110 (as opposed to the drawing indications) would be expressed in computer sensible form. The information concerning material specifications, surface attributes and tolerances and the surface shapes peculiar to the optical industry would be mapped onto the STEP Generic Resources to produce a NODIF AP.

Optical information outside the scope of ISO 10110 would also be defined and standardized as a part of the NODIF AP. This would include optical system usage specifications such as relative aperture, focal length, transverse magnification, wavelength band and image format. It would also include information significant to packaging optical systems such as ray bundle definitions. It is possible that different conformance levels for the NODIF AP could be introduced for this status of an International Standard (IS). The STEP standards themselves, 10 years after they were initiated, have recently reached IS status and commercial tools and implementations are being used in production environments. Continued development of a NODIF AP is thus timely.

THE BRIGHT FUTURE OF OPTICAL STANDARDIZATION

Standardization in the U.S. is a creature of contrasts, in some areas energetic and in others lethargic. On the energetic side, the STEP effort is heavily supported by major U.S. companies through the IGES-PDES Organization (IPO). (You may visit their website at http://pdesinc.scra.org/) Dues for major corporations range from $50K to $100K per year with 1 to 2 man years of employee support in addition. Those are pretty scary numbers for companies of modest size, but there is a way for modestly sized companies, or individuals, to be involved as well. U.S. PRO is the parent organization that provides management and direction for IPO, for the U.S. Technical Advisory Group (TAG) and for the National IGES Users Group (NIUG). Depending on the size of your company, dues range from $1K to $5K yearly. For this sum you will be kept informed as to STEP's progress and you will be involved in the work! (You may visit their website at https://www.uspro.org/)

On the lethargic side, wherever there is no involvement in standardization, it becomes poorly understood and even becomes a source of fear. The U.S. optical industry had been on the verge of letting the standards committees of OSA and SPIE slip into oblivion. This would have been a sad event for the U.S. because future advanced technology will be described and transmitted via standard protocols. These standard descriptions of optical systems will become a source of new technology, from which the U.S. cannot afford to be cut off. The response of both OSA and SPIE to this threatening situation was to propose the formation of a joint U.S. standards committee that would represent the following trade and professional organizations:

- APOMA
- COM
- IEEE/LEOS
- LEOMA
- OIDA
- OSA
- NAPM
- SPIE

The resulting organization is the Optics and Electro-Optics Standards Council (OEOSC), which is funded by its member organizations, including individual companies, trade associations and professional societies. OEOSC supports those involved in standards work, sets priorities and provides communication within the optics community. Dues to the OEOSC depend on the size of the member organization, but are only $100 per year for a small company and up to $5K for a large company. (You may visit their website at http://www.optstd.org/)

To get an idea as to the future of NODIF, one may look at some of the accomplishments up to the present. First, there are two decisions by ISO leadership that support the continuing development of NODIF:

1. The original optical task group spawning NODIF (ISO TC172/SC1/ TG2) has been converted to full working group status, ISO TC172/SC1/ WG4. (You may visit our website at http://optics.org/optical_standards/wg4.html/)
2. A Class A liaison between (ISO TC172/SC1/ WG4) and the technical group for STEP product modeling and analysis (ISO TC184/SC4/WG3/T9) was approved at the October 1991 Tokyo Plenary.

Second, and even more important, is the evidence that both the IGES protocol as well as STEP APs that are a precursor of NODIF are already being incorporated into commercial opto-mechanical CAD software. So far these software packages include:

- ASAP ™ from Breault Research Organization (IGES) -- http://www.breault.com/
- LightTools ™ from Optics Research Organization (IGES and STEP) -- http://www.opticalres.com/
- SOLSTIS/SPEOS ™ from Optis (IGES and STEP) -- http://www.optis.fr/
- TracePRO ™ from Lambda Research (IGES and STEP) -- http://www.lambdares.com/
- and others to be added to the growing list

Third, to actually see STEP passing data through the opto-mechanical interface is inspiring. If only I could slip a copy of LightTools ™, for example, to you over the web and show you what is now possible! However, failing that, please take a look at Figure 1 which depicts a simple 2D profile of what is really a full, 3D solid model residing in LightTools ™. This model is a Double-Gauss lens design, like the 50 mm lens in your favorite SLR camera. For demonstration purposes only, I have added a simple aluminum can around the lens elements, traced rays through it to show that they are well-focused and then written this design out to a file in STEP AP214 format. Figure 2 shows the results of reading this design back in from the STEP file and retracing the rays. Now there is good news and bad news about this round trip. The bad news is that the rays no longer focus because, without the NODIF protocol in place, the lens prescription data are lost: no unique refractive indices for the glasses and inadequate dimensional precision for most lens designs. The really good news is that:

- both the optical and mechanical structure were faithfully retrieved
- the structure could be amazingly complicated and the retrieval would be just as successful, like the LightTools model of a SLR camera
- Phase I of NODIF will fill in the missing information

Lastly, the really bright part of the future lies with you, because, as the current convener of TC172/SC1/WG4 and chairman of the OEOSC, I solicit *your* involvement, as part of our highly diverse technical community, in the process that lies ahead. We need your participation and support, at whatever level you can provide, for the remainder of this decade. Please share your ideas as to how we can maintain good communication with you, so that NODIF will become a welcome new tool with which we can all do good work.

ACKNOWLEDGEMENTS

The author gratefully acknowledges the leadership of Mr. Eckart Wieder, who was with Carl Zeiss in the years between 1988 and 1993 when our task group was finding its place in the world of standardization, and who is now a member of our working group representing Germany. Also to be thanked are the other members of our working group who are not only hard-working and intelligent, but are often our gracious hosts:

- Dr. Mikhail Gan of the S.I.Vavilov State Optical Institute, Russia
- Mr. Michael Hayford of Optical Research Associates, US
- Mrs. Prudence M. J. H. Wormell of Imperial College, UK
- Dr. Kimiaki Yamamoto of Olympus, Japan

REFERENCES

1. “Harnessing Light”, Optical Science and Engineering for the 21st Century, Committee on Optical Science and Engineering, Board on Physics and Astronomy, National Materials Advisory Board, Commission on Physical Sciences, Mathematics, and Applications, Commission on Engineering and Technical Systems, National Research Council, National Academy Press, Washington, D.C. 1998

Table I. NODIF Definition of a Conic Surface Using EXPRESS

conic_optical_surface -> CONI
The conic surface object is a surface form parameterized by the radius and the conic constant. The sign of the radius is such that: r > 0 convex surface r < 0 concave surface r = 0 plano surface
The value of the conic constant, k, generates the following surface shapes: k > 0 oblate ellipse k = 0 circle -1 < k < 0 prolate ellipse k = -1 parabola k < -1 hyperbola
EXPRESS Specification: *) ENTITY conic_optical_surface SUBTYPE OF (spherical_optical_surface); conic_constant : REAL; END_ENTITY; (*
Attribute Definitions: conic_constant: conic constant, k.

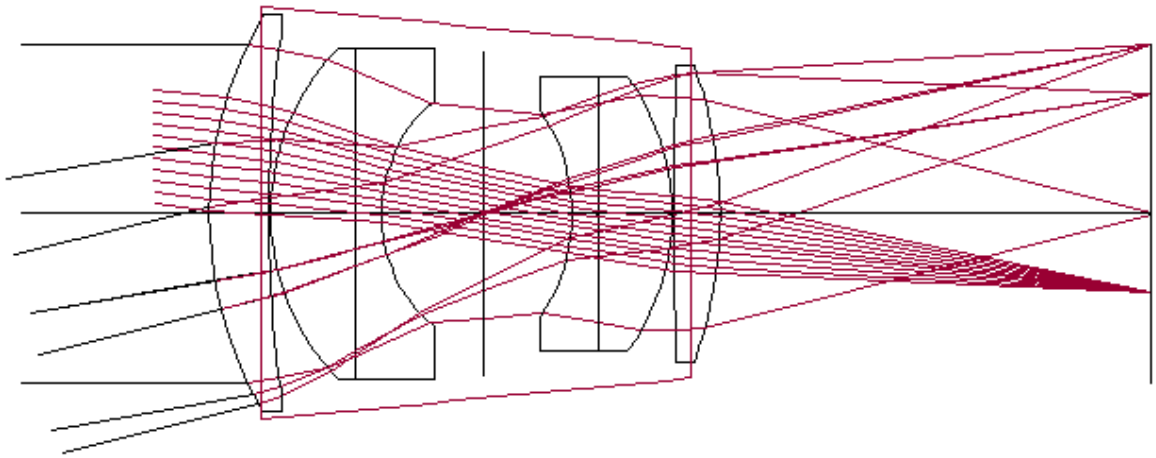

Figure 1 Mounted Double-Gauss lens in LightTools ™

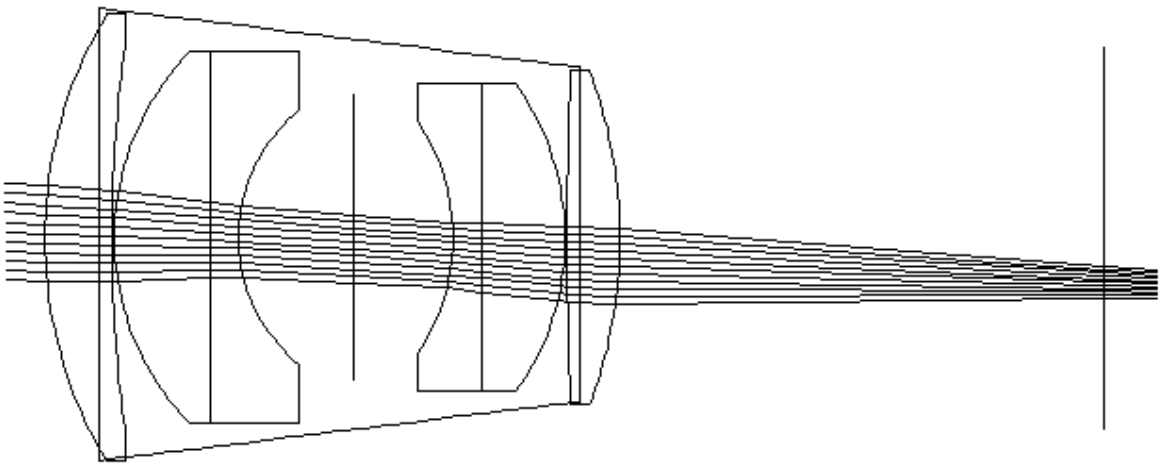

Figure 2 Mounted Double-Gauss lens after being read back into LightTools ™ from a STEP file

REPORT DOCUMENTATION PAGE

Form Approved
OMB No. 0704-0188

Public reporting burden for this collection of information is estimated to average 1 hour per response, including the time for reviewing instructions, searching existing data sources, gathering and maintaining the data needed, and completing and reviewing the collection of information. Send comments regarding this burden estimate or any other aspect of this collection of information, including suggestions for reducing this burden, to Washington Headquarters Services, Directorate for Information Operations and Reports, 1215 Jefferson Davis Highway, Suite 1204, Arlington, VA 22202-4302, and to the Office of Management and Budget, Paperwork Reduction Project (0704-0188), Washington, DC 20503.

1. AGENCY USE ONLY (*Leave blank*)

2. REPORT DATE
November 1999

3. REPORT TYPE AND DATES COVERED
Conference Publication

4. TITLE AND SUBTITLE
Ninth Thermal and Fluids Analysis Workshop Proceedings

5. FUNDING NUMBERS
WU–940–30–08–21

6. AUTHOR(S)
Barbara Sakowski, compiler

7. PERFORMING ORGANIZATION NAME(S) AND ADDRESS(ES)
National Aeronautics and Space Administration
John H. Glenn Research Center at Lewis Field
Cleveland, Ohio 44135–3191

8. PERFORMING ORGANIZATION REPORT NUMBER
E–11411

9. SPONSORING/MONITORING AGENCY NAME(S) AND ADDRESS(ES)
National Aeronautics and Space Administration
Washington, DC 20546–0001

10. SPONSORING/MONITORING AGENCY REPORT NUMBER
NASA CP—1999-208695

11. SUPPLEMENTARY NOTES
Proceedings of a workshop held at NASA Lewis Research Center, August 31—September 4, 1998. Responsible person, Barbara Sakowski, organization code 7730, (216) 433–8725.

12a. DISTRIBUTION/AVAILABILITY STATEMENT
Unclassified - Unlimited
Subject Category: 34 Distribution: Nonstandard

This publication is available from the NASA Center for AeroSpace Information, (301) 621–0390.

12b. DISTRIBUTION CODE

13. ABSTRACT ***(Maximum 200 words)***

The Ninth Thermal and Fluids Analysis Workshop (TFAWS 98) was held at the Ohio Aerospace Institute in Cleveland, Ohio from August 31 to September 4, 1998. The theme for the hands-on training workshop and conference was "Integrating Computational Fluid Dynamics and Heat Transfer into the Design Process." Highlights of the workshop (in addition to the papers published herein) included an address by the NASA Chief Engineer, Dr. Daniel Mulville; a CFD short course by Dr. John D. Anderson of the University of Maryland; and a short course by Dr. Robert Cochran of Sandia National Laboratories. In addition, lectures and hands-on training were offered in the use of several cutting-edge engineering design- and analysis-oriented CFD and Heat Transfer tools. The workshop resulted in international participation of over 125 persons representing aerospace and automotive industries, academia, software providers, government agencies, and private corporations. The papers published herein address issues and solutions related to the integration of computational fluid dynamics and heat transfer into the engineering design process. Although the primary focus is aerospace, the topics and ideas presented are applicable to many other areas where these and other disciplines are interdependent.

14. SUBJECT TERMS
Computational fluid dynamics; CFD; Heat transfer; Thermal analysis; Collaborative engineering; TFAWS; STEP; Computational heat transfer; SINDA

15. NUMBER OF PAGES
278

16. PRICE CODE
A13

17. SECURITY CLASSIFICATION OF REPORT
Unclassified

18. SECURITY CLASSIFICATION OF THIS PAGE
Unclassified

19. SECURITY CLASSIFICATION OF ABSTRACT
Unclassified

20. LIMITATION OF ABSTRACT